UNIVERSITY OF CALIFORNIA
SANTA CRUZ

RUPTURE CHARACTERISTICS OF LARGE EARTHQUAKES

A dissertation submitted in partial satisfaction
of the requirements for the degree of

DOCTOR OF PHILOSOPHY

in

EARTH SCIENCES with an emphasis in GEOPHYSICS

by

Lingling Ye

September 2015

The Dissertation of Lingling Ye is approved:

_____
Professor Thorne Lay, chair

_____
Professor Emily Brodsky

_____
Professor Quentin Williams

_____
Tyrus Miller
Vice Provost and Dean of Graduate Studies

Contents

List of Figures

List of Tables

Rupture Characteristics of Large Earthquakes

Lingling Ye

Abstract

The occurrence of many large and/or destructive global earthquakes over the past ten years has provided unprecedented seismic, geodetic, and tsunami recordings that reveal complex rupture processes advancing our understanding of earthquake physics. This thesis research has focused on seismological analysis of recent large earthquakes to extract observational insights that address two fundamental questions, "*how do great earthquake rupture?*", and "*what controls large earthquakes?*". We approach these two questions by providing an improved seismological understanding of large earthquake rupture processes, exploring the variation of kinematic source parameters, and placing the ruptures into the context of tectonic plate motions that drive the deformation.

Given the great diversity of earthquakes, various seismic tools have been explored to give a better robust characterization of large earthquake ruptures. It includes W-phase point source inversion, back projection of seismic array data to map the space-time distribution of high-frequency coherent seismic radiation, determination of broadband source spectra and radiated energy, waveform inversion for co-seismic finite-source slip distribution, and forward modeling of and joint inversion with tsunami and GPS data. By applying these methods, I have studied large events located in different areas, including 1) megathrusts (subduction zone plate boundaries) along the Japan trench, Middle American Trench, and globally; 2) the

large transform fault boundary near Scotia-Sea-Antarctic plate boundary, and 3) intraplate events in subducted slabs near the Philippine trench, at intermediate depth (70-300 km) beneath Rat Island earthquake and in the mantle transition zone (300-700 km) beneath Sea of Okhotsk and Ogasawara Islands. The controlling parameters for earthquake-related hazards (e.g. tsunami and strong ground shaking) and earthquake physical mechanisms (e.g. brittle failure, thermal weakening process, stress transfer) have been investigated with an emphasis on the frequency-dependence seismic radiation.

To

Professor Thorne Lay

and

Professor Hiroo Kanamori.

Acknowledgements

First, I owe thanks to Thorne Lay and Hiroo Kanamori for shaping the line of study that I have pursed in this thesis. They provided lots of thorough and in-depth discussion on the source modeling and diverse source parameters with great patience, which facilitated a greater understanding of the problems. My sincere thanks to them for making our research work into a very pleasant process, which prompts me to pursue a long-term career in seismology.

I also thank many collaborators who provided me their program codes, data and expertise on research in this thesis. Keith Koper shared unselfishly his back-projection code with a great training and discussion on several large earthquakes. I thank Luis Rivera for calculating the near-field Green's Function and providing his code on W-phase and stress drop calculation. Robert Smalley and Jeffrey T. Freymueller provided their recordings and expertise on geodetic observations for the 2013 Scotia and 2014 Rat Islands earthquakes respectively. Zhongwen Zhan provided his subevent analysis on the 2015 Bonin deep earthquake.

I thank many people at UC Santa Cruz, including teachers, students and staff, who have enriched my Ph. D. study beyond this thesis. To Emily Brodsky I owe special thanks for extending my view to other earthquake-related topics, and providing extensive guidance in research career development. Quentin Williams provided lots of interesting discussion on the deep earth process. Ru-Shan Wu provided extensive guidance on the inversion theory. Xiao-bie Xie, Yingcai Zheng and Yu Geng shared several numerical codes to calculate synthetic seismogram.

Chapter 1

Introduction

The occurrence of many large and/or destructive global earthquakes over the past ten years has provided unprecedented seismic, geodetic, and tsunami recordings that reveal complex rupture processes advancing our understanding of earthquake physics [*Kanamori*, 2014; *Lay*, 2015]. Many of the events have had surprising attributes, which cautions us against placing high confidence in conceptual models that had developed from previous limited information.

Recognizing the great diversity of earthquakes, we have developed expertise in a variety of seismological tools to quantify the rupture process of major and great earthquakes. By inverting the very-long period, ~100-1000 s, W-phase signals [*Kanamori*, 1993; *Kanamori and Rivera*, 2008], we can obtain robust seismic moment, moment tensor with two possible fault planes, source duration (centroid time shift), and centroid source depth. To constrain the rupture dimension and directivity effects, we have applied two strategies: 1) directivity analysis by aligning the body-wave or surface-wave seismic recordings with the directivity parameter ($\Gamma = -p \cos\phi$, where p and ϕ are the ray parameter and station azimuth relative to assumed rupture direction, respectively); and 2) back projection of seismic array data to map the space-time distribution of high-frequency, usually 0.5-2 Hz, coherent seismic radiation. In addition, we have obtained additional constraints on effective rupture area, slip, and fault orientation by collaborating with tsunami modeling experts for great shallow earthquakes [*Lay* et al., 2013a; 2013b; *Bai* et al., 2014]. With this information, we set-up finite-fault representations and invert teleseismic body waves in the frequency band 0.005-0.9 Hz, for co-seismic slip distribution linearly with spatial smoothing and moment penalty, modified from *Kikuchi and Kanamori* [1991]. For some shallow great earthquakes, there are regional static and high-rate (hr) GPS data, and we have explored the constraints on rupture process from these observations by forward modeling using teleseismic-based slip models, or joint inversion with

teleseismic data. In addition, we have analyzed the source spectrum for frequency-dependence seismic radiation and determining the total seismic radiated energy. Combination of these methods enables robust characterization of large earthquake ruptures. By applying these methods, I have explored diverse aspects of **earthquake cycles** and **seismotectonics**, **earthquake interaction**, **earthquake physical mechanism**, and **sources of hazard**, as presented in Chapters 2-11 subdivided in parts I, II, and III according to the tectonic environments where earthquakes occurred (Figure 1.1).

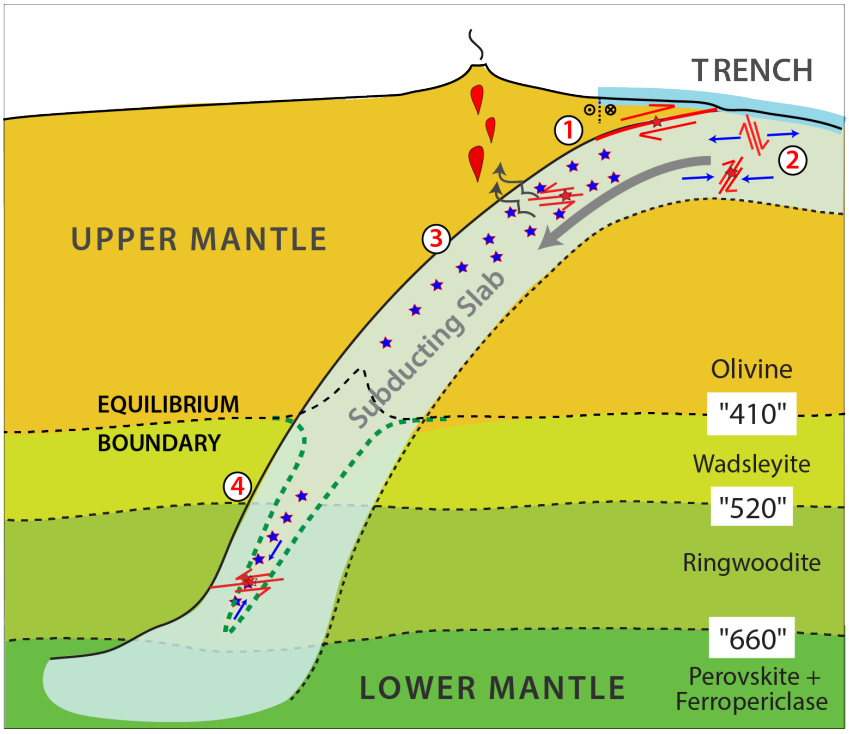

Figure 1.1 Schematic figure showing subducting slab related earthquakes failures: interplate earthquakes occur along the subduction zone megathrust at plate boundaries ①, and intra-slab earthquakes including normal faulting occur in the shallow outer-rise ②, deeper compressional near-trench failure ②, and earthquakes at intermediate depth ③ and in the mantle transition zone ④.

Motivated by the 2011 M_W 9 Tohoku earthquake, I began research on the variable frictional properties along megathrusts (① in Figure 1.1). By studying frequency-dependent seismic radiation for earthquakes along the Japan Trench [Chapter 3] and Middle American Trench [Chapter 4], I found that distinct regions along megathrust are responsible for

producing strong ground shaking (deeper portion) and devastating tsunamis (shallower portion). Isolation of the earthquake source spectra using an empirical Green's function method for regional observations further demonstrated that both depth-varying rupture properties and path attenuation variations contribute to observed ground shaking and hazard patterns [Chapter 3]. Building on these regional studies, we conducted a uniform finite-fault inversion and source spectral analysis of 114 major and great ($M_W \geq 7$) megathrust earthquakes since 1990, providing the most comprehensive evaluation of megathrust energy release and rupture process for investigation of large earthquake mechanics and hazards. We performed an extensive evaluation on the source scaling relationships [Chapter 5] and frictional heterogeneity along megathrust [Chapter 6] from the systematically determined rupture duration, static stress drop, spectral shape, and radiated energy, and derived apparent stress, radiation efficiency and fracture energy. A step-change or rapidly increasing trend with source depth of the moment-scale duration and apparent stress from this data set may be associated with depth-evolving properties of sediments at shallow < ~15 km depth, and the progressive tends of short-period seismic radiation with depth may be related with gradually increasing percentage of isolated, small-scaled asperities [Chapter 6].

The variation of rupture along-strike in subduction zones is also enigmatic, for example, why the huge rupture from the 2011 M_W 9 Tohoku earthquake produced very little slip in the offshore-Sanriku region interested me. By investigating the seismicity, repeating earthquake behavior and geodetic deformation, I argued that low "seismic" coupling with significant stable sliding exists along this region, producing a strain energy deficit that limited the northward down-dip extent of the 2011 M9 rupture [Chapter 2]. Study on slip distributions and seismic radiation from the large regional thrust events indicate strong variations along the strike of Middle America Trench: relatively strong seismic coupling near Costa Rica; patchy zones of strong seismic coupling in the shallowest megathrust region along Nicaragua and El Salvador; and small deeper patchy zones of strong seismic coupling near Guatemala, which can be reconciled with the geodetic observations [Chapter 4].

Enhanced high-frequency seismic radiation from large earthquakes within the subducted oceanic slab (② and ③ in Figure 1.1) has also presented significant seismic hazard by causing strong ground shaking. This intra-slab faulting, although less well-recognized due to their infrequent occurrence, can be very damaging for populated regions above subduction zones such as Japan, Taiwan, Chile, Peru, and Indonesia. For example, the most deadly event in Chile was the 1939 Ms 7.8 earthquake, with ~28,000 fatalities. Our studies on the 2012 M_W 7.6 below-trench compressional Philippine earthquake [Chapter 7] and the large intermediate-depth earthquake beneath Rat Islands (M_W 7.9; depth 100 km) [Chapter 8] show that there are systematically large moment-scaled radiated energy, high stress drop and relatively compact slip distributions for these earthquakes.

The spatial and temporal variation of interplate megathrust events and seaward intraplate events, including shallow tensional (normal-faulting) events and deep compressional (thrusting) events, in subduction zones has been studied for indication of elastic interactions that may be useful for evaluating seismic coupling and earthquake hazard. Figure 1.2a shows a schematic model that considers elastic plate bending and temporally changing stress for coupled and uncoupled subduction zones [*Christensen and Ruff*, 1988]. Based on this, occurrence of a large near trench thrust earthquake is of interest as a possible indicator of strong interplate coupling and compressional strain accumulation prior to a future interplate rupture. Our study on the 2012 M_W 7.6 Philippine earthquake shows that this event is possibly as a result of horizontal compressional stress accumulation offshore of a locked megathrust [Chapter 7]. In addition, aftershock mechanisms provide clues about stress transfer in subduction zones. To identify the possible activated fault planes, we have developed a waveform correlation method to classify the possible focal mechanism type for small aftershocks with very few recordings. Coulomb stress calculations show that static stress perturbations may contribute to the mix of intraplate and interplate aftershock faulting offshore of the Philippines [Chapter 7]. We also used this correlation procedure in studies of aftershocks along the Middle American trench [Chapter 4] and along the Haida Gwaii thrust event adjacent to the Queen Charlotte Fault [*Lay et al.*, 2013a].

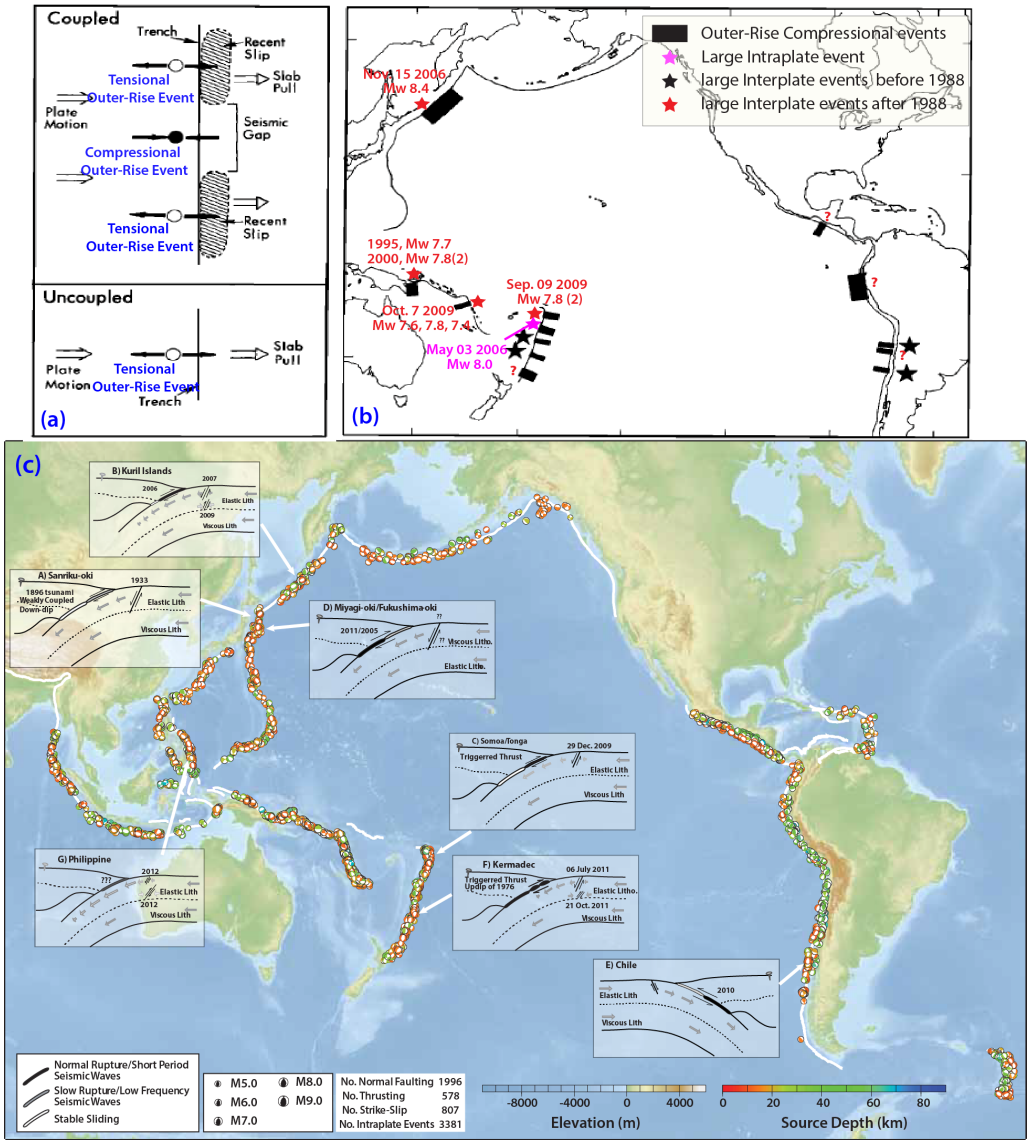

Figure 1.2 (a) Schematic representation of the model for coupled and uncoupled subduction zones by Christensen and Ruff [1988]. Solid and open circles indicate compressional and tensional outer-rise events with arrows depicting the orientation of the principle stress axes, respectively. (b) Distribution of compressional outer-rise events (heavy bars) with adjacent interplate events (stars) in circum-Pacific subduction zones. Black colors indicate the results from *Christensen and Ruff* [1988] and red stars indicate large interplate events that occurred after 1988 in regions where they had identified outer rise compression. The 2006 Tonga event is not a megthrust event, but is a large intraplate compressional event about 60 km deep, so the outer rise compression correctly indicated strong compression around the megathrust. The 2009 events were triggered megathrust events after an outer rise normal faulting event, but the outer rise compression again correctly indicated the potential for such thrusting. (c) Distribution of all near-trench intraplate earthquakes identified in the GCMT catalog from 1976-2012. Insets show schematic cross-sections of A) Sanriku-oki, B) Kuril, C) Samoa, D) Miyagi-oki, E) Maule, F) Kermadec and G) Philippine subduction zones where large outer-rise earthquakes appear to relate to megathrust earthquakes.

While not usually as destructive as large shallow earthquakes, deep-focus (400-700km) events (④ in Figure 1.1) provide important constraints on our understanding of earthquake physics. Distinguishing between the possible mechanisms for deep earthquake is difficult due to challenges in resolving the fault dimensions and lack of knowledge of the deep slab environment. To quantify the rupture properties of deep earthquake we have applied radiation efficiency, the ratio between seismic radiated energy and total available strain energy from a rupture, as a criterion for differentiating dissipative rupture processes (such as a melting process) from brittle failures enriched in high-frequency seismic radiation. Our work on the 2013 Okhotsk deep earthquake (M_W 8.3; 610 km) shows that this largest deep event ever recorded behaved like a shallow, brittle failure earthquake [Chapter 9], whereas the second largest deep earthquake, the 1994 M_W 8.2 Bolivia earthquake (640 km) involved a distinct dissipative rupture process. By analyzing a huge global seismic dataset for the 2015 isolated deep Bonin earthquake (M_W 7.9; 680 km), we found that it involves a moderately dissipative rupture process intermediate to that of the two largest deep earthquakes [Chapter 10]. The isolated occurrence of the event suggests that localized stress concentration associated with the pronounced deformation of the Izu-Bonin slab likely played a role in generating this major earthquake. These studies, along with previous work, raise questions about the fundamental behavior responsible for diversity of deep ruptures.

In additional to these subducting slab related earthquakes, I have expanded my studies to strike-slip earthquakes located on transform fault boundaries. By combining the seismic data and GPS recordings for two large strike-slip earthquakes in 2003 and 2013 along the south Scotia Ridge transform boundary, we found two unusual and surprising aspects: the shallow dip of the strike-slip faulting suggests reactivation of a thrust fault which may have formed due to compression from past convergence or continental fragmentation, and a complementary pattern of fault slip of the two events, with rupture during 2013 straddling slip in the 2003 failure zone [Chapter 11].

PART I MEGATHRUST EARTHQUAKE

Chapter 2

The Sanriku-Oki Low Seismicity Region on the Northern Margin of the Great 2011 Tohoku-Oki Earthquake Rupture

This chapter has been published as:
Ye, L., T. Lay and H. Kanamori (2012), "The Sanriku-Oki Low Seismicity Region on the Northern Margin of the Great 2011 Tohoku-Oki Earthquake Rupture", *J. Geophys. Res.*, Vol. 117, B02305, 17.

Abstract. We examine a region of the megathrust fault offshore of northeastern Honshu (38.75°-40.25°N, 141.5°-143.25°E) that we designate as the Sanriku-Oki Low Seismicity Region (SLSR). The SLSR, located near the northern termination of the 2011 Tohoku-Oki (M_w 9.0) rupture, lacks historical great earthquake ruptures, and has relatively low levels of moderate size ($M_j \geq 5.0$) earthquakes with subregions having many small events (M_j 2.5-5.0) in the JMA-unified catalog. The SLSR is located down-dip along the megathrust from the rupture zone of the great 1896 Sanriku tsunami earthquake and the great 1933 Sanriku outer trench slope normal faulting event; weak seismic coupling of the SLSR had been deduced based on occurrence of those unusual events. Relatively low slip deficit on the SLSR megathrust was estimated based on GPS deformations prior to 2011 compared to adjacent areas with strong inferred locking to the south and north. The southern portion of the SLSR appears to have had at most modest levels (< 5 m) of coseismic slip during the 2011 event. Some thrust-faulting aftershocks did occur in the SLSR, primarily at depths near 40 km where there had previously been small (M_j ~ 5.0) repeating earthquakes (e.g., the Kamaishi-repeater). An M_w ~7.4 underthrusting aftershock occurred in the northeastern edge

of the SLSR ~22.5 minutes after the great 2011 event. Postseismic convergence along the megathrust is peaked in the SLSR. The collective observations indicate that the SLSR is primarily undergoing quasi-static aseismic convergence, and the lack of regional strain accumulation likely delimited the northern extent of the great 2011 rupture as well as the down-dip extent of the 1896 rupture. The triggering of the M_w 7.4 aftershock and heightened activity in the down-dip repeater regions suggest that high postseismic strain rates drove the region to have ephemerally increased seismic failure, but it appears unlikely that a great earthquake will nucleate or rupture through this region. Similar properties may exist on the megathrust near the southern end of the 2011 rupture.

2.1 Introduction

The subduction zone megathrust fault offshore of northeastern Honshu, Japan, accommodates ~8-10 cm/yr of plate convergence with spatially varying slip behavior, ranging from quasi-static slip to slowly rupturing tsunami earthquakes to 60+ m coseismic displacements. Anticipating the nature of slip in regions of the megathrust for which we have limited seismological history has been difficult given the regional variability, and it is important to understand the distribution and nature of the diverse fault behavior. The Sanriku-Oki region of the plate boundary fault (Figure 2.1) (38.75°-40.25°N, 141.5°-143.25°E) has been characterized as having low seismic coupling and very uncertain potential for hosting a large earthquake due to a lack of large historic earthquake ruptures (Figure 2.1b; Kanamori, 1972, 1977; Earthquake Research Committee hereinafter, ERC, 1998;

Yamanaka and Kikuchi, 2004), low levels of moderate size earthquakes (Figure 2.1a) and the relatively low regional slip deficit inferred from several years of GPS observations (e.g., Mazzotti et al., 2000; Nishimura et al., 2000; Kawasaki et al., 2001; Suwa et al., 2006; Hashimoto et al., 2009; Loveless and Meade, 2010).

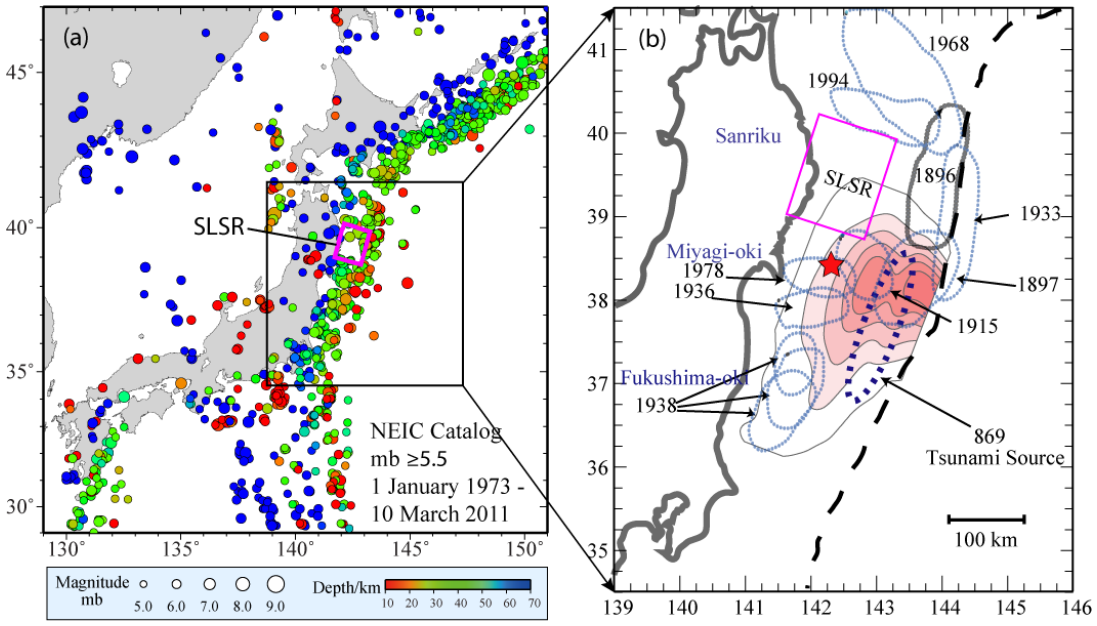

Figure 2.1 (a) Seismicity from the NEIC catalog around Japan from 1973-2011 prior to the 11 March 2011 Tohoku-Oki earthquake with $m_b \geq 5.5$. Hypocentral depths are indicated by the color scale, and symbol size increases with seismic magnitude. The magenta rectangular region indicates the SLSR. The black rectangle indicates the zoomed-in region in (b). (b) Map showing the location of the Sanriku Low Seismicity Region (SLSR), and schematic rupture zone of historic large earthquakes along the northeast Honshu coast (ERC, 1998) with blue dotted ellipsoidal shapes and a gray dotted shape for the 1896 tsunami earthquake source area (Tanioka and Satake, 1996) up-dip of the SLSR. Slip contours of 1, 10, 20, 30, 40 and 50 m for 2011 Tohoku-Oki rupture model of Yue and Lay (2011) are shown along with a red star for the USGS/NEIC epicentral location. The darkly dotted ellipse indicates the approximate location of the 896 Jogan Tsunami source region (Minoura et al., 2001). The dashed curve indicates the position of the trench.

Over the past 115 years, this region has been framed on three sides (Figure 2.1b) by large

and great earthquake ruptures on the megathrust (ERC, 1998; Yamanaka and Kikuchi, 2004). To the north, the 1994 Sanriku-Haruka-Oki earthquake (M_w 7.6) had almost equal amounts of coseismic and postseismic moment (Heki et al., 1997; Kawasaki et al., 2001); to the east (up-dip), the great 1896 Sanriku tsunami earthquake (M_S 7.2, M_w 8.0-8.2, M_t 8.2-8.6) (Kanamori, 1972; Aida, 1977; Abe, 1979; Tanioka and Satake, 1996) and the great 1933 Sanriku outer trench slope normal-faulting event (M_w ~8.6) (Kanamori, 1971) both generated huge tsunamis that devastated the coast of Iwate prefecture; and to the south, the sequence of large Miyagi-Ken-Oki earthquakes (M ~7.2-8.2) of 1793, 1835, 1861, 1897, 1936, 1978, and 2005 (ERC, 1998; Kanamori et al., 2006) repeatedly ruptured the down-dip portion of the megathrust. The great 2011 Tohoku earthquake (M_w 9.0) recently ruptured the entire width of the megathrust to the south with large fault displacements, particularly in the up-dip half of the fault zone, but limited coseismic slip appears to have occurred in the Sanriku-Oki region and many aftershocks in the area appear to be upper plate events (Asano et al., 2011).

While the Sanriku-Oki region has numerous small earthquakes ($M_w \leq 5.0$), as we show here, it has few moderate to large size events (M_w ~5.0-7.5) and no very large to great earthquakes ($M_w > 7.5$) in earthquake catalogs dating back to 1900 (Figure 2.1), so we designate it the Sanriku-Oki Low Seismicity Region (SLSR).

The SLSR was first characterized as being nearly completely seismically decoupled in early considerations of plate coupling based on subducting plate geometry, models of

subduction zone evolution, and historical earthquake behavior (e.g., Kanamori, 1977). This perspective emerged from the observed along-strike variation from repeated great underthrusting earthquakes along the Kuril and Hokkaido regions to smaller, less regular events along the Honshu coast, with the intervening 1896 tsunami earthquake suggesting a transition in seismic coupling (Kanamori, 1972; Tanioka and Satake, 1996). The 1896 thrust event involved large displacement of the shallow portion of the megathrust, and with no historical record of large down-dip thrusting events, it is logical to infer that the deeper megathrust slips aseismically (i.e., it is seismically 'decoupled'), allowing stress to build-up and rupture the shallow, perhaps somewhat weakly-coupled region.

This notion of decoupling of the down-dip portion of the megathrust is strengthened by considering the great 1933 Sanriku normal-fault earthquake, which involved tensional fracture of the oceanic lithosphere near the trench 37 years after the 1896 tsunami earthquake (Kanamori, 1971). The 1933 event is still the largest known outer trench slope normal faulting earthquake, and it is plausible that significant loading of the plate bending stresses by deep slab negative buoyancy was involved, again suggesting that the deep megathrust is essentially decoupled or it would have shielded the shallow plate from the deep slab pull. These ideas played a role in the widely held assessment that the Japan megathrust further to the south was relatively unlikely to support earthquakes larger than M_w ~8.5 (estimated size of the 896 Jogan earthquake located south of the 1896 event (e.g., Minoura et

al., 2001)). That assessment, taken by some as an absolute upper bound on viable earthquake size, influenced earthquake hazard estimates along the Japan Trench using the characteristic earthquake model, but this perspective was evolving in the face of geodetic evidence for large megathrust slip deficits offshore of Miyagi and Fukushima prefectures (e.g., Loveless and Meade, 2010) and reconsiderations of the seismic history (e.g., Minoura et al., 2001; Watanabe, 2001; Kanamori et al., 2006; Satake et al., 2007), and was demonstrated to be an underestimate by the great event in 2011.

The rupture zones of the 1896 and 1933 earthquakes are not very well constrained, but the shallow subduction zone up-dip of the SLRS is seismically very active and probable rupture regions of the earlier great events are suggested by present day microseismicity distributions (e.g., Gamage et al., 2009). The nature of any down-dip transition to aseismic displacement in the SLSR is not known in detail, but a relatively abrupt lower edge of the high microseismicity domain is shown below.

The SLSR has also been regarded as a predominantly stable sliding portion of the megathrust with small asperities that fail in small repeating earthquakes (e.g., Igarashi et al., 2003; Matsuzawa et al., 2002; Matsuzawa et al., 2004; Uchida et al., 2003). A recurrence interval of 5.35 ± 0.53 years for M ~4.7 repeating earthquakes with very similar waveforms has been determined for the megathrust region offshore the coastal town of Kamaishi in the down-dip region of the SLSR (~39.4°N, ~142.2°E). This has been interpreted as repeated

rupture of the same asperity with a dimension of ~1 km surrounded by a creeping zone on the plate boundary (Matsuzawa et al., 2002). Uchida and Matsuzawa (2011) build on these observations to propose a notional hierarchical structure of asperities along the northeastern Japan coast and estimate low interplate coupling in the SLSR based on repeating earthquake analysis.

During the 2011 Tohoku event, minor slip on the order of a few meters may have occurred in the southern SLSR (Ammon et al., 2011; Lay et al., 2011b; Ozawa et al., 2011; Shao et al., 2011; Yue and Lay, 2011), far less than the tens of meters of slip on the megathrust to the south, but GPS data indicate that postseismic slip following the 2011 event is largest, albeit > 1 m, in this region (Ozawa et al., 2011). It appears likely that the SLSR played a role in delimiting the great event's northern rupture extent. Observations of how this region, including its repeating earthquake patches, was affected by the 2011 event are relevant to seismic hazard, frictional behavior, and earthquake interactions and stress transfer on a megathrust with variable slip behavior.

We use earthquake catalogs and seismic waveforms to examine the seismicity and focal mechanism of events in the SLSR in the context of it being located on the margins of the large slip zones of the 1896 and 2011 ruptures. Our attention focuses on interplate thrust events to the extent possible using as criteria event locations and regional or global Centroid Moment Tensor (CMT) focal mechanisms.

2.2 Characteristics of SLSR faulting

2.2.1 Seismicity and Focal Mechanisms

We use the USGS/NEIC Preliminary Determination of Epicenters (PDE) catalog (1 January 1973 - 7 July 2011) and the Japan Meteorological Agency (JMA)-unified catalog (2 January 1925 - 7 July 2011) to establish basic attributes of the seismicity in the SLRS. The NEIC catalog is expected to be reasonably complete for events near Japan with $m_b > 5.0$ for the 1973-2011 time interval, and some events down to m_b ~2.0 are included. The JMA-unified catalog is likely to be reasonably complete back to 1925 for $M_j \geq 6.5$, and back to 1973 for $M_j \geq 5.0$. The most recent 15 years of the JMA-unified catalog incorporate large numbers of observations from the high sensitivity seismograph network (Hi-net) that was rapidly deployed after the 1995 Kobe earthquake, with the detection and completeness levels for events within the SLSR lowering with time. For the past decade, events down to M_j ~2.5 have been very well recorded in the SLSR due to its proximity to the coast. The time-varying attributes of the catalogs are complex, and we will not attempt to quantify them or differences between m_b and M_j, given that the SLSR is quite distinctive without need for any special processing. Data for two seismicity and moment tensor catalogs are presented to ensure that our interpretations do not depend on specific catalog parameters.

We consider seismicity distributions prior to, and for 4 months following, the 2011 Tohoku-Oki earthquake. Before the 2011 earthquake, the framing of the SLSR by large earthquake ruptures in Figure 2.1b is also apparent in maps of JMA-unified catalog seismicity

along Honshu dating back to 1925 for large earthquakes (Figure 2.2a; $M_j \geq 6.5$), and back to 1973 for medium to large earthquakes (Figure 2.2c; $M_j \geq 5.0$). However, on the same map scale, the SLSR is not as clearly distinctive in the distribution of smaller events since 2001 (M_j ~ 2.5-5.0) as was noted by Uchida et al. (2009), although there is a somewhat sparse, patchy distribution of seismicity (Figure 2.2e). The hypocentral depths of the events in the SLSR are mostly 40-50 km in the west, shallowing to ~30 km in the east, consistent with many events being located on the megathrust, but some events have depths that place them in the upper or lower plates.

To date, the SLSR has hosted numerous aftershocks of the 11 March 2011 great earthquake with $M_j \geq 6.5$ and $M_j \geq 5.0$ (Figure 2.2b, d), and moderate numbers of smaller events, many in a well-defined north-south lineation in the upper plate in the southern SLRS (Figure 2.2f). The overwhelming task of processing the intense aftershock activity raises questions about the catalog completeness of the aftershock sequence for the lower magnitudes.

The low historical seismicity for large events in the SLSR is particularly striking given the intensity of large earthquakes at comparable down-dip positions on the megathrust to the south along the Miyagi-Ken-Oki zone. It is clear in Figures 2.2a and 2.2c that the near-trench portion of the megathrust that ruptured with large slip up-dip of the hypocenter in 2011 (Figure 2.1b) had relatively few large or small preceding events in the JMA-unified catalog,

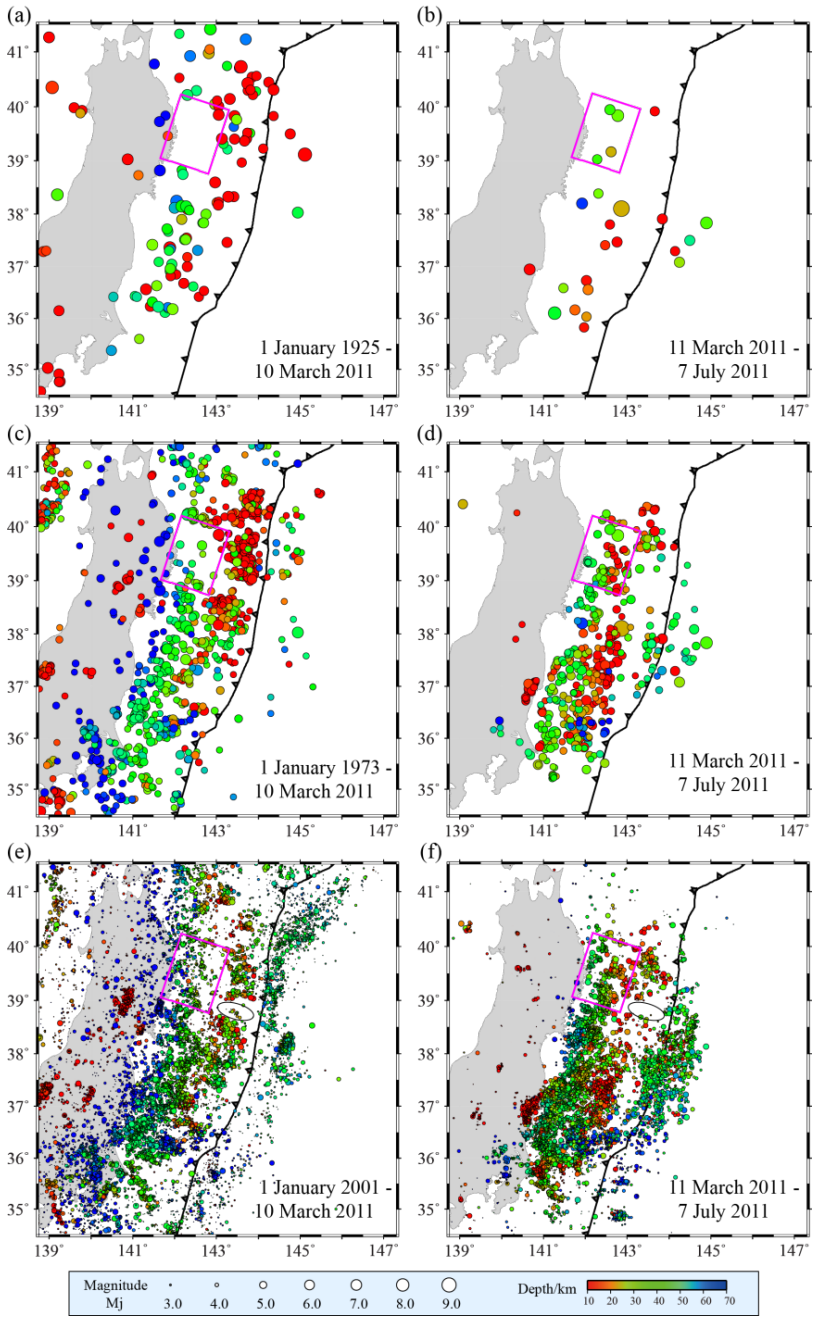

Figure 2.2 Seismicity from the JMA-unified catalog around northeast Honshu prior to (left column) and after (right column) the 11 March 2011 Tohoku-Oki Earthquake with (a) $M_j \geq 6.5$ from 1925 to 10 March 2011, (c) $M_j \geq 5.0$ from 1973 to 10 March 2011, (e) M_j 2.5 - 5.0 from 2001 to 10 March 2011. Aftershocks of the Tohoku-Oki event with (b) $M_j \geq 6.5$, (d) $M_j \geq 5.0$, and (f) M_j 2.5 – 5.0 up until 7 July 2011. The ellipses in the lower panels denote the "seismic gap" for small earthquakes (Uchida et al., 2004). The toothed black line indicates the Japan Trench. Other symbols are the same as those in Figure 2.1.

and also few aftershocks. This is also the case in the latitude range 35°-36°N, on the southern margin of the large slip region in the 2011 event. A localized region from 38.8°-39.0°N, 143°-144°E up-dip from the SLSR (ellipses in Figures 2.2e and 2.2f) has very low activity at all magnitude levels, as was discussed by Uchida et al. (2004). We will discuss these low seismicity regions later, although it is clear that a relative lack of seismicity alone can be misleading with respect to seismogenic potential. Overall, the SLSR appears to have general similarities to the creeping section of the San Andreas fault, where there are many small events but no large events, and large adjacent ruptures do not seem to be able to penetrate through the region (e.g., Wyss et al., 2004).

We now zoom-in on the SLSR and examine the regional seismicity in more detail. The up-dip portion of the megathrust extends to ~144°E, near the trench. The NEIC catalog (Figure 2.3a) and JMA-unified catalog (Figure 2.4a) show that there is much higher seismic activity for m_b or $M_j \geq 5.0$ since 1973 in the up-dip portion of the megathrust, where the 1896 earthquake rupture occurred. Both catalogs indicate a transition in seismicity levels near ~143°E or somewhat further to the east. Due to limited teleseismic location capabilities, the NEIC catalog has moderate numbers of small earthquakes for $m_b \sim 2.5$-5.0 (Figure 2.3c). Many more small events (M_j 2.5-5.0) are found in the JMA-unified catalog in the SLSR region from 1973-2011 (Figure 2.4c) with most of the smaller events in the catalog being since 1995. Several distinct clusters are indicated by the smaller activity, but are not as evident for

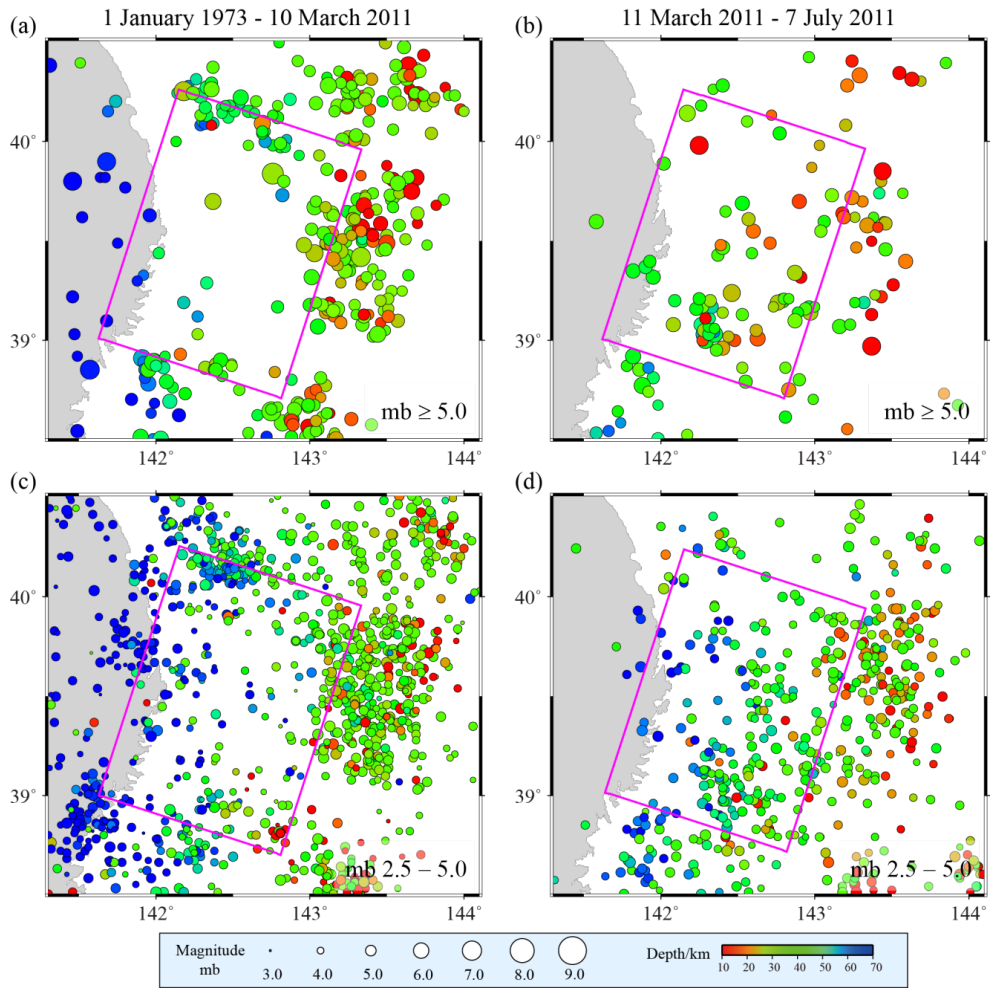

Figure 2.3 Seismicity from the NEIC catalog around the SLSR from 1973-2011 prior to the 11 March 2011 Tohoku-Oki earthquake with (a) $m_b \geq 5.0$ and (c) $m_b < 5.0$, and after the Tohoku-Oki earthquake with (b) $m_b \geq 5.0$ and (d) $m_b < 5.0$. Other symbols are the same as those in Figure 2.1.

the larger events. Both catalogs define the almost completely aseismic region extending to the trench within 38.8°-39°N, 143°-144°E corresponding to the ellipses in Figures 2.2e and 2.2f. This low seismicity region, with a particularly strikingly well-defined northern edge in Figure 2.4c, may demark the southern limit of the 1896 rupture zone (Aida, 1977), although some estimates indicate a more southerly rupture limit near 38.4°N (e.g., Figure 2.1b; Tanioka and

Satake, 2006). The aseismic region extending to the trench lies near the northern edge of the large up-dip slip region for the 2011 event (Figure 2.1b) as well.

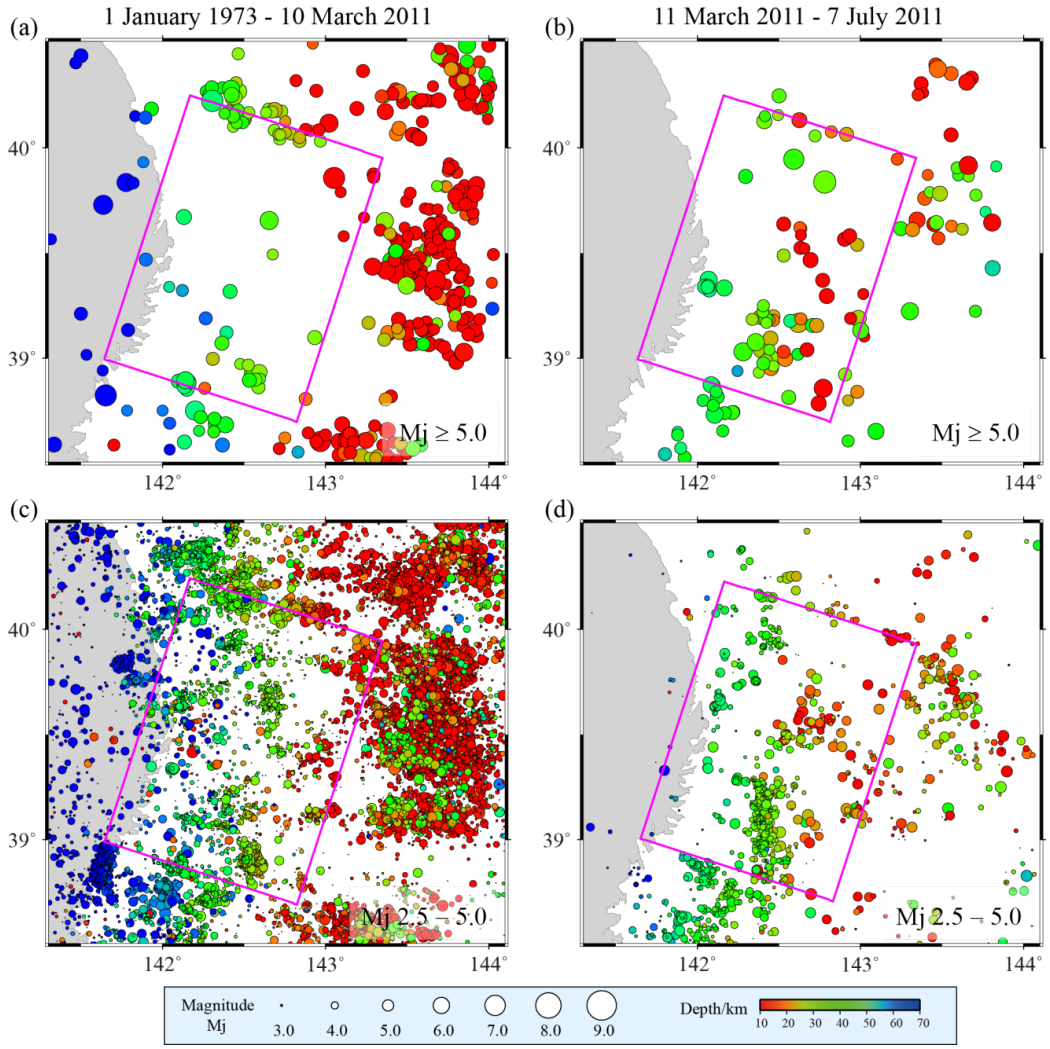

Figure 2.4 Seismicity from the JMA-unified catalog around the SLSR from 1973-2011 prior to the 11 March 2011 Tohoku-Oki earthquake with (a) $M_j \geq 5.0$ and (c) $M_j < 5.0$, and after the Tohoku-Oki earthquake with (b) $M_j \geq 5.0$ and (d) $M_j < 5.0$. Other symbols are the same as those in Figure 2.1.

Aftershock activity in the SLSR for the 2011 Tohoku-Oki earthquake is substantial relative to the preceding several decades as seen for both the NEIC catalog (Figures 2.3b,

2.3d) and the JMA-unified catalog (Figures 2.4b, 2.4d). The differences between catalog locations for the aftershocks are clearly apparent, with larger events tending to locate further off-shore in the JMA-unified catalog than in the NEIC catalog, and smaller events tending to be more clustered in the JMA-unified catalog, notably for the north-south lineation apparent in Figure 2.4d. It is interesting that the aseismic patch near 38.9° that extends to the trench is remarkably devoid of aftershocks in the JMA-unified catalog (Figures 2.4b, 2.4d) and there are regions within the SLSR that appear similarly devoid of aftershocks. As is true for the mainshock rupture zone to the south, many of the aftershocks are actually shallow, upper plate events (most red symbols in the SLSR regions in Figures 2.3b, 2.3d, 2.4a, and 2.4b), and it is useful to examine aftershock focal mechanisms to help identify events on the SLSR megathrust, which is of primary interest here.

We extracted all focal mechanisms in the Sanriku region from the Global Centroid Moment Tensor (GCMT) catalog back to 1976 (Figure 2.5) and the NIED regional CMT mechanism catalog back to 1997 (Figure 2.6). All available solutions are shown, separated by magnitude less than or greater than M_w 6.0 and by timing relative to the great 2011 Tohoku event. For the GCMT solutions, the lowest value of M_w is 4.7, and the events are plotted at the GCMT centroid locations. Most of the GCMT events around the SLSR margins appear to be interplate thrust events, and there are about a dozen such events within the SLSR prior to 2011 (Figures 2.5a and 2.5c) and only a few GCMT events with $M_w > 6.0$ (Figure 2.5a).

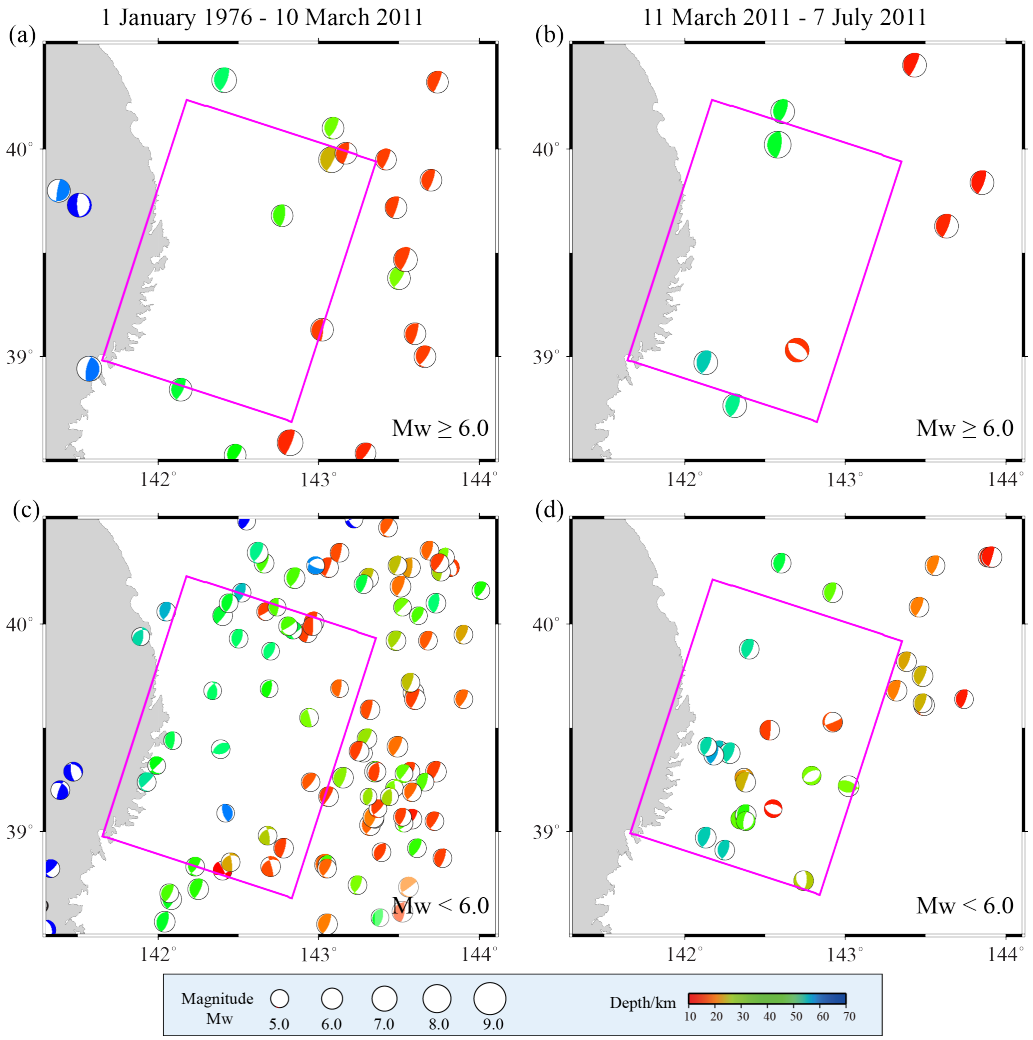

Figure 2.5 Focal mechanisms from the GCMT catalog around the SLSR since 1976 prior to the 11 March 2011 Tohoku-Oki earthquake with (a) $M_w \geq 6.0$ and (c) $M_w < 6.0$, and after the Tohoku-Oki earthquake with (b) $M_w \geq 6.0$ and (d) $M_w < 6.0$. Other symbols are the same as those in Figure 2.1.

The upper plate in the SLSR had some compressional activity prior to the 2011 Tohoku-Oki event, but experienced diffuse extensional activity afterward. Thrust faulting aftershocks occurred in the northern region of the 1896 rupture zone and in the down-dip SLSR region just offshore of the coastline, with a cluster near the off-Kamaishi repeater zone at 39.4°N, 142.2°E (Figures 2.5b and 2.5d).

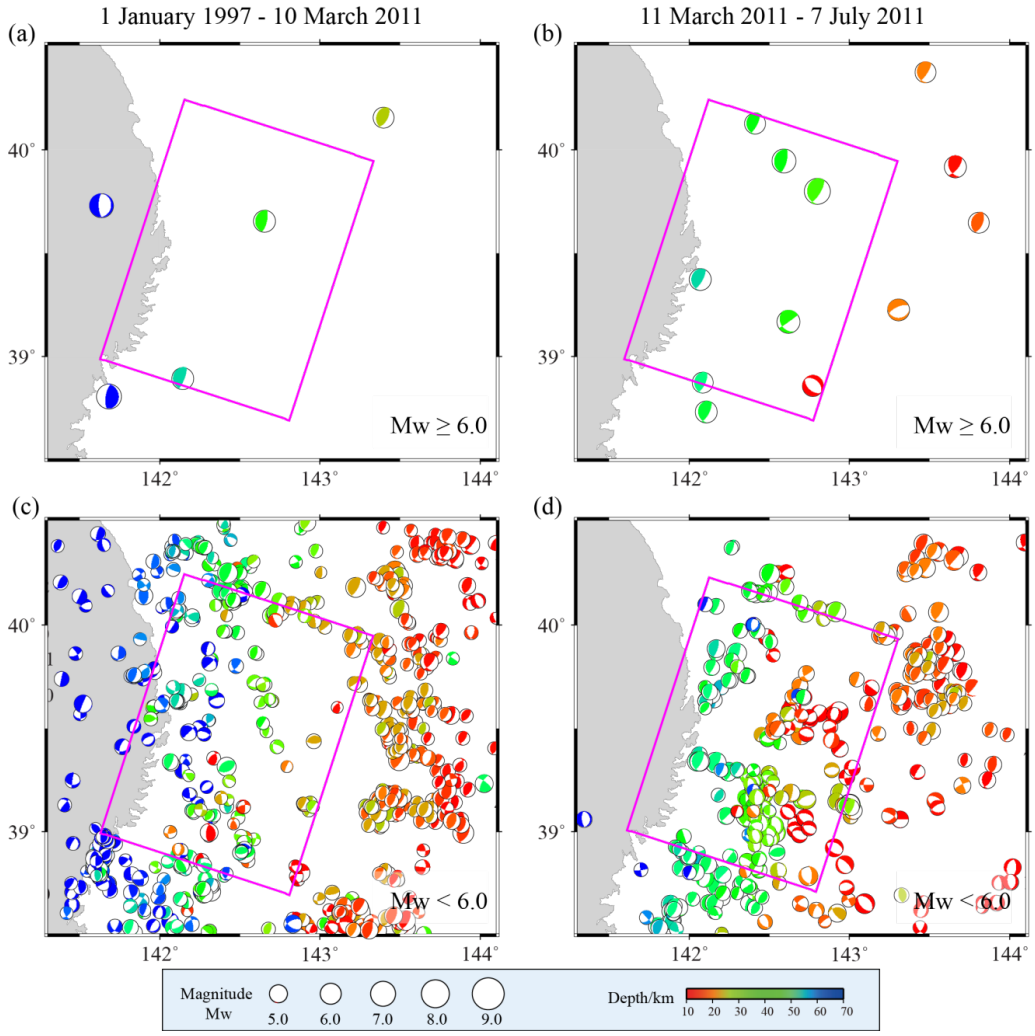

Figure 2.6 Focal mechanisms from the NIED CMT catalog since 1997 around the SLSR prior to the 11 March 2011 Tohoku-Oki earthquake with (a) $M_w \geq 6.0$ and (c) $M_w < 6.0$, and after the Tohoku-Oki earthquake with (b) $M_w \geq 6.0$ and (d) $M_w < 6.0$. Other symbols are the same as those in Figure 2.1.

The NIED moment tensors (Figure 2.6) are based on inversion of broadband waveforms from F-net stations and provide many more solutions for events as small as $M_w = 3.2$. There are differences in M_w between the GCMT and NIED solutions, and 50% more NIED $M_w > 6$ events are apparent for the aftershock sequence (compare Figures 2.5b and 2.6b). Many of the NIED mechanisms for lower M_w values located in the SLSR before 2011 (Figure 2.6c)

appear to be intraplate events within the Pacific plate (most blue mechanisms), including a prominent sequence near 38.9°N, 141.8°E. There are again only a few large events with thrusting mechanisms within the SLSR before 2011 relative to the surrounding regions.

The expanded sampling of small aftershock mechanisms provided by the NIED catalog (Figure 2.6d) indicates several 20-km scale subregions with underthrusting aftershocks in the SLSR close to the coastline (including the off-Kamaishi events), with most events eastward of 142.5° having extensional faulting that is likely located within the upper wedge. The overall activity levels in the SLSR are clearly elevated for the 4-month interval after the 11 March 2011 event, and several of the patches with thrusting aftershocks had only experienced a few events in the preceding decades. The concentration of NIED underthrusting aftershocks in the northern region of the 1896 zone (Figures 2.6b and 2.6d) is similar to the GCMT pattern (Figures 2.5b and 2.5d). It is interesting that so few underthrusting aftershocks are found south of 39.5°N and east of 142.5°E, as very large coseismic slip occured just to the south of this region during the 2011 rupture (Figure 2.1b).

2.2.2 Interplate slip deficit around the SLSR

Observations from the dense nation-wide global positioning system (GPS) network (GEONET) in Japan since 1996 revealed the crustal strain distribution in Honshu prior to the 2011 Tohoku-Oki earthquake, and this has been modeled by several groups to estimate the spatial distribution of offshore interplate coupling. While estimates of the spatial slip deficit

across the megathrust are dependent on assumptions and boundary conditions in the modeling, particularly regarding the degree of coupling allowed at shallow megathrust depths near the trench (Loveless and Meade, 2011), slip deficits on the plate boundary 30-50 km deep in the SLSR should be relatively well resolved because of proximity to the GPS network. Figure 2.7 shows examples of spatial distributions of inverted "back slip" (the slip deficit required to account for the crustal strain while fully accommodating overall plate convergence) translated into degree of locking around the SLSR.

Assessment of any slip deficit in the SLSR is made more difficult by the coseismic and postseismic deformation of large events like the 1989 (M_w 7.4), 1992 (M_w 6.9), and 1994 (M_w 7.7) Sanriku-Oki events (Heki et al., 1997; Kawasaki et al., 2001; Yamanaka and Kikuchi, 2004) north of the SLSR. Nishimura et al. (2000) regard the SLSR as a region of slip velocity-strengthening (aseismic) due to the unusually large postseismic displacement on the megathrust following the 1992 and 1994 earthquakes and the lack of historical large earthquakes. The distribution of back slip rate in the SLSR during 1997-2001 estimated by Suwa et al. (2006) is ~2 cm/yr lower than that in the surrounding region (Figure 2.7a).

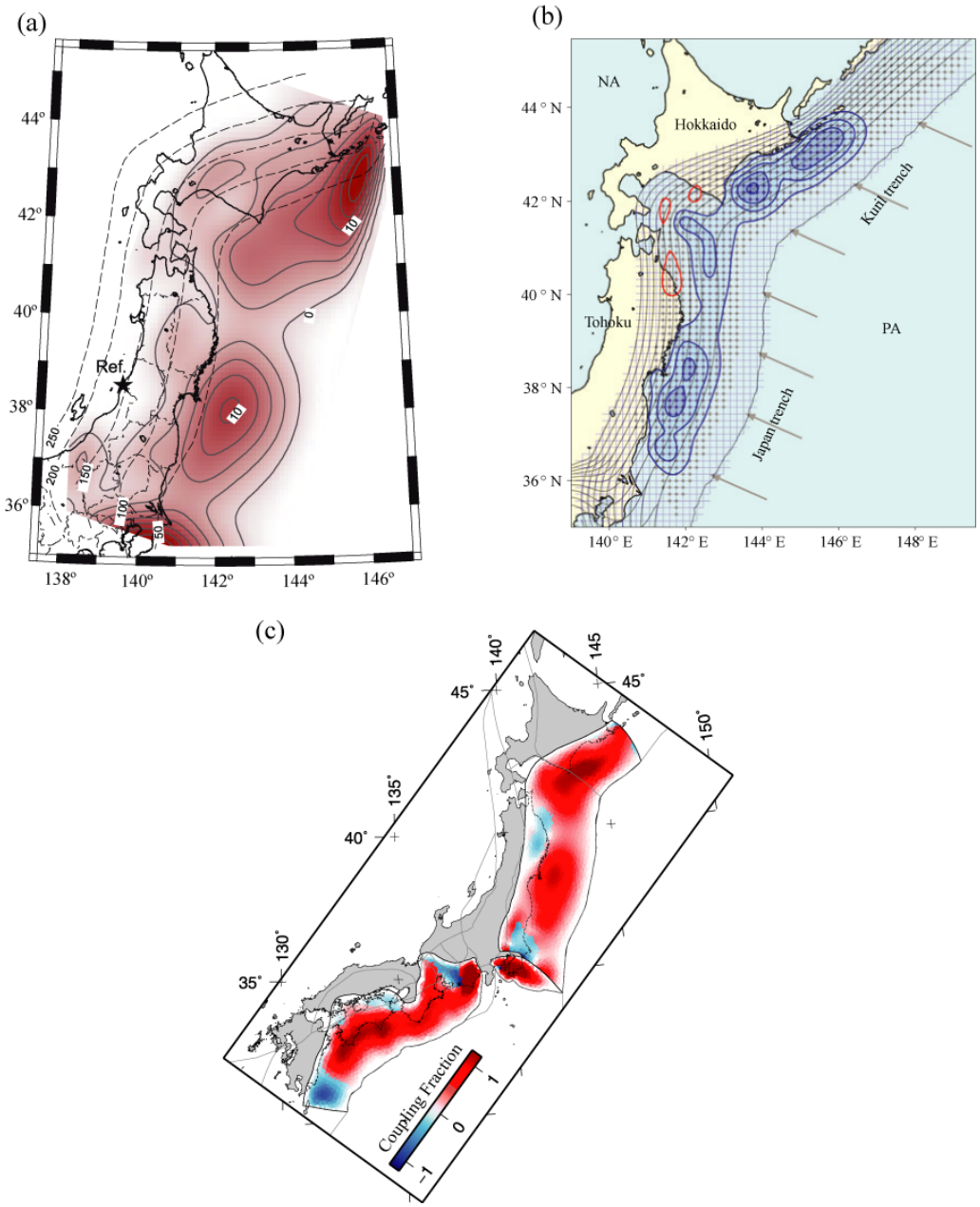

Figure 2.7 Slip deficit maps. (a) Distribution of back slip rate estimated by inverting three-dimensional velocity data with a contour interval of 2cm/yr with continuous GPS data from 1997 to 2001. Dashed lines indicate the slab depth every 50km. (Modified from Suwa et al., 2006). (b) The distribution of slip-deficit rates (blue contours) and slip-excess rates (red contours) inverted with the GPS data between 1996 and 2000. (Modified from Hashimoto et al., 2009). (c) Coupling fraction estimated from GPS observation from 1997 to 2000. A zone of large thrust sense slip around SLSR may reflect postseismic deformation triggered by 1994 Mw 7.7 Sanriku-Oki earthquake. Thin gray lines indicate the block geometry. (Modified from Loveless and Meade, 2010).

Hashimoto et al. (2009) argue that slip-deficit zones are the potential source regions of large interplate earthquakes ($M_w \geq 7.5$), and infer that the smaller slip deficit found for GPS data from 1996-2000 (Figure 2.7b) indicates a low likelihood of large earthquakes in the SLSR. Loveless and Meade (2010) estimated forward slip of up to 2.5 cm/yr and very low coupling on the subduction zone interface beneath northernmost Honshu in and around the SLSR (Figure 2.7c). They attribute part of the deformation signal in GPS data from 1997 to 2000 to postseismic dislocation triggered by the 1994 Sanriku-Oki earthquake, giving the forward slip indicated by negative (blue) values.

Overall, GPS inversions for back slip rate distribution and/or postseismic deformation in northeastern Japan prior to the great 2011 earthquake indicated strong megathrust coupling in two large regions off Tokachi north of the SLSR, and off Miyagi south of the SLSR, with relatively weak plate coupling in the SLSR (Figure 2.7). Inversions for back-slip tend to be heavily smoothed and the SLSR is not resolved to have zero slip deficit, just reduced slip deficit relative to adjacent regions. Specific testing of the hypothesis that there is zero slip deficit could be performed using the seismically defined spatial extent of the SLSR in the future. Given the available inversion models and accepting that there is some lateral smearing of the strains caused by the adjacent region with up to 100% slip deficit (totally locked) that ruptured in the great 2011 event, the geodetic observations indicate that the SLSR has relatively low slip deficit as a result of aseismic displacement involving either stable sliding or

episodic slow slip events.

2.3 2011 Mainshock Effects

2.3.1 Coseismic slip and Postseismic Slip in the SLSR in 2011

Several coseismic finite-faulting slip distribution models for the 11 March 2011 Tohoku-Oki earthquake have now been inverted for using teleseismic, geodetic, and tsunami data (e.g., Ammon et al., 2011; Ito et al., 2011; Lay et al., 2011b; Ozawa et al., 2011; Shao et al., 2011; Simons et al., 2011). These models have notable differences, but they are consistent in indicating minor slip on the order of zero to a few meters coseismic slip in the southern SLSR (e.g., Figures 2.1 and 2.8). It appears that despite the SLSR lacking large previous seismic events, it was able to delimit the great 2011 event's northern rupture extent either due to lack of accumulated strain energy available to tap or due to high frictional strength.

On the other hand, GPS data indicate that the postseismic slip following the 2011 Tohoku event is largest in the SLSR, on the order of 0.4-0.8 m (Figure 2.8, Ozawa et al., 2011). The lack of coseismic slip and concentration of postseismic slip in the SLSR indicates frictional conditions that are generally unfavorable for seismic failure. However, some aftershocks did occur in the SLSR.

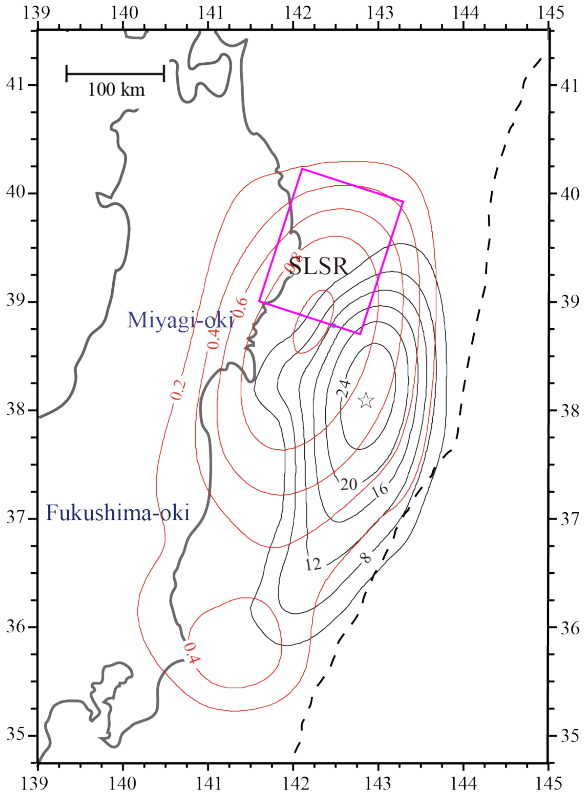

Figure 2.8 Coseismic slip (black lines, 4-m interval, 10-11 March 2011) and postseismic slip (red lines, 0.2-m interval, 12-25 March 2011) distribution of the 2011 Tohoku estimated from GPS observation (Ozawa et al., 2011). Other symbols are the same as those in Figure 2.1.

2.3.2 Large aftershocks in the SLSR

As shown above, there are relatively numerous aftershocks located in the SLSR compared with preceding activity. About ~22.5 minutes after the mainshock an M_w 7.4 (39.84°N, 142.78°E; JMA) aftershock (strike = 179°; rake = 60°; dip = 23°; depth = 35 km from NIED focal mechanism, shown in Figure 2.6d) occurred near the northeastern corner of the SLSR. This is located close to the 1 November 1989 M_w 7.4 event (39.84°N, 142.76°E, NEIC) event (the GCMT centroid location, 39.95°N, 143.08°E is just inside the SLSR in Figure 2.5). The 1989 event has been analyzed by Yamanaka and Kikuchi (2004) and Uchida et al. (2004). That event ruptured close to a prior event on 21 March 1960 (M_w 7.3), possibly

with overlapping rupture area (Yamanaka and Kikuchi, 2004), so the 2011 M_w = 7.4 aftershock is not in a surprising location. Both the 1960 and 1989 events were followed by large aftershock sequences in the shallow megathrust region up-dip of the SLSR (Yamanaka and Kikuchi, 2004).

Numerous moderate size underthrusting aftershocks (M_w ~5.0-6.5) have occurred on the down-dip portion of the SLSR about 40 km beneath the coastal margin (Figures 2.5b, 2.5d, 2.6b, 2.6d), with activity extending along the length of the SLSR, but clustered in 2-3 groups. There is very little aftershock thrust activity from 142.5°E-143.25°E. Numerous normal fault events occurred at upper plate depths in this eastern portion of the SLSR, but only the down-dip portion appears to have had thrust aftershocks.

We modeled teleseismic P waves for the larger recent thrust events in and near the SLSR to confirm the source depths and to evaluate whether they had unusual rupture characteristics. Adequate broadband teleseismic P wave data were found for 6 aftershocks (M_w 5.9-6.2) and 2 earlier events (M_w 6.3-6.4) with low dip angle faults and hypocentral depths consistent with interplate events (Figure 2.9). A few P-wave recordings at azimuths of ~300° with high signal-to-noise ratios were forward modeled, holding the GCMT mechanism fixed and varying the source depth and source duration.

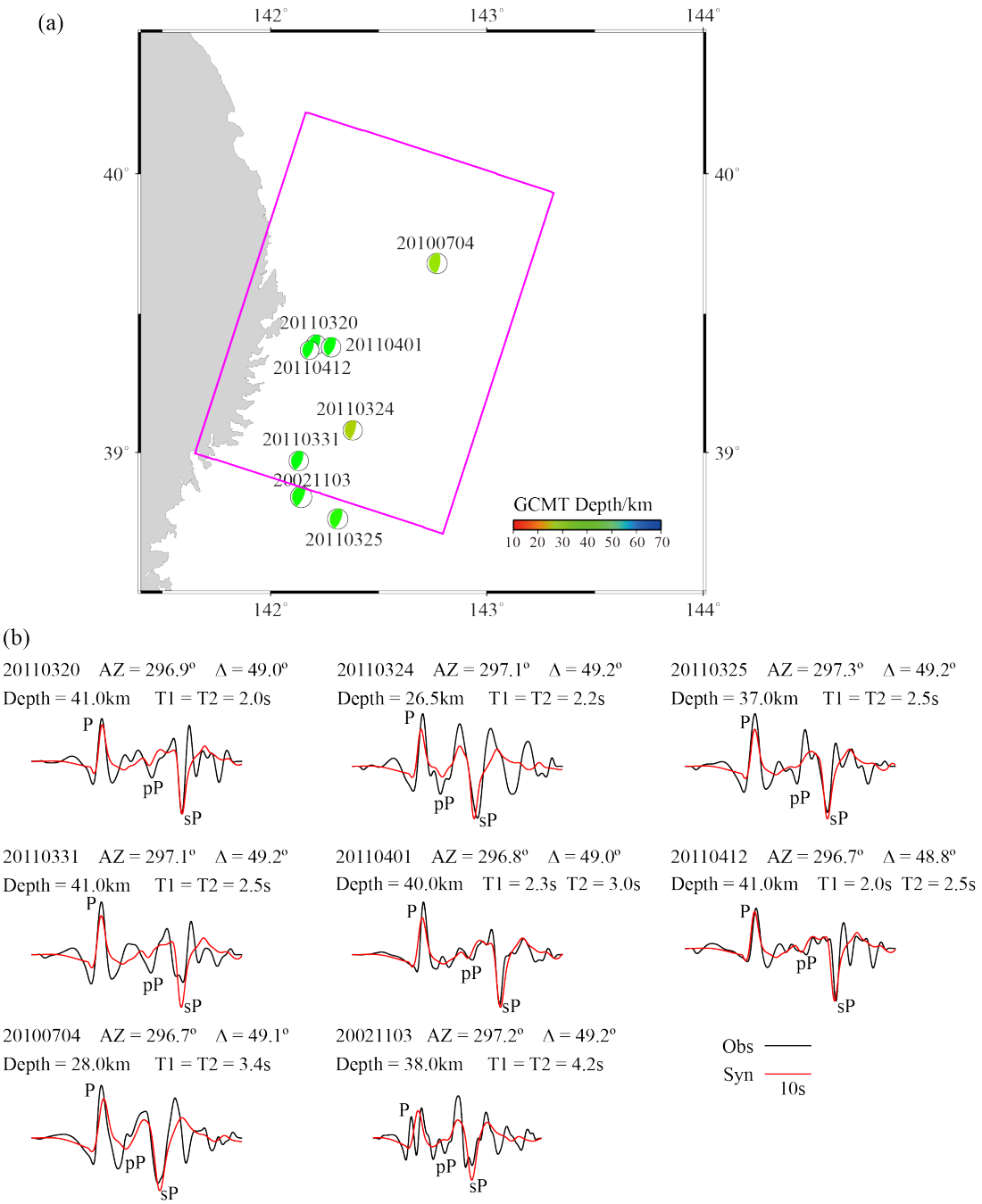

Figure 2.9 (a) The GCMT location and focal mechanism of the thrusting aftershocks used in waveform modeling in section 2.3.1. Other symbols are the same as those in Figure 2.1. (b) Observed (black lines) and synthetic (red lines) teleseismic P, pP and sP waves for aftershocks in (a) recorded in the station KN.TKM2. The azimuth, epicentral distance, preferred depth, and preferred trapezoidal source duration for each record are indicated above each waveform.

The depths of these larger thrust events (Table 2.1) are determined to be ~40 km except the 4 July 2010 event (depth = 26.5 km) located northeast of the other events. The modeling depth estimates are consistent with those from the JMA-unified and NEIC catalogs and shallower than the GCMT centroid depths by ~15 km. The P wave signals used have weak pP arrivals compared to sP, which is consistent with the focal mechanisms having low dip angles of ~19°-26°. In each case ~2-3 s trapezoidal source durations provide good matches to the P waveforms. This duration is typical of M_w 6.0 events, and these SLSR events do not show any distinctive waveforms relative to comparable size events elsewhere, and the aftershocks are not distinctive from the earlier events. The 3 November 2002 events has complex double-pulse P waves, but we do not model the details, as we mainly wanted to confirm the depth.

Table 2.1. Aftershocks selected for waveform modeling

	Origin Time/UT	**Lat./°N**	**Lon./°E**	**Depth/km**				**M_W**
				PDE	GCMT	JMA	Modeling	
1	2011 03 20 12:03:46.72	39.35	141.82	42.0	55.3	47.8	41.0	5.8
2	2011 03 24 08:21:00.14	39.08	142.08	27.0	37.1	33.7	26.5	5.9
3	2011 03 25 11:36:24.49	38.77	141.88	39.0	51.0	44.7	37.0	6.2
4	2011 03 31 07:15:30.19	38.92	141.82	42.0	54.0	47.4	41.0	6.0
5	2011 04 01 11:57:54.39	39.32	141.95	41.0	52.7	45.2	40.0	5.9
6	2011 04 12 19:37:48.29	39.37	141.90	45.0	56.6	48.3	41.0	5.6
7	2002 11 03 03:37:42.07	38.89	141.98	39.0	44.0	45.8	39.0	6.4
8	2010 07 04 21:55:51.98	39.70	142.37	27.0	35.3	34.5	28.0	6.3

2.3.3 Repeating Earthquakes off-Kamaishi

Seven underthrusting aftershocks with M_w 4.3-5.9 occurred on the plate boundary offshore of Kamaishi (~39.4°N, ~142.0°E) where the M_j 4.8 ± 0.1 repeating earthquake sequence was observed by Matsuzawa et al. (2002). To identify whether they are the repeating earthquakes of this sequence, we calculated the cross-correlation of the waveforms of these 7 aftershocks with those for earlier identified repeating earthquakes in 2001 and 2008 (Okada et al., 2003; Shimamura et al., 2011). We used signals recorded by the broadband network F-net in Japan for the time window from 10 s before predicted P arrival to 10 s after predicted S wave arrival. Waveform cross-correlations indicate that at least two of the events, event #13 and #15 in Table 2.2 (group A), are precisely co-located with earlier off-Kamaishi repeating events in 2001 and 2008. The other four events, #11, #12, #14 and #16 (group B) show high waveform similarity with each other but are clearly somewhat different from the earlier repeaters. Also, the magnitudes of these events (M_j = 5.3 to 5.9) are consistently larger than those of earlier repeating events (M = 4.7 to 5.1) and events #13 and #15. Increase in size of repeaters and initiation of new repeater sequences were observed for the 2004 Parkfield earthquake as well (Chen et al., 2010). Event #17 has few high cross-correlation coefficients with the signals for the two groups, so it appears distinctive.

Even though there appear to be at least two groups based on waveform similarities, cross-correlation coefficients between events from the two groups are still ~0.8 for the most

Table 2.2. Possible Repeating earthquakes off-Kamaishi

Event	Origin Time (JST)	Lat./°N	Lon./°E	Depth/km	Mag. (Mj)
#1	1957 09 27 21:43:27.20	39.3170	142.0000	49.0	4.9
#2	1962 07 30 19:51:04.30	39.3330	142.0670	50.0	4.9
#3	1968 10 17 22:28:22.50	39.3000	142.1170	50.0	4.9
#4	1973 12 08 06:07:21.80	39.3330	142.0500	50.0	4.8
#5	1979 07 19 10:30:00.20	39.3500	141.9330	50.0	4.8
#6	1985 03 01 11:35:06.00	39.3430	142.0520	51.0	4.9
#7	1990 07 16 21:35:10.00	39.3400	142.0420	52.0	5.0
#8	1995 03 11 13:49:56.90	39.3250	142.1220	57.1	5.1
#9	2001 11 13 16:45:05.40	39.3370	142.0690	48.0	4.8
#10	2008 01 11 08:00:31.70	39.3410	142.0670	47.2	4.7
#11	2011 03 11 15:40:49.50	39.3260	142.0720	51.4	5.7
#12	2011 03 20 21:03:47.50	39.3440	142.0480	47.8	5.9
#13	2011 03 29 08:51:31.10	39.3440	142.0550	49.1	4.3
#14	2011 04 13 04:37:48.40	39.3440	142.0650	48.3	5.5
#15	2011 04 29 15:54:48.10	39.3400	142.0640	48.2	4.8
#16	2011 05 31 21:28:35.70	39.3420	142.0620	48.0	5.3
#17	2011 07 11 13:29:28.38	39.3417	142.0605	50.0	5.1

near-by stations. Since digital data for the off-Kamaishi repeating sequence are only available at our stations for the 2001 and 2008 events, it is hard to evaluate definitively whether the events in group B and event #17 are or are not repeaters of prior events in the off-Kamaishi group. The occurrence of at least two definite repeating earthquakes, events #13 and #15, supports the notion of a local asperity with a size of ~1 km loaded to failure by steady sliding of the surrounding megathrust (Matsuzawa et al., 2002). Since the other events are very similar to each other and may be repeats of earlier off-Kamaishi events, it appears that the large postseismic deformation following the great 2011 earthquake accelerated the repeated

failure of one or two asperities rather dramatically (Figure 2.10).

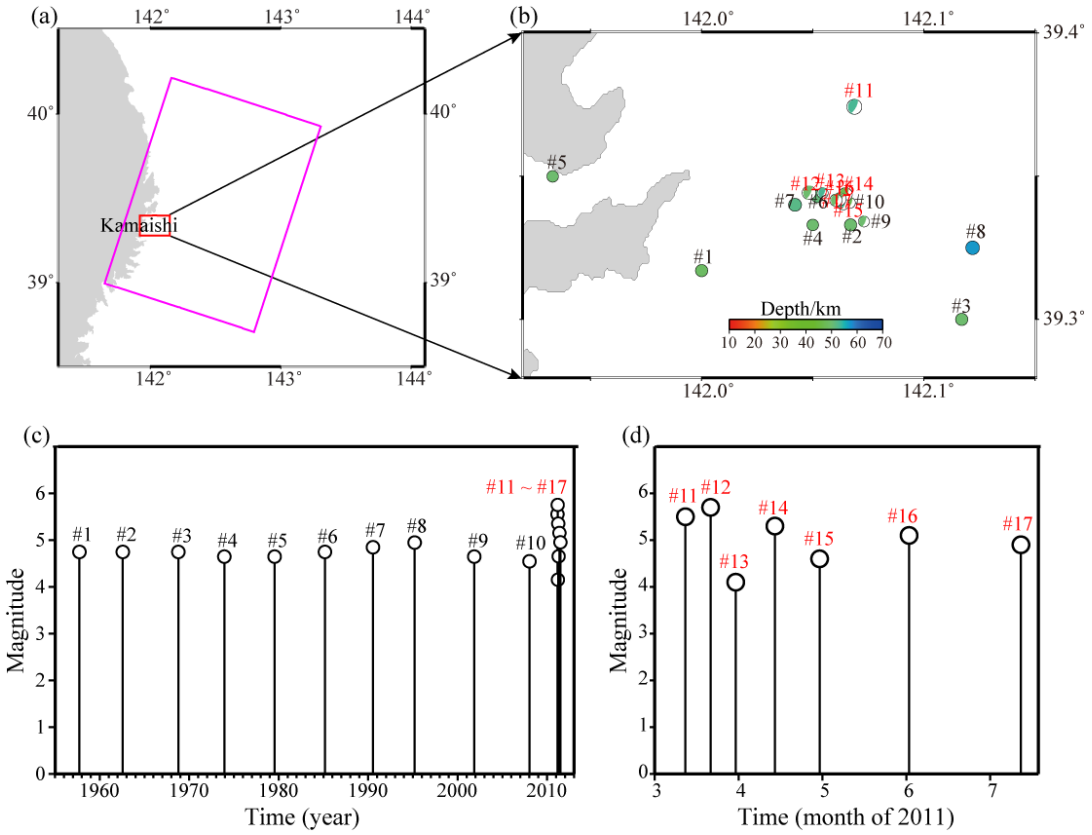

Figure 2.10 (a) Location of the region of the off-Kamaishi repeater sequence (red box) within the SLSR (magenta box) (b) Locations from the JMA-unified catalog of 7 aftershocks with M_w 4.3-5.9 off-Kamaishi and 10 earthquakes in the M 4.8±0.1 repeating sequences there (Matsuzawa et al., 2002). (c) Magnitude versus time diagram of all 17 events. (d) Expanded time scale of the aftershock sequence.

2.3.4 Stress Changes in the SLSR Thrust Zone

The limited and localized occurrence of thrusting aftershocks indicates that most of the postseismic deformation in the SLSR is taking place aseismically. Evaluating the stress perturbation produced by the main shock displacement can give some guidance on the stress changes in the SLSR. We used Coulomb 3 software, provided by S. Toda, R. Stein, J. Lin

and V. Sevilgen, to estimate the stress perturbation for the coseismic slip model from Yue and Lay (2011) (Figure 2.1b), obtained by inversion of high-rate GPS observations across Honshu.

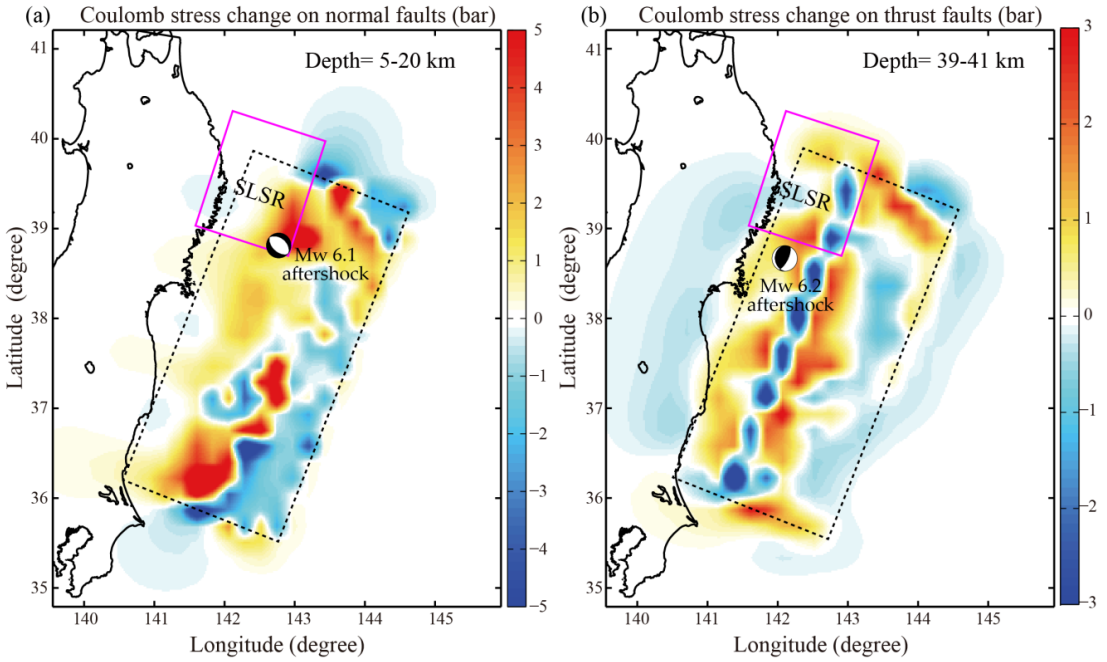

Figure 2.11 Maps of Coulomb stress change predicted for the coseismic slip model from Yue and Lay (2011). (a) The Coulomb stress change averaged over the depth range 5-20 km for normal faulting geometry given by the westward dipping plane of an M_w 6.1 aftershock located in the SLSR (2011/03/11 20:11 UTC; strike=140°, dip=41°, rake=-76°; NIED CMT solution). (b) The Coulomb stress change over the depth range 39-41 km for a shallow-dipping thrust faulting geometry given by an M_w 6.2 aftershock (2011/03/25 11:36:28.2 UTC; strike=185°; dip=26°; slip=74°; NIED CMT solution) which is the largest aftershock modeled in section 2.3.1.

We calculated the average stress change over the depth range 5-20 km for the westward dipping fault plane of a normal faulting geometry (Figure 2.11a) given by an M_w 6.1 aftershock located in the SLSR (2011/03/11 20:11 UTC; strike=140°, dip=41°, rake=-76°; NIED CMT solution) and the average stress change over the depth range 39-41 km for a shallow-dipping thrust faulting geometry (Figure 2.11b) of an M_w 6.2 aftershock (2011/03/25

11:36:28.2 UTC; strike=185°; dip=26°; slip=74°; NIED CMT solution), which is the largest aftershock modeled in section 3.1. For shallow normal faulting, the driving stress increased by ~5 bars in the SLSR, which is compatible with the occurrence of numerous extensional aftershocks in the upper plate (Figures 2.5 and 2.6). At greater depth within the SLSR near the megathrust, the driving stress for thrusting increased ~3 bars near the coastline, which is consistent with the band of thrusting aftershocks in the SLSR discussed above.

Coulomb stress calculations provide only first-order guidance with respect to changes in the SLSR stress environment, as the ambient stresses are not known. However, the general shift from compressional activity to extensional activity in the intraplate environment (Figure 2.6) does suggest relatively low stress (e.g., Hasegawa et al., 2011). Thus, aseismic convergence may be inferred to be occurring in the region due to low frictional resistance rather than as a result of very high stress stable sliding.

2.4 Discussion and Conclusions

Source process analysis of large earthquakes and interplate coupling distribution estimated from GPS observation for northeast Japan provide support for an asperity model characterization of the SLSR megathrust (Figure 2.12), as has been suggested by Yamanaka and Kikuchi (2004), Hashimoto et al. (2009) and Uchida and Matsuzawa (2011). The deeper portion of the SLSR has moderate size thrust events, in concentrated patches both before and

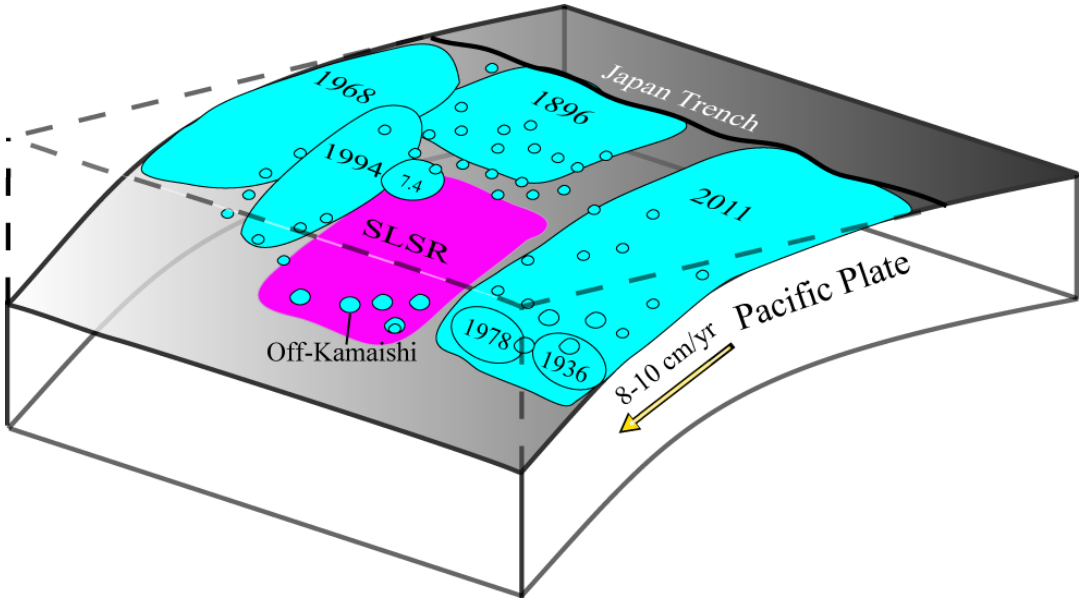

Figure 2.12 Schematic map of the Japan megathrust fault showing the distribution of rupture zone of historic large events and the 2011 Tohoku earthquake (large blue regions), and aftershocks (small blue regions) along the megathrust from Japan Trench. We plot the southern end of the 1896 rupture zone as extending to about 39°N, north of the aseismic zone seen in Figure 2e, consistent with the southern extent of the tsunami model of Aida (1977) and the region of strong inundation on the Iwate coast indicated by Hatori (1974). The convergence velocity of Pacific Plate is indicated by yellow arrow. The magenta region highlights the SLSR on the megathrust. The SLSR is largely aseismic, but does have modest size patches of seismogenic regions down-dip, including the off-Kamaishi repeater zone. The shallower portion of the SLSR is almost devoid of moderate size thrust events, but seismic activity is high in the 1896 rupture zone region further up-dip.

after the 2011 Tohoku-Oki mainshock. These patches normally failed at a slow rate before the great 2011 event, but the rate increased after the event. This is particularly clear for the off-Kamaishi repeating earthquake sequence where two confirmed repeaters, and many additional events on a nearby asperity, occurred within four months after the mainshock. This increase in failure rate is generally consistent with the predicted Coulomb stress change for models of the mainshock slip and with the concentration of postseismic deformation in the

vicinity of the SLSR. The up-dip portion of the SLSR megathrust has very few thrusting events and the total seismic moment of thrusting for the whole SLSR constitutes a tiny fraction of plate convergence slip.

Postseismc slip is accelerated creep following a mainshock, and is generally thought to happen on weak or stably sliding areas of the fault in response to increased strain rate in the mainshock vicinity. The <5 m slip during the 2011 rupture and the ~0.4-0.8 m postseismic slip in the SLSR support the idea that the region is weakly coupled and that resulting low strain accumulation may have served as an elastic energy sink that bounded the 2011 rupture. The high ratio of the number of repeating earthquakes to the total number of earthquakes (Igarashi et al., 2003), and the fringing of the SLSR by slow slip events, such as accompanied the 1989 Sanriku-Oki (M_w 7.4), 1992 Sanriku-Oki (M_w 6.9) and 1994 Sanriku-Oki (M_w 7.7) earthquakes, indicate that little strain has accumulated in the SLSR with convergence having been accommodated by aseismic slip. It is likely that this region is either totally decoupled or is in a slip strengthening state given the lack of induced thrust faulting aftershocks.

The cause of the distinct nature of the frictional state on the SLSR relative to adjacent regions of the megathrust is unclear. There is evidence for volumetric velocity heterogeneity in the vicinity of the 2011 Tohoku-Oki large slip zone where relatively high Vp is observed (Zhao et al., 2011) and in the transition from large up-dip slip to lower down-dip slip (Kennett et al., 2011), where low shear/bulk sound velocity is observed. The latter study finds low

shear/bulk sound velocity near the megathrust in the upper portion of the SLSR as well, with an increase in the ratio down-dip below the coastline. Presence of fluids could reduce the shear velocity and possibly the frictional strength in the aseismic region of the SLSR, but specific causes of the frictional behavior are not known.

The up-dip region of the Ibaraki-Oki megathrust region to the south of the 2011 rupture zone has some similar attributes to the SLSR. While the down-dip region has had historical M > 7+ events, such as the 1938 sequence with cumulative seismic moment equivalent to M_w ~ 8.1 (Abe, 1977), the up-dip activity in this region is low (Figure 2.2). Relatively low back slip and low slip deficit have also been estimated in this region (Figure 2.7c; Loveless and Meade, 2010). A large underthrusting aftershock (M_w 7.9) occurred in the down-dip megathrust (36.18°N, 141.17°E) ~30 minutes after the Tohoku-Oki earthquake (e.g., Lay et al., 2011a), but the up-dip region from 35°-36°N, 141.2°-142.2°E appears not to have had coseismic slip and had relatively few aftershocks (Figure 2.2). These observations suggest that weak interplate coupling and little strain accumulation might have also bounded the 2011 slip zone to the south in the same way the SLSR appears to have bounded it to the north. The aseismic zone extending from the SLSR to the trench (ellipse in Figures 2.2e and 2.2f) may have bounded the extent of up-dip rupture for the 2011 event and plausibly the southern extent of the 1896 rupture.

The SLSR appears to be a region where great earthquakes will not nucleate and through

which they do not manage to rupture. The lines of evidence supporting this interpretation include the low GPS-inferred slip deficit, the lack of historical great events, localized zones of repeating earthquakes that appear to be surrounded by quasi-static deformation and were accelerated by the 2011 rupture, significant 2011 postseismic slip, and lack of triggered thrust aftershocks from adjacent giant earthquake over the up-dip portion. Occurrence of large postseismic deformation for large earthquakes to the north of the SLRS and slow rupture up-dip in the 1896 tsunami earthquake, with abrupt transition in microseismicity at about 143°E further indicate transitions to a distinct frictional regime in the SLRS. The overall evidence suggests that this region is not storing strain that will release in a future great event, but rather is accommodating most plate convergence with aseismic sliding of most of the SLRS fault surface. Characterizing other regions with similar properties may help to define bounds on adjacent large earthquake ruptures.

Acknowledgments. This work made use of GMT and SAC software. Seismic catalogs and focal mechanisms were obtained from JMA, NIED, NEIC and GCMT. K. Katsumata provided a convenient version of the JMA-unified catalog. Y. Asano kindly provided a copy of his unpublished focal mechanism catalog of regional CMT inversions. N. Uchida shared his catalog of repeating events in the Japan Trench. B. L. N. Kennett provided a preprint of his velocity tomography results. C. Ammon provided seismicity maps that motivated this examination of the SLSR. This work was supported by NSF grant EAR0635570.

Chapter 3

Ground Shaking and Seismic Source Spectra for Large Earthquakes Around the Megathrust Fault Offshore of Northeastern Honshu, Japan

This chapter has been published as:

Ye, L., T. Lay, and H. Kanamori (2013), "Ground shaking and seismic source spectra for large earthquakes around the megathrust fault offshore of northeastern Honshu, Japan", *Bull. Seismol. Soc. Am.*, 103, no. 2B, 1221–1241.

Abstract. Large earthquake ruptures on or near the plate boundary megathrust fault offshore of northeastern Honshu, Japan, produce variable levels of regional high frequency ground shaking. Analyses of 0.1-10 Hz strong ground motion recordings from K-net and KiK-net stations and 0.3-3.0 Hz short-period recordings from Hi-net stations establish that the shaking variations result from a combination of differences in seismic source spectra and path attenuation. Eleven earthquakes with M_w = 6.0 to 7.6 are analyzed, including interplate events at different positions on the megathrust within the rupture zone of the 11 March 2011 Tohoku (M_w 9.0) event, and nearby intraplate events within the underthrusting Pacific slab. The relative ground shaking for frequencies of 5-10 Hz is strongest for the 7 April 2011 (M_w 7.2) intra-slab event near the coast, followed by intraplate events beneath the outer trench-slope. Decreasing levels of high frequency shaking are produced by interplate megathrust events moving from the down-dip edge of the seismogenic zone to the up-dip region near the trench. Differential attenuation measurements from averaged spectral ratios of strong-motion recordings indicate that average path attenuation is lower for events deeper on the megathrust or within the slab below the coast. Empirical Green's function analysis isolates the

source spectra for the passband 0.3-3.0 Hz, indicating higher corner frequencies for intraplate events and deep megathrust events than for shallow megathrust events. Similar differences in average source spectra are found for teleseismic P waves. Depth-varying source radiation and path attenuation thus account for the high frequency shaking for the 2011 Tohoku mainshock originating from the down-dip portion of the megathrust.

3.1 Introduction

The 11 March 2011 M_w 9.0 Tohoku earthquake ruptured across the entire 200 km seismogenic width of the megathrust fault offshore of northeastern Honshu, producing strong ground motions in Japan and generating a devastating tsunami. Seismological, geodetic, and tsunami data indicate that seismic radiation characteristics varied over the fault surface. Concentrated sources of coherent short-period P wave radiation to teleseismic distances (signal energy that has good phase alignment on a localized grid point when the teleseismic P waves are back-projected to the source region) were located down-dip on the megathrust beneath the coastal environment (e.g., Ishii, 2011; Koper et al., 2011a,b; Meng et al., 2011; Wang and Mori, 2011; Yao et al., 2011), whereas very large slip with little coherent short-period radiation dominated in the up-dip portion of the megathrust from around the hypocenter to the Japan trench (e.g., Ammon et al., 2011; Fujii et al., 2011; Hayes, 2011; Ide et al., 2011; Iinuma et al., 2011; Ito et al., 2011; Koketsu et al., 2011; Lay et al., 2011a; Lee et al., 2011; Maeda et al., 2011; Ozawa et al., 2011; Pollitz et al., 2011; Shao et al., 2011; Simons et al., 2011; Yagi and Fukahata, 2011; Yamazaki et al., 2011; Yokota et al., 2011; Yoshida et al., 2011; Yue and Lay, 2011). Analysis of strong-motion recordings by Kurahashi and Irikura (2011) also indicates that the down-dip region radiated the primary high

frequency energy observed in Japan, with a wide region onshore experiencing strong ground accelerations and moderately high ground velocities (Figure 3.1).

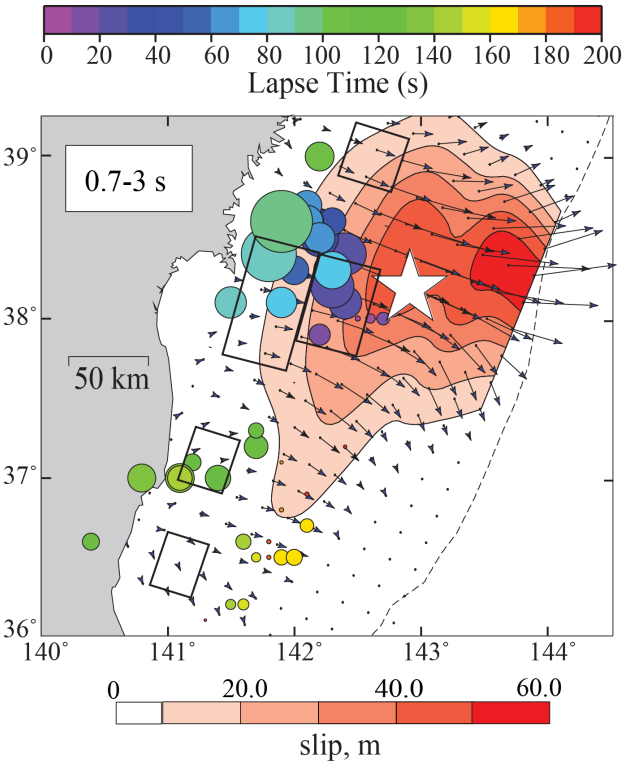

Figure 3.1 Map summarizing rupture characteristics for the 11 March 2011 Tohoku earthquake. The coseismic slip distribution is from inversion of regional continuous GPS observations by Yue and Lay (2011). The vectors orientations indicate the slip direction, and the vector magnitudes and contoured color scale indicate the total slip on each subfault. The white star indicates the epicentral location from Zhao et al. (2011). The position and timing of sources of coherent short-period teleseismic P wave radiation in the bandpass imaged by back-projection of recordings at North American seismic stations, mainly from the EarthScope Transportable Array, are shown by the colored circles, with radius scaled proportional to relative beam power (Koper et al., 2011b). The rectangles indicate estimated source locations of high frequency strong ground motions determined by Kurahashi and Irikura (2011). Note that the regions with large slip locate up-dip, toward the trench (dashed line), whereas the coherent short-period radiation is from down-dip, near the coastline.

The variation in seismic radiation from different portions of the rupture zone for the great 2011 Tohoku event may be the result of intrinsic differences in rupture behavior across the megathrust. Kanamori (1972) recognized that the shallowest part of the plate boundary megathrust just to the north of the 2011 event produced the great 1896 tsunami earthquake, with apparently long rupture duration and anomalously low short-period seismic wave amplitudes. Estimates of moment-scaled rupture durations inferred from teleseismic P wave data for moderate size (M_w ~5.8-6.8) events on the megathrust offshore of northeastern

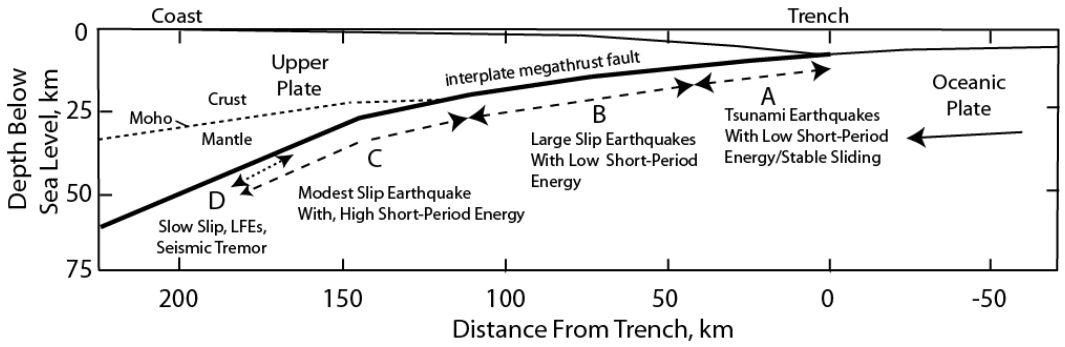

Figure 3.2 Schematic cross-section of a generic interplate megathrust fault with 4 domains of depth-varying rupture characteristics: A – near-trench domain where tsunami earthquakes or anelastic deformation and stable sliding occur; B – central megathrust domain where large slip occurs with minor short-period seismic radiation; C – down-dip domain where moderate slip occurs with significant coherent short-period seismic radiation; D – transitional domain, only present in some areas, typically with a young subducting plate, where slow slip events, low frequency earthquakes (LFEs), and seismic tremor can occur. (Modified from Lay et al., 2012).

Honshu have along-strike and along-dip variations, with a general tendency of decreasing moment-scaled duration as depth increases on the megathrust (Bilek and Lay, 1998; Lay and Bilek, 2007; Bilek et al., 2012). Systematic patterns as a function of depth in the seismic radiation spectra of great and moderate size events on the megathrusts in other subduction zones have also been observed. Lay et al. (2012) proposed a general megathrust rupture segmentation scenario with depth-varying Domains, A, B, and C (Figure 3.2), based on a large suite of observations. Domain A extends across the shallowest ~10 km depth extent of the megathrust, and hosts tsunami earthquake ruptures with low moment-scaled energy and weak short-period radiation like the 1896 event; Domain B spans the central portion of the megathrust over a depth range of ~25 km with large coseismic slip but modest coherent short-period radiation, and Domain C has smaller coseismic slip and strong coherent bursts of short-period radiation over the deepest 10-15 km depth range of the seismogenic megathrust. Subduction zones with shallow dipping megathrusts and young subducting oceanic plates (Southwest Japan, Cascadia, Mexico) appear to have an additional Domain D at relatively

shallow depths of 30-45 km, with slow slip events, low frequency earthquakes, and seismic tremor. This transitional Domain D may not exist down-dip of Domain C in all regions; as yet, there is no indication of Domain D behavior for the northeastern Honshu megathrust, which dips fairly steeply and involves a very old underthrusting Pacific plate.

The great 2011 Tohoku earthquake ruptured across the entire width of the megathrust, so Domains A, B, and C appear to have failed in a single event. The spatial partitioning of high- and low-frequency seismic radiation from the rupture zone of such a great earthquake is difficult to resolve, so the conceptual model of megathrust rupture segmentation requires quantification by characterizing the overall source spectra of events that have ruptures confined to within each candidate Domain. We address this for the source region of the 2011 Tohoku earthquake using regional and teleseismic data. This is still challenging because the frequency-dependent attenuation structure is not known in detail. As a result, most studies of source spectrum variations across the megathrust have been restricted to frequencies <2 Hz using teleseismic data (see a summary by Lay et al., 2012). We use regional data to extend the spectral bandwidth to 3-10 Hz, thereby also connecting the megathrust rupture segmentation behavior to local ground shaking effects and seismic hazard.

We also consider source spectrum variations between large events on the megathrust and nearby large intraplate events within the subducting slab. The intraplate events include shallow outer trench slope normal-faulting events and deep thrust-faulting events below the megathrust near the coast. These commonly observed intraplate events are caused by large-scale deformation of the bending and sinking slab, influenced by temporally varying interplate stresses on the megathrust (e.g., Christensen and Ruff, 1988; Lay et al., 1989). Both types of intraplate events can produce stronger regional shaking relative to comparable seismic moment events on the megathrust, so they have particular seismic hazard significance. Outer

rise normal-faulting events commonly radiate large amplitude short-period seismic waves that generate strong shaking even though they are far offshore (Kanamori, 1971; Ammon et al., 2008; Hino et al., 2009; Lay et al., 2011b). The intra-slab earthquakes at depths of ~40-100 km often lie below populated areas and can cause considerable damage to buildings because of high-frequency-rich strong ground motions with large peak ground accelerations, as were observed for the 15 January 1993 Kushiro-Oki (M_w 7.6) earthquake under Hokkaido (e.g., Morikawa and Sasatani, 2004), the 24 March 2001 Geiyo (M_w 6.8) earthquake under southwestern Honshu (e.g., Miyatake et al., 2004; Kanamori et al., 2012), the 26 May 2003 Miyagi-Oki (M_w 7.0) earthquake under the Honshu coast (e.g., Tsuda et al., 2006), and the 23 July 2008 (M_w 6.8) Northern Iwate, Japan earthquake (e.g., Suzuki et al., 2009; Kanamori et al., 2012). It is well-recognized that the strong ground shaking for intraplate events tends to be systematically higher amplitude than the ground motions from interplate events (e.g., Youngs et al., 1997; Si and Midorikawa, 1999; Purvance and Anderson, 2003), and this is commonly attributed to higher stress drops for intraplate events. Investigations of the frequency content of the ground shaking and source processes of events near the northeastern Japan megathrust are important both for understanding the variations in rupture process between intraplate and interplate faults, and for considering the seismic hazard from all types of faulting near the megathrust.

Japan's extensive deployment since 1995 of high-quality strong motion stations of K-net and KiK-net, and the High Sensitivity Seismographic Network (Hi-net) provides superb data for investigating variations of frequency content of large earthquake ruptures on the Tohoku megathrust and nearby intraplate faults and relating the behavior to observations for the 2011 mainshock. We analyze the ground shaking and earthquake source spectra for 11 large (M_w 6.0-7.6) earthquakes from 2003-2011 (Table 3.1), including a large thrust event (M_w 7.1; 7

April 2011) that occurred in the Pacific slab below the down-dip limit of the 2011 Tohoku earthquake and an outer-rise normal-faulting event (M_w 7.6; 11 March, 2011) that occurred 40 minutes after the great 2011 event. Both events were probably triggered by stress changes resulting from the large fault slip in the great 2011 event (Ohta et al., 2011; Lay et al, 2011b). Nakajima et al. (2011) suggest that the thrust event possibly involved reactivation of a pre-existing hydrated fault with over-pressurized fluids or serpentine minerals that had originally formed during bending near the trench. We also consider another outer trench slope normal-faulting event (M_w 7.0, 14 November 2005) and its preceding 2005 Miyagi-Oki interplate event (M_w 7.3, 16 August 2005) located in the down-dip region of the megathrust, along with seven other underthrusting events located in megathrust Domains A, B or C. To suppress path effects we use the empirical Green's function method (EGF) (e.g., Irikura, 1986), extracting reliable average source spectra that we can relate to the type of faulting and position along the megathrust. The characteristics of these large events are thus relevant to both basic earthquake source physics and regional seismic hazard.

Table 3.1 Event Information

No.	Event	Centroid Time	Longitude (°N)	Latitude (°E)	Depth (km)	Magnitude (M_j)	Cut-off Freq. (Hz)	Rupture Domain
1	2003-10-31	01:06:41.00	142.9790	37.8555	19	6.8	-	B
-	2003-11-01	11:24:41.00	142.7596	37.9219	24	3.8	4.0	-
-	2003-11-05	00:27:23.00	142.8120	37.9042	28	3.9	5.0	-
-	2003-11-19	10:49:41.00	142.9150	37.7806	25	3.8	5.0	-
2	2005-08-16*	02:46:25.70	142.2780	38.1500	42	7.2	-	C
-	2004-11-07	18:28:46.00	141.9120	38.3093	46	4.1	5.0	-
-	2006-05-06	11:45:43.00	142.2240	38.4476	40	4.2	3.0	-
-	2009-03-25	01:23:14.00	142.0270	38.2189	48	4.2	4.0	-
-	2011-04-04	21:52:57.00	141.9910	38.2976	52	4.2	2.0	-
-	2011-04-19	03:02:52.00	141.8360	38.1597	57	4.0	2.0	-

-	2011-04-26	04:52:21.00	141.8667	38.3331	53	4.0	2.0	-
3	2005-11-14*	21:38:51.30	144.9450	38.0270	45	7.2	-	(1)
-	2011-03-21	10:43:08.00	144.8160	38.0613	9	4.6	3.0	-
-	2011-03-27	14:44:25.00	144.7700	38.0255	18	4.5	1.0	-
4	2005-12-02	13:13:12.00	142.5730	38.0276	34	6.5	-	B
-	2003-11-01	11:24:41.00	142.7596	37.9219	24	3.8	3.0	-
-	2003-11-04	15:15:40.00	142.6650	37.8829	30	3.6	4.0	-
-	2006-01-26	16:41:31.00	142.6720	38.0060	30	3.9	5.0	-
-	2007-12-02	15:41:50.00	142.7030	37.9037	33	4.0	3.0	-
-	2008-11-17	17:27:01.00	142.6460	37.9837	28	4.1	2.0	-
-	2010-04-02	18:32:57.00	142.6750	38.0069	30	4.1	2.0	-
5	2008-07-19	02:39:35.00	142.5460	37.5138	18	6.9	-	B
-	2003-11-01	05:54:39.00	142.8664	37.4729	17	3.7	5.0	-
-	2003-11-06	23:55:24.00	142.7880	37.4759	22	3.7	5.0	-
-	2005-12-20	22:44:53.00	142.5540	37.5132	24	4.0	3.0	-
-	2008-02-11	09:31:42.00	142.7980	37.4625	17	4.0	3.0	-
-	2009-09-03	05:29:17.00	142.6727	37.5596	28	3.7	5.0	-
6	2010-03-14*	17:08:04.10	141.8180	37.7240	39.8	6.7	-	C
-	2004-08-23	11:48:10.00	141.8740	37.7544	43	4.2	3.0	-
-	2007-10-11	16:19:55.00	141.9550	37.9106	45	3.9	3.0	-
-	2007-10-23	01:22:58.00	141.7500	37.7012	45	4.0	3.0	-
-	2010-05-12	08:52:59.00	141.9800	37.9535	47	4.1	3.0	-
-	2011-04-04	15:47:06.00	141.5730	37.5818	49	4.1	3.0	-
7	2011-03-09	02:45:32.00	143.0820	38.5372	19	7.3	-	B
8	2011-03-09(1)	21:22:10.00	143.6240	38.1150	32	6.0	-	A or B
9	2011-03-09(2)	21:24:08.00	143.0380	38.2203	25	6.4	-	B
-	2003-09-08	21:15:59.00	143.2530	38.5579	26	3.8	5.0	-
-	2008-05-28	20:43:33.00	143.1946	38.5662	22	3.9	3.0	-
-	2008-12-04	01:42:24.00	143.2728	38.5131	23	4.2	2.0	-
-	2008-12-04(1)	18:42:05.00	143.1360	38.5527	23	4.1	3.0	-
-	2008-12-07	20:39:34.00	143.2500	38.5438	27	4.2	3.0	-
-	2009-02-03	15:22:49.00	143.1856	38.4286	25	3.9	4.0	-
-	2011-03-11	05:46:08.10	142.8610	38.1040	23.7	9.0	-	A/B/C

10	2011-03-11(1)	06:26:05.00	144.8980	38.1871	19	7.6	-	(1)
-	2011-03-21	10:43:08.00	144.8160	38.0613	9	4.6	3.0	-
-	2011-03-27	14:44:25.00	144.7700	38.0255	18	4.5	1.0	-
11	2011-04-07	14:32:50.00	142.1950	38.2478	57	7.2	-	(2)
-	2004-11-07	18:28:46.00	141.9120	38.3093	46	4.1	5.0	-
-	2006-05-06	11:45:43.00	142.2240	38.4476	40	4.2	3.0	-
-	2009-03-25	01:23:14.00	142.0270	38.2189	48	4.2	4.0	-
-	2011-04-04	21:52:57.00	141.9910	38.2976	52	4.2	2.0	-
-	2011-04-11	21:03:37.00	141.9620	38.4233	58	4.2	2.0	-
-	2011-04-18	10:56:05.00	142.0010	38.4951	54	4.2	2.0	-
-	2011-04-19	03:02:52.00	141.8360	38.1597	57	4.0	2.0	-
-	2011-04-26	04:52:21.00	141.8667	38.3331	53	4.0	2.0	-

***** The origin time, location and magnitude come from the GCMT catalog for event 2005-08-16, 2005-11-14 and 2010-03-14, while for other events this information comes from the regional CMT catalog (Asano et al., 2011). Events numbered from 1 to 11 are large events, followed by from 2 to 8 small events used as EGFs in the source spectra analysis.

3.2 Ground Shaking Analysis

Reliable measurements of ground shaking for large earthquakes are of central importance for guiding appropriate building standards and proper design of critical facilities such as nuclear power plants located close to subduction zones. In this section we examine spectral characteristics of ground motion induced by the large events in Figure 3.3, which are located on and around the rupture zone of the great 2011 Tohoku earthquake. We consider spectral ratios of ground motions relative to the large foreshock event on 2011-03-09 (M_w 7.3) located near the hypocenter of the 2011 mainshock. This foreshock is located in Domain B and we use it as a reference, as we are interested in relative levels of high-frequency ground motions produced as a function of depth of the source along the Tohoku megathrust, and the relative frequency content of ground motions from megathrust versus intra-slab faulting.

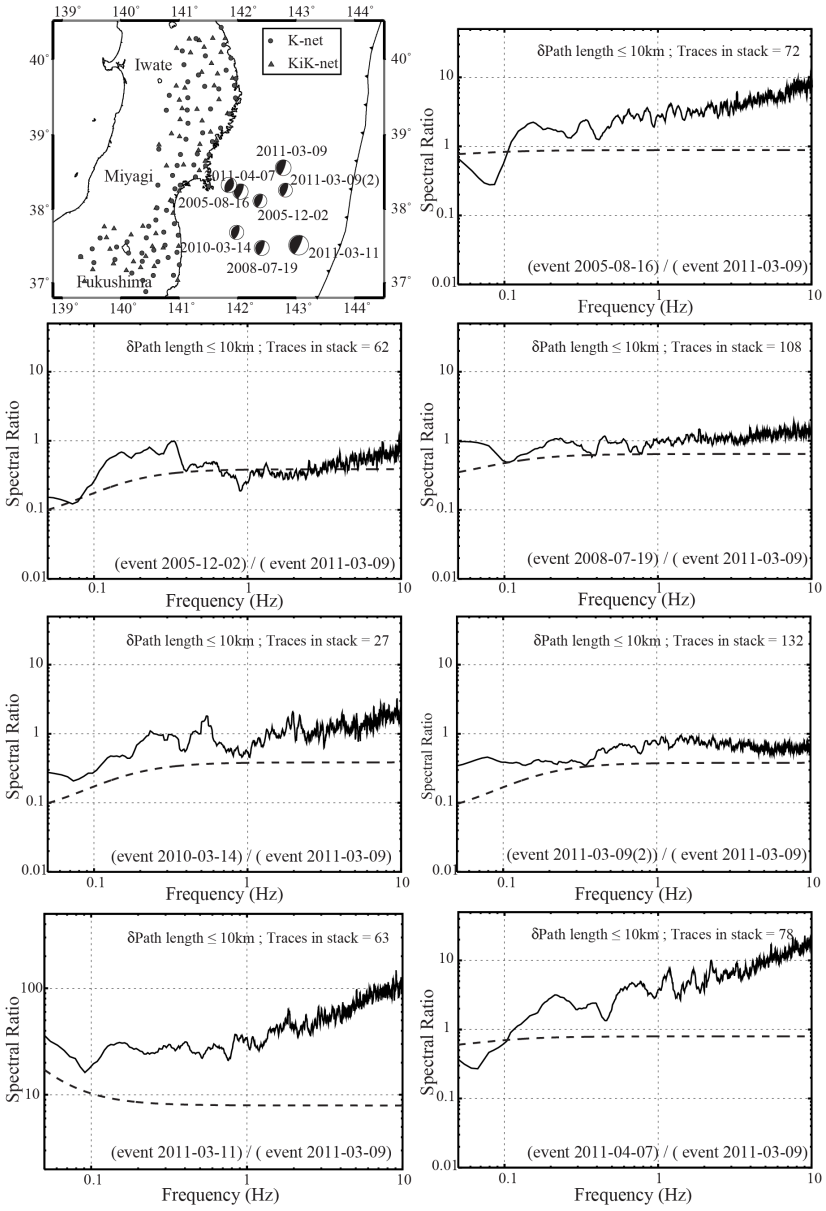

Figure 3.3 Stacked spectral ratios of ground accelerations for large events in the Japan subduction zone around Tohoku relative to the foreshock on 2011-03-09 (Mw 7.3) being the reference (denominator) in each case. Subsets of K-net and KiK-net strong motion sensors in Iwate, Miyagi, and Fukushima prefectures (map) with common path lengths from sources and receiver (within 10 km) are used. The stacked, smoothed spectral ratios from all three components 100-s-long signals for the indicated number of channels are shown. The dashed curves are predicted spectral ratios for reference Brune w-2 source models for a 3 MPa constant stress drop and the regional CMT seismic moments. The barbed solid curve in the map indicates the position of the trench.

We use accelerometer recordings from the K-net and KiK-net strong ground motion networks operated by NIED (National Research Institute for Earth Science and Disaster Prevention), which provide many on-scale recordings for each of the large regional events. We restrict our analysis to the closest stations, located in Iwate, Miyagi and Fukushima

Prefectures (Figure 3.3). The KiK-net stations have three component dual surface/borehole accelerometers while K-net stations are all located at the surface. The borehole records provide higher signal-to-noise ratios with less influence of site effects, particularly nonlinear affects that can occur for surface sensors with particularly strong shaking for stations on either low velocity materials or high velocity materials (e.g., Tsuda et al., 2006; Assimaki et al., 2008). Our approach involves computing spectral ratios of recordings for two events at the same station component by component with emphasis on frequencies in the passband 0.1-10.0 Hz. Spectral ratios cancel out the instrument responses and, to the degree that they do not vary rapidly with backazimuth or due to nonlinearity, site effects. The individual spectral ratios for all stations and components are averaged to give the spectral ratio for each event relative to the foreshock.

We initially computed average ratios of spectra for complete, 100-s-long ground motions for all common station components for each event relative to the 2011-03-09 foreshock. We find systematic spatial trends, with relatively high spectral ratios for events near the coast and in the outer rise (Figure 3.3). There is no significant difference between the event-averaged spectral ratios calculated separately for data from KiK-borehole observations, KiK-surface observations and K-net surface observations below 10 Hz (Figures S1-S8 in the electronic supplement compare the average ratios for stations in each azimuthally distinct prefecture for each instrument type). This indicates negligible contributions to the averaged ratios from any nonlinearity in the site responses within our passband for the modest range of large earthquake size considered in this section, so the ratios in Figure 3.3 combine all types of sensors. Given that the spectral ratios are influenced by multiple factors such as relative source spectra, relative geometric spreading factors, relative radiation pattern factors, and relative path attenuation, we include in the average spectral ratio stacks in Figure 3.3 only

those ratios for which the hypocenter to receiver direct line path lengths from the numerator event are within 10 km of the path lengths from the denominator (reference) event. Requiring common path lengths for each ratio restricts the azimuthal sampling and reduces the effects of geometric spreading differences and common attenuation effects (as for a uniform Q model), so the ratios can be viewed as direct measures of relative ground shaking referenced to the foreshock event. This restriction to common path lengths mainly affects the baselines of the ratios, but the frequency-dependent trends of the ratios remain similar to those for the ratios of all data grouped by prefecture shown in Figures S1-S8 in the electronic supplement.

We use the global centroid moment tensor (GCMT) centroid locations for each event to compute the source-receiver distances, recognizing that these centroid estimates may have some absolute bias, but it is likely to be in common for the full set of events considered here because they are relatively close together and have similar size and mechanisms. Similar results are found using Japan Meteorological Agency (JMA) hypocenters, or regional centroid moment tensor (CMT) centroids obtained by NIED or Asano et al. (2011), although the specific groups of stations that get included can vary (the subset of stations used in the equal path length stacks for each event in Figure 3.3 are indicated in the corresponding Figures S1-S8 in the electronic supplement). The individual spectra were smoothed with an 11-sample running mean and the spectral ratios were averaged over all components to give the spectral ratios extending to 10 Hz shown in Figure 3.3. The numbers of channels used for averaging are from 60 to 130 with the exception of just 27 channels for the event 2010-03-14 which is located furthest away from the reference event 2011-03-09. The constraint to similar path lengths within 10 km eliminated all stations for outer rise events, but those will be considered below (spectral ratios for all strong-motion observations are shown for the 2011-03-11(1) outer rise event in Figure 3.S7 in the electronic supplement).

To provide a consistent reference source spectrum behavior, we use an "omega-squared" spectrum, $\hat{\hat{M}}(f)$, given by

$$\hat{\hat{M}}(f) = \frac{M_0 f_c^2}{f^2 + f_c^2} \tag{1}$$

where M_0, f $(\omega = 2\pi f)$ and f_c are, respectively, the seismic moment, frequency (angular frequency), and the corner frequency given by

$$f_c = c\beta \left(\frac{\Delta\sigma}{M_0} \right)^{1/3} \tag{2}$$

Here β, Δσ, and c are the shear wave velocity, a stress parameter, and a constant, respectively. This is the form introduced by Brune (1970) to explain the S-wave radiation. The constant c is 0.49 if all the quantities are given in SI units. In the context of our study, Δσ is just a scaling parameter (Boore, 1983) and is not necessarily meant to be the stress drop at the source. The stress drop of an earthquake can be defined unambiguously if it is spatially uniform. However, the stress drop in real earthquakes is most likely spatially very complex and cannot be defined in a simple way. In this paper we use the term stress drop for the stress parameter, Δσ in (2). The stress parameter does not necessarily equate to the stress drop of the source, but for purposes of qualitative interpretations, we use Δσ as a rough approximation of the source stress drop. In our reference spectrum, we use β =3.75 km/s, and Δσ =3 MPa. The predicted spectral ratios for each event pair assuming these parameters are constant are shown by dashed lines in Figure 3.3.

The common path-length average spectral ratios in Figure 3.3 indicate that overall ground shaking has systematic variation with event position on the megathrust, as is indicated by the average ratios of all data in each prefecture (Figures S1-S8 in the electronic

supplement). The spectral ratios for events 2005-12-02, 2008-07-19 and 2011-03-09(2), all located in Domain B near the reference event 2011-03-09, are quite consistent with predictions for the Brune ω^{-2} source models. This does not mean the assumption of 3 MPa stress drop is correct, but there is at least relative consistency in ground shaking spectra produced by nearby ruptures within the central megathrust domain. The ground shaking spectral ratios show a rapid increase in amplitude with increasing frequency from 0.1 Hz to 10 Hz for the Miyagi-Oki 2005-08-16 event in Domain C, the mainshock of 2011-03-11 which ruptured Domains A, B and C, and the 2011-04-07 intraslab event, all relative to the reference Domain B event.

Figure 3.4 shows variation of average spectral ratio amplitudes at 10 Hz for these total ground shaking measurements (from Figure 3.3) relative to the reference ω^{-2} source model spectral ratios, as a function of distance of each event's JMA location from the trench. Along the megathrust, relatively larger ground shaking is produced by events 2005-08-16 and 2010-03-14, which are in the down-dip (Domain C) portion of the megathrust, and there is no systematic high-frequency ground shaking enhancement for up-dip events 2005-12-02, 2008-07-19 and 2011-03-09(2) near the reference Domain B event 2011-03-09. Relatively high-frequency ground shaking was produced by the 2011 Tohoku mainshock, which ruptured across the entire width of the megathrust as indicated by the line with arrows. It is plausible that the short-period content in the mainshock signals originates primarily from the down-dip region of the fault, as suggested by the location of subsources of strong-ground motion energy radiation inferred by Kurahashi and Irikura (2011). These spectral variations are a combined effect of source radiation and path attenuation differences, but directly indicate that large near-coast events on the down-dip part on the megathrust produce a factor of 2 to 4 stronger 10 Hz ground shaking on Honshu. This tendency of increasing high-frequency shaking from

up-dip region to down-dip region along the megathrust could be accounted for by using distance-from-trench ground shaking predictions for offshore megathrust events, given the geometry of the subduction zone, like that shown in Figure 3.4.

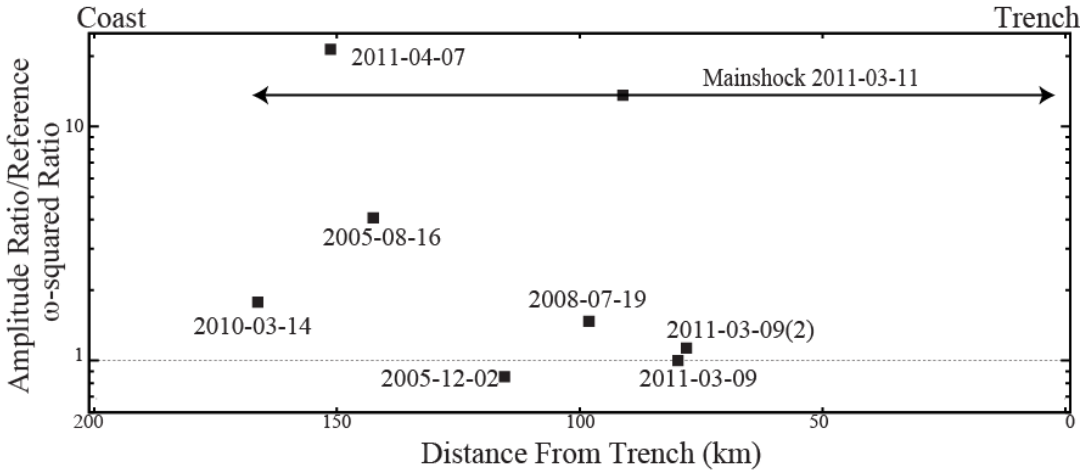

Figure 3.4 The 10 Hz spectral ratio amplitudes for large events around the Tohoku megathrust relative to the foreshock on 2011-03-09 normalized by spectral ratios for the Brune w-2 source models, plotted as a function of perpendicular distance from the trench to the JMA source locations.

The average spectral ratio of the intraplate event 2011-04-07 is significantly larger at high frequencies (Figure 3.3). The normalized spectral ratio of this event at 10 Hz (Figure 3.4) is ~ 23 times larger than that for the reference Domain B event 2011-03-09 and ~5 times larger than that for the nearby Domain C interplate event 2005-08-16. Strong short-period radiation has also been observed from large intra-slab earthquakes (the 1993 Kushiro-Oki and 1994 Hokkaido Toho-Oki earthquakes) along the southern Kurile–Hokkaido arc by Morikawa and Sasatani (2003), and the source rupture process on those events show that the observed high-frequency-rich ground motion is due to the short duration rupture over a small source area with high stress drop (Morikawa and Sasatani, 2004). Since there are significant differences in the propagation paths and the focal mechanisms between the intraplate event 2011-04-07 and the interplate event 2011-03-09, we cannot yet directly attribute the

difference to the source properties, but from the earthquake hazard perspective, the ground shaking from the intra-slab event at intermediate depth clearly poses significantly greater hazard for large events. This is supported by comparison with the relative spectra for the 2011 Tohoku mainshock (Figures 3 and 4). At approximately common propagation distances, the M_w 7.2 intraplate event produced about twice as high average ground shaking at 10 Hz compared to the M_w 9.0 mainshock (Figure 3.4). Because distance from the mainshock is ambiguous, direct comparisons at common stations are perhaps more meaningful, but even in that case, the amplitudes of shaking from the intraplate event are about 30-50% of those for the great event despite their great difference in seismic moment (Figures S6 and S8 in the electronic supplement).

The complete ground motion spectra for 100-s-long time windows capture total ground shaking behavior, but clearly multiple seismic phases are included in those windows, with the high frequency signal being dominated by shear wave energy. While those measurements allow us to include the mainshock spectra for comparison, for the shorter rupture duration $M_w \sim 7.0$ events we can measure the spectra for specific P and S time windows to evaluate any differences in ground shaking for different phases, and for measuring overall relative attenuation differences. We manually picked the arrival times of P and S waves, and calculated the P spectral ratios for vertical components for the interval from a few seconds before the P arrival to the arrival time of the S wave. For S and SH spectral ratios we use 30 s time windows beginning just before the S arrivals using three components and tangential components, respectively. The spectral ratios were again made relative to the corresponding signals for the foreshock on 2011-03-09 (Figure 3.5), for stations with distance differences of less than 10 km for each event pair. The isolated phase spectral ratios are not calculated for the 2011 Tohoku event because of the long source duration and ambiguity of S wave onsets.

The behavior of the isolated phase spectral ratios is very similar to what was found for the total ground shaking spectra. Figure 3.5 shows that the P, S and SH spectra all have similar frequency enrichment for the intraplate event 2011-04-07, and Domain C events 2005-08-06 and 2010-03-14, with clear distinction from the other three Domain B events.

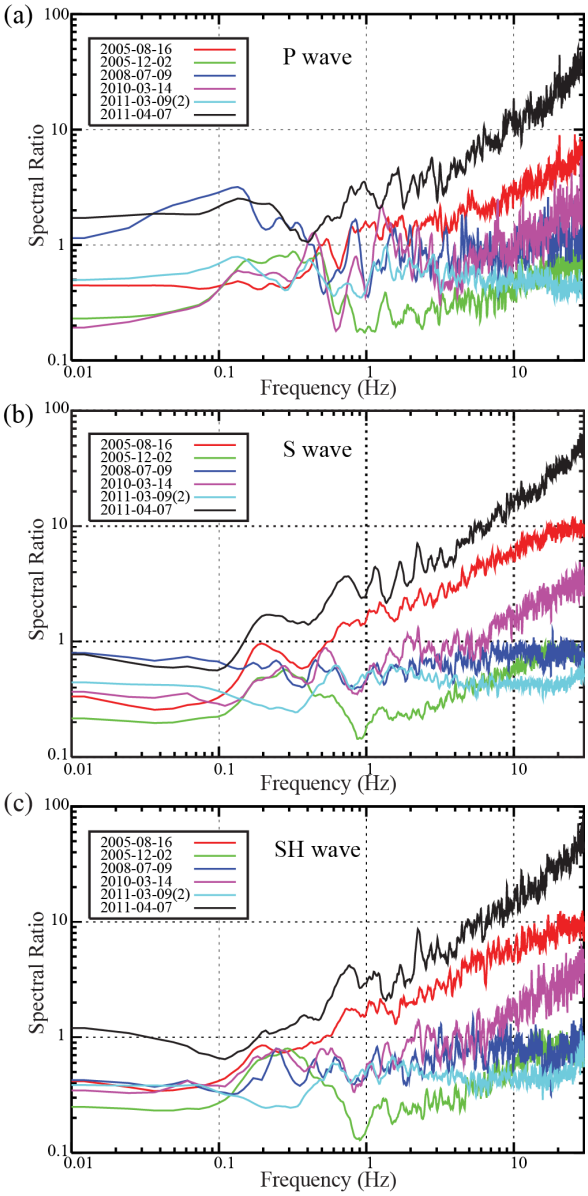

Figure 3.5 Stacked P, S and SH ground acceleration spectral ratios for large events relative to the foreshock on of 2011-03-09 for the same K-net and KiK-net strong motion data used in Figure 3.3. Only event-stations pairs with path-length difference within 10 km of each other are used. The time window for P spectral ratios is from the arrival time of P wave to the arrival time of S wave and only vertical components are used. 30 s time window after the arrival time of S wave are used for calculating S and SH wave spectra using three components and tangential components, respectively.

The log-log spectral ratio plots in Figures 3.3 and 3.5 show some characteristic upward curvature of the spectral ratios suggestive of differential attenuation relative to the reference

event 2011-03-09. These spectral ratio trends can result from combined effects of differential path attenuation and differential source spectral shape (e.g., Purvance and Anderson, 2003). To provide a first-order quantification of the size of possible differential attenuation effects, we assume that the spectral shape differences are negligible (later we will show that this is actually not the case for the intraplate events) and use a simple convolution model for the ground motions to estimate average differential attenuation affecting frequencies out to 10 Hz:

$$\ln\left(\frac{U(f)}{U_{ref}(f)}\right) = \ln\left(\frac{S(f)R^{pt}G(f)R(f)I(f)}{S_{ref}(f)R^{pt}{}_{ref}G_{ref}(f)R_{ref}(f)I_{ref}(f)}\frac{e^{-\pi ft^*}}{e^{-\pi ft^*_{ref}}}\right) \quad (3)$$

where U(f) is the ground motion, S(f) is the source function, R_{pt} is an average radiation pattern term for the signal in the time window, G(f) is the elastic propagation effect, R(f) is the receiver site response effect, I(f) is the instrument response, and t^* = travel time/Q, where the quality factor, Q, is assumed to be independent of frequency, f, for frequencies less than 10 Hz. The assumption of constant Q may not be valid for many of the spectral ratios extending to higher frequencies; our goal here is not to characterize detailed path attenuation parameters (which should be done on a path by path basis rather than for an aggregate spectral ratio measure), but to give a first-order parameterization of the magnitude of differential attenuation that could account for the linear slopes of the event-averaged spectral ratios below 10 Hz. The reference event parameters are represented by the subscript ref. We assume that the instrument response and site response terms cancel quite precisely for each component ratio, and that the elastic propagation terms cancel to first order for geometric spreading and overall amplitude of energy flux over the equal path lengths despite the differences in actual paths for each ratio. The source terms are assumed to have the w-squared model form of (1), for which the ratios are expected to flatten to a constant beyond

the corner frequency of the smaller event in the pair, as indicated by the predicted ratios for 3 MPa stress drop models in Figure 3.3. The differential attenuation $Dt^* = t^*-t^*_{ref}$, can then be estimated over the high frequency portion of the spectral ratio to the extent that it behaves linearly (as expected for a constant Q situation). We measured Dt^* by least squares linear regression of the natural log spectral ratios across the linear frequency band 0.3-10.0 Hz, over which roughly linear relationships are observed, solving for both slope and intercept of the regression curve. The intercept is allowed to vary to accommodate the uncertainties in precise seismic moments, stress drops, and geometric spreading factors, which shift the ratios up or down.

The Δt^* estimates for the total ground motion ratios and the P, S, and SH ratios relative to the reference event 2011-03-09 are listed in Table 3.2. Corresponding regressions are shown in Figures 3.A9-A12 in the electronic supplement. For frequencies higher than 10 Hz, the spectral ratios begin to flatten and appear to be dominated by noise (or possibly frequency-dependence of Q). The differential attenuation measurements indicate that average path attenuation is lower for events deeper on the megathrust ($Dt^* \sim$ -0.03 to -0.05 s) and within the slab below the coast ($Dt^* \sim$ -0.06 s), while the differential attenuation is smaller ($Dt^* \sim$ 0.0 to -0.03 s) for the three events in the up-dip region of the Tohoku megathrust close to the reference event. The outer rise event 2011-03-11(1) has a negative differential attenuation as well, as indicated by positive slope of the spectral ratio (Figure 3.A7 in the electronic supplement), which suggests that the paths dive into the high velocity, high Q slab rather than traversing the sedimentary wedge. When the differential attenuation is larger, the values for the 100-s-long total ground shaking are closer to those for the S waves, as expected. While we do not believe non-linear effects are significant in the averaged spectral ratios, they would

likely have greater effect for the S wave measures and for the events closer to the coast, possibly giving some variation between P and S behavior.

Table 3.2 Δt^* from Spectral Ratios in Figure 3.3 and Figure 3.5

Event	Δt^*_100s, s	Δt^*_P, s	Δt^*_S, s	Δt^*_SH, s
2005-08-16	-0.0457	-0.0306	-0.0525	-0.0502
2005-12-02	-0.0280	-0.0126	-0.0327	-0.0300
2008-07-19	-0.0159	0.0003	-0.0151	-0.0165
2010-03-14	-0.0314	-0.0126	-0.0348	-0.0344
2011-03-09(2)	0.0057	0.0067	0.0055	0.0040
2011-03-11	-0.0445	-	-	-
2011-04-07	-0.0572	-0.0588	-0.0640	-0.0606

Δt^* is measured for the passband 0.3-10.0 Hz relative to the event 2011-03-09. Δt^*_100s is calculated by fitting the three-component averaged spectral ratios in Figure 3.3 for 100-s-long signals, and Δt^*_P, Δt^*_S and Δt^*_SH are calculated from the spectral ratios of P waves, three-component S waves and SH waves in Figure 3.5, respectively.

Because the data used in the stacked spectral ratios come from a moderate range of paths (tending to be nearby stations in one prefecture or another due to the equal propagation distance requirement, as can be seen in the Figures 3.A1-A8 in the electronic supplement), these differential attenuation estimates provide only an estimate of the average relative attenuation for the large events around the megathrust on paths to the mainland for frequencies less than 10 Hz, under the assumption that source spectral differences are negligible. We emphasize that these differential attenuation measures are provided to indicate the likelihood of systematic variations in attenuation, not as robust measures of the medium properties. The enhancement in high frequency spectra is clearly partly the result of differences in attenuation caused by three-dimensional Q distribution (since the path lengths are similar, the Q must decrease for the paths from events near the coast). Thus, part of the trend seen in Figure 3.4 is caused by systematic differences in attenuation due to

heterogeneous Q structure varying with distance from the coast. However, the baseline shifts in the spectral ratios in Figures 3.3 and 3.5 relative to the reference model indicate that not all of the differences are due to attenuation variations. One could use the estimated differential attenuation values to measure the source spectrum differences, but because of the averaging involved, this is not very precise, and it requires the assumption that all spectra fall off as w^{-2}. In the next section, we will suppress the individual path effects using the EGF method with several small events near each large event to extract reliable average source spectra free of that assumption.

3.3 Source Spectra Analysis

Ground motions produced by an earthquake depend on the event source properties, including seismic source spectrum and focal mechanism, propagation effects including geometric spreading, scattering due to the lateral heterogeneities and anelasticity along the propagation path, and near-surface site amplification effects due to the shallow geological layers beneath the station. The propagation and site effects are very difficult to model for high frequencies, and the empirical Green's function (EGF) method is designed to isolate the source spectrum effects for a large earthquake using records of nearby small earthquakes recorded at the same station. We apply this method to estimate the source spectra of the large megathrust and intra-slab events around the 2011 Tohoku rupture zone.

The EGF method is very dependent on the selection of small events, which should be nearly co-located with the large event, have the same focal mechanism, and have a large difference in corner frequency, which requires a large difference in seismic moment, while still having good signal-to-noise ratio over substantial bandwidth. For offshore events, this is usually difficult to achieve, due to the long paths involved and low signal levels from small

events near the large earthquakes. For the KiK-net and K-net strong ground motion recordings, small events located near to the large earthquakes considered here tend to be poorly recorded except for events close to the coast (where attenuation is relatively low as we have seen). So, we primarily use data from the High Sensitivity Seismographic Network (Hi-net) operated by NIED. This is one of the finest arrays in the world, and each station is equipped with a borehole short-period instrument typically deployed about 100 m below the surface to suppress surface noise, enabling high gain recording of high-quality seismograms for low-magnitude events offshore at many of the same stations for which the large events produce on-scale records. The use of Hi-net borehole data also insures the EGF method will not be affected by nonlinear site responses that sometimes exist for surface sensors when weak-motions are compared with strong-motions (Si and Midorikawa et al., 199l; Tsuda et al., 2006; Assimaki et al., 2008).

Eleven large (M_w 6.0-7.6) earthquakes, including three intra-slab events and eight interplate events around the Tohoku megathrust from 2003-2011 are analyzed using recordings for both the large and small events at the same station. Average spectral ratios for the large events relative to the reference foreshock for P, S, and SH phases are shown in Figure 3.A13 in the electronic supplement. Most of our EGF events have JMA magnitudes M_j ~ 4.0, which is about as small as viable while retaining good signal bandwidth. We use the focal mechanisms, centroid locations, and seismic moment determinations from a revised (relative to NIED rapid determinations) regional Centroid Moment Tensor (CMT) catalog (Asano et al., 2011), which is based on waveform inversion of seismograms from regional Hi-net and broadband F-net stations. For each large event, we have collected data for from 2 to 8 nearby EGF events with M_j 3.8-4.2 except for the distant outer-rise events 2005-11-14 and 2011-03-11(1) for which the EGF magnitudes are a bit larger (M_j ~ 4.5 - 4.6). High-quality

strong ground motion data from KiK-net borehole and a few K-net stations for the near-shore events 2005-08-16, 2011-04-7 and a few of their corresponding small EGF events are included, but we did not find many useful strong motion records for the small events further offshore. The strong-motion spectral ratios are very consistent with those for the Hi-net data for the same and other EGF events over the 0.3-3.0 Hz passband, and we are confident that this subset of data also has no nonlinear behavior of significance. Table 3.1 lists the regional CMT event information for the EGF events used for each large earthquake.

The locations, magnitudes and focal mechanisms of the 11 large earthquakes and their EGF events and the stations used are shown in Figure 3.6. The calculations of P, S and SH spectral ratios between the large events and the EGF events use the same windowing as described in the previous ground shaking section, with all ratios for a given EGF event being averaged for each phase. We then shifted the event-averaged spectral ratios according to the CMT seismic moment of each EGF event to a common reference EGF moment level corresponding to M_w 4.0. For the intraplate event 2011-04-07, the number of EGFs with focal mechanisms matching the mainshock is limited, so we shifted each EGF-average spectral ratio first relative to the EGF event of 2011-04-11 (which has the most favorable focal mechanism) by least-squares fitting the spectral ratios from 0.3-3 Hz, and then shifting all the curves to the reference moment level of M_w 4.0. These moment-corrected spectra are shown in Figure 3.7(a-c), with each curve being for a different EGF event. The degree to which the curves overlay indicates the relative consistency of the CMT seismic moment estimates. The ratios of the 3 MPa constant stress drop w^{-2} reference spectrum for each large event to that of an M_w 4.0 event are shown as reference. For that stress drop, the predicted flattening of the spectral ratios caused by the corner frequency of the EGF event (denominator) is expected to

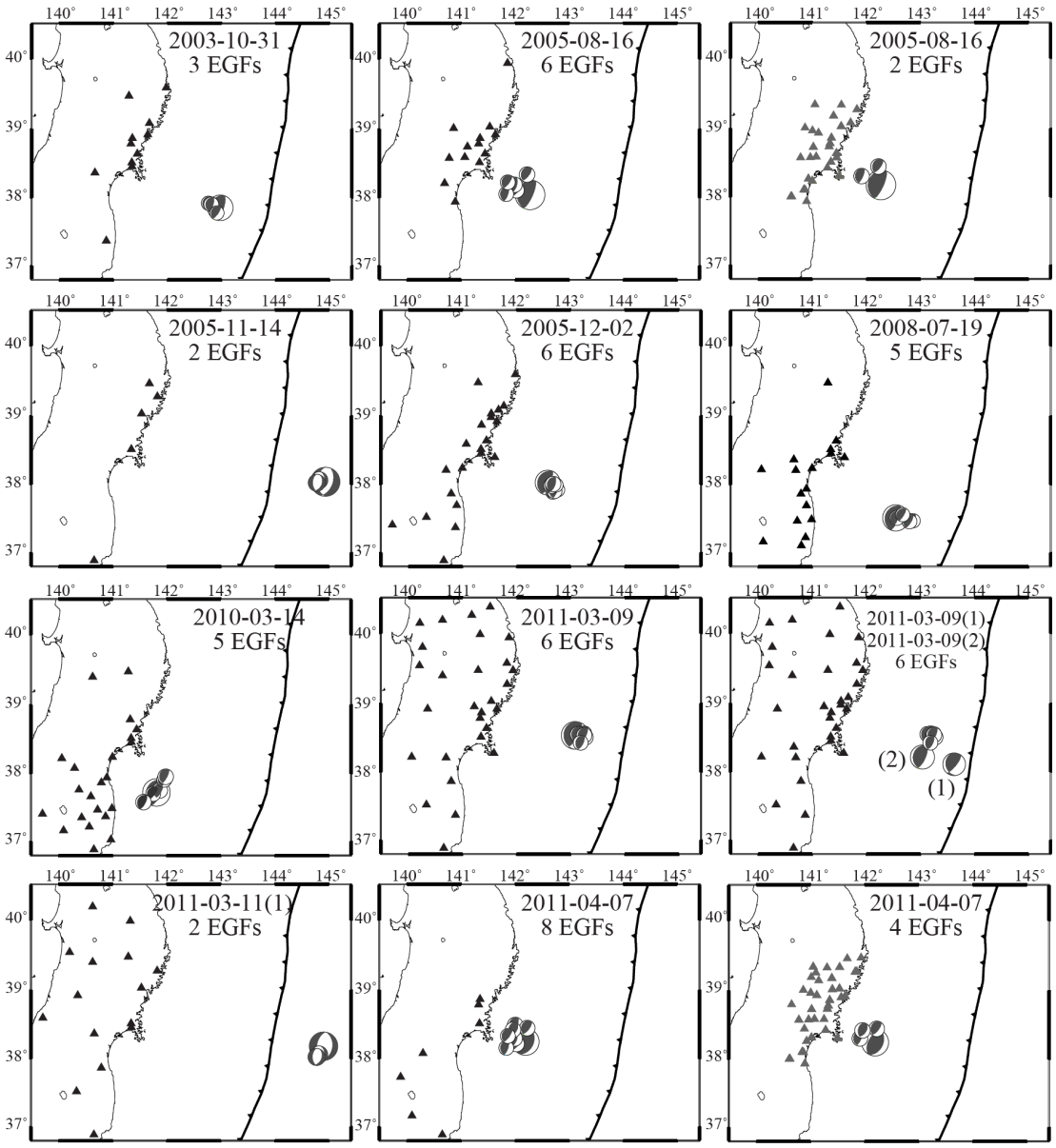

Figure 3.6 Focal mechanisms of the large events around the Tohoku megathrust with from 2 to 8 nearby small events used as empirical Green's functions to correct for path effects on each path to regional seismic stations. Focal mechanisms are mainly from a regional CMT catalog (Asano et al., 2011), although GCMT solutions are used for events 2005-08-16, 2005-11-14 and 2010-03-14, which are not in the regional catalog. The triangles show the stations with large event and EGF recordings, with black symbols for Hi-net stations and the gray symbols for K-net and KiK-net stations (2005-08-16 and 2011-04-07 events only). The barbed solid curves indicate the position of the trench.

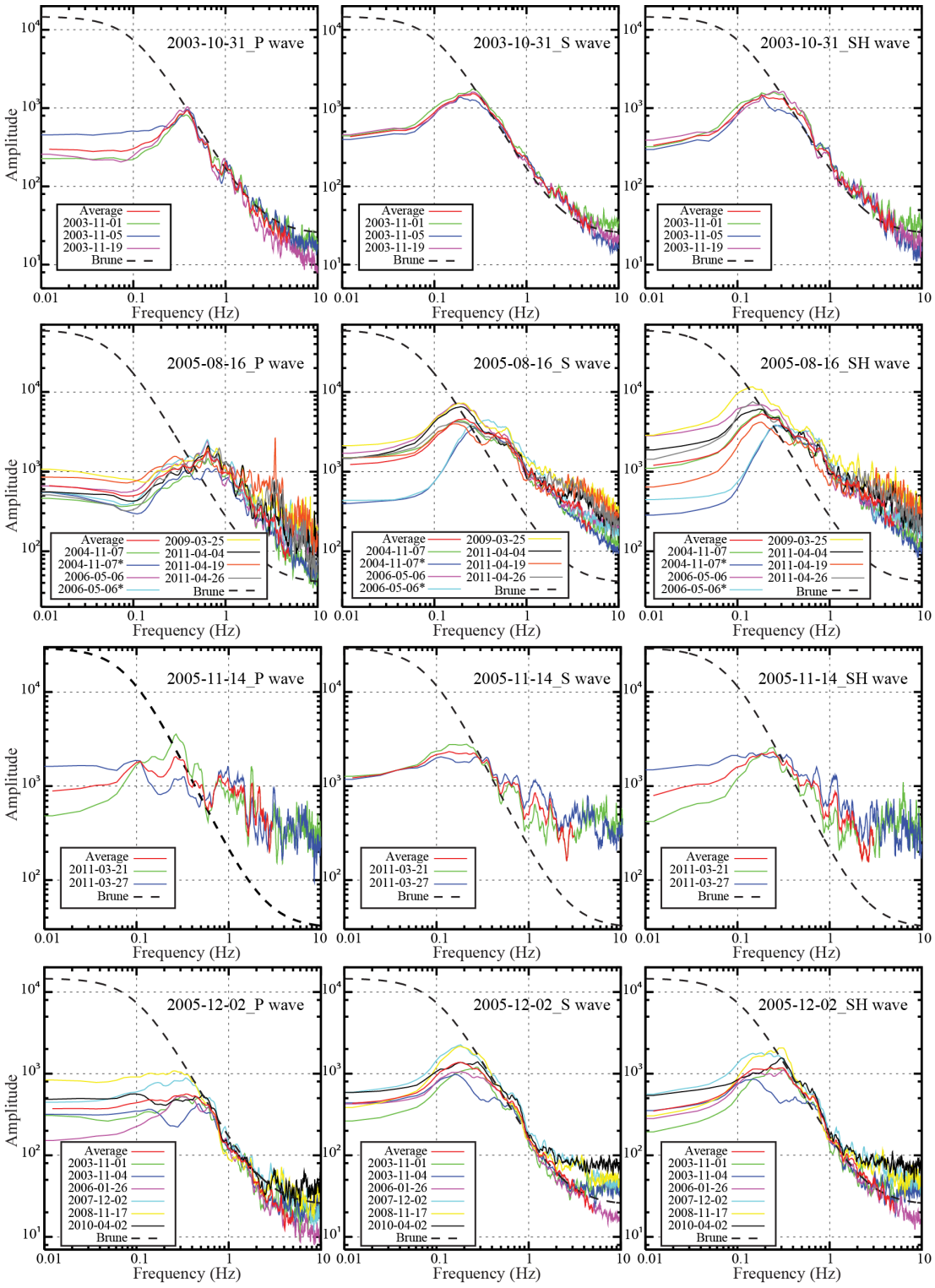
2003-10-31_P wave
2003-10-31_S wave
2003-10-31_SH wave
2005-08-16_P wave
2005-08-16_S wave
2005-08-16_SH wave
2005-11-14_P wave
2005-11-14_S wave
2005-11-14_SH wave
2005-12-02_P wave
2005-12-02_S wave
2005-12-02_SH wave
Amplitude
Frequency (Hz)
Average
2003-11-01
2003-11-05
2003-11-19
2003-11-04
2004-11-07
2004-11-07*
2006-05-06
2006-05-06*
2006-01-26
2007-12-02
2008-11-17
2010-04-02
2009-03-25
2011-04-04
2011-04-19
2011-04-26
2011-03-21
2011-03-27
Brune

Figure 3.7a

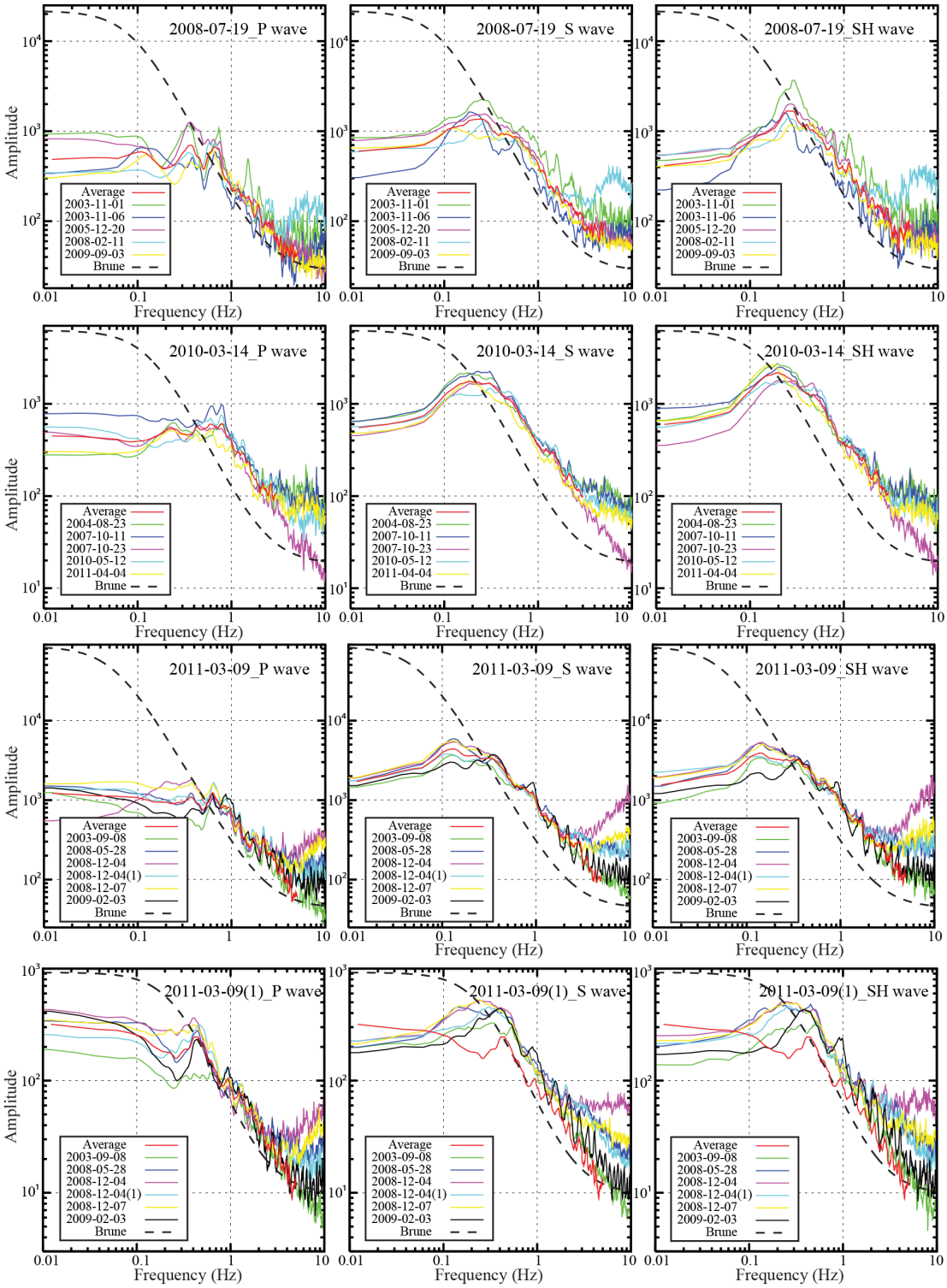
2008-07-19_P wave
2008-07-19_S wave
2008-07-19_SH wave
2010-03-14_P wave
2010-03-14_S wave
2010-03-14_SH wave
2011-03-09_P wave
2011-03-09_S wave
2011-03-09_SH wave
2011-03-09(1)_P wave
2011-03-09(1)_S wave
2011-03-09(1)_SH wave
Amplitude
Frequency (Hz)
Average
2003-11-01
2003-11-06
2005-12-20
2008-02-11
2009-09-03
Brune
2004-08-23
2007-10-11
2007-10-23
2010-05-12
2011-04-04
2003-09-08
2008-05-28
2008-12-04
2008-12-04(1)
2008-12-07
2009-02-03

Figure 3.7b

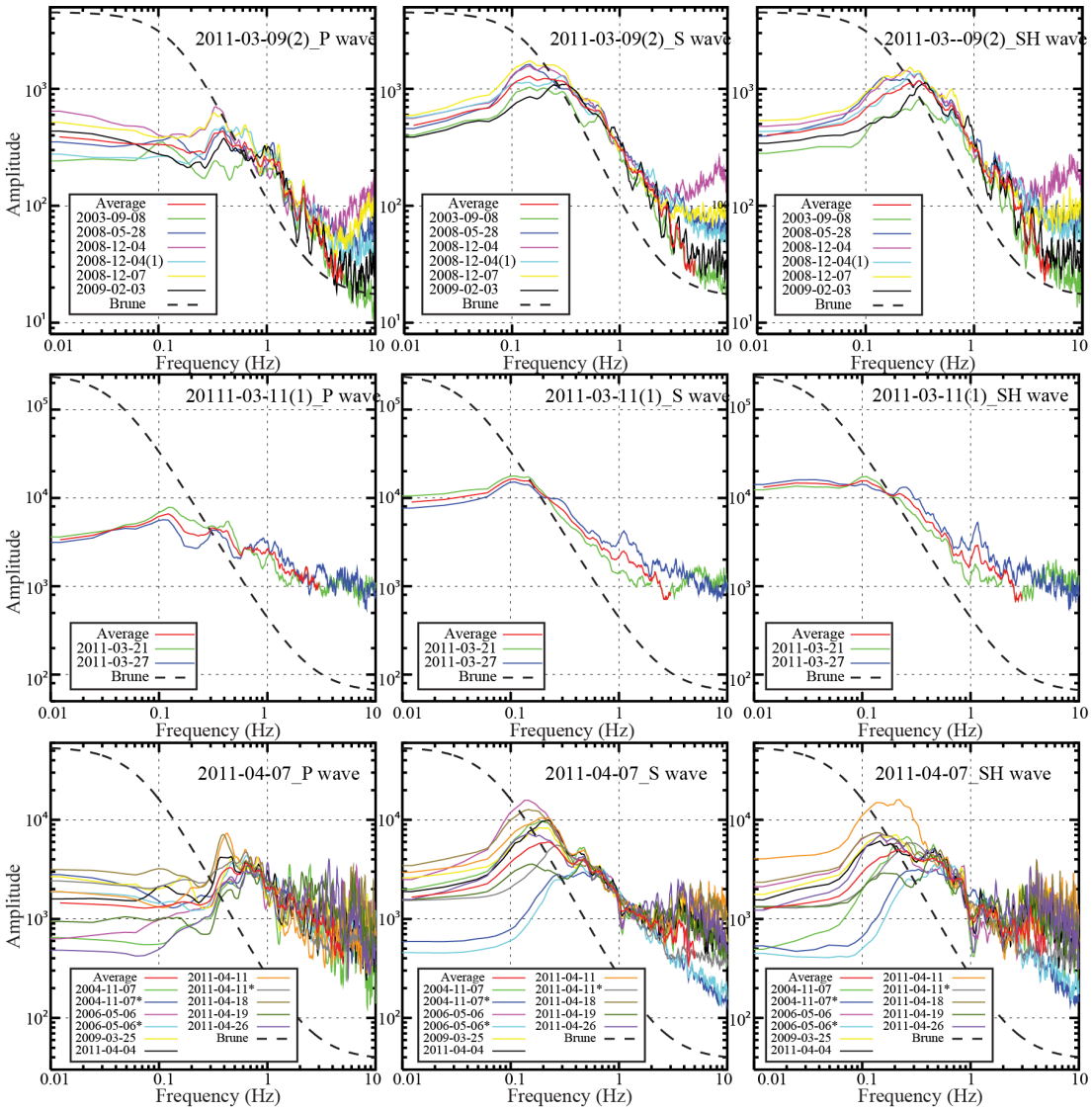

Figure 3.7c

Figure 3.7 P, S and SH source spectra determined using the EGF spectral ratio method. Each curve is the stacked spectral ratio of the large event relative to the indicated EGF event for all stations with data as shown in Figure 3.6. The data time windows and components are the same as in Figure 3.5. The asterisks indicate data from the K-net and KiK-net, with all others being from Hi-net. The red curves are the average source spectra computed from the stacked EGF spectra for frequencies up to the cut-offs indicated in Table 3.1, which is where the EGF corner frequency begins to flatten the spectral ratios. The dashed curves are predicted source spectral ratios for the reference Brune w-2 source models relative to an Mw 4.0 event, with a 3 MPa constant stress drop and the regional CMT seismic moments (GCMT moments are used for the events 2005-08-16, 2005-11-14 and 2010-03-14). The source spectra are reliable from about 0.3 to 3.0 Hz in each case.

initiate at about 2.5 Hz. Because our EGF magnitudes vary somewhat and the stress drops may differ from 3 MPa, some ratios indicate flattening at higher frequency or lower frequency, although noise levels clearly increase above 3 Hz. At low frequency, below ~0.3 Hz, the limited bandwidth of the instruments and the weak long period wave excitation for the small events, lead to a flattening of the ratios. Thus, the reliable bandwidth over which we can estimate the source spectra is limited to the range 0.3-3.0 Hz, which is above the corner frequency for all of the large events. Nonetheless, we obtain stable estimates of the source spectra over this range of frequencies in each case.

We identified the high frequency limit for each EGF-corrected average spectrum before the onset of the flattening effect caused by the small event corner frequency based on linearity of the spectral decay to that point and used these as cut-off frequencies for each case (listed in Table 3.1). We then averaged the EGF-corrected source spectra for each large event over the varying bandwidth provided by each EGF event (essentially extending the bandwidth at high frequency when smaller EGF events were available). The final P, S and SH source spectra estimates for the 11 events are shown in Figure 3.8. The spectra below 0.3 Hz are not reliably estimated. These spectra should now be free of any contribution from site effects, path attenuation, geometric spreading, focal mechanism, or instrument response. The absolute amplitudes are relative to the seismic moment of the M_w 4.0 reference event (M_o = 1.26 x 10^{15} Nm). The dashed curves for the ratio of the w^{-2} reference spectrum with a constant 3 MPa stress drop provide a common reference, with most spectra lying on or above that reference. It appears that the estimated source spectra fall off linearly to 3 Hz indicating that they are free of bias from the EGF corner frequency, except for the outer trench-slope event spectra (2005-11-14 and 2011-03-11(1)) for which the larger EGF events had to be used. The spectra in those cases may be valid only below 2 Hz. In general, the spectral decay slope is -2 or less,

with the slopes appearing to be somewhat less for 2005-08-16 and 2010-03-14 (the two Domain C events), 2005-11-14 and 2011-03-11(1) (the two trench-slope intraplate events), and 2011-04-07 (the intra-slab thrust event).

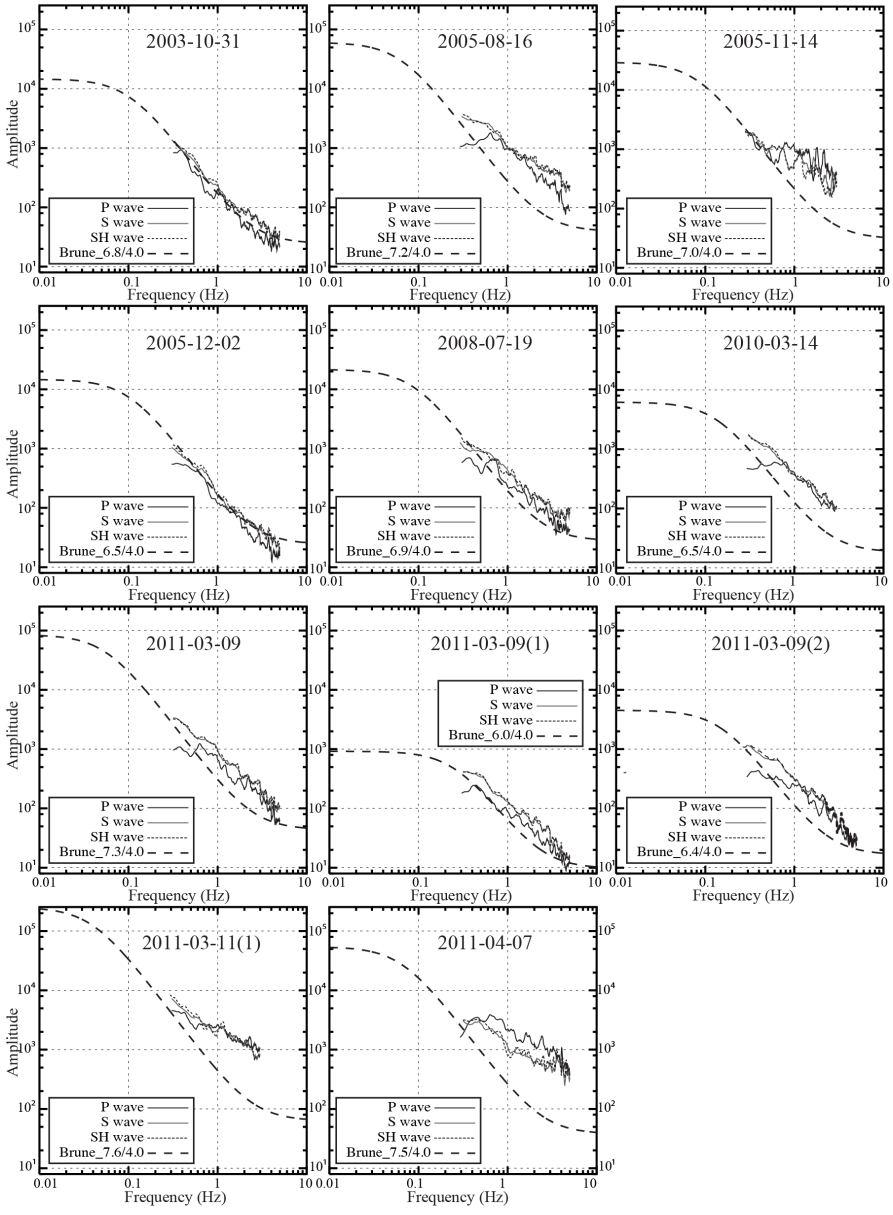

Figure 3.8 Average P, S and SH source spectra for the large events around the Tohoku mega thrust determined using the EGF method, with a nominal Mw 4.0 reference event. The dashed curves show the spectral ratio relative to an Mw = 4.0 event for the reference Brune w-2 source models with parameters as in Figure 3.7. The source spectra are valid from about 0.3 Hz to 3.0 Hz, and all are above the expected corner frequency of the large event, and the flattening of the spectra below 0.3 Hz is not to be inferred as a corner frequency effect. Some of the EGF events are smaller than Mw 4.0, so the estimated source spectra do not all flatten at 2 Hz as expected for the reference model.

To facilitate comparison with the strong-motion spectral ratios described in the preceding section, we compute spectral ratios of the event average source spectra relative to the reference foreshock 2011-03-09, along with the corresponding spectral ratios for the constant stress drop models, and show these in Figure 3.9. The S and SH ratios tend to track quite closely; and they differ from P spectra only for the 2005-11-14, 2011-03-11(1) and 2011-04-07 events. The ratios are flatter than seen in Figures 3.3 and 3.5 as a result of the explicit correction for attenuation and radiation pattern effects, but there are still systematic variations in absolute level, and for the 2005-08-16 and 2011-04-07 events there are clear differences in slope over the spectral range 0.3-3.0 Hz. The P wave spectra for the trench slope events (2005-11-14 and 2011-03-11(1)) are high relative to the 3 MPa model, as are the spectra for the Domain C event on 2010-03-14. The other events have relatively flat spectra, but the levels are low for events 2003-10-31, 2005-12-02, 2008-07-19 and 2011-03-09(1), suggestive of lower stress drop than for the reference event. The overall differences in spectra in Figure 3.9 can mostly be interpreted as departures from constant stress drop w^{-2} source variations.

Interpretation of spectral ratios provides limited resolution of the absolute spectra, but we can at least estimate differences in stress drop and high-frequency falloff rate, since the EGF-corrected spectra are presumably free of site, path, and radiation pattern effects. To give a sense for the level of stress drop variations that are involved, we fit the spectral ratios with theoretical spectra assuming the reference event of 2011-03-09 has a 3 MPa stress drop and a standard w^{-2} spectral decay. We then varied the stress drop parameter, and if necessary, the spectral decay of the numerator event to roughly match the overall level and shape of the observed source spectral ratios around 0.3 – 3 Hz. The high frequency enhancement in spectral ratios of down-dip events on the megathrust and intra-slab events, and the anomalous

spectral slope of event 2011-04-07 are of primary interest here. We keep the shear velocity constant in the calculations.

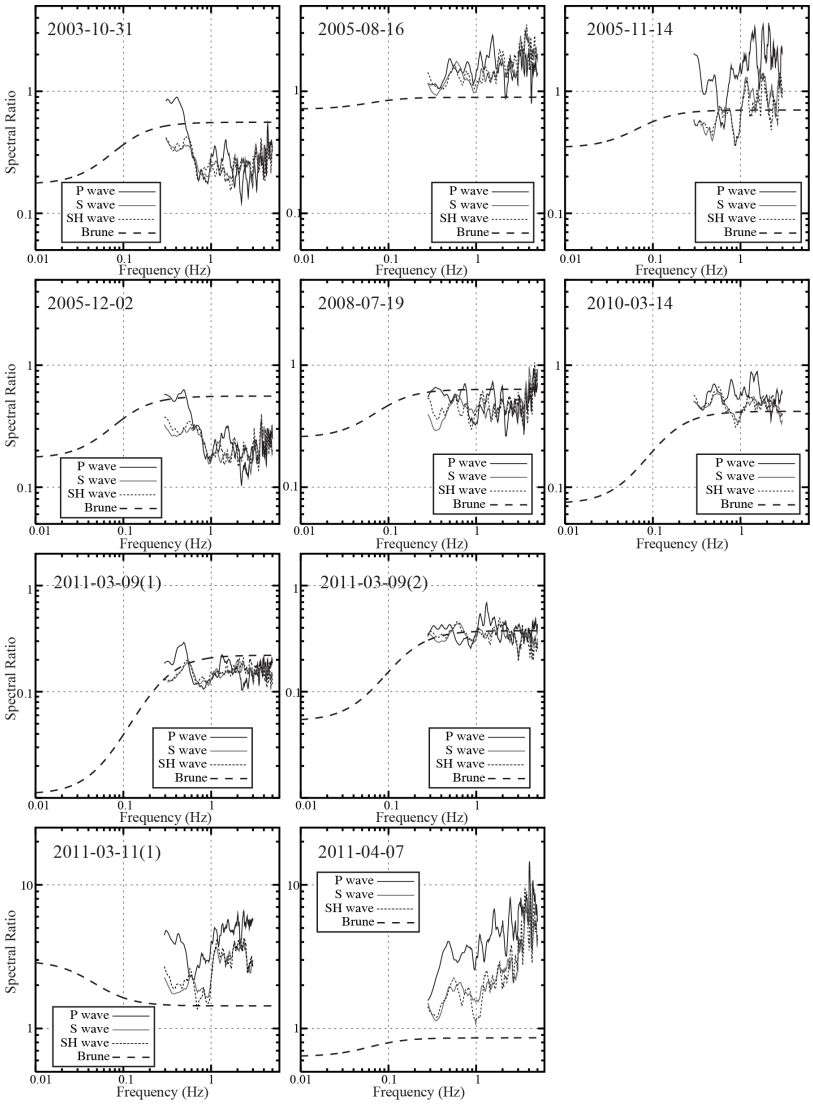

Figure 3.9 The spectral ratios of P, S and SH EGF-corrected source spectra relative to the foreshock on 2011-03-09. The dashed curves show the spectral ratios for the reference 3 MPa Brune w-2 source models. The spectral ratios are valid from about 0.3-3.0 Hz.

The estimates from fitting the spectral ratios are shown in Figure 3.10. The estimated stress parameters are ~ 1.5–2.0 times higher for the down-dip events 2005-08-16 and 2010-03-14, and ~ 2.0–4.0 times higher for the outer-rise normal faulting events 2005-11-14 and 2011-03-11(1), relative to the reference foreshock 2011-03-09 in Domain B. This general behavior is consistent with the factor of 2-5 difference in stress drops estimated between populations of interplate and intraplate events globally (e.g., Allmann and Shearer, 2009;

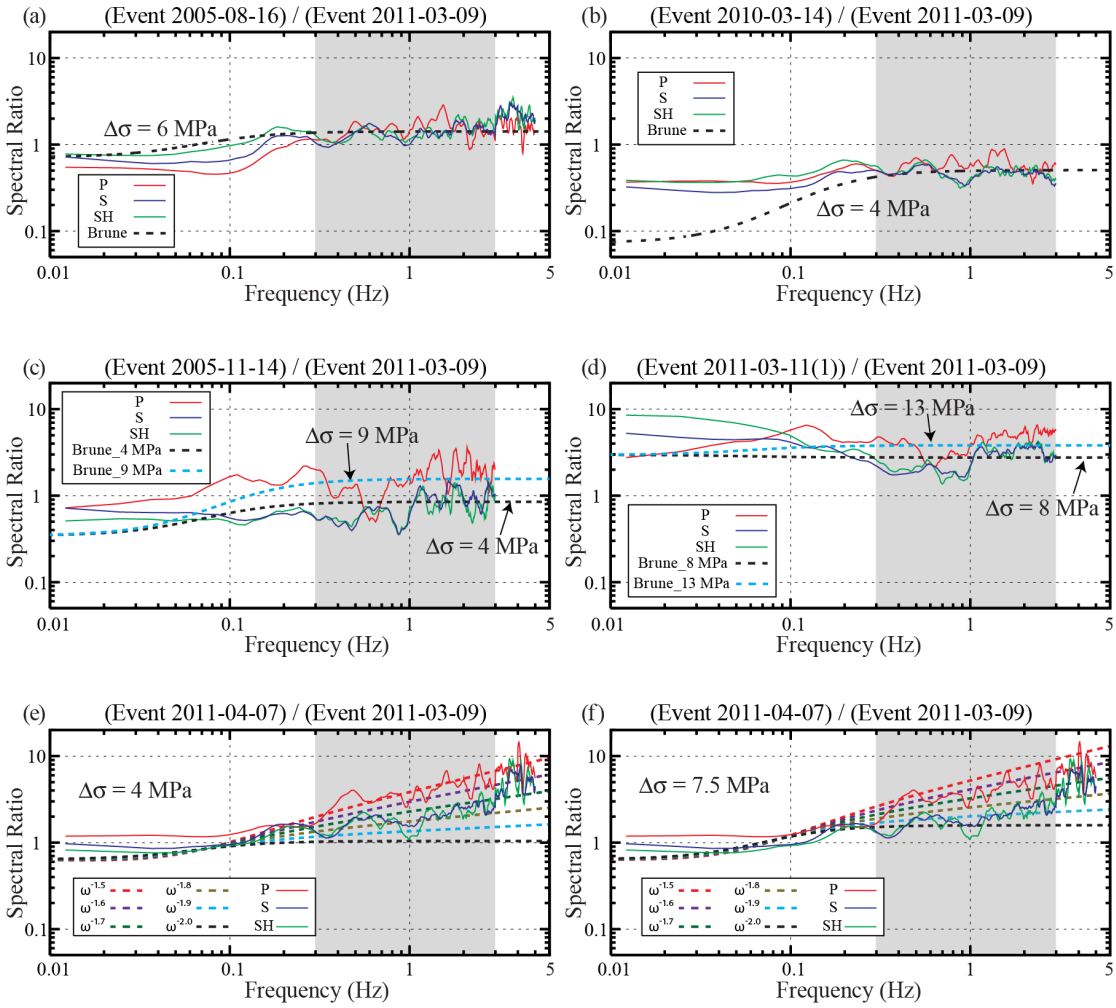

Figure 3.10 Estimation of relative stress drops for the Domain C events 2005-08-16 (a) and 2010-03-14 (b), outer-rise normal-faulting events 2005-11-14 (c) and 2011-03-11(1) (d), and the intra-slab compressional event 2011-04-07 (c and d) based on the spectral ratios from Figure 3.9. The reference (denominator) is the 2011-03-09 foreshock, for which we assume a stress drop of 3 MPa and w-2 source model. Dashed lines in (a)-(d) indicate the spectral ratios predicted by w-2 source models with the indicated stress drop for the numerator event, which provide a good fit on the observed spectral ratios relative to the constant 3 MPa results in Figure 3.9. The set of dashed lines in (e) and (f) are the spectral ratios predicted by w-n models for the numerator event with the value of n ranging from 1.5 to 2.0 for stress drops of 4 MPa and 7.5 MPa, respectively. The n ~1.6 and ~1.8 with stress drop 7.5 MPa provide a good fit on the spectral ratios of 2011-04-07 relative to the event 2011-03-09 for P wave and S/SH wave respectively. The shaded regions show the frequency band where the spectral ratios are valid from the EGF method.

Iwata and Asano, 2011) and with source spectra in the Mexico subduction zone (Purvance and Anderson, 2003), another region with long-term dense strong ground motion recordings. While variations in stress drop are not unexpected within any single faulting domain, the higher stress drop for the event 2011-03-11(1) relative to the nearby event 2005-11-14 may possibly be influenced by large stress perturbations associated with the great 2011 mainshock. The difference of P and S spectral ratios between the two outer-rise events could be due to the P waves having a higher corner frequency than S waves as predicted for the quasi-dynamic circular crack model (Madariaga, 1976). The data are too limited to justify very detailed analysis, and the main result is the tendency to have factor of 2-3 higher stress drop parameter for the intraplate and down-dip megathrust events relative to the Domain B events.

The intra-slab event of 2011-04-07 has the most anomalous source spectra (Figures 8 and 9), and the most negative Dt^* (Table 3.2), which combine to give the large ground shaking difference for this event (Figures 3, 4 and 5). The shape of the spectral ratio in Figure 3.9 cannot be matched just by difference in stress drop, even for very large (>100 MPa) stress drops that give extreme shifts of the corner frequency of the event. Figures 10(e) and 10(f) explore predictions of the spectral ratio for this event for w^{-n} models with n ranging from 1.5 to 2.0, for stress drops of 4 MPa and 7.5 MPa. For n ~1.6 or ~1.8 with a stress drop of 7.5 MPa good fits of the spectral ratios of this event relative to the foreshock 2011-03-09 are found for P waves and S/SH waves, respectively. With the spectral decay rate exponent being lower than -2, the negative Dt^* values in Table 3.2 are likely overestimates, as there is trade-off in the source spectrum decay rate and the differential attenuation estimation.

Given the limited bandwidth over which we can reliably resolve the source spectra and the modest size of the overall data set, we view these stress drop parameters and spectral slope estimates as good only to the first-order, and provide them mainly to quantify the magnitude

of variations involved, not to provide absolute measures with high fidelity. However, the isolated source spectra for these large events do indicate systematic variations of source radiation properties along the megathrust and significant high frequency radiation from the intra-slab events, which may result from local frictional differences on the fault surface and/or different stress drops. This information is more quantitative than obtained by back-projection methods, which resolve only the spatially-coherent part of short-period signals without establishing the overall spectral levels involved.

3.4 Far-field P-wave Spectral Analysis

To provide a connection between the regional spectral analysis and teleseismic observations, we calculated the average far-field P wave spectra for four large events around the megathrust fault offshore of Honshu, as shown in Figure 3.11. The observed far-field P wave spectra are estimated at frequencies < ~0.05 Hz using finite-fault models inverted from teleseismic body wave observations and at frequencies > ~0.05 Hz from broadband teleseismic P wave spectra directly. Reference source spectra for the Brune ω^{-2} model with 3 MPa stress drop are shown in each case. The observed spectra have systematic variations in high frequency slope in the passband around 0.1 – 1 Hz, with event 2005-08-16 in Domain C and intra-slab thrust event 2011-04-07 having relative enrichment of spectral amplitudes above ~ 0.3 Hz, the foreshock on 2011-03-09 in Domain B having lower spectral amplitudes above ~ 0.02 Hz, and the 2011-03-11 Tohoku mainshock which ruptured Domain A, B and C showing spectral amplitudes comparable to the reference source spectrum. In this case, we are estimating the full bandwidth of the spectra, establishing the corner frequency and moment level of the spectra, which we cannot achieve with the EGF-method using the regional data due to the bandwidth constraints. For the corresponding resolved portions of

the source spectra, from 0.3-1.0 Hz, the regional and teleseismic spectral variations are very consistent. For example, the ratio of the 2005-08-16 spectra to the foreshock spectra is about 2 over the entire passband, which agrees very well with the ratio for P energy in Figure 3.9. Similarly, the teleseismic P wave ratio for the 2011-04-07 event relative to the foreshock increases with frequency (up to 2 Hz, in this case) about the same amount as in the regional ratio in Figure 3.9. This consistency indicates that the teleseismic spectral estimates provide robust relative spectral behavior up to 1-2 Hz, which is encouraging for future analysis of

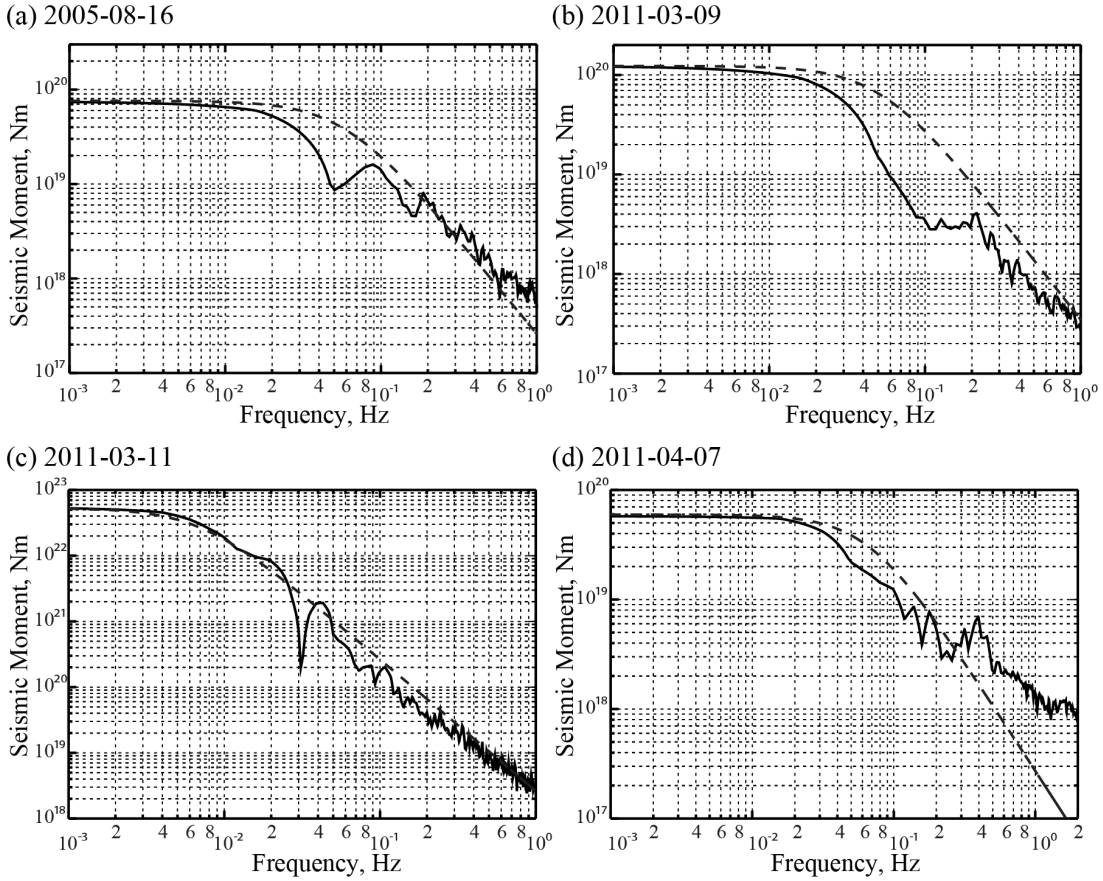

Figure 3.11 The stacked source spectra for far-field P waves for large events around the Tohoku megathrust. In each panel, the black line indicates the observed spectra, estimated at frequencies less than ~0.05 Hz using finite-fault models inverted from teleseismic body wave observations and at frequencies > ~0.05 Hz calculated from broadband teleseismic P waves directly. The dashed lines are reference source spectra for the Brune w-2 model with 3 MPa stress drop and the GCMT seismic moments.

larger numbers of events, as it is not necessary to use EGF deconvolution to suppress average attenuation variations because they appear to be minor (although slab effects may cause differential effects for some paths). There is still a direct dependence on the attenuation correction used in the analysis but that is likely to at least be uniform for nearby events. The consistency also reinforces the interpretation of depth varying source radiation properties along the megathrust and the high frequency enrichment of seismic waves from intra-slab events.

3.5 Discussion and Conclusions

Observed variations in seismic wave radiation from different portions of megathrust faults motivated this investigation of ground motion and source spectra for earthquakes around the rupture zone of the 2011 Tohoku earthquake. The results build upon many prior observations that indicate strength of ground motion generally decreases as source location moves further offshore, that intraplate events tend to have higher apparent corner frequencies in general, and that sources deviate from constant stress drop behavior even on a single fault. The main contribution here is the quantitative resolution of source spectra (for at least portions of the high-frequency range) to supplement qualitative indicators such as back-projection of teleseismic short-period P waves. We clarify how energy release can vary over the megathrust and in the proximate intra-slab environment.

Figure 3.12a shows the cross-section modified from the megathrust domain Figure 3.of Lay et al. (2012) (Figure 3.2), adding two intra-slab environments, Region (1) in the outer trench slope, and Region (2) below the leading edge of the seismogenic portion of the megathrust, together with a list of the events we studied. Only one of our events, (2011-03-09(1)), possibly

locates in Domain A, for the JMA location. This event is uncertain in placement (the GCMT location places it in Domain B). We do not yet have a clear isolated large tsunami earthquake in the Tohoku region similar to the 1896 event to the north, but the mainshock appears to have ruptured all the way through Domain A to the trench with shallow rupture attributes being consistent with a tsunami earthquake.

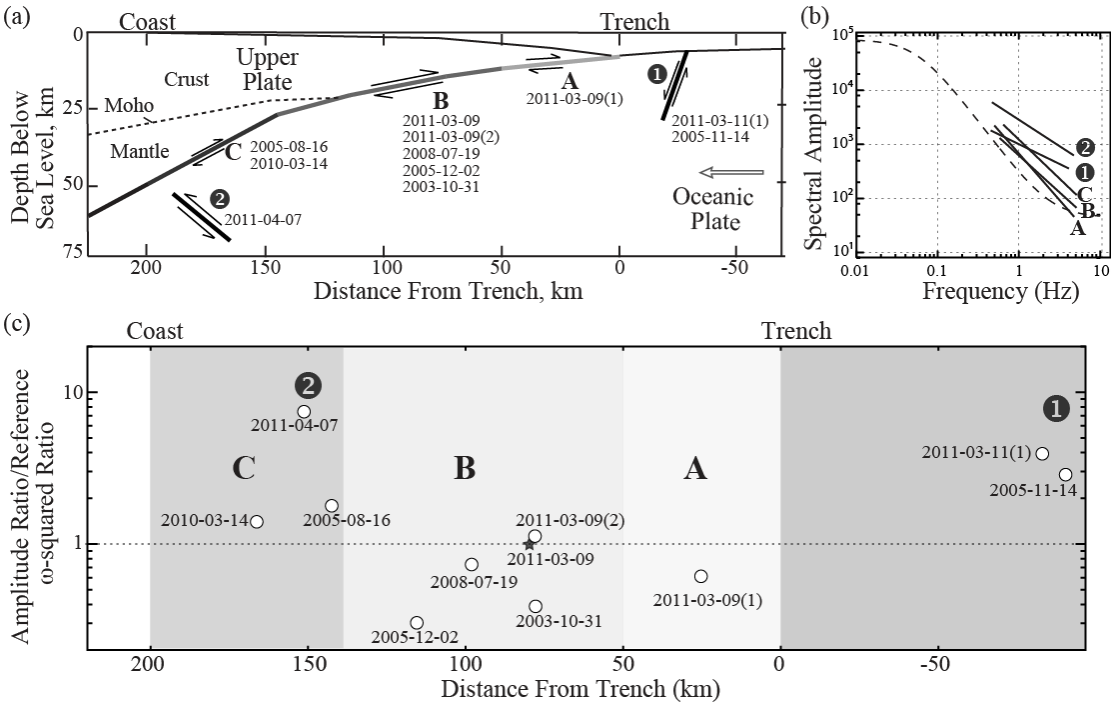

Figure 3.12 Schematic cross-section (a) around Tohoku megathrust with five environments of distinct source spectral characteristics with Domains A, B and C located on the megathrust, and intraplate Regions (1) and (2) in the Pacific plate. The dashed line in (b) show the spectral ratio of event 2011-03-09 relative to an Mw = 4.0 event for the reference Brune w-2 source models with 3 MPa stress drop and the regional CMT seismic moments, and the solid lines are liner approximation of averaged source spectra of the events 2011-03-11(1) in Region (1), 2011-03-09(1) in Domain A, 2011-03-09 in Domain B, 2005-08-16 in Domain C and 2011-04-07 in Region (2), scaling by the corresponding expected spectra for Brune w-2 source models. (c) The 3 Hz amplitude ratio of the EGF-corrected source spectra relative to the foreshock 2011-03-09 normalized by spectral ratios for the Brune w-2 source models with regional CMT seismic moment, plotted as a function of perpendicular distance from the trench to the JMA source locations. The star shows the location of the foreshock 2011-03-09 with relative spectral ratio of 1.

Figure 3.12b illustrates the spectral amplitudes for each of the megathrust Domains and intraplate Regions taken from the actual spectra shown in Figure 3.9. All of the megathrust events have similar spectral decay rates, but the Domain C events have higher amplitude due to the higher corner frequency for a given moment. The intra-plate events have lower decay rates and higher spectral amplitudes, indicating both higher stress drop and distinct high-frequency spectral fall-off.

Figure 3.12c shows the EGF-corrected source spectral ratios from Hi-net data (Figure 3.9) at 3 Hz relative to the foreshock (2011-03-09) as a function of distance from the trench (the JMA locations are used). The 3 Hz amplitudes (adjusted relative to the 3 MPa constant stress drop reference spectrum as in Figure 3.4) are large for the Domain C and Region (1) and (2) events. These EGF-corrected ratios should represent rupture physics effects isolated from propagation effects, whereas Figure 3.4 represents ground shaking variations that have both source and propagation contributions.

Overall, the behavior of large earthquake sources around the Tohoku rupture indicates that, for a given magnitude, the greatest shaking hazard is associated with the events near the coast, not just due to proximity to the land but also because the events have higher spectral amplitudes at short-period and higher Q along the path from the source to the site. It is advisable to treat the deep megathrust and down-dip intra-slab events distinctly from other shallow earthquakes in ground motion predictions.

The variations in source spectra reflect the variations in basic source physics; the model of depth-dependent source radiation advanced by Lay et al. (2012) is supported by the results of the large events that rupture in Domain C and Domain B. More sampling of Domain A is needed to establish the characteristics of Domain A events, but the characteristics of tsunami earthquakes elsewhere, including the 1896 Sanriku event to the north, are now well-

established (e.g., Polet and Kanamori, 2000; Lay and Bilek, 2007; Convers and Newman, 2011). The favorable comparison between carefully measured teleseismic spectra and regional EGF-corrected source spectra indicates that the source variations can be reliably isolated with full spectral amplitude determinations. This is an important supplement to procedures such as back-projection, which view the short-period wavefield through the lens of a strong coherency-filter that does not necessarily reflect the absolute (or even relative) spectral levels. In combination, these methods are unveiling the systematic spatial and mechanism dependent variations in source radiation that can guide both ground shaking hazard analysis and further fundamental studies on the causes of stress drop and spectral decay rate variations.

Data and Resources. Seismograms used in this study included regional strong ground motion recordings from K-net and KiK-net stations and short-period recordings from Hi-net stations by National Research Institute for Earth Science and Disaster Prevention (NIED), and broadband teleseismic P wave data from Incorporated Research Institutions for Seismology (IRIS) Data Management System (DMS) at http://www.iris.edu (last accessed March, 2012). Data from KiK-net, K-net and Hi-net can be obtained from http://www.kik.bosai.go.jp, http://www.k-net.bosai.go.jp and http://www.hinet.bosai.go.jp (last accessed March, 2012), respectively. The Global Centroid Moment Tensor (GCMT) catalog can be obtained from http://www.globalcmt.org/CMTsearch.html (last accessed March 2012). K. Katsumata provided the JMA-unified catalog (via personal communication) and Y. Asano provided the regional CMT solutions (via personal communication; Asano et al., 2011). Some plots were made using the Generic Mapping Tools (www.soest.hawaii.edu/gmt; Wessel and Smith, 1998), and some data processing the software SAC (http://www.iris.edu/software/sac/manual.html).

Acknowledgements. This work made use of GMT and SAC software and Federation of Digital Seismic Networks (FDSN) seismic data. The Incorporated Research Institutions for Seismology (IRIS) Data Management System (DMS) provided the teleseismic P wave data and the F-net, K-net, Kik-net and Hi-net data were obtained from National Research Institute for Earth Science and Disaster Prevention (NIED) data centers. We thank Y. Asano for sharing his catalog of redetermined regional CMT solutions with us. We thank an anonymous reviewer and J. Anderson for thoughtful comments that improved the manuscript. This work was supported by NSF grant EAR0635570.

3.6 Supplementary Figures

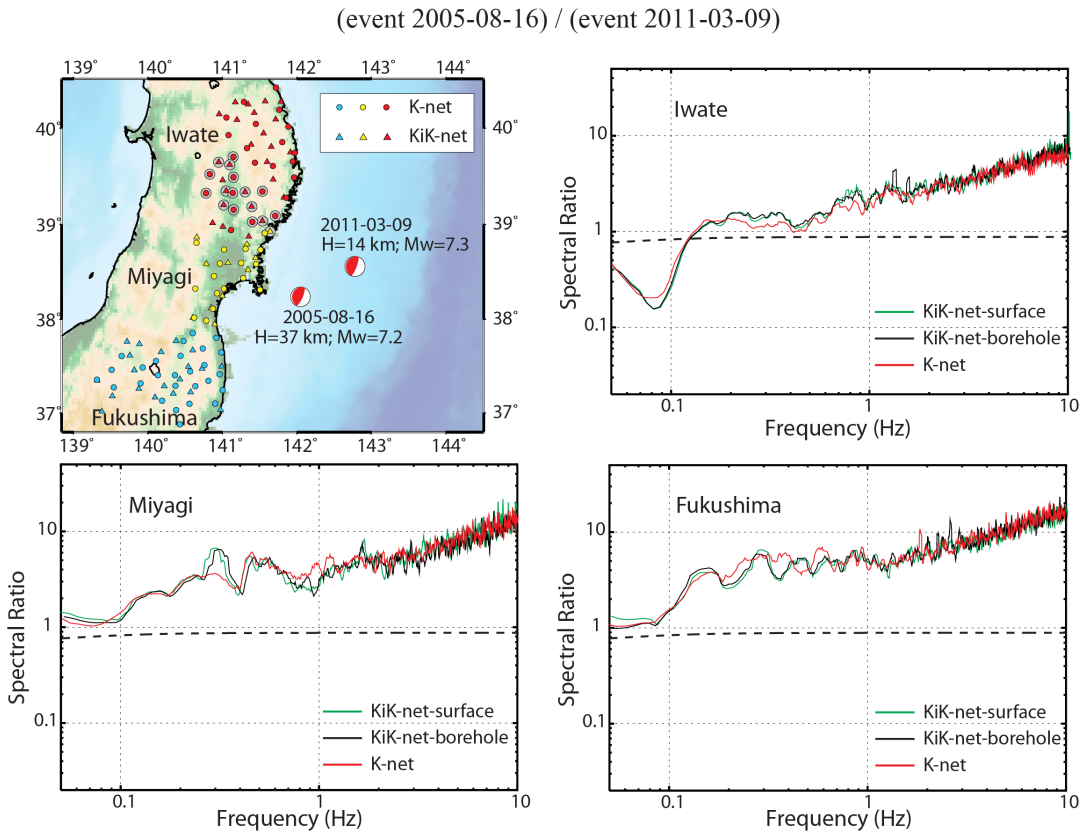

Figure 3.A1. Spectral ratios for (event 2005-08-16)/(event 2011-03-09).

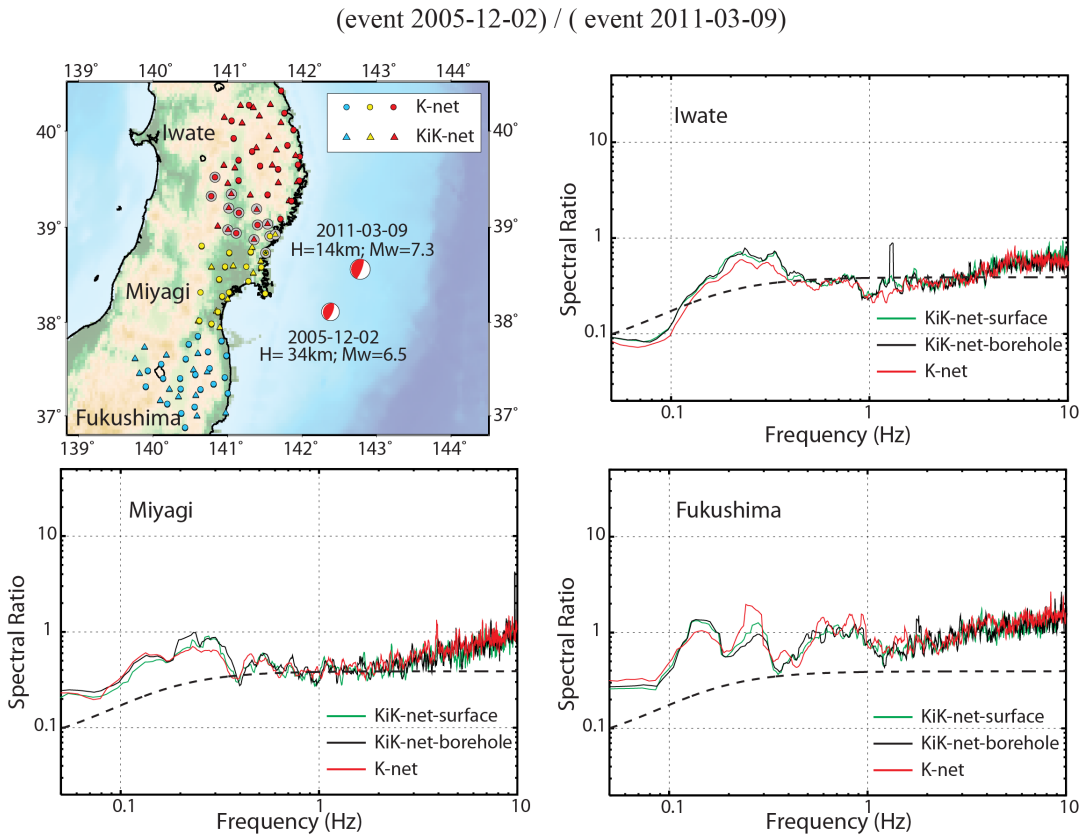

Figure 3.A2. Spectral ratios for (event 2005-12-02)/(event 2011-03-09).

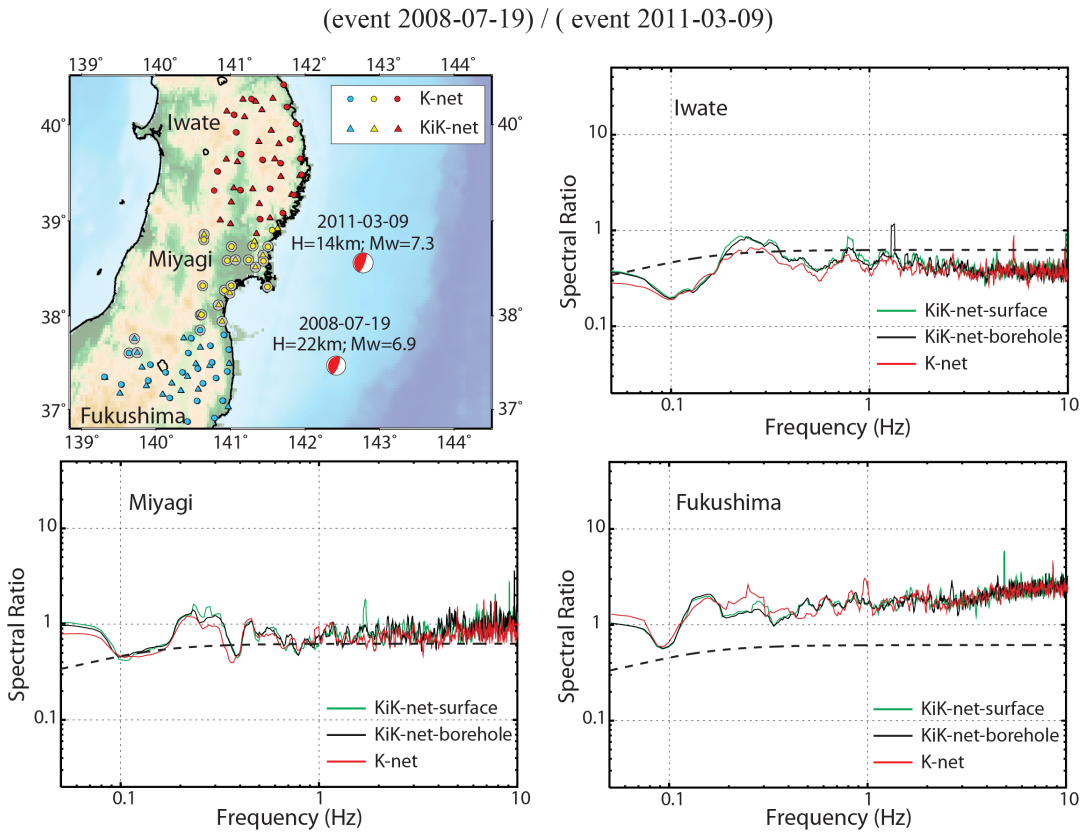

Figure 3.A3. Spectral ratios for (event 2008-07-19)/(event 2011-03-09).

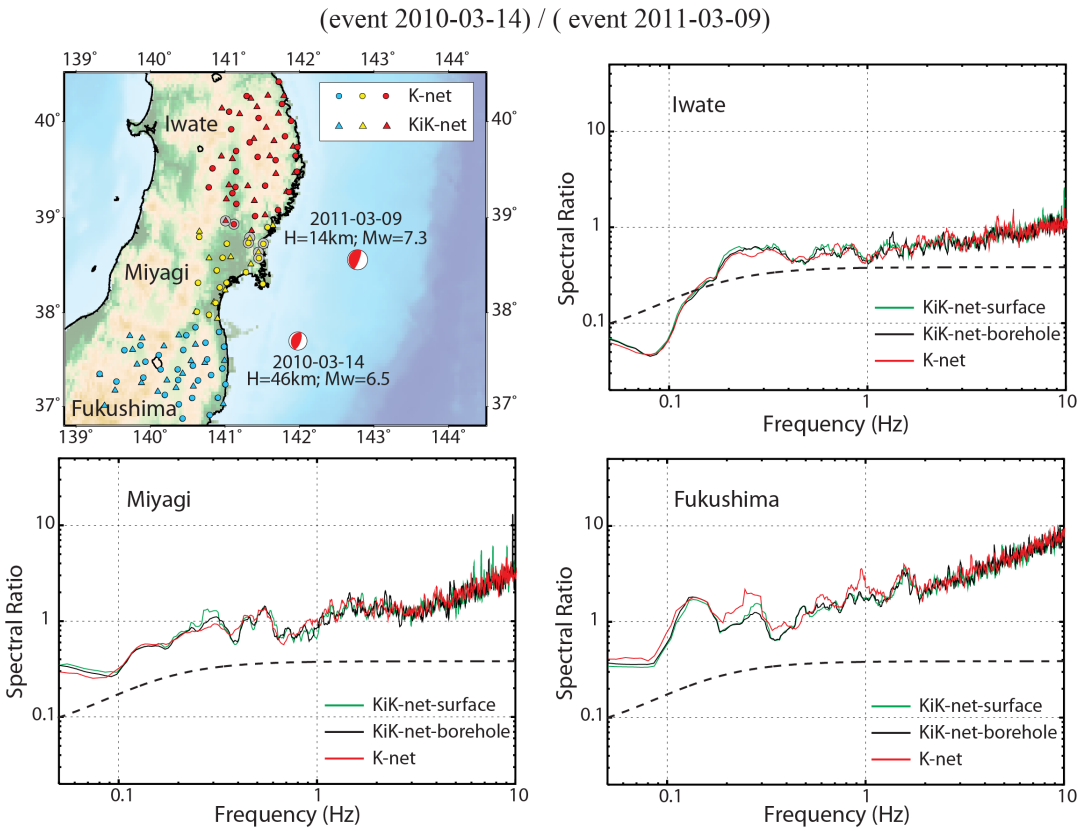

Figure 3.A4. Spectral ratios for (event 2010-03-14)/(event 2011-03-09).

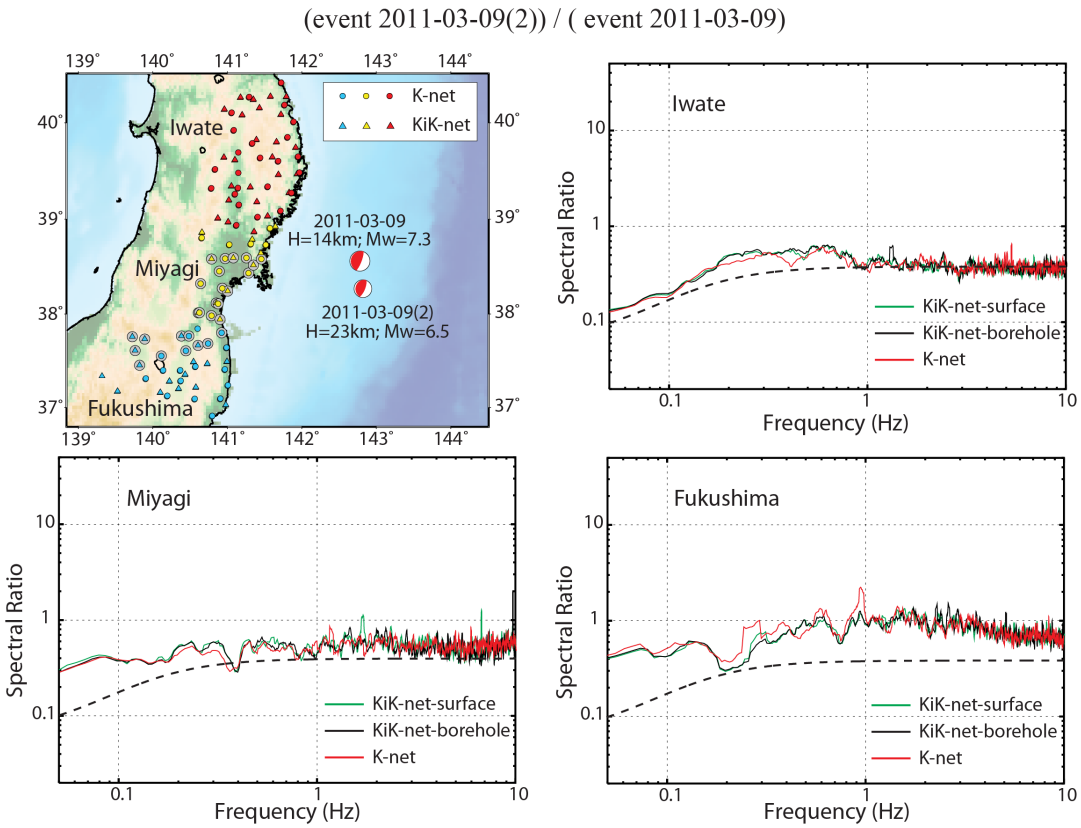

Figure 3.A5. Spectral ratios for (event 2011-03-09(2))/(event 2011-03-09).

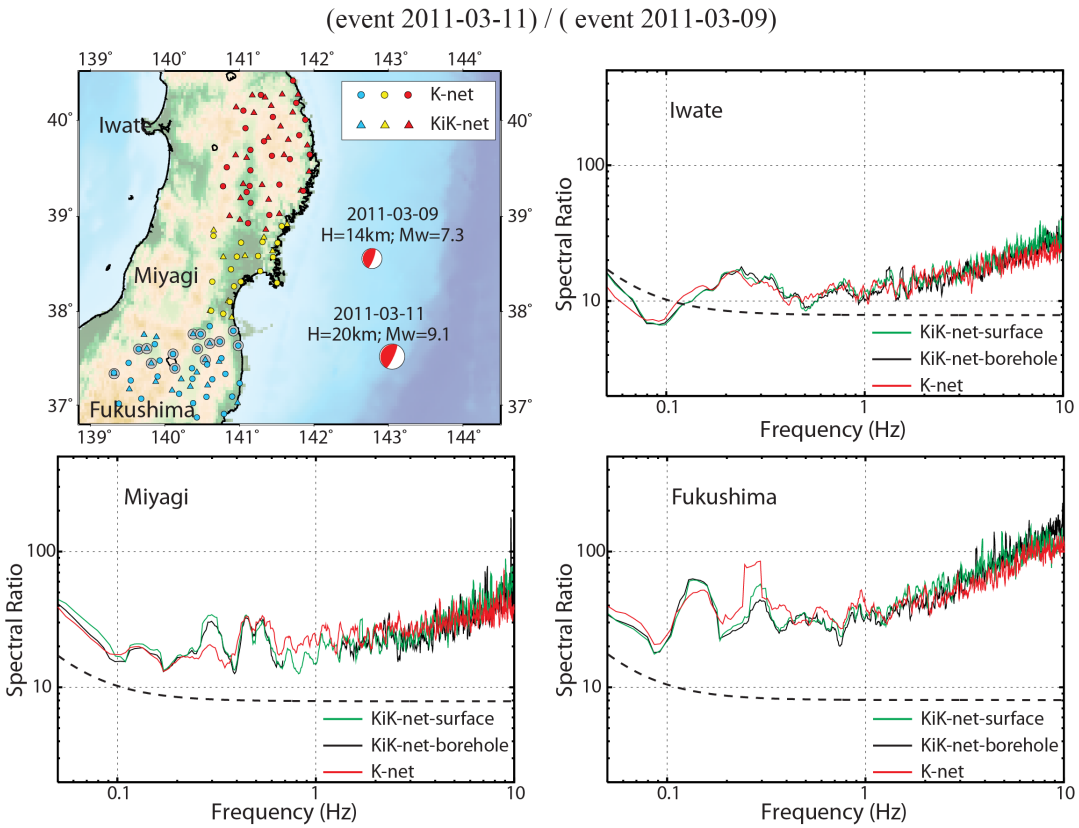

Figure 3.A6. Spectral ratios for (event 2011-03-11)/(event 2011-03-09).

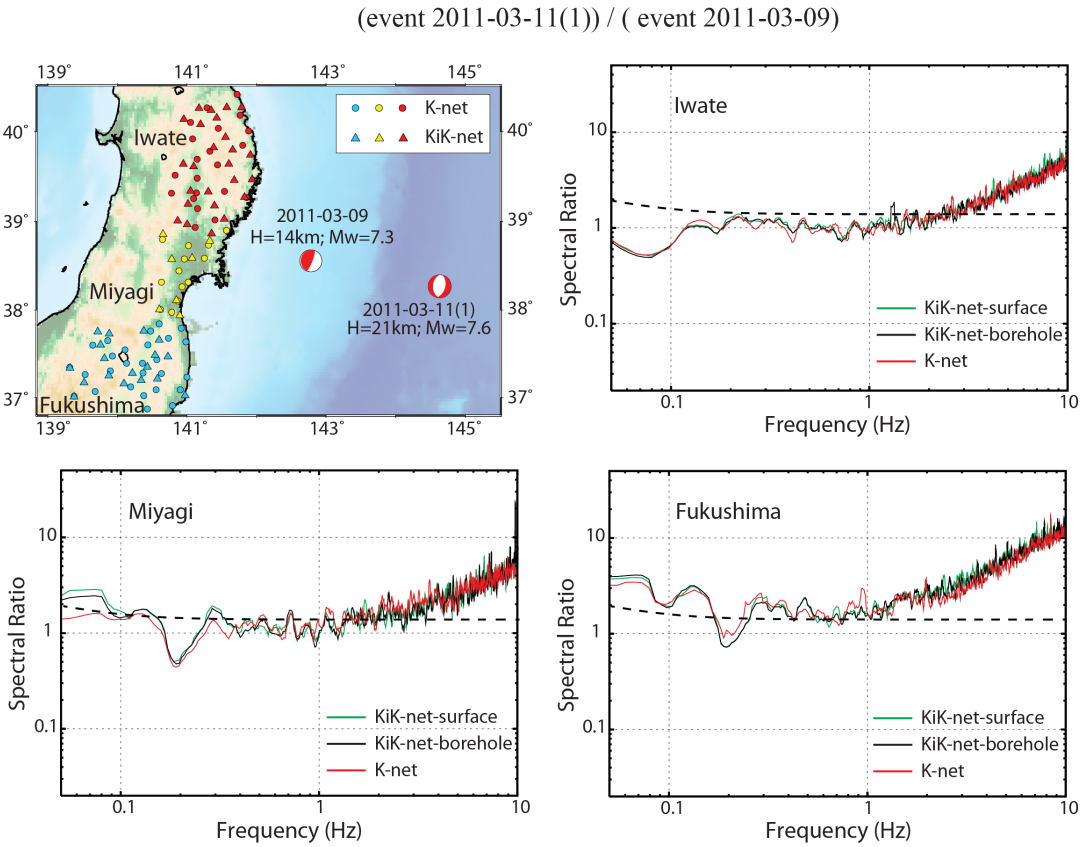

Figure 3.A7. Spectral ratios for (event 2011-03-11(1))/(event 2011-03-09).

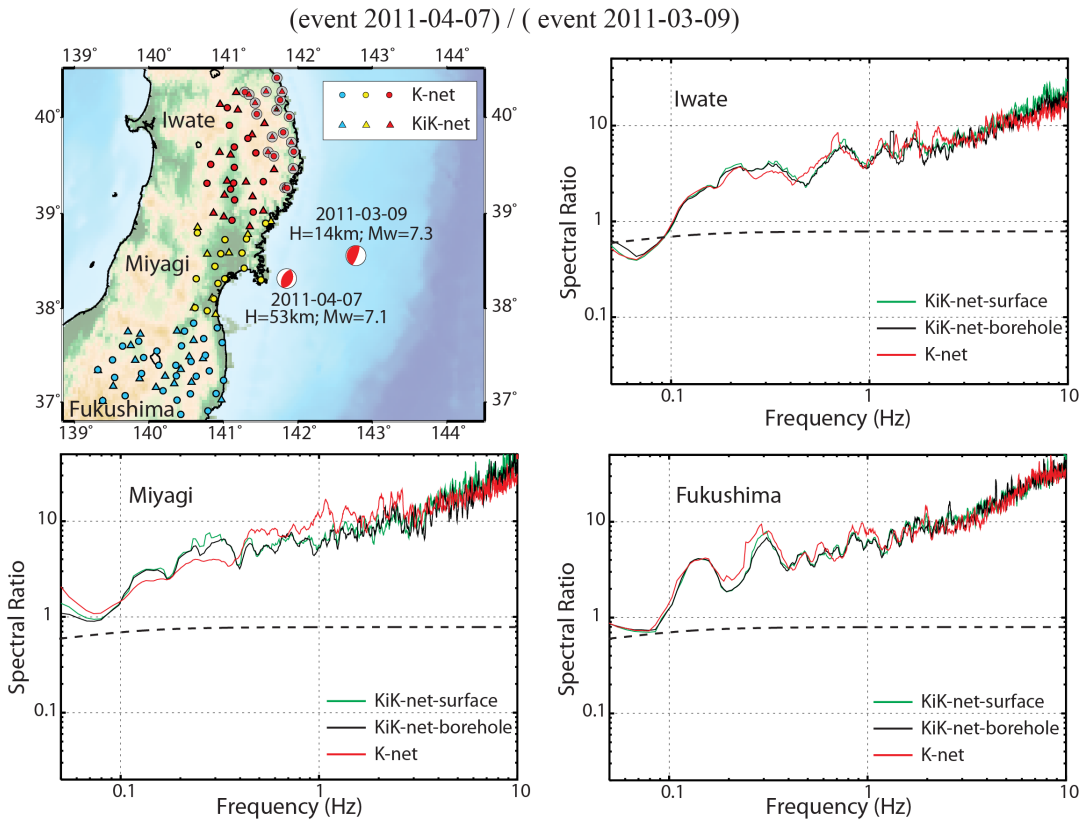

Figure 3.A8. Spectral ratios for (event 2011-04-07)/(event 2011-03-09).

Figure 3.A1 – A8. Spectral ratios relative to the foreshock of 2011-03-09 from K-net and Kik-net strong motion sensors in Iwate, Miyagi, and Fukushima prefectures (map). The stacked, smoothed spectral ratios from all three components of recorded ground accelerations over 100 s windows are shown, with separate averaged computed for K-net and KiK-net observations. The gray circles show the sensors with common path lengths from sources and receivers (within 10 km) used for spectral ratios calculation in Figure 3. The dashed curves show the spectral ratios for the reference 3 MPa Brune omega-square source models.

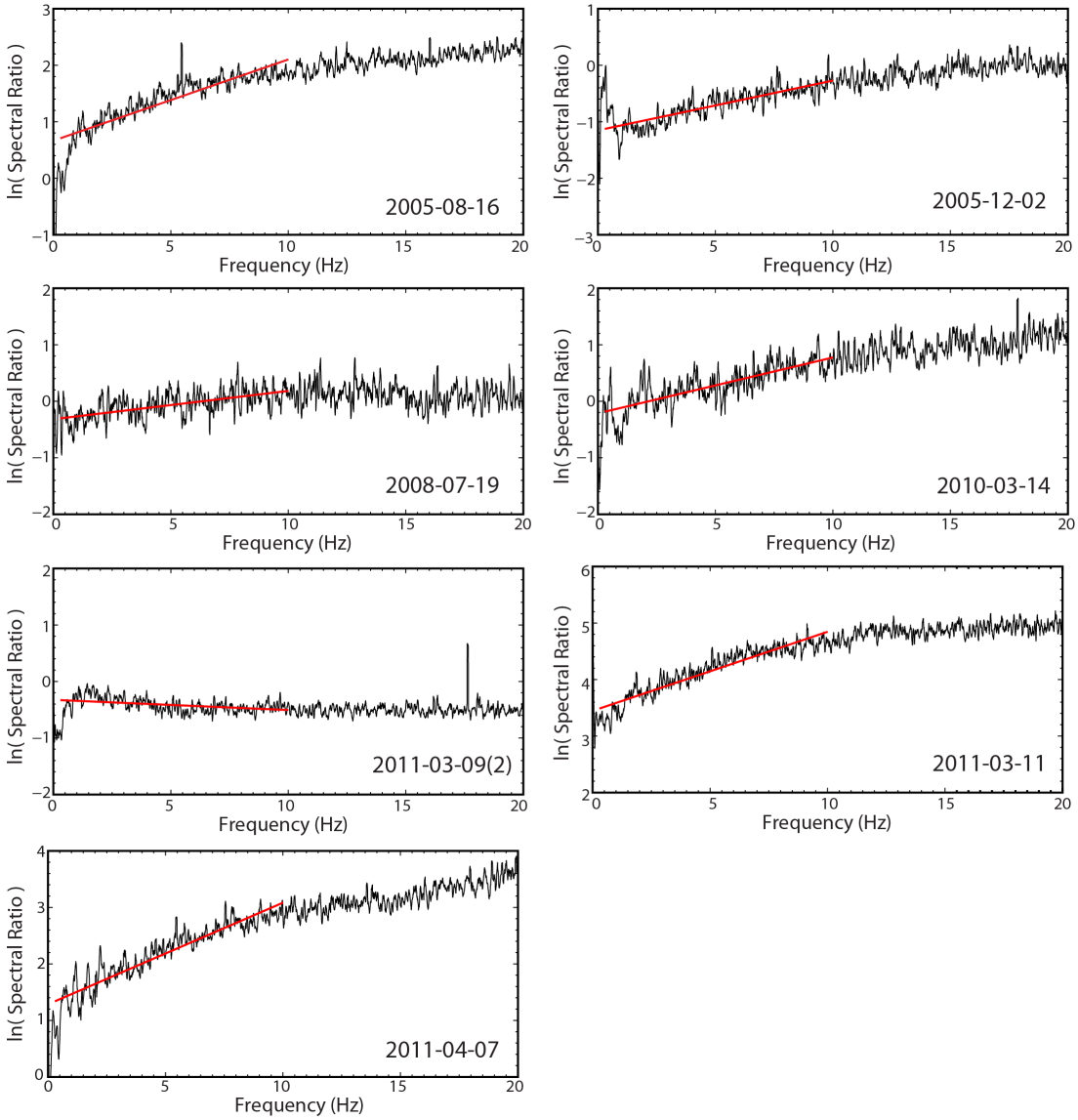

Figure 3.A9. Least squares linear regression of the natural log of averaged spectral ratios in the frequency band 0.03-10.0 Hz in Figure 3 for three-component signals 100 s long.

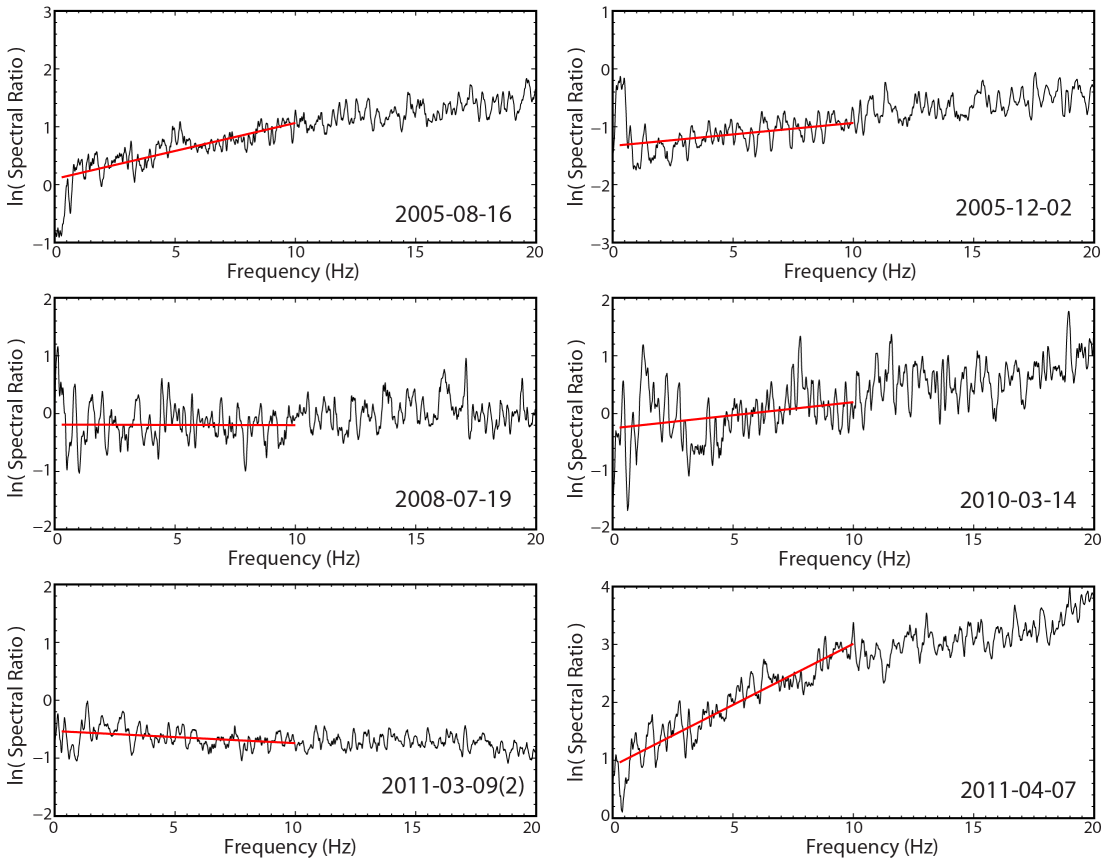

Figure 3.A10. Least squares linear regression of the natural log of averaged P wave spectral ratios in the frequency band 0.03-10.0 Hz in Figure 5(a) for vertical component.

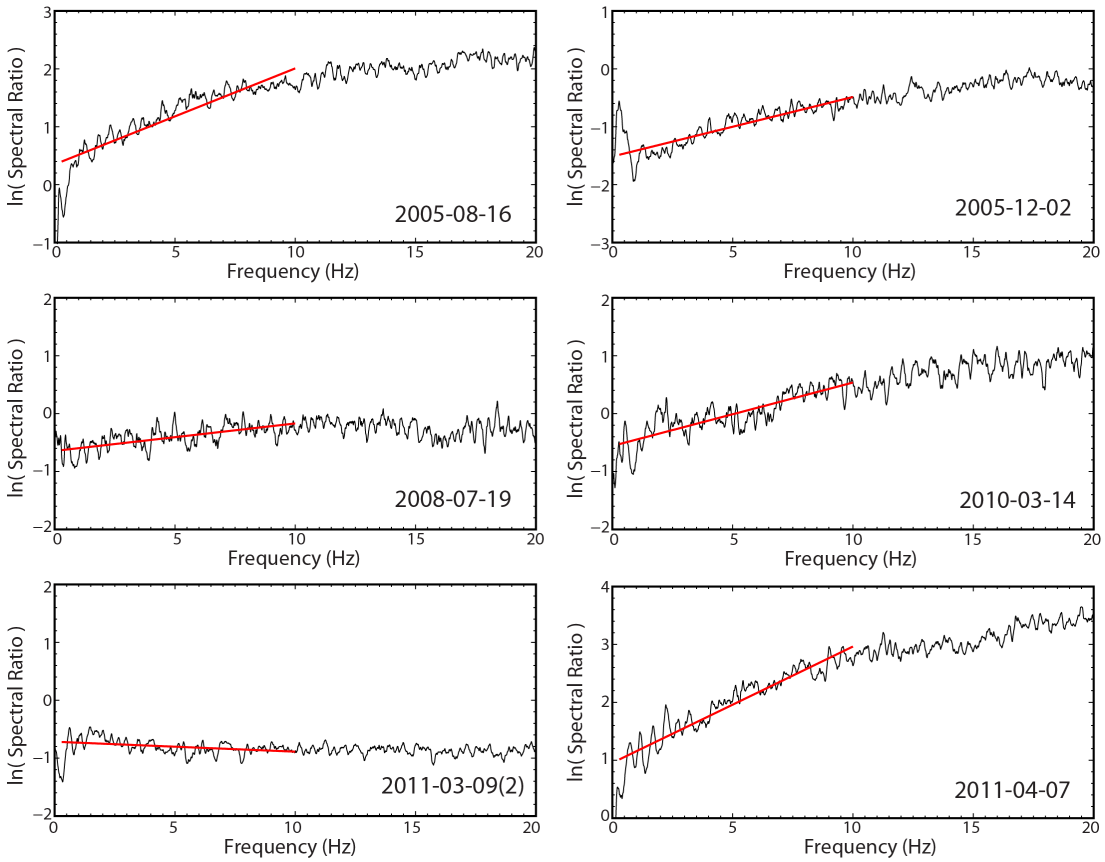

Figure 3.A11. Least squares linear regression of the natural log of averaged S wave spectral ratios in the frequency band 0.03-10.0 Hz in Figure 5(b) for three-components signals.

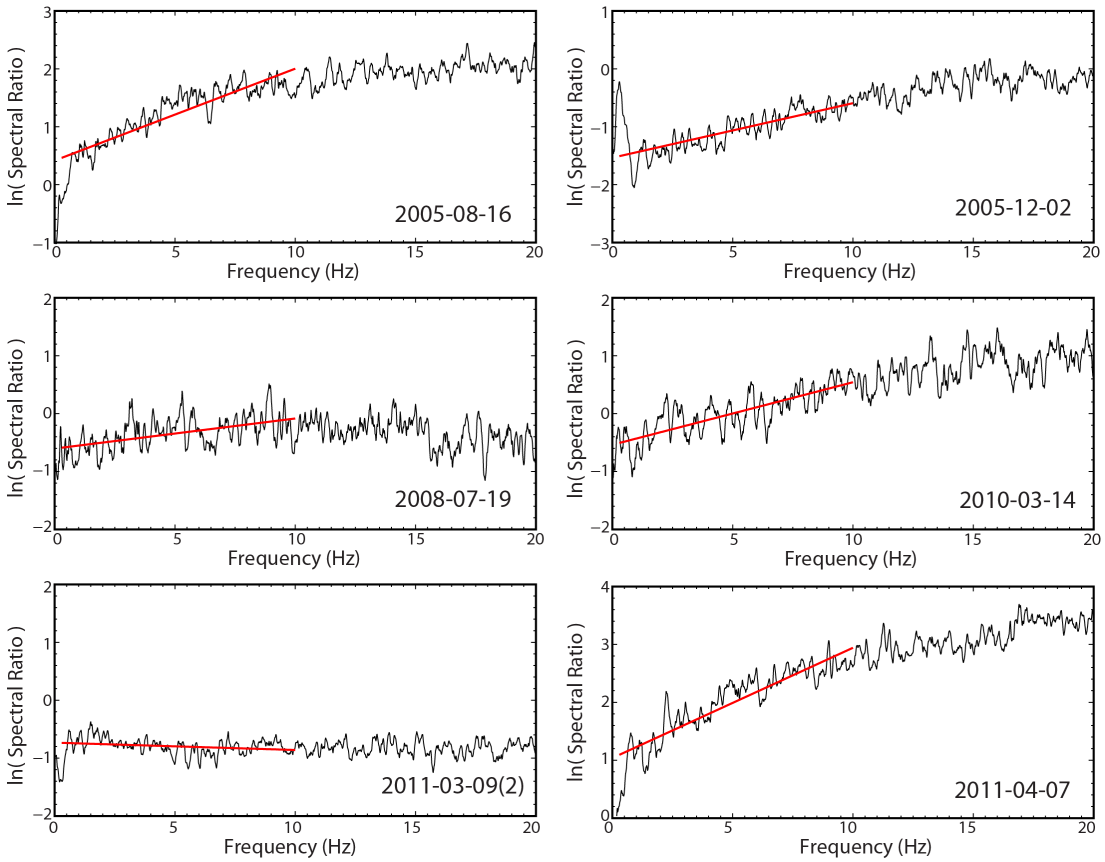

Figure 3.A12. Least squares linear regression of the natural log of averaged SH wave spectral ratios in the frequency band 0.03-10.0 Hz in Figure 5(c) for tangential component.

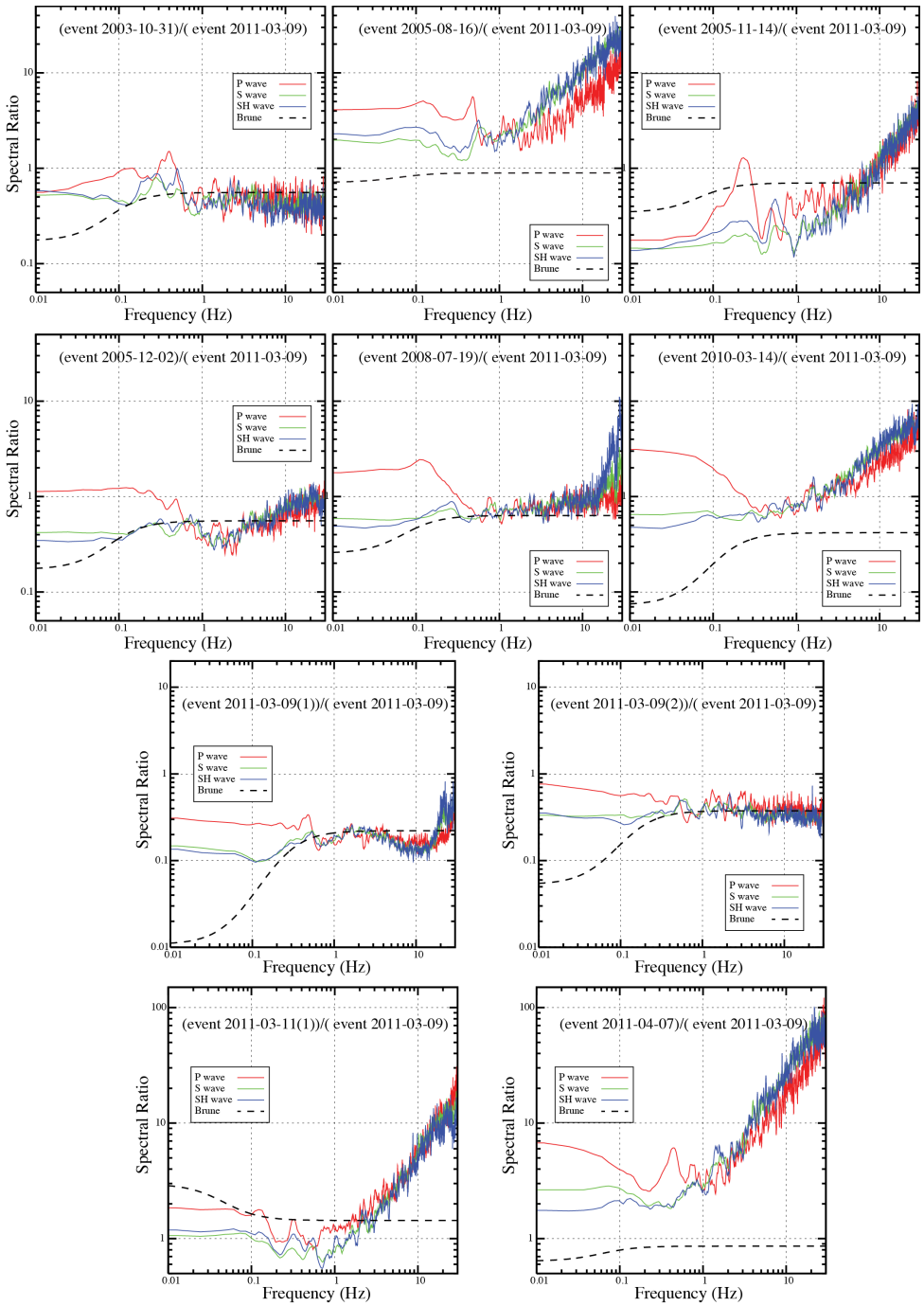

Figure 3.A13. Stacked spectral ratios of ground velocity recorded by short period Hi-net stations (Figure 6) for large events in the Japan subduction zone around Tohoku with the foreshock on 2011-03-09 (Mw 7.3) being the reference (denominator) in each case. The stacked, smoothed spectral ratios are from all three components of recorded for 100 s time windows. The dashed curves are predicted spectral ratios for reference Brune omega-square source models for a 3 MPa constant stress drop and the regional CMT seismic moments.

Chapter 4

Large Earthquake Rupture Process Variations on the Middle America Megathrust

This chapter has been published as:
Ye, L., T. Lay, and H. Kanamori (2013), "Large earthquake rupture process variations on the Middle America megathrust", Earth Planet. Sci. Lett., 381,147-155.

Abstract. The megathrust fault between the underthrusting Cocos plate and overriding Caribbean plate recently experienced three large ruptures: the August 27, 2012 (M_W 7.3) El Salvador; September 5, 2012 (M_W 7.6) Costa Rica; and November 7, 2012 (M_W 7.4) Guatemala earthquakes. All three events involve shallow-dipping thrust faulting on the plate boundary, but they had variable rupture processes. The El Salvador earthquake ruptured from about 4 to 20 km depth, with a relatively large centroid time of ~19 s, low seismic moment-scaled energy release, and a depleted teleseismic short-period source spectrum similar to that of the September 2, 1992 (M_W 7.6) Nicaragua tsunami earthquake that ruptured the adjacent shallow portion of the plate boundary. The Costa Rica and Guatemala earthquakes had large slip in the depth range 15 to 30 km, and more typical teleseismic source spectra. Regional seismic recordings have higher short-period energy levels for the Costa Rica event relative to the El Salvador event, consistent with the teleseismic observations. A broadband regional waveform template correlation analysis is applied to categorize the focal mechanisms for larger aftershocks of the three events. Modeling of regional wave spectral ratios for clustered events with similar mechanisms indicates that interplate thrust events have corner frequencies, normalized by a reference model, that increase down-dip

from anomalously low values near the Middle America trench. Relatively high corner frequencies are found for thrust events near Costa Rica; thus, variations along strike of the trench may also be important. Geodetic observations indicate trench-parallel motion of a forearc sliver extending from Costa Rica to Guatemala, and low seismic coupling on the megathrust has been inferred from a lack of boundary-perpendicular strain accumulation. The slip distributions and seismic radiation from the large regional thrust events indicate relatively strong seismic coupling near Nicoya, Costa Rica, patchy zones of strong seismic coupling in the shallowest megathrust region along Nicaragua and El Salvador, and small deeper patchy zones of strong seismic coupling near Guatemala, which can be reconciled with the geodetic observations as long as the strong coupling is limited to a small fraction of the megathrust area.

4.1 Introduction

The Middle America subduction zone (Figure 4.1) is distinctive in having pronounced forearc translation parallel to the trench despite the lack of strong obliquity of the plate convergence direction along much of the plate boundary. The extensive GPS data collected over the past two decades (Alvarado et al., 2011; Alvarez-Gomez et al., 2008; Correa-Mora et al., 2009; DeMets, 2001; Franco et al., 2012; Guzman-Speziale and Gomez-Gonzales, 2006; LaFemina et al., 2009; Lyon-Caen et al., 2006; Rodriguez et al., 2009; Turner III et al., 2007) indicate forearc trench-parallel motions along Nicaragua and El Salvador relative to a fixed Caribbean plate have a velocity of 14-15 ± 2 mm/yr toward the diffuse triple junction between the Cocos (CO), Caribbean (CA) and North America (NA) plates. The geodetic observations also indicate very little trench-perpendicular ground velocity that would be expected if the offshore megathrust boundary is locked and significant upper plate convergent strain accumulating.

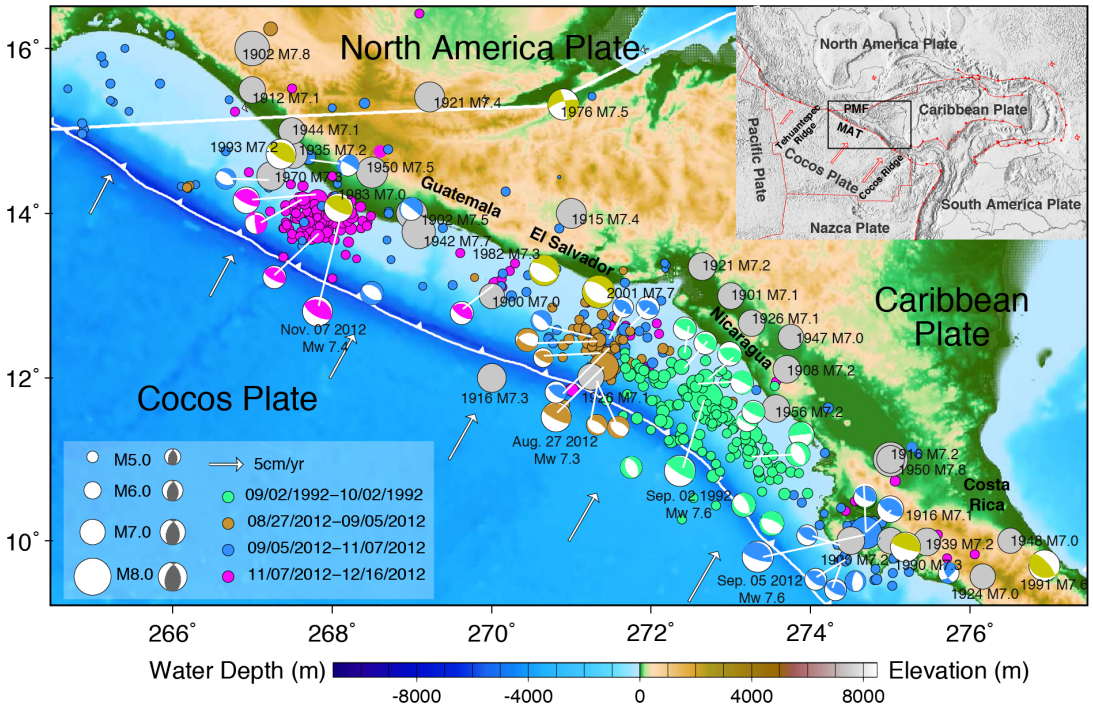

Figure 4.1. Large earthquakes around the Middle American subduction zone from Costa Rica to Guatemala. Gray circles are M ≥ 7.0 events from 1900 to 1975 from PAGER-CAT (Allen et al., 2009). Focal mechanisms are global centroid moment tensor (gCMT) solutions for M ≥ 7.0 events from 1976 to 2012 (Olive) plotted at the NEIC epicenters. Color-coded circles are epicenters for aftershock sequences following the September 2, 1992 Nicaragua (M_W 7.6) tsunami earthquake (Green), the August 27, 2012 El Salvador (M_W 7.3) earthquake (Brown), the September 5, 2012 Costa Rica (M_W 7.6) earthquake (Blue), and the November 7, 2012 Guatemala (M_W 7.3) earthquake (magenta). Correspondingly colored gCMT mechanisms for these four sequences are shown. White curves indicate the Middle America Trench (MAT) boundary (barbed) between the Cocos Plate and Caribbean Plate, and the approximate North America and Caribbean plate boundary. Arrows indicate plate motion direction and rate relative to a fixed Caribbean plate computed using model NUVEL-1 (Argus and Gordon, 1991). The Cocos Plate subducts northeastward beneath the Caribbean Plate at 75 to 85 mm/yr with ~20-25% obliquity along Nicaragua, and at 65 to 75 mm/yr offshore of El Salvador and Guatemala with negligible obliquity. The inset map shows the regional plate tectonic setting. The red vectors indicate the plate motions relative to a fixed Caribbean Plate for model NUVEL-1. The relative motion between North America and Caribbean plates is left-lateral with rate of ~ 20 mm/yr across the Polochic-Motagua Fault zone (PMF).

These geodetic observations have led to the notion of a relatively rigid forearc sliver, or Middle America microplate, extending all the way from Costa Rica to Guatemala. During at

least the last several decades of GPS measurements there appears to be very weak interplate coupling between the CO plate and the CA plate forearc sliver along El Salvador and Nicaragua with, at most, limited regions of strong megathrust coupling located offshore of Guatemala and southern Nicaragua. To account for the block-like motion of the forearc sliver in the presence of weak interplate coupling and lack of oblique convergence offshore of El Salvador and southeastern Guatemala, the driving force for the sliver has been attributed to the Cocos Ridge collision with the CA plate along southern Costa Rica and/or pinning of the westernmost triangular region of the CA plate between the converging CO and NA plates near the triple junction (Franco et al., 2012; LaFemina et al., 2009). In contrast to the Mexican subduction zone to the northwest, where generally strong seismic coupling between the converging NA and CO plates is found, the upper CA plate is moving away from the MAT such that lower tectonic and seismic coupling may be expected. However, the inference of little megathrust coupling is complicated by the GPS sites being located far from the MAT, as well as by uncertainty in the locations and rupture characteristics of historical seismic events in the region.

Large subduction zone earthquakes do occur along the MAT (Figure 4.1), including sources that produce destructive tsunami, like the 1902 Guatemala and 1992 Nicaragua tsunami earthquakes (Fernandez et al., 2000; Kanamori and Kikuchi, 1993), and there are an unusual number of outer-rise and down-dip normal faulting events along the arc (Supplemental Figure 4.A1). Casual inspection of the seismicity in Figures 4.1 and A1 does not immediately suggest very weak seismic coupling, especially allowing for possible landward mislocation of some of the historical large events in the regions. As a result, there is substantial uncertainty regarding the potential for much larger underthrusting events in the region than have been documented in the seismological record.

Earthquake focal mechanism and seismic strain rate analyses (DeMets, 2001; Guzman-Speziale and Gomez-Gonzales, 2006; Harlow and White, 1985; McNally and Minster, 1981; White and Harlow, 1993; Pacheco et al., 1993) indicate that only ~10% to 20% of the CO-CA plate motion is seismically manifested in trench-perpendicular underthrusting events, so the cumulative seismic activity in Figures 4.1 and S1 actually does fall far short of the plate motion convergence rate even allowing for uncertainty in older event locations and mechanisms. Despite this, numerous strike-slip events occur along the Middle America volcanic arc, as is typically observed for strain partitioning that accompanies oblique subduction in strongly-coupled regions (DeMets, 2001; Fitch, 1972; McCaffrey, 1992). It has been estimated that the strike-slip earthquake strain budget may match the geodetic rates, suggesting 80-100% seismic coupling of that boundary of the sliver (Correa-Mora et al., 2009).

In 2012, the megathrust between the CO and CA plate sliver experienced three large ruptures: the August 27, 2012 M_w 7.3 El Salvador, September 5, 2012 M_w 7.6 Costa Rica, and November 7, 2012 M_w 7.4 Guatemala earthquakes (Table 4.A1). Together with the September 02, 1992 M_w 7.7 Nicaragua event (Table 4.A1), these large thrust earthquakes shed light on the nature of the Middle America megathrust rupture processes in the context of the geodetic inferences of very weak plate boundary seismic coupling extending from Guatemala to northern Costa Rica. We analyze the rupture characteristics of the four large events and aftershock sequences for the three 2012 events (Figure 4.1) to explore the nature of megathrust failure properties along the MAT.

4.2. Rupture Process Characteristics of Large Earthquakes

We first quantify the overall faulting parameters for the four large thrust events along the MAT. These are the largest events on the megathrust for which we have high quality

observations, and they define the minimum degree of seismic coupling of the plate boundary.

4.2.1 W-Phase Inversion

Three component W-phase signals in the 1.67-5.0 mHz passband were inverted for point-source moment tensors for the 1992 and 2012 events. Figure 4.A2 shows that the preferred solutions for: a) the 1992 Nicaragua event with seismic moment of 4.1×10^{20} Nm (M_w 7.7), centroid time shift of 47.8 s, depth 15.5 km, and a best double-couple solution with strike 289.0°, dip 14.7°, and rake 65.3°; b) the 2012 El Salvador event with seismic moment of 9.6×10^{19} Nm (M_w 7.3), centroid time shift of 23.0 s, depth 15.5 km, and a best double-couple solution with strike 284.4°, dip 17.2°, and rake 78.9°; c) the 2012 Costa Rica event with seismic moment 3.3×10^{20} Nm (M_w 7.6), centroid time shift of 19.5 s, depth 30.5 km, and a best double-couple solution with strike 303.4°, dip 15.7°, and rake 94.2°; and d) the 2012 Guatemala event with seismic moment of 1.2×10^{20} Nm (M_w 7.3), centroid time shift of 10.6 s, depth 23.5 km, and a best double-couple solution with strike 293.1°, dip 28.5°, and rake 77.8°. Examples of waveform fits for each case are shown in Supplemental Figure 4.A3. The estimates of depth and centroid time shift are similar to the centroid depths of 15 km, 12.0 km, 29.7 km, and 21.3 km, and centroid time shifts of 44.5 s, 20.1 s, 15.4 and 9.6 s from the global Centroid Moment Tensor (gCMT) project (http://www.globalcmt.org/CMTsearch.html) for the 1992 Nicaragua and 2012 El Salvador, Costa Rica, and Guatemala events, respectively. Although their magnitudes are similar, the W-phase centroid time shift of the El Salvador event is ~3 times larger than for the Guatemala event, and about half that for the 1992 Nicaragua tsunami earthquake, whose overall source time function duration is ~100 s (Kanamori and Kikuchi, 1993). This indicates a relatively slow rupture process of the 2012 El Salvador earthquake.

4.2.2 Finite-fault rupture inversions

Finite-fault rupture models were developed using teleseismic P waves for all four large events. Figure 4.2 summarizes the slip distribution models found from the P wave ground motions in the frequency band 0.005-0.9 Hz using the linear inversion procedure of Kikuchi and Kanamori (1991). This inversion method assumes a constant rupture velocity for a fault geometry with specified strike and dip, allowing variable rake, and uses modest smoothing to stabilized the temporal and spatial moment distribution.

For the September 2, 1992 Nicaragua earthquake, 13 broadband P waves with 130 s duration signals were inverted (examples of waveform fits are shown in Supplemental Figure 4.A4a). We assumed a hypocenter depth of 15 km, 3 km water depth, a rupture velocity of 1.6 km/s, a strike of 303°, a shallow 15°-dipping fault plane extending from the MAT to about 23 km depth, and subfault source time functions parameterized by 4 overlapping 2 s rise-time triangles (total subfault duration of 10 s) with variable rake. These choices were guided by previous studies of the limited number of broadband teleseismic P waves, surface waves and tsunami observations (e.g. Kanamori and Kikuchi, 1993; Imamura et al., 1993; Satake, 1994; Velasco et al., 1994).

The rupture model (Figure 4.2a) has three slip concentrations; a ~60 km wide patch to the southeast (with peak slip ~ 1.4 m) and two smaller 30 km wide patches (with peak slip ~ 0.9 m) on either side of the hypocenter, with rupture extending from the trench to ~23 km deep. The slip model supports the slow asymmetric bilateral rupture model of Velasco et al. (1994). The seismic data do not provide strong constraints on the along-dip width of the rupture; narrower rupture models with width of 40 km extending to 10 km deep, as proposed from tsunami modeling by Satake (1994), can be reconciled with the data, as can wider models. The seismic moment of this model, 3.6×10^{20} Nm is compatible with the long-period

estimates of 4.1 × 10^{20} Nm from W-phase inversion and 3.7 × 10^{20} Nm (Kanamori and Kikuchi, 1993) and estimates of 3.4 × 10^{20} Nm from the gCMT and from body wave inversions (Kikuchi and Kanamori, 1995). The 100 s duration of the source time function, with a centroid time of 45 s, is also consistent with earlier studies. Given the limited data available, the resolution of the model is lower than for the more recent events, but we believe this model captures first-order attributes of the rupture well.

For the August 27, 2012 El Salvador event we inverted 83 broadband P waves with 100 s durations for a fault geometry with strike 296° and dip 16°, again extending from the trench to about 23 km deep, and a hypocentral depth of 15 km. A rupture velocity of 2 km/s, was used, with little direct constraint on that choice. The subfault source time functions had six overlapping 2 s rise-time triangles spanning a 14 s long total duration. The resulting model (Figure 4.2b) has a single large slip patch, extending across the fault width and ~50 km along strike, with peak slip of ~1.2 m and total seismic moment of 1.2 × 10^{20} Nm (M_w 7.3), about 20% larger than the W-phase solution. The source time function has ~40 s duration with a centroid time of 19 s. Waveform comparisons are shown in Supplemental Figure 4.A4b. The waveforms are relatively simple and the source model has limited spatial resolution as a result. Using a deeper hypocenter gives a more compact slip distribution, but our model is compatible with the 12 km centroid depth of the gCMT solution.

For the Costa Rica and Guatemala events larger centroid depths are indicated by the gCMT and W-phase long-period solutions. We explored a range of source depths and dip angles guided by the regional slab geometry to find our preferred finite-faulting inversions of ~70 broadband teleseismic P signals in each case (examples of the waveform fits are shown in Figure 4.A4c and S4d). For the September 5, 2012 Costa Rica earthquake we settled on a hypocenter depth of 24 km and fault plane dip of 24° dip and strike of 310°, a rupture

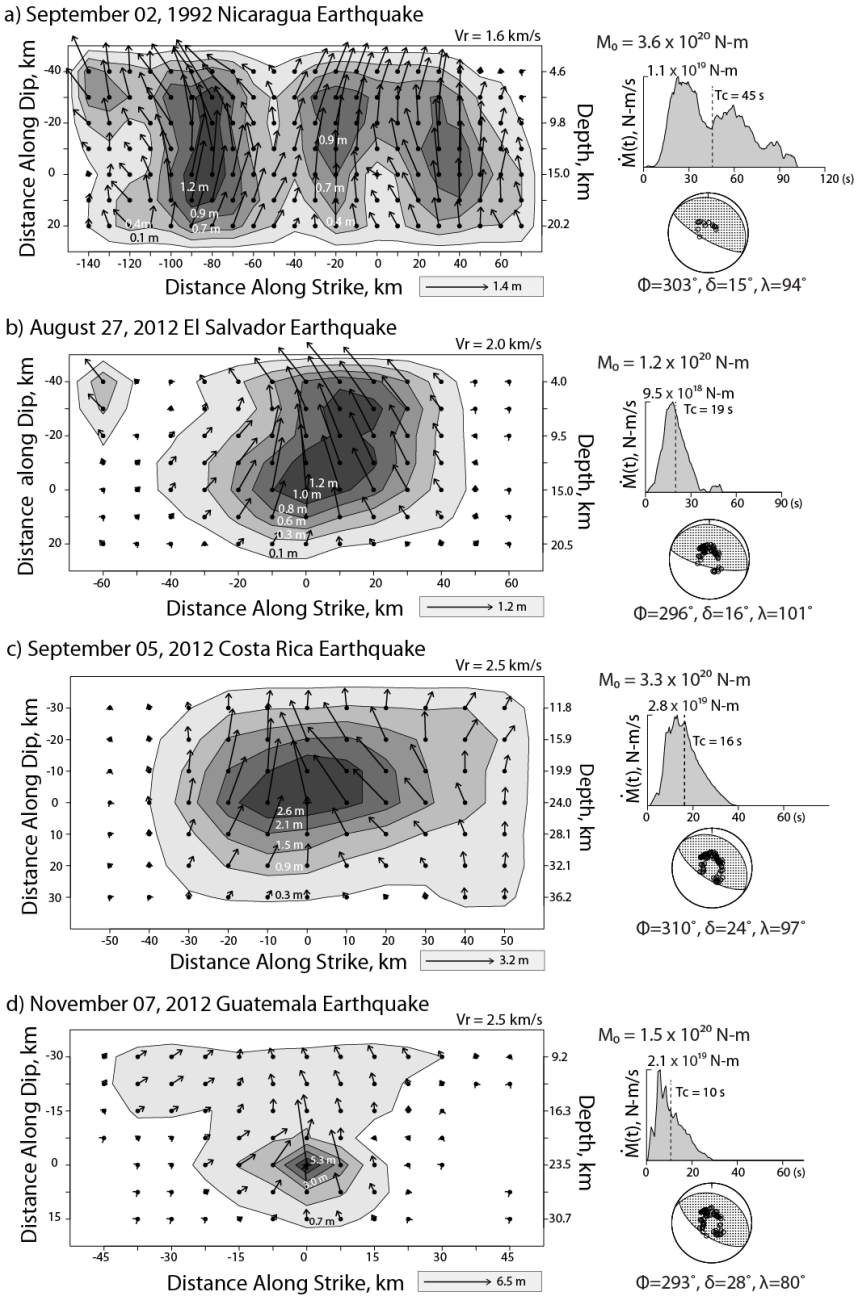

Figure 4.2 Finite-fault slip models from teleseismic P wave inversion for a) September 2, 1992 Nicaragua, b) August 27, 2012 El Salvador, c) September 5, 2012 Costa Rica and d) November 7, 2012 Guatemala earthquakes. The slip distribution on the fault plane is shown for each case with the arrows indicating average rake of each subfault, and the slip magnitude being contoured. Peak slip is indicated for each model, along with the rupture expansion velocity, Vr. The moment rate functions, seismic moments, centroid times (Tc), and average focal mechanisms are shown, with the lower hemisphere equal area projections indicating the positions sampled by teleseismic P waves used in the inversions. Observed and synthetic P wave comparisons are shown in supplementary Figure 4.A4.

velocity of 2.5 km/s, and subfault source time functions with 4 overlapping 3 s rise-time triangles (total subfault duration of 15 s). The slip model in Figure 4.3c has a large-slip patch with peak slip of ~3.2 m extending from 10 – 35 km in depth and ~80 km along strike, with a total seismic moment of 3.3×10^{20} Nm (M_w 7.6) and centroid rupture time of 16 s. For the November 7, 2012 Guatemala earthquake, the hypocenter depth is 23.5 km, with dip of 28° and strike of 293°, a rupture velocity of 2.5 km/s and subfault source time functions comprised of 4 overlapping 1.5-s rise-time triangles (total subfault rupture durations of 7.5 s). A slip concentration with peak slip of 5.3 m, is found near the hypocenter, spread from 20 – 25 km in depth and ~20 km along strike. The centroid time is 10 s. Minor, poorly resolved slip extends up-dip to ~10 km depth, and the total seismic moment is 1.5×10^{20} Nm (M_w 7.4), about 20% higher than the W-phase estimate. The moment rate functions for Costa Rica and Guatemala events have more pronounced jagged short-duration pulses than the shallower events, which may correspond to relative enrichment in high frequency radiation.

4.3 Short-period seismic wave radiation characteristics

We extend the rupture characterization of the four large thrust events to include their short-period seismic wave radiation, computing azimuthally-averaged P wave source spectra, seismic moment-scaled radiated energy, E_r/M_0, and ~1 s period P wave magnitudes measured over the full duration of the source radiation, $\hat{m}_b$ (Houston and Kanamori, 1986).

Broadband source spectra were obtained by combining the spectra of the moment-rate functions for the preferred finite-fault models in Figure 4.2 for frequencies less than ~0.05 Hz with averages of radiation-pattern- and attenuation-corrected teleseismic broadband P wave spectra for frequencies from 0.05 to 1 Hz. Figure 4.3 shows the resulting source spectra, along with reference source spectra for an ω^{-2} model with 3 MPa stress parameter (Brune, 1970).

The spectra for the El Salvador and Guatemala events are normalized to the W-phase moment estimates because the P wave estimates appears about 20% high. The source spectra were fit with ω^{-2} models by varying the stress parameter and holding the shear velocity (β) fixed at 3.75 km/s. The best fitting models have low stress parameters of 0.08 and 0.09 MPa for the 1992 Nicaragua and 2012 El Salvador events, respectively, and more typical interplate stress parameters of 0.91 and 1.35 MPa for the 2012 Costa Rica and 2012 Guatemala events, respectively.

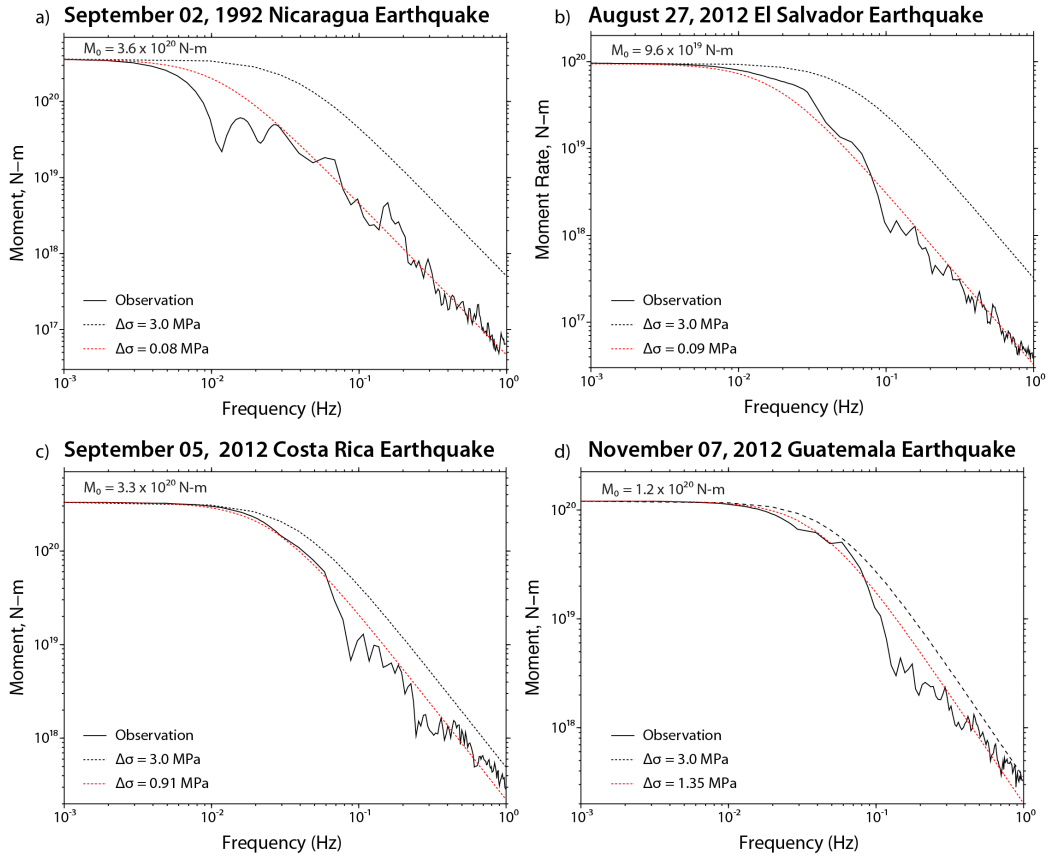

Figure 4.3 The average source spectra for teleseismic P waves for the large thrust events in Middle America. In each panel, the black line indicates the observed spectra, estimated at frequencies less than ~0.05 Hz from the moment rate function inverted from teleseismic P wave observations (Figure 4.2) and at frequencies > ~0.05 Hz from stacking of broadband teleseismic P wave spectra. The dashed lines are reference source spectra for an w-2 model with 3 MPa stress parameter (black) and best fitting w-2 models with different stress parameters (red), with fixed shear velocity, b = 3.75 km/s, and seismic moments given by the W-Phase inversions (2012 El Salvador and 2012 Guatemala events) or P-wave inversions (1992 Nicaragua and 2012 Costa Rica events).

Total radiated seismic energy was estimated using the energy fraction computed for 0.05-1.0 Hz teleseismic P wave ground velocity spectra relative to the lower frequency energy content following the theory and method of Venkataraman and Kanamori (2004) and Rivera and Kanamori (2005). Large uncertainties are introduced by poor knowledge of the average P and S wave velocities around the sources, as well as limited data bandwidth and uncertainty in propagation corrections, particularly attenuation. The inclusion of the low-frequency energy contribution is essential for the 1992 Nicaragua and 2012 El Salvador events, for which the spectra are depleted in short-period energy. The total radiated energy estimates are 2.24×10^{14} J, 1.67×10^{14} J, 3.36×10^{15} J and 1.37×10^{15} J for the Nicaragua, El Salvador, Costa Rica and Guatemala events, respectively. The USGS estimates of energy magnitude, M_e, are 7.4 for the El Salvador and 7.9 for the Costa Rica and Guatemala events.

Figure 4.4a shows the seismic moment-scaled radiated seismic energy for the large Middle America subduction zone events along with values for other interplate and intraplate events. Known tsunami earthquakes are highlighted. The 1992 Nicaragua event has the lowest E_r/M_0, 6.22×10^{-7}, among all events in Figure 4.4a, while the 2012 El Salvador event also has a low E_r/M_0, 1.85×10^{-6}, similar to tsunami earthquakes. The 2012 Costa Rica and 2012 Guatemala events have E_r/M_0 ratios, 1.02×10^{-5} and 1.13×10^{-5}, respectively, similar to interplate events in other subduction regions.

The relative short-period seismic wave radiation levels are also measured by the $\hat{m}_b$ values, which are 5.6, 5.5, 6.4 and 6.4 for the Nicaragua, El Salvador, Costa Rica and Guatemala events, respectively. These values generally track the USGS m_b values given above, although the value for the 1992 Nicaragua event is relatively increased by using the full P wave signal window to measure the 1 Hz signal level. Figure 4.4b shows that the magnitude difference between M_w and $\hat{m}_b$ is ~ 2 for the 1992 Nicaragua and 2012 El

Salvador events and 0.8 for the 2012 Costa Rica and Guatemala events.

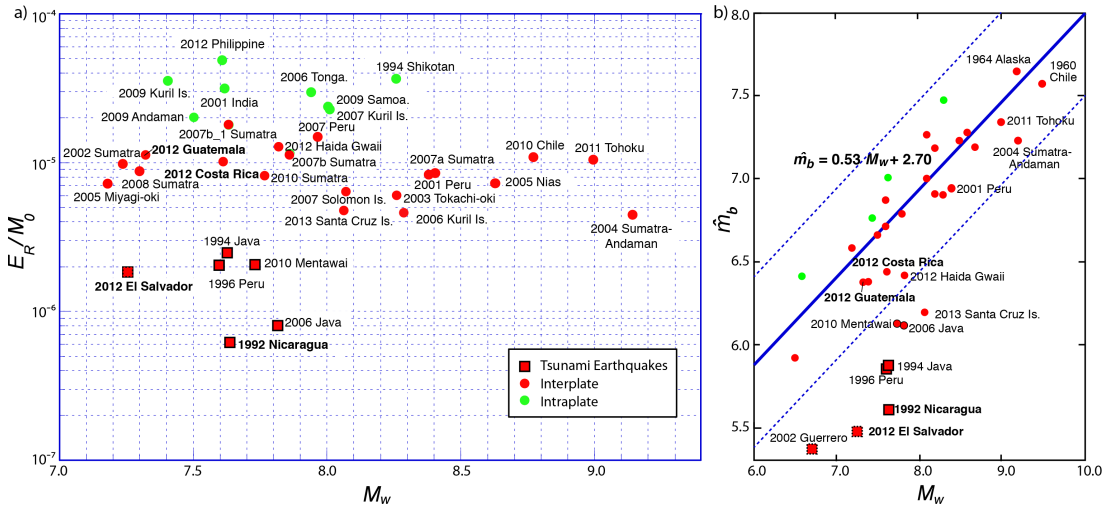

Figure 4.4 (a) Estimates of seismic moment-scaled radiated seismic energy from teleseismic P wave ground velocity spectra and broadband source time functions from finite source inversions for recent large earthquakes. The 2012 El Salvador event has low moment-scaled energy typical of larger tsunami earthquake ruptures. Note that the 2012 Costa Rica and 2012 Guatemala events have ~ 5-6 times higher seismic moment-scaled radiated energy. (b) Short-period $\hat{m}_b$ measurements for large earthquakes, plotted versus their seismic moment magnitudes. $\hat{m}_b$ is similar to conventional mb, but uses the peak 1 s period amplitude over the full duration of the P waves rather than just the first few cycles of the waveforms, so it gives a better estimate of the overall ~1 s spectral level. Color-coded circles indicate interplate earthquakes (red) and intraplate earthquakes (green), and red squares with black outline indicate interplate tsunami earthquakes. The 2012 El Salvador earthquake has a similar value to the 1992 Nicaragua tsunami earthquake, but was too small to generate a large tsunami. The 2012 Costa Rica event and 2012 Guatemala event have $\hat{m}_b$ similar to typical interplate ruptures, although on the low end of the suite of observations. The blue line shows the $\hat{m}_b$ - seismic moment magnitude relationship obtained by Houston and Kanamori (1986).

To further establish the radiation characteristics, we compare teleseismic and regional P wave signals for the 2012 El Salvador and 2012 Costa Rica earthquakes at common stations. Figure 4.A5 shows that the teleseismic P waves are not dramatically different waveforms, but the first arrivals do have more impulsive character for the Costa Rica event. The regional P wave ground velocity recordings at comparable propagation distances have signal amplitude ratios for frequencies > 1 Hz relative to < 0.1 Hz that are a factor of 3.6-5.6 larger for the Costa Rica event than for the El Salvador event, consistent with the factor of 5.5 higher

seismic moment-scaled radiated energy (Figure 4.A5).

4.4 Aftershock Sequence Characterization

Substantial aftershock sequences (Figure 4.1) followed the three large 2012 thrust earthquakes, with 141 events with $m_b \geq 4.0$ including the mainshocks (Table 4.A2) being well recorded by regional broadband station TGUH and several Nicaragua broadband network (NU) stations (Figure 4.5). 24 of the aftershocks have gCMT solutions with normal faulting or thrust fault mechanisms, as shown in Figure 4.5. We are particularly interested to identify events with faulting mechanisms similar to the mainshocks which are likely to be on the plate interface. The main objective is to evaluate the seismic radiation efficiency for small events to see whether there are similarities to the large event characteristics.

We used cross-correlations of three-component broadband recordings at TGUH filtered in the passband of 0.01-0.05 Hz for the vertical components and 0.02-0.05 Hz for horizontal components to identify similar waveform clusters for nearby events. We use template waveforms from events with known gCMT focal mechanisms (Figure 4.A6). There are 28, 10 and 10 events with focal mechanisms similar to the 2012 El Salvador, Costa Rica and Guatemala mainshocks, respectively. 4 events have waveforms similar to two near-trench intraplate normal faulting events (012 and 017), and 7 events have waveforms similar to forearc normal faulting event 016. 7 events have similar waveforms to thrust event 104, which has distinct waveforms from the 2012 Guatemala event, and 3 events with similar waveforms to offshore thrust event 133 between Guatemala and El Salvador. Other events are too small or have focal mechanisms distinct from the nearby template events. The activation of normal faulting by the 2012 El Salvador event is similar to other large tsunami earthquakes, possibly indicating relatively complete stress release on the megathrust and/or slip extending up to the

trench. Figure 4.5 indicates the spatial and temporal distribution of the clusters of similar mechanism events, along with the distribution of unclassified events.

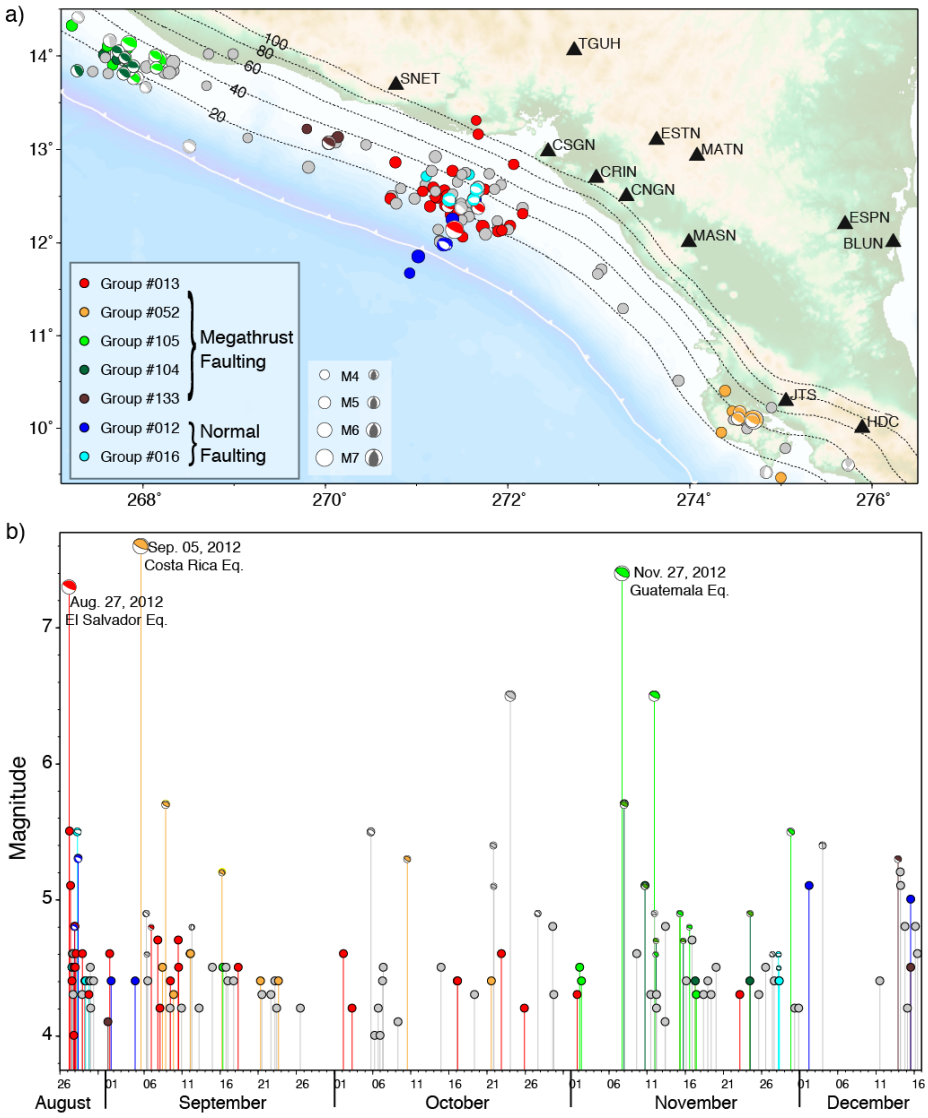

Figure 4.5 (a) Locations of mb ≥ 4.0 events in the aftershock sequences for the three 2012 mainshocks from the USGS/NEIC catalog. Color-coded circles indicate similarity of three-component waveforms at station TGUH (triangle) to reference under-thrusting events 013 (red) and 133 (dark brown) offshore of El Salvador, 052 (tan) under Costa Rica, 104 (dark green) and 105 (green) offshore of Guatemala, and offshore El Salvador normal-faulting events 012 (blue) and 016 (light blue). The reference event focal mechanisms are from gCMT. Grey circles are events with no classification of mechanism. Waveforms are shown in Figure 4.A6. White barbed curve indicates the position of the trench. Triangles indicate stations used for spectral analysis. The white barded curve indicates the position of the MAT, and dash lines show the slab depth contours in km. (b) Time series for the aftershock sequence color-coded as in the map.

Having identified events with similar focal mechanisms in close spatial proximity, we use the regional broadband waveforms to estimate basic source spectral characteristics. This involved modeling of spectral ratios of common component recordings at the same station for events with similar mechanisms separated in location by ≤ 50 km. The data distribution allows us to examine spectral differences among the thrust populations along the megathrust and the difference between the thrust and normal faulting populations along El Salvador. Time windows of 10 s before to 150 s after the manually picked P arrivals in the regional broadband recordings from TGUH and the NU network stations shown in Figure 4.5 are used. The most reliable spectral ratios with substantial bandwidth are baseline adjusted in the 0.1-0.2 Hz spectral band relative to the vertical component ratios for TGUH, and average spectral ratios computed from 3 to 10 individual ratios. These averaged spectral ratios were then modeled, with propagation and site effects ideally being cancelled out, isolating the source spectrum differences.

For the spectral ratio modeling we assumed the spectral shape of the ω^{-2} source model, parameterized by a moment level and a corner frequency parameter. We varied the seismic moment of the denominator event relative to specified gCMT seismic moment for the numerator event, along with the corner frequencies of both numerator and denominator events. The procedure is most robust for event pairs with large differences in corner frequency and seismic moment, and good signal-to-noise ratio over substantial bandwidth. Examples of the spectral ratio averaging and modeling are shown in Figure 4.A7. The ratios have increasing variance at higher frequencies, and not all of the spectral ratios tightly define the smaller event's corner frequency, but this mainly affects the smallest events. The spectral ratios are not reliable above 3 Hz where the ratios abruptly rise or drop off, so modeling was constrained to frequencies ≤ 3 Hz. The parameter estimation was performed by grid

searching over the 3 adjustable spectral parameters rather than by inversion. In general the spectral ratios are modeled adequately with the simple point-source parameterization although some event pairs have spectral ratio complexity not represented by the simple sources. Our signal windows capture essentially the full regional waveform, so body and surface waves are included. This allows us to have substantial bandwidth and avoids challenges of phase windowing, but does mean that our source spectral characterizations are gross measures of the seismic radiation, not individual phase spectra.

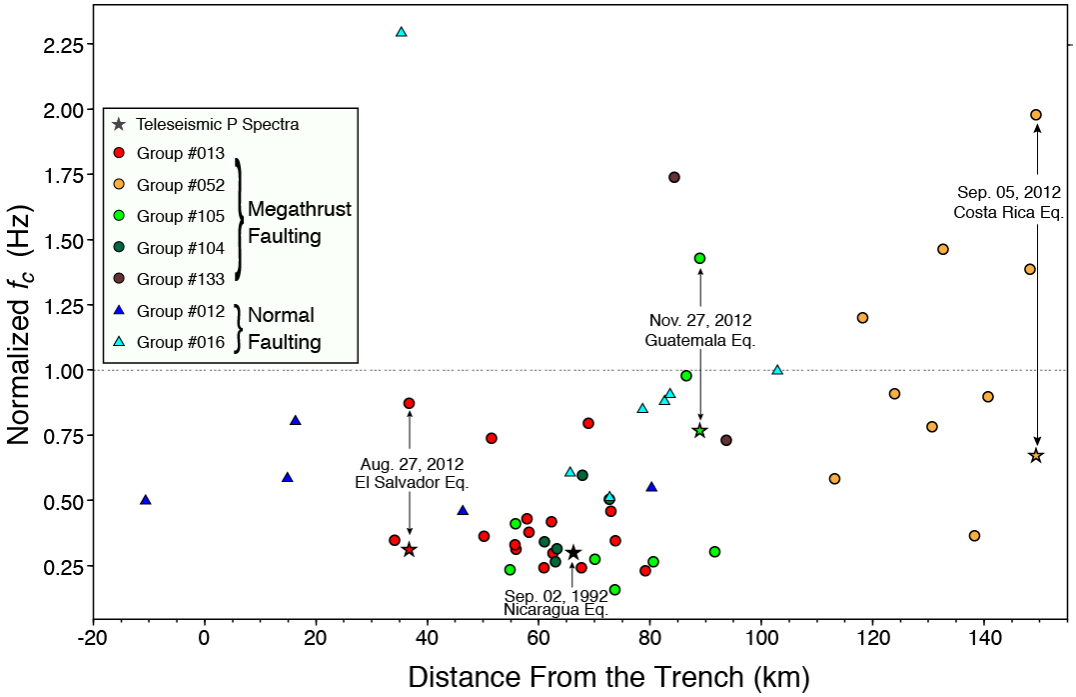

Figure 4.6 Corner frequencies, normalized by 3 MPa w-2 source model with shear velocity 3.75 km/s, from fitting the spectral ratios of similar focal mechanism events for likely interplate thrust events (circles) and intraplate normal faulting events offshore El Salvador (triangles), plotted as a function of perpendicular distance from the trench to the USGS/NEIC source locations. The stars show the normalized corner frequencies from fitting teleseismic P wave spectra (Figure 4.3). Note the trend of increasing normalized corner frequencies for (likely) interplate thrust events from anomalously low values closer to the trench to higher values at greater distances, and the high normalized corner frequencies offshore Costa Rica. Intraplate normal faulting events tend to have higher normalized corner frequencies than interplate earthquakes offshore El Salvador. Examples of the spectral ratio fitting are shown in supplementary Figure 4.A7.

Figure 4.6 shows that the corner frequency estimates, normalized relative to a reference constant stress parameter (3 MPa) ω^{-2} source model with shear velocity 3.75 km/s, exhibit systematic spatial distributions. The normalized corner frequencies for thrust faulting events tend to increase from anomalously low values closer to the MAT to higher values, scattered around the reference model further down-dip. This trend may involve along-strike variation as well, given that the deeper events are mainly near Costa Rica, with many shallower events being along El Salvador. Intraplate normal faulting events tend to have higher normalized corner frequencies than interplate earthquakes along El Salvador. The source parameter estimates from the regional wave spectra for the three large thrust events have higher normalized corner frequencies from regional data than inferred from the teleseismic P wave spectra (Figure 4.3), although the relative shifts are similar. This may due to spectral superposition of multiple arrivals and source-finiteness effects in the full regional waveform spectra (Molnar et al., 1973; Savage, 1972) relative to the single phase measures given by the teleseismic data.

While there is a lot of scatter and the approximate uncertainty for each estimate is ±30%, the basic pattern of difference in spectral character between the El Salvador (red) and Guatemala (green) events relative to the Costa Rica (tan) events appears reliable, as does the tendency for intraplate normal faulting to have higher normalized corner frequencies along El Salvador. Allmann and Shearer (2009) find that the Central America region has very low stress drop measures for thrust events along the Cocos subduction zone, including along Mexico, Guatemala and Nicaragua, whereas intraplate events had more typical stress drop estimates. The basic trend seen in Figure 4.6 is also compatible with the results of Convers and Newman (2011) who analyzed radiated seismic energy for 53 large thrust events along the MAT with $M_w \geq 6.7$. They found that on average the $\log_{10}$(radiated energy/seismic

moment) discriminant value along the MAT (-5.15) is lower than the global average value (-4.74) for thrust events, indicating energy deficiency by about a factor of 3. All of their events off of Nicaragua and Costa Rica were energy deficient, with some events off of Chiapas, Mexico and Guatemala having higher energy. They observed a slight trend of increasing energy with depth, but there is again a lot of scatter, so it is difficult to distinguish from lateral variations. Overall, the tendency for interplate events on the megathrust along the MAT to have lower corner frequencies and lower radiated energy appears to hold for events ranging in size from m_b ~4 to M_w ~7.6, suggesting that this is related to the interplate frictional properties, not just unusual rupture of the largest events.

4.5 Discussion

The nature of interplate coupling along the Middle America megathrust can now be considered in the light of joint seismic and geodetic observations. The large thrust events of 2012 provide a significantly expanded sampling of well-quantified seismological observations of earthquake ruptures to supplement the extensive geodetic data sets acquired in the past few decades. We update and refine the seismic strain rate estimates from previous studies by focusing exclusively on shallow-dipping thrust earthquakes in the gCMT catalog since 1976, which is fairly complete down to about M_w 5.0. We only consider events with centroid depths less than 40 km along the plate boundary from northern Guatemala to Nicoya, Costa Rica as shown in Figure 4.7a. There is some depth uncertainty in the gCMT catalog, and some events with overestimated source depths or deeper coupled portions of the plate boundary may be excluded, but the number of such events is small and their inclusion would not change the basic result we find here. The cumulative seismic moment for these events is ~ 1.01×10^{21} Nm, of which 9.54×10^{20} Nm is from the 1992 Nicaragua, 2012 El Salvador, 2012

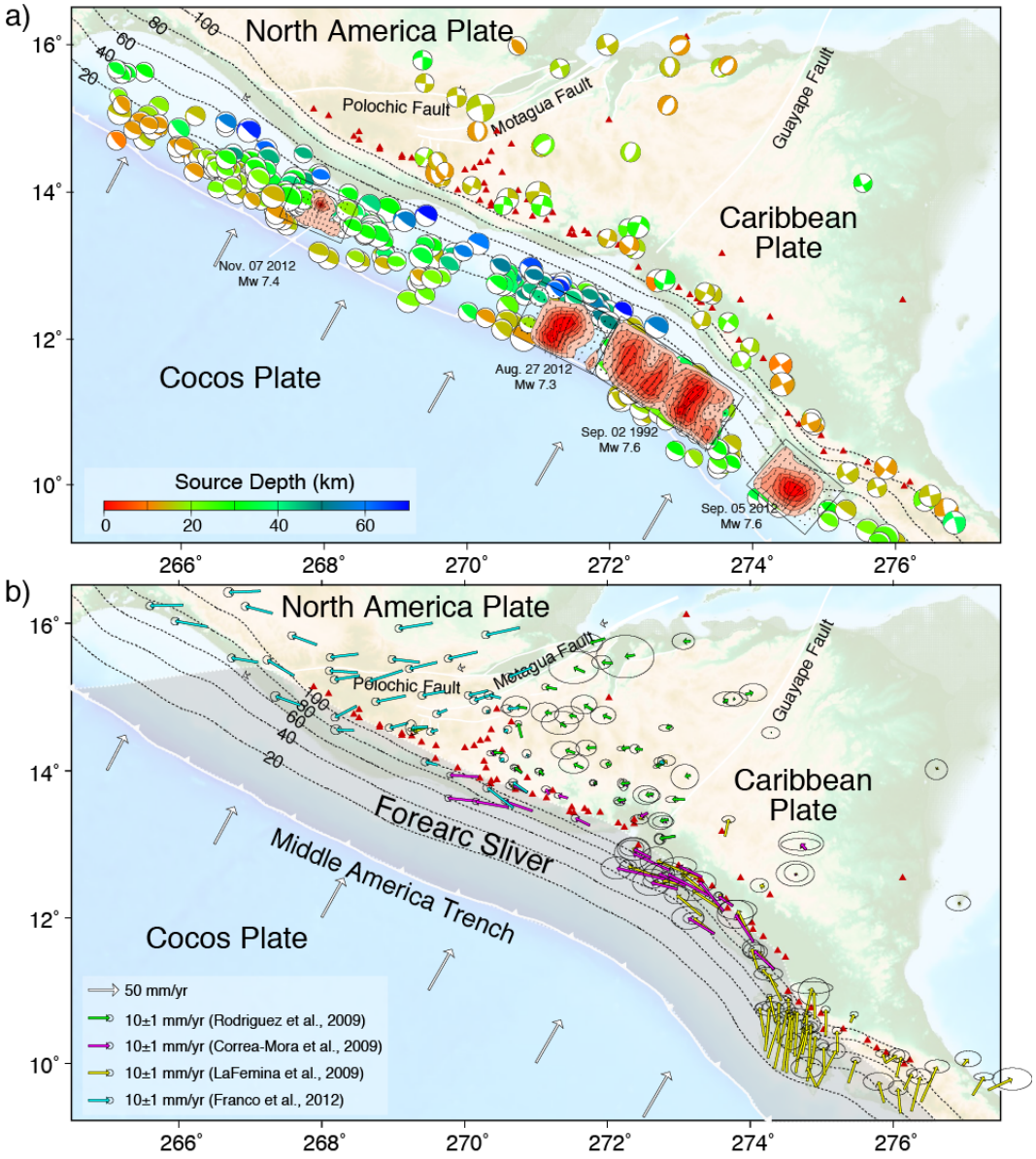

Figure 4.7 a) Map of gCMT focal mechanisms from 1976 to 2013 for interplate earthquakes on the MAT megathrust, strike-slip earthquakes along the volcanic arcs and the Polochic-Motagua faults, and shallow normal faulting events in the Caribbean Plate. Fault slip models for the 1992 Nicaragua, 2012 El Salvador, 2012 Costa Rica, and 2012 Guatemala earthquakes from finite fault inversions (Figure 4.2) are also shown. b) Summary of the GPS velocity field measurements from four recent studies (Rodriguez et al., 2009; LaFemina et al., 2009; Correa-Mora et al., 2009; Franco et al., 2012) in the fixed Caribbean Plate reference frame. The white barbed curve indicates the position of the MAT, and dashed lines indicate 20-km increment slab depth contours. The forearc sliver that is undergoing boundary-parallel motion is shaded.

Costa Rica and 2012 Guatemala events. We estimate a seismogenic megathrust length of 1300 km, width of 100 km, and area of ~1.3×10^5 km^2. The CO-CA convergence rate is ~72 mm/yr along Guatemala to ~85 mm/yr along Nicoya (DeMets, 2001), so we assume an average value of 78 mm/yr for the region. The 37 year interval seismic moment rate to tectonic convergence rate ratio is ~6.7%, assuming an average rigidity of 40 GPa along the megathrust. This estimate is comparable with the seismic coupling estimates of ~3%-20% along the MAT by Pacheco et al. (1993) and ~10% from 1976-2003 by Guzman-Speziale and Gomez-Gonzalez (2006). The 37 year period is certainly too short for robust seismic coupling estimation given the regional estimate of recurrence time of ~50-70 years for M7+ events (Nishenko, 1991), but it is very difficult to justify inclusion of historical events with uncertain locations and focal mechanisms, especially given the well-documented and extensive occurrence of intraplate normal faulting and strike slip faulting in the nearshore and offshore regions. We note that the measure of cumulative moment release over a fixed interval of time is not the ideal measure of seismic coupling, which would use time intervals between repeated ruptures of the same fault subregions, but we lack information about slip in any prior large ruptures in the regions of the recent events so this is all that can be done.

We summarize the extensive GPS observations and inferences that have accumulated and been published over last two decades, plotting them relative to a fixed Caribbean plate in Figure 4.7b. The inferred relative motions between NA, CO, CA and the forearc sliver, as well as the internal deformation are noted. The NA/CA motion decreases from ~20 mm/yr in eastern Guatemala along the Polochic-Motagua fault zone down to a few millimeters per year in western Guatemala. There is ~ 5-10 mm/yr E-W extension within the CA plate in northwestern Honduras adjacent to Guatemala and El Salvador, where shallow normal faulting events have occurred (Figure 4.7a) (Franco et al., 2012; Lyon-Caen et al., 2006). The

geodetic studies consistently indicate low or no coupling on the deeper portion of the megathrust below the forearc sliver, which is translating at ~10-16 mm/yr toward the NA-CO-CA triple junction in the CA reference frame. Given that the CA is moving away from the subduction zone, the relative motion of the sliver can be viewed as the forearc being left behind the retreating CA. 85-100% seismic coupling is estimated from strike-slip events along the volcanic arc on the northeast boundary of the sliver (Figure 4.7a) (Franco et al., 2012). Two patches with ~10% and ~25-50% locking near El Salvador and Costa Rica, respectively, are suggested by Correa-Mora et al. (2009), with less than 2% on average over the entire megathrust along the sliver. Estimates of from 5 to 100% localized coupling over different scale lengths for the shallow megathrust along the sliver extending to about 20 km depth have been proposed in various studies (LaFemina et al., 2009; Rodriguez et al., 2009; Franco et al., 2012). Relatively strong locking of ~60% near the triple junction has been suggested, although part of this region is the Tehuantepec seismic gap, where no large historical earthquake activity has been recorded. These geodetic coupling estimates are summarized in Figure 4.A8.

Considering the seismic activity along the Middle America megathrust in the context of the cumulative moment estimate and the geodetic observations, we provide a schematic map (Figure 4.8) that indicates generally low coupling on the megathrust below the forearc sliver, with localized asperities that had/have high seismic coupling inferred from the slip models and focal mechanisms of interplate thrusting events. This characterization is now much better defined as a result of our quantification of the three recent large earthquakes along the MAT. The region along Nicoya, Costa Rica has repeatedly experienced large interplate thrust events, suggesting a high-percentage of strong coupling, and this is consistent with the geodetic estimates of substantial areas of 100% locking prior to the 2012 event. Offshore of

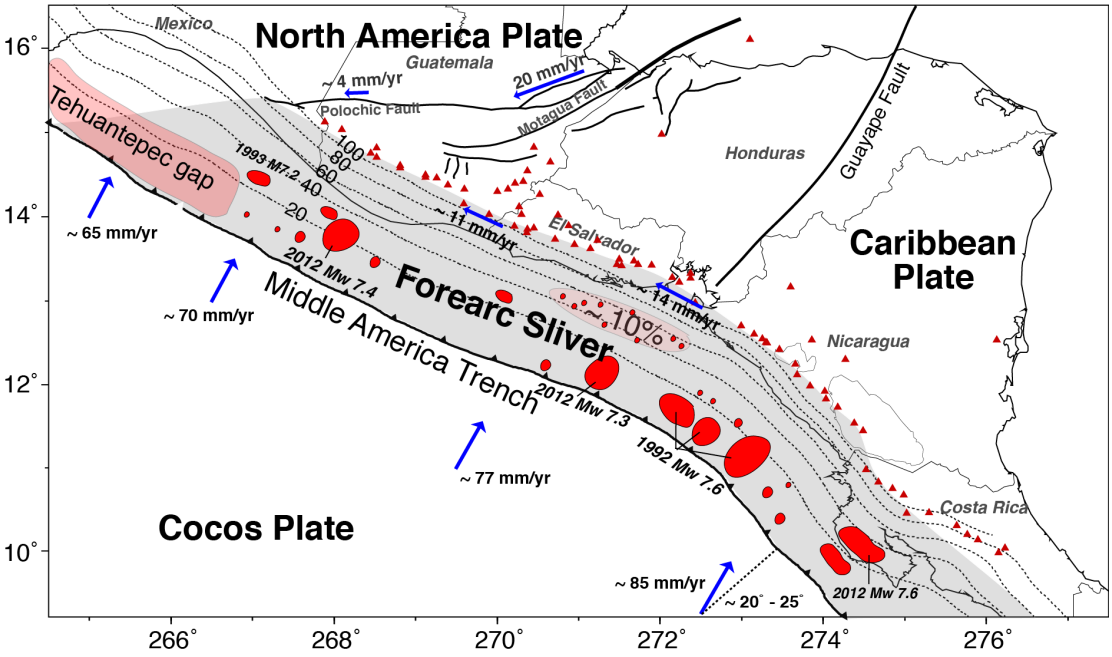

Figure 4.8 Map showing plate and forearc motions relative to a fixed Caribbean Plate (blue) and schematic seismic asperities (red patches) that had/have high seismic coupling as inferred from slip models for large interplate thrusting events. The pale pink region offshore of El Salvador at depths from 30-60 km is inferred to have ~10% locking inverted from geodetic data (Correa-Mora et al., 2009). The Tehuantepec gap lacks any recorded large earthquake activity, but has been inferred to have about 60% locking based on geodetic observations (Franco et al., 2012).

Nicaragua and El Salvador, the larger asperities appear to be located at depths from the trench to about 20 km deep, with patchy areas of ~40 km length scale, surrounded by weaker coupling. Failure of either several or individual patches led to the 1992 Nicaragua and 2012 El Salvador earthquakes with depleted short-period seismic radiation, low rupture velocity and tsunami-earthquake characteristics. Many of the smaller interplate events in this region appear to have anomalously low corner frequencies. Presence of subducted sediments on the megathrust may account for the low rupture velocities and weak short-period radiation during failure of the shallow megathrusts (e.g., Kanamori and Kikuchi, 1993; Polet and Kanamori, 2000). Intermediate size asperities exist on the megathrust at somewhat deeper depths along this region, giving rise to a few moderate size thrusting aftershocks and events

like the October 9, 2004 M_w 6.9 event located down-dip of the 1992 Nicaragua event. Offshore of Guatemala and Chiapas, Mexico, localized asperity failures gave rise to the November 7, 2012 M_w 7.4 event and the September 10, 1993 M_w 7.2 event to the north, with normal radiation characteristics.

There is a large segment between El Salvador and Guatemala without a recent large event; it is hard to preclude isolated events like the 2012 events occurring in this region. However, the absence of upper plate strain in the convergence direction along the sliver from Nicaragua to Guatemala strongly suggests the patchy asperity distribution in Figure 4.8 is about the upper limit of the seismically strongly coupled portion of the megathrust in terms of what can be reconciled with the recent geodetic history. At face value, this appears to reduce the likelihood of a great earthquake rupturing along this boundary. There are several caveats to this interpretation: the 1992 Nicaragua event itself appears to involve a sequence of asperities failing in a single rupture, enhancing the tsunami excitation greatly relative to a single asperity failure like the 2012 El Salvador event. A cascade of multiple asperities failing along the megathrust, perhaps following rupture of one particularly large one, could give rise to a great rupture even without requiring uniform strong coupling. The relative timing of the three 2012 earthquakes and the overlap of their aftershock sequences indicates the potential for synchronization of proximity to failure along the arc. There is also a fundamental question about time-varying coupling; the shallow megathrust off of the Nicaragua event may have unusually slow healing and accumulation of upper plate strain due to the shallow frictional properties of that source region. These considerations make it difficult to rule out great events entirely.

4.6 Conclusions

Motivated by recent geodetic findings of little strain accumulation in the upper Caribbean plate along the Middle America subduction zone, we analyzed the seismological rupture characteristics of and unusual suite of three large thrust earthquakes that occurred in 2012, along with the 1992 Nicaragua tsunami earthquake. A relatively long source duration, low seismic moment-scaled radiated energy, and depleted short-period seismic source spectrum is found for the 2012 El Salvador event, similar to the 1992 Nicaragua tsunami event which ruptured the adjacent shallow portion of the plate boundary. The 2012 El Salvador event was too small to generate a large tsunami but has attributes shared with other recent tsunami earthquakes. It seems quite plausible that other tsunami earthquakes can occur along the shallow megathrust extending from Guatemala to Nicaragua. Large 2012 ruptures along Costa Rica and Guatemala occur at greater depth on the megathrust and have more typical seismic moment-scaled radiated energy and source spectra. Underthrusting aftershocks of the El Salvador and Guatemala events have anomalously low relative corner frequencies, whereas deeper aftershocks of the Costa Rica event appear to be rather typical. This suggests that both large and small events are influenced by depth- or laterally-varying frictional properties, with events closer to the trench having lower than typical corner frequencies. The slip distributions, radiated energy and spectral variations suggest a patchy distribution of seismic coupling along the shallow megathrust, with cumulative seismic moment release over the past 37 years accounting for less than 10% of the plate motion budget. This is generally consistent with the geodetic inferences of weak interplate coupling and trench-parallel transport of a forearc sliver with little trench-perpendicular strain accumulation in the upper plate. While the potential for a great earthquake along the boundary may appear to be low given the inferred weak coupling, seismic hazard along the

arc remains high due to the very seismogenic strike-slip system accommodating the sliver motions and the presence of large intraplate normal faulting in the slab just off the coast, along with upper plate deformation in the westernmost portion of the Caribbean plate. The possibility of a multi-asperity rupture growing into a great event along the arc cannot be ruled out, nor can concerns about time-varying plate coupling, given the short observational history.

Acknowledgments. This work made use of GMT and SAC software. We appreciate comments from two anonymous reviewers. The IRIS DMS data center was used to access the seismic data from Global Seismic Network and Federation of Digital Seismic Network stations. This work was supported by NSF grants EAR0635570 (T. L.).

4.7 Supplementary Figures

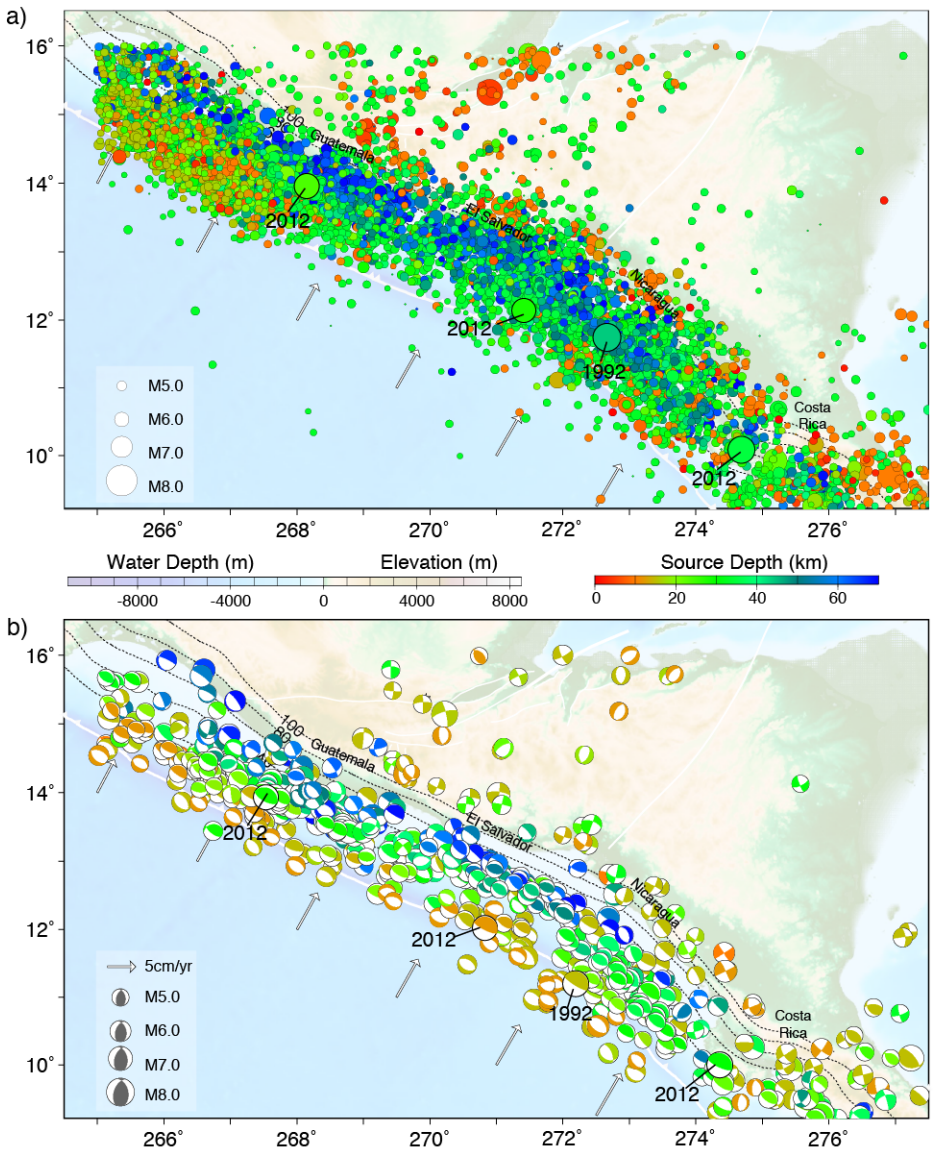

Figure 4.A1 (a) Shallow seismicity along Middle America with mb ≥ 5.0 between 1973 and 2013 from the USGS/NEIC catalog. Symbol diameters are scaled with magnitude and colored by source depth. The epicenters of the November 7, 2012 Guatemala (Mw 7.4), August 27, 2012 El Salvador (Mw 7.3), September 2, 1992 Nicaragua (Mw 7.6), and September 5, 2012 Costa Rica (Mw 7.6) events are highlighted. The white curve indicates the position of the Middle America trench, and dashed lines show slab depth contours in km. The arrows show the estimated Cocos plate motion direction and rate relative to a fixed Caribbean plate computed using model NUVEL-1. (b) Best double-couple solutions from the Centroid-Moment Tensor catalog from 1976-2013 for events less than 70 km deep are plotted at the centroid locations. The symbol sizes are scaled relative to Mw. The mechanisms of the three events highlighted at the top are labeled.

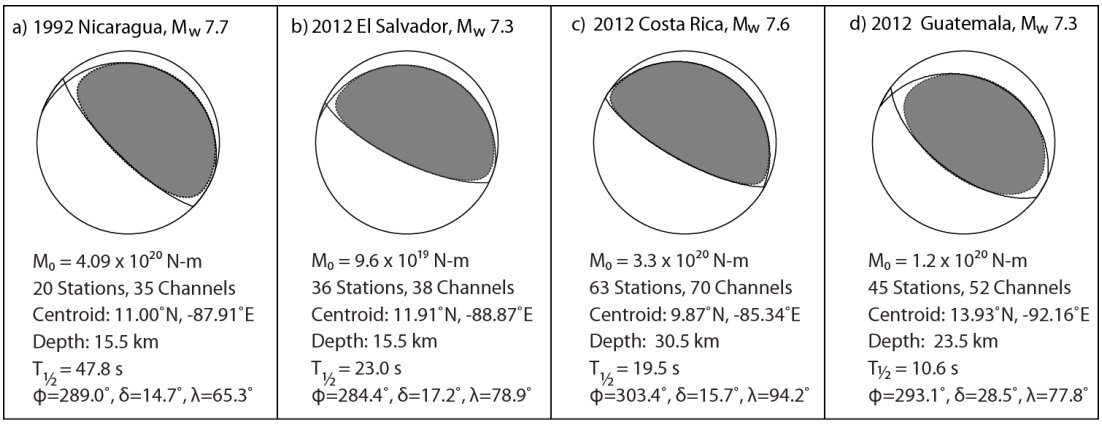

Figure 4.A2 Point-source moment tensor from W-phase inversion for a) the September 2, 1992 Nicaragua event, b) the August 27, 2012 El Salvador event, c) the September 5, 2012 Costa Rica event and d) the November 07, 2012 Guatemala event. These solutions are for inversion of W-phase observations in the frequency band 1.67-5.0 mHz (200-600 s) from the indicated number of stations and channels, with the seismic moment (M0), centroid epicenter and depth, centroid time shift ($T_{1/2}$) and strike (φ), dip (δ) and rake (λ) of the best double couple being given for each case. Observed and synthetic W-phase comparisons are shown in supplementary Figure 4.A3.

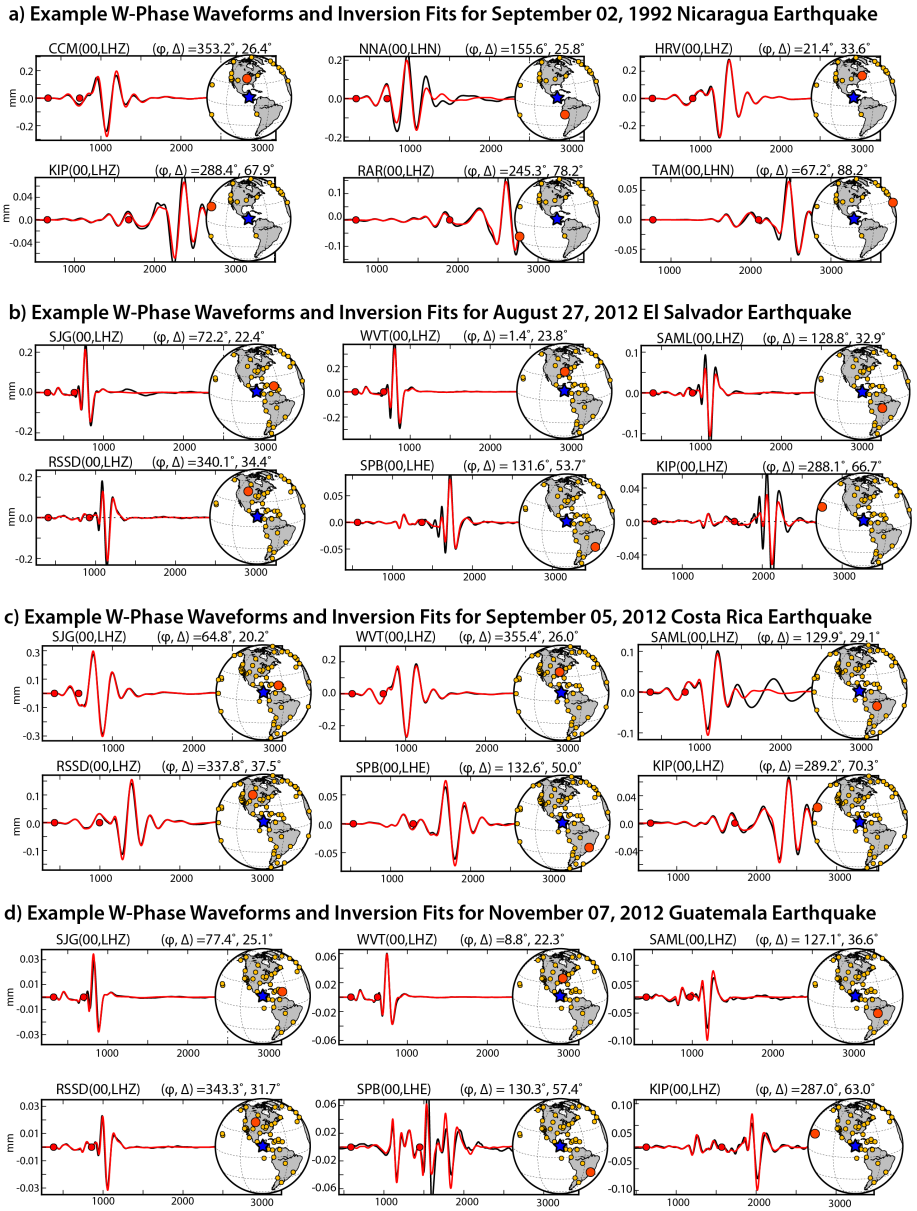

Figure 4.A3 Example W-phase observations (black traces) and computed waveforms (red) for the point-source moment tensors in Figure 4.A2 for a) the September 2, 1992 Nicaragua evetn, b) the August 27, 2012 El Salvador event, c) Costa Rica event and d) the November 7, 2012 Guatemala event. The data are from global seismic network stations with ground displacement filtered in the frequency band 1.67-5.0 mHz. The W-phase signal used in the inversions is the waveform interval between the red dots. The large amplitude signals after the W-phase are fundamental mode surface waves and the waveform comparisons are predictions for those signals. The maps indicate the position of the station (red dot) among the total set of stations (gold dots) used in the corresponding W-phase inversion.

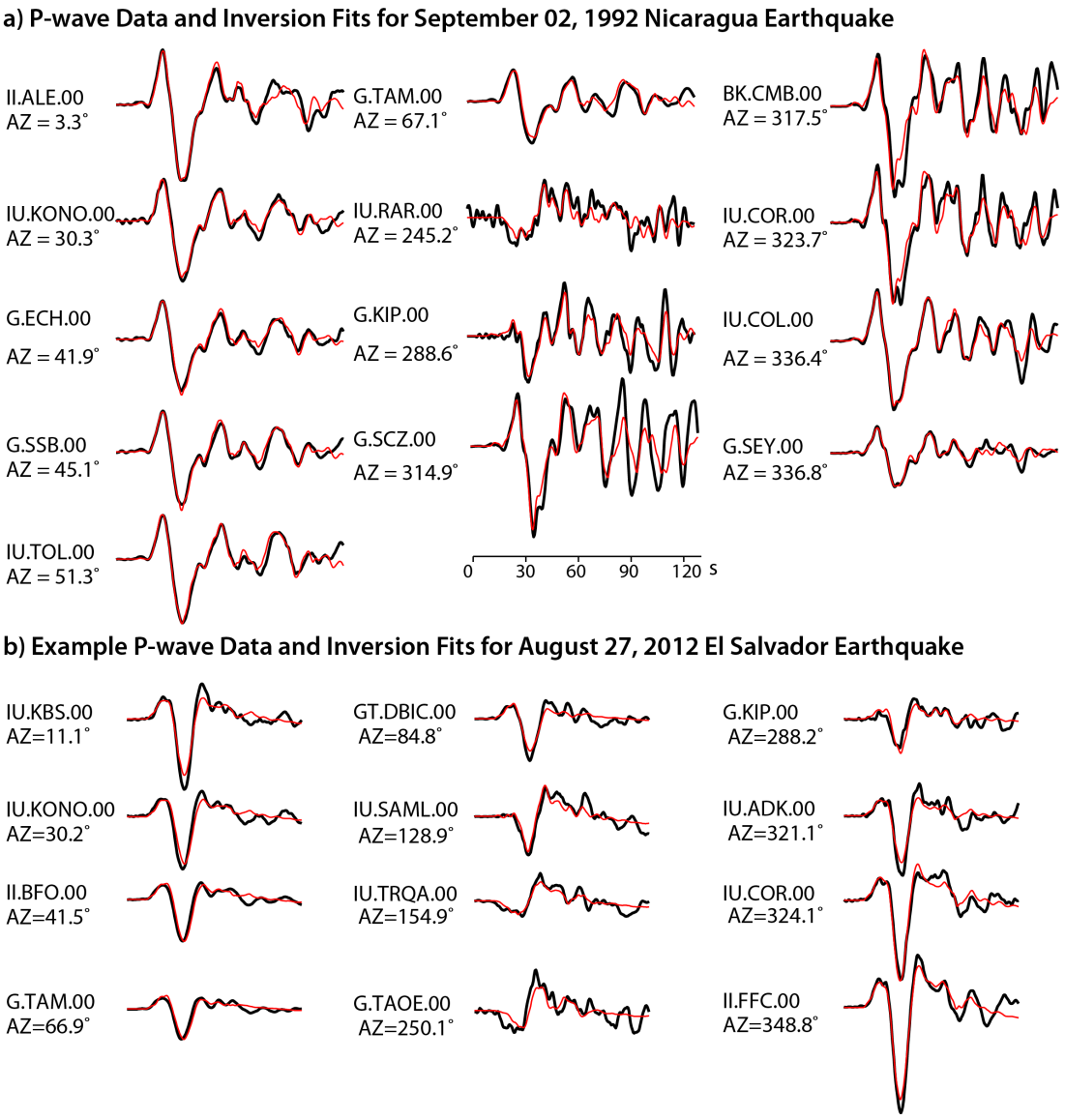

Figure 4.A4 Comparison of representative observed (black lines) and modeled (red lines) teleseismic P waves for a) September 2, 1992 Nicaragua, b) August 27, 2012 El Salvador, c) September 5, 2012 Costa and d) November 7, 2012 Guatemala earthquakes. The models shown in Figure 4.2 are used for the computations. The signals are broadband ground displacements in the passband 0.005-0.9 Hz. Comparable waveform matches are found for all of the stations used in the inversions.

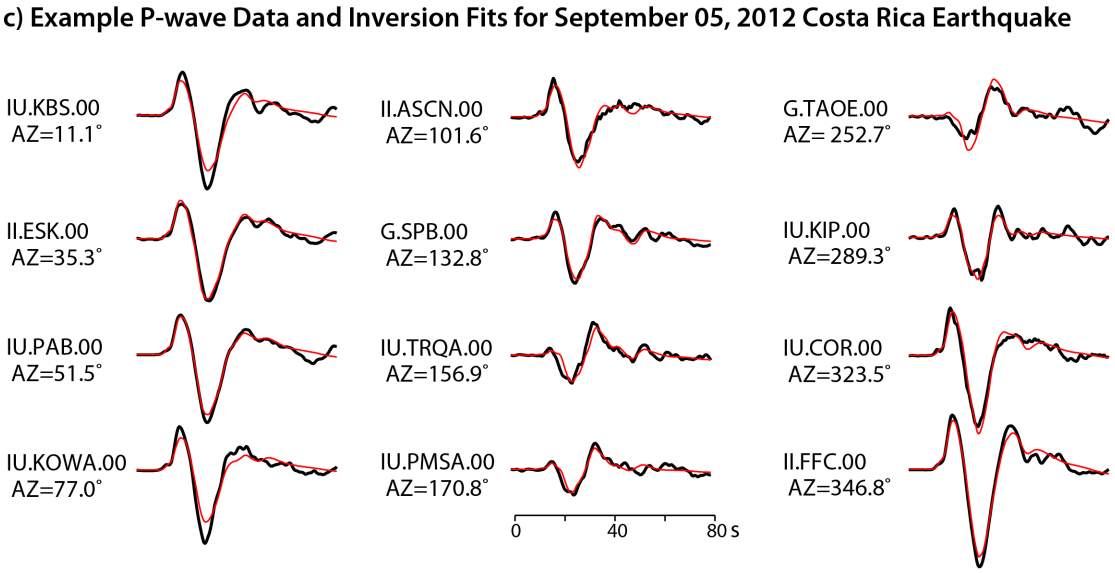

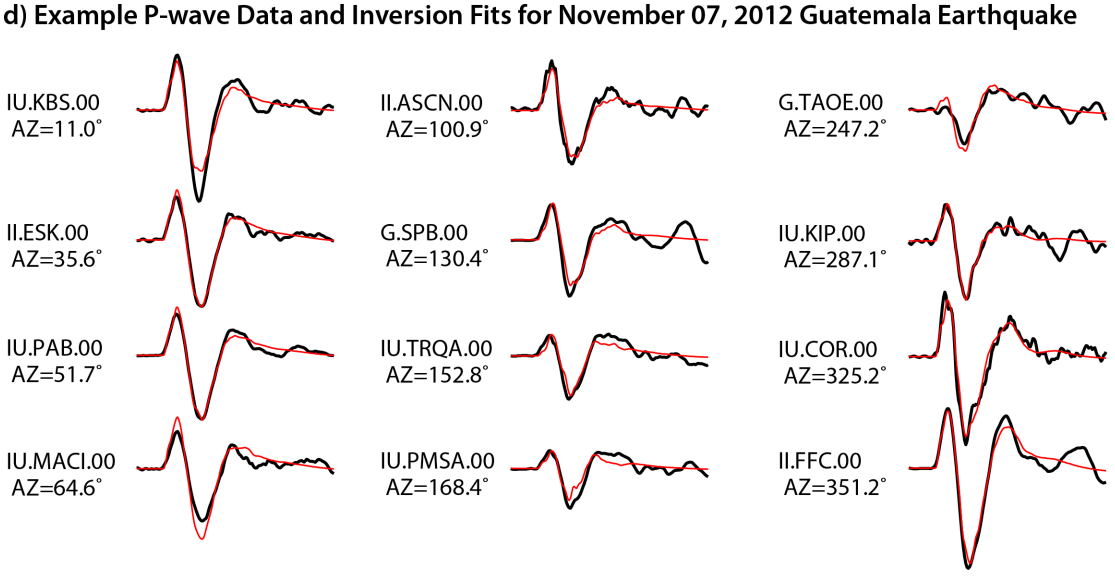

Figure 4.A4 Continued.

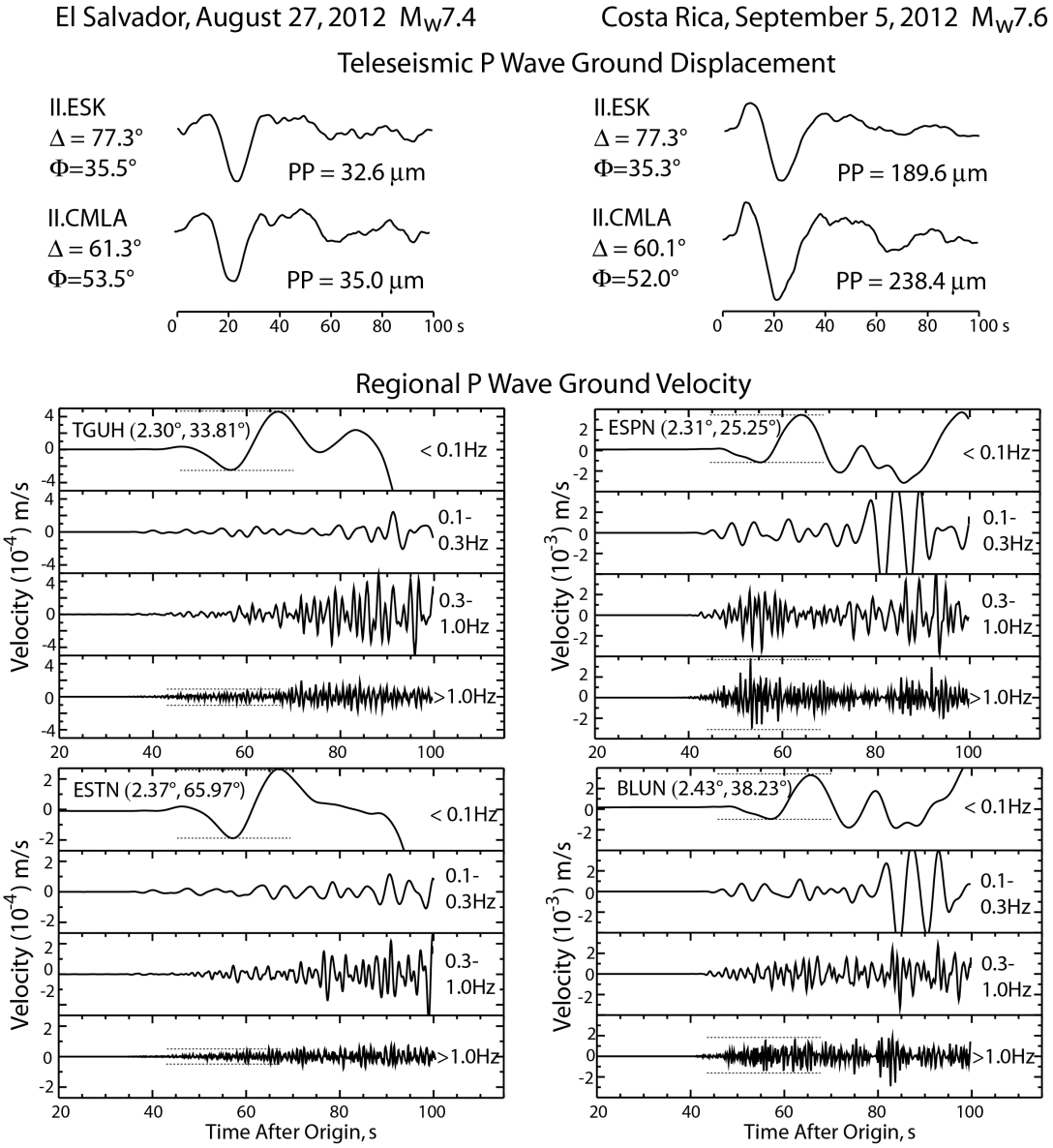

Figure 4.A5 Comparison of teleseismic and regional P wave signals for the August 27, 2012 El Salvador (Mw 7.3) earthquake (left column) and the September 5, 2012 Costa Rica (Mw 7.6) earthquake (right column). The teleseismic P waves at common stations are not dramatically different in appearance, but the first arrival has more impulsive, short-period-rich onsets for the Costa Rica event. The spectral differences are more apparent in regional recordings at comparable propagation distances (station locations are shown in Figure 4.5), with narrow-band filtered ground velocities being shown below with true relative amplitudes. The ratio of the signal amplitudes in the P arrival for frequencies > 1 Hz relative to below 0.1 Hz is higher for the Costa Rica event by a factor of 3.6-5.6, consistent with the factor of 5 higher seismic moment-scaled radiated energy in Figure 4.4.

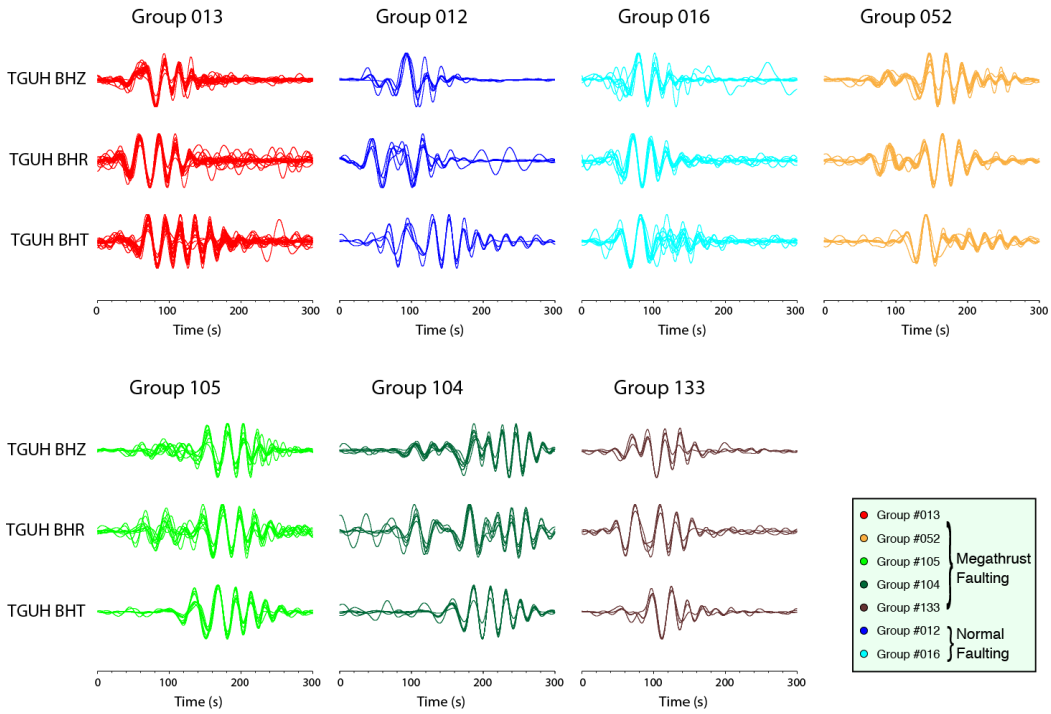

Figure 4.A6 Aligned three-component 300-s long regional wave recordings at station TGUH that have been clustered by waveform correlations based on similarity to reference events 013, 012, 016, 052, 105, 104 and 133. The correlations are for waveforms band-passed in the frequency band 20 to 100 s for vertical components and 20 to 50 s for horizontal components. Amplitudes are normalized on the peak amplitude. Note the distinct waveform character for the different groups. The faulting geometry for each group is inferred using the gCMT solutions for the reference events.

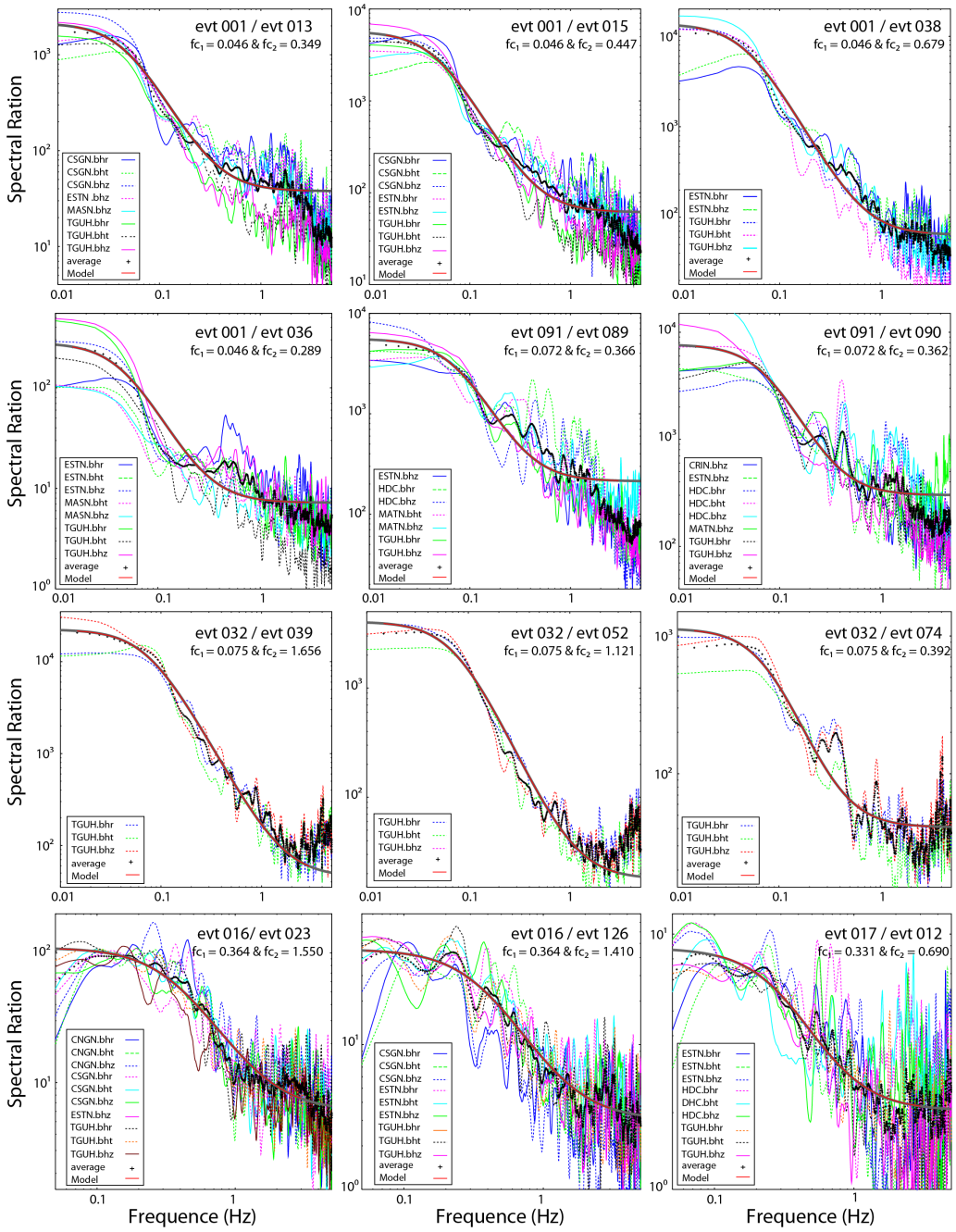

Figure 4.A7 Example fitting of the stacked spectral ratios (heavy blank curves) between two nearby events (separation distance < 50 km) with similar focal mechanism using an ω^{-2} source model. 150-s-long signals after P arrivals are used and the individual spectral ratios (colors) used for calculating the average spectral ratios are indicated by the station name and component in each panel. The smooth curves show the best fitting spectral ratio (gray curves highlighted in red for the reliable frequency band used for fitting), with corner frequencies for denominator and numerator events being indicated by f_{c1} and f_{c2}.

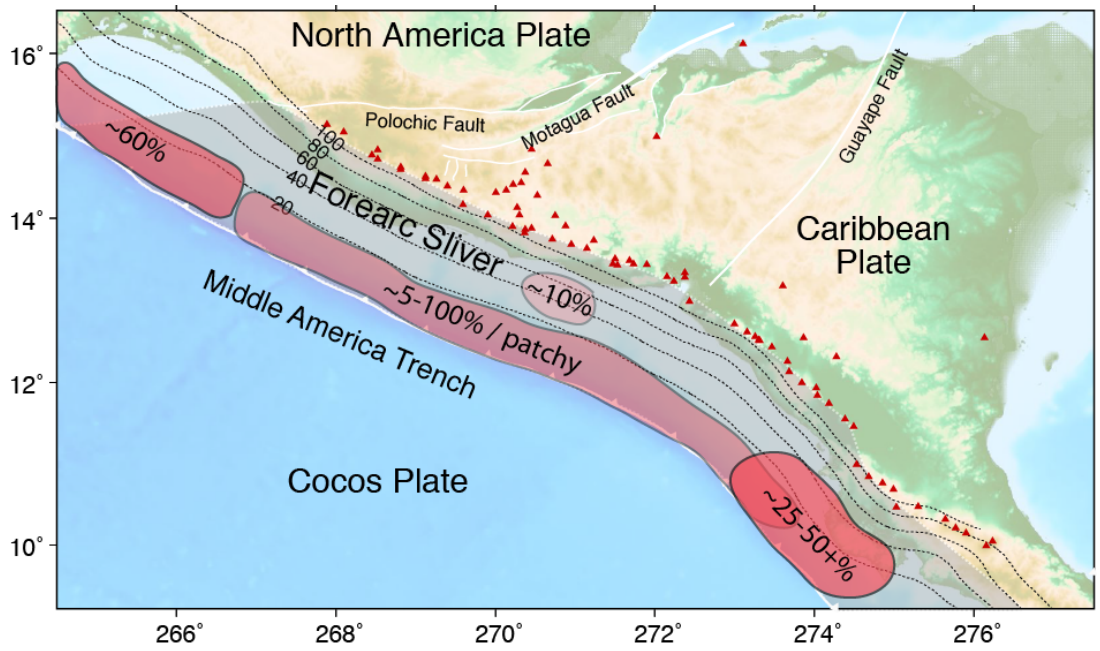

Figure 4.A8 Map indicating inferences of megathrust locking based on several studies of GPS observations in Figure 4.7. The studies consistently indicate low or no coupling on the deeper portion of the megathrust below the forearc sliver, which is translating at about 15 mm/yr toward the triple junction of the North American, Cocos and Caribbean plates. Two patches with ~ 10% and ~ 25-50+% locking near El Salvador and Costa Rica, respectively are suggested by Correa-Mora et al. (2009) with less than 2% on average over the entire megathrust. Estimates ranging from 5 to 100% coupling for the shallow megathrust along the sliver extending to about 20 km depth have been proposed in various studies (LaFemina et al., 2009; Rodriguez et al., 2009; Franco et al., 2012). Relatively strong locking of ~60%, near the triple junction has been proposed (Franco et al., 2012).

Table 4.A1 Events Information from USGS/NEIC Catalog for Large Interplate Earthquakes

Event	Date	Time	Location			Magnitude		
			Lon.	Lat.	Depth /km	m_b	M_s	M_w
1992 Nicaragua Eq.	09/02/1992	00:16:01	-87.340	11.742	44	5.3	7.2	7.7
2012 El Salvador Eq.	08/27/2012	04:37:19	-88.590	12.139	28	6.0	6.9	7.3
2012 Costa Rica Eq.	09/05/2012	14:42:07	-85.315	10.085	35	6.8	7.7	7.6
2012 Guatemala Ea.	11/07/2012	16:35:46	-91.854	13.963	24	6.6	7.4	7.4

Table 4.A2 Events Information from USGS/NEIC Catalog for Aftershock Sequence Characterization

No.	Date	Time	Lon.	Lat.	Mag
001	08/27	04:37:19.43	-88.59	12.14	7.3
002	08/27	05:38:04.42	-88.61	12.30	5.5
003	08/27	09:05:03.87	-88.28	12.17	5.1
004	08/27	12:55:18.98	-88.46	12.39	4.5
005	08/27	13:34:20.61	-88.26	12.57	4.4
006	08/27	13:46:15.21	-88.54	12.10	4.5
007	08/27	14:36:36.29	-89.03	12.47	4.6
008	08/27	17:09:28.32	-88.11	12.17	4.3
009	08/27	17:17:34.21	-87.84	12.37	4.6
010	08/27	18:27:20.10	-89.24	12.86	4.5
011	08/27	18:44:41.50	-88.35	13.31	4.0
012	08/27	21:13:28.86	-88.68	11.98	4.8
013	08/27	22:07:39.31	-88.66	12.39	4.8
014	08/27	23:05:49.56	-88.70	12.56	4.5
015	08/28	10:11:31.30	-88.86	12.39	4.6
016	08/28	06:08:16.10	-88.65	12.46	5.5
017	08/28	08:53:36.88	-88.71	11.98	5.3
018	08/28	21:28:34.44	-88.91	12.62	4.3
019	08/28	22:02:48.50	-88.61	12.77	4.6
020	08/29	05:55:29.41	-88.56	12.32	4.4
021	08/29	08:39:39.27	-88.90	12.71	4.4
022	08/29	18:52:10.21	-88.39	12.47	4.3
023	08/29	19:27:02.11	-88.43	12.73	4.4
024	08/29	23:18:02.52	-86.98	11.71	4.5
025	08/30	00:16:58.72	-88.75	12.02	4.2
026	08/30	00:27:00.79	-88.12	12.23	4.4
027	08/30	09:03:02.24	-88.45	12.36	4.4
028	09/01	06:05:53.63	-90.21	13.22	4.1
029	09/01	11:55:30.33	-88.82	12.59	4.6
030	09/01	15:54:41.00	-88.35	12.46	4.4
031	09/04	20:09:04.53	-89.08	11.67	4.4
032	09/05	14:42:07.80	-85.31	10.09	7.6
033	09/06	06:47:34.45	-88.52	12.37	4.9

034	09/06	09:07:12.09	-85.34	10.11	4.6
035	09/06	11:38:57.67	-88.52	12.42	4.4
036	09/06	23:30:03.03	-88.33	12.37	4.8
037	09/07	19:12:25.03	-88.67	12.50	4.7
038	09/08	02:27:21.38	-88.50	12.06	4.2
039	09/08	09:50:22.22	-85.62	10.40	4.5
040	09/08	20:29:31.21	-85.32	10.08	5.7
041	09/09	09:50:01.59	-88.61	12.52	4.2
042	09/09	11:08:43.99	-88.94	12.55	4.4
043	09/09	21:37:34.01	-85.01	9.46	4.3
044	09/10	11:31:19.36	-88.69	12.40	4.7
045	09/10	13:15:31.07	-88.78	12.48	4.5
046	09/10	22:22:04.00	-88.47	12.75	4.2
047	09/12	01:13:27.38	-88.75	12.01	4.6
048	09/12	02:13:02.07	-85.39	10.07	4.6
049	09/12	06:29:34.70	-85.17	9.52	4.8
050	09/13	05:46:13.45	-91.02	14.02	4.2
051	09/14	23:13:12.87	-85.41	10.08	4.5
052	09/16	05:51:09.45	-85.46	10.17	5.2
053	09/16	08:25:42.87	-92.79	14.32	4.5
054	09/16	18:33:25.51	-89.28	12.50	4.5
055	09/16	23:22:26.17	-89.18	12.58	4.4
056	09/17	18:02:59.31	-89.88	13.12	4.4
057	09/18	08:20:41.83	-89.29	12.47	4.5
058	09/21	06:37:02.60	-85.54	10.18	4.4
059	09/21	11:12:04.29	-88.77	12.14	4.3
060	09/22	14:57:01.00	-89.56	13.05	4.3
061	09/23	03:43:10.05	-85.38	9.99	4.4
062	09/23	08:52:53.81	-88.56	12.65	4.2
063	09/23	14:58:26.43	-85.41	10.11	4.4
064	09/26	11:37:27.55	-85.11	10.22	4.2
065	10/02	03:10:51.36	-88.11	12.12	4.6
066	10/03	06:26:40.74	-87.84	12.31	4.2
067	10/05	18:22:56.83	-91.50	13.03	5.5
068	10/06	05:52:52.81	-90.86	13.12	4.0
069	10/06	17:11:10.00	-88.08	12.62	4.2
070	10/06	22:55:03.00	-88.81	12.92	4.0
071	10/07	07:00:56.13	-84.96	9.78	4.4
072	10/07	09:16:49.34	-89.23	12.42	4.5
073	10/09	07:50:13.56	-91.31	13.68	4.1
074	10/10	12:19:44.93	-85.48	10.10	5.3
075	10/14	22:40:55.31	-88.84	12.77	4.5
076	10/17	01:26:40.20	-91.29	14.02	4.4
077	10/17	02:55:22.90	-88.80	12.49	4.4
078	10/19	07:42:28.46	-88.43	12.28	4.3
079	10/21	13:31:57.45	-85.66	9.95	4.4
080	10/21	20:28:17.00	-88.34	12.56	5.4
081	10/21	20:44:15.00	-88.33	12.59	5.1
082	10/22	20:31:28.30	-87.98	12.18	4.6
083	10/24	00:45:32.99	-85.30	10.09	6.5
084	10/25	21:24:11.26	-88.33	13.16	4.2

085	10/27	16:22:05.80	-92.72	14.41	4.9
086	10/29	14:35:13.68	-88.25	12.09	4.8
087	10/29	17:14:14.55	-88.15	12.57	4.3
088	11/01	19:33:58.59	-87.94	12.84	4.3
089	11/02	03:28:21.00	-92.18	14.08	4.5
090	11/02	08:57:07.29	-92.34	13.90	4.4
091	11/07	16:35:46.69	-91.85	13.96	7.4
092	11/07	22:42:48.22	-92.16	13.85	5.7
093	11/09	14:42:42.52	-92.25	14.06	4.6
094	11/10	17:15:09.90	-92.22	13.81	5.1
095	11/11	10:32:16.49	-88.00	12.14	4.3
096	11/11	22:14:59.24	-92.16	14.13	6.5
097	11/11	22:44:30.37	-92.07	13.76	4.9
098	11/12	03:02:59.72	-92.20	13.98	4.6
099	11/12	03:31:14.60	-92.28	14.05	4.7
100	11/12	04:35:07.07	-92.42	14.03	4.2
101	11/12	05:03:06.70	-92.39	13.81	4.3
102	11/13	08:28:12.48	-85.53	10.09	4.1
103	11/13	09:08:02.55	-92.26	13.99	4.8
104	11/15	06:42:34.80	-92.73	13.84	4.9
105	11/15	08:01:01.40	-91.87	14.00	4.9
106	11/15	17:11:19.69	-92.11	13.89	4.7
107	11/16	03:04:56.24	-92.56	13.83	4.4
108	11/16	13:02:01.28	-91.86	13.87	4.8
109	11/16	21:06:47.88	-88.80	12.92	4.7
110	11/17	06:47:44.49	-92.44	14.01	4.4
111	11/17	10:13:57.06	-92.40	14.10	4.3
112	11/18	08:56:18.48	-86.74	11.29	4.3
113	11/18	22:12:50.64	-92.42	13.98	4.4
114	11/19	08:15:39.01	-91.67	13.84	4.3
115	11/20	00:59:18.96	-91.77	13.82	4.5
116	11/23	03:38:44.33	-88.07	12.13	4.3
117	11/24	10:12:50.36	-92.29	13.96	4.4
118	11/24	11:21:07.53	-92.21	13.98	4.9
119	11/25	15:10:40.71	-87.02	11.66	4.3
120	11/26	12:27:57.51	-88.40	12.43	4.5
121	11/27	10:15:27.32	-91.98	13.66	4.6
122	11/27	15:05:30.49	-88.51	12.24	4.4
123	11/28	05:28:23.99	-88.38	12.46	4.6
124	11/28	05:43:23.52	-88.35	12.38	4.4
125	11/28	06:46:37.20	-88.35	12.57	4.5
126	11/28	07:00:37.27	-88.36	12.50	4.4
127	11/29	19:32:31.75	-92.11	13.76	5.5
128	11/30	08:26:24.00	-88.80	12.55	4.2
129	11/30	20:02:47.00	-88.21	12.74	4.2
130	12/02	04:44:37.27	-88.99	11.85	5.1
131	12/03	23:58:35.43	-92.37	14.16	5.4
132	12/11	12:14:55.91	-88.51	12.73	4.4
133	12/13	21:26:39.18	-89.97	13.07	5.3
134	12/14	04:04:06.86	-91.68	13.93	5.2
135	12/14	04:58:48.46	-91.72	13.82	5.1

136	12/14	19:18:51.00	-90.19	12.81	4.8
137	12/15	02:53:18.94	-89.89	13.07	4.2
138	12/15	12:43:30.09	-88.61	12.25	5.0
139	12/15	13:03:26.04	-89.87	13.13	4.5
140	12/16	03:06:47.62	-91.97	13.88	4.8
141	12/16	10:23:42.50	-86.13	10.51	4.6

Chapter 5

Rupture Characteristics of Major and Great ($M_W \geq 7.0$) Megathrust Earthquakes from 1990-2015: I. Source Scaling Relationships

This chapter has been submitted as:

Ye, L., T. Lay, H. Kanamori and L. Rivera (2015), "Rupture Characteristics of Major and Great ($M_W \geq 7.0$) Megathrust Earthquakes from 1990-2015: I. Source Parameter Scaling Relationships", *J. Geophys. Res.*, submitted.

Abstract Source parameter scaling for major and great thrust-faulting events on circum-Pacific megathrusts is examined using finite-fault inversions and radiated energy estimates for 114 $M_W \geq 7.0$ earthquakes. To address the limited resolution of source spatial extent and rupture velocity (V_r) from teleseismic observations, the events are subdivided into either group 1 (18 events) having independent constraints on V_r from prior studies, or group 2 (96 events) lacking independent V_r constraints. For group 2, finite-fault inversions with V_r = 2.0, 2.5, and 3.0 km/s are performed. The product $V_r^3\Delta\sigma_E$, with stress drop $\Delta\sigma_E$ calculated for the slip distribution in the inverted finite-fault models, is very stable for each event across the suite of models considered. It has little trend with M_W, although there is a baseline shift to low values for large tsunami earthquakes. Source centroid time (T_c) and duration (T_d), measured from the finite-fault moment-rate functions vary systematically with the cube root of seismic moment (M_0), independent of assumed V_r. There is no strong dependence on magnitude or V_r for moment-scaled radiated energy (E_R/M_0) or apparent stress (σ_a). $\Delta\sigma_E$ averages ~4 MPa, with direct trade-off between V_r and estimated stress drop, but little dependence on M_w. Similar behavior is found for radiation efficiency (η_R). We use $V_r^3\Delta\sigma_E$ and $T_c/M_0^{1/3}$ to explore

variation of stress drop, V_r and radiation efficiency, along with finite-source geometrical factors. Radiation efficiency tends to decrease with average slip for these very large events, and fracture energy increases steadily with slip.

5.1 Introduction

How earthquake source parameters vary with event size and the extent to which there may be deterministic characteristics for all earthquake failures, have been the subjects of investigations for several decades [e.g., *Aki*, 1967; *Kanamori and Anderson*, 1975; *Ohnaka*, 2003]. Earthquake source parameter scaling is fundamental for understanding mechanics of earthquake ruptures. Many studies have sought to measure fundamental rupture parameters, such as source duration, static stress drop, radiated seismic energy, apparent stress, dynamic stress drop, rupture area, etc., from seismic observations, and to establish their scaling relationships with seismic moment. Diverse results and implications have been found for different earthquake magnitude ranges and tectonic environments [e.g., *Venkataraman and and Kanamori*, 2004], or using different seismological methods.

There have been numerous estimates of the static stress drop or apparent stress for minor to moderate (M_W < ~6) earthquakes by fitting average source amplitude spectra with parameterized point-source representations [e.g., *Abercrombie*, 1995; *Choy et al.*, 2006; *Shearer et al.*, 2006; *Allmann and Shearer*, 2009] that involve a corner frequency (f_c) and high-frequency (ω) spectral decay rate (often assumed to be ω^{-2}) [e.g., *Brune*, 1970; *Madariaga*, 1976]. Relatively little magnitude dependence of estimated static stress drop inferred from such spectral modeling is apparent for event sizes varying over several orders of magnitude [e.g., *Allmann and Shearer*, 2009], although there is large scatter in stress drop estimates. Some studies report systematically increasing apparent stress estimates as earthquake size increases [e.g.,

Abercrombie, 1995; *Kanamori et al.*, 1993; *Abercrombie and Rice*, 2005; *Walter et al.*, 2006], while others find no dependence of apparent stress on seismic moment [e.g., *McGarr*, 1999; *Ide and Beroza*, 2001; *Perez-Campos and Beroza*, 2001; *Ide et al.*, 2003; *Baltay et al.*, 2014]. Bandwidth limitations [*Ide and Beroza*, 2001], attenuation uncertainty [*Ide et al.*, 2002; *Baltay et al.*, 2011], and variability of stress drop estimates due to errors in corner frequency measurement [*Prieto et al.*, 2007] may all have contributed to the discrepancies. *Walter et al.* [2006] provided a comprehensive summary of the debate over whether there is significant scaling of seismic energy with moment.

For events with magnitude larger than ~6, it is unclear that earthquakes can be treated as point sources with simplified spectral amplitude methods being used to estimate source parameters. Even for strong earthquakes (M_W 6.0-6.9), point-source moment rate functions show significant variability [e.g., *Bilek and Lay*, 2000] that is not well captured by average spectral amplitude analysis alone (i.e., ignoring phase information). Determining the stress evolution over space and time during the rupture process is required for many source parameters to be meaningfully estimated (this is likely also true of smaller sources, but there are observational limits for globally determining finite-source properties for small events).

Over the past twenty five years the occurrence of many major and great global earthquakes, along with rapid advances in seismic and geodetic data collection and analysis, have reinforced the tremendous range of complexity of large earthquakes [*Kanamori*, 2014; *Lay*, 2015]. The source complexity of major and great earthquakes ($M_w \geq 7$) certainly cannot be well captured by point-source spectral amplitude averages. To account for the finiteness of large earthquakes, we investigate scaling relations for megathrust events obtained from finite-fault inversions along with short-period spectral stacking and radiated energy estimates.

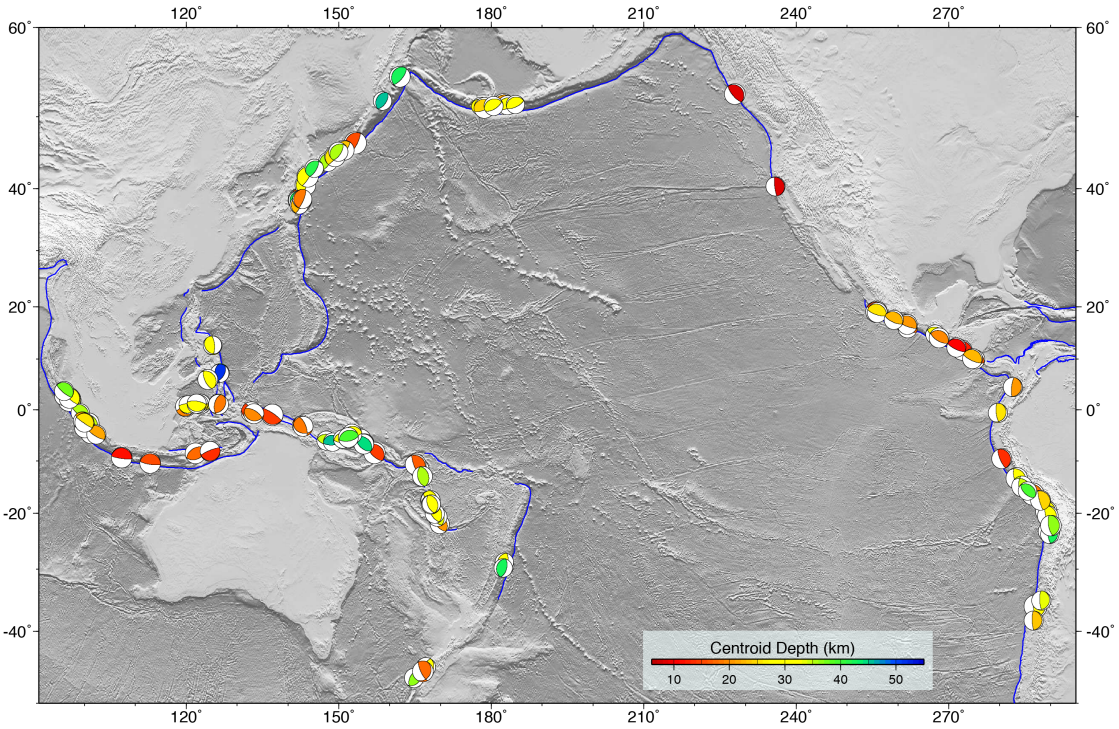

Figure 5.1 Epicentral locations indicated by best-double-couple focal mechanisms from the global Centroid Moment Tensor (gCMT) catalog for the 114 major and great ($M_w \geq 7$) megathrust earthquakes from 1990-2015 analyzed in this study. Focal mechanism radius is scaled proportional to M_w and color indicates gCMT centroid depth. All major and great interplate thrust events for which reliable source parameter estimates could be made are included.

We document the primary source characteristics for all major and great ($M_W \geq 7$) subduction zones interplate earthquakes from 1990-2015 (Figure 5.1) using global broadband body wave observations (for frequencies below 1 Hz). There are systematic differences in some source characteristics between interplate and intraplate events [e.g., *Venkataraman and Kanamori*, 2004*; Allman and Shearer*, 2009*; Ye et al.*, 2013a*; Kanamori*, 2014], so this study does not span the entire range of shallow major earthquake behavior. Given the intrinsic limitations of estimating source parameters from teleseismic body wave analyses associated with limited slowness coverage, and uncertainties in attenuation and model parameterization, we will not strive for quantitative rupture mechanics interpretations, but focus on evaluation of basic

scaling relations. We consider a suite of rupture models for each event, computed for varying rupture expansion velocity, V_r. We then discuss scaling relationships for the measured source parameters: the product $V_r^3\Delta\sigma_E$, with stress drop $\Delta\sigma_E$ calculated for the slip distribution in the inverted finite-fault models, source centroid time and total duration, moment-scaled radiated energy, and apparent stress. We explore the variability in geometric terms for the megathrust ruptures, along with variations in source models for ranges of stress drop and radiation efficiency. Combining our results with previous work [*Abercrombie and Rice*, 2005] we investigate radiation efficiency and fracture energy behavior over a wide range of earthquake average slip. In a companion paper, we will explore these source parameter variations with tectonic environment and source depth.

5.2 Teleseismic Finite-Fault Inversions

In order to focus on rupture characteristics along plate boundary megathrust faults we select events using criteria that include having a shallow-dipping thrust-fault focal mechanism from the global Centroid-Moment-Tensor (gCMT) catalog [http://www.globalcmt.org/CMTsearch.html], location near the interplate contact, and source depth less than 60 km. We consider all $M_w \geq 7$ events from the gCMT and USGS/NEIC catalogs [http://earthquake.usgs.gov/earthquakes] from 1990 to July 2015. This spans the time interval when substantial numbers of global digital broadband seismograms are available for each event from the Incorporated Research Institutions for Seismology (IRIS) data center [http://www.iris.edu/wilber3/find_event]. Several events meeting the above selection criteria, but having very limited azimuthal coverage of data (mainly events in the early 1990s), low signal-to-noise ratios (typically as a result of being preceded by another large event), or unusually strong water/sediment reverberations that we

were unable to model satisfactorily, are excluded. Several additional likely intraplate thrust events are also eliminated. The 26 December 2004 M_w 9.2 Sumatra earthquake is excluded from the finite-fault characterization because the extremely long source duration prevents us from isolating teleseismic P-waves and SH-waves for the finite-source inversion method used in this study. The final data set is comprised of 114 events globally distributed as shown in Figure 5.1.

For each earthquake we obtain systematic estimates of the slip distribution, moment-rate function, source centroid depth and time, total source duration, static stress drop, broadband source spectrum, radiated seismic energy, apparent stress, and radiation efficiency. The variations of these source characteristics with seismic moment are then examined for scaling behavior. The precision with which these source parameters can be estimated using only teleseismic observations varies with event location (affects data distribution), date of occurrence (affects number of available data), and required information for each measurement (level of dependence on velocity structure, faulting parameterization, etc.). Some source attributes are relatively robustly determined by teleseismic data (moment-rate function, centroid time), whereas measures that depend on estimates of rupture dimension (static stress drop, radiation efficiency), or dynamic source properties (radiated energy, apparent stress) are strongly affected by modeling parameters. Errors associated with the assumptions are very hard to quantify, as they propagate into the estimates in complex ways. Some recent analysis [e.g., *Gallovic et al.*, 2015] demonstrates trade-off between spatial and temporal smoothing in resolving the kinematic slip distribution and evolution during the rupture process, and additional effects of parameterization and neglect of 3D structure in computing Green's functions. For a global study, we cannot realistically address 3D source structure effects and it is most useful to instead adopt relatively uniform parameterization of

faulting. As a result, we will evaluate uncertainties qualitatively, conveying the level of confidence appropriate for each type of measurement, but we do not attempt to quantify model error effects rigorously, as it is unrealistic to do so and the earthquakes appear to have large intrinsic variations that are real.

For each of the 114 earthquakes identified as a large megathrust rupture we perform a finite-fault inversion using ground displacements in the passband 0.005-0.9 Hz for teleseismic P-waves, and in a few cases also SH-waves. We use the least-squares kinematic inversion method with positivity constraint for constant rupture front expansion velocity (V_r), specified planar fault geometry, and subfault source time functions parameterized by several overlapping triangles. The inversion code was written by *Kikuchi and Kanamori* [1991], is archived at http://www.eri.u-tokyo.ac.jp/ETAL/KIKUCHI/, and uses a method similar to that developed by *Hartzel and Heaton* [1983]. We modify the teleseismic body wave inversion code to include a constraint to minimize the difference of the inverted total seismic moment from the long-period seismic moment estimate (gCMT). This stabilizes the inversion process and allows flexibility in the number of triangles assigned for each subfault and use of subfaults with relatively small grid size, as needed for the smaller events. For each event, we adjust the subfault source time functions to give a stable rupture pattern with limited model parameters. The hypocentral depth (h_0) is typically set as the value from the USGS-NEIC bulletin, but this is perturbed when it appears to be inaccurate based on waveform misfits or overall inconsistency with long-period centroid depth constraints. The fault geometry is generally specified with strike and dip from the gCMT best-double couple solution, unless the body wave modeling motivated perturbations from those solutions. The source region crustal model is usually obtained from Crust 2.0 [*Bassin et al.*, 2000], with 1D layered structure Green's functions being computed using a propagator matrix method [*Bouchon*, 1981].

Given the limited resolution of source finiteness from teleseismic body wave observations, in order to best constrain the rupture expansion velocity (V_r) we classified the 114 events into two groups. Group 1 (18 events) has independent constraints from prior detailed rupture analyses and we adopt the preferred values of V_r from those studies. Group 2 (96 events), for which independent constraints are lacking, is analyzed with a suite of models for each event with different V_r. For each earthquake in group 1 (Appendix III), the rupture model parameterization and dimensions from the literature (citations in Appendix III) are used in new inversions, applying the same seismic moment constraint and spatial smoothing as used for all other events. The final rupture models and waveform fits for each event in this group are presented in Appendices I and II.

For each earthquake in group 2 (Table 5.S2), three finite-fault inversions with V_r =2.0 km/s, 2.5 km/s and 3.0 km/s, and proportionally-scaled grid spacing of 8 km, 10 km, and 12 km, respectively, have been performed. The final rupture models and waveform fits for V_r = 2.5 km/s are all presented in Appendix II. As a representative example, Figure 5.2 shows the results for finite-fault models with V_r =2.0, V_r 2.5, and V_r 3.0 km/s for the 18 April 2014 M_w 7.2 Guerrero earthquake. For this event, and for all others, we determine the overall fault-perpendicular moment-rate function from the combined source time functions for each subfault (Figure 5.a), the average focal mechanism (Figure 5.2a1), the variable rake space-time slip distribution with subfault source time functions (Figure 5.2b) and the shear stress distribution (Figure 5.2c). The computation of shear stress distribution for the inverted slip models uses the analytic methods developed by *Mansiha and Smylie* [1971] and *Okada* [1992], assuming a homogeneous half space and computing the shear stress at the center of each subfault. Only a subset of the observed and modeled waveforms are shown in Figure 5.2d(1-3); the entire data sets are displayed in Appendix II for this event and for all others. About 90

percent of the P waveform power is accounted for by the source models shown in Figure 5.2. The moment-rate functions are very similar between the models, and the spatial pattern of slip is similar. However, the spatial dimensions, the amount of slip and the static stress drop vary significantly with the rupture expansion velocity, V_r. This applies to all solutions. The goodness of waveform fits varies little with V_r, and optimization of the source model based on waveform misfit is not a well- constrained procedure. This is, in part, due to the large number of parameters in the models and the intrinsically variable degrees of freedom for fitting the data from using variable grid dimensions and multiple subfault subevents. It is misleading to hold all parameters fixed and to optimize any one parameter, such as V_r, based on waveform fits when all the parameters are coupled and not uniquely resolved independently. As a result, we treat the range of models as a sampling of viable models for a reasonable suite of key kinematic parameters.

For these finite-fault rupture solutions, we computed the seismic moment (M_0), rupture centroid depth estimated from the average depth of the slip distribution (H_c), averages of source rigidity (μ), P-wave velocity (V_p), S-wave velocity (V_s) and density (ρ) weighted by the slip distribution, source centroid time (T_c) and total duration (T_d) computed from the moment-rate function, effective rupture areas and corresponding average slip for specific trimming factors (discussed in section 3.2), and average static stress drop ($\Delta\sigma_E$) weighted by the slip distribution following the method of *Noda et al.* [2013]. Table 5.1 shows these source parameters for the three slip models for the 18 April 2014 Guerrero Mexico event. For all events the corresponding values are presented in Appendix III for group 1 events and group 2 events, respectively. In the following discussion, the values for source parameters such as seismic moment, average centroid depth, and source duration that have little dependence on V_r are given for the results of slip models with V_r 2.5 km/s for group 2 events.

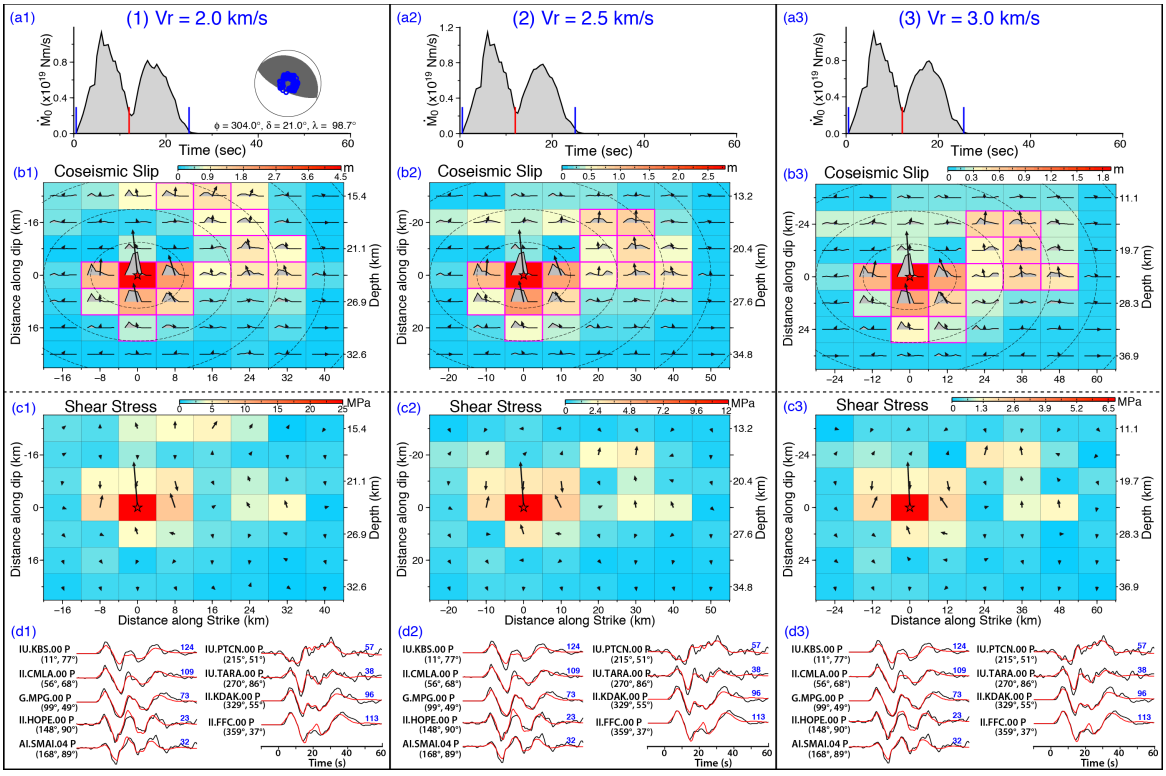

Figure 5.2 Example of finite-fault inversions using different rupture expansion velocity, V_r, with subfault grid-spacing proportional to V_r for the 18 April 2014 Guerrero, Mexico event (M_w 7.3). Solution parameters are listed in Table 5.1. The moment rate function for each inversion is shown in row (a). Blue ticks indicate the time span used to determine total duration, Td, and the centroid time, T_c, is indicated by the red tick. The average focal mechanism with double couple strike (ϕ), dip (δ), and rake (λ) is almost identical for each inversion. Row (b) shows the subfault grid, with average subfault slip direction and magnitude indicated by the vectors, and slip magnitude is color-coded. Dashed circles indicated rupture front position in 5 s intervals. Row (c) indicates the average stress vector at the center of each subfault used to compute stress drop for the variable slip solution. Comparisons of sampled observed (black) and predicted (red) P waveforms are shown in row (d). Below each station name the azimuth and distance of the station relative to the source is indicated. The peak-to-peak amplitude of the data trace in microns is shown in blue; each waveform is normalized to uniform amplitude. All waveforms used in the finite-fault inversion for this event are shown in the Appendix II.

Table 5.5.1 Source Parameters for the 18 April 2014 Guerrero, Mexico event (M_w 7.3)

Vr (km/s)	Vari.	M_0 (N-m)	T_d (s)	T_c (s)	H_0 (km)	H_c (km)	Rake (°)	Grid (km)	A_{eff}^* (km^2)	$\Delta\sigma_E$ (MPa)	D^* (m)	$Vr^3\Delta\sigma_E$ (km^{3}MPa)
2.0	0.127	9.43 x10^{19}	24.5	12.0	24.0	22.8	98.7	8.0	1088	6.36	1.27	50.88
2.5	0.120	9.41 x10^{19}	24.5	12.0	24.0	22.9	98.7	10.0	1800	2.94	0.80	45.94
3.0	0.118	9.41 x10^{19}	25.0	12.2	24.0	22.8	98.8	12.0	2736	1.63	0.53	44.01

*The trimming factors of 0.14, 0.12 and 0.12, which provide circular rupture models with uniform average slip that give stress drops that match $\Delta\sigma_E$ calculations, are used in estimating the effective rupture area and the corresponding average slip for slip models with V_r 2.0, 2.5 and 3.0 km/s respectively.

The total duration measure is sometimes subjective, as it is influenced by the adequacy of the Green's functions for accounting for water reverberations and late scattered waves. We obtained the T_d estimates by ignoring very weak tails in the moment-rate functions, as these may be artifacts due to inaccurate modeling of the coda. The nature of inversions with moment rate function positivity constraint is such that these measurements may be biased a bit long, but our application of a penalty function relative to the long-period seismic moment suppresses instability.

Teleseismic body waves for major and great events generally do not tightly constrain seismic moment due to bandwidth limitations and dependence on the model parameterization. By imposing an *a priori* constraint on the seismic moment, the inverted moment estimates are in general comparable with gCMT seismic moment estimates obtained by inversion of long-period (~40-350 s) seismic waves, with discrepancies less than 20% (Figure 5.3a). The systematically larger seismic moment estimates from the finite-fault inversions for earthquakes with magnitude < 7.4 may be the result of differences in the source velocity models (gCMT uses PREM, while local crustal models are used in the finite-fault inversions) or differences in source centroid depth for spatially concentrated sources, along

with effects of the positivity constraint on poorly resolved, low moment regions of the compact rupture models for smaller events. These effects appear to be insignificant for larger ruptures.

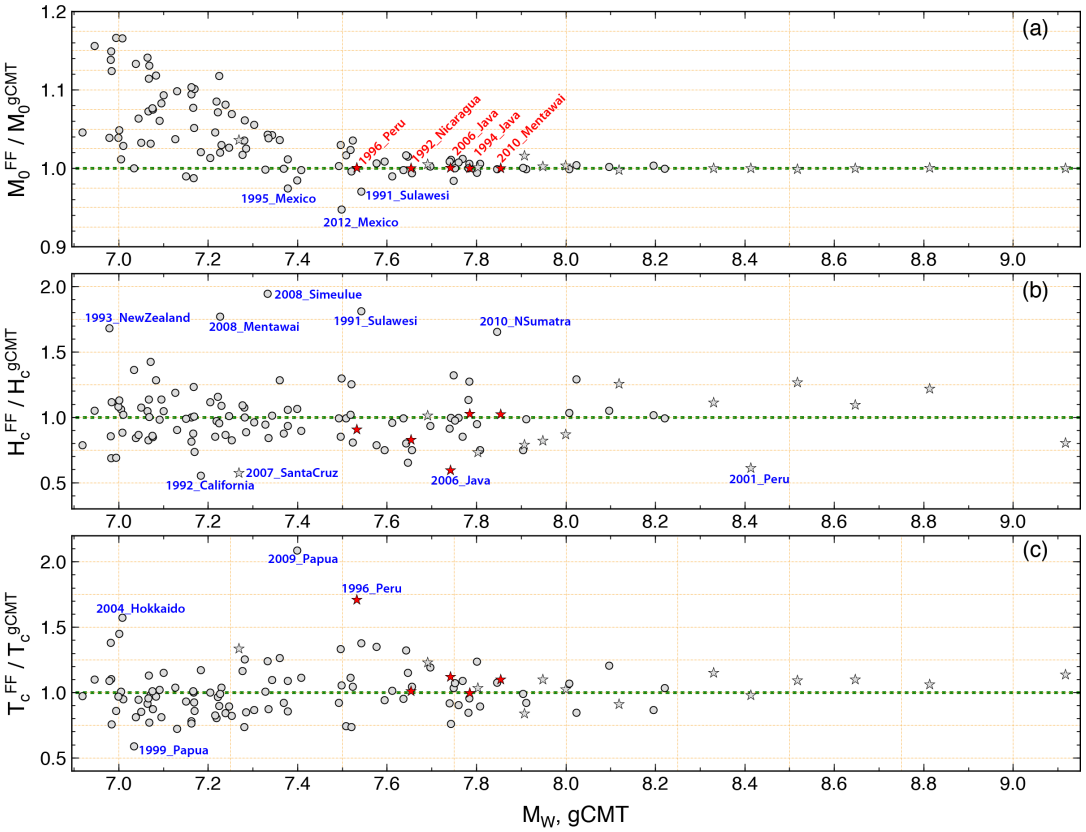

Figure 5.3 Ratios of finite-fault inversion (FF) estimates with V_r = 2.5 km/s (circles) or independent specific V_r (stars) to global Centroid Moment Tensor (gCMT) estimates for (a) seismic moment, (b) centroid depth H_c, and (c) centroid time T_c. Similar behavior is found for the ratios for finite-fault inversions with V_r of 2.0 km/s or 3.0 km/s. Events with outlying ratios are labeled. Five notable tsunami earthquakes, 1992 Nicaragua, 1994 Java, 1996 Peru, 2006 Java and 2010 Mentawai are highlighted with red labels and stars.

The finite-fault inversion slip-weighted average source depths and centroid time are generally consistent with values from the gCMT catalog for all magnitudes (Figure 5.3b,c), although there are a few outliers. We also find general consistency with corresponding values

from W-phase inversions [*Duputel et al.*, 2013]. Most estimates are within ±10 km for depths and ±5 s for centroid time. Some of the variability in depth estimates stems from using localized crustal structures for the finite-fault inversions in contrast to the PREM structure uniformly used in the long-period inversions.

As shown in Table 5.1, there is a strong trade-off between the V_r and the stress drop, $\Delta\sigma_E$. This is the well-known difficulty in constraining $\Delta\sigma_E$ with slip inversion. The trade-off is generally given by $\Delta\sigma_E \propto V_r^{-3}$. Thus, the product $V_r^3\Delta\sigma_E$ is very stable for the inverted slip models for each event with V_r ranging from 2 km/s to 3 km/s as clearly shown in the last column of Table 5.1. This is true for all other events, as shown in Figure 5.4. In other words, slip inversion can constrain $V_r^3\ \Delta\sigma_E$ tightly despite the strong trade-off between V_r and $\Delta\sigma_E$.

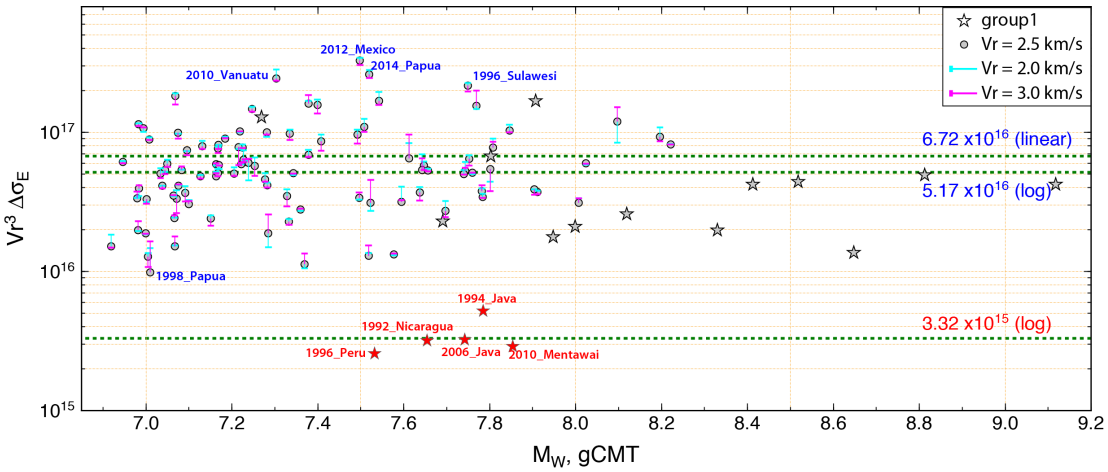

Figure 5.4 The products of $Vr^3\Delta\sigma_E$ from the finite fault slip models for V_r = 2.5 km/s (circles), 2.0 km/s (cyan bars) and 3.0 km/s (magenta bars) for group 2 events or the independently constrained V_r for group 1 events (stars), plotted versus M_W. Tsunami earthquakes are highlighted with red stars. Outlier events are labeled. The linear and log averages of the entire population are indicated by the labeled green dashed lines with units of Nm/s^3. Note the very tight range of values for each event. The tsunami earthquakes appear to have a distinct baseline value of ~3.0x10^{15} Nm/s^3.

Figure 5.4 clearly distinguishes five well-known tsunami earthquakes that have unusually large tsunami excitation relative to their short-period seismic magnitudes [*Polet and Kanamori*,

2009] from the other events, reflecting the significant difference in the rupture physics. Generally tsunami earthquakes have been recognized to have low stress drop and low rupture speed, but $V_r^3\Delta\sigma_E$, or the rupture speed-scaled stress drop, $\left(\frac{V_r}{V_{r0}}\right)^3 \Delta\sigma_E$ (V_{r0} is a reference rupture speed, e.g., 2.5 km/s) is another good diagnostic parameter for tsunami earthquakes.

5.3 Scaling Relationships

Given the intrinsic limitations of source parameters estimated from teleseismic analyses, we will explore the scaling relationships for 1) relatively robustly measured source parameters, including source total duration and centroid time, moment-scaled radiated energy and apparent stress; 2) less-well resolved source parameters such as stress drop and rupture area estimated from slip models with variable rupture expansion velocities; and 3) dynamic earthquake source parameters such as radiation efficiency and fracture energy, which have high uncertainty due to combined errors in both radiated energy and stress drop estimates.

5.3.1 Robust Scaling Relationships

5.3.1.1 Source Duration and Centroid Time

We can approximately relate the source duration t for a simple rupture to other seismic parameters by

$$\tau \propto \frac{L}{V_r} \propto \frac{(M_0 / \Delta\sigma)^{1/3}}{V_r} \ , \qquad (1)$$

where L is the fault length, V_r is the rupture velocity, M_0 is the seismic moment, and $\Delta\sigma$ is the stress drop. Here, the fault width, W, and final slip, D, are assumed to scale with L. The centroid time T_c has a similar basic scaling relation. If we assume uniform slip on a rectangular rupture area, we can more explicitly write the centroid time T_c as:

$$T_c = \left(\frac{C\alpha^2}{\gamma^3} \right)^{1/3} \left(\frac{1}{V_r \Delta\sigma^{1/3}} \right) M_0^{1/3}, \quad (2a)$$

where $\alpha = L/W$ is the fault aspect ratio, C is a rupture shape factor for stress drop calculation, and $\gamma = L/(V_r T_c)$. γ is 2 or 4 depending on whether the rupture is unilateral or bilateral, respectively. The term in the first parentheses is a geometrical factor, and the term in the second parentheses includes the source physical parameters $\Delta\sigma$ and V_r.

Figure 5.5a shows that centroid time T_c estimated from the finite-fault inversions generally scales with $M_0^{1/3}$ with a few significant outliers such as the 17 July 2006 M_W 7.8 Java, 21 February 1996 Peru M_W 7.5, and 2 September 1992 M_W 7.6 Nicaragua tsunami earthquakes, and the 15 August 2007 M_w 8.0 Peru earthquake. The 2007 Peru event was characterized by a compound earthquake by *Lay et al.* [2010b] with a ~60 s hiatus in the seismic radiation between doublet subevents, and cannot be modeled as a simple rupture. As shown in Figure 5.4, tsunami earthquakes have a distinct value of $V_r\Delta\sigma^{1/3}$ from the other earthquakes (here, we ignore the difference between $\Delta\sigma$ and $\Delta\sigma_E$). Thus, the term given by the second parentheses should be different, which explains the deviations of tsunami earthquakes from the general trend. The 2007 Peru earthquake's distinct rupture complexity explains its deviation from the general trend.

Although Figure 5.5a shows an approximately linear relationship between T_c and $M_0^{1/3}$, tsunami earthquakes and some other earthquakes cause considerable scatter because of the distinct value of $V_r\Delta\sigma^{1/3}$ and the geometrical factor, respectively. Considering this, we determine the relation between centroid time, T_c, and seismic moment, M_0, by linear regression for all the events excluding the significant outliers. We obtain the relationship

$$T_c = 2.58 \times 10^{-6} \times M_0^{1/3} \quad (2)$$

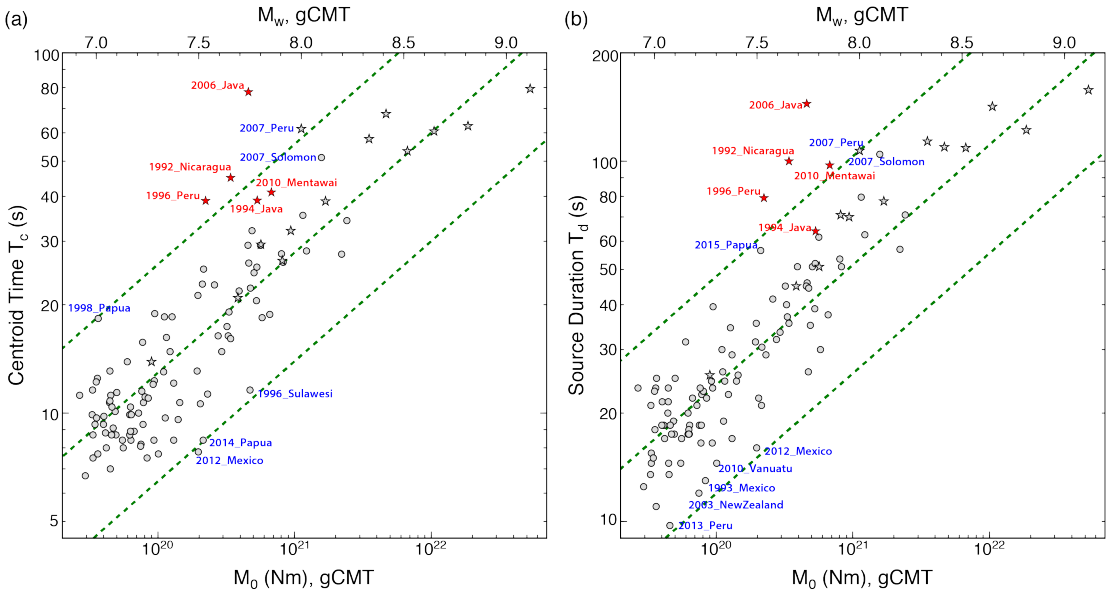

Figure 5.5 Comparison of finite-fault model estimates of (a) source time function centroid time shift, T_c, and (b) total source time function duration, T_d, with seismic moment (lower scale) and M_W (upper scale). The circles indicate solutions found assuming V_r = 2.5 km/s. The stars use independently constrained V_r from detailed studies. Tsunami earthquakes are highlighted in red, and outlying events are identified. The green dashed lines correspond to slopes of 1/3 with intercepts varying by factors of two.

where M_0 is in units of N-m and T_c is in second. The coefficient 2.58x10^{-6} is close to the value, 2.59x10^{-6} (1.2x10^{-8} with M_0 in dyne-cm) obtained in *Duputel et al.* [2013] using the centroid time determined by long period W-phase inversion. *Duputel et al.* [2013] applied a regression analysis to all the events without excluding the outliers such as tsunami earthquakes, but the outliers are few and the relation is not very different. If we include all the earthquakes in the regression analysis, we obtain $T_c = 2.76 \times 10^{-6} \times M_0^{1/3}$. With this scaling relationship, we can predict the centroid time (T_r) for a given seismic moment, to within a factor of 2, except for tsunami earthquakes, over the magnitude range M_W = 6.9-9.0. The ratios between the measured and predicted centroid time are shown as a function of earthquake magnitude

(Figure 5.6a) and earthquake occurrence time (Figure 5.6b). As emphasized by *Duputel et al.* [2013] the scaling relationship (2) provides one of the more robust seismological scaling behaviors for major megathrust earthquakes. The outliers in these plots also provide a useful means of identification of unusual earthquakes such as tsunami earthquakes.

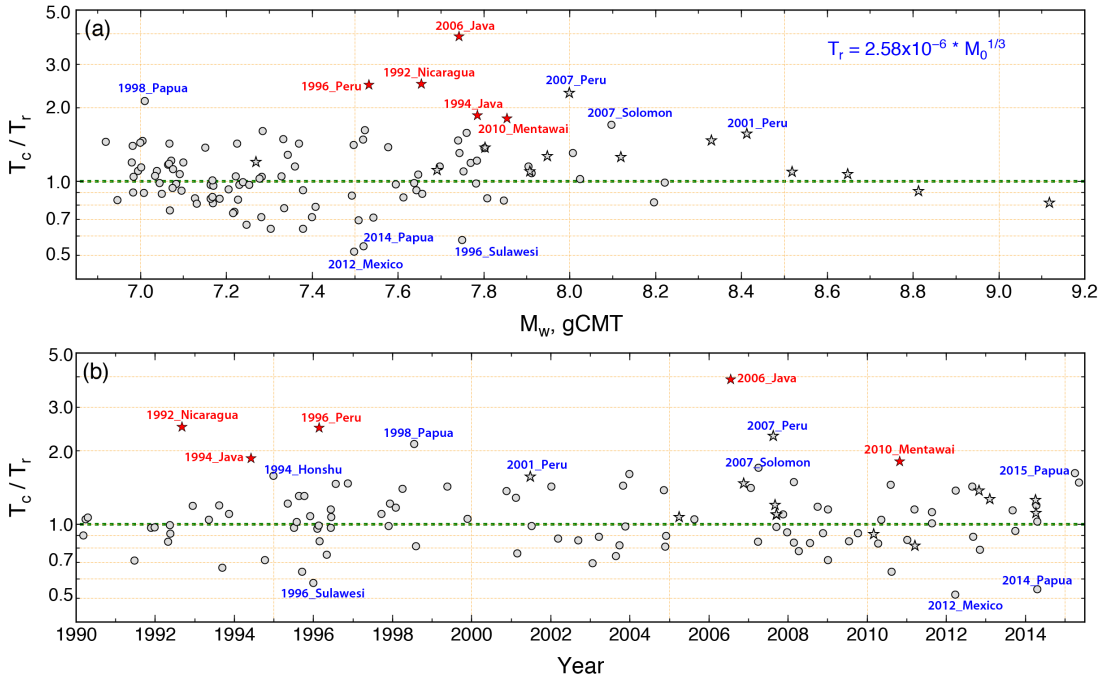

Figure 5.6 Source time function centroid times, T_c, from finite-fault inversions assuming V_r = 2.5 km/s (circles) or independent determinations of V_r (stars) normalized by the duration (T_r) estimated by regression of T_c and $M_0^{1/3}$ (M_0 has the unit of Nm) with zero intercept, plotted as functions of (a) M_W and (b) time. Events with anomalously large or small ratios are labeled. The long-duration events tend to be tsunami earthquakes (red stars), or have long intervals of weak initial slip (e.g., 2001 Peru), or are doublet ruptures (2007 Peru and 2007 Solomon Islands earthquakes).

If we perform the regression allowing for a non-zero intercept there is a ~2 s offset as seismic moment approaches zero (Figure 5.A1), which has been observed previously for the gCMT catalog [*Dziewondski and Woodhouse*, 1983] and the W-phase catalog [*Duputel et al.*, 2013]. This may be an artifact caused by limitations of the moment-rate function

parameterizations in the various methods, (we use subfault source time functions with multiple triangles with 0.5 s half-duration, and 0.5 s sample rate for the data in our finite-fault inversions), along with uncertainties in the absolute origin times used as references for the centroid time estimation (we align our P waves by eye, and that has some uncertainty). We tested whether there is any bias in the scaling by including the intercept shift, but the overall pattern of scaled centroid time do not show significant difference (Figure 5.A2).

We apply a similar analysis to the total duration, T_d, and the result is shown in 5b. The weak positive trend relative to cube-root scaling is likely due to the bias discussed above concerning the total duration estimates from the moment rate functions determined with the finite-fault inversion with positivity constraints. T_d comparisons with earlier studies for smaller events are considered in the companion paper.

5.3.1.2 Geometrical Factor

To isolate the geometrical factor, we rewrite (2a) as

$$\frac{C\alpha^2}{\gamma^3} = \left(V_r^{\,3}\Delta\sigma\right)\Big/\left(M_0/T_c^{\,3}\right), \tag{2b}$$

which means that the ratio of the well-constrained $V_r\Delta\sigma^{1/3}$ determined by slip inversion to M_0/T_c^3 (Figure 5.A3 shows this term as a function of M_W) determined by the M_0 vs. T_c^3 relation gives the geometrical factor. For purposes of illustration, we consider a reference fault geometry with a unilateral ($\gamma = 2$) thrust fault and an aspect ratio $\alpha = 3$. For this geometry the geometrical factor, $C\alpha^2/\gamma^3$, is close to 1. Figure 5.7 shows the ratio, $(V_r^3\Delta\sigma_E)/(M_0/T_c^3)$, as a function of M_W. For most events, the ratio is close to 1. Small $C\alpha^2/\gamma^3$ can be due to strong bilateral rupture, such as for the 11 March 2011 M_W 9.0 Tohoku earthquake. Large values can result from large aspect ratio ruptures like the 17 July 2006 M_W 7.8 Java and 1

April 2007 M_w 8.1 Solomon Islands earthquakes, or unusually long duration doublet earthquakes, like the 15 August 2007 M_w 8.0 Peru earthquake. Although the cause of some of the outliers in Figure 5.7 is not obvious, the overall trend is what is expected.

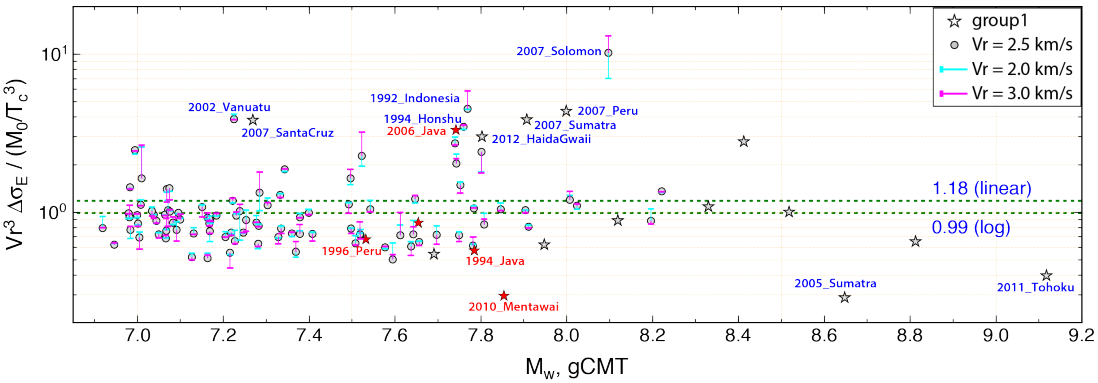

Figure 5.7 The ratio of $V_r^3 \Delta\sigma_E$ (Figure 5.4) and M_0/T_c^3 plotted as a function of M_W. This ratio isolates the geometrical factors that differ between events. The non-dimensional linear and log averages are indicated by labeled dashed green lines. Tsunami earthquakes are highlighted with red stars, and outliers are labeled in both panels.

Source scaling analyses often assume that the geometrical factors are constant for all earthquakes. For that assumption we can predict a stress drop ($\Delta\sigma_{T,G}$) using the measured seismic moments and centroid source durations along with a specified rupture speed and equation 2b. If $C = 1, \alpha = 3, \text{and } \gamma = 2$ for unilateral rupture, $C\alpha^2/\gamma^3$ is about 1.125 which is close to the average value from the ratios of M_0/T_c^3 and $V_r^3\Delta\sigma_E$ in Figure 5.7. Assuming a constant V_r = 2.5 km/s for all events we obtain estimates of $\Delta\sigma_{T,G}$ that are compared with our measured energy-related stress drops $\Delta\sigma_E$ using the same V_r for group 2 events in Figure 5.A4a. For most earthquakes, there is reasonable similarity of the two stress drop estimates, but there can be significant errors for some events if the real geometric factor is not determined by finite-fault inversion.

5.3.1.3 Moment-Scaled Radiated Energy and Apparent Stress

We estimate the radiated energy E_R for each station from the observed ground velocity spectra following the method of *Venkataraman and Kanamori* [2004], and then average the station estimates in a logarithmic sense (i.e., geometric average) to estimate the radiated energy for frequencies above 0.05 Hz. The time window for each signal is carefully chosen to include most of P-wave group energy arrivals while minimizing the effect of scattered coda energy and PP phases. A broadband source spectrum is obtained for each event by combining the spectrum of the moment rate functions estimated with finite-fault inversions for frequencies below 0.05 Hz and the average displacement spectrum estimated from attenuation-corrected P waves for frequencies in the range 0.05-1.0 Hz. The broadband spectrum thus obtained is used to estimate the total radiated energy by adding in the low frequency contribution. In some cases there is a substantial contribution from frequencies less than 0.05 Hz, especially for tsunami earthquakes [*Ye et al.*, 2013b; *Lay et al.*, 2013a].

The total radiated energy E_R scaled by seismic moment is an important characterization of earthquake dynamics. There are numerous observations and debates about the influence of earthquake size on E_R/M_0 [e.g. *Venkataraman and Kanamori*, 2004; *Walter et al.,* 2006]. Figure 5.8a shows our measurements of this ratio using the radiated energy estimates up to 1 Hz as a function of M_W and M_0. The tsunami earthquakes clearly stand out from the other large megathrust events in this study (Figure 5.8a), along with a few other earthquakes with strong observed tsunami or very shallow ruptures, such as the 17 November 2000 (21:01) Papua [*Geist and Parsons*, 2005], 27 August 2012 El Salvador [*Ye et al.*, 2013b], 6 February 2013 Santa Cruz Islands [*Lay et al.*, 2013a], and 5 May 2015 Papua earthquakes. The low E_R/M_0 of tsunami events relative to comparably large earthquakes is compatible with the results of *Newman and Okal* [1998] despite our values being systematically larger. Moment-scaled

radiated energy measures have large scatter from 1 x 10^{-6} to 4 x 10^{-5}, but no obvious magnitude dependence. The average value of E_R/M_0 for the 114 events in this study is 1.22 x 10^{-5}, or $\theta = \log_{10}(E_R/M_0) = -4.91$, which is consistent with the value $\theta = -4.74$ from *Convers and Newman* [2010] for all $M_w > 6.7$ thrust events from 1997 to mid-2010 and with the compilation of all measurements for events from M_w 1.5-9.2 by *Baltay et al.* [2014], for which our data fill in a large gap in the M_w 7.0-8.5 range.

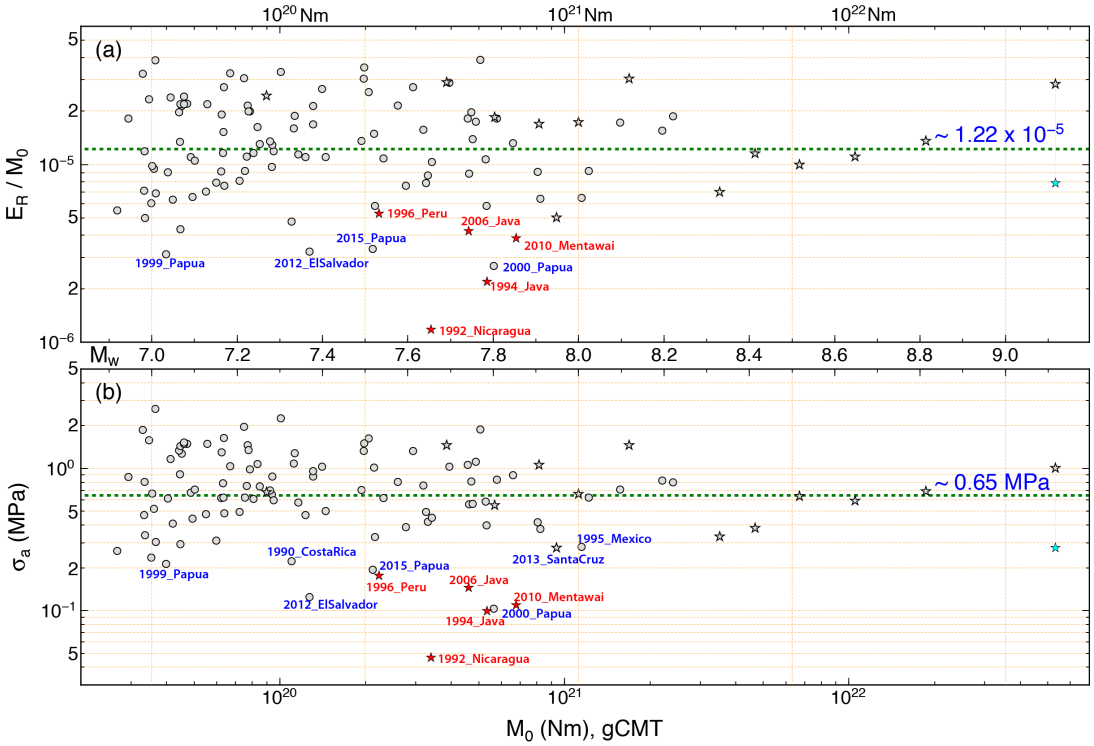

Figure 5.8 (a) Moment-scaled radiated energy estimates and (b) apparent stress versus gCMT seismic moment and M_W. Circles indicate determinations that estimate low frequency energy contributions from finite fault models with V_r = 2.5 km/s and stars indicate finite fault models with independently estimated V_r. The low frequency energy estimates are very weakly dependent on V_r, so the plot is very similar to those for different choices of V_r. Tsunami events are highlighted with red stars. Outliers are labeled. The average values over the entire range are given by the labeled dashed green lines. The cyan star indicates the moment-scaled radiated energy and apparent stress calculated with the radiated energy for the 2011 Tohoku event from *Lay et al.* [2012].

A related source parameter that is often considered is apparent stress, defined as the product of rigidity and moment-scaled radiated energy,

$$\sigma_a = \mu \frac{E_R}{M_0} = \frac{E_R}{A \cdot D} \ , \tag{3}$$

where D is average slip, A is source rupture area, and μ is rigidity. The apparent stress was used by Wyss (1980) to study the difference in the state of stress between shallow and deep earthquakes. The recent advances in broadband seismology have enabled us to estimate E_R accurately, making this parameter more meaningful. The total strain (potential) energy release in an earthquake is given by $\Delta W = \bar{\sigma} DA = \left(\frac{\bar{\sigma}}{\mu}\right) M_0$, where $\bar{\sigma}$ is the average stress on the fault plane [*Kostrov*, 1973; *Dahlen*, 1977]. Then the radiated energy E_R can be written as $E_R = \eta \bar{\sigma} DA = \sigma_a DA$ where η is the seismic efficiency, and $\sigma_a = \eta \bar{\sigma}$ is the apparent stress. Thus, σ_a is a part of the average stress that is responsible for seismic energy radiation, and is the stress that represents the dynamic characteristics of an earthquake. The remainder of the average stress is used as work done on the fault plane.

From equation (3), we can think of apparent stress as radiated energy per unit rupture area, per unit slip, although the energy is not necessarily radiated from the fault plane [*Rivera and Kanamori*, 200]. It has been used for interpreting fracture energy and slip-weakening models [e.g., *Abercrombie and Rice*, 2005; *Rice*, 2006]. If the rigidity, μ, is assumed to be constant for all earthquakes in various environments, say 30 GPa, as used in many previous studies, the apparent stress is directly proportional to the moment-scaled radiated energy that we show in Figure 5.8a. Given that we have variable rigidity in our source models, we compute apparent stress parameters using the slip-weighted average rigidity for each rupture model. Resulting variations of apparent stress with seismic moment for our large events (Figure 5.8b) are naturally quite similar to those of E_R/M_0, but the shallow tsunami/tsunamigenic earthquakes

are more separated from the general trend, due to the product of low E_R/M_0 and low source region rigidity. The average apparent stress for the entire population of events is about 0.65 MPa. Because the actual values of rigidity, particularly at very shallow depth in the megathrust environment are not well constrained, it is difficult to formally estimate uncertainties in the apparent stress values. However, apart from the baseline shift to low values around 0.1 MPa for tsunami earthquakes, there is no clear dependence on earthquake size for our population of major and great megathrust events.

5.3.2 Stress Drop

Stress drop is an important measure of the change of static stress on a fault before and after an earthquake. Despite this importance, the static stress drop cannot be defined precisely, and some ambiguity remains. The stress drop is a function of spatial derivatives of slip, but detailed slip distribution is usually difficult to determine in practice. Given this difficulty, it is typically estimated from the ratio of the average coseismic slip to a characteristic fault dimension, and is therefore subject to large uncertainty due to the resolution of estimates of both of those parameters. In reality, the stress drop varies spatially over the rupture area, as expected from the heterogeneous slip distributions of kinematic finite-fault models; it evolves at each point during nucleation, rupture and healing processes, as demonstrated in dynamic rupture simulations. Because of this complexity, estimations of stress drops by different investigators vary even for similar slip distributions depending on how averaging is done. To stabilize the stress drop estimation procedure we use the following two methods for all of the events: 1) averaging the stress drop distribution for finite-fault models weighted by the spatially varying slip distribution, and 2) using the rupture area of the well-resolved slip regions and the average slip over it.

5.3.2.1 Energy-related Stress Drop

Based on consideration of energy partitioning, the energy-related stress drop ($\Delta\sigma_E$) has been proposed as the spatial average of the stress drop weighted by slip [*Noda et al.*, 2013; *Ye et al.*, 2013c],

$$\Delta\sigma_E = \frac{\int_\Sigma \Delta\sigma_1 \Delta u_1 \, dS}{\int_\Sigma \Delta u_1 \, dS}, \tag{4}$$

where $\Delta\sigma_1$ and Δu_1 are components of stress drop and slip at each sub-fault in the overall slip distribution, as shown in the Figure 5.2 and Appendices I and II for all earthquakes.

As mentioned earlier, strong trade-off exists between the stress drop and V_r. Given this trade off, we compute $\Delta\sigma_E$ for three slip models with V_r = 2 km/s, 2.5 km/s and 3 km/s, and use the case with $V_r = 2.5$ km/s as a reference model. However, the rupture speed for the individual event may differ from 2.5 km/s, and variations of V_r over a range of at least 2 to 3 km/s is possible.

Figure 5.9a shows $\Delta\sigma_E$ thus calculated as a function of M_W. No systematic variation in $\Delta\sigma_E$ with M_W is seen. The average $\Delta\sigma_E$ is ~ 3.4-4.6 MPa for the 114 $M_W \geq 7$ events we analyzed with the assumed V_r of 2.5 km/s for group 2 events. There is a factor of ~2 variation of $\Delta\sigma_E$ for rupture velocities varying from 2.0 km/s to 2.5 km/s or from 2.5 km/s to 3.0 km/s. The values of $\Delta\sigma_E$ with different V_r for all the earthquakes ranges from ~0.4 MPa to ~40 MPa, with $\Delta\sigma_E$ less than 2 MPa for tsunami earthquakes. Only a few events have $\Delta\sigma_E$ larger than 10 MPa. While there is no overall magnitude dependence, there is a tendency for scatter to decrease from a factor of ~100 for M_w 7.0-7.9 events to a factor of ~10 for $M_w > 8$ (Figure 5.9a). For earthquakes smaller than 7, stress drops are most frequently estimated from the spectral corner frequencies, and the estimates of stress drop show a 3 to 4 orders of magnitude variation [e.g., *Shearer et al.*, 2006; *Allman and Shearer*, 2009]. The large scatter in

stress drop estimates reflects uncertainty in source modeling, but also represents actual variations of stress heterogeneity in the crust. The heterogeneous state of stress in the crust is indicated by the variations in observed body wave frequency content, waveform complexity, and ground shaking duration (see the individual rupture models and data fits in Appendices I and II). The reduced scatter in stress drop as event size increases may be a result of more extensive averaging over stress heterogeneity on the fault plane for larger ruptures.

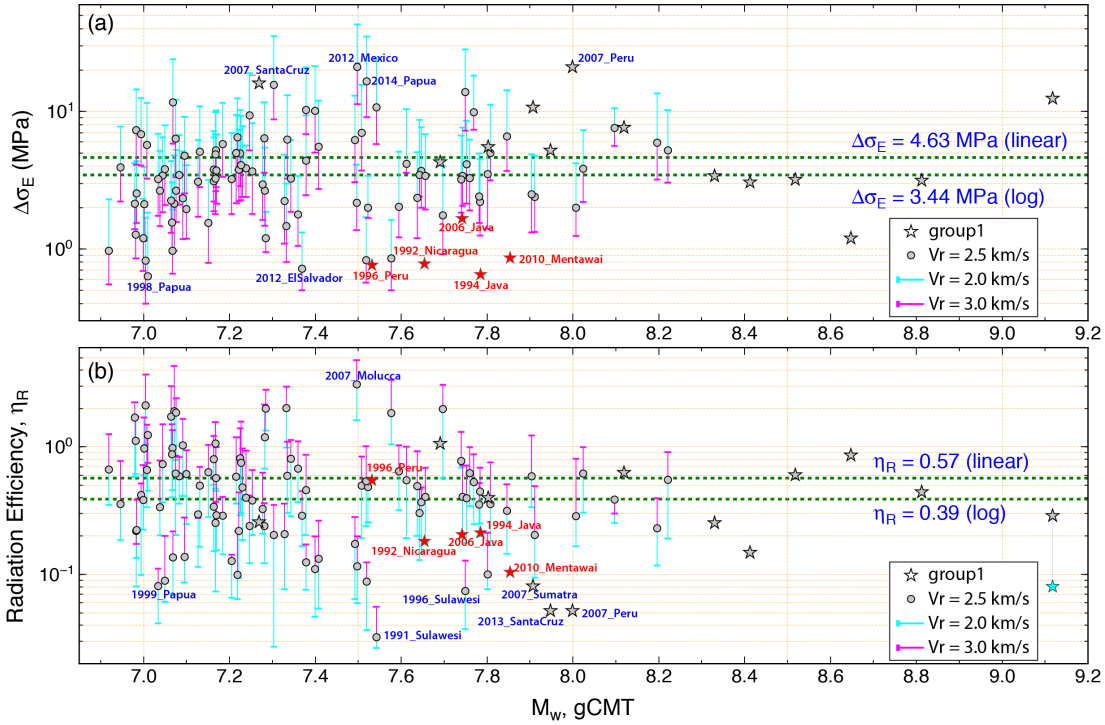

Figure 5.9 (a) The range of stress drop, Ds_E, from variable slip finite source models with V_r = 2.0 km/s (upper cyan estimates), to V_r =2.5 km/s (circles), to V_r =3.0 km/s (lower magenta estimates), plotted versus M_w. The stars are for group 1 finite fault models with independent estimates of V_r. (b) Corresponding values of radiation efficiency for models with different V_r versus magnitude. Linear and logarithmic averages of $\Delta\sigma_E$ and η_R are indicated by labeled horizontal green lines. Events with high or low values are labeled. Tsunami earthquakes are highlighted with red stars. The cyan star indicates radiation efficiency calculated with the radiated energy for the 2011 Tohoku event from *Lay et al.* [2012].

The stability of individual event values of $V_r^3\Delta\sigma_E$ for a range of finite-fault models allows us to estimate the rupture velocities for a range of assumed stress drops. Figure 5.10a shows the rupture velocities consistent with stress drops varying from 2 MPa to 7 MPa for each event, as a function of seismic moment. The inferred rupture velocities range from ~1 km/s (for tsunami earthquakes) to ~4 km/s, with an average of 2.26 km/s.

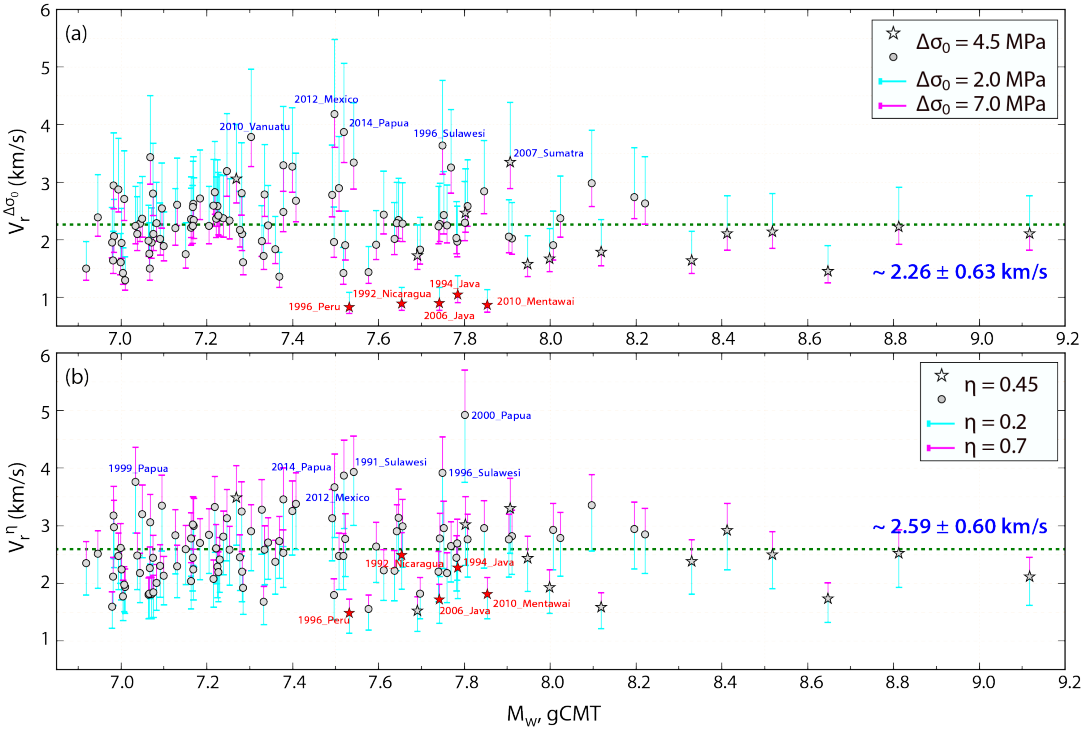

Figure 5.10. (a) Calculations of rupture expansion velocity V_r for each event consistent with constant stress drop $\Delta\sigma_0$ of 2.0 MPa (cyan bars), 4.5 MPa (circles and stars) and 7 MPa (magenta bars) plotted versus M_W. The individual event values of $V_r^3\Delta\sigma$ from finite-fault models (Figure 5.4, V_r 2.5km/s for group 2 events) are used to estimate V_r. (b) Calculations of rupture velocity for each event consistent with the stress drops derived with constant radiation efficiency of 0.2 (cyan bars), 0.45 (circles and stars), and 0.7 (magenta bars) plotted versus M_W. The individual event values of $Vr^3\Delta\sigma$ from finite fault models (Figure 5.4) are also used to estimate V_r. Tsunami earthquakes are highlighted with red stars and outliers in the V_r estimates are identified. The average V_r for each population is indicated by the labeled dashed green line in each panel.

5.3.2.2 Trimming Factor and Effective Rupture Area

The most common seismological estimates of average static stress drop ($\Delta\sigma_s$) for large earthquakes are based on the seismic moment and fault dimensions with assumed fault geometry. For large subduction zone interplate earthquakes, stress drop is often calculated using the average slip from finite-fault models using the relation [*Kanamori and Anderson*, 1975],

$$\Delta\sigma_s = \frac{7\pi}{16}\mu\frac{D}{a} = \frac{7\pi^{3/2}}{16}\frac{M_0}{A^{3/2}}, \quad (5)$$

where D is the average slip, a is a radius of circular fault area equal to the estimated source rupture area A, and μ is rigidity. The relation (5) is for a circular crack, but it is approximately used for any fault with an area A. The seismic moment M_0 can be taken from the well-determined long-period measurements; we use gCMT estimates in this study. The critical issue is the estimation of the rupture dimension or rupture area, which is difficult to determine from teleseismic body wave data, as mentioned above. In our finite-fault inversions, we initially use a large enough fault plane to accommodate the slip zone well within it, adjusting the model dimensions based on the source complexity and any independent information about the rupture velocity. After settling on a final grid and rupture velocity, we apply a trimming threshold ζ, to our final inverted slip distribution. This removes subfaults with a seismic moment smaller than ζ times the moment of the subfault with the largest moment. The choice of ζ, has a direct effect on the estimates of effective rupture area (A_{eff}) and the associated equivalent circular fault radius, a, and to a lesser extent on the estimated value of D. Typical values of ζ used in our own previous work have been 0.1 to 0.2. ζ is not theoretically constrained, and can vary from event to event depending on the nature of the slip distribution, the data coverage, and the fault model parameterization.

Instead of computing $\Delta\sigma_s$ with an arbitrarily chosen ξ, we varied ξ to find $\Delta\sigma_s$ that matches the energy-related stress drop $\Delta\sigma_E$ for the same event. Figure 5.11a shows that the resulting trimming threshold ranges from ~0.08 to 0.4 with an average of ~0.17. This is compatible with the results of numerical calculations of strain energy for many heterogeneous stress drop distributions [*Noda et al.*, 2013]. Overall, a use of $\xi \sim 0.17$ is sufficient to remove most of the poorly resolved model components and to provide a reasonable source area for the stress drop determination. The energy-related $\Delta\sigma_E$ presented in this study can be compared directly with the static stress drop estimated with ξ ~0.15 in our previous studies [e.g., *Ye et al.*, 2013c; *Lay et al.*, 2013a; 2013b]. The values of ξ do not depend much on the assumed rupture expansion velocity as shown in the Figure 5.11a.

The scaling between rupture area and seismic moment for major megathrust events is important for many applications, including tsunami early warning and long-term earthquake hazard estimation. For the specific ξ values that give $\Delta\sigma_s = \Delta\sigma_E$, we have corresponding effective rupture areas (A_{eff}) with significant slip from the finite-fault models. Figure 5.11b shows that A_{eff} generally scales with $M_0^{2/3}$ with small scatter, ranging over one order of magnitude of A_{eff}. The relation shown by Figure 5.11b is consistent with the result of previous studies. For example, Figure 5.2 of *Kanamori and Anderson* (1975) indicates a relation $\log M_0 = 1.5 \log A + 15.05$ (M_0 in N-m, A in km^2), and Figure 5.16 of *Wells and Coppersmith* (1994) indicates a relation $\log M_0 = 1.515 \log A + 15.0$. The middle dotted line on Figure 5.11b which passes through the group 1 events and the middle of the points for group 2 events calculated with $V_r = 2.5$ is given by $\log M_0 = 1.5 \log A + 15.3$. Thus, the rupture speed $V_r = 2.5$ km/s seems to be a reasonable average rupture speed.

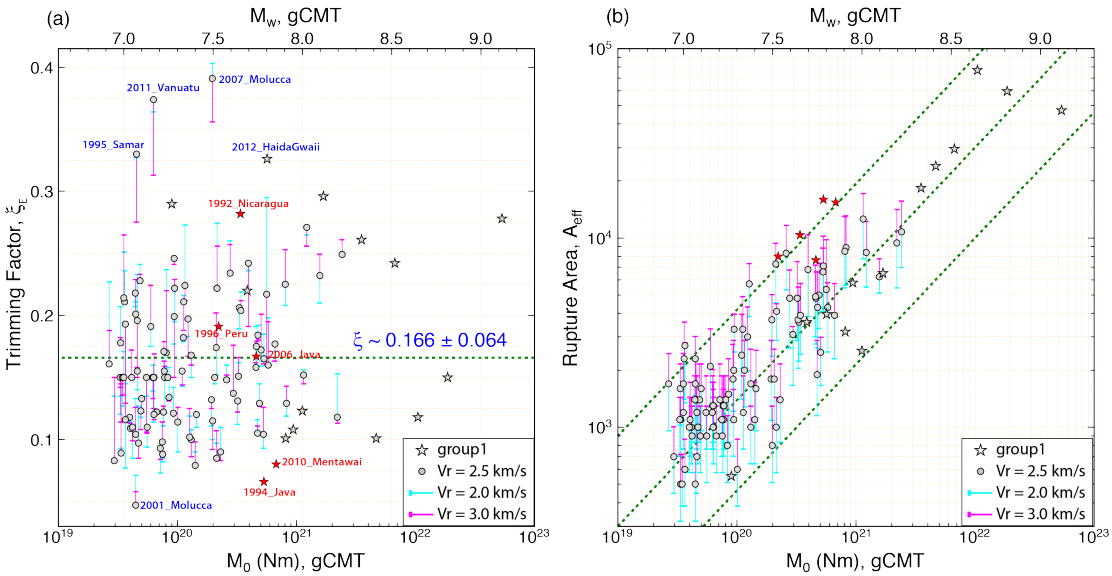

Figure 5.11 (a) Determinations of finite fault model trimming factors ζ_E that provide circular rupture models with uniform average slip that give stress drops that match $\Delta\sigma_E$ calculations, and (b) the corresponding trimmed rupture area (A_{eff}) for each model, plotted versus seismic moment (lower axis) and M_W (upper axis). Circles are trimming factors for finite source models that assume V_r = 2.5 km/s, cyan bars indicate the trimming for models with V_r = 2.0 km/s that match the corresponding model estimates of $\Delta\sigma_E$, magenta bars indicate the trimming for models with V_r = 3.0 km/s that match the corresponding model estimates of $\Delta\sigma_E$, and stars are for finite source models with independently constrained V_r. The average trimming factor is about 0.17 (horizontal green line in (a)).

5.3.3 Radiation Efficiency

A parameter that is commonly used to connect kinematic observations with earthquake dynamic models is radiation efficiency, η_R, defined as

$$\eta_R = \frac{E_R}{\Delta W_0} = \frac{2\mu}{\Delta\sigma}\frac{E_R}{M_0} = 2\cdot\frac{\sigma_a}{\Delta\sigma}\ , \qquad (6)$$

where E_R, $\Delta W_0, \sigma_a,$ and $\Delta\sigma$ are radiated energy, available potential energy, apparent stress and static stress drop, respectively. The radiation efficiency, η_R, is different from the efficiency, η, which is the ratio of E_R to the total potential energy change ΔW. Thus,

$$\eta = \frac{\Delta\sigma}{2\bar{\sigma}}\eta_R \leq \eta_R . \quad (7)$$

Radiation efficiency is useful for understanding the energy partitioning between the radiated energy and the mechanically and thermally dissipated energy in the fault zone, and can be related to the rupture speed. *Kanamori et al.* [1998] found very low radiation efficiency for the slowly rupturing main phase of the 1994 M_w 8.3 deep Bolivia earthquake, indicative of a dominant role of dissipative mechanical and thermal processes during that deep earthquake faulting. The physical requirement of $\eta_R < 1$ (assuming no final stress undershoot) has subsequently been used to constrain the rupture dimension of the 24 May 2013 M_w 8.3 deep-focus Sea of Okhotsk earthquake by *Ye et al.* [2013c]. The rupture of the Okhotsk earthquake appears to have been faster and more brittle with higher radiation efficiency than the Bolivia earthquake.

Theoretically, the radiation efficiency varies between 0 and 1 as a function of rupture speed, V_r, for mode II and III type ruptures [e.g., *Kanamori and Rivera*, 2006]. It is physically possible that radiation efficiency as defined by (6) can exceed 1 if there is stress recovery that results in small final stress drop, and the available energy defined by $\Delta W_0 = \frac{\Delta\sigma}{2\mu} M_0$ in (6) is underestimated. We computed the radiation efficiency using our independently estimated source parameters and examine the distribution of values. We find that about 15% of the total set of events have a calculated radiation efficiency larger than 1 if we use the energy-related stress drop $\Delta\sigma_E$ and average rigidity from the finite-fault models (Figure 5.9b). About 10% of our events have very low estimates of radiation efficiency (<0.1), which suggests strongly dissipative processes, likely with strong thermal heating effects. It is interesting that several events in Papua and Sulawesi regions have particularly low values (Figure 5.9b). The average estimates of radiation efficiency are 0.57 (linear) and 0.39 (logarithmic).

The scatter of the radiation efficiency decreases with the magnitude (Figure 5.9b), and a negative correlation between radiation efficiency and stress drop for our measurements (Figure 5.A5a) results from the relative constancy of moment-scaled radiated energy. The trend is quite systematic even for events with low radiation efficiency, so this behavior indicates that stress drop variations dominate the radiation efficiency estimates. Correlations between radiation efficiency and moment-scaled radiated energy are more scattered (Figure 5.A5b,c). Essentially, moment-scaled radiated energy does not increase as fast as stress drop increases, lowering the efficiency. A possible interpretation is that when higher stress is involved during fault slip more energy is dissipated by micro-cracking, deformation or some thermal process.

We can use equation (6) to predict a stress drop ($\Delta\sigma_\eta$) under the assumption of a specific value of radiation efficiency, together with the measured values of moment-scaled radiated energy for each earthquake. Figure 5.A4b shows that $\Delta\sigma_\eta$ for $\eta = 0.5$, has some correlation with measured $\Delta\sigma_E$, but less than that for $\Delta\sigma_{T,G}$. The overall population of values of $\Delta\sigma_\eta$ is slightly low relative to $\Delta\sigma_E$, which could be redressed by assuming a somewhat lower value of h. Estimates of V_r can again be made using the stable event-specific values of $V_r^3\Delta\sigma_E$ replacing $\Delta\sigma_E$ with the stress drop values estimated from specified values of radiation efficiency ($\Delta\sigma_\eta$, h = 0.2 to 0.7). Figure 5.10b shows that this gives a range of inferred rupture velocities from ~1.5 km/s to ~4 km/s with an average ~2.6 km/s. The less distinct rupture velocity estimates for tsunami earthquakes indicate that this procedure has limitations, but retrieves the overall behavior fairly well. While V_r is directly parameterized in finite-fault models rather than stress drop or radiation efficiency, the overall consistency of the V_r values with reasonable ranges of stress drop and radiation efficiency indicates that reasonable values are used.

Figure 5.12a plots estimates of radiation efficiency for our very large events along with measurements from *Abercrombie and Rice* [2005] for smaller events as a function of average slip D for each event. The η_R values for major and great events are for the source models with stress drop $\Delta\sigma_E$ and the average rigidity across the slip distribution, while a uniform source rigidity of 30 GPa is assumed for the smaller events. There is a trend of slightly increasing radiation efficiency with increasing average slip from 1 mm up to 1 m, but then radiation efficiency appears to decrease for yet larger slip up to 20 m. The pattern involves data from different faulting geometries and source environments for the small and major events, so it is possible that different mechanisms affect η_R across the combined population. If we consider just the major and great events, radiation efficiency tends to decrease with slip. Diverse mechanisms may operate for the largest slip events that distinguish them from lower slip events.

While our results for radiation efficiency are obtained from an extensive data set of very large megathrust events, further constraints on source parameters using regional data with better spatial resolution of rupture dimensions are likely needed before drawing more definitive conclusions from these measurements.

5.3.4 Fracture Energy

Fracture energy per unit area, G, which involves all resistance to rupture expansion at the rupture tip including plastic yielding, cracking, and latent heat due to thermal pressurization and melting, is another important source characteristic for the energy budget of earthquake ruptures [e.g., *Kanamori and Heaton*, 2000; *Abercrombie and Rice*, 2005; *Rice*, 2006; *Kanamori and Rivera*, 2006]. The available energy ΔW_0 (which excludes the frictional energy

associated with work done against the resistance to sliding on the fault plane) is equal to the radiated seismic energy plus the total fracture energy for rupture with total surface area A:

$$\Delta W_0 = E_R + GA \tag{8}$$

Rewriting this to express G in terms of E_R and η_R gives:

$$G = E_R(\eta_R^{-1} - 1)/A \tag{9}$$

Using (9) and our estimates of radiated energy, radiation efficiency, and effective rupture area we can estimate G (we denote these estimates as G'), or from the equivalent expression for the proxy for fracture energy used by *Abercrombie and Rice* [2005]:

$$G' = 0.5(\Delta\sigma - 2\mu\, E_R/M_0\,)D = 0.5(1 - \eta_R)\Delta\sigma D \tag{10}$$

G' is equal to G if the final stress is equal to the final dynamic stress (i.e., there is no stress undershoot or overshoot).

Various mechanisms could cause G'/D to vary with earthquake size or total slip [e.g., *Rice*, 2006]. Variation in G' could result from η_R varying with event size or total slip. *Abercrombie and Rice* [2005] and *Rice* [2006] inferred variation of G' with slip for a data set they compiled. We show the G' values computed for our data set in Figure 5.12b together with those compiled by *Abercrombie and Rice* [2005]. Our major and great earthquake population extends the overall trend of G' with slip displayed by *Abercrombie and Rice* [2005] and *Rice* [2006], and our observations overlap the averaged results for large events they show (those values have been omitted here). The G' values computed for the events with nominal values of η_R>1 become negative. This is obviously an artifact arising from the non-physical η_R (>1), and we omit those events (18 from our major-event set and 6 from the smaller events) in Fig. 12b. However, omission of these events does not affect the overall trend defined by other events. The cause of the baseline shifts apparent in the segmented trends is not clear, but the data show similar slopes close to 2 in each segment population due to correlation of $\Delta\sigma$ and D

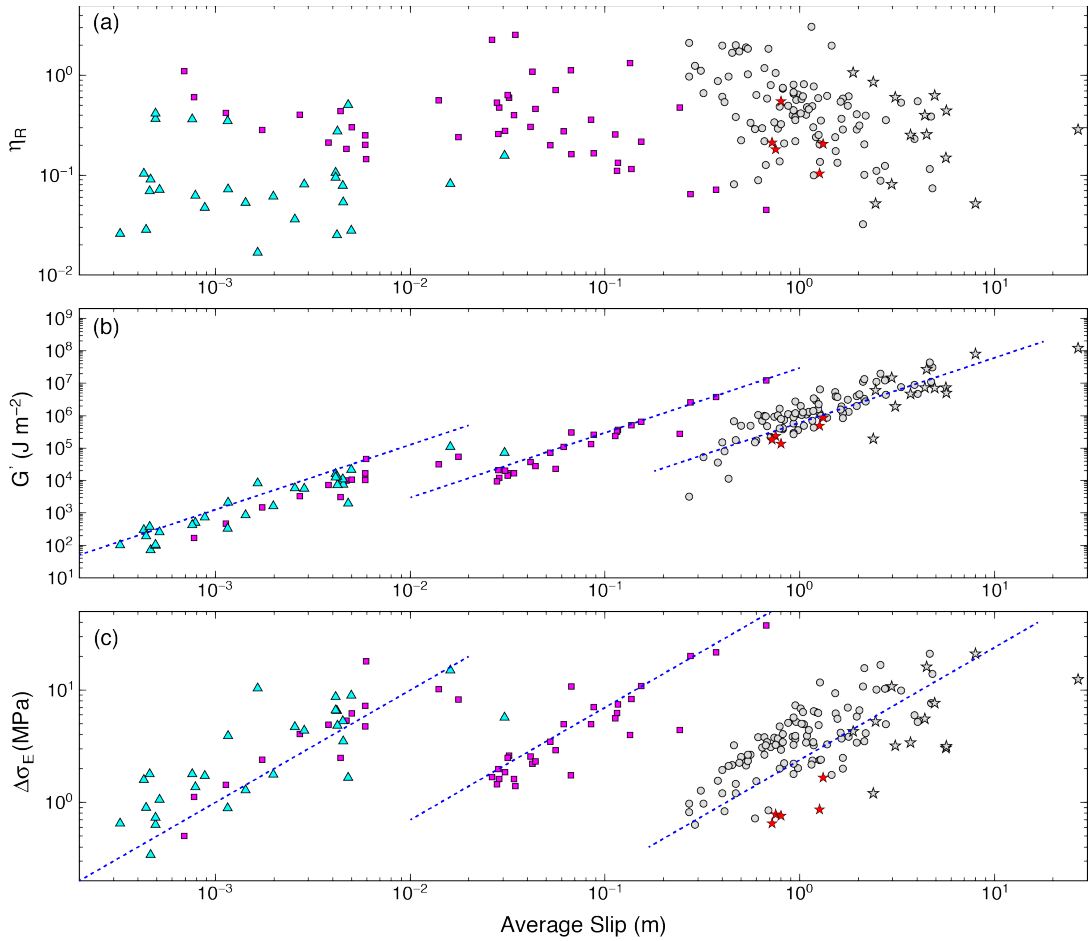

Figure 5.12. (a) Radiation efficiency, (b) fracture energy and (c) energy-related stress drop $\Delta\sigma_E$, derived from the source parameters from the finite fault models for both group 1 (stars) and group 2 events (circles, V_r = 2.5 km/s), versus the average slip calculated from the finite fault models for the area with trimming factors from Figure 5.10a. Cyan triangles and purple boxes are values from *Abercrombie and Rice* [2005]. Tsunami earthquakes are highlighted with red stars and text. The blue dashed lines in (b) and (c) show the linear trends with slopes of 2 and 1, respectively, in log-log scale.

(Figure 5.12c), for a moderate range of η_R in (7). The baseline shifts (reproduced from the previous papers) could be due to comparison of events in different environments, differences in measurement procedures, and differences in material parameters. Thermal weakening models predict some downward curvature of the log G' – log D relations [*Rice*, 2006], but our data for large slip values do not exhibit such a trend. Further work to understand the

segmentation of these measurements, to account for the negative G' estimates, and to reduce uncertainty in the measurements appears to be necessary before drawing firm conclusions about thermal weakening or other slip dependent processes.

5.4 Discussion and Conclusions

As we discussed earlier, the most difficult kinematic parameter to constrain with slip inversion of only teleseismic data is the rupture speed, V_r. Thus, we consider a range from $V_r = 2.0$ km/s to 3.0 km/s, and use the model with $V_r = 2.5$ km/s as a reference model. The rupture speed of individual event can vary over a range even larger than the range from 2 to 3 km/s, but we believe that the reference speed 2.5 km/s is a reasonable average for group 2 events for the following reason. As shown in Table 5.2, the geometrical average of $\Delta\sigma_E$ is 0.89 and 5.61 for five tsunami earthquakes, and the other 13 group 1 earthquakes, respectively. For these events, the rupture speed is independently constrained. In Table 5.2 we show the geometrical average of $\Delta\sigma_E$ and η_R computed with V_r = 2.0 km/s, 2.5 km/s and 3.0 km/s for all group 2 events. Although there may be some small tsunami-earthquake-like events (e.g., 2012 El Salvador event) in group 2, most events are deeper on their megathrust. The values of $\Delta\sigma_E$ for $V_r = 2.0$ and 3.0 km/s bracket the average $\Delta\sigma_E$ of the 13 non-tsunami earthquakes listed in Table 5.2. The value of $\Delta\sigma_E$ for $V_r = 2.5$ km/s is somewhat larger than $\Delta\sigma_E$ of the 13 non-tsunami earthquakes listed in Table 5.2, but is comparable. Thus, we believe that $V_r = 2.5$ km/s is a reasonable average rupture speed for group 2 events. The same argument can be made for η_R, and for the arithmetic average of $\Delta\sigma_E$, and η_R. Also, as shown in the previous section, $V_r = 2.5$ km/s gives a A_{eff} vs. M_0 relation that is consistent with the previous studies.

Table 5.2 Stress Drop and Radiation Efficiency Averages

	Group 1 Earthquakes				Group 2 Earthquakes					
	5 Tsunami EQ.		13 Others EQ.		$V_r = 2.0$ km/s		$V_r = 2.5$ km/s		$V_r = 3.0$ km/s	
	$\Delta\sigma_E$ (MPa)	η_R	$\Delta\sigma_E$ (MPa)	η_R	$\Delta\sigma_E$ (MPa)	η_R	$\Delta\sigma_E$ (MPa)	η_R	$\Delta\sigma_E$ (MPa)	η_R
Geometric Average	0.89	0.21	5.61	0.27	7.00	0.21	3.45	0.43	1.99	0.71
Arithmetic Average	0.94	0.25	7.47	0.39	9.07	0.30	4.44	0.62	2.53	1.01

Extensive efforts have been made over recent decades to obtain constraints on earthquake physics from seismically measurable parameters. Much of this has focused on establishing scaling relationships between small and large earthquakes and characterization of stress heterogeneity on faults. Our catalog of finite-fault solutions, rupture durations, static stress drops, and radiated energy estimates for 114 $M_w \geq 7$ interplate megathrust events from 1990-2015 continues this process of accumulation of observational constraints on earthquake ruptures. The essential data are global broadband seismic wave recordings that are processed by relatively uniform procedures intended to recover first-order parameters of the large magnitude events, extending prior systematic point-source treatment of smaller events. We are very cognizant of the assumptions, limitations, and uncertainties of the parameter estimation, and proceed with limited consideration of some implications of the kinematic parameters for earthquake dynamic processes.

Scaling relations of earthquake rupture characteristics for these major and great subduction zone megathrust earthquakes have been explored. The source duration, moment-scaled radiated energy, apparent stress and radiation efficiency estimates generally follow expected self-similarity relationships overall, albeit with large variability, extending previous studies to the large magnitude range. The energy-related stress drop, $\Delta\sigma_E$, calculated from

inverted finite-fault slip models, averages ~4 MPa, with there being a direct trade-off between assumed V_r and estimated stress drop for individual events, but little overall dependence on earthquake magnitude. By performing a series of finite-fault inversions with assumed rupture velocities of 2 km/s, 2.5 km/s and 3 km/s, the product $V_r^3\Delta\sigma_E$, is found to be very stable for each event over the suite of models, and this product has little trend with M_W, although there is a baseline shift to low values for large tsunami earthquakes. By investigating $V_r^3\Delta\sigma_E$, $T_c \sim M_0^{1/3}$, trimming factor, and assumptions of variable radiation efficiency, uniform rupture geometry parameters, or variable stress drop, we have examined observations and predictions of stress drop, effective rupture area and rupture velocity measurements. Using simple scaling assumptions can help to highlight unusual events, but full finite-source analysis is required to account for the combined variability in geometric factors, stress drop and radiated energy for very large earthquakes. In contrast to the increasing trends observed for small earthquakes in previous studies, radiation efficiency tends to decrease with average slip for major interplate events, and estimates of fracture energy increase steadily with slip. Further work to understand the possible discrepancy between small and major/great earthquake measurements is necessary before drawing conclusions on the responsible mechanical process.

Acknowledgements. This work made use of GMT and SAC software. The Incorporated Research Institutions for Seismology data management center was used to access the seismic data from Global Seismic Network and Federation of Digital Seismic Network stations. This work was supported by NSF grant EAR1245717 (T.L.).

5.5. Supplementary Figures

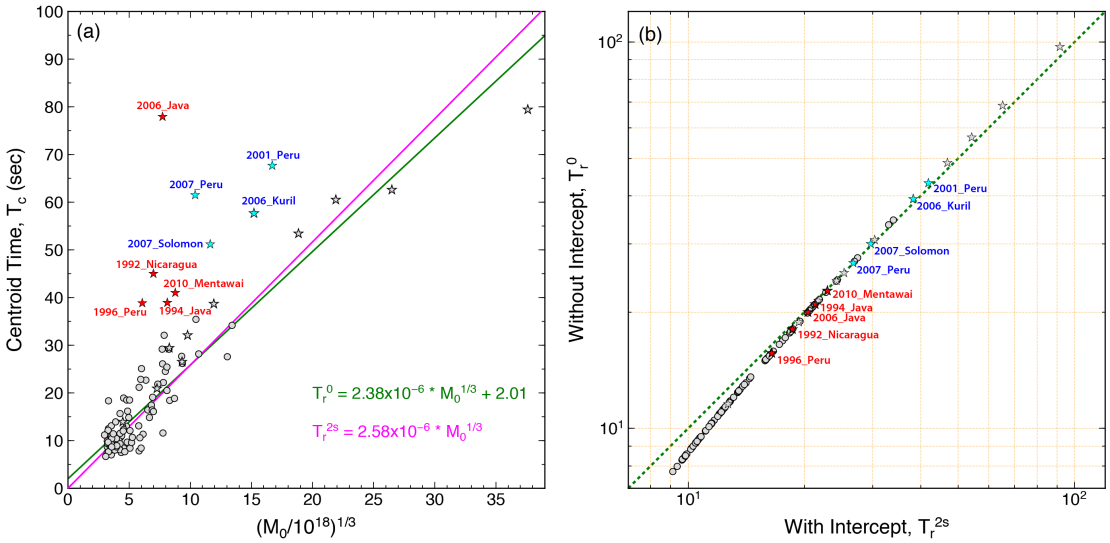

Figure 5.A1 (a) Source time function centroid times, T_c, from finite-fault inversions assuming V_r = 2.5 km/s (circles) or independent determinations of V_r (stars) plotted as functions $M_0^{1/3}$. The red and blue lines indicate linearly regressions of $T_c \sim M_0^{1/3}$ with non-zero intercept (green equation) and zero intercept (purple equation), respectively. Events with anomalously long centroid times are all tsunami earthquakes (red stars), have long intervals of weak initial slip (2001 Peru and 2006 Kuril events), or are doublet ruptures (2007 Solomon and 2007 Peru event). (b) The predicted time shifts with zero intercept versus values with intercept, ~ 2 s.

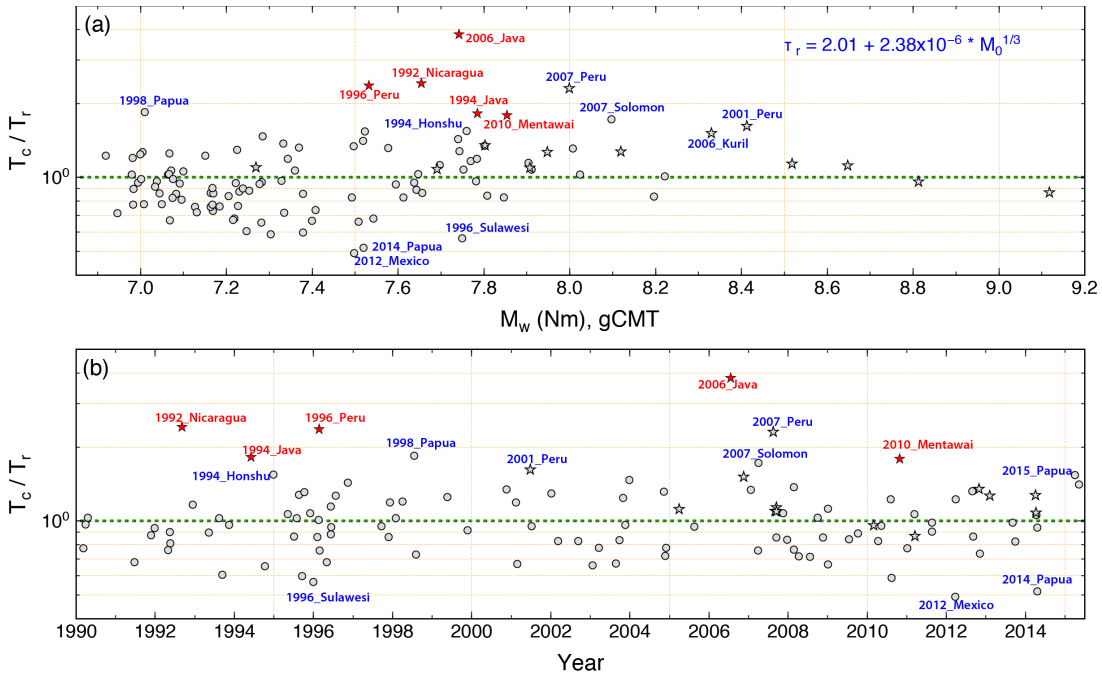

Figure 5.A2 Source time function centroid times, T_c, from finite-fault inversions assuming V_r = 2.5 km/s (circles) or independent determinations of Vr (stars) normalized by the duration (T_r) estimated by regression of T_c and $M_0^{1/3}$ with non-zero intercept, plotted as functions of (a) M_W and (b) time. Events with anomalously large or small ratios are labeled. The long-duration events tend to be tsunami earthquakes (red stars), or have long intervals of weak initial slip (e.g., 2001 Peru event), or are doublet ruptures (2007 Peru and 2007 Solomon Islands events).

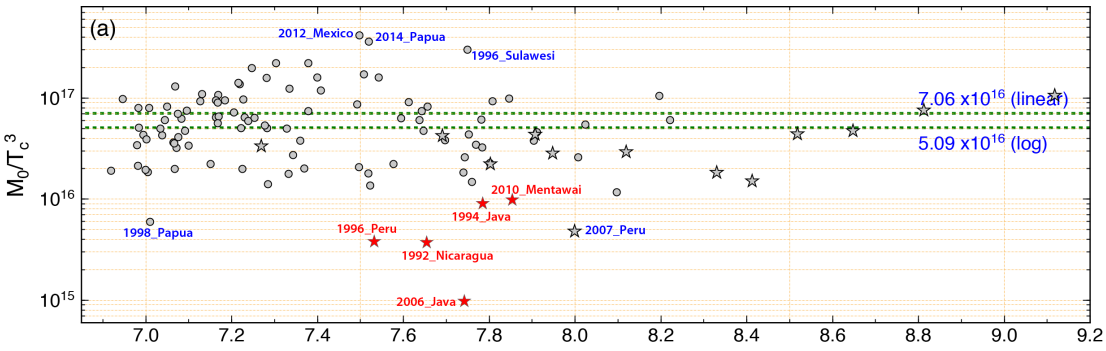

Figure 5.A3 The ratio of seismic moment M_0 and cube of centroid time, T_c^3, for each event (circles indicate group 2 events and stars indicated group 1 events), plotted as a function of M_W. Linear and log averages of the population are indicated by dashed labeled dashed green lines with units of Nm/s^3.

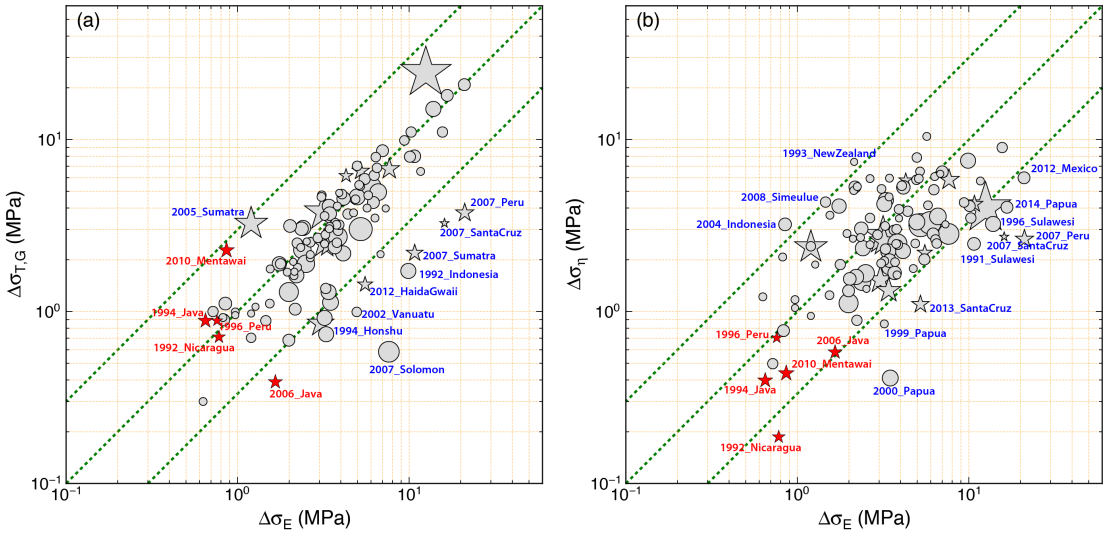

Figure 5.A4 (a) Estimated stress drop $\Delta\sigma_{T,G}$ calculated using seismic moment and centroid source duration with constant geometrical factors for a reference model (C = 1, γ = 2, a = 3), and (b) estimated stress drop $\Delta\sigma_{\eta}$ with constant radiation efficiency of 0.5 calculated using the moment-scaled radiated energy for each event, plotted relative to the stress drop $\Delta\sigma_E$ for finite source models for both group 1 (stars) and group 2 events (circles, V_r = 2.5 km/s). The size of symbols is proportional to the earthquake magnitude. Tsunami earthquakes are highlighted in red stars. Outliers are labeled in both panels. Dashed green lines have slope of unity.

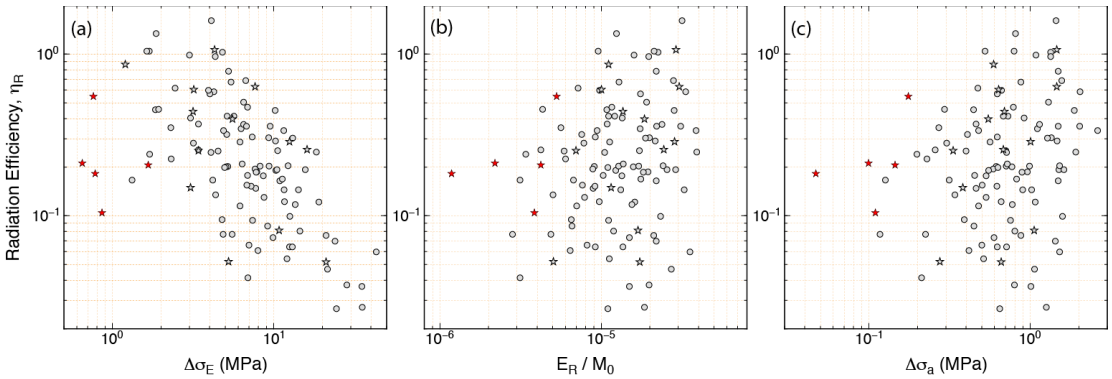

Figure 5.A5 Radiation efficiency versus (a) energy-based static stress drop $\Delta\sigma_E$ estimated from finite-fault models, (b) moment-scaled radiated energy, and (c) apparent stress.

Chapter 6

Rupture Characteristics of Major and Great ($M_W \geq 7.0$) Megathrust Earthquakes from 1990-2015: II. Depth-Dependence

This chapter has been submitted as:

Ye, L., T. Lay, H. Kanamori and L. Rivera (2015), " Rupture Characteristics of Major and Great ($M_W \geq 7.0$) Megathrust Earthquakes from 1990-2015: II. Depth-Dependence", *J. Geophys. Res.*, submitted.

Abstract Seismic wave radiation from megathrust earthquakes provides an important probe of fault zone properties and interplate rupture attributes. Depth varying characteristics of short-period seismic radiation for earthquakes along megathrusts have been inferred from several recent giant earthquakes and large tsunami earthquakes. To quantify any depth-dependence more extensively, we analyzed 114 $M_w \geq 7.0$ thrust-faulting earthquakes with centroid depths from 5 to 55 km on circum-Pacific megathrusts using teleseismic body wave finite-fault inversions and source spectrum determinations. Large tsunami earthquakes and some other shallow events at depths less than about 18 km have unusually long source durations, and low values of static stress drop ($\Delta\sigma_E$), $V_r^3\Delta\sigma_E$, and apparent stress, with relatively depleted short-period radiation. Deeper events have no clear global trend with source depth for moment-normalized centroid or total duration, static stress drop, moment-scaled radiated energy, apparent stress, or radiation efficiency. Regional behavior among the 17 sampled subduction zones generally conform to the global composite. The source spectra have high-frequency logarithmic spectral decay slopes averaging ~-1.6. There is relative enrichment in short-period spectral levels with increasing source depth manifested in reduced high-frequency spectral decay slope. The ratio of high-frequency (0.3-1Hz) radiated energy to

total energy increases correspondingly. These observations suggest that overall dynamic rupture processes are relatively insensitive to source depth, but varying scale lengths of megathrust heterogeneity may contribute to enrichment of short-period seismic radiation for events deeper on the megathrust. A weak correlation of higher estimated average megathrust temperature at 30 km depth with higher spectral decay rate indicates that the depth-varying pattern may in part result from frictional properties being influenced by temperature variations or systematic reduction of average attenuation with increasing depth along the megathrust.

6.1 Introduction

Devastating tsunami and strong ground shaking are two principal hazards from large earthquakes located in subduction zones [e.g., *Kanamori*, 2014]. Motivated by recent occurrence of several giant earthquakes and large tsunami earthquakes, along with improved resolution of finite-fault slip distributions from inversions of seismic and geodetic observations and new back-projection methods for imaging coherent short-period radiation from the rupture area, *Lay et al.* [2012] proposed the conceptual model for megathrust ruptures shown in Figure 6.1. They introduced depth-varying domains A, B, C and D with distinct seismic radiation characteristics that provide a general framework for considering hazards for large interplate events. There is very little short-period seismic radiation but strong tsunami excitation from the shallowest domain A where tsunami earthquakes and some slow slip events occur. Modest levels of spatially distributed short-period radiation and large slip are typical for the central domain B where most megathrust events occur. Concentrated bursts of short-period radiation during domain C events at depths of 30-50 km accentuate strong ground shaking hazard from the deeper ruptures. Domain D represents a transition at the

deep edge of the seismogenic zone, observed only in some regions, with diverse occurrence of slow slip events, low-frequency earthquakes, and/or seismic tremor.

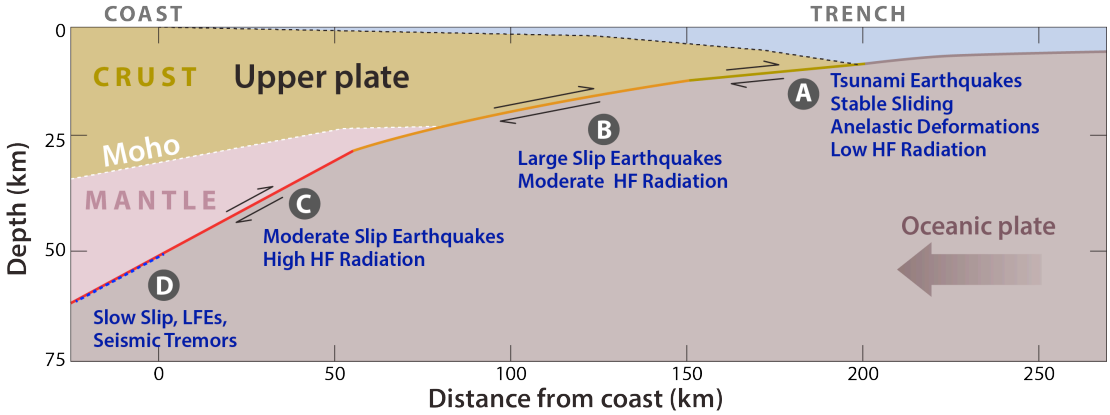

Figure 6.1 Schematic cross-section of a generic interplate subduction zone megathrust fault with four domains of depth-varying rupture characteristics: A, near-trench domain where either low-radiated-energy tsunami earthquakes occur or anelastic deformation and stable sliding accommodate interplate deformation; B, central megathrust domain where large co-seismic slip occurs with moderate short-period seismic radiation; C, down-dip domain where moderate co-seismic slip occurs with relatively enhanced levels of short-period seismic radiation; D, transitional domain, only present in some areas, typically those with a young subducting plate, where slow slip events, low-frequency earthquakes (LFEs), and seismic tremor occur. (Modified from *Lay et al.* [2012] and *Kanamori* [2014]).

A few tests of this conceptual model using teleseismic and regional spectral estimates have been applied to events in individual subduction zones along the Japan Trench offshore of Honshu [*Ye et al.*, 2013a] and along the Middle American trench [*Ye et al.*, 2013b; *Geirsson et al.*, 2015], yielding general support for depth-dependence of some aspects of megathrust ruptures. Isolation of the source spectra for magnitude 6.0-7.6 events off-shore Honshu with an empirical Green's function (EGF) method for regional network observations in Japan demonstrated that both depth-varying source radiation and path attenuation variations account for observed ground shaking patterns [*Ye et al.*, 2013a]. Studies such as *Choy et al.* [2006], *Venkataraman and Kanamori* [2004] and *Ye et al.* [2012, 2013a,b] have demonstrated the distinct seismic radiation characteristics of off-megathrust intraplate faulting, both for outer

trench slope faulting and intraslab faulting down-dip of the megathrust. Thus careful identification of megathrust events is required. It is still challenging to seek any depth-varying rupture characteristics for confidently identified events on global subduction zone megathrusts due to limited availability of regional broadband observations and because earthquakes are intrinsically diverse, with substantial variability in rupture processes and strong along-strike variations [*El Hariri et al.*, 2013; *Ye et al.*, 2011; 2013b]. Fortunately, *Ye et al.* [2013a] found good consistency in overall characteristics of teleseismic and regional EGF-corrected source spectra, giving confidence that teleseismic estimates can provide reliable relative source characteristics up to 1-2 Hz. Building on that study, we systematically analyze source characteristics using teleseismic data for large interplate earthquakes in global subduction zones.

The data set used in this study is the same as in *Ye et al.*, [2015, *submitted: Chapter 5*]. *Chapter 5* focuses on scaling relationships for various source parameters of major and great interplate earthquakes. We use the same measurements for 114 $M_W \geq 7$ earthquakes from 1990-2015 (Figure 6.2), identified as megathrust ruptures based on their locations, source depths (from ~5 km to 55 km), and focal mechanisms. All of the measurements and finite-fault inversions use only global broadband body wave observations for frequencies below 1-2 Hz. This paper focuses on the faulting characteristics in the context of tectonic environment and source depth, drawing upon the scaling relations established in *Chapter 5*. Given the intrinsic limitations of source parameter estimates inferred from finite-fault inversions that use only teleseismic data and far-field source spectrum estimates and the variety of subduction zone environments in which the earthquakes occur, large scatter is expected. We seek any systematic behavior that can be confidently resolved.

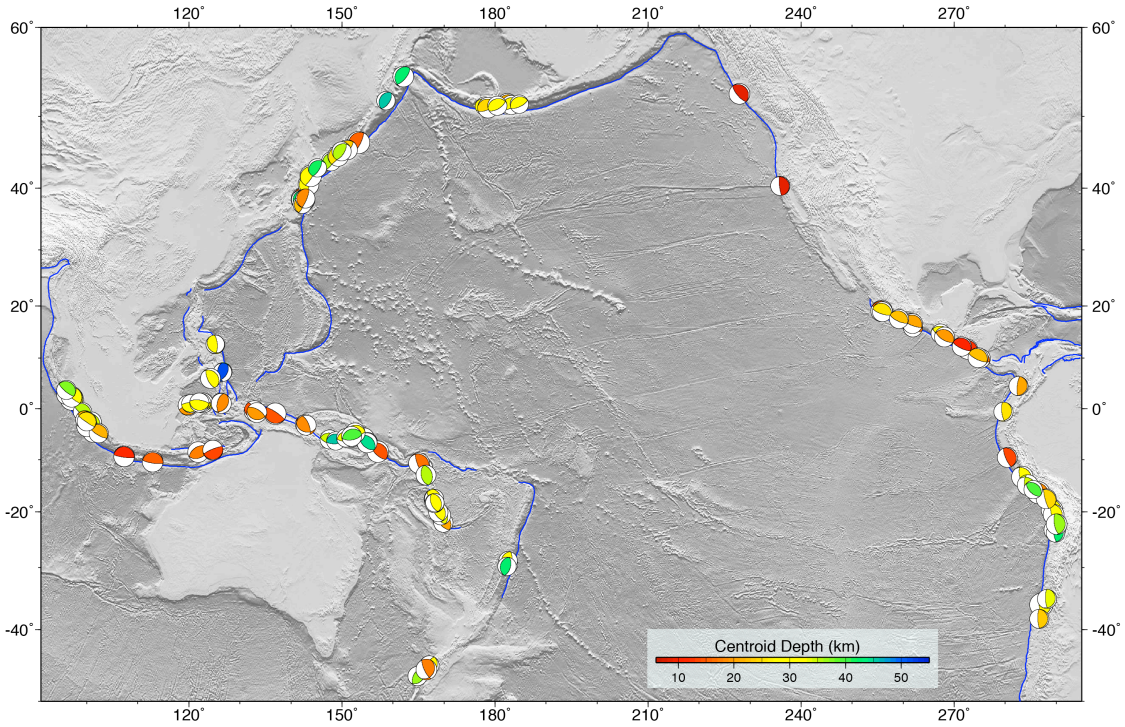

Figure 6.2 Epicentral locations indicated by best-double-couple focal mechanisms from the global Centroid Moment Tensor (gCMT) catalog for the 114 major and great ($M_w \geq 7$) megathrust earthquakes from 1990-2015 analyzed in this study. Focal mechanism radius is scaled proportional to M_w and color indicates gCMT centroid depth. All major and great interplate thrust events for which reliable source parameter estimates could be made are included.

Due to the strong trade-off between estimated static stress drop and assumed rupture expansion velocity (V_r) for time-domain finite-fault inversions using only teleseismic data, we follow *Chapter 5* in subdividing all events into either group 1 (18 events) having independent constraints on V_r from prior studies, or group 2 (96 events) lacking independent V_r constraints. For group 2, finite-fault inversions with V_r = 2.0, 2.5, and 3.0 km/s were performed. Details of the data selection and finite-fault inversion are presented in *Chapter 5*. Figure 6.3 shows three example finite-fault models for earthquakes at various depths. Appendix I displays all the finite-fault solutions for group 1 and V_r = 2.5 km/s models for group 2 on regional maps for the 17 subduction zones sampled by our events. For each event we determined the

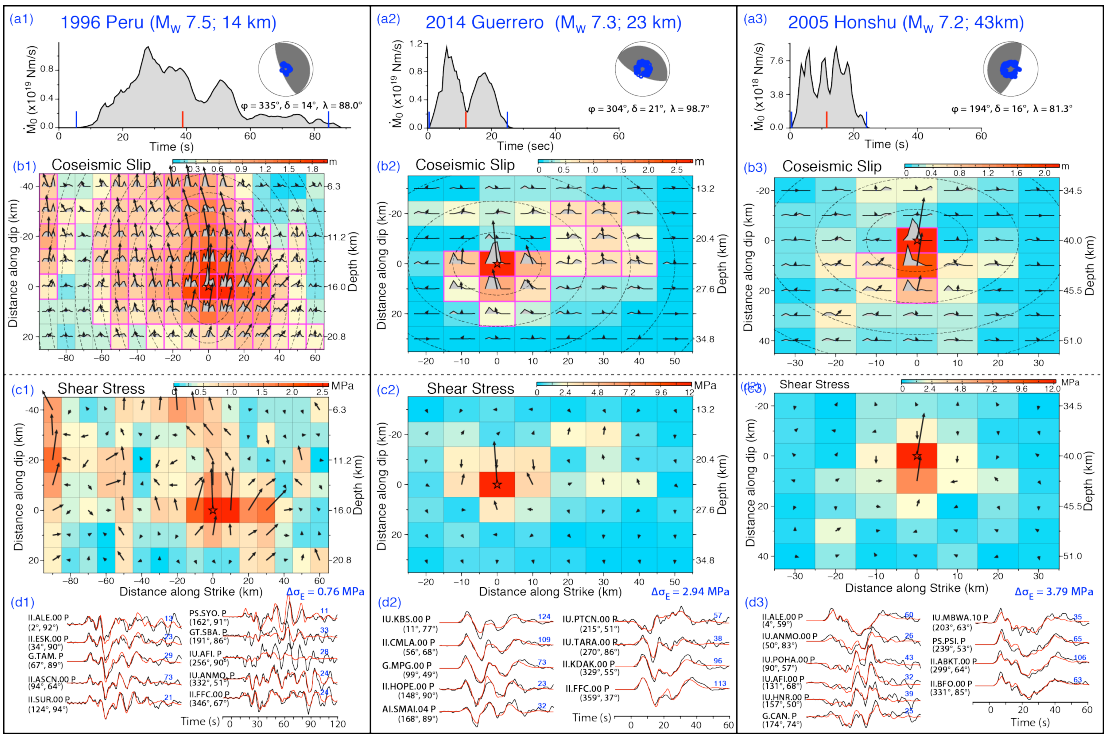

Figure 6.3 For each event in Figure 6.2, a finite-source model has been determined by linear least-squares inversion of teleseismic P- (and in some cases SH-) waves. Representative examples of finite-fault inversions are shown for the (1) 21 February 1996 Peru event (M_w 7.5), (2) 18 April 2014 Guerrero, Mexico event (M_w 7.3) and (3) 16 August 2005 Japan event (M_w 7.2). Solution parameters are listed in Table S1. The moment rate function for each inversion is shown in row (a). Blue ticks indicate the time span used to determine total duration, T_d, and the centroid time, T_c, is indicated by the red tick. The average focal mechanism with double couple strike (ϕ), dip (δ), and rake (λ) is almost identical for each inversion. Row (b) shows the subfault grid, with average subfault slip direction and magnitude indicated by the vectors, and slip magnitude color-coded. Dashed circles indicated rupture front position in 5 s intervals. Row (c) indicates the average stress vector at the center of each subfault used to compute stress drop for the variable slip solution. Example waveform fits are shown in row (d) (data are black, model predictions are red). Below each station name the azimuth and distance of the station relative to the source is indicated. The peak-to-peak amplitude of the data trace in microns is shown in blue; each waveform is normalized to uniform amplitude.

moment-rate function from finite-fault inversions of teleseismic body waves filtered in the frequency band 0.005 – 0.9 Hz, the average focal mechanism from planar fault models with variable subfault rake, the space-time slip distribution and subfault source time functions

parameterized by multiple overlapping triangular subevents, and the shear stress distribution for the final slip model. For these finite-fault rupture solutions, we computed the seismic moment (M_0), rupture centroid depth (H_c) estimated by average depth of the slip distribution, and averages of source rigidity (μ), P-wave velocity (V_p), S-wave velocity (V_s) and density (ρ) over the slip distribution. The source centroid time (T_c) and total duration (T_d) measured from the origin time are determined from the corresponding moment-rate function. Average static stress drop (Ds_E) weighted by the slip distribution is computed following the method of *Noda et al.* [2013]. In *Chapter 5*, summary rupture parameters for all the finite-fault models were evaluated by comparing the seismic moment, centroid time and centroid source depths with corresponding values from the global Centroid-Moment Tensor (gCMT) catalog [http://www.globalcmt.org/CMTsearch.html], and W-phase inversions [*Duputel et al.*, 2013]. Given the spatial finiteness of the large earthquakes considered, we use the average source depths, with ±5 km uncertainty, rather than hypocentral depths, when examining depth-varying characteristics in this paper. The actual average slip versus depth distribution for each rupture model is displayed in Appendix III.

6.2 Source Duration and Static Stress Drop

6.2.1 Source Duration

Earthquake characteristic source duration, t, (parameterized by source duration T_d or centroid time T_c in our measurements) generally scales with seismic moment, M_0, and other source parameters by

$$\frac{\tau}{\left(M_0\right)^{1/3}} \propto \frac{\tau}{\left(L^3 \cdot \Delta\sigma\right)^{1/3}} \propto \frac{1}{V_r \Delta\sigma^{1/3}}, \tag{1}$$

where L is a general rupture dimension, V_r is the rupture velocity, and $\Delta\sigma$ is stress drop.

This assumes a simple rupture expansion and that width scales with *L. Chapter 5* confirmed the dominance of cube-root scaling of seismic moment for both characteristic source time measurements for our events, with little dependence on parameters used in obtaining the corresponding finite-fault models. Figure 6.4a shows the moment-scaled centroid time, $T_c^N = T_c \times \left(M_{0ref} / M_0 \right)^{1/3}$, where M_{0ref} is 1.16 x 10^{18} Nm (M_w ~ 6), and centroid time T_c is measured from the moment-rate function of our finite-fault models. The average moment-scaled centroid time for all 114 great and major events is ~2.9 s. It is ~2.8 s if we exclude the 5 labeled tsunami earthquakes [*Polet and Kanamori*, 2009]. There is no significant depth variation in the moment-scaled centroid time estimations, T_c^N, apart from the shallow tsunami earthquake behavior (Figure 6.4a). The 15 August 2007 M_w 8.0 Pisco, Peru earthquake stands out with a significantly long centroid time due to its compound rupture process with a ~60 s hiatus in the seismic radiation between doublet events [*Lay et al.*, 2010].

The total source duration measure, T_d, is a somewhat more uncertain parameter, as it is influenced by the inadequacy of the Green's functions for accounting for water reverberations and late scattered waves. We obtained T_d estimates by ignoring very weak tails in our moment-rate functions, as these may be artifacts due to inaccurate modeling of the coda, and the nature of the inversions with positivity constraint is such that these measurements may be biased a bit long. In Figure 6.4b we combine our large event T_d measurements with corresponding source duration measurements for smaller events from *Bilek et al.* [2012] and *El Hariri et al.* [2013]. The latter two studies estimated source duration from point-source moment-rate functions obtained by simultaneous deconvolution of teleseismic broadband P-wave recordings without positivity constraint for 613 globally distributed interplate thrusting events with M_w = 5.0-7.0.

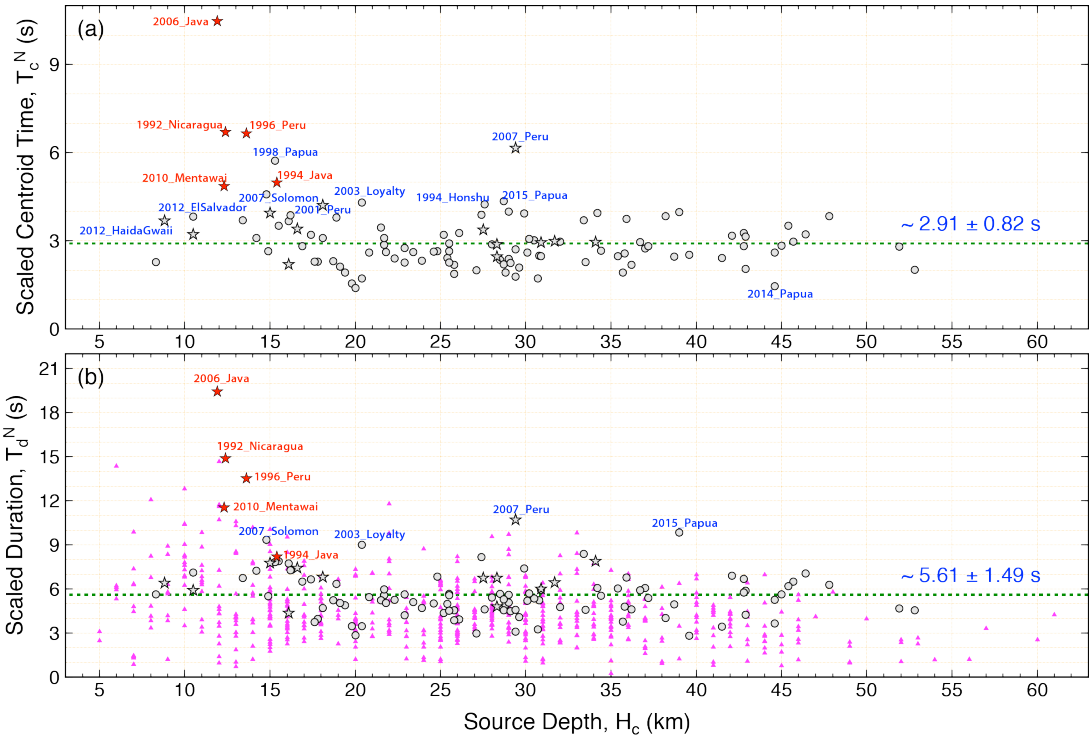

Figure 6.4 The moment-scaled estimates of (a) the centroid time, T_c^N and (b) the source duration, T_d^N, by cube-root scaling of seismic moment relative to a reference seismic moment M_{ref} = 1.122 × 10^{18} Nm (M_w ~ 6). Circles in (a) and (b) are results from this study, with source duration estimated from the moment rate function and average source depth from the slip distribution of finite-fault inversions. Triangles in (b) are results for 613 events (M_w 5 -7) between 1989 and 2011 from *Bilek et al.* [2012] and *El-Hariri et al.* [2013] with source duration and depth estimated by point-source simultaneous deconvolution of teleseismic broadband P wave recordings. The horizontal dashed lines in (a) and (b) indicate the average values of ~2.9 s and ~5.6 s for the moment-scaled durations and centroid times in this study, respectively. In both panels the measures for large tsunami earthquakes are labeled in red, and some events with anomalous long duration/centroid times are labeled in blue, like the 15 August 2007 M_w 8.0 Peru and 2007 M_w 7.9 Sumatra doublet events.

The T_d values in Figure 6.4b are again scaled by $M_0^{1/3}$ relative to the reference M_{0ref} = 1.16 × 10^{18} Nm, and show similar behavior with source depth to that for centroid times (Figure 6.4a). Here, the preferred point-source depths for the simultaneous deconvolutions [*Bilek et al.*, 2012; *El Hariri et al.*, 2013] are used for the smaller events. There is a greater spread in moment-scaled T_d estimates for depths less than about 18 km (~15 km below the

seafloor, assuming there is on average about 3 km of water above the subduction zone). While some of these are large tsunami earthquakes, others are smaller events that were not particularly tsunamigenic but do have very long scaled source durations. This shallow depth range corresponds to domain A in the model of *Lay et al.* [2012] (Figure 6.1).

There is no clear trend for either moment-scaled T_d or moment-scaled T_c for depths larger than 18 km. The average moment-scaled T_d for our large events is ~8.0 s for 24 events with depths less than 18 km, ~5.4 s for 90 events with larger depths, and ~6.0 s overall (or ~5.6 s excluding the 5 tsunami earthquakes). The average moment-scaled T_c is ~4.1 s and ~2.8 s for the shallower and deeper event populations, respectively, which is consistent with the factor of slightly less than 2 ratio of T_d/T_c expected for the typical asymmetric triangular shapes of the moment-rate functions. For the population of events with M_w < 7.0 from *El Hariri et al.* [2013] and *Bilek et al.* [2012], the average moment-scaled T_d for all 123 shallower (< 18 km) events is ~5.5 s and for 490 deeper (18-60 km) events it is ~4.3 s, both of which are shorter than our finite-faulting based durations. Our inclusion of large tsunami earthquakes affects the shallower distribution. The difference for deeper events may be due to intrinsic differences in estimating the total duration from simultaneously deconvolved point-source source time functions without positivity constraint versus our estimates from moment rate functions for finite-fault inversions with a positivity constraint, or it may reflect differences in signal-to-noise ratios between the populations.

The composite behavior of duration measures versus source depth is similarly reflected in the individual subduction zones. Plots of moment-scaled T_c versus depth for events in the 17 sampled subduction zones are shown for each region in Appendix III. Some regions have few major and great earthquakes, but others have moderate numbers allowing any local

trends to be detected. The regional plots do not reveal any distinct behavior from the global composite in Figure 6.4.

6.2.2 Static Stress Drop

The average static stress drop, proportional to the ratio of coseismic slip to a characteristic rupture dimension, is an important measure of the change of stress level on the fault due to the earthquake rupture process. There is large estimation uncertainty for stress drop due to limited resolution of rupture finiteness from teleseismic data only. This issue is extensively addressed in *Chapter 5*, and the energy-related stress drop $\Delta\sigma_E$, given by the spatial average of the stress drop weighted by slip [*Noda et al.*, 2013; *Ye et al.*, 2013c], is preferred as a relatively robust stress drop measurement. $\Delta\sigma_E$ still varies systematically with rupture expansion velocity used in our finite-fault inversions for group 2 events (Table 2 in *Chapter 5*).

Figure 6.5a shows that there is no systematic global variation in stress drop $\Delta\sigma_E$ for the range of finite-fault inversions performed for each group 2 event as a function of source depth H_c. The overall average static stress drop is ~4 MPa for all 114 M_w 7-9 earthquakes we analyzed, with the estimates spanning values from ~0.4 MPa to ~40 MPa. *Chapter 5* demonstrated that $\Delta\sigma_E$ does not have systematic magnitude dependence either. The variation in $\Delta\sigma_E$ is largest among earthquakes with depths less than 18 km, and large tsunami earthquakes have relatively low values. However, the pattern is not as systematic or distinct as found for the duration estimates (Figure 6.4) as there are comparably low stress drop events deeper on the megathrust as well as ordinary stress drop shallow events. The large stress drop for the 2 September 2007 M_W 7.3 Santa Cruz event is uncertain due to difficulty in modeling strong P coda reverberations at some azimuths. The 28 October 2012 Haida Gwaii M_W 7.8 earthquake, with a stress drop of ~5 MPa, is well constrained to have shallow depth by both

seismic and tsunami modeling [*Lay et al.*, 2013b] and has a rupture velocity of 2.3 km/s, significantly larger than that for comparably shallow tsunami events; thus the variability at shallow depth appears to be real.

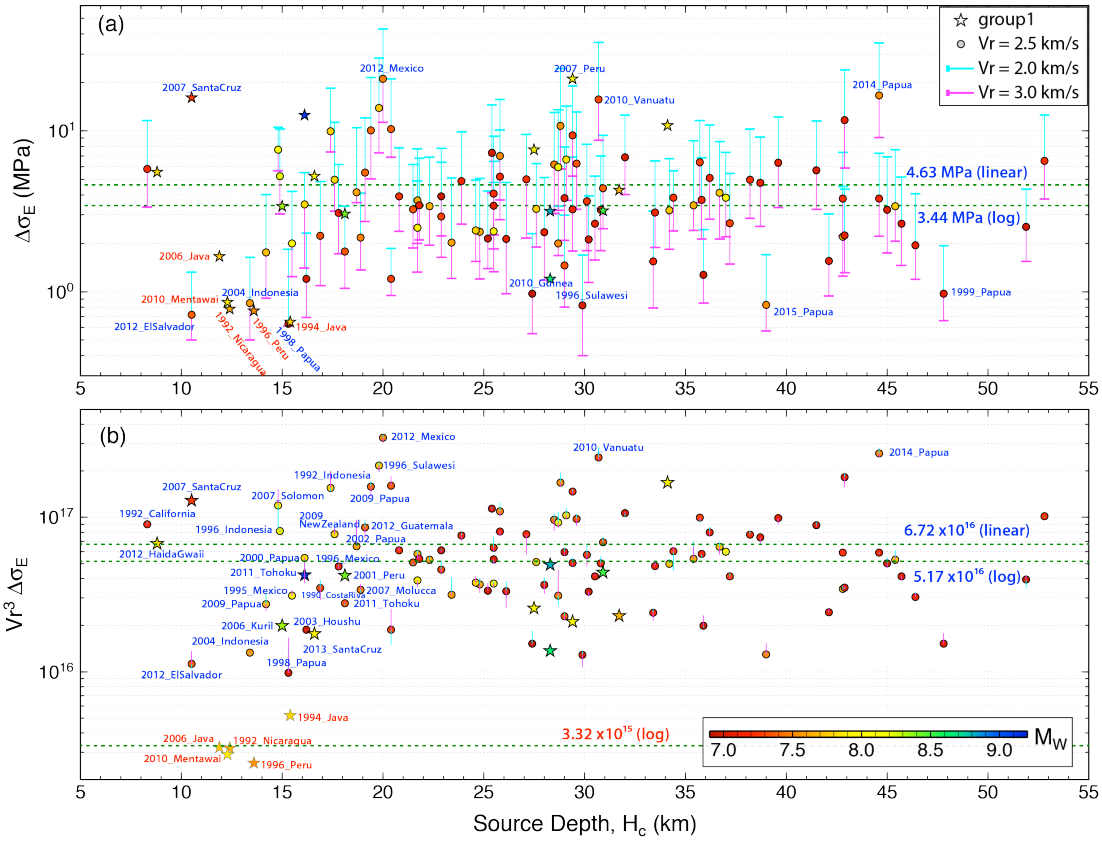

Figure 6.5 The ranges of (a) stress drop , D_{SE}, and (b) the product of $V_r^3 D_{SE}$, plotted versus average depth of the slip distribution from the finite-fault inversion. The stress drop, D_{SE}, is calculated from variable slip finite source models with V_r = 2.0 km/s (upper cyan estimates), to V_r = 2.5 km/s (circles), to V_r =3.0 km/s (lower magenta estimates). The stars are for group 1 finite fault models with independent estimates of V_r. Events with high or low values are labeled. Tsunami earthquakes are highlighted with red text. The symbol colors denote M_w. The linear and log averages of the entire population are indicated by the labeled green dashed lines.

Examination of $\Delta\sigma_E$ versus H_c for each of the 17 subduction zones separately (Appendix III) shows general similarity with the composite behavior in Figure 6.5a. Central America displays a trend of increasing stress drop with depth from 10 to 30 km, but the scatter is too

large or the number of data is too small to resolve depth dependence in any of the other regions. We do not detect significant baseline shifts in stress drop between regions either. Detailed analysis of larger numbers of events in each region, including smaller events, is warranted, but our large events do not indicate strong regional patterns.

In *Chapter 5*, it was established that the product $V_r^3\Delta\sigma_E$ is very stable for each event across the suite of models with V_r ranging from 2 – 3 km/s. It is appealing to explore this parameter, as it is relatively free of modeling assumptions. Figure 6.5b shows that $V_r^3\Delta\sigma_E$ has a pattern with source depth opposite to that for the duration estimates, consistent with equation (1). The low rupture velocity tsunami earthquakes now is well-isolated from the other events with average values about a factor of 20 lower than the overall population. The behavior appears to be either a step-change or a rapidly increasing trend for source depths from 5 to ~18 km, although events like 2012 Haida Gwaii deviate from either pattern.

6.3 Far-field Source Spectrum Analysis

To investigate frequency-dependent seismic radiation characteristics across the megathrust, we evaluate whether there is any variation with source depth in high-frequency spectral decay, moment-scaled radiated energy or apparent stress parameters for these 114 $M_w \geq 7$ interplate thrust events.

The moment-rate spectrum ($\hat{\dot{M}}(f)$), or source spectrum, at frequencies higher than 0.05 Hz in this study is obtained from the observed ground displacement spectrum ($\hat{u}(f)$) at a station by:

$$\left|\hat{\dot{M}}(f)\right| = \frac{4\pi\rho_h V_{\alpha,\beta}^3 R_E}{g(\Delta)R(\theta,\phi)} \cdot \frac{\left|\hat{u}(f)\right|}{C\left|\hat{I}(f)\right|} \cdot e^{\pi f t^*}, \qquad (2)$$

where $V_{a,\beta}$ and ρ_h are the P-wave or S-wave velocity, and density at the source region, R_E= 6371 km is the radius of the earth, $g(\Delta)/R_E$ is the geometric spreading for each path at teleseismic distances, C is the free surface receiver effect, and $\hat{I}(f)$ is the instrumental response. t^* is the attenuation factor (equal to the travel time divided by the path-average Q factor); we use the attenuation model from *Perez-Campos et al.* [2003], with t^* reducing with increasing frequency, as determined by reconciling teleseismic and regional estimates of seismic energy. $R(\theta,\phi)$ is the average radiation pattern for P, pP, and sP phases for the final average focal mechanism and centroid source depth from the finite-fault inversions. Because the depth phases are difficult to separate for large shallow earthquakes, we applied the combined correction formulated by *Boatwright and Choy* [1986]. These corrections are appropriate only for frequencies above 0.05 Hz. To obtain the average source spectrum for frequencies above 0.05 Hz, we logarithmically average the individual corrected moment-rate spectra from (2) for stations with good azimuthal coverage and stable radiation pattern coefficients.

To estimate the source spectrum at frequencies lower than 0.05 Hz, we use the spectrum computed from the moment-rate functions obtained by the finite-fault inversions of teleseismic body-waves. We normalize the low frequency level to the long-period gCMT seismic moment.

We combine the source spectra from the finite fault moment-rate functions and from the average P-wave observations to obtain broadband source spectra for frequencies up to about 1-2 Hz. In most cases, the spectral estimates are consistent in the vicinity of the cross-over frequency of 0.05 Hz. The gray curves in Figure 6.6 show representative source spectra for the 21 February 1996 Peru, 18 April 2014 Guerrero and 16 August 2005 Honshu earthquakes thus computed. These are typical of the source spectra for major and large events in the shallow domain A, domain B, and deep domain C regions, respectively. There is some

scalloping structure near the corner frequency, with a relatively stable low frequency level and smoothly decaying spectrum above 0.1 Hz. The source spectra for all events are shown in Appendix III, grouped by subduction zone.

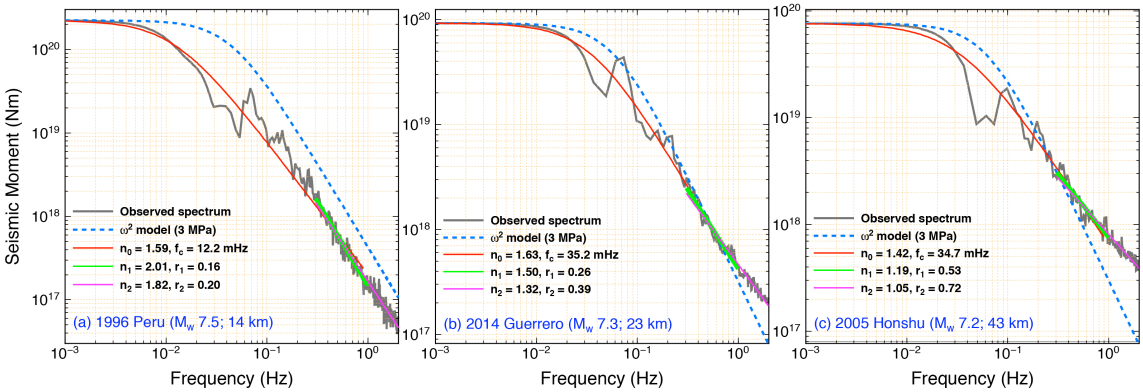

Figure 6.6 For each event in Figure 6.2 an average source spectrum was estimated, and various parameters were measured to characterize the shape of the spectrum. Representative examples are shown (gray lines) for the (a) 21 February 1996 Peru event (M_w 7.5), (b) 18 April 2014 Guerrero, Mexico event (M_w 7.3) and (c) 16 August 2005 Japan event (M_w 7.2). The source spectra for frequencies less than ~0.05 Hz is from the moment rate function of the finite-fault model inversion of teleseismic P-wave observations (Figure 6.3) and for frequencies higher than ~0.05 Hz the spectrum is calculated by averaging broadband teleseismic P wave spectra corrected for an attenuation model, radiation pattern, and geometric spreading. The blue dash lines are the reference source spectra for ω^{-2} model with 3 MPa stress parameter, shear velocity 3.75 km/s and seismic moments from gCMT solutions. The red lines are best-fitting ω^{-n0} model with optimized corner frequency (f_c) and high-frequency fall-off rate (n_0). The green and megenta lines show linear regressions for slope of the high-frequency spectrum from 0.3-1.0 Hz and 0.3-2.0 Hz with slopes of n_1 and n_2, respectively.

We fit each average far-field source spectrum by a spectrum, w^{-n0}, given by

$$\left|\hat{M}(f;M_0,f_c,n_0)\right| = \frac{M_0}{1+\left(f/f_c\right)^{n_0}}, \tag{3}$$

where M_0 is the seismic moment, f_c is the corner frequency and n_0 is a constant that determines the high-frequency fall off. This form is similar to that of the standard Brune w^{-2} squared spectrum, but we allow a more general spectral decay rate. We determined f_c and n_0

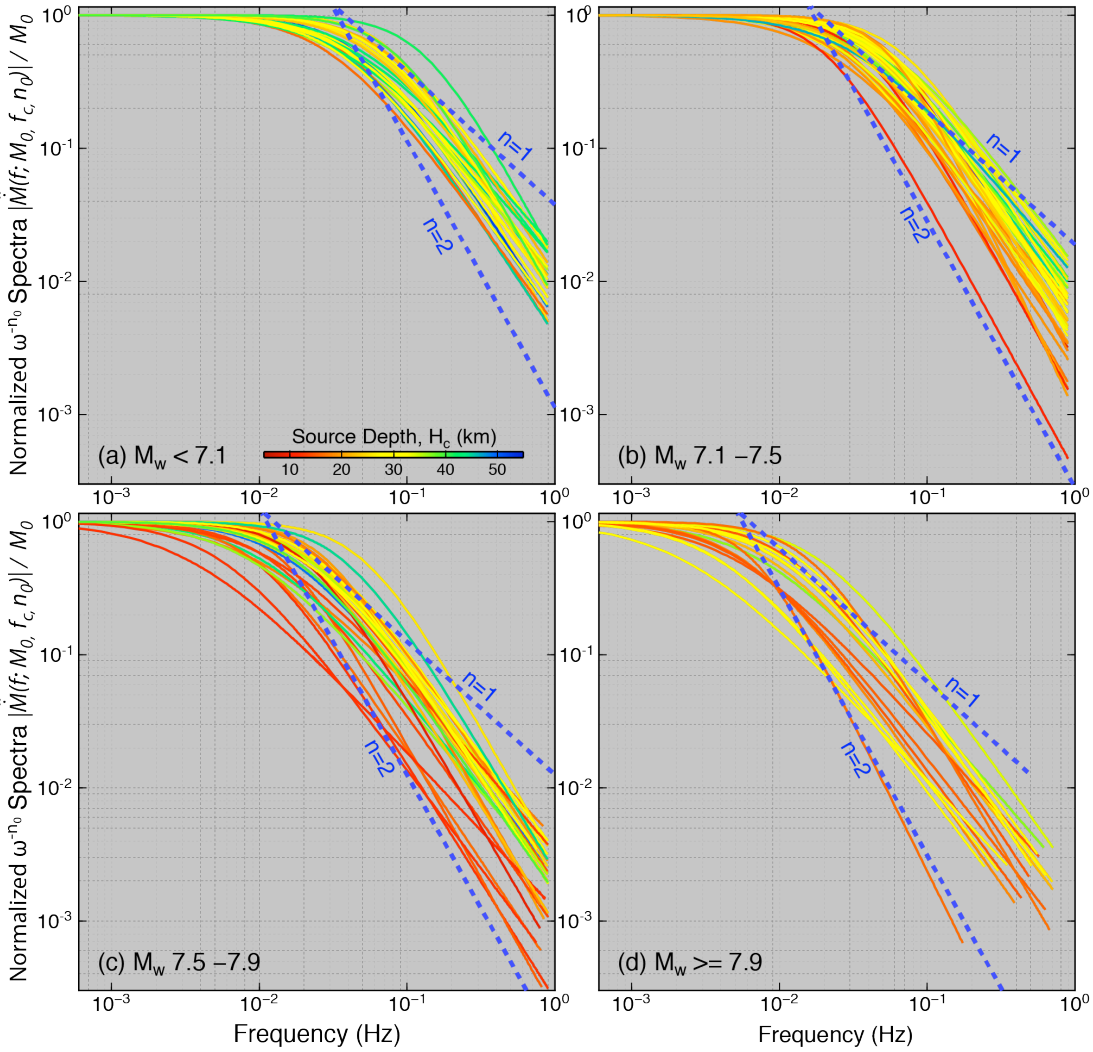

Figure 6.7 The best-fitting ω^{-n0} models, $\left|\hat{M}(f;M_0,f_c,n_0)\right|$, (normalized by seismic moment) for events with (a) M_w < 7.1, (b) M_w 7.1-7.5, (c) M_w 7.5-7.9 and (d) M_w > 7.9. Two blue dashed straight lines in each panel indicate reference high-frequency decay slopes of 1 and 2. Colors indicate average depth of the slip distribution for each event.

by minimizing the difference between the predicted moment-rate spectrum given by equation (3) and the observed spectrum. We use the seismic moment M_0 from the gCMT catalog, which is consistent with our finite-fault inversion solutions. The frequency band used for the spectral fitting is from 0 Hz to a high frequency cut-off about 25 times the corner frequency,

but 1 Hz is used as an upper limit for smaller events with large corner frequency. The red curves in Figure 6.6 shows the best-fitting w^{-n0} model for the 21 February 1996 Peru, 18 April 2014 M_w 7.3 Guerrero and 16 August 2005 Honshu earthquakes; these capture the basic features of the corresponding average source spectrum (gray curves) other than the notching at intermediate periods which is a manifestation of the specific shape of the individual moment rate functions. We obtained f_c = 12 mHz, 35 mHz, 35 mHz, and n_0 = 1.59, 1.63 and 1.42 for the three earthquakes with increasing source depths, respectively. A strong trade-off between the corner frequency and high-frequency decay rate is more evident for larger earthquakes, like the 1996 Peru, than for smaller earthquakes, like the 2014 Guerrero and 2005 Honshu, and this parameterization trade-off may blur the high-frequency characteristics presented below.

Our objective is not to precisely estimate the specific parameters of the spectral models and their formal uncertainties, but rather to obtain stable overall characterizations of the spectra that permit comparisons between events. Figures 6.7 and 6.8 display the moment-normalized best-fitting w^{-n0} models and the ratios of each observed spectrum with respect to a reference w^{-2} model, respectively, for all 114 events. The reference spectrum uses the seismic moment for each event and a Brune model stress parameter of 3 MPa with a shear velocity of 3.75 km/s and a scaling constant of 0.49. Because the corner frequency varies with magnitude, we compare the spectra for four magnitude bins (a) $M_w < 7.1$, (b) M_w 7.1-7.5, (c) M_w 7.5-7.9 and (d) $M_w \geq 7.9$. Figure 6.7 includes reference curves for spectral decay rates of w^{-1} and w^{-2}, and it is apparent that most events are fit by spectra with intermediate decay rates out to 1 Hz. Given that a consistent attenuation model is used for all events, we believe that the variability between events for different depths is a real feature, although both the absolute attenuation level and regional distribution of attenuation may vary between events. In both

figures, there are systematic increases of the high-frequency radiation with source depth for magnitude ranges 7.1-7.5, 7.5-7.9 and 7.9-9.0 (Figures 6.7b-d and 6.8b-d), but large scatter for small events (M_w < 7.1) (Figures 6.7a and 6.8a). We explore this depth-varying behavior in the following sections 3.1-3.4.

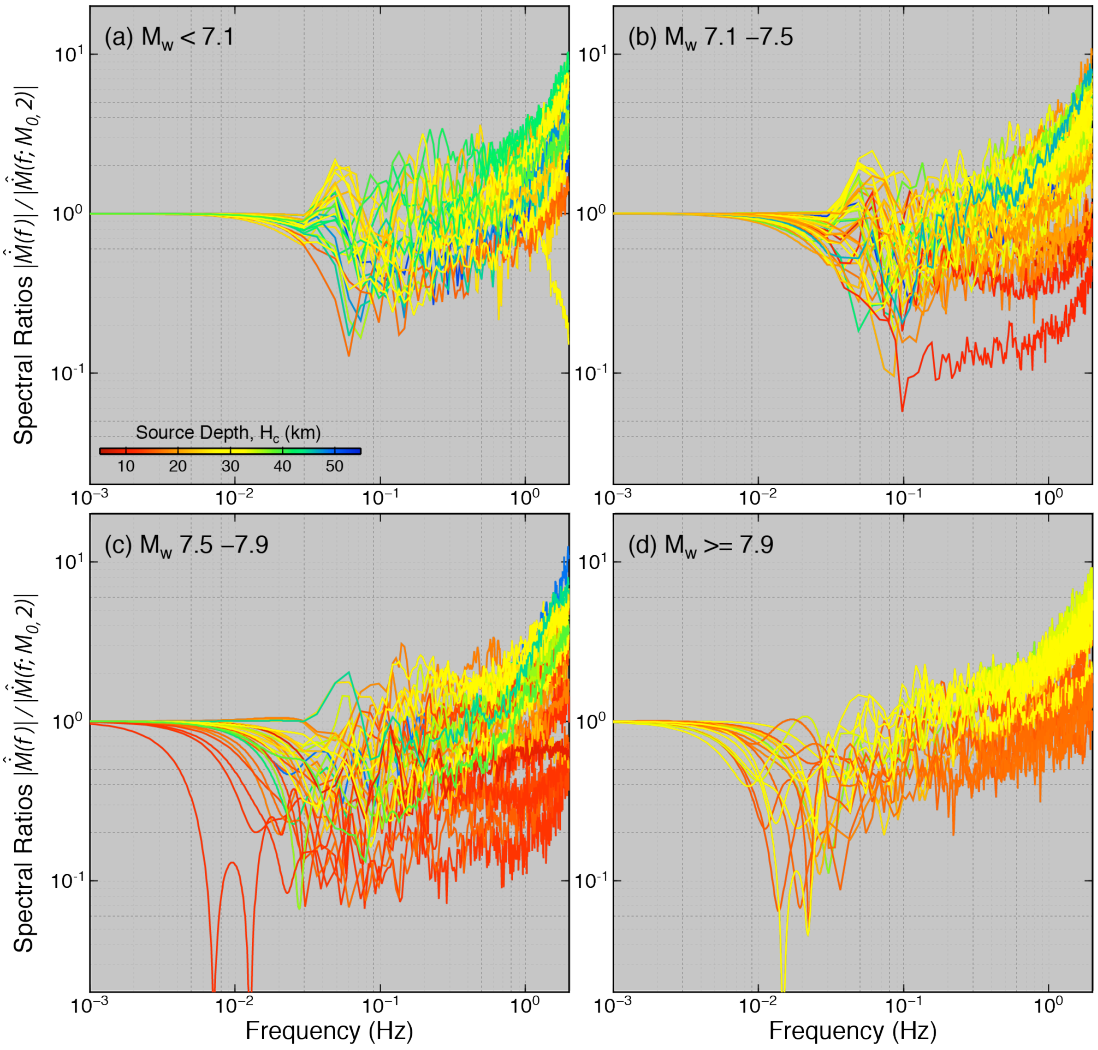

Figure 6.8 The ratios of observed spectra, $\left|\hat{M}(f)\right|$, with respect to corresponding event ω^{-2} models ($\left|\hat{M}(f;M_0,2)\right|$), assuming a constant stress parameter of 3 MPa and β = 3.75 km/s, for events with (a) M_w < 7.1, (b) M_w 7.1-7.5, (c) M_w 7.5-7.9 and (d) M_w > 7.9. Colors indicate average depth of the slip distribution for each event.

6.3.1 High-Frequency Spectral Decay

Figure 6.9a shows the variation of high-frequency fall-off rate parameter, n_0, obtained from the spectral fitting (Figure 6.7) with the average source depth, H_c, from finite-fault inversions. The value of n_0 exhibits a large scatter for shallow events including the large tsunami earthquakes without obvious dependence on magnitude (indicated by symbol size). The average value of n_0 is about 1.64, and the mild depth dependence indicated by the regression curve suggests that deeper megathrust events may have slight enrichment in high-frequency spectral levels.

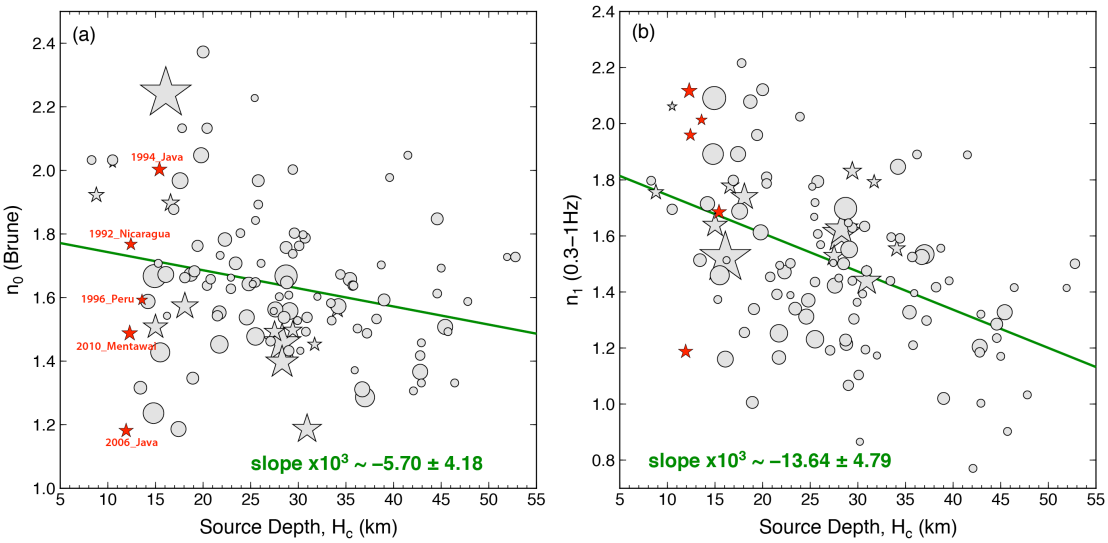

Figure 6.9 (a) High-frequency fall-off rate for the best-fitting ω^{-n0} model for average event spectra, and (b) regression slopes for the frequency band 0.3-1.0 Hz as functions of average depth of the slip distribution from the finite-fault source models. Symbols sizes are scaled with M_w from 7 to 9. Tsunami earthquakes are indicated by the red stars.

Since there is some trade-off between n_0 and f_c in the spectral fitting and there is often notching of the source spectrum around the corner frequency, we use two additional simple parameters to characterize the high-frequency spectral decay. We made simple linear regressions of the high-frequency source logarithmic spectrum to determine the high-

frequency slope (decay parameters) for frequency bands 0.3-1 Hz (n_1) and 0.3-2Hz (n_2). These frequency bands are typically well beyond the corner frequency, as apparent in Figure 6.7. In most cases, we are confident about the source spectrum estimates up to ~1 Hz. For some events, the spectrum tends to flatten rapidly above 1 Hz as a result of hitting a noise floor, abruptly reducing n_2 compared to n_1, while in some cases mild concave-upward curvature of the spectra is observed, also reducing n_2 compared to n_1. But in many cases the spectrum falls off smoothly out to 2 Hz with no indication of noise contamination (spectral slope fitting for all events shown in Appendix III). While still having large variability, these measures display clear trends of decreasing n_1 (Figure 6.9b) and n_2 (Figure 6.A1a) with source depth, stronger than for n_0. The depth variation is more pronounced for n_2, but we consider those estimates less reliable overall.

The trend in Figure 6.9b, while capturing a limited bandwidth spectral behavior, further supports the interpretation that the relative level of high-frequency seismic radiation increases for deeper megathrust events [*Lay et al.*, 2012]. However, the pattern is rather subtle, with large variability. Although tsunami earthquakes are notable in having depleted short-period radiation, they are not distinct from other shallow earthquakes in their high-frequency decay rate (Figure 6.9b), indicating that the source radiation for all shallow megathrust events is slightly different from that of deeper events. Consideration of the regional subduction zone patterns (Appendix III) shows similar trends, albeit with lots of scatter, in several regions with sufficient data over a wide range of depths, including Central America, Peru/N.Chile, Vanuatu (New Hebrides), Solomon Islands, Sumatra, the Philippines, and Kuril/Kamchatka. This suggests that a wide-spread behavior underlies this depth dependence.

The various estimates of spectral decay slope (absolute values, n_0, n_1, n_2) for $M_w \geq 7$ events are systematically smaller than 2 (Figure 6.9), whereas many smaller earthquakes

appear to follow a standard w^{-2} model [e.g., *Hough and Seeber*, 1991; *Shearer et al.*, 2006]. Such low spectral decay rates are similar to observations by *Polet and Kanamori* [2000] and *Allmann and Shearer* [2009]. Since extrapolation of the lower decay rates to higher frequency would result in unbounded energy, the decay rate must increase at a higher frequency. The observed low decay rate may be a manifestation of 'compound' ruptures of different scale asperities. As depth increases, a distribution of more small (high corner frequency) asperities and fewer large (low corner frequency) asperities could yield a composite spectrum that has a reduced slope over a limited frequency band. This scenario is consistent with the notion from *Lay et al.* [2012] that deeper events tend to be enriched in short period radiation due to sampling a distinct population of small-scale asperities as the deep limit of the seismogenic zone is approached. Dynamic modeling of source spectra for models with multi-scale heterogeneities would offer one way to test this idea further.

6.3.2 Radiated energy

The total radiated seismic energy from a double couple point source in a homogeneous whole space can be calculated from source spectrum, $\hat{\dot{M}}(f)$, by

$$E_R = \left[1 + \frac{3V_\alpha^5}{2V_\beta^5}\right] \cdot \frac{8\pi}{15\rho_h V_\alpha^5} \cdot \int_0^\infty f^2 \left|\hat{\dot{M}}(f)\right|^2 df \,, \tag{4}$$

or from the ground velocity spectrum, $\hat{u}(f)$, by

$$E_R = \left[1 + \frac{3V_\alpha^5}{2V_\beta^5}\right] \cdot \frac{128\pi^3 R_E^2}{15R(\theta,\phi)^2} \cdot \frac{\rho_h V_\alpha}{g(\Delta)^2} \cdot \int_0^\infty \hat{u}(f)^2 e^{2\pi f t^*} df \,. \tag{4'}$$

Based on equation (4'), we determine the radiated energy for each station from the observed ground velocity spectra following the method of *Venkataraman and Kanamori* [2004], and then

average the station estimates in a logarithmic sense to estimate the radiated energy for frequencies above 0.05 Hz. The time window for each event is carefully chosen to include most P-wave group energy arrivals while minimizing the scattered coda energy and PP phases. For some events there is a substantial fraction of radiated seismic energy for frequencies less than 0.05 Hz, especially for tsunami earthquakes [*Ye et al.*, 2013b; *Lay et al.*, 2013a]. We account for the low-frequency radiated energy as follows. First, from each moment rate spectrum as shown in Figure 6.6, we estimate the ratio of cumulative energy over the low frequency band, f ≤ 0.05 Hz, to the high-frequency band, f ≥0.05 Hz. This does not involve the absolute energy. Then we scale the average radiated energy estimations for f ≥0.05 Hz using (4') with this ratio to retrieve the low-frequency contribution and total radiated energy.

Uncertainties in radiated energy estimates are introduced by a lack of constraint on the average P- and S-wave velocities around the source, limited data bandwidth, uncertainty in wave propagation corrections (particularly attenuation), uncertainties in radiation pattern corrections, and source directivity effects. It is also recognized that the free surface interaction for very shallow events may lead to overestimation of the low frequency energy [*Rivera and Kanamori*, in preparation]. *Venkataraman and Kanamori* [2004] show that the directivity corrections for dip-slip earthquakes with rupture that expands primarily along strike are generally less than a factor of 2, and we tried to include data with as uniform azimuthal coverage as possible to reduce this effect.

Figure 6.10a shows our radiated energy estimates for the 114 Mw ≥ 7 events in this study computed for an upper frequency limit of 1 Hz. For three events larger than M_w 8.5, we adopt E_R estimates reported by *Lay et al.* [2012] (Table S1 in *Chapter 5*) because special efforts were made to determine the long-period energy contributions for those events. It is hard to

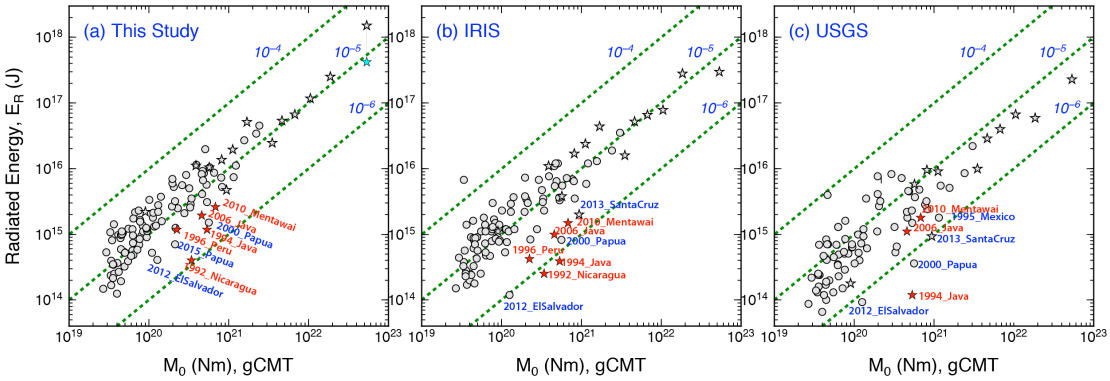

Figure 6.10 Estimates of radiated energy for the events considered in this study from (a) this analysis, using the procedure described in the text (circles for models with assumed V_r, stars for models with independent estimates of V_r). Most results for this study for giant earthquakes (M_w > 8.5) are comparable with those from *Lay et al.* [2012], except large discrepancy for the 2011 Mw 9.1 Tohoku earthquake as indicated by the cyan star. (b) IRIS implementation of the method of *Convers and Newman* [2011], and (c) USGS-NEIC [*Boatwright and Choy*, 1986], as functions of gCMT seismic moment. The measures for large tsunami earthquakes are labeled in red. The dashed curves are for constant logarithmic scaling of E_R versus M_0.

define a uniform upper limit of frequency given the low S/N ratio in teleseismic P-wave recordings for events of variable size, but 1 Hz appears to be compatible with most of the observed source spectral noise levels. The absolute levels of the short-period energy estimates depend on the attenuation model, which is approximated as being uniform but certainly has path-dependent variations that are averaged in each case. Many spectra appear to be well-behaved up to about 2 Hz (or higher), but some are contaminated by noise. If we uniformly compute radiated energy estimates using frequencies up to 2 Hz, higher radiated energy estimates are, of course, obtained. There are substantial differences, up to about a factor of 2, in radiated energy estimates for smaller events (M_W ~ 7.0-7.4) when using upper frequency limits of 1 Hz versus 2 Hz, and modest differences for large events (M_W > ~ 7.5), but no obvious bias for events at different source depths. If we compare our up-to-1 Hz estimates of radiated energy with routine catalog estimates for the same events, we find good consistency

with broadband estimates from the IRIS SPUD implementation of the method of *Convers and Newman* [2011] (http://www.iris.edu/spud/eqenergy) (Figure 6.10b), but somewhat higher values than the USGS estimates based on *Boatwright and Choy* [1986] (Figure 6.10c). The latter difference may be due to our inclusion of the additional contribution from low frequencies, differences in frequency bandwidth used, or differences in the attenuation models used. The large tsunami earthquakes stand out as having low radiated energy for all three databases. The depth-dependent distribution of radiated energy will be quantified in detail below.

6.3.3 Moment-Scaled Radiated Energy and Apparent Stress

The radiated energy E_R scaled by seismic moment M_0 is an important measure of the rupture processes, and has been explored for investigation of depth-varying characteristics [e.g. *Lay et al,* 2012*; Ma and Hirakawa,* 2013]. Figure 6.11a shows our measurements of this ratio using the radiated energy estimates up to 1 Hz as functions of source depth H_c. The highlighted notable tsunami earthquakes clearly stand out from the other large megathrust events in this study, along with other earthquakes with strong observed tsunami or very shallow ruptures such as the 17 November 2000 (21:01) Papua event [*Geist and Parsons,* 2005], 27 August 2012 El Salvador earthquake [*Ye et al.,* 2013b], and 6 February 2013 Santa Cruz Island earthquake [*Lay et al.,* 2013a]. The low E_R/M_0 of the tsunami events relative to other comparably large earthquakes is compatible with the results of *Newman and Okal* [1998]. Moment-scaled radiated energy measures have large scatter from 1×10^{-6} to 4×10^{-5} with an average of $\sim 1.22 \times 10^{-5}$, but no apparent magnitude (*Chapter 5*) or depth dependence apart from the shallow tsunami event population. There is a subtle increasing trend with source depth in some individual subduction zones such as Mexico, Central America, Vanuatu (New

Hebrides) and Japan (see Appendix III), but the data are too sparse to place much confidence in those trends at this time.

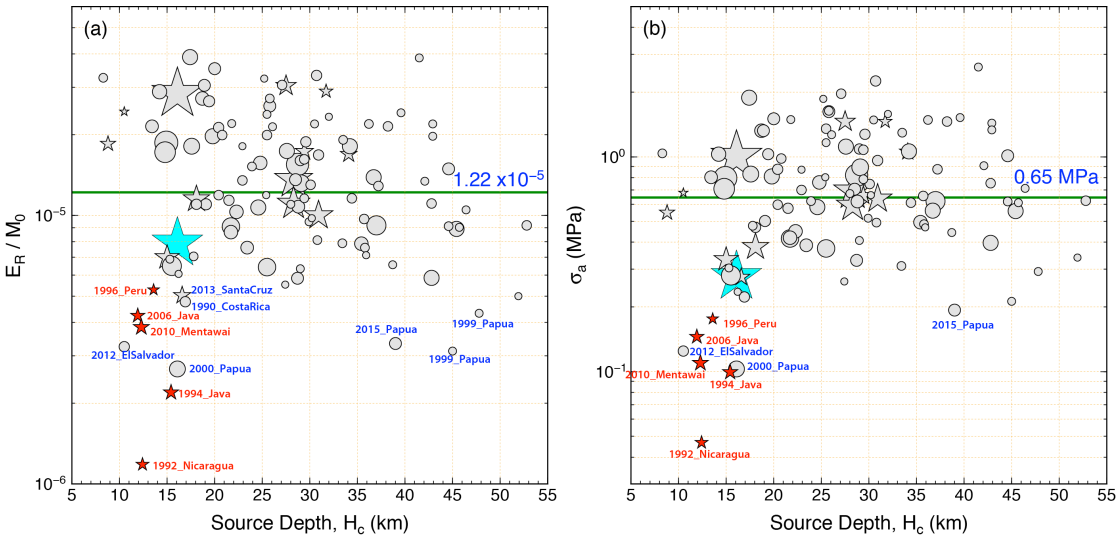

Figure 6.11 (a) Moment-scaled radiated energy and (b) apparent stress, plotted as functions of average depth of the slip distribution for the finite-fault models. Symbols sizes are scaled with M_w from 7 to 9. The cyan star indicates the moment-scaled radiated energy and apparent stress for the 2011 Mw 9.1 Tohoku earthquake calculated with the radiated energy from Lay *et al.* [2012]. Tsunami earthquakes are indicated by the red stars.

Apparent stress, defined as the product of the rigidity and moment-scaled radiated energy, has often been related to dynamic rupture processes (*Chapter 5*). If rigidity is assumed to be constant for all megathrust environments, say 30 GPa, as used in many previous studies, the apparent stress would be directly proportional to moment-scaled radiated energy presented in Figure 6.11a. We compute apparent stress using the depth-dependent rigidity determined from the velocity models incorporated in our finite-fault inversions. The slip-weighted average rigidity for the rupture model is used as the effective rigidity. Resulting variations of apparent stress with the source depth for our major and large events (Figure 6.11b) are naturally quite similar to the moment-scaled radiated energy patterns, but the

shallow tsunami/tsunamigenic earthquakes are more distinctive, due to the product of low E_R/M_0 and low source region rigidity. The average value is 0.65 MPa. The overall pattern of apparent stress, with an increasing trend at shallow depth (H_c < ~18 km) but no trend at large depth, is similar to that in moment-scaled source duration and $V_r^3\Delta\sigma_E$. Because the actual values of rigidity, particularly at very shallow depth, in the megathrust environment is not well constrained, it is hard to formally estimate uncertainties in the apparent stress values. However, apart from the baseline shift to low values around 0.1 MPa for the tsunami earthquakes and some other shallow events, there is no clear dependence on earthquake depth over the megathrust for our global population of major and great events at large source depths. The individual subduction zones with a pattern of increasing moment scaled radiated energy with increasing depth noted above all have slightly more pronounced patterns for apparent stress due to the increase in rigidity with depth in our source models (Appendix III).

6.3.4 High-Frequency Radiated Energy Fraction

A systematic way to quantify any depth-variations of relative high-frequency radiated energy above a frequency, f_1, is to compute the ratio, $r(f_1)$, of high-frequency radiated energy to the total radiated energy. For an w^{-2} model this ratio is given by,

$$\begin{aligned} r(f_1) &= \frac{E_R(f_1 \to \infty)}{E_R(0 \to \infty)} \\ &= \frac{4f_c}{\pi}\int_0^\infty \frac{f^2}{\left(f^2+f_c^2\right)^2}df \\ &= 1-\frac{2}{\pi}\left[\tan^{-1}\left(\frac{f_1}{f_c}\right)-\frac{f_1\cdot f_c}{f_1^2+f_c^2}\right] \end{aligned} \quad . \qquad (5)$$

As $f_1 >> f_c$, the ratio approaches:

$$r(f_1) \rightarrow \frac{2}{\pi}\frac{f_c}{f_1}. \quad (6)$$

This shows that the high-frequency radiated energy ratio is essentially controlled by the corner frequency. Since $f_c \propto M_0^{-1/3}$, this ratio is magnitude-dependent for a uniform f_1. To assess any variation of high frequency energy with centroid depth, we show the high-frequency ratios for 2 magnitude bins in Figure 6.12. There is a clear trend of the ratio (high frequency energy from 0.3-1 Hz))/(total radiated energy), or say $f_1 = 0.3$, with source depth for events with M_w 6.9-7.5 and M_w 7.5-9.1. Even stronger trends are found for energy ratios using the radiated energy computed from 0.3-2.0 Hz (Figure 6.A1b). This behavior is consistent with what was found for the high-frequency decay rate of the source spectrum, as it is essentially an integral measure of the same spectral behavior.

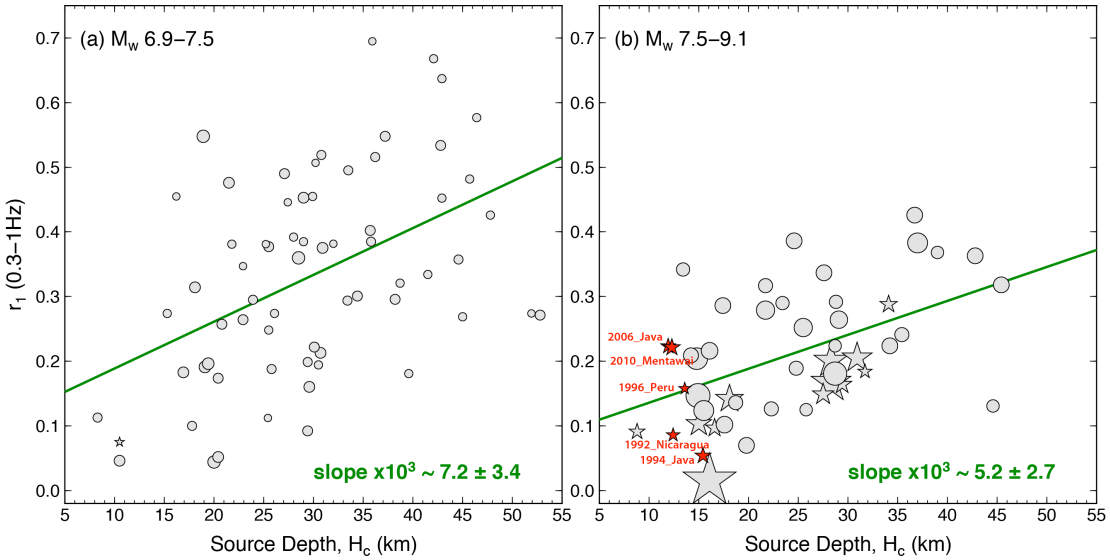

Figure 6.12 Ratios of high frequency (0.3-1.0 Hz) radiated energy over total radiated energy for events with (a) M_w 6.9 – 7.5 and (b) M_w 7.5-9.1, plotted as functions of average depth of the slip distribution for the finite-fault models. Tsunami earthquakes are indicated by the red stars.

Among the individual subduction zones, a corresponding pattern is observed for Peru/N.Chile, New Zealand, Vanuatu (New Hebrides), Sumatra and Kuril/Kamchatka (Appendix III). The increase in relative amount of high-frequency radiated energy is systematic, but too weak to cause the total moment-scaled radiated energy to display a strong trend with source depth. The increase in r with depth is important for understanding strong ground shaking hazard produced by the high-frequency part of the spectrum.

6.4 Discussion

Constraining physical controls on seismic rupture characteristics of plate boundary megathrust faults is challenging due to observational limitations of both the seismic and environmental parameters, as well as the existence of both along-strike and along-dip variations. Distinctive tsunami earthquake rupture properties, such as unusually long source duration, low rupture velocities, low static stress drop, low moment-scaled radiated energy, and large slip to the trench, have been related to low source region rigidity associated with subducted sediments [*Kanamori and Kikuchi*, 1993]. Additionally, tsunami earthquake characteristics have been related to rupture on splay faults or backstop frontal faults in addition to the main megathrust [*Moore et al.*, 2007]. Anelastic deformation of the sedimentary wedge during shallow ruptures has also been proposed to explain properties of tsunami earthquakes [*Ma and Hirakawa, 2013*]. Several physical parameters, such as fluid distribution and pore pressures, mineralogical composition related with dehydration processes, incoming plate morphological structure, and rate- and state-dependent frictional conditions, have been invoked to explain variable high-frequency seismic radiation for deep events along megathrusts [e.g., *Lay and Bilek, 2007*].

6.4.1 Frictional Heterogeneity on the Megathrust

The lack of depth-dependence of static stress drop ($\Delta\sigma_E$) for major and great megathrust earthquakes globally and in individual subduction zones indicates that the observed seismic radiation characteristics are largely insensitive to normal stress variations. In addition, we find no clear trends with source depth for the dynamic source parameters discussed in *Chapter 5*, radiation efficiency η_R and fracture energy per unit area G (Figure 6.13). The radiation efficiency is defined as the ratio of radiated energy to the total available potential energy (ΔW_0), i.e. $\eta_R = \frac{E_R}{\Delta W_0} = \frac{2\mu}{\Delta\sigma} \cdot \frac{E_R}{M_0} = 2 \cdot \frac{\sigma_a}{\Delta\sigma}$, which involves the ratio of the apparent stress to static stress drop. The absence of depth-dependence of radiation efficiency implies that there is no systematic variation of energy partitioning during earthquake rupture with source depth. These observations suggest that overall dynamic rupture processes are relatively insensitive to source depth, and the enrichment of high-frequency seismic radiation may be the results of heterogeneity on the rupture surface along the megathrust.

The notion of depth-dependent scale lengths of megathrust heterogeneities (Figure 6.14) has been advanced as a means for explaining the depth-variation of seismic radiation illustrated by the schematic model in Figure 6.1 [*Lay et al.*, 2012]. Large aseismic or conditionally stable regions at shallow depth (domain A with source depth < ~ 15 km) arising from the presence of sediments and pore fluids may produce slow rupture expansion and inefficient seismic wave generation, resulting in low moment-scaled radiated energy and significantly low apparent stress enhanced by low rigidity, even though large displacements occur in tsunami earthquakes. At source depths spanning from 15-30 km, there are large, relatively uniform regions with unstable sliding frictional properties, i.e. asperities, or area with large coseismic slip, that generate modest amounts of spatially distributed short-period

radiation upon failure. The down-dip part of the megathrust may be enriched in patchy, smaller-scale asperities surrounded by "aseismic" conditionally stable areas, which would produce enhanced localized bursts of short-period seismic radiation during rupture. In general, the depth-varying properties of sediments at shallow depths from 5 to ~18 km may contribute to a step-change or rapidly increasing trend of moment-scaled duration and apparent stress; the increase of high-frequency radiated energy fraction, and the associated decrease of high-frequency decay rate, with source depth may be related with gradual increase of the percentage of isolated, small-scale asperities as shown in Figure 6.14. Further quantitative modeling of effects on seismic radiation from sediments and multiple-scale heterogeneities along the megathrust, such as that done by *Noda and Lapusta* [2013], framed by the extensive kinematic observations presented in this study, is desirable.

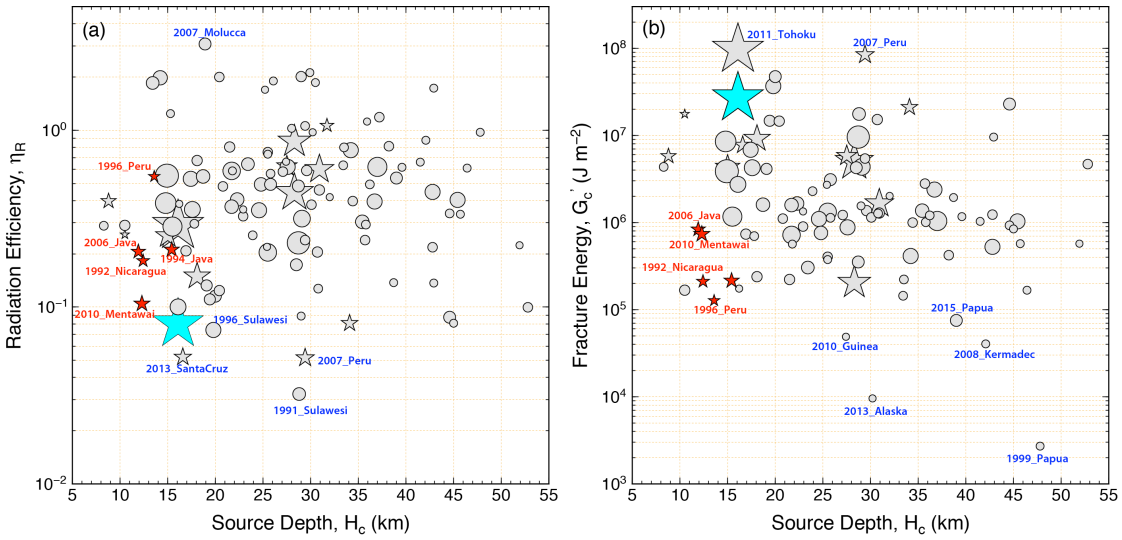

Figure 6.13 (a) Radiation efficiency and (b) fracture energy *G'* (for those cases with radiation efficiency less than 1.0), plotted as functions of average depth of the slip distribution for the finite-fault models. Symbols sizes are scaled with M_w from 7 to 9. The cyan star indicates the radiation efficiency and fracture energy for the 2011 Mw 9.1 Tohoku earthquake calculated with the radiated energy from Lay *et al.* [2012]. Events with high or low values are labeled. Tsunami earthquakes are indicated by the red stars.

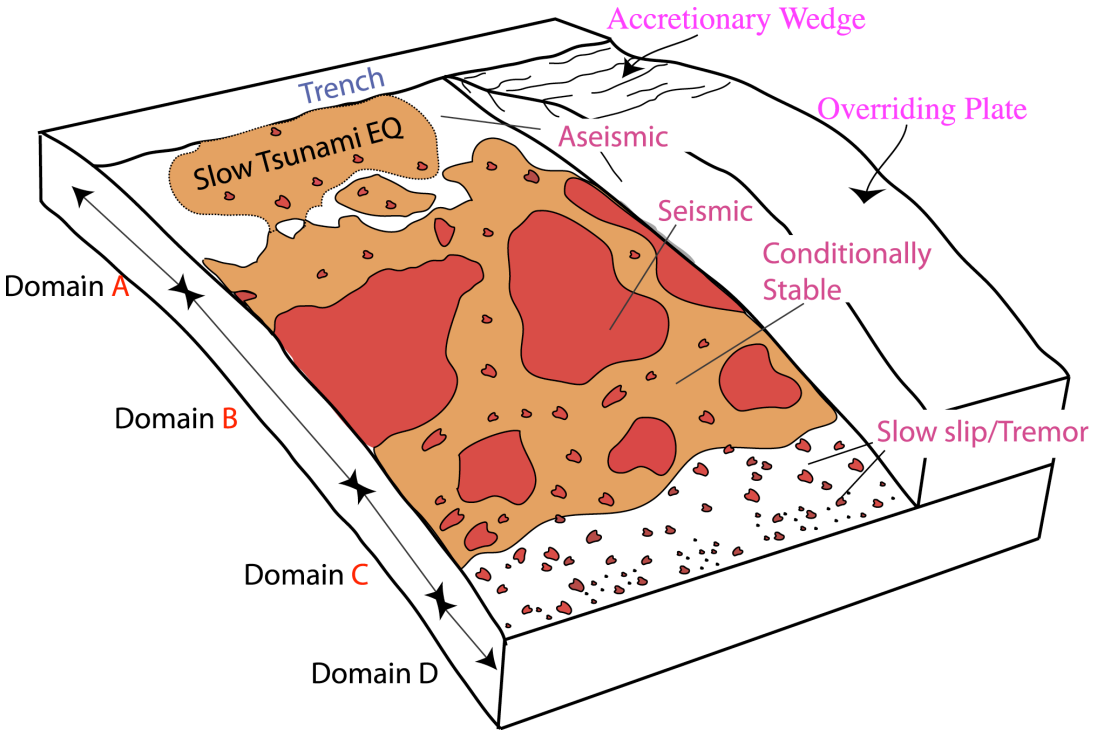

Figure 6.14 Cut-away schematic characterization of the megathrust frictional environment, related to Domains A, B and C defined in Figure 6.1. Regions of unstable frictional sliding are red regions labeled "seismic". Regions of aseismic stable or episodic sliding are white regions labeled "aseismic". Orange areas are conditional stability [*Scholz, 1998*] regions, which displace aseismically except when accelerated by failure of adjacent seismic patches. Domain A is at shallow depth where sediments and pore fluids cause very slow rupture expansion even if large displacements occur in tsunami earthquakes. Domain B has large, relatively uniform regions of stable sliding that can have large slip, but generate modest amounts of short-period radiation upon failure. Domain C has patchy, smaller scale regions of stable sliding surrounded by conditionally stable areas. When these areas fail, coherent short-period radiation is produced. Small, isolated patches may behave as repeaters when quasi-static sliding of surrounding regions regularly load them to failure. Domain D is dominated by aseismic sliding, but many small unstable patches can rupture in seismic tremor when slow slip events occur. Modified from *Lay* [2015].

6.4.2 Correlation with Slab Properties

The global sampling provided by the data set in this study enables some tests of correlation of seismic radiation attributes with pressure- and/or temperature-dependent

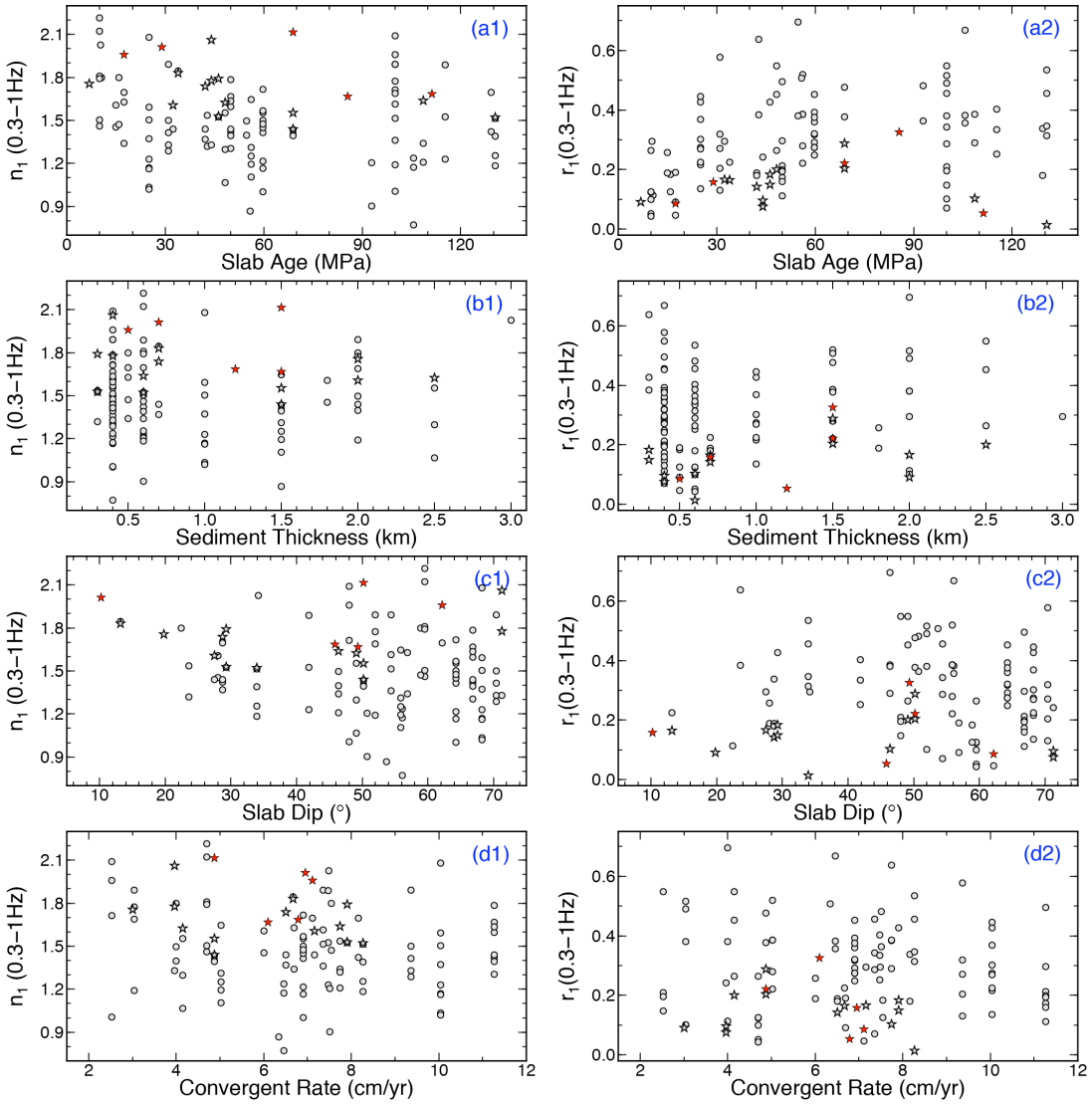

Figure 6.15 High-frequency regression slopes for the 0.3-1.0 Hz spectral range (left), and ratios of high frequency (0.3-1Hz) radiated energy over the total radiated energy (right), versus (a) subducted slab ages, (b) sediment thickness, (c) slab dip angles, and (d) convergent velocities [*Syracuse et al.*, 2010]. Tsunami earthquakes are indicated by the red stars.

properties of the megathrust. We correlated the depth-varying high-frequency spectral decay and high-frequency radiated energy ratio estimates from this study with estimates of slab age, slab dip angle, plate convergence velocity, and sediment thickness as summarized by *Syracuse et al.* [2010], along with 2D kinematically-modeled slab surface temperature at 30 km depth

for 56 segments of global subduction zones [*Syracuse et al.*, 2010]. We did not find systematic trends for high-frequency seismic radiation measures as a function of slab age, geometry, convergent rate or sediment thickness (Figure 6.15).

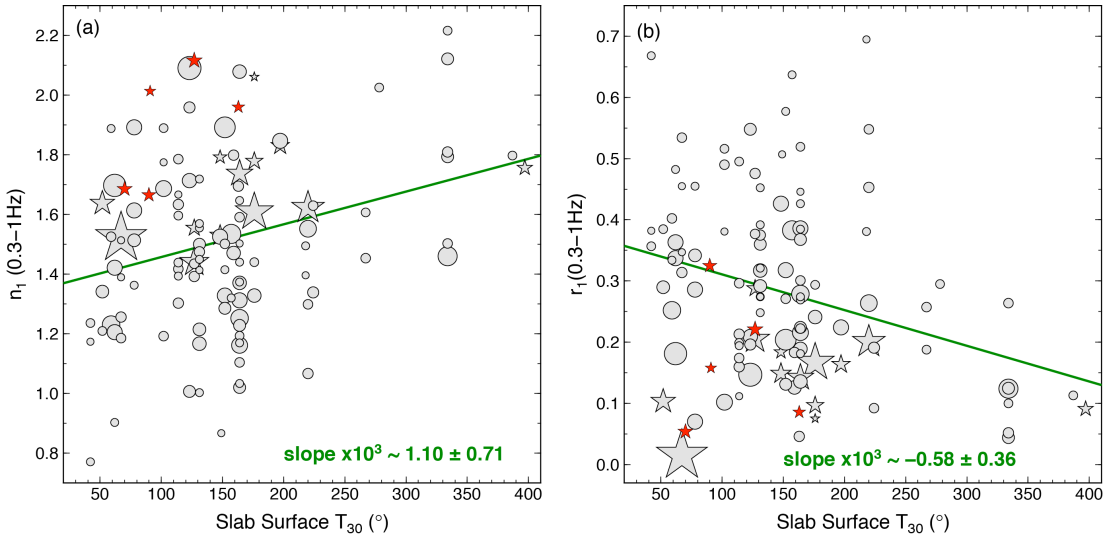

Figure 6.16 (a) High-frequency regression slopes for the 0.3-1 Hz spectral range, and (b) ratios of high frequency (0.3-1 Hz) radiated energy over the total radiated energy, versus estimates of surface temperature of the subducting slab at 30 km depth [*Syracuse et al.*, 2010]. Symbols sizes are scaled with M_w from 7 to 9. Tsunami earthquakes are indicated by the red stars.

However, we find some (admittedly weak) correlation between high-frequency spectral slopes and high-frequency radiated energy ratios with slab temperature at 30 km (Figures 6.16 and 6.A2), with the sense that relatively enriched high-frequency seismic radiation correlates with colder slab interface conditions. As there could be a systematic reduction of average attenuation factor with increasing depth or decreasing slab interface temperature, we cannot uniquely attribute this tendency to temperature effects on frictional properties or on stress heterogeneity, but further work to explore any temperature relationships to seismic radiation is encouraged. The sense of correlation that we find for the global data set is consistent with the regional results found for the Japan trench megathrust, where the extensive high-qualify

regional seismic data allowed the inference that observed strong high-frequency ground shaking from deep megathrust events is due to a combination of enriched high-frequency source spectra and low attenuation path effects [*Ye et al.*, 2013a].

6.5 Conclusions

Depth-dependent variations of rupture characteristics for 114 $M_W \geq 7$ interplate subduction zone megathrust earthquakes from 1990-2015 have been explored. The source characteristics are estimated using uniform methodologies, finite-fault inversion and source spectrum analysis, applied to teleseismic body wave observations. There is no trend of moment-scaled source duration and centroid time, static stress drop or moment-scaled radiated energy with depth other than low values being found for very shallow tsunami earthquakes and a few other shallow events. However, there is a systematic increase in the relative amount of short-period seismic radiation for deeper megathrust events, manifested in reduced high-frequency fall-off slopes of the average source spectra and increased ratios of high-frequency radiated energy to total radiated energy as depth increases. There is a weak correlation of these high-frequency measures with estimated average megathrust temperature, with colder megathrust environments tending to have somewhat enriched short-period radiation. This raises the possibility that the depth-varying seismic characteristics may result from frictional and/or attenuation variations influenced by temperature. Statistical comparisons of seismic measurements with slab and plate interface parameters require larger data sets to consider two-dimensional and regional variations. Efforts to directly estimate physical variations of large ruptures, such as size and patterns of large-slip patches on megathrusts could potentially help to reveal the mechanisms of the observed depth-varying rupture characteristics.

Acknowledgements. This work made use of GMT and SAC software. We appreciate comments from the Associate Editor, Rachel Abercrombie, and an anonymous reviewer on an earlier version of the manuscript. The Incorporated Research Institutions for Seismology data management center was used to access the seismic data from Global Seismic Network and Federation of Digital Seismic Network stations. This work was supported by NSF grant EAR1245717 (T.L.).

6.6 Supplementary Figures

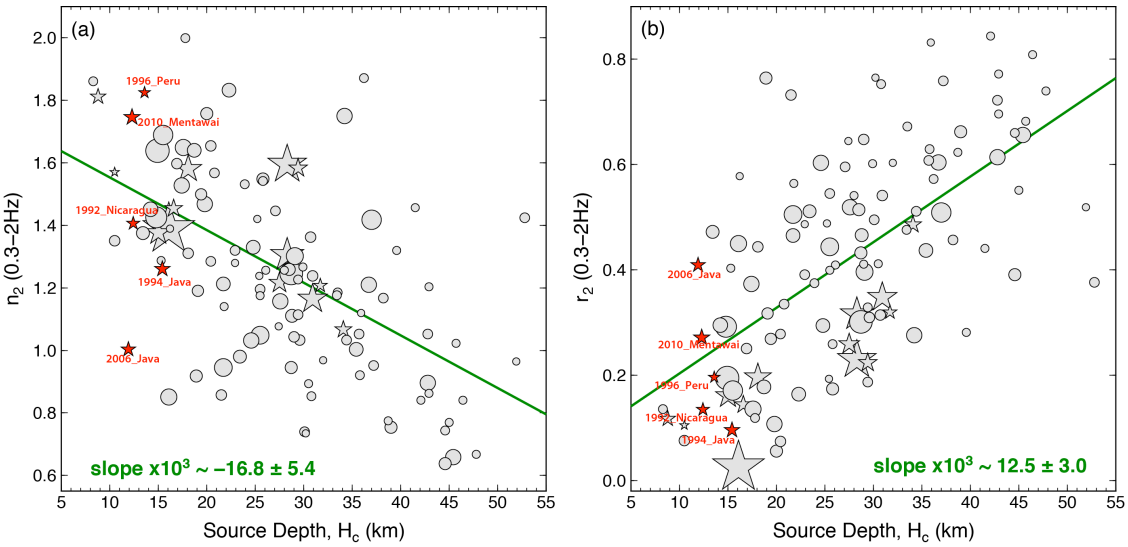

Figure 6.A1 (a) High-frequency regression slopes of the source spectra and (b) ratios of high-frequency radiated energy over total radiated energy, for the frequency band 0.3-2 Hz as functions of average depth of the slip distribution from the finite-fault source models. Symbols sizes are scaled with Mw from 7 to 9. Tsunami earthquakes are indicated by the red stars.

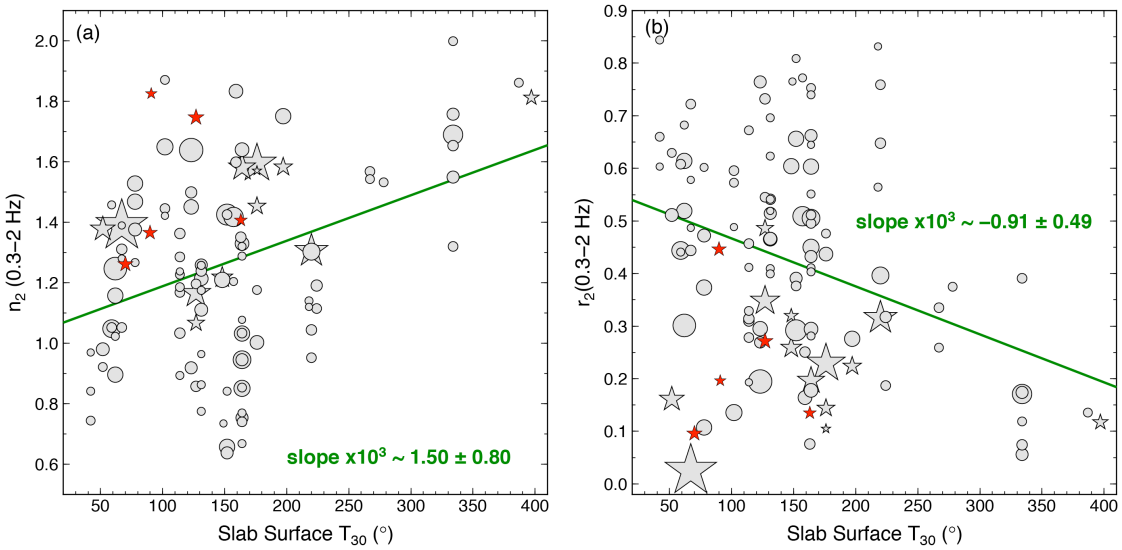

Figure 6.A2 (a) High-frequency regression slopes for the 0.3-2 Hz spectral range, and (b) ratios of high frequency (0.3-2 Hz) radiated energy over the total radiated energy, versus estimates of surface temperature of the subducting slab at 30 km depth [Syracuse et al., 2010]. Symbols sizes are scaled with Mw from 7 to 9. Tsunami earthquakes are indicated by the red stars.

PART II INTRA-SLAB EARTHQUAKES

Chapter 7

Interactions During the August 31, 2012, Philippine Trench Earthquake (M_W 7.6) Sequence

This chapter has been published as:
Ye, L., T. Lay, and H. Kanamori (2012), "Intraplate and interplate faulting interactions during the August 31, 2012, Philippine Trench earthquake (Mw 7.6) sequence", Geophys. Res. Lett., 39, L24310.

Abstract. On August 31, 2012, a large (M_w 7.6) thrust earthquake occurred within the subducting Philippine Sea plate seaward of a low seismicity region of the plate boundary (9.5°N-11.5°N), possibly as a result of horizontal compressional stress accumulation offshore of a locked megathrust. The mainshock ruptured from ~30-50 km depth, with high radiated-energy/seismic-moment ratio and enriched short-period P-wave radiation. The nine largest aftershocks with global centroid moment tensor solutions (M_w ~5.2-5.6) were shallow (10-13 km) normal-faulting outer-rise events, and a waveform template analysis using regional broadband data indicates many (48/101) similar normal faulting events (m_b 4.0-5.5) and a few (8/101) likely shallow thrust faulting events on the megathrust with additional very small unidentified events. Coulomb stress perturbations may contribute to the mix of intraplate and interplate faulting. Geodetic assessment of any slip deficit on the megathrust is essential for quantifying the potential for a future large interplate rupture in this region.

7.1 Introduction

Large thrust-faulting earthquakes within subducting plates seaward of plate boundaries

are rare, but have been observed to correlate with subsequent occurrence of great thrust events on the adjacent megathrusts [Christensen and Ruff, 1988]. Together with the common occurrence of normal faulting seaward of the plate boundary following large megathrust events and temporal patterns of deeper slab activity, it has been proposed that intraplate elastic stresses offshore and down-dip of the megathrust are modulated by the fluctuating cycle of locking and rupturing of the plate boundary [Dmowska et al., 1988; Lay et al., 1989, 2009, 2011; Taylor et al., 1996; Ammon et al., 2008]. Thus, occurrence of a large outer rise or outer trench slope thrust earthquake is of interest as a possible indicator of interplate coupling and strain accumulation prior to a future interplate rupture. We examine the earthquake sequence associated with a large thrust earthquake below the Philippine Trench seaward of a plate boundary megathrust region with uncertain seismic potential.

7.2 The 2012 Mw 7.6 Philippine Trench Earthquake

The Philippines region has extensive large earthquake activity documented back to 1600 [e.g., Bautista and Oike, 2000; Abe, 1994; Allen et al., 2009] (Fig. 7.1) involving several subduction zones and the long Philippine Fault. On August 31, 2012, an M_w 7.6 earthquake struck beneath the Philippine Trench (10.838°N, 126.704°E, hypocentral depth 34.9 km, 12:347:34 UTC; [USGS NEIC, http://earthquake.usgs.gov/earthquakes/]). Long-period seismic waves used in a W-phase inversion indicate a centroid depth of 44 to 50 km (Fig. 7.2b), which is comparable to depths for other well-studied large thrust events near oceanic trenches [Christensen and Ruff, 1988; Lay et al., 2009; Raeesi and Atakan, 2009; Todd and Lay, 2012]. Elastic bending stresses in subducting plates might account for relatively deep thrust activity below shallower normal faulting activity [e.g., Chapple and Forsyth, 1979; Lay et al., 1989], but very large trench slope thrust events may require that interplate locking decrease

the depth of the elastic bending neutral surface in the plate, bringing a larger fraction of the brittle lithosphere into the compressional regime [e.g., Taylor et al., 1996; Liu and McNally, 1993].

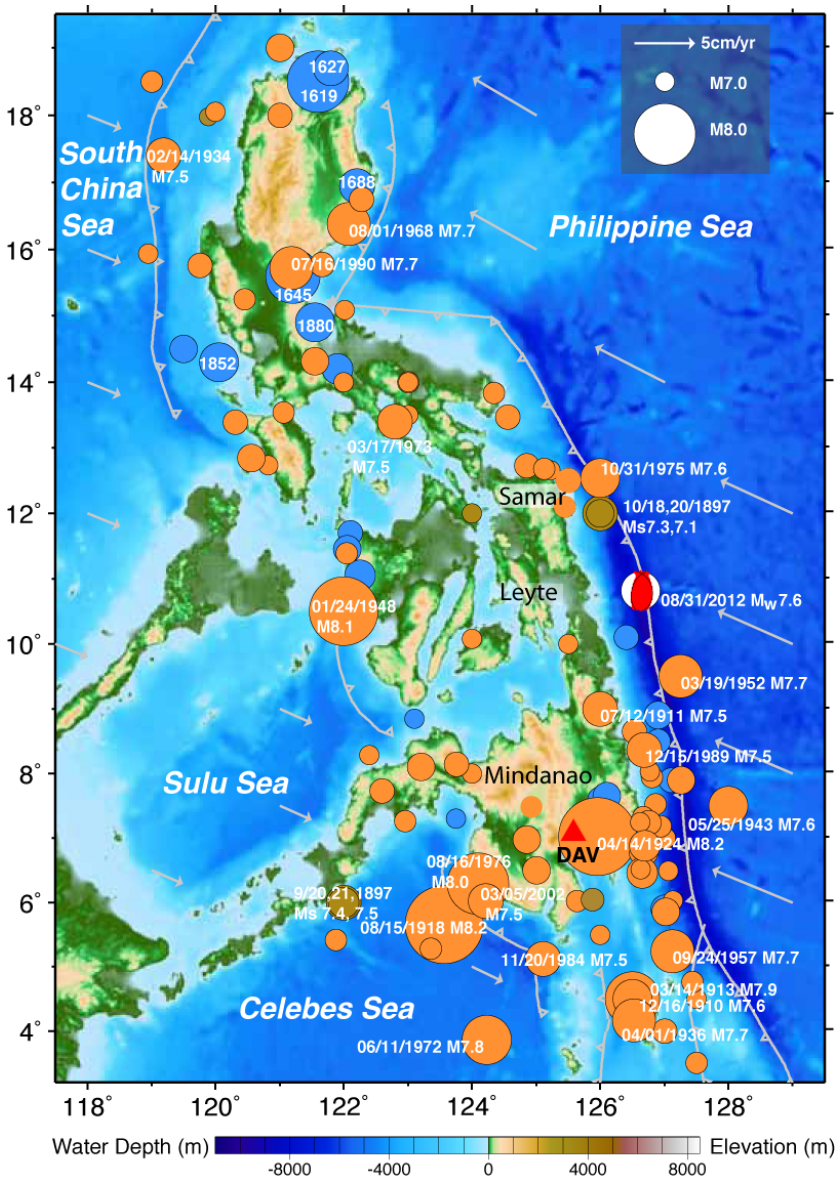

Figure 7.1 Large earthquakes around the Philippines: blue circles are M ~7+ events (inferred from Intensity information) from 1600 to 1895 [Bautista and Oike, 2000], the brown circles are large events in 1897 with M_s from Abe [1994], including the northern Samar event of October 18, 1897 (M_s 7.3), and orange circles are M ≥ 7.0 events from 1900 to 2008 from PAGER-CAT [Allen et al., 2009]. The red focal mechanism is the W-Phase solution for the August 31, 2012 Philippine Trench event plotted at the NEIC epicenter. The red triangle shows the location of GSN station DAV. Barbed curves indicate subduction zones. Arrows indicate plate motion directions and rates computed using model GSRM 1.2 [*Kreemer et al.*, 2003, with updates].

The 2012 Philippine Trench event is located offshore of a region of the subduction zone from 9.5°N-11.5°N, where there is no record of great earthquake activity dating back to 1600 (Fig. 7.1), and there is large uncertainty in the seismic potential [Bautista and Oike, 2000; Nishenko, 1991]. This region also has had few moderate size events with $m_b \geq 5.0$ since 1973 (see Auxiliary Figure 7.A1), so it can be described as a low seismicity region extending 150-200 km along the trench. The adjacent portions of the subduction zone have experienced large earthquakes (Fig. 7.1): the October 18, 1897 northern Samar (M_s 7.3) earthquake struck to the north and the April 14, 1924 (M_s 8.2) event struck eastern Mindanao to the south. The faulting geometries of these events are not known. There have been large intraplate normal-faulting events to the north and south, for example the October 31, 1975 (M_w 7.6) event involved normal faulting [Christensen and Ruff, 1988]. There is no clear disruption of the trench bathymetry, upper plate structure or incoming bathymetric features on the Philippine Sea plate that might suggest distinct coupling of the megathrust in this region [Bilek et al., 2003; Song and Simons, 2003]. Relatively sparse observations of GPS velocities indicate east-west compressional strain across the southern Philippines [e.g., Rangin et al., 1999] and convergence in the Philippine Trench varies from 5.4 cm/yr near 13°N to 3.2 cm/yr near 7°N [Yumul et al., 2008]. However, the relative contributions of internal upper plate deformation, especially near the Philippine fault, and any plate boundary localized slip deficit in the central Philippine trench are not well-established by published GPS observations.

The point-source moment tensor for the August 31, 2012 event was determined by W-phase inversion using three-component observations from 64 channels at 47 Global Seismic Network (GSN) stations for the passband 0.00167-0.005 Hz. The scalar moment is 3.2×10^{20} N-m, with the optimal centroid depth of 50.5 km yielding the solution shown in Fig. 7.2. Corresponding waveform fits are shown in Auxiliary Fig. 7.A2. The depth appears to be quite

well constrained and the centroid location is 11°N, 127°E. The solution has a minor non-double-couple component.

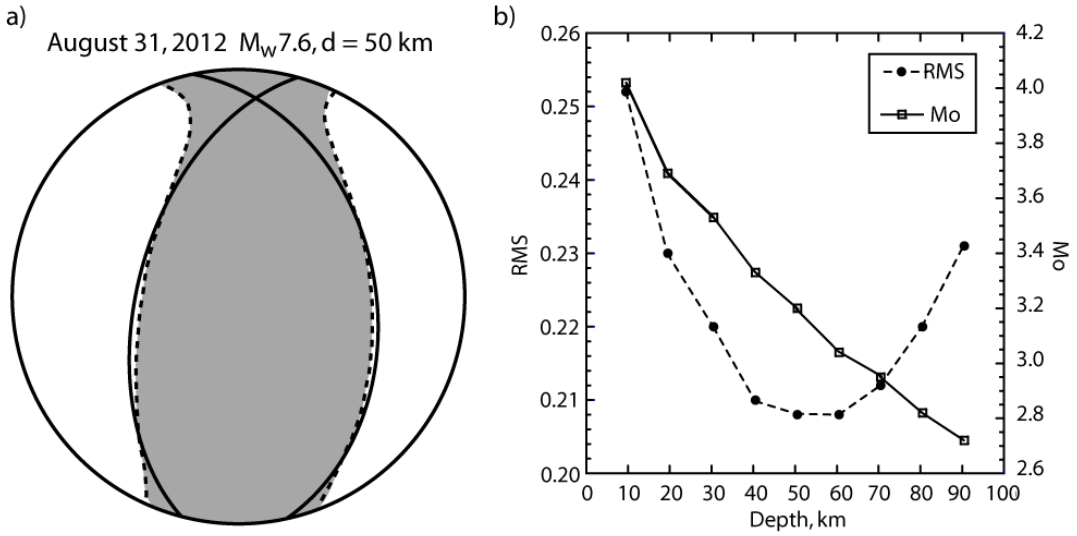

Figure 7.2 a) Point-source moment tensor from W-phase inversion for the August 31, 2012 Philippine event. The best double couple for a source depth of 50 km has nodal plane orientations: strike, $\phi_1 = 348.2°$, dip, $\delta_1 = 40.1°$, rake, $\lambda_1 = 68.9°$; and $\phi_2 = 195°$, $\delta_2 = 53.0°$, $\lambda_2 = 106.9°$. The waveform fits are shown in Fig. 7.A2. b) W-phase inversion RMS and estimated seismic moment, Mo, dependence on assumed source depth. A centroid time of 15 s was used.

Using the two possible fault plane geometries from the best double-couple for the W-phase moment tensor (Fig. 7.2), we performed finite-fault inversions using 81 teleseismic broadband P waves with 75 s long signals. Comparable fits were obtained using either nodal plane, and we show the result for a fault model with strike ϕ=348.2° and dip δ=40.1° in Fig. 7.3a. We assumed the hypocentral depth of 35 km from the NEIC location, but found little resolution of hypocenter between 30 km and 45 km depth. A rupture velocity of 3 km/s was assumed, and the subfaults were parameterized to have 4 overlapping 2-s duration triangles (allowing total subfault duration of up to 5 s), with variable rake. A large slip concentration is

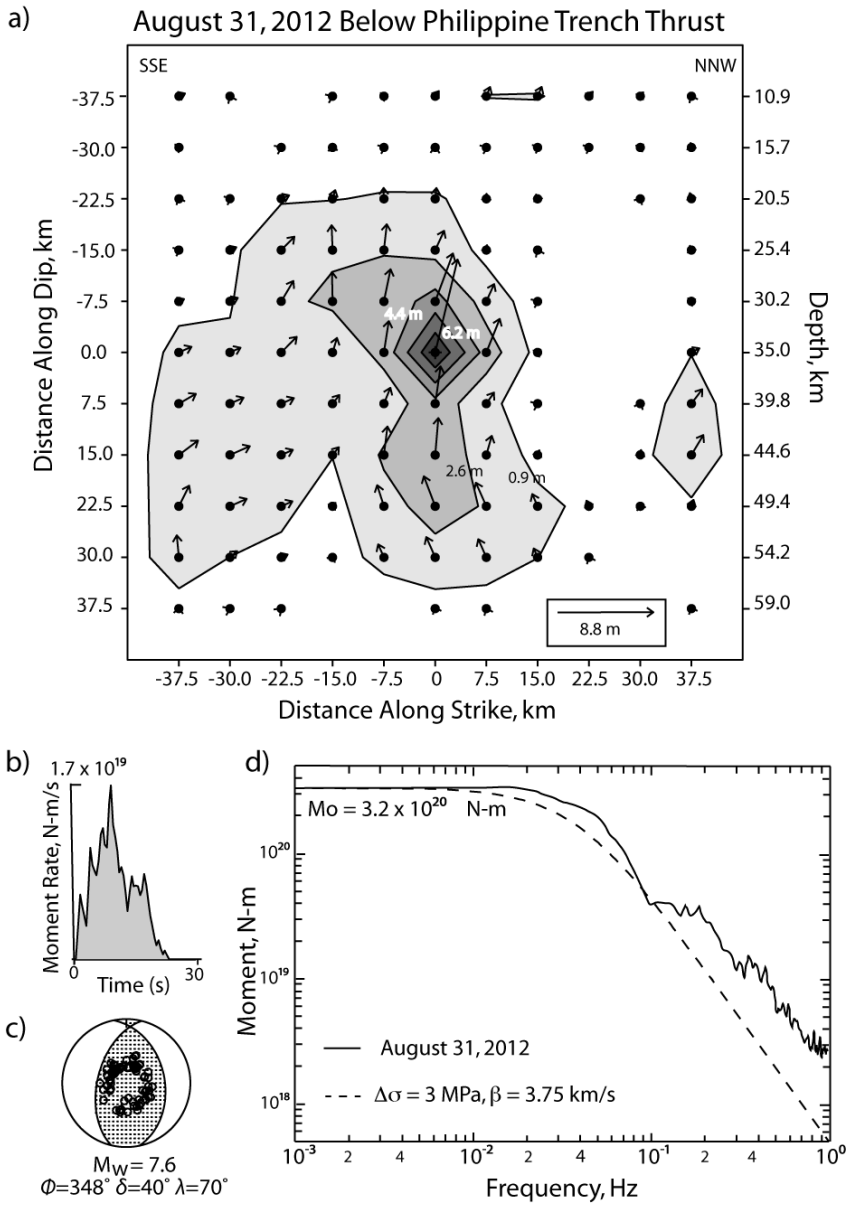

Figure 7.3 a) Rupture model slip distribution for the August 31, 2012 Philippine event obtained by inverting 81 75-s long teleseismic P wave signals for a fault plane with ϕ = 348.2° and δ = 40.1°. The vectors indicate the direction of slip of the hanging-wall side of the fault relative to the foot-wall. b) The ~25 s duration moment rate function for the slip model, with a centroid time of 10 s. c) Average focal mechanism with P wave sampling of the focal sphere. Waveform fits are shown in Fig. 7.A3. d) The average far-field P wave source spectrum is shown by the black line, estimated at frequencies less than ~0.03 Hz from the moment rate function in b) and at frequencies > ~0.03 Hz from stacking of broadband teleseismic P wave spectra. The dashed line is a reference source spectrum for an ω^{-2} model with 3 MPa stress drop, shear velocity, b = 3.75 km/s, and seismic moment given by the W-phase inversion in Fig. 7.2.

found near the hypocenter, with rupture extending from 25-55 km in depth and about 50 km along strike, with greater extent toward the SSE. The moment rate function (Fig. 7.3b) has jagged short-duration pulses over a 25-s duration, stemming from short period roughness in the P waves (waveforms and fits are shown in Auxiliary Fig. 7.A3). If we evaluate the stress drop over the well-resolved part of the fault model with subfault moments at least 12% of the peak subfault moment, the estimated slip area is 2300 km^2, the moment is 3.2 x 10^{20} N-m, the static stress drop is ~7 MPa (assuming a circular rupture), and the average slip is ~2.0 m. Similar results are found using the conjugate plane (Auxiliary Fig. 7.A4).

The enriched level of short-period energy in the P waveforms is particularly evident in the average source spectrum shown in Fig. 7.3d compared to a reference w^{-2} spectrum with 3 MPa stress parameter. The spectrum is obtained from the moment rate function for frequencies below ~0.03 Hz and from stacking of 41 broadband P-wave spectra for higher frequencies. The radiated energy is estimated as E_r = 1.6 x 10^{16} J over the frequency range 0-1.0 Hz [following Venkataraman and Kanamori, 2004]. There is some additional energy at higher frequencies that we have not accounted for. The USGS estimate of energy is 1.8 x 10^{16} J, which is quite compatible. The E_r/M_o ratio we obtain is 5.0 x 10^{-5}, which is relatively high even among large intraplate ruptures (Auxiliary Figure 7.A5).

7.3 Aftershock Sequence Characterization

A substantial aftershock sequence (Fig. 7.4a) occurred following the mainshock, with events having M_w up to 5.6. Nine of the larger events (N1-N9 in Fig. 7.4a) have Global Centroid Moment Tensor (GCMT, http://www.globalcmt.org) solutions, all of which have shallow (10-13 km centroid depth) normal faulting mechanisms, all but one being clustered near the trench south of the mainshock. A total of 110 distinct aftershocks with $m_b \geq 4.0$ were

listed in the NEIC and PHIVOLCS (Philippine Institute of Volcanology and Seismology) bulletins from August 31 to September 16, 2012.

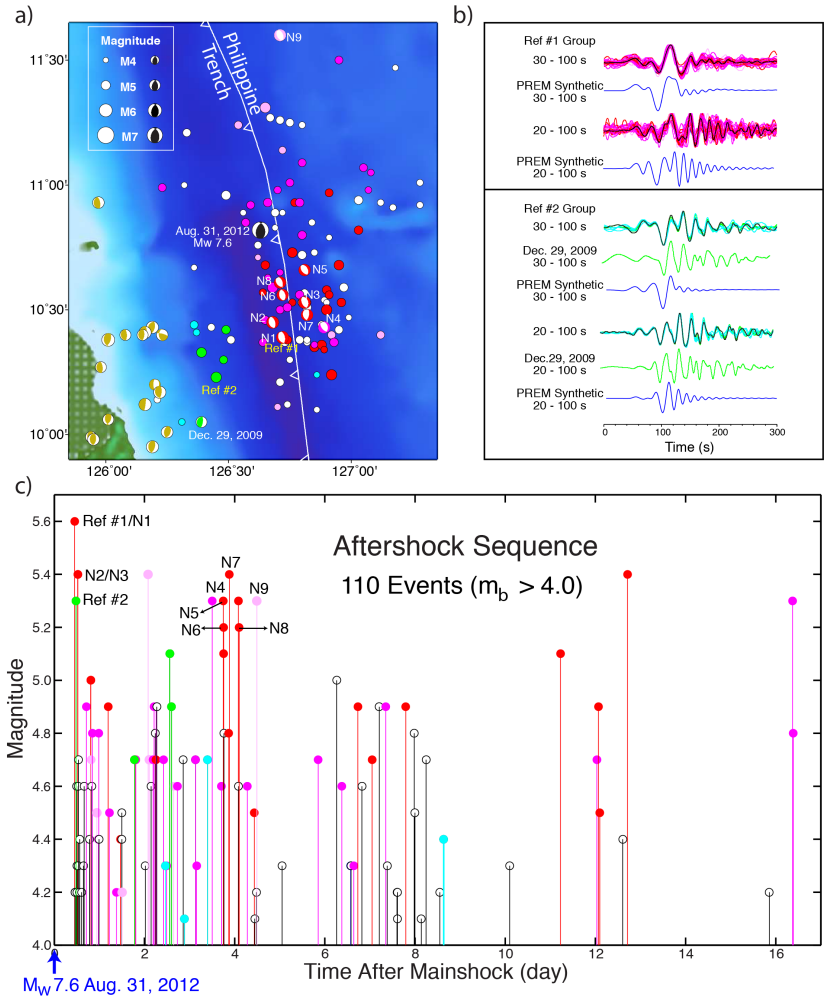

Figure 7.4 a) Locations of events in the aftershock sequence from combined catalogs of NEIC and PHIVOLCS (Philippine Institute of Volcanology and Seismology), and GCMT focal mechanisms of earlier events (brown mechanisms and December 29, 2009 underthrusting event). The blue mechanism is the GCMT solution for the August 31, 2012 mainshock. The red, pink, and pale pink symbols (including GCMT mechanisms) indicate similarity of waveforms at station DAV to that for normal-faulting reference event #1: with very high waveform cross-correlation coefficients (≥ 0.9 for 30-100 s and ≥ 0.7 for 20-100 s), high cross-correlation coefficients (≥ 0.8 for 30-100 s and ≥ 0.5 for 20-100 s), and medium coefficients (≥ 0.8 for 30-100 s waveform, but < 0.5 for 20-100 s), respectively. The green and cyan symbols indicate events with very high or high cross-correlation coefficients with reference event #2 waveforms, including the December 29, 2009 event. White circles are events with no classification of mechanism. The white barbed curve indicates the position of the trench. b) Superimposed waveforms for the groups of events similar to the two template waveforms in two pass bands, along with synthetic seismograms for station DAV. For group 2, the very highly correlated December 29, 2009 waveform is shown as well, indicating that these are likely shallow thrust events. c) Time series for the aftershock sequence color-coded as in the map, indicating the predominance of normal faulting throughout the sequence.

We attempted to identify events with faulting mechanisms similar to the mainshock that might be on the main rupture plane, hoping to resolve between the two nodal planes. We used broadband vertical component recordings of the aftershocks at regional GSN station DAV about 350 km to the south-southwest (Fig. 7.1), filtered in passbands of 0.01-0.03 Hz and 0.01-0.02 Hz to evaluate distinct waveform clusters using template waveforms (Auxiliary Fig. 7.A6). One of the normal faulting aftershocks (N1) was found to have good waveform correlations with 56 of the aftershocks (Fig. 7.4), while 8 other events have distinct waveforms similar to those for an event on December 29, 2009, for which a GCMT mechanism indicates shallow-dipping thrust faulting. The other events are all very small at DAV and their mechanisms are uncertain. The aftershock sequence (Fig. 7.4c) thus appears to be dominated by shallow near-trench normal faulting with a patch of triggered thrust-faulting apparently on or near the megathrust to the west. GCMT solutions for prior earthquakes in the region (at NEIC epicenters in Fig. 7.4a) indicate deeper thrust faulting near the southern end of the seismic gap zone. The aftershocks do not reveal which nodal plane ruptured for the main event, but they do indicate activation of distinct fault systems by the mainshock.

7.4 Faulting Interactions

The aftershock sequence likely involves both intraplate and interplate faulting. While dynamic triggering produced by the strong waves from the mainshock may play an important role in activating different fault systems, static stress changes may as well. There are several recent examples of large shallow normal faulting events being followed by deeper thrust events below the outer trench slope in the Kuril Islands [Lay et al., 2009] and in northern Kermadec [Todd and Lay, 2012]. There has also been clear activation of megathrust faulting by large trench-slope normal faulting in Tonga [Lay et al., 2010] and northern Kermadec

[Todd and Lay, 2012]. Seismic activity can also be suppressed by stress changes from large faulting [Toda et al., 2012], although the seismicity in the central Philippines Trench region has been too sparse to detect regional decreases.

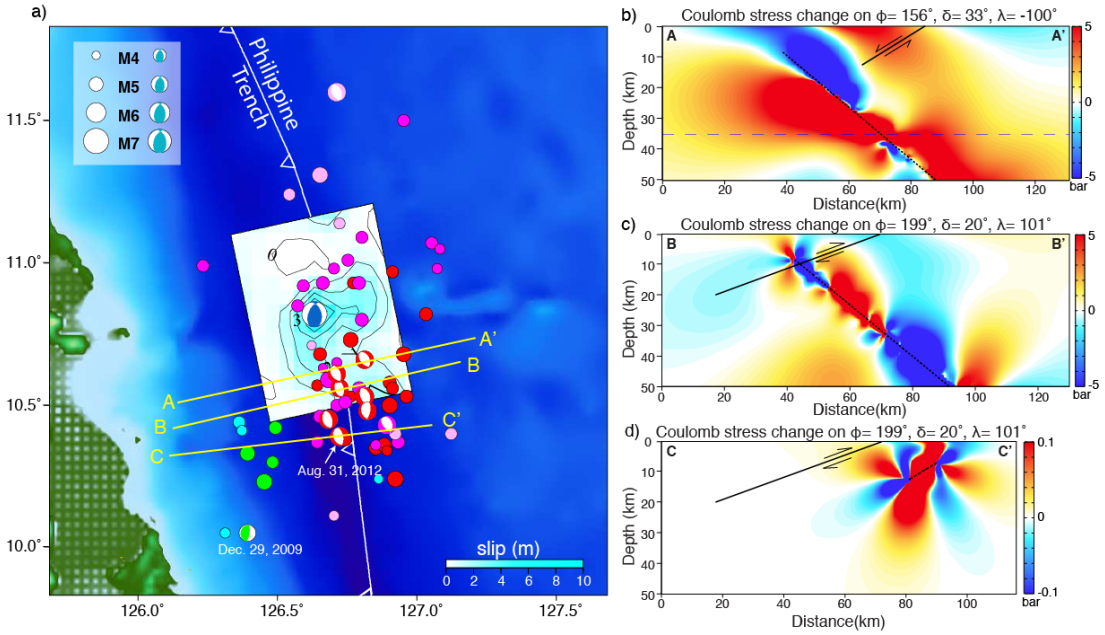

Figure 7.5 a) Map view of the slip model (Fig. 7.3) for the August 31, 2012 Philippine event with aftershock locations from NEIC and PHIVOLCS indicated by dots and GCMT focal mechanisms color-coded as in Fig. 7.4. Positions of three cross-section, AA', BB' and CC', are indicated for which the Coulomb stress changes are computed in vertical profiles. b) Vertical cross section showing Coulomb stress change calculated for the mainshock finite fault model (dotted line) on target normal faults with the GCMT geometry (black solid line) of shallow reference event #1. c) Coulomb stress change calculated for the mainshock finite fault model (dotted line) on target shallow dipping thrust faults with the GCMT geometry of the December 29, 2009 event (black solid line). d) Coulomb stress change calculated for a uniform slip model for the Mw 5.5 normal faulting reference event #1 (dotted line) on shallow dipping thrust faults with the GCMT geometry of the December 29, 2009 event (black solid line).

We compute Coulomb stress changes induced on the shallow normal faulting and interplate thrust faulting geometries that appear active in the aftershock sequence (Fig. 7.5). Figs. 5b,c shows cross sections through the stress change volume calculated for the mainshock

slip model in Fig. 7.3 with target fault geometries corresponding to the two populations of waveforms found in the aftershocks. Fig. 7.5b indicates that several bar increase in driving stress is likely for normal faulting events above the deep thrust event in the vicinity of the observed cluster of normal fault aftershocks. Figure 7.5c indicates that the driving stress on the megathrust produced by the mainshock decreased at depths larger than 10 km, but there may have been about a 1 bar increase in the shallowest part of the megathrust where the observed thrust aftershocks occurred. Comparable stress changes are predicted for a slip model using the alternate mainshock rupture plane, as shown in Auxiliary Fig. 7.A7. The normal faulting at shallow depth involves only small events, but a large number of them occurred, and these should have produced small increases in driving stress (fractional bar increases per event) on the shallow megathrust as well. It is difficult to further characterize the faulting interactions, especially since we are ignorant of the precise aftershock faulting geometries and the ambient stress regimes that the stress perturbations are superimposed on, but this is another clear case of complex faulting interactions in the shallow subduction zone.

7.5 Conclusions

The August 31, 2012, M_w 7.6 earthquake below the Philippine trench is a high energy release thrust-faulting event that ruptured from about 25-55 km deep in the subducting plate offshore of a long-term seismic gap of uncertain seismic potential. The thrust mechanism may indicate strong interplate coupling along the megathrust from 9.5°N-11.5°N, but that possibility requires direct evaluation by geodetic mapping of strain within the upper plate. The long time interval (> 400 years) over which there is no documented larger interplate rupture in this region, combined with the ~5 cm/yr convergence rate, suggest the potential for a great earthquake in this region if it is significantly seismically coupled. The shallow

normal faulting that dominates the aftershock sequence and the triggering of what appears to be very shallow megathrust events represents interaction between different fault systems in the subduction zone, but does not establish whether interplate strain accumulation is occurring.

Acknowledgments. This work made use of GMT and SAC software. Coulomb 3 software produced by S. Toda, R. Stein, J. Lin, and V. Sevilgen was used. The IRIS DMS data center was used to access the seismic data from Global Seismic Network and Federation of Digital Seismic Network stations. We thank two anonymous reviewers for their helpful comments on the manuscript. This work was supported by NSF grants EAR0635570 (T. L.).

7.6 Supplementary Figures

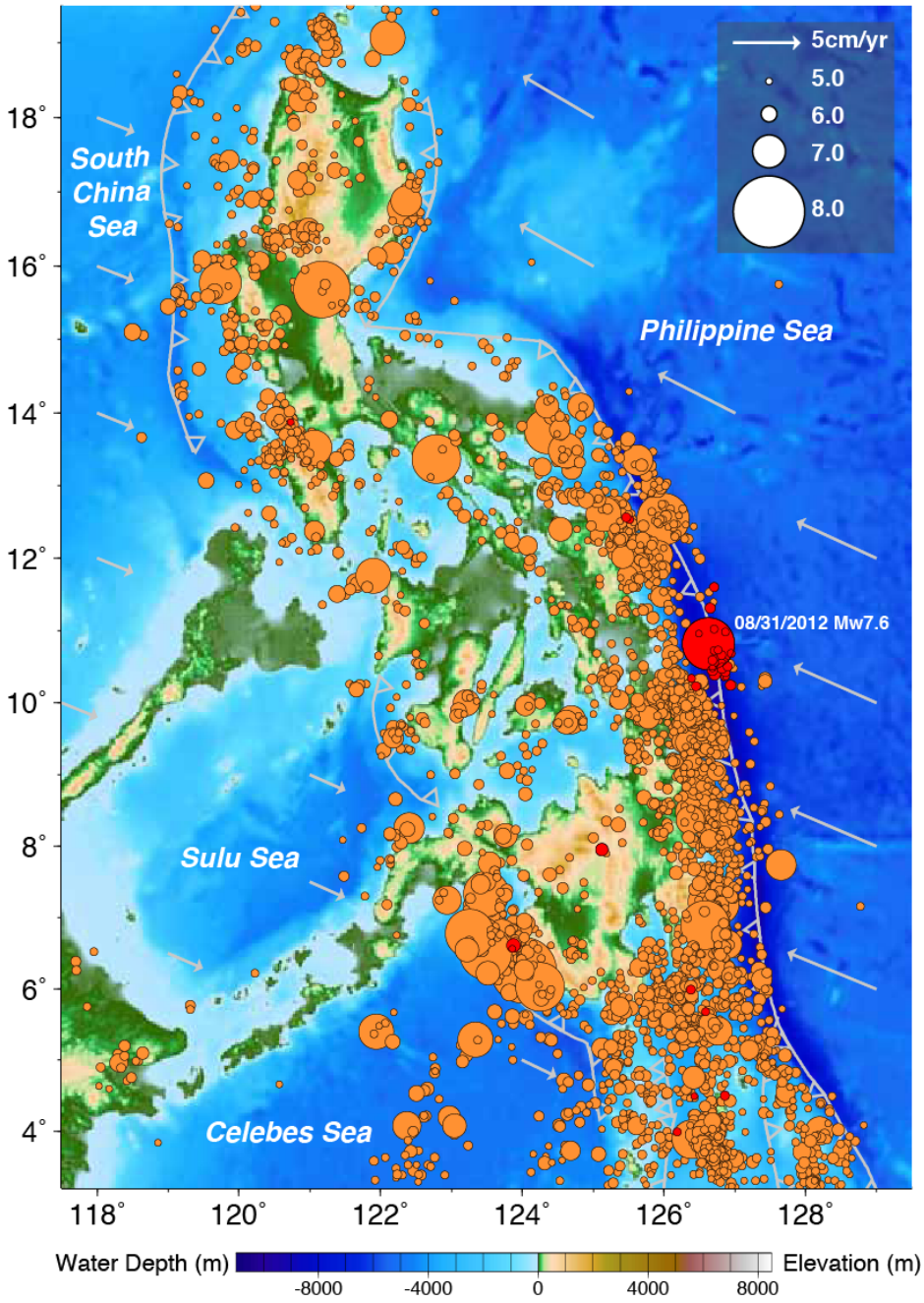

Figure 7.A1 Shallow seismicity around the Philippines with mb ≥ 5.0 between 1973 and 2012 from the NEIC catalog. Earthquakes on and after August 31, 2012 have red symbols. Symbols are scaled with magnitude. The barbed gray curves indicate subduction zones and the arrows show the estimated plate motion directions and rates computed using model GSRM 1.2 [*Kreemer et al.*, 2003 with updates].

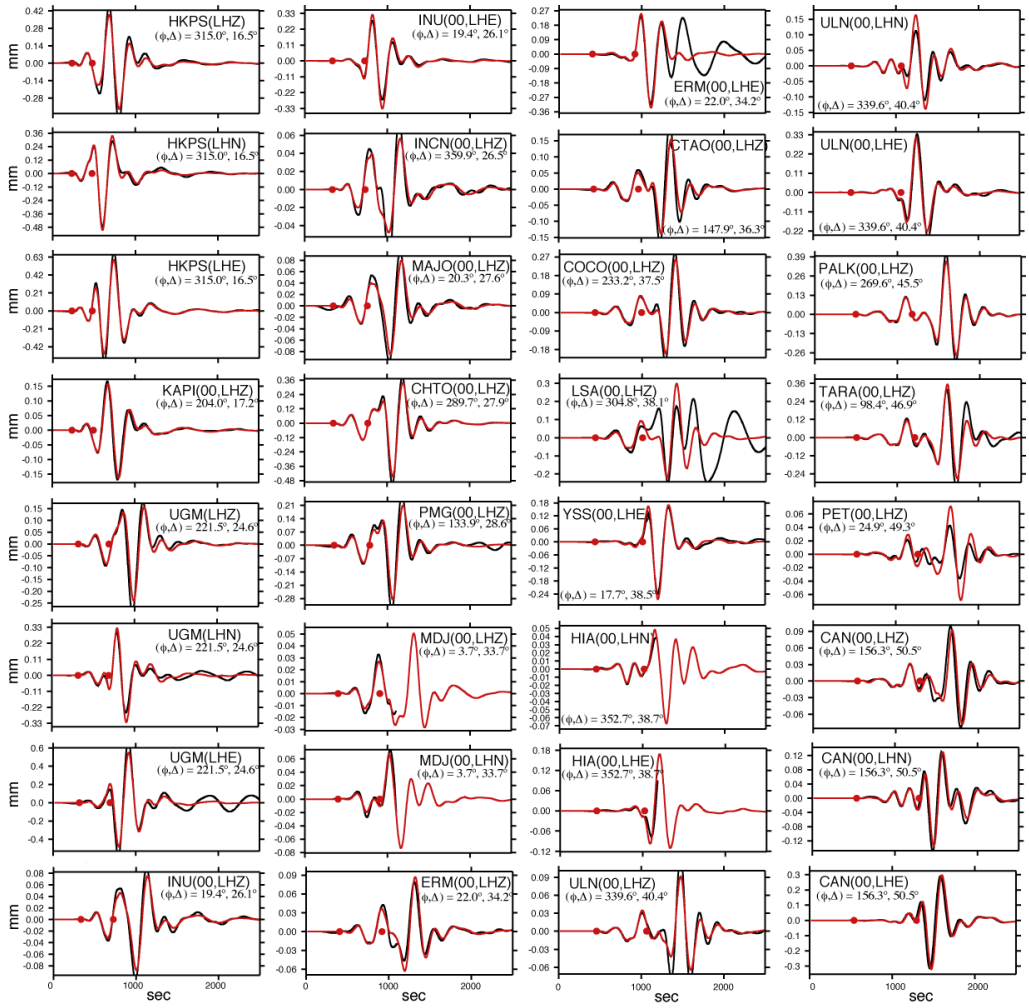

Figure 7.A2 Observed waveforms (black traces) and synthetic waveforms computed for the W phase moment tensor solution (red traces) for the August 31, 2012 Philippine event (Fig. 7.2). The passband is 0.00167 to 0.005 Hz. The station name, component, azimuth (Φ) and epicentral distance (Δ) are indicated. The W phase time window used in the inversion is bounded by red dots. The fit to the fundamental mode surface waves following the W-phase interval is generally good, although some stations clipped or had nonlinear responses during the surface wave arrivals.

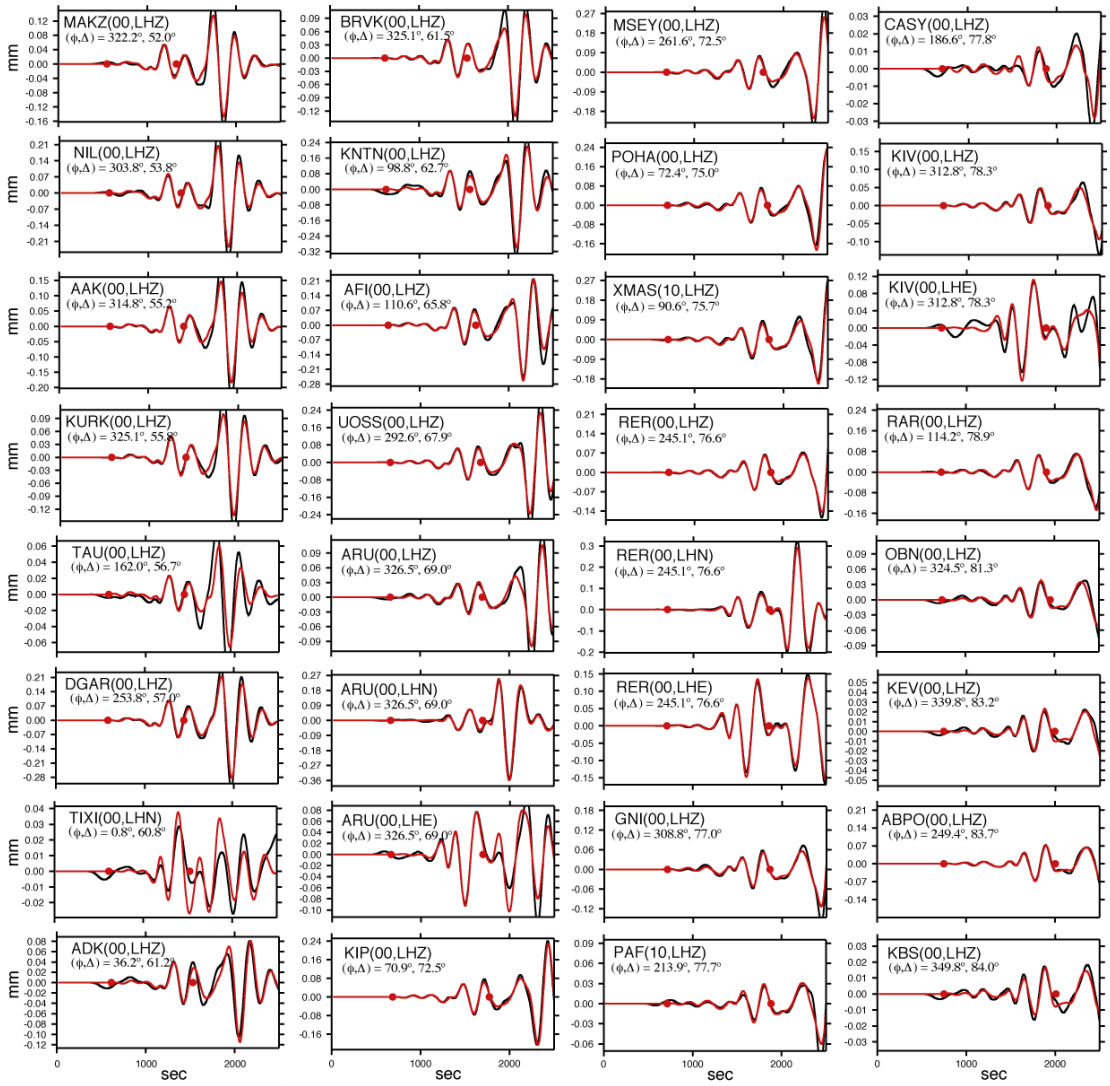

Figure 7.A2. Continued.

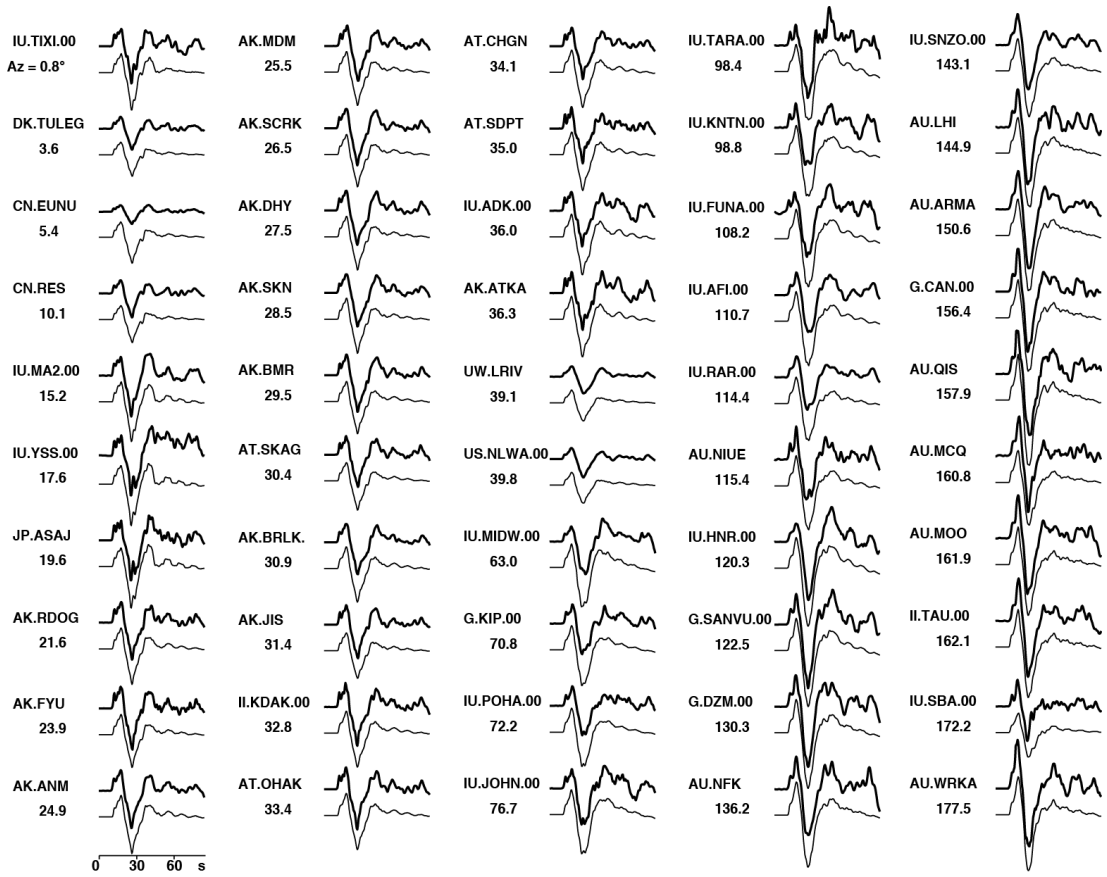

Figure 7.A3 Observed teleseismic P wave vertical ground displacement waveforms (upper bold traces) and synthetic waveforms for the finite fault inversion shown in Fig. 7.3 (lower light traces) for the August 31, 2012 event. There is a 10 s leader before the first P arrivals, and the total time window used in the inversions is 75 s. Globally distributed data in the epicentral distance range of 35°-95° with high signal to noise ratio were used in the slip inversion. The azimuth from the source to each station is shown. All signals are plotted with actual relative amplitudes.

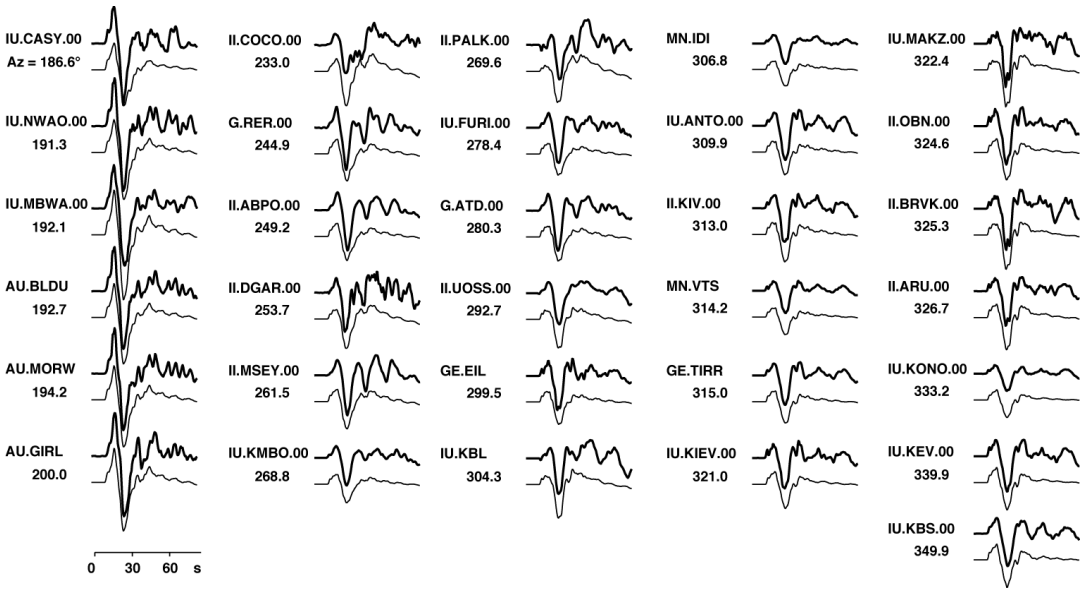

Figure 7.A3. Continued.

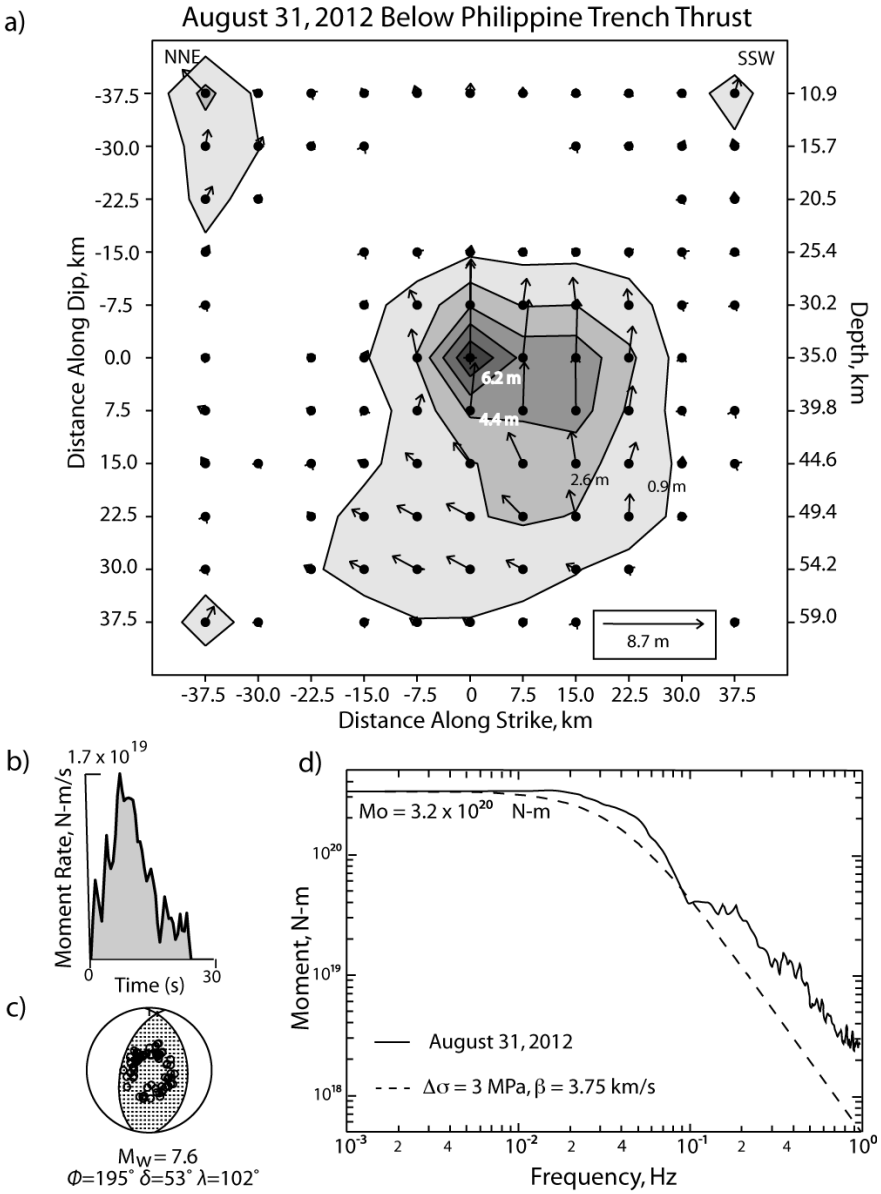

Figure 7.A4. a) Rupture model slip distribution for the August 31, 2012 Philippine event obtained by inverting 81 75-s long teleseismic P wave signals for a fault plane with ϕ= 195° and δ = 53°. The vectors indicate the direction of slip of the hanging wall side of the fault relative to the footwall. b) The ~25 s duration moment rate function for the slip model. c) Average focal mechanism with P wave sampling of the focal sphere. Waveform fits are very similar to those shown in Fig. 7.A3 for the conjugate fault model (Fig. 7.3). d) The average far-field P wave source spectrum is shown by the black line, estimated at frequencies less than ~0.03 Hz from the moment rate function in b) and at frequencies > ~0.03 Hz from stacking of broadband teleseismic P wave spectra. The dashed line is a reference source spectrum for an ω^{-2} model with 3 MPa stress drop, shear velocity, β= 3.75 km/s, and seismic moment given by the W-phase inversion in Fig. 7.2.

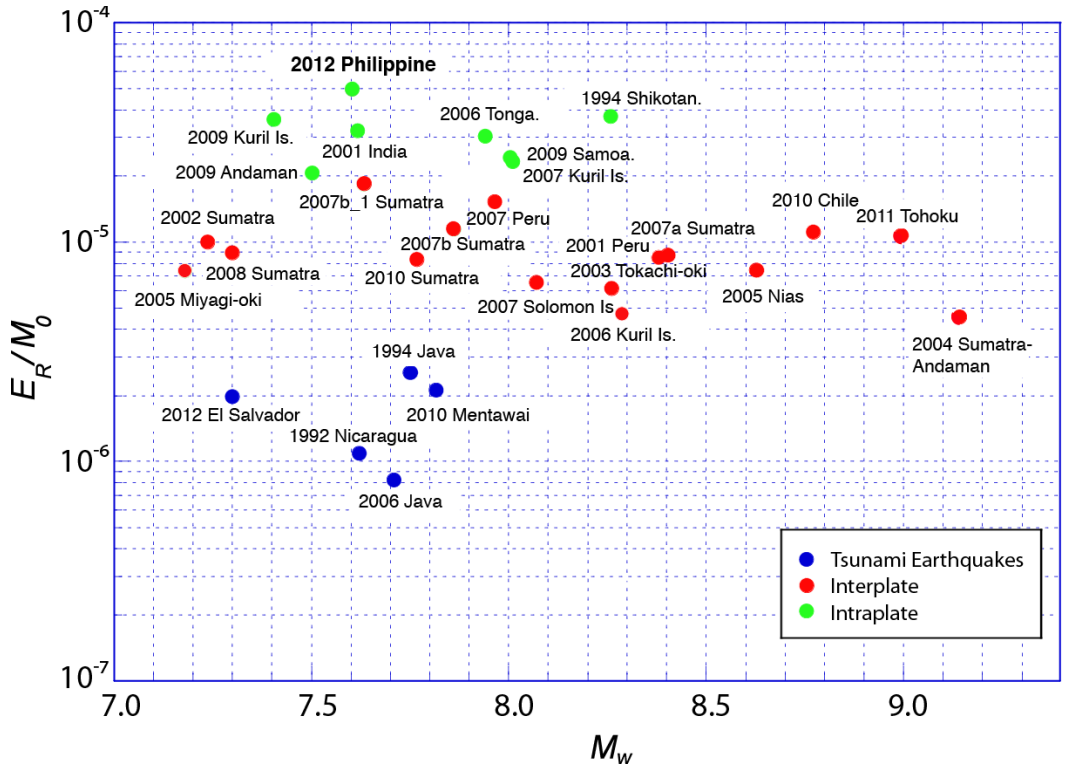

Figure 7.A5. Estimates of radiated seismic energy scaled by seismic moment from teleseismic P wave ground velocity spectra and broadband source time functions from finite-fault source inversions for recent large earthquakes. Color-coded circles indicate the tsunami earthquakes (blue), interplate earthquakes (red) and intraplate earthquakes (green). The August 31, 2012 Philippine event has high moment-scaled energy typical of intraplate ruptures.

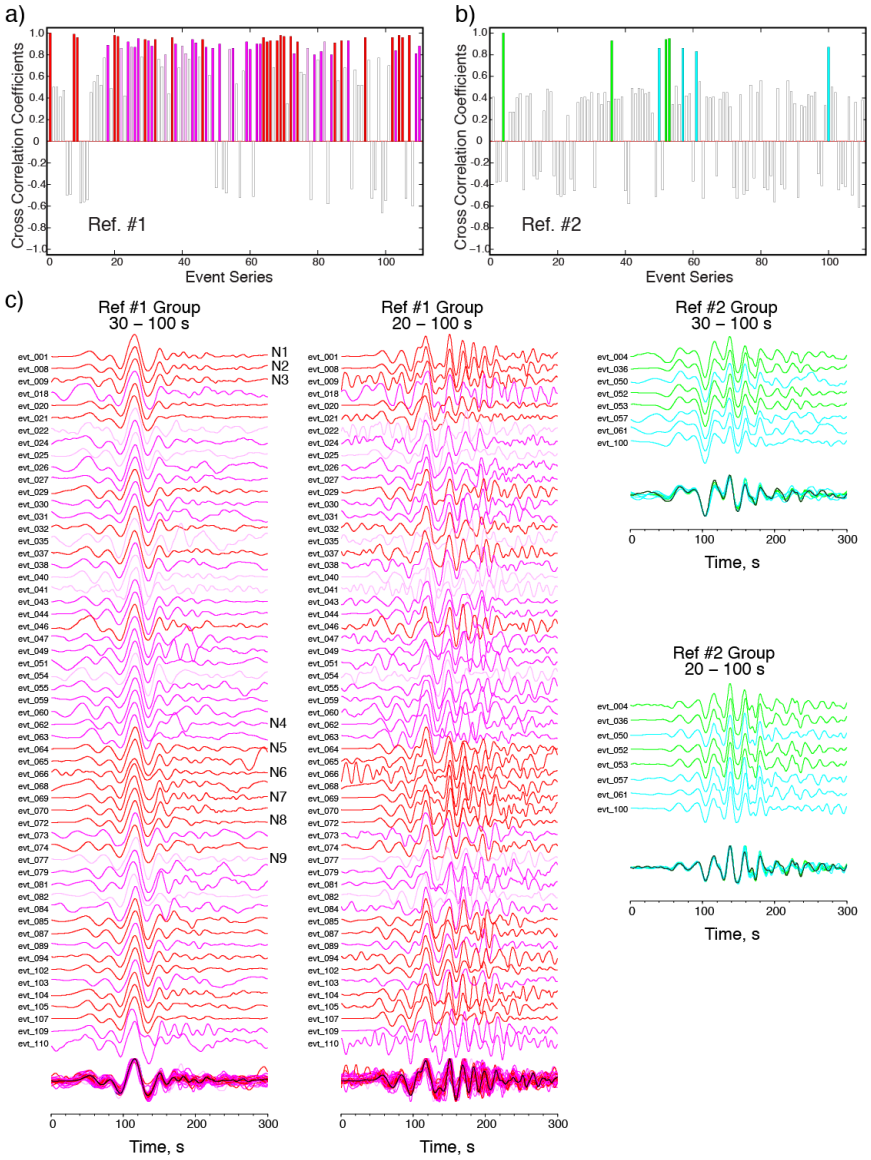

Figure 7.A6. Cross correlation coefficients of DAV waveforms for 300-s long signals with periods of 30-100 s for all aftershocks from August 31, 2012 to September 16, 2012 with mb>4.0 with waveforms for a) reference event #1 and, b) reference event #2. The colors in a) sort the aftershocks into four categories according to red: very high coefficients (≥ 0.9 for 30-100 s and ≥ 0.7 for 20-100 s periods), pink: high coefficients (≥ 0.8 for 30-100 s and ≥ 0.5 for 20-100 s periods), pale pink: intermediate coefficients (≥ 0.8 for 30-100 s waveform, but < 0.5 for 20-100 s waveform) and white: low coefficients (<0.8 for 30-100 s periods), respectively. The colors in b) indicate events with green: very high, bluegreen: high, and white: low correlations. c) Aligned waveforms characterized as similar to reference events #1 and #2 in the 30-100 s and 20-100 s period ranges, along with superimposed traces and average traces at the bottom. Amplitudes were normalized on the peak amplitude. Note the distinct waveform character for the two groups.

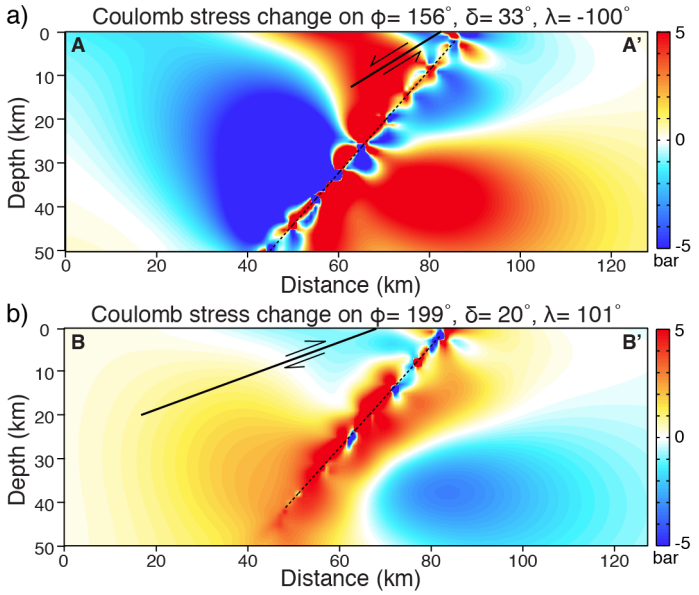

Figure 7.A7. a) Vertical cross section showing Coulomb stress change calculated for the alternate mainshock finite fault model (dotted line) with strike 195° and dip 53° (Figure 7.A4) on target normal faults with the GCMT geometry (black solid line) of shallow reference event #1. The location of cross-section A-A' is the same as in Figure 7.5. b) Coulomb stress change calculated for the mainshock finite fault model (dotted line) on target shallow dipping thrust faults with the GCMT geometry of the December 29, 2009 event (black solid line). The location of cross-section B-B' is the same as in Figure 7.5.

Chapter 8

The 23 June 2014 (M_W 7.9) Rat Islands archipelago, Alaska, intermediate depth earthquake

This chapter has been published as:

Ye, L., T. Lay and H. Kanamori (2014), "The 23 June 2014 Mw 7.9 Rat Islands archipelago, Alaska, intermediate depth earthquake", *Geophys.Res. Lett.*, 41(18), 6389–6395
Ye, L., T. Lay, H. Kanamori, J. Freymueller, and L. Rivera (2015), "Joint inversion of high-rate GPS and teleseismic observations for rupture process of the 23 June 2014 (Mw 7.9) Rat Islands archipelago, Alaska, intermediate-depth earthquake", *Natural Hazards and Plate Boundaries (invited)*, *AGU Book*, in press.

Abstract On 23 June 2014, a large (M_w 7.9) earthquake ruptured within the subducting Pacific plate ~100 km below the Rat Islands archipelago, Alaska. The focal mechanism indicates two possible rupture orientations, 1) on a shallowly dipping fault plane (strike 206°, dip 24°, rake -14°) striking perpendicular to the trench, possibly related to curvature of the underthrust slab, or 2) on a steeply dipping fault (strike 309°, dip 84°, rake -113°) striking parallel to the trench, possibly associated with a slab detachment process. Joint inversion of teleseismic body waves and regional high-rate (1 Hz) GPS recordings indicate a slip zone spanning 50 km x 30 km with a maximum slip of ~11 m on the shallowly dipping plane, or a more distributed slip pattern extending upward to ~70 km, with maximum slip of ~14 m on the steeply dipping plane. Estimated stress drops are 16 to 25 MPa. The radiated energy is ~1.8 x 10^{16} J, and the inferred low radiation efficiency, ~0.1, is compatible with the assumed low rupture velocity, 1.5 km/s. The finite-fault models and aftershocks do not indicate a preferred fault plane. This type of intermediate-depth intraslab faulting can be very damaging

for populated regions above subduction zones such as Japan, Taiwan, Chile, Peru, and Indonesia.

8.1 Introduction

Most large subduction zone earthquakes involve shallow thrust faulting offshore on the plate boundary megathrust fault, producing both shaking and tsunami hazards for nearby regions. However, large intraplate earthquakes also occur in subduction zones, including normal-faulting events near the outer trench slope; the largest known example being the great (M_S ~8.3+) 1933 Sanriku-oki earthquake [e.g., *Kanamori*, 1971]. The shaking and tsunami hazard of these near-trench events is now broadly recognized [e.g., *Lay et al.*, 2009, 2011], although the frequency of occurrence of normal-faulting events remains difficult to quantify [e.g., *Sleep*, 2012].

Less well-recognized are the hazards presented by large intraslab earthquakes at depths of ~70 to 130 km, located below the coastline and volcanic arc. While not usually tsunamigenic, the relatively high stress drops and high moment-scaled radiated energy commonly observed for intraplate events [e.g., *Ye et al.*, 2012] can result in strong ground shaking from these intraslab events. Several great intraslab events have occurred in this depth range (e.g., 4 November 1963 Banda Sea (M_w 8.3) ~120 km deep [*Welc and Lay*, 1987]; 22 June 1977 Tonga earthquake (M_w 8.2) ~96 km deep [*Zhang and Lay*, 1989]; M ~8.1 events on 11 August 1903 beneath Kythira, Greece [*Papadopoulos and Vassilopoulou*, 2001] and 15 June 1911 under the Ryukyu Islands [*Allen et al.*, 2009], 9 December 1950 (M_S 8, M_w 7.9) Antofagasta, Chile earthquake [*Kausel and Campos*, 1992], and an M_w 8.3 event on 17 August 1906 near the Rat Islands, Aleutians [*Okal*, 2005]). Recent examples of damaging events of this type include the ~78 km deep 30 September 2009 (M_w 7.6) Indonesia earthquake which

struck near the city of Padang [e.g., *McCloskey et al.*, 2010], taking more than 1100 lives, and the ~95 km deep 13 June 2005 (M_w 7.8) Tarapaca, Chile earthquake [e.g., *Delouis and Legrand*, 2007]. Comparable size events at these depths have struck beneath Fiji, the Philippines, Hokkaido, Peru, the Solomon Islands, Tonga, and Romania in the past 35 years. Some large population centers such as Taipei, Taiwan and Tokyo, Japan are exposed to risk from this type of intermediate depth faulting [e.g., *Kanamori et al.*, 2012]. Complex internal slab deformation is usually involved in such events, and the seismic hazard framework of these events is not well defined due to their infrequent occurrence and lack of a straightforward tectonic strain accumulation model.

On 23 June 2014, the largest magnitude (M_w 7.9) intermediate depth (70-300 km) earthquake (51.849°N, 178.735°E, 109 km deep, 20:53:09.7 UTC, USGS/NEIC: http://earthquake.usgs.gov/) to strike the Aleutians in ~109 years ruptured within the subducting Pacific slab beneath the Rat Islands archipelago of the Western Aleutians, Alaska (Figure 8.1). Due to the large source depth, the earthquake produced only small tsunami amplitudes of ~2 cm ~300 km to the south at DART (Deep-ocean Assessment and Reporting of Tsunamis) site 21414, and run-ups of up to ~10 to 20 cm were recorded by tide gauges in Alaska and Hawaii (http://ntwc.arh.noaa.gov). While fortunately located below an unpopulated region, this event is representative of the intermediate depth intraslab ruptures that can pose shaking hazards in many subduction zones. Aftershocks spread northwestward from the hypocenter with depths spanning 70 to 140 km and the USGS/NEIC locations indicate about 50 km horizontal extent of the main aftershock zone (Figure 8.2b). Two of the largest early aftershocks are isolated shallow strike-slip events to the west (red focal mechanisms in Figure 8.2b); apparently these are triggered events in the Aleutian arc crust.

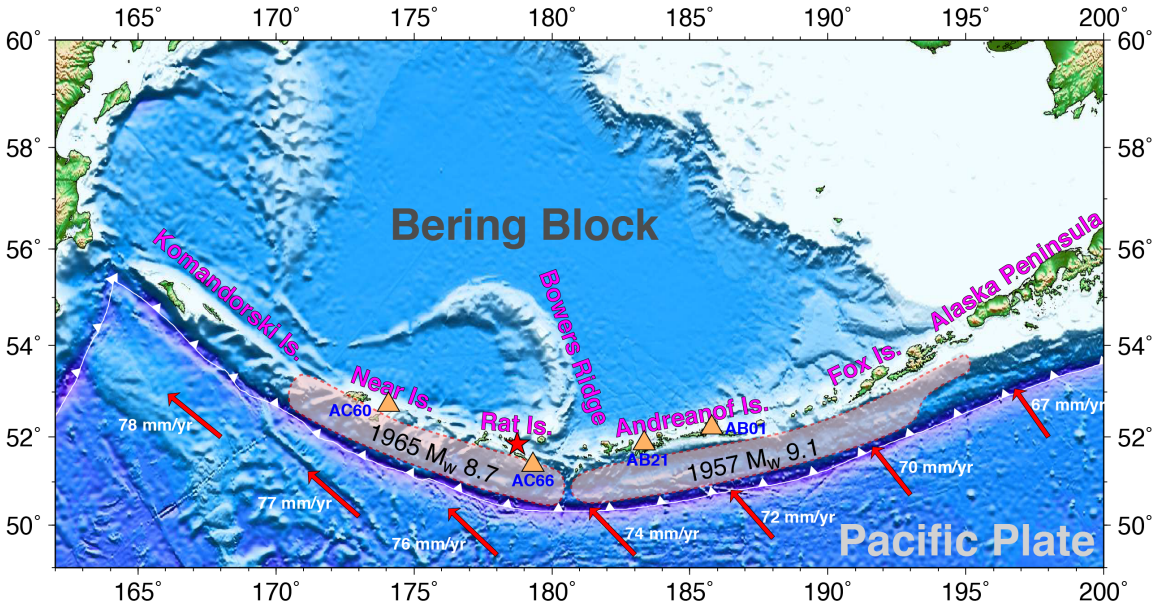

Figure 8.1 Geographic features of the Aleutian island arc and the Bering block around the 2014 M_w 7.9 Rat Islands earthquake (red star) along with the aftershock zones of the 1957 M_w 9.1 and 1965 M_w 8.7 earthquakes [*Sykes et al.*, 1971]. Brown triangles show the location of the four hr-GPS sites used in the joint inversion. The red arrows indicate the motions of the Pacific plate relative to a fixed North America plate (model MORVEL [*DeMets et al.*, 2010]). The Bering block has a westward motion and rotation relative to fixed North America that reduces obliquity of convergence in the Aleutian trench near the Rat Islands.

The 2014 earthquake occurred in the underthrust Pacific slab down-dip of the hypocenter of the great 1965 (M_w 8.7) Rat Islands [*Wu and Kanamori*, 1987; *Beck and Christensen*, 1987] and 17 November 2003 (M_w 7.8) interplate events, west of the bend in the central Aleutian arc at around 180°E (Figures 8.1, 2a). This region has right-oblique relative motion between the Pacific and North American plates at ~75 mm/yr [e.g., *DeMets et al.*, 2010]. However, rotation or westward extrusion of a "Bering block" relative to North America [e.g., *Mackey et al.*, 1997; *Redfield et al.*, 2007; *Cross and Freymueller*, 2008; *Gabsatarov et al.*, 2011] reduces the rate of the right-oblique component and slightly increases the trench-normal convergence rate along the Rat Islands region [e.g. *Carver and Plafker*, 2008]. *Cross and Freymueller* [2008] favor existence of a separate Bering plate, with arc-parallel translation of 4-

8 mm/yr and a variable few mm/yr trenchward component of motion in the western Aleutians. There is evidence for incomplete slip partitioning along the western Aleutians; using the observed rotation of megathrust slip vectors, *Ekström and Engdahl* [1989] estimated that the trench-parallel motion of the arc crust amounted to about 50% of the oblique component of plate motion. This means that the slip vectors for large megathrust earthquakes near the Rat Islands are significantly rotated from both the arc-normal and plate convergence directions (Figure 8.2a). The arc crust in the western Aleutians is also segmented into blocks with rotations that may locally influence slip partitioning [e.g., *Geist et al.* 1988; *Ruppert et al.*, 2012] and interplate coupling [*Beck and Christensen*, 1987]. Strike slip faulting on roughly trench normal faults in the upper plate has been observed in several locations in the arc, and is likely due to block rotation or other internal deformation of the arc [*Ruppert et al.*, 2012]; the shallow aftershocks located well to the west of the mainshock appear to outline one such fault (Figure 8.2b).

Amchitka Pass (at 180°E) is one of the major block boundaries within the arc [*Geist et al.*, 1988], and it is inferred to be a major structural discontinuity. It separates the slip zones of the 1965 M_w 8.7 and 1957 M_w 9.1 megathrust earthquakes [*Johnson et al.*, 1994] (Figure 8.1), and *Geist et al.* [1988] identified it as the transition point between arc blocks that were largely rotating in place and arc blocks that were translating westward due to slip partitioning. *Cross and Freymueller* [2008] found an abrupt increase in the degree of slip partitioning observed by GPS measurements on the arc islands at this location, in contrast to the gradual increase of slip partitioning inferred from the slip azimuths for focal mechanisms of megathrust earthquakes. This led them to propose that the roughly arc-parallel strike slip faults involved in the partitioning were located in the forearc east of Amchitka Pass and crossed into the

backarc at Amchitka Pass. The maximum depth of intraslab seismicity also changes from ~250 km east of Amchitka Pass to ~180 km beneath the Rat Islands [*Engdahl et al.*, 1998].

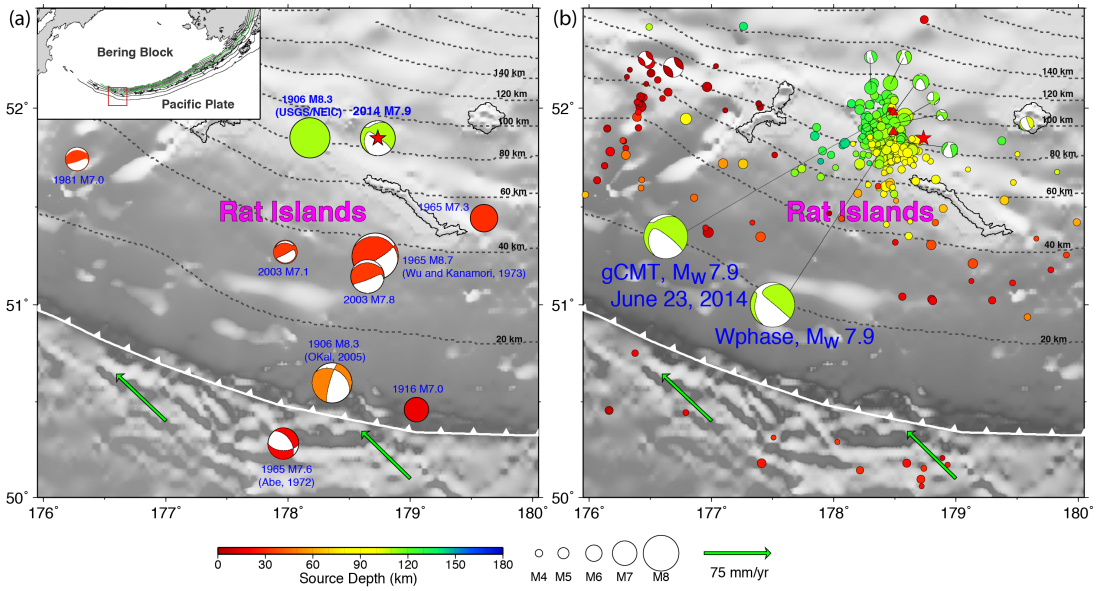

Figure 8.2 (a) Large earthquakes (M ~ 7+) from 1900-2014 in the vicinity of the 23 June 2014 M_w 7.9 Rat Islands archipelago earthquake (red star). Event locations and magnitudes (circles scaled with magnitude and color-coded for depth) are from the USGS/NEIC catalog and focal mechanism solutions from 1976-2014 are global Centroid-Moment Tensor (gCMT) solutions. The focal mechanisms for the 1906 *M* 8.3, 1965 *M* 8.7 and 1965 *M* 7.6 events are from *Okal* [2005], *Wu and Kanamori* [1973] and *Abe* [1972], respectively. The inset locates the source region in the western Aleutian Islands, Alaska, with the slab contours indicates the upper surface of the underthrust Pacific slab from model slab 1.0 [Hayes *et al.*, 2012]. (b) Aftershock sequence (circles) of the 2014 M_w 7.9 Rat Islands archipelago earthquake, color coded with source depth and scaled proportional to magnitude, including available gCMT solutions. The gCMT and W-phase moment tensor solutions for the main shock are shown along with their associated centroid locations (red triangles) relative to the hypocenter from the USGS/NEIC (red star). The barbed curve indicates the position of the Aleutian trench. The green arrows indicate the highly oblique motion of the Pacific plate relative to a fixed North America plate (model MORVEL [*DeMets et al.*, 2010]).

The 17 August 1906 M_w 8.3 earthquake hypocenter is located near the 2014 event in the ISC-GEM catalog [http://www.isc.ac.uk/iscgem/; *Storchak et al.*, 2013], but relocation by *Okal* [2005] shifts it to the south (Figure 8.2a). The 1906 focal mechanism estimated by *Okal* [2005] has a steeply dipping plane with strike perpendicular to the arc (Figure 8.2a); plausibly

this may have been a slab-tearing event. The data are very limited, so the location, magnitude and focal mechanism have substantial uncertainty, but *Okal* [2005] suggests that the presence of the Bowers ridge in the upper plate near 180°E (Figure 8.1) may contribute to strain accumulation and tearing of the subducted slab through collision of the ridge system with the subduction zone.

The 2014 event is the largest intermediate depth event in the Aleutian slab for which extensive geophysical recordings can be used to investigate the source process. This study was motivated by availability of ground motion records from nearby high-rate (1Hz) GPS (hr-GPS) stations along the arc (Figure 8.1) and by ambiguity of faulting geometry in an initial teleseismic-only investigation of the source process [*Ye et al.*, 2014]. Few intermediate depth events have been large enough to be well observed with GPS displacements, and even fewer have had hr-GPS data available. By combining the regional hr-GPS data and teleseismic data, we will improve characterization of the slip distribution for this earthquake, although specification of the fault plane remains uncertain.

8.2 Rupture Analysis

8.2.1 Long-period point-source solutions

Point-source moment tensors for the 2014 Rat Islands earthquake obtained from long-period seismic wave inversions have consistent, predominantly double-couple, source mechanisms with centroid locations about 50 km to the west of the USGS/NEIC hypocenter (Figure 8.2a). The global Centroid-Moment Tensor (gCMT) solution (http://www.globalcmt.org/CMTsearch.html) has best double-couple nodal planes with strike f_f = 207°, dip d = 27°, rake l = -13°, and strike f_f = 309°, dip d = 84°, rake l = -117°, a centroid depth of 104.3 km, a centroid time shift of 24 s, and a seismic moment M_0 = 9.7 x

10^{20} Nm. We performed a moment tensor inversion of 1 to 5 mHz passband W-phase signals. W-phase inversions provide stable focal mechanisms with little dependence on the earth model [*Kanamori and Rivera*, 2008]. We use 132 ground motion recordings from 58 stations, obtaining a solution with best double-couple nodal planes with ϕ_f = 205.9°, δ=23.6°, λ= -14.1° and ϕ_f = 308.8°, δ =84.4°, and λ= -113.0°, a centroid depth of 100.5 km, a centroid time shift of 22.9 s, and M_0 = 1.0 x 10^{21} N m. These long-period solutions both give M_w 7.9, and both have a null axis striking close to the Pacific-North America relative plate motion direction (Figure 8.2b), representing either sub-horizontal or nearly vertical shearing of the slab.

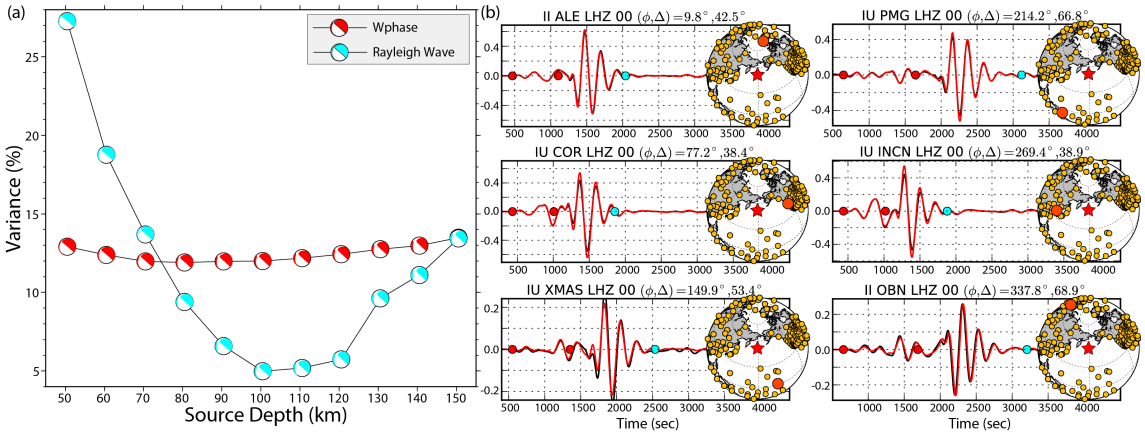

Figure 8.3 (a) Residual waveform variance of W-phase inversions (red focal mechanisms) using three-component observations in the period range 100-600 s for varying assumed source depths for the 2014 Rat Islands earthquake. The cyan focal mechanisms show the residual waveform variance for predicted vertical component Rayleigh waves in the period range 100-600 s for the W-phase solution at each source depth. (b) Example W-phase (waveform intervals between red dots) and Rayleigh wave (waveform intervals between second red dot and cyan dot) observations (black traces) and computed waveforms (red traces) for the point-source moment tensor solution at 100.5 km for the 2014 Rat Islands earthquake. The maps indicate the position of each station (red dots) among the total set of stations (gold dots) used in the corresponding W-phase inversion. Comparable waveform matches are found for all of the stations indicated in the maps.

There is limited resolution of centroid depth for the long-period W-phase inversions (Figure 8.3a). However, there is greater sensitivity to depth for the fundamental mode Rayleigh waves that arrive after the W-phase window. Figure 8.3a shows the residual

waveform variance of observed minus predicted vertical component Rayleigh wave displacements for a frequency band of 1.667 to 10 mHz for the W-phase inversion solution in the same bandwidth at each target source depth. We compute this for the time window from the end of the W-phase window to the 2.3 km/s group velocity arrival time (cyan dots in Figure 8.3b). Note the excellent prediction of the Rayleigh waveforms for the 100 km deep source. PREM [*Dziewonski and Anderson*, 1981] is used in these calculations, but for frequencies lower than 10 mHz only small propagation errors due to neglecting aspherical Earth structure are expected for the propagation distances less than 90° used in the inversion. Point-source depths around 100 to 110 km give the best fits to the long-period Rayleigh waves (Figure 8.3a), compatible with the long-period inversion centroid estimates.

Non-double-couple components caused by superposition of subevents with different double-couples have often been observed for large intermediate-depth and deep earthquakes [e.g., *Kuge and Kawakatsu*, 1992]. The long-period moment tensors for the 2014 Rat Islands event do not have significant non-double-couple components, but the body waves do have weak early amplitudes for about 15 s, raising the possibility of some initial mechanism change. To evaluate this, we applied multiple point-source iterative deconvolution [*Kikuchi and Kanamori*, 1991] to teleseismic body waves filtered in the frequency band of 0.005 to 1 Hz. The largest moment subevents from this inversion have mechanisms similar to the long-period best double-couple solutions and locate ~45 km to the west from the hypocenter, consistent with the centroid locations from the gCMT and W-phase inversions, and with short-period P wave back-projection images [*Ye et al.*, 2014]. The iterative inversions do not fit the first 15 s of low amplitude P wave ground motions very well and variable mechanisms are found for small subevents, but these are not very stable and are influenced by precise alignment of the weak P wave onsets. A W-phase inversion of the first 15 s of long-period

ground motions yields a focal mechanism that is close to the overall solution. Overall, it is hard to resolve any change in mechanism during the rupture, or to identify complexity such as en echelon faulting with similar orientations, so we will proceed to model the rupture using single fault planes, acknowledging that there is a possibility of more complex faulting, particularly in the early phase of the rupture.

8.2.2 Back-Projection Analysis

Back-projections of teleseismic P wave recordings from large networks of stations in Japan (Hi-net), Europe (EU), Australia and the South Pacific (AU), and North America (NA) were performed using the method of Xu et al. [2009]. The four networks all indicate 50 to 100 km westward rupture propagation over an interval of about 40 s, as shown by time-integrated maps of the coherent short-period energy release in the passband 0.5-2.0 s (Figure 8.3).

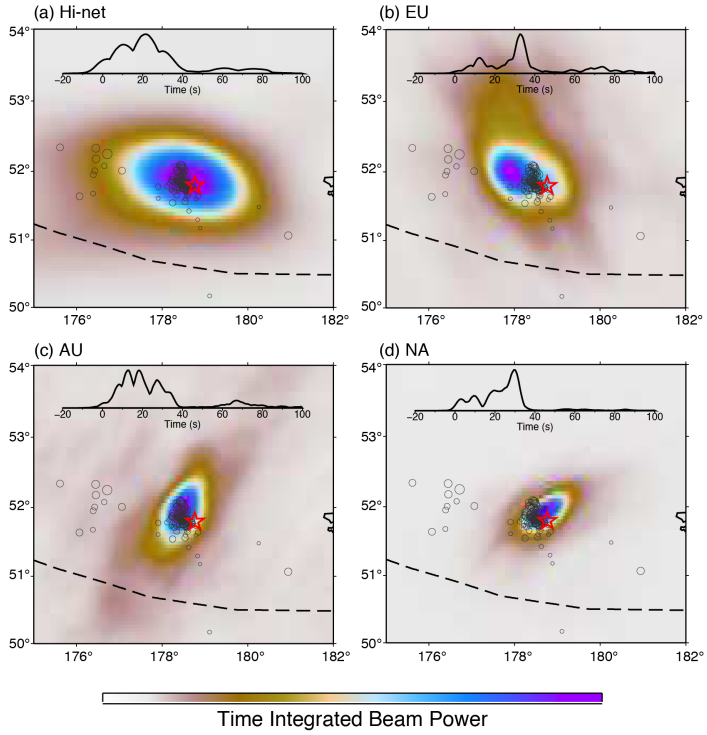

Figure 8.4 Imaged locations of coherent short-period seismic energy release from the 2014 Rat Islands archipelago earthquake obtained by backprojection of teleseismic P wave recordings in the period range of 0.5 to 2.0 s from networks of (a) Hi-net stations in Japan, (b) broadband stations in Europe (EU), (c) Australia and South Pacific (AU), and (d) North America (NA). The time-integrated normalized beam power for each back-projection is shown with the color scale ranging from zero (white) to 1.0 (purple). The peak beam amplitudes as a function of time are shown at the top of each panel.

The slightly west-northwestward distribution of energy release corresponds with the distribution of aftershocks in the first ten days after the event. Array response artifacts smear the images slightly along the great-circle directions to the networks, and there is no direct resolution of depth-extent of the rupture from this method. However, indications of modest north-south broadening of the rupture are apparent in the animations, which slightly favors the shallow-dipping nodal plane. The limited spatial resolution does not tightly bound the rupture velocity (the apparent horizontal rupture expansion rate appears to be on the order of 1.5 km/s), but all the images favor a modest horizontal extent of the rupture zone, which indicates a low apparent horizontal rupture expansion velocity.

8.2.3 Finite-Fault modeling

Guided by the long-period point-source solutions, we determine finite-fault rupture models for the 2014 Rat Islands earthquake by joint inversion of teleseismic body waves and regional hr-GPS (1 Hz) recordings, including long time averaged estimates of their static displacement offsets. We use the least-squares kinematic inversion method with positivity constraint for specified fault geometry, constant rupture expansion velocity (V_r), variable subfault rakes, and subfault source time functions parameterized by several overlapping triangles developed by *Hartzell and Heaton* [1983] and *Kikuchi and Kanamori* [1991].

The teleseismic P and SH waves used in the inversion are the same as those analyzed by *Ye et al.* [2014]. These include ground displacements for 63 P waves and 49 SH waves, filtered in the frequency band 0.005 to 1 Hz.

Regional ground motions were recorded at four GPS stations, AC60, AC66, AB21, and AB01 (Figure 8.1), along the Aleutian arc. Site AC66 is only ~60 km eastward from the USGS/NEIC epicenter, and provides sensitivity to absolute location of the faulting. Daily

positions were estimated in the ITRF2008 reference frame using the GIPSY-OASIS software in point positioning mode [*Zumberge et al.*, 1997], following the analysis methods described in *Fu and Freymueller* [2012]. The three-component co-seismic static offsets for all four stations are obtained by the difference of the average daily positions for 5 days before and 5 days after the earthquake, skipping the day of the earthquake (we call these the final static offsets to distinguish them from static offsets estimated from the hr-GPS solutions after passage of the seismic waves). These offsets may include minor afterslip contribution, but comparison with the hr-GPS estimates indicates that any such contribution is small. AC66 subsided 3.3±0.2 cm and AC60 showed 0.6±0.2 cm subsidence. AB01 also shows subsidence but this may be short-term noise, as a longer time series shows no systematic offset at the time of the event; horizontal displacements at this site are within 1 sigma of zero. Horizontal motions at AC66 are 3.6±0.1 cm to northwest, and at AC60 are 1.7±0.1 cm to the west. AB21 shows small SE-directed motion but has a very low signal-to-noise ratio.

The hr-GPS solutions with 1 s time sampling were obtained using a kinematic Precise Point Positioning (PPP) approach following the methods described in *Ding et al.* [2015]. We used the GIPSY software with very similar models as in the static processing, except that we used the JPL high rate clock products interpolated from 30 s to 1 s sampling, and estimated the station positions with a random walk noise model. The hr-GPS solutions for this event have slightly higher noise levels than the solutions of for the 2013 Craig earthquake [*Ding et al.*, 2015], perhaps because the remote location relative to sites used in JPL's global orbit and clock solution. Estimates of the static offsets from the hr-GPS kinematic solutions have a noise level of about ±1 cm due to oscillatory variations seen in the solutions after the passage of the seismic waves. By comparing the final static offset estimates and the offsets several minutes after the origin in the hr-GPS solutions, along with assessing the signal to noise character of

each component, we assign different weights to the GPS data for the joint inversions. Among the GPS observations, both hr-GPS signals and static offsets of the NS and EW components at sites AC60 and AC66 (which have amplitudes of several cm), and the vertical static offset at site AC66 are given full weight; and the EW components (hr-GPS and static offset) at more distant sites AB01 and AB21, are given a lower weight (about one third), in the joint inversions. The other components, which have too little signal, are not used in the joint inversion, although we show comparisons of all observed data with the inverted model predictions. The estimated models do predict near-zero static displacements for these remote sites, even though the data were not included in the inversion.

The Green's functions for both teleseismic and GPS modeling are computed for a structural model with a simple 34.5 km thick crust with 0.5 km thick low-velocity sedimentary layer from Crust 2.0 model [*Bassin et al.*, 2000] underlain by PREM mantle structure. Complete ground motion Green's functions including time-varying and static offsets for the regional hr-GPS signals are computed using a frequency-wavenumber (F-K) integration method [Computer Programs in Seismology, Robert Herrmann; *Hermann, 2013*]. We low-pass filter the observed hr-GPS signals and the Green's functions with a single-pass Butterworth filter with a corner of 0.05 Hz to eliminate wave energy that cannot be well-modeled with a 1D structure. Given that the crustal structure is uncertain, we also perform inversions using the PREM structure for both crust and mantle, finding negligible differences in modeling the hr-GPS and static offsets from the local crustal structure used.

The data lack strong directivity effects, making it difficult to resolve the rupture velocity. Based on our earlier investigation with back-projection imaging and body wave inversion [*Ye et al.*, 2014], we adopt a rupture expansion velocity of 1.5 km/s. The subfault source time functions are parameterized by three overlapping triangles with 3 s rise time and 3 s time

shifts, giving 12 s possible subfault source durations. The rupture expansion velocity defines the initiation time of the first triangle for each subfault, which need not be activated in the inversion, allowing for a variable actual rupture velocity. We modify the teleseismic body wave inversion code to include the weighted hr-GPS signals and static displacement offsets, and add a constraint to minimize the difference of the inverted total seismic moment from the long-period seismic moment estimate (~1.0 x 10^{21} Nm). The effect of the seismic moment constraint is small for this event. The teleseismic data, regional hr-GPS signals, and static offsets are relatively weighted by balancing signal power contributions of the observations and the coefficient matrix used to assign the relative weight of each data set. We empirically explore modifications of the relative weighting, but given the limited number of GPS observations and the good fits obtained across the suite of data, the precise relative weighting of data sets is not too important in this case. Given that there is no strong constraint to favor either possible fault plane from the seismological data or aftershock locations [*Ye et al.*, 2014], finite-fault inversions for both nodal planes from our W-phase inversion are performed.

The regional hr-GPS ground motions at site AC66 provide valuable constraints on the absolute placement of the fault geometry due to the proximity of the station. This is particularly the case for the steeply dipping fault plane choice, as there is limited horizontal fault width extent and small variation of up-going radiation pattern to AC66. Figure 8.5 shows waveform predictions for the NS and EW components at AC66 for joint inversions of all data using steeply dipping fault planes with hypocentral locations shifted along SW-NE offsets from the USGS/NEIC hypocenter. Models with the initial rupture location at the USGS/NEIC hypocenter (Model B) or shifted northeastward (Model A), can not match the early motion on the NS component, or the entire EW motion at AC66, and there are strong mismatches of the final static offsets as well. This could be interpreted as favoring the

shallowly dipping fault plane choice, as the AC66 fits are much better for that option for corresponding hypocenters, but the absolute location of the USGS/NEIC hypocenter is subject to bias due to slab structure, which should tend to pull the hypocenter estimate in the down-dip (northeastward) direction. We explore modest hypocentral shifts to the southwest to evaluate whether the signals at AC66 can be reconciled with the steeply dipping fault plane choice. There is progressive improvement in the prediction of both hr-GPS recordings and static offsets at AC66 as the hypocenter (and rupture plane) shifts to the southwest, and very good agreement is obtained for shifts larger than ~20 km (Models D and E).

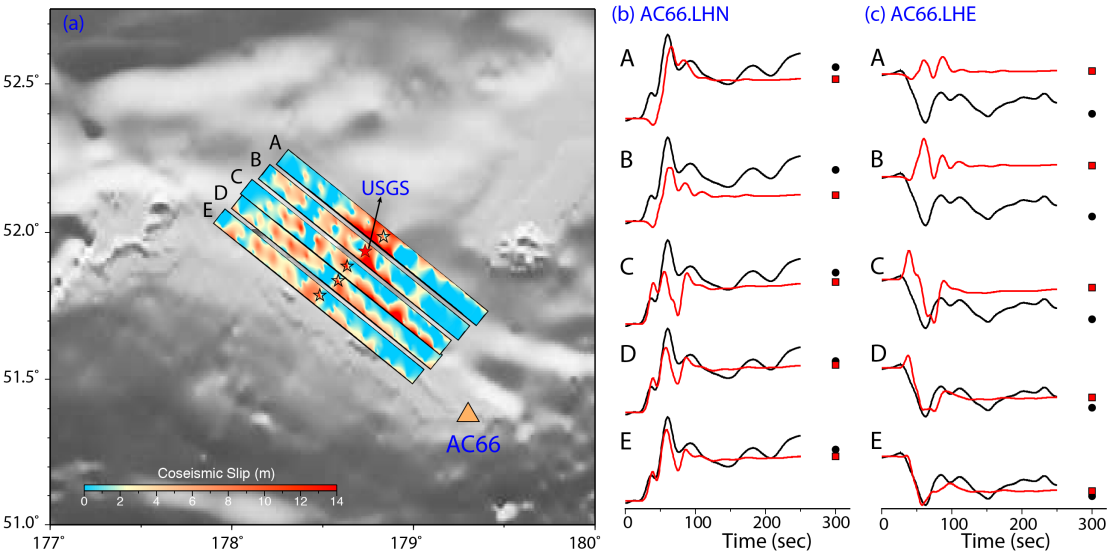

Figure 8.5 (a) Map view of five inverted slip distributions, A-E, using the steeply dipping fault plane for the 2014 Rat Islands earthquake with shifted hypocentral locations (stars), for joint inversions of teleseismic body-waves, hr-GPS observations, and static displacement offsets (e.g. Figure 8.8). The red star shows the epicenter location from the USGS/NEIC catalog. Model E is the slip model on the steep fault plane shown in the Figure 8.9. The position of local hr-GPS station AC66 is indicated by the orange triangle. (b) Comparisons of the observed north-south (LHN) and east-west (LHE) hr-GPS observations at station AC66 (black traces) and predicted waveforms (red traces) for slip models A-E. The black dots and red squares indicate the corresponding observed (daily averaged) and predicted static displacement offsets.

To systematically explore the spatial sensitivity to the precise fault positioning for different

data sets, we perform finite-fault joint inversions for different assumed hypocentral locations over a 0.05°-spaced grid of longitude and latitude positions around the USGS/NEIC epicenter for both choices of fault plane. Figures 8.5a and 5b show that the teleseismic body waves can be well fit in joint inversions with either shallowly or steeply dipping fault plane with almost no resolution of the placement of the fault. The shallowly dipping fault inversions can fit both hr-GPS signals and static offsets very well with epicenters close to the USGS/NEIC location or slightly to the west (Figure 8.6a), so the total waveform misfit does not favor a specific hypocentral location for the shallowly dipping plane. On the other hand, there is an abrupt spatial change in the residual misfit for the hr-GPS and static offsets for the steeply dipping fault solutions (dominated by the fit to station AC66), as expected given the results in Figure 8.5. Shifts of the hypocenter of more than 15 km are required for the fit to the GPS data to be acceptable.

Some regional short-period P arrivals at stations along the east-west trending island arc were used in the USGS/NEIC hypocenter location, so the error in the hypocenter is expected to be fairly small, but hypocentral depth and position can still trade-off and are subject to errors from the velocity model and non-uniform coverage. For our final models we adopt a hypocenter (red circles in Figure 8.6) ~25 km SW of the USGS/NEIC solution for both fault planes, as this gives good matches for all data sets. Given that the steep plane can only fit the data well if the hypocenter is shifted from the USGS/NEIC location, a more accurate relocation using a 3-D velocity model might be able to rule out the steep plane if it can rule out this location. There is slightly better fit for the shallowly dipping fault plane if we use a hypocenter depth of 95 km, compared to the USGS/NEIC hypocentral depth of 109 km, while we have similar fits for the steeply dipping fault using hypocenters at either 95 km or 109 km. The finite-fault inversion centroid depths vary with assumed hypocentral depth for

both fault planes (Figure 8.6c), and we find better agreement with the long-period seismic wave centroid estimates if adopt 95 km and 109 km hypocentral depths for the shallowly and steeply dipping faults, respectively.

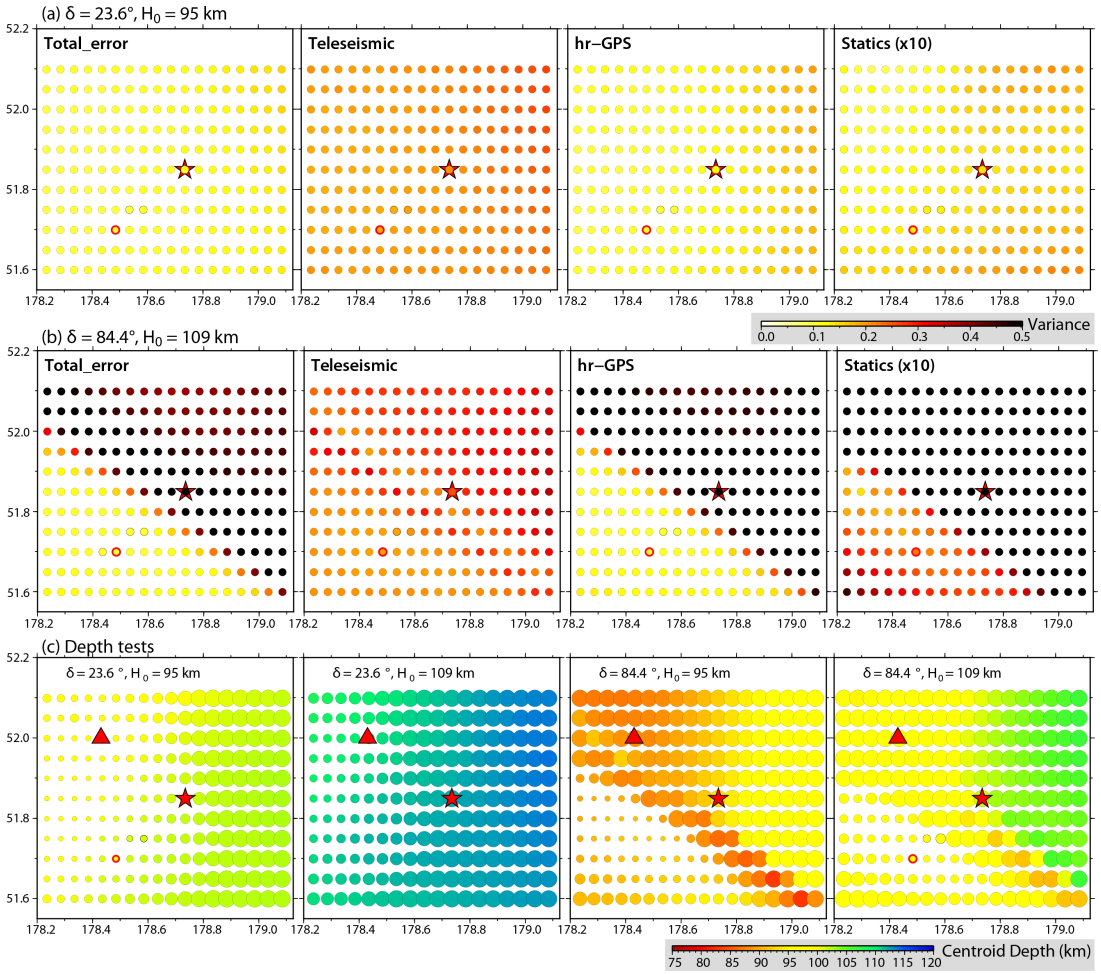

Figure 8.6 Spatial plots of residual waveform misfit of teleseismic body wave, hr-GPS, static offset, and all three data sets together (total) for inverted slip models using different assumed hypocentral locations (each point) on (a) the shallowly dipping fault plane with hypocentral depth 95 km and (b) the steeply dipping fault plane with hypocentral depth 109 km. (c) The centroid depth for the finite fault models for the shallowly dipping (dip, δ= 23.6°) and steeply dipping fault planes (δ = 84.4°) with hypocentral depths of 95 km or 109 km at different initial locations. The radius of the circles is scaled with the total residual waveform misfit, saturated with variance of 0.12. The red stars and triangles show the epicentral location from the USGS/NEIC catalog and the centroid location from gCMT catalog, respectively. The circles outlined in red highlight the selected models shown in Figure 8.7 and Figure 8.9, with initial location ~25 km SW of the USGS/NEIC epicenter.

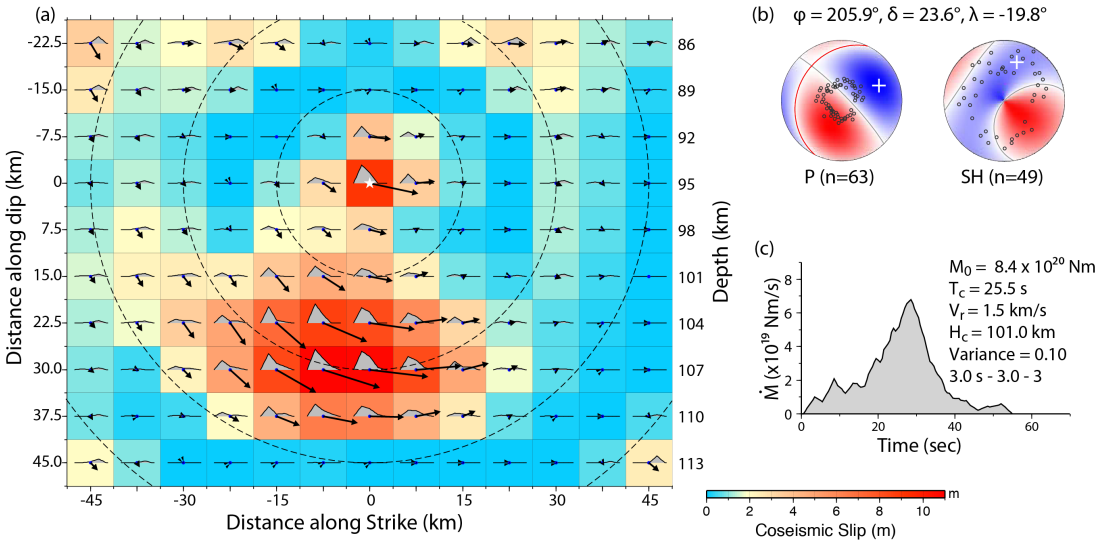

Figure 8.7 Finite-fault slip model for the shallowly dipping fault plane from the joint inversion of teleseismic body waves (P and SH), hr-GPS and static displacement offsets for the 2014 M_w 7.9 Rat Islands earthquake. The slip distribution on the fault plane is shown with the arrows indicating average rake of each subfault, and slip magnitude being color-coded. A rupture expansion velocity of V_r = 1.5 km/s is used, and the isochrones for the expanding rupture front in 10 s increments are indicated by the dashed circles. The moment-rate function, seismic moment, centroid time shift (T_c) and the average focal mechanism for each fault segment are shown, with lower hemisphere equal area projections indicating the positions sampled by teleseismic P and SH waves used in the inversions. Observed and synthetic waveform comparisons are shown in Figure 8.8.

The finite-fault model from joint inversion using the shallowly dipping plane with a hypocentral depth of 95 km and the 25 km offset location is shown in Figure 8.7, with observed and predicted seismic and GPS signals shown in Figure 8.8. The finite-fault model from joint inversion using the steeply dipping plane with a hypocentral depth of 109 km and the 25 km offset location is shown in Figure 8.9, with corresponding signal comparisons in Figure 8.10. The moment rate functions are similar for both solutions, with a relatively low amplitude interval for ~15 s followed by a large triangular pulse with about 25 s duration. The slip distribution on the shallowly dipping plane (Figure 8.7) has about 9 m slip near the hypocenter and a 30 km x 20 km patch of large slip centered about 25 km downdip (toward the northwest), with peak slip of ~11 m. The gap in slip between the hypocenter and the main

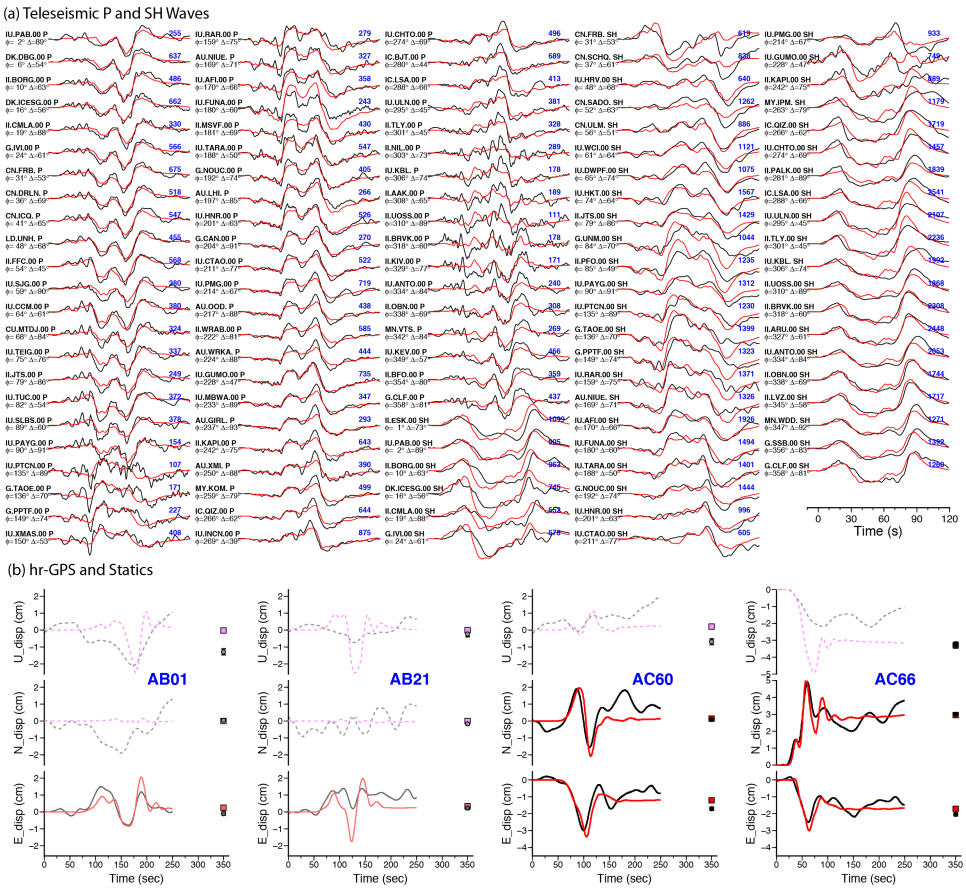

Figure 8.8 Comparison of (a) observed (black) and synthetic (red) P and SH ground motions and (b) 1-Hz high-rate GPS ground motions and static displacement offsets for the selected rupture model on the shallowly dipping fault plane shown in Figure 8.7. For each station in (a), the azimuth from the source (ϕ) and epicentral distance (Δ) are indicated, along with the peak-to-peak ground motion in microns (blue numbers). The observed signal amplitudes are normalized. The red curves are true relative amplitude synthetic waveforms. For GPS observations in (b), both hr-GPS and static offsets of the NS and EW components at sites AC60 and AC66, and the vertical static offset at site AC66 have been given full weight in the joint inversion; and the EW component (hr-GPS and static offset) at more distant GPS sites, AB01 and AB21, have been given a low weight (about one third), in the inversion. The dashed black and purple curves show the other observed and forward modeled GPS observations, which are not used in the inversion, due to the low signal-to-noise ratio.

slip patch is consistently found for inversions with the shallowly dipping plane. The subfault source time functions within the region of significant slip activate at the rupture expansion velocity time, so it is an actual rupture velocity. The waveform matches in Figure 8.8 are quite good for P and SH waves apart from some of the early low amplitude P arrivals and the nodal P waveforms at azimuths to the southeast and northwest (along the slab strike). The

EW motions at GPS sites AB01 and AB21 are fit adequately and good fits are found for the horizontal motions at AC60 and AC66, along with the vertical static offset at AC66. As indicated by Figure 8.6a, comparable waveform matches are found for hypocentral locations at or around the USGS/NEIC location, so this solution is quite stable.

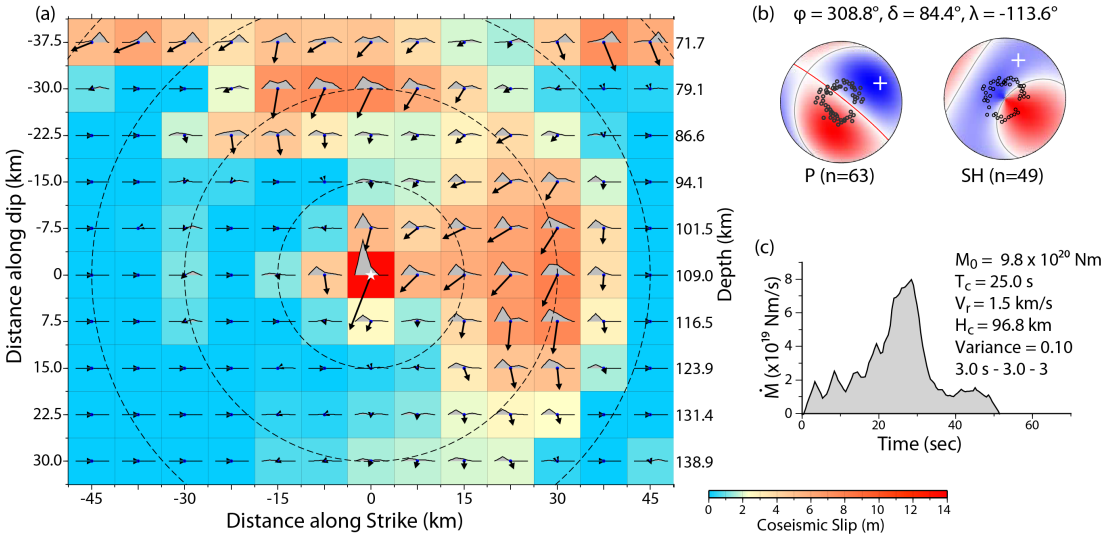

Figure 8.9 Finite-fault slip model for the steeply dipping fault plane from the joint inversion of teleseismic body waves (P and SH), hr-GPS and static displacement offsets for the 2014 M_w 7.9 Rat Islands earthquake. Format is the same as in Figure 8.7.

The slip distribution found for the steeply dipping plane (Figure 8.9) also has some large slip near the hypocenter, with peak slip of ~ 14 m, and a patch with peak slip of ~10 m at similar depth located to the northwest along strike. But this fault plane choice results in a widely spread slip distribution with a peak slip of ~11 m near 70 km depth, which is near the upper edge of the underthrust plate. The model domain is intentionally restricted so that it does not extend to depths above the subducted slab, but if we do allow shallower slip, the inversion tends to place some slip at the upper edge of the model. It is uncomfortable to have large slip at the edge of finite-fault models, but it is plausible that this broadening of slip is located within the subducted oceanic crust, which may have pore fluids that facilitate

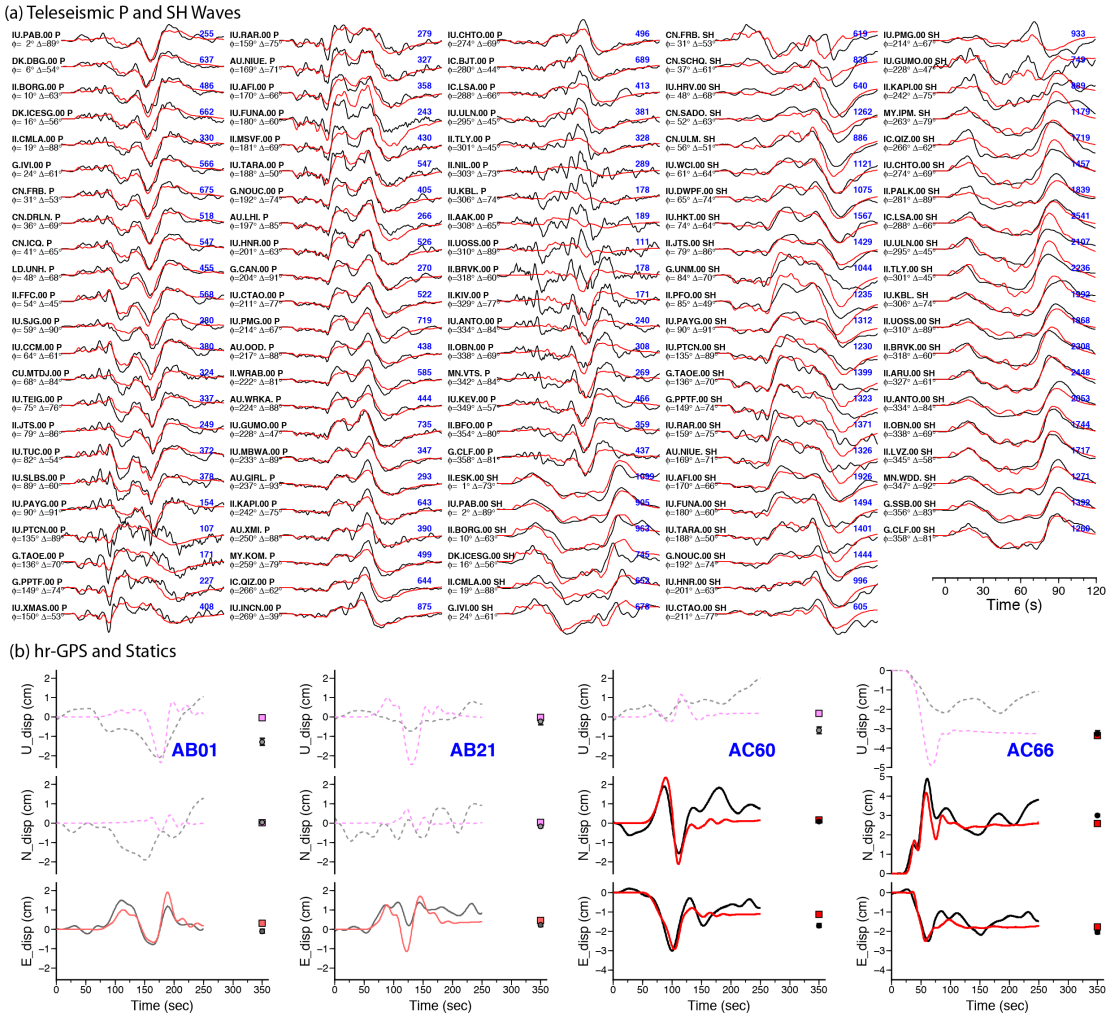

Figure 8.10 Comparisons of (a) observed (black) and synthetic (red) P and SH ground motions and (b) 1-Hz high-rate GPS ground motions along with static displacement offsets for the selected rupture model on the steeply dipping fault plane shown in Figure 8.9. Format is the same as in Figure 8.8.

expansion of the rupture. The overall waveform matches for the steeply dipping fault (Figure 8.10) are comparable to those for the shallowly dipping plane and the joint inversion residuals are very similar. The steeply dipping plane fits the nodal P wave data to the southeast a bit better than the shallowly dipping plane, but has more severe waveform mismatches to the northwest, so it is very difficult to favor one geometry over another based on data mismatch. The finite-fault seismic moment estimate is a bit lower for the shallowly dipping plane (8.4 x

10^{20} Nm) than for the steeply dipping plane (9.8 x 10^{21} Nm), but the centroid time shifts of ~25.5 - 25.0 s, and average slip depths, H_c, ~101 - 96.8 km for the shallowly and steeply dipping planes, respectively, are compatible with values from the long-period point-source solutions. Given the simple earth structure, kinematic constraints, and simplified faulting representations used, the overall characteristics of all data are quite well modeled by either the shallowly or steeply dipping fault models. Map views of the two fault models, along with comparison of the observed and predicted GPS static motions are shown in Figure 8.11. The primary slip regions are located in the vicinity of the aftershock distribution, but the NE-SW spread of the aftershock distribution may somewhat favor the shallowly dipping fault geometry. These models are generally similar to those obtained from inversion of only teleseismic signals by *Ye et al.* [2014], but some of the isochronal smearing of slip apparent in the latter models is suppressed by the addition of the hr-GPS data and there are minor differences in seismic moment. The overall waveform matches are comparable.

Using the slip models from the two finite-fault inversions, we estimated the stress drop weighted by the slip distribution. *Noda et al.* [2013] show that the stress drop averaged this way is more appropriate for estimating the strain energy. We first computed the stress drop by embedding our slip models in a homogeneous half space with an appropriate depth and geometry, and numerically computed the stress drop for the spatially heterogeneous slip distribution. The computation is based on the methods developed by *Mansiha and Smylie* [1971] and *Okada* [1992]. The average stress drop estimates, are ~16.4 MPa and ~24.8 MPa for the slip models on the shallowly and steeply dipping faults, respectively. These values are consistent with stress drop estimates obtained from a slip model with trimming threshold ξ ~0.15 to 0.2, in which the stress drop is estimated for a circular crack model with the area given by summing the subfaults with a moment larger than ξ times the moment of the

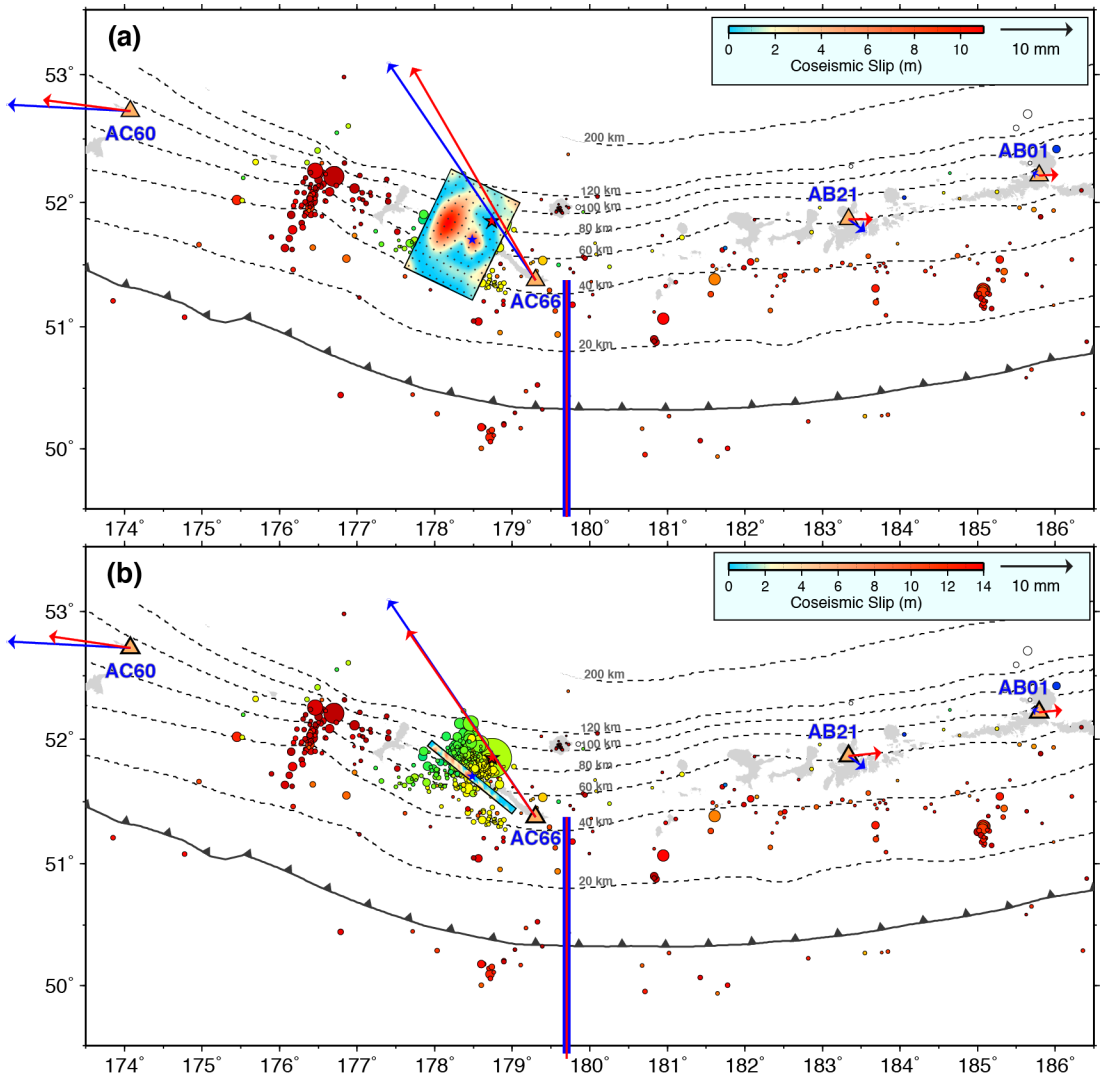

Figure 8.11 Map of the selected (a) shallowly dipping and (b) steeply dipping fault slip models for the 2014 Mw 7.9 Rat Islands earthquake from Figure 8.7 and Figure 8.9, respectively, along with the aftershock sequence from Figure 8.2. The observed (blue) and predicted (red) horizontal static ground motions at the 4 hr-GPS sites used in the joint inversion are shown with arrows. The bold blue and superimposed red bars show the observed and predicted vertical displacement offset at site AC66. The red and blue stars show the epicenter from the USGS/NEIC catalog and the epicenter of the finite fault models, respectively.

subfault with the largest moment. These stress drop estimates are very dependent on the rupture area, and that, in turn, is dependent on the rupture expansion velocity. We performed inversions with varying rupture velocity for both fault models, scaling the grid

spacing proportional to the rupture velocity so that the slip distribution shapes are similar but the areas vary systematically. Estimates of the average stress drop from the heterogeneous slip models are shown in Figure 8.12a, with expected large variation. By computing radiated energy we can explore radiation efficiency constraints on the rupture expansion velocity.

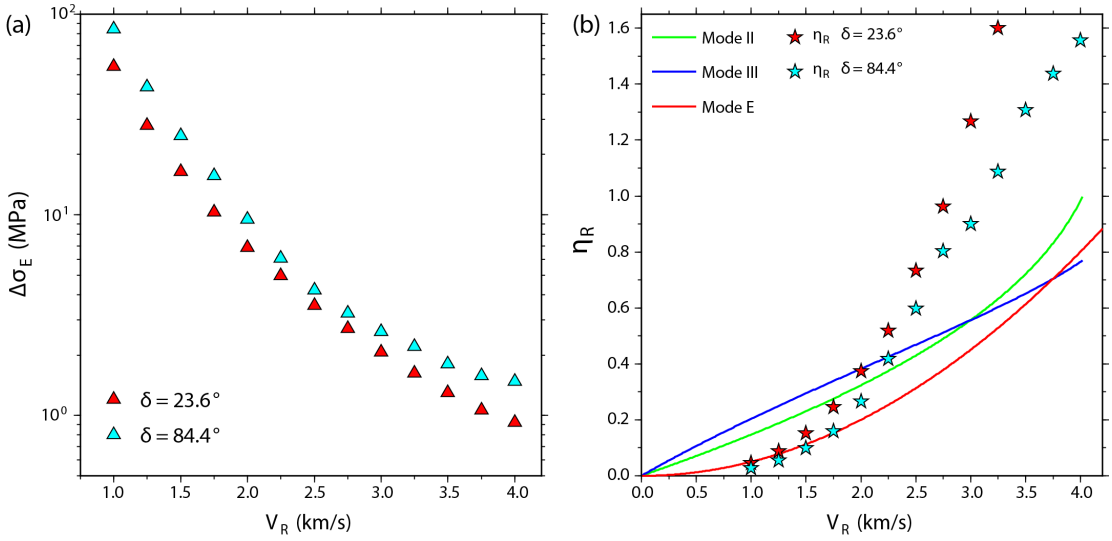

Figure 8.12 Variation of (a) calculated average stress drop and (b) radiation efficiency as functions of assumed rupture expansion velocity for finite-fault models using the shallowly dipping (red) and steeply dipping (cyan) fault planes. The green, blue and red curves in (b) show the predicted radiation efficiency with reference shear-wave velocity ~4.5 km/s for mode II and III cracks, and an energy-based model (mode E). The radiated seismic energy, 1.8×10^{18} J, estimated from the spectrum method (Fig.12a), and seismic moment from gCMT catalog are used to estimate the radiation efficiencies. For our selected models with V_R 1.5 km/s shown in Figure 8.7 and Figure 8.9, the stress drop are ~16.4 MPa and ~24.8 MPa, and the radiation efficiency are ~0.15 and ~0.10, for the shallowly and steeply dipping fault planes, respectively.

8.2.4 Seismic Radiated Energy

The average source spectrum and estimated total radiated energy are shown in Figure 8.13a. The source spectrum at frequencies less than ~0.05 Hz is obtained from the moment rate function from the finite-fault inversion (here we use the shallowly dipping fault plane solution from Figure 8.7) and at frequencies of 0.05 – 2 Hz from the stack average of

broadband P wave displacement spectra, corrected for the radiation pattern and an attenuation operator, t* = travel time / Q, where Q is the quality factor defined by loss of amplitude per cycle. Large uncertainties are introduced by limited knowledge of the average P and S wave velocities around the source, as well as limited data bandwidth and uncertainty in propagation corrections, particularly for attenuation. Relatively low attenuation is expected for the 2014 Rat Islands earthquake because of the source depth and location within the steeply dipping subducting slab traversed by the down-going P signals. To estimate t*, we downward interpolate the t*(f) model of *Perez-Campos et al.* [2003] from a depth of 50 km to halved values at 650 km. This provides consistent values with the empirical Green's function corrected radiated energy for the great M_w 8.3 deep Sea of Okhotsk earthquake [*Ye et al.*, 2013]. For the 2014 Rat Islands event, which is not very deep, the frequency-dependent t* model has t* ~ 1.0 s, 0.9 s and 0.5 s at frequencies of 0.01 Hz, 0.1 Hz and 2 Hz, respectively.

The average source spectrum for this earthquake is slightly enriched in high-frequency spectral level relative to a reference ω–squared source spectrum with a stress parameter of 3 MPa. The measured total radiated seismic energy for frequencies less than 2 Hz is, E_R ~1.8 x 10^{16} J. This was estimated using the energy fraction computed for high-frequency teleseismic P wave ground velocity spectra relative to the low-frequency energy content following the theory and method of *Venkataraman and Kanamori* [2004]. This estimate falls within the range of 1.1 x 10^{16} J – 2.7 x 10^{16}J found assuming constant t* values of 0.7 s to 0.4 s [*Ye et al.*, 2014]. The corresponding seismic moment-scaled radiated energy ratio is E_R/M_0 = 1.85 x 10^{-5}. This is near the low end of typical values for large intraplate earthquakes (average ~3.0 x 10^{-5}), and near the upper end of typical large interplate event values (average ~1.5 x 10^{-5}) [e.g., *Ye et al.*, 2012].

8.3 Discussion and Conclusions

Joint inversions of teleseismic body waves, regional hr-GPS (1Hz) recordings and their corresponding static displacement offsets for the 2014 Rat islands earthquake, yield slip distributions with a compact slip zone spanning 50 km x 30 km with a maximum slip of ~11 m for a shallowly dipping plane, or a more distributed slip pattern extending upward to ~70 km, with maximum slip of ~14 m on a steeply dipping plane. Maximum slip is not a well-resolved parameter in finite fault inversions, as it depends on model parameterization. The values given here are for the 7.5 km x 7.5 km grid spacing of our models. The centroid depths, centroid time shifts and the total seismic moment from both slip models are comparable with values determined from long-period seismic waves.

Radiation efficiency, proportional to the ratio between the moment-scaled radiated energy and static stress drop, has been used in evaluating heating effects, which are important for considering possible physical mechanisms for intermediate-depth and deep earthquakes in very high pressure and temperature environments [e.g., *Kanamori et al.*, 1998; *Ye et al.*, 2013]. However, as apparent in Figure 8.12a, there is large uncertainty in estimating static stress drops from finite-fault slip distributions for this event, mainly due to lack of directivity effects and resulting poor constraint on the rupture velocity. There are strong trade-offs between the rupture velocity and subfault source time function parameters, and subfault grid size in our finite-fault parameterization method. Estimated stress drop decreases dramatically with increasing rupture expansion velocity for finite-fault slip models on the shallowly and steeply dipping planes that give comparable fits of the observations. Comparison of the corresponding radiation efficiency for Mode II and III cracks, suggests that a rupture velocity around 1.5 to 2.0 km/s is favored (Figure 8.12b). This supplements the finding that slip models for a 1.5 km/s rupture expansion rate have large-slip areas compatible with the spatial

extent of the aftershock distribution (Figure 8.11). We infer that a rupture velocity, Vr = 1.5 km/s, as used in our selected models, is reasonable. The corresponding radiation efficiency estimates are ~0.15 and ~0.10 for the static stress drops of ~16.4 MPa and ~24.8 MPa for the slip models on the shallowly and steeply dipping fault planes, respectively. The low radiation efficiency and high stress drop suggest that a relatively dissipative source process, possibly involving melting or thermal shear runaway [e.g., *Prieto et al.*, 2013], occurred during the 2014 Rat Islands event.

Reactivation of inherited oceanic faults formed at shallow depths has been commonly invoked to account for intermediate-depth faulting. Shallow intraplate faulting, such as the large M_w 7.6 trench slope normal faulting earthquake on 30 March 1965 (Figure 8.2a), may provide hydrated fault zones that can be reactivated as the slab sinks to intermediate depths and undergoes dehydration reactions that release fluids, reducing confining stresses on the fault zone [*Peacock*, 2001]. Observations supporting this scenario involve similarity of the fault orientations relative to the plate surface [e.g., *Warren*, 2014]. However, the faulting orientations for the 2014 Rat Islands event are not easily related to the likely geometry of shallow plate bending faults, with the deeper slab either displacing northeastward on the shallow-dipping plane or almost vertically downward on the steeply dipping plane, at relatively low angle to the slab surface. Given the obliquity of the relative plate motions along the curving Aleutian trench, contortion of the subducted Pacific plate [e.g., *Creager and Boyd*, 1991; *Ruppert et al.*, 2012] is expected to affect the intraplate stresses in the slab beneath the Rat Islands archipelago, but the faulting may be controlled by inherited fault zone structure. Even if correct in general, reactivation of prior fault systems does not provide a simple strain accumulation and release context like that for the relative plate motions driving megathrust faulting to provide guidance on the frequency of large intermediate depth events. The best

approach seems to characterize the attributes of such events based on the limited number of recorded examples and to recognize their general potential in circum-Pacific earthquake hazard assessments.

Figure 8.13 shows comparisons of source time functions from finite-fault inversions and teleseismic source spectra for the 2014 Rat Islands earthquake and similar magnitude events in different tectonic regions, such as the 13 June 2005 Tarapaca, Chile intraslab earthquake (M_w 7.8), the 3 May 2006 Tonga intraslab earthquake (M_w 8.0), the 13 January 2007 Kuril outer rise intraplate earthquake (M_w 8.1) [*Ammon et al.*, 2007], the 1 April 2014 Iquique interplate earthquake (M_w 8.1), and the 6 February 2013 Santa Cruz Islands interplate earthquake (M_w 7.9) [*Lay et al.*, 2013]. Compared to a typical megathrust earthquake like the

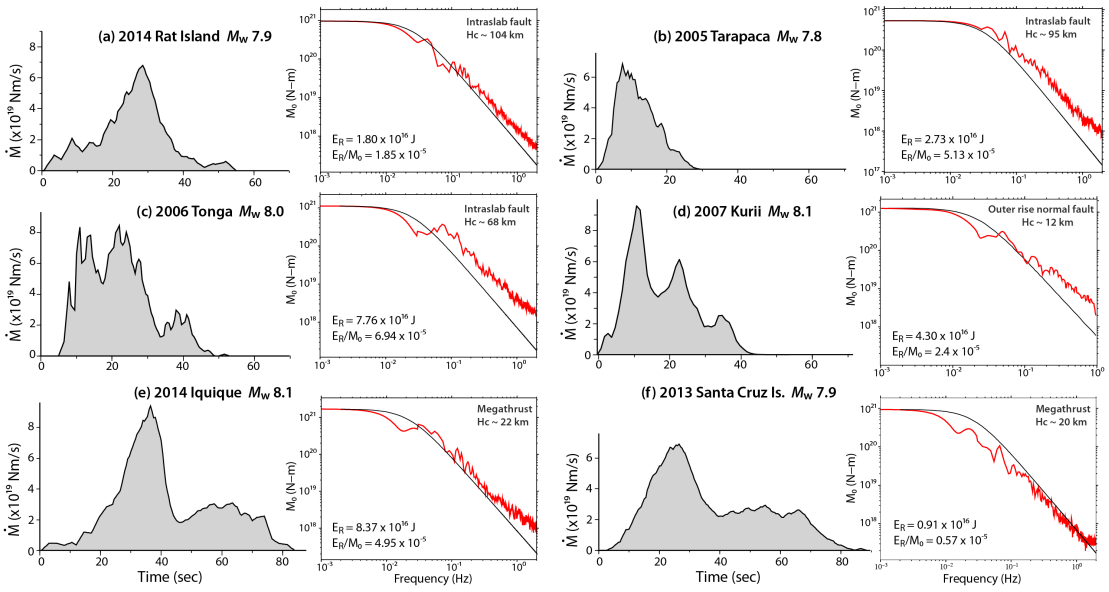

Figure 8.13 Comparison of moment rate functions and source spectra (red curves) for (a) the 23 June 2014 Rat Islands intraslab earthquake (M_w 7.9), (b) the 13 June 2005 Tarapaca intraslab earthquake (M_w 7.8), (c) the 3 May 2006 Tonga intraslab earthquake (M_w 8.0), (d) the 13 January 2007 Kuril outer rise intraplate earthquake (M_w 8.1) [*Ammon et al.*, 2008], (e) the 1 April 2014 Iquique interplate earthquake (M_w 8.1) and (f) the 6 February 2013 Santa Cruz Island interplate earthquake (M_w 7.9) [*Lay et al.*, 2013]. The centroid depth (H_c) for each earthquake is from gCMT catalog. Reference w-squared spectra for a 3 MPa stress parameter and seismic moment of each event are shown by the black curves.

2013 Santa Cruz earthquake and to reference 3 MPa w-squared spectra, the intraslab earthquakes are generally enriched in high-frequency seismic radiation, which contributes to strong ground shaking damage. Both high stress drop and low attenuation along some wave paths under the arc may contribute to strong shaking [*Ye et al.*, 2013]. The 2014 Iquique event has an unusually spatially-concentrated slip distribution for a megathrust event, and it also has a somewhat enriched high-frequency source spectrum, so the Rat Islands spectrum is not particularly distinctive, as indicated by the E_R/M_0 value.

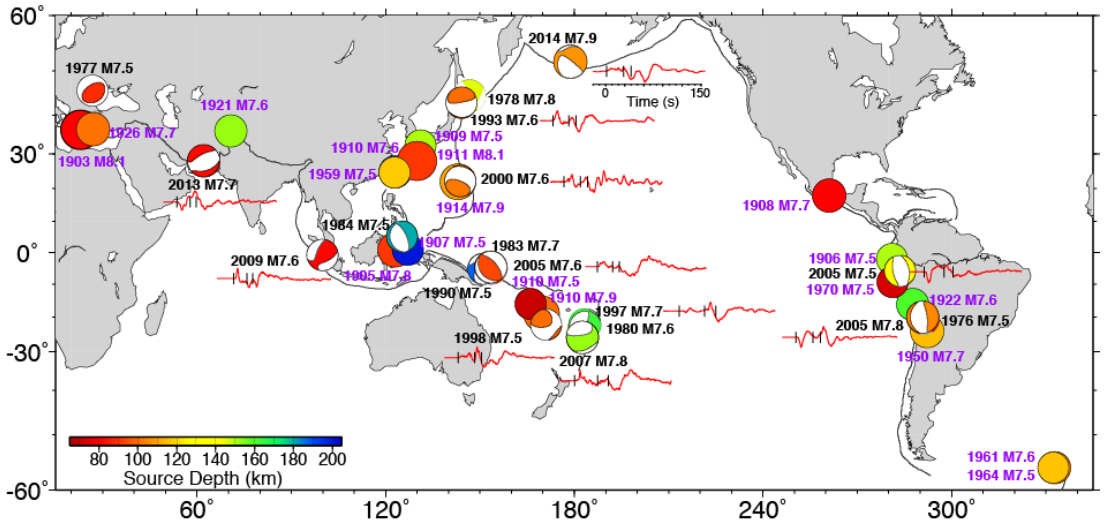

Figure 8.14 Map showing the global distribution of all 38 earthquakes in the depth range 70 to 200 km between 1900 and 2014 with $M_w \geq 7.5+$ from the PAGER-cat [*Allen et al.*, 2009], with events since 1976 displayed as the GCMT moment tensor. For the recent large events, a broadband P wave ground displacement is shown with tick marks indicating the P, pP, and sP arrival times (all have the same time scale with 20 s leader ahead of the P arrival and 150 s of signal after that). Figure 8.A2 identifies the specific stations shown for each event. Some events may actually be shallower events with overestimated depth in the catalog and some events actually in this depth range may be missed because the catalog depths are incorrectly estimated as less than 70 km.

The distribution of large earthquakes at depths from 70 to 200 km with Mw ≥ 7.5 from the seismological record is shown in Figure 8.14. Epicenters of events dating back to 1900 are shown by circles, and GCMT focal mechanisms are shown for the events since 1976.

Comparisons of teleseismic P waveforms from several of the larger recent events are included, demonstrating the overall similarity of the 2014 event signals to events in other regions. The map indicates the global extent of this class of intraslab earthquakes relative to population centers. Slabs with varying thermal structures, convergence rates, and geometries experience large events, and detailed work is required to evaluate any tectonic controls on their occurrence. Each region likely has unique tectonic stresses and inherited faulting geometries from shallower plate bending, making it difficult to infer recurrence and total distribution of such events from the short seismological record along with the lack of geologic record, but at a minimum, recognition of this class of infrequent large ruptures should be incorporated into seismic hazard assessments in populated subduction zone environments.

Acknowledgements. The IRIS DMS data center (http://www.iris.edu/hq/) was used to access the seismic data from Global Seismic Network and Federation of Digital Seismic Network stations. This work made use of GMT and SAC software. This work was supported by NSF grant EAR1245717 (T.L.).

8.4 Supplementary Figures

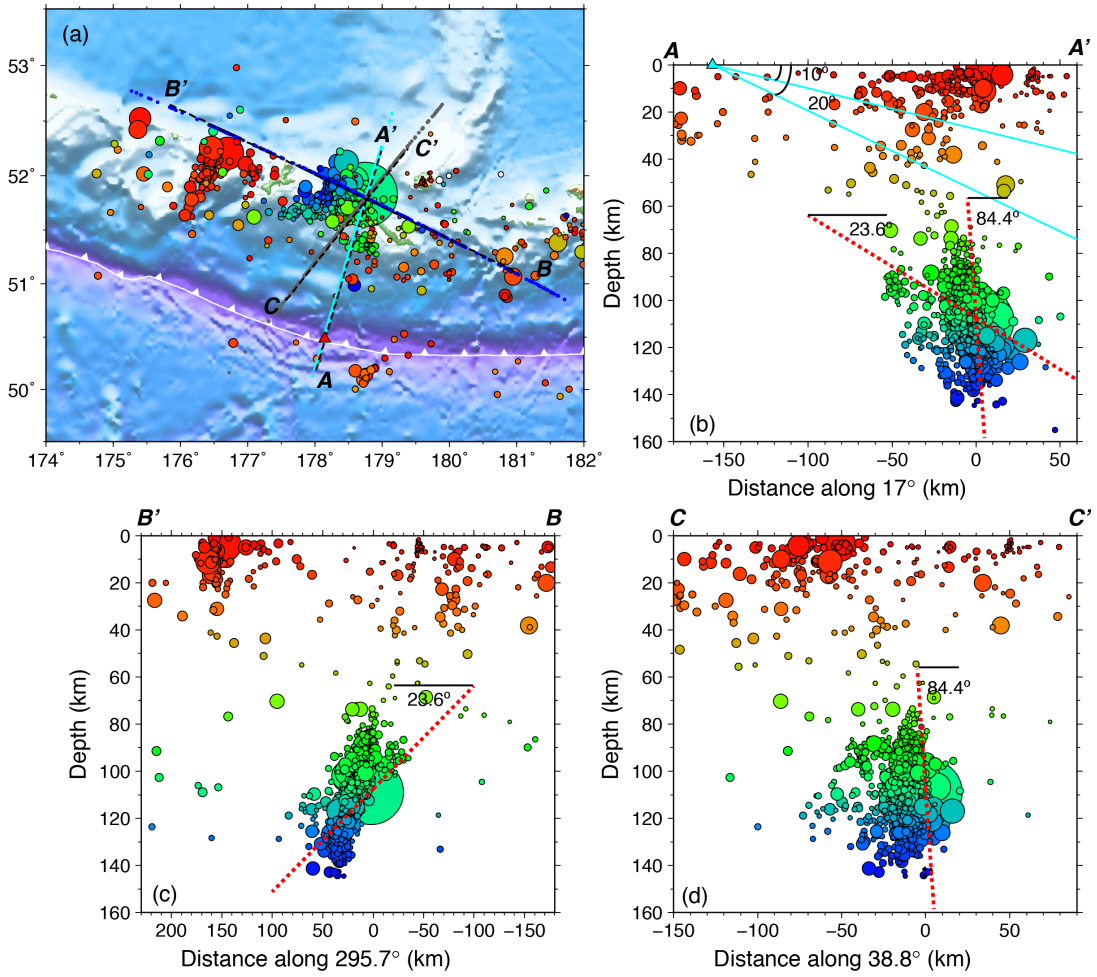

Figure 8.A1 Aftershock locations from the USGS-NEIC are viewed in (a) map view with bathymetry and Aleutian trench (barbed line) shown, (b) vertical cross-section A-A' along an azimuth of 17° through the mainshock hypocenter, which is perpendicular to the local strike of the Aleutian trench with the red triangle indicating the trench position and the dashed cyan lines indicating the possible slab dipping angles, (c) vertical cross-section B-B' along an azimuth of 295.7° in the plunge direction of the shallow-dipping nodal plane, and (d) vertical cross-section C-C' along an azimuths of 84.4° in the plunge direction of the steeply-dipping nodal plane. Earthquake hypocenters are shown by circles, color-coded with source depth and radius-scaled proportional to magnitude. The spread of aftershock locations does not allow unambiguous preference for a fault-plane, but in either case the source region appears to be spatially concentrated over a 50 km x 50 km extent.

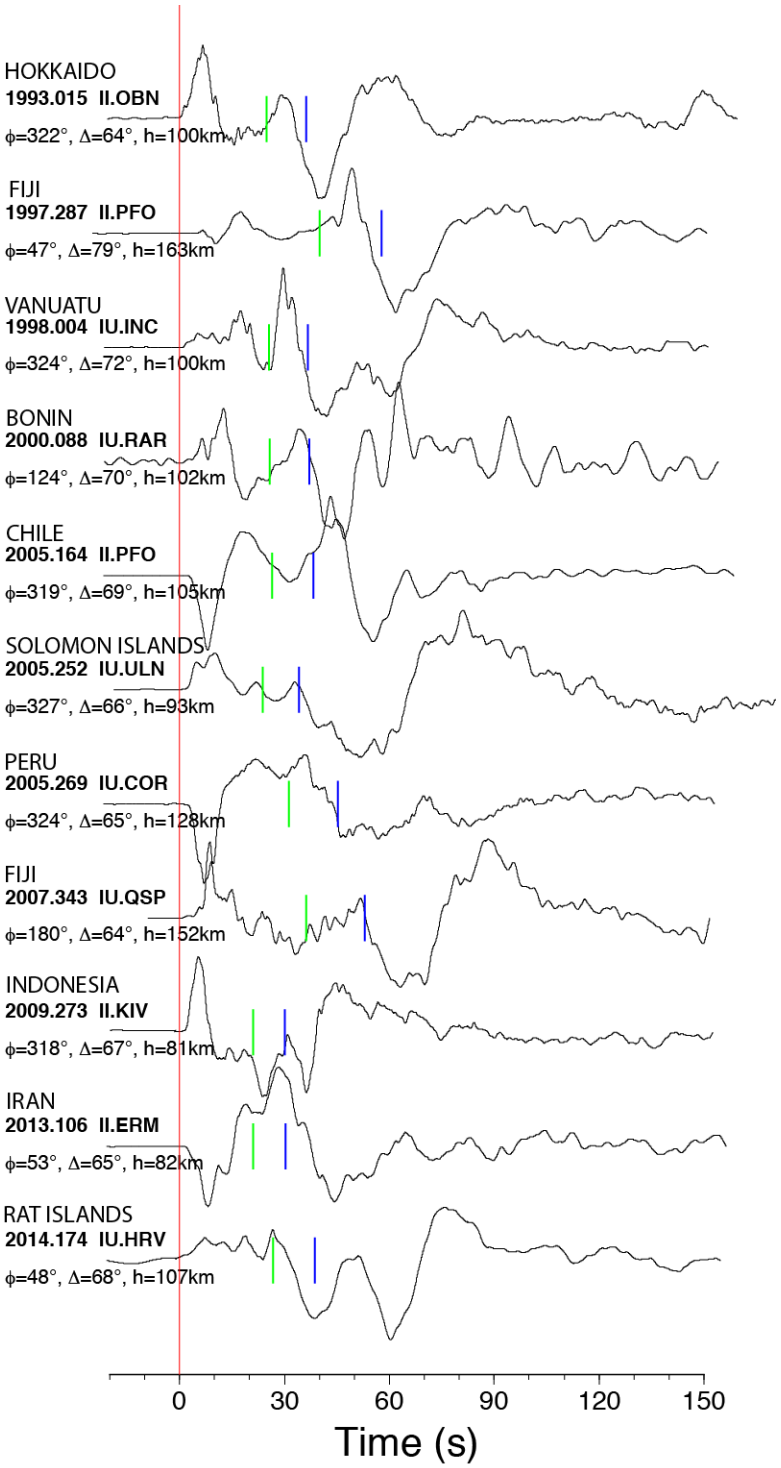

Figure 8.A2 Details about the seismograms shown for recent large intermediate depth earthquakes from 1993 to 2014 in Figure 8.14. For each event, a representative teleseismic P wave ground displacement recording from 64° to 79° is shown with a 20 s leader and 150 s of motion. Data are filtered in the passband 0.005 to 4.0 Hz. The waveforms are aligned on the P arrival, with the predicted arrival time of pP indicated by green tick marks and the sP arrival time indicated by blue tick marks. The amplitudes are normalized by the peak amplitude of each recording. The event location, year, Julian day, and station name are indicated, with the station azimuth (f) and epicentral distance (D) and the PAGER-cat source depth (h) indicated.

Chapter 9

Energy Release of the 2013 Mw 8.3 Sea of Okhotsk Earthquake and Deep Slab Stress Heterogeneity

This chapter has been published as:
Ye, L., T. Lay, and H. Kanamori (2013), "Large earthquake rupture process variations on the Middle America megathrust", Earth Planet. Sci. Lett., 381,147-155.

Abstract Earth's deepest earthquakes occur in subducting oceanic lithosphere where temperatures are lower than ambient mantle. On 24 May 2013 a magnitude 8.3 earthquake ruptured a 180 km long fault within the subducting Pacific plate about 609 km below the Sea of Okhotsk. Global seismic P wave recordings indicate a radiated seismic energy of ~1.5 x 10^{17} J. A rupture velocity of ~4.0 - 4.5 km/s is determined by back-projection of short-period P waves, and the fault width is constrained to give static stress drop estimates (~12 - 15 MPa) compatible with theoretical radiation efficiency for crack models. A nearby aftershock had a stress drop 1 to 2 orders of magnitude higher, indicating large stress heterogeneity in the deep slab, and plausibly within the rupture process of the great event.

9.1 Introduction

The occurrence of earthquakes in the depth range 400-720 km (the mantle transition zone) has long been enigmatic, given the immense pressure exerted by the overlying rock mass on any fault surface. Seismic radiation from deep earthquakes indicates that they likely involve shear faulting basically indistinguishable from shallow earthquakes despite the extreme pressure conditions. Deep earthquakes only initiate in relatively low temperature

regions of subducted oceanic lithosphere. Very high deviatoric stresses may be present in the core of the subducted slab and some mechanism must exist to offset the inhibiting effects of pressure to allow shear faulting to initiate [Green II and Houston, 1995]. For the depth range 50-400 km, it is generally believed that release of water by mineral dehydration reactions or production of other fluid phases reduces the effective normal stress on surfaces and enables fluid-assisted frictional sliding. It is not clear whether such mechanisms can account for transition zone earthquakes, the largest of which tend to occur below 600 km depth. Much research has focused on processes such as abrupt phase transitions [Green II and dBurnley, 1989] that may be able to nucleate rupture under tremendous confining stress. Once deep fault slip initiates and becomes substantial, frictional heating can lead to melting of the fault surface, abetting run-away rupture expansion for large deep earthquakes [Kanamori et al., 1998].

On 24 May 2013 the largest deep earthquake yet recorded occurred near a depth of 609 km [05:44:49 UTC, 54.874°N, 153.281°E; http://earthquake.usgs.gov/earthquakes/eventpage/usb000h4jh#summary] in the Pacific plate subducting along the Kuril-Kamchatka subduction zone (Figure 9.1). The event locates under the Sea of Okhotsk. Globally recorded long-period seismic waves indicate that the overall earthquake process appears to involve shear-faulting with a seismic moment of ~4.1 x 10^{21} Nm (M_w 8.3) (http://www.globalcmt.org/CMTsearch.html). The event is slightly larger than the 637 km deep Bolivia earthquake of 9 June 1994 that had a seismic moment of ~3 x 10^{21} Nm (M_w 8.3) [Silver et al., 1995; Kikuchi and Kanamori, 1994].

Both great events have similar faulting geometries with very shallow-dipping normal fault mechanisms and only minor deviations from shear double-couple solutions. The 1994 Bolivia earthquake was interpreted as having a relatively slow rupture velocity, Vr~1-2 km/s, with a

40s rupture duration and a spatially compact rupture zone with a scale of about 40km x 60km [Silver et al., 1995; Kikuchi and Kanamori, 1994; Beck et al., 1995; Ihml, 1998, Chen, 1995; Antolik et al., 1996], leading to large stress drop estimates of around 110-150 MPa [Kikuchi and Kanamori, 1994; Antolik et al., 1996].

In the first four days after the 2013 earthquake, 9 aftershocks were detected, 8 having small magnitudes of 4.1-4.4 at depths from 487 km to 627 km, and an M_w 6.7 event struck nine hours after the mainshock [14:56:31, 52.222°N, 151.515°E, 623 km deep; USGS/NEIC] about 200 km to the southwest (Figure 9.1). Six nearby aftershocks with depths of around 600 km define a north-south trend about 90 km long, preferentially extending southward from the mainshock hypocenter. The trend is generally compatible with rupture along either of the two nodal planes of the mainshock focal mechanism, but slightly favors the shallow plane. Aftershock occurrence for large deep earthquakes is highly variable [Wiens and McGuire, 1995], and the large depth range for the 2013 aftershocks suggests that some are triggered away from the mainshock rupture zone. The 2013 event was preceded by nearby large earthquakes in 2008 (M_w 7.3, 7.7, Figure 9.1), the larger of which was ~100 km along strike to the south.

9.2 Source Spectrum and Radiated Seismic Energy

Two of the most fundamental seismological properties of a large earthquake are the source spectrum and the radiated seismic energy. We analyzed extensive global seismic recordings of P waves for the 2013 event to estimate both. Source spectrum estimates obtained from two distinct approaches provide estimates of the radiated seismic energy (Figure 9.2). The radiated energy estimates depend on attenuation corrections. The attenuation corrections are parameterized by t^*, the ratio of total P wave travel time to

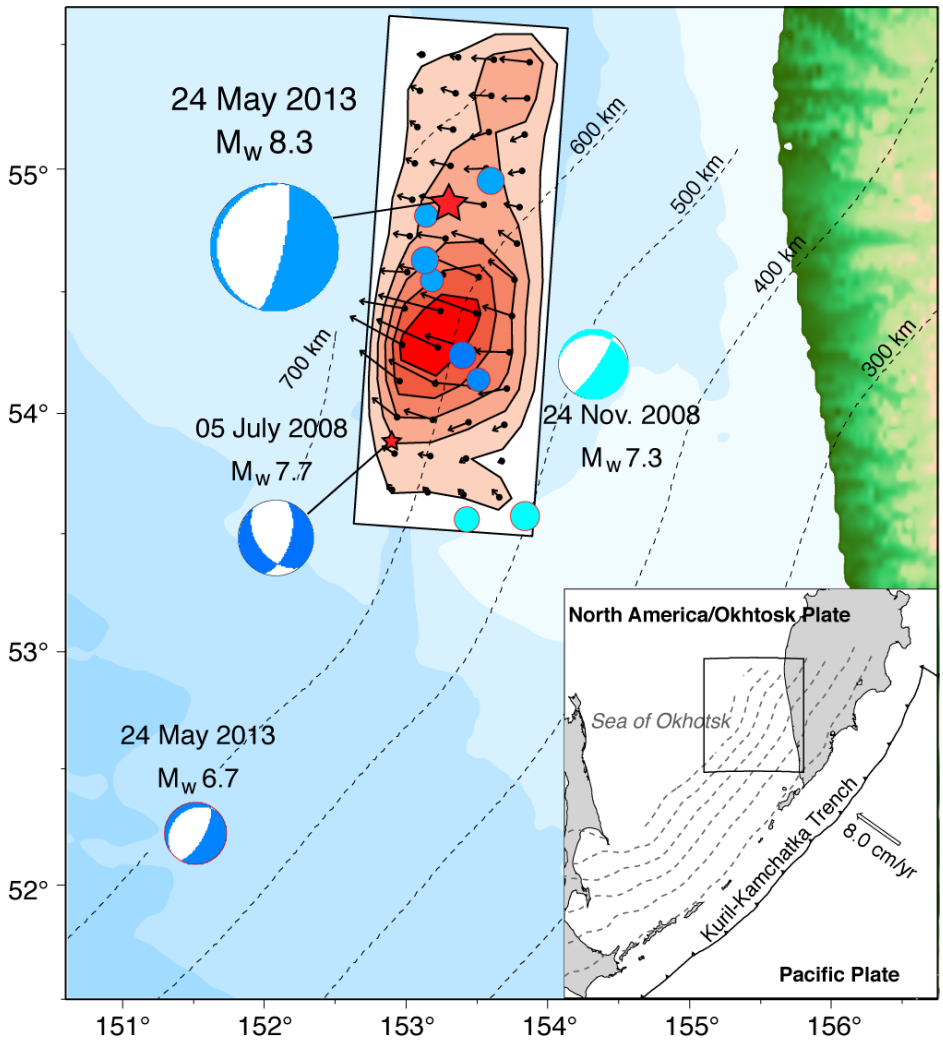

Figure 9.1 Tectonic setting of the 2013 M_w 8.3 deep Sea of Okhotsk slab earthquake. The inset map indicates the plate configuration, with the Pacific plate underthrusting the North American/Sea of Okhotsk plate along the Kuril-Kamchatka subduction zone at a convergence velocity of ~8.0 cm/yr. Dashed lines are depth contours for the subducted oceanic slab beneath the Sea of Okhotsk. The main map shows best-double couple faulting mechanisms from global centroid-moment tensor inversions for recent large earthquakes in the deep slab, with blue indicating events below 600 km depth and cyan indicating events around 500 km deep. Focal mechanisms are at the event epicenter unless offset with a tie-line. Small circles are locations of aftershocks of the 24 May 2013 event with magnitudes 4.1-4.4. The contoured plot indicates the slip distribution of the preferred rupture model for the mainshock, with the large red star being the hypocenter at a depth of 608.9 km. The arrows indicate the magnitude and direction of slip of the upper side of the fault, with the fault dipping 10° toward the west. The peak slip is 9.9 m and the colors indicate about 2.2 m slip contour increments.

average attenuation quality factor, $Q(f)$, along each path as a function of frequency, f. The precise $Q(f)$ on each path is not known in detail, and is expected to vary strongly due to upper mantle heterogeneity in attenuation structure beneath the seismic stations. For deep focus earthquakes, the t^* values are expected to be on average ~0.5 s at 0.1 Hz for teleseismic P waves (half of the t^* value for a shallow source), and about 0.25-0.5 s at 1.0 Hz, with t^* likely decreasing as frequency increases above 1.0 Hz. Lacking knowledge of specific path or even best average attenuation parameters, we show spectral estimates for a range of constant t^* values from 0.1-0.5 s, with a value of 0.3 s deemed to be a reasonable value. The uncertainty in t^* affects the high frequency spectral levels which are very important for radiated seismic energy estimates. We averaged the energy values obtained from 102 stations by integrating the energy spectrum from the P-wave ground-motion velocities (13-16) after correcting for faulting geometry and propagation effects. Using $t^* = 0.3$ s for each station and frequencies up to 3 Hz gives radiated energy of $E_R = 1.5 \times 10^{17}$ J, with a range of reasonable estimates being given by results for $t^* = 0.2$ s ($E_R = 1.0 \times 10^{17}$ J) to 0.4 s ($E_R = 2.8 \times 10^{17}$ J). For $t^* = 0.3$ s the moment-scaled energy is $E_R/M_0 = 3.7 \times 10^{-5}$.

To confirm the source spectrum estimate, we used P wave observations of the nearby M_w 6.7 aftershock at the same stations as for the mainshock to explicitly cancel out the unknown path effects. The large aftershock is remarkably short-duration, with impulsive P wave motions that have average pulse widths of about 1.8 s. The average source spectrum for the aftershock found assuming $t^* = 0.3$ s for 22 stations has a very flat spectrum up to ~0.5 Hz (Figure 9.2), indicating that this event can serve as an impulse response, or empirical Green's function (EGF) up to near that frequency. For $t^* = 0.3$ s, $E_R = 2.36 \times 10^{15}$ J for the EGF from log averaging of the 22 individual station energies, and $E_R/M_0 = 2.8 \times 10^{-4}$, using our finite-fault inversion estimates of $M_0 = 8.4 \times 10^{18}$ N-m.

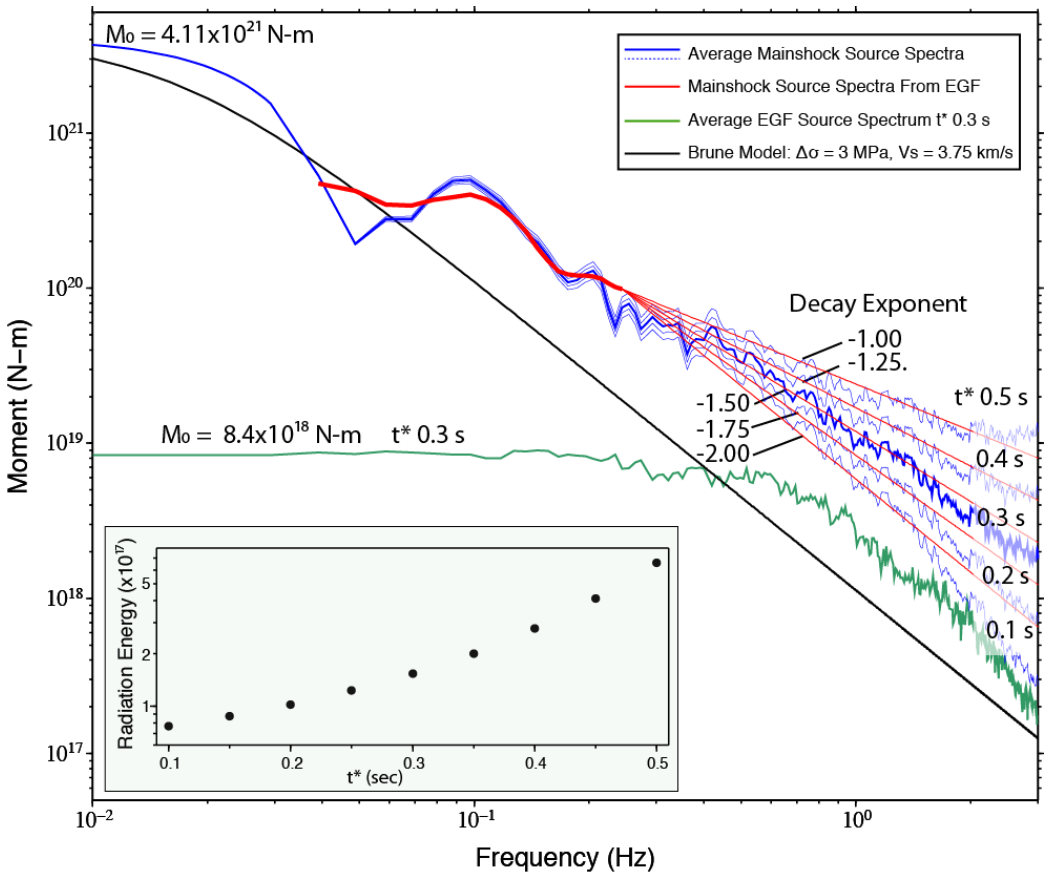

Figure 9.2 Source spectra estimates for the 2013 Mw 8.3 Sea of Okhotsk mainshock and Mw 6.7 aftershock. The mainshock spectrum is estimated by two methods. The blue curves are estimates based on the spectrum of the source time function from finite-fault inversion for frequencies less than 0.05 Hz and from averaging many teleseismic P wave spectra with propagation and radiation pattern corrections from 0.05-3.0 Hz. Results are shown for different attenuation parameters of t^* = 0.1 to 0.5 s. The red curve is an estimate of the mainshock source spectrum from 284 spectral ratios of the mainshock and the aftershock (empirical Green's function) spectra at the same station for the frequency band 0.03 to 0.25 Hz. The extrapolated spectra to 3 Hz assume source spectrum decay exponents of from -1.0 to -2.0. The green curve is the average source spectrum for the M_w 6.7 event based on the first method, using an assumed t^* = 0.3 s. The inset shows the dependence of estimates of radiated energy, E_R, on the assumed value of t^* for the mainshock signals, given by averaging energy estimates from individual path-corrected P wave spectra.

We computed mainshock/EGF spectral ratios for 284 broadband P wave observations (Figure 9.A1), correcting for differences in radiation pattern, geometric spreading and multiplying by the EGF M_0. The ratios are in close agreement with the averages of mainshock

P spectra over the corresponding passband (Figure 9.2). This ensures that uncertainties in t^* do not bias the average spectrum estimate in this passband.

Extrapolations of the spectral ratios from 0.25 Hz to 3.0 Hz are made for various assumed mainshock spectral decay slopes with frequency exponents varying from -1 to -2. For reference, a shallow interplate earthquake source spectrum for a moment equal to that of the mainshock has a decay exponent of -2, a stress parameter of 3 MPa, and source velocity of 3.75 km/s. The deep earthquake spectral amplitudes are enriched in high-frequency relative to the reference model, in part due to higher source velocity and in part due to higher stress drop. The precise spectral decay slope expected near 1 Hz is not known, as it depends on the detailed space-time history of slip on the fault, but values around -1.5 to -2 are consistent with assuming t^* values around 0.3 s. We conclude that $E_R \sim 1.5 \times 10^{17}$ J, with about a factor of 2 uncertainty. This is about three times as large as for the 1994 Bolivia event [$E_R \sim 5.2 \times 10^{16}$ J, (*Kanamori et al.*, 1998; *Winslow and Ruff*, 1999)].

9.3 Rupture Finiteness Analysis

The spatial extent of the 2013 Sea of Okhotsk deep earthquake faulting is critical for estimating additional properties of the source such as slip pattern and static stress drop. Back-projection of teleseismic short-period P waves was used to estimate the rupture velocity, *Vr*, and the source rupture dimensions (Figure 9.3). The data are from large continental seismic networks in Europe and North America that recorded coherent broadband waveforms (Figure 9.A4). For both array geometries, the back-projections indicate asymmetric bilateral extent of short-period radiation extending 50-60 km to the north of the hypocenter and about 120 km to the south, along the trend of the deep aftershocks, with a source time duration of

about 30 s. Animations of the back-projections show the space time evolution of the short-period radiation (Movie M1).

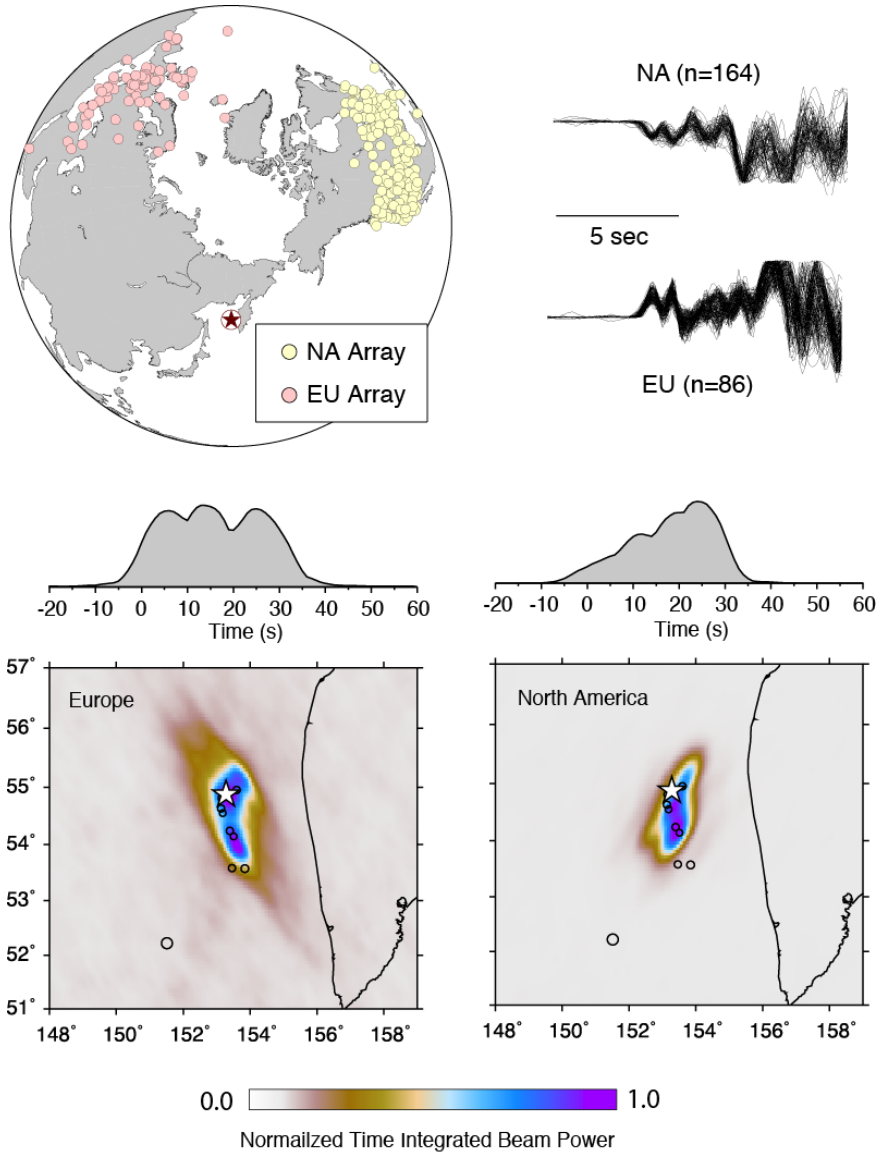

Figure 9.3 Constraints on rupture velocity from P wave back-projection. Teleseismic P waves in the frequency band 0.5-2.0 Hz from large networks of stations in North America and Europe were used to image the space-time history of coherent high frequency seismic radiation from the 2013 M_w 8.3 Sea of Okhotsk earthquake. The time-integrated power stacked on a grid around the source are shown here, relative to the mainshock epicenter (white star). The darker blue colors indicate coherent energy release with an asymmetric spread of source radiation in the north-south direction being resolved by the images from both networks. Supplementary information Animation A1 shows the time-varying images throughout the rupture process.

If we adopt the *Vr* estimate of 4.0 km/s obtained from the back-projections as a constraint on the finite-fault inversions, rupture models are found with average slip of 1.9-2.3 m and average static stress drop of 4-5 MPa for rupture areas that have a radius of about 74-82 km (Figures 9.A2, 9.A3) for the two fault plane choices. For these estimates, only subfaults with moment at least 15% of the peak subfault moment are retained to diminish sensitivity to poorly resolved low-slip areas of the model [Noda et al., 2013].

A problem with these solutions is that they can give large (>1) estimates of calculated radiation efficiency, η_R, which is the ratio of the radiated energy E_R to the available potential energy ΔW_0:

$$\eta_R = E_R / \Delta W_0 = 2\mu E_R / (\Delta\sigma_S M_0) \quad (1)$$

where $\Delta\sigma_s$ is the static stress drop, μ is the rigidity and M_0 is the seismic moment.

Radiation efficiency has been calculated as a function of *Vr* for Mode II, Mode III and energy-based (Mode E) crack models (Figure 9.4) [Freund, 1972; Fossum and Freund, 1975; Kostrov 1966; Mott, 1948; Kanamori and Brodsky, 2004]. For higher *Vr* there is less energy dissipation near the crack tip, so the radiation efficiency approaches 1 as *Vr* approaches the limiting speed (the Rayleigh velocity for Mode II and the shear velocity for Mode III and Mode E). For the 2013 Sea of Okhotsk event, *Vr* < 2.5 km/s is required for the circularly-expanding rupture models to have large enough calculated stress drop to lower the seismic efficiency to intersect the predictions of crack theory (Figure 9.4). Such a low *Vr* cannot account for the faulting dimensions indicated by the back-projections for the 2013 Sea of Okhotsk event. In order to obtain radiation efficiency consistent with the crack models, the width of the ruptures for high *Vr* must be constrained, essentially increasing the static stress drop by imposing rectangular rather than circular fault expansion.

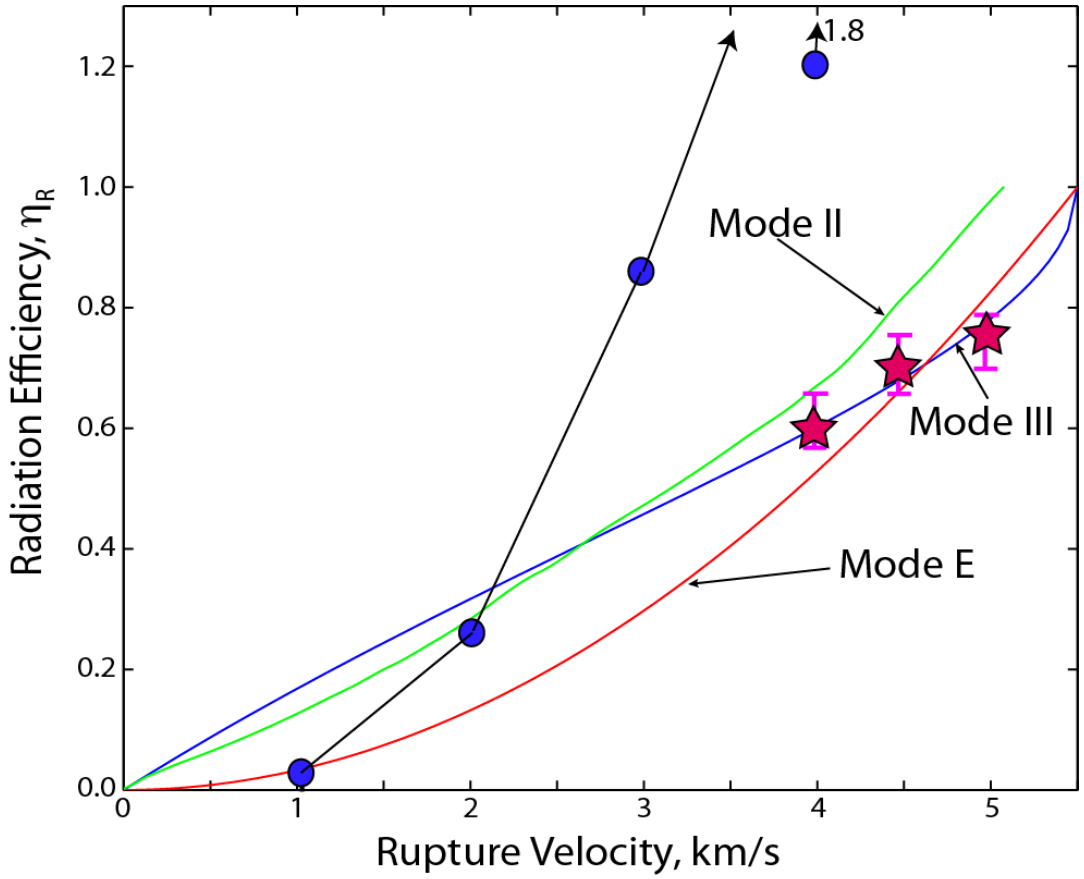

Figure 9.4 Model constraints from consideration of radiation efficiency for crack models with varying rupture speed. Reference curves for Mode II and Mode III cracks and an energy-based model (Mode E) have radiation efficiencies, h_R, that approach 1 as the rupture speeds approach their limiting velocities (~5.1 km/s for Mode II, ~5.5 km/s for Mode III and Mode E at a depth of 610 km) [Newman and Okal, 1998; Kanamori and Brodsky, 2004]. The blue circles indicate calculated radiation efficiency for rupture models (Figure 9.A2) with varying rupture velocity, *Vr*, with fault dimensions scaling proportional to *Vr*. These models are only compatible with the crack theory for *Vr* ~1.5-2.0 km/s, but this is inconsistent with the rupture extent indicated by back-projection in Figure 9.3, which favor *Vr* of 4.0 to 5.0 km/s. By constraining the width of the slip models, we find high *Vr* models consistent with the theoretical radiation efficiency, with preferred models giving the red stars. The solution shown in Figure 9.1 is the 15 MPa stress drop model for *Vr* = 4.0 km/s. The pink bars indicate variation in estimates for different thresholds (0.1-0.2, with stars for 0.15) used to remove poorly resolved low slip regions of the fault models.

For Vr = 4.0 km/s, $\Delta\sigma_s$ = 15 MPa is needed to give η_R = 0.6 for a Mode III rupture (Figure 9.4). For a 180 km rupture length, imposing a fault width of 60 km yields an effective rupture area that gives the required stress drop. For Vr = 5 km/s the fault width is increased to 68 km and gives $\Delta\sigma_s$ = 12 MPa and η_R = 0.75 (Figure 9.4). These models are now physically acceptable, and the slip distribution for the shallow-dipping plane for Vr = 4 km/s has average slip of 4.4 m (Figures 9.1 and 9.A9a). Good fits to observed P waveforms are obtained (Figure 9.A10). The slip distribution has asymmetric bilateral extent of 60 km NNE and 120 km SSW. Large slip is concentrated between 30 and 90 km south of the hypocenter, with the area of significant slip being 9675 km^2. We have some preference for the shallow-dipping plane, but very similar results are found for the steeply dipping plane (Figure 9.A9b); the narrow rectangular faults give similar waveforms at most stations for the along-strike rupture.

9.4 Discussion and Conclusions

While there are limitations in the precision of the back-projection constraints and the theoretical crack-model efficiency is calculated for very simple models, the basic model with Vr ~ 4.0 km/s and $\Delta\sigma_s$ ~15 MPa appears to be a valid representation of the overall source rupture. The Vr and rupture area are both about a factor of 4 larger than for the 1994 Bolivia event, and $\Delta\sigma_s$ is about an order of magnitude lower. The $\Delta\sigma_s$ ~15 MPa estimate is comparable values for shallow intraplate earthquakes [Venkataraman, 2004; Allmann and Shearer, 2009; Convers and Newman, 2011] and the fault dimensions are similar to those for the shallow trench-slope intraplate normal faulting event in the Kuril Islands of 13 January 2007 (M_w 8.1) [Lay et al., 2009]. The fault geometry is compatible with re-rupture of such an

outer rise normal fault surface within the plate, rotated by the dip of the deep slab. However, the M_w 6.7 aftershock has an unusually short rupture duration and finite-fault inversions for variable assumed rupture velocities for that event give $\Delta\sigma_s$ estimates in the range 157 to 5856 MPa (Figure 9.A12). Independent constraints on the aftershock fault area or rupture velocity are not available, but there is no question that it has a localized stress drop greatly exceeding the average stress drop for the 8.3 mainshock, and significantly lower radiation efficiency suggestive of a more dissipative source process. It is plausible that within the mainshock rupture zone there were corresponding very high stress drop slip patches that cannot be resolved. The envelope of teleseismic P wave ground accelerations for the mainshock follow the source-time function shape (Figure 9.A13), so a very heterogeneous stress distribution on the fault does appear likely (Houston et al., 1998; Chung and Kanamori, 1980; Wu and Chen, 2001], and the average parameters do not represent the total degree of slip and stress heterogeneity.

The 2013 mainshock rupture extends along the slab strike, with slip likely confined to the low temperature core of the slab. The subducted plate is older and colder than the slab where the 1994 Bolivia earthquake occurred, and this difference in thermal state may have fundamentally affected how rupture expanded for the two events [Tibi, 2003]. The Sea of Okhotsk event is similar to a shallow intraplate earthquake, with a large aspect ratio fault area defined by the brittle core of the slab. For the Bolivia event the brittle core volume is smaller and surrounding ductile or plastic material with a finite strength may dominate. Faulting for the Bolivia event involved a rupture with a very dissipative source process that deposited a large amount of energy into the rupture zone, likely leading to melting. This behavior may be akin to that of a shear band. The Sea of Okhotsk mainshock rupture appears to have been

less dissipative and little or no melting may have occurred, although seismology cannot directly constrain the amount of melting.

The stress drops found for the 2013 mainshock and large aftershock suggest preexisting zones with strong and weak regions, likely inherited from shallow faulting of the slab. The warm plate in Bolivia may have more strong, less-brittle patches than weak brittle patches, while the cold plate in the Sea of Okhotsk has more weak brittle patches than strong less-brittle patches. Strong patches may be distributed only sparsely in the Sea of Okhotsk slab, with one rupturing in the aftershock, and may act to stop rupture propagation on weak patches. The difference in the distribution of strong, less-brittle and weak, brittle patches caused by the difference in the thermal state is likely responsible for the drastically different source characteristics of the Bolivian and the Sea of Okhotsk events.

Acknowledgments. We thank E. Brodsky for helpful discussions, and three anonymous reviewers for their thoughtful comments. The Incorporated Research Institutions for Seismology (IRIS) data management center provided the seismic recordings. This work was supported in part by NSF under grant EAR-1245717 (T.L.). All data used are available from the IRIS data center.

9.5 Supplementary Methods

9.5.1 Radiated Energy Estimation

Teleseismic broadband P wave observations were analyzed for hundreds of recordings from stations of the Federation of Digital Seismic Networks (FDSN), accessed through the Incorporated Research Institutions for Seismology (IRIS) Data Management Center (DMC). High-quality signals were retained for the M_w 8.3 mainshock and M_w 6.7 aftershock for stations with computed P-wave radiation pattern coefficients higher than 0.5. Data were corrected for radiation pattern, instrument response, geometric spreading and attenuation parameterized with varying values of t^*. The low frequency portion of the average spectrum, below 0.05 Hz, is obtained from the source spectrum of the moment rate function determined by finite-fault inversion of teleseismic P waves and the long-period estimate of seismic moment, M_0 = 4.1 x 10^{21} Nm. The moment rate function characterizes the time history of the seismic radiation from the fault and is one of the most robust source attributes that can be determined using seismic waves. The higher frequency part of the source spectrum is obtained from averaging the corrected broadband P wave spectra for many stations. Subsets of 102 observations for the mainshock and 22 for the aftershock with good azimuthal distribution were used for computing individual estimates of seismic energy, and the estimates were averaged logarithmically to give the average radiated energy estimates and the average source spectra in Figure 9.2.

284 pairs of recordings for the mainshock and aftershock with both signals having radiation pattern coefficients higher than 0.2 were used to compute the spectral ratio average in the passband 0.03-0.25 Hz. Examples of spectra are shown in Figure 9.A1. The individual spectral ratios were binned in 30° azimuthal windows and then averaged logarithmically to compute the mean value, scaled by the seismic moment of the aftershock, shown in Figure 9.2.

9.5.2 Finite-fault model inversions

We use a multi-time-window linear least-squares kinematic inversion procedure [Hartzell and Heaton, 1983; Kikuchi and Kanamori, 1991]. Our initial finite-fault models (Figures 9.A2 and A3) are parameterized with 17 nodes (central positions of subfaults) along strike and 17 nodes along dip with spacing proportional to imposed rupture velocity (3.75 km for 1 km/s, 7.5 km for 2 km/s, 11.25 km for 3 km/s, and 15 km for 4 km/s). We consider both nodal planes of the USGS W-phase point source moment tensor solution (best-double couple). The shallow-dipping plane has strike 184°, dip 10° and the steeply dipping plane has strike 12°, dip 81°. Each subfault source time function is parameterized with 4 2-s rise time symmetric triangles, allowing subfault rupture durations of up to 10 s. Rake is allowed to vary for each subevent of each subfault by allowing two rake values ±45° from the average given by the W-phase solution, with a non-negative moment constraint [Lawson and Hanson, 1995]. The hypocenter is 609 km deep. We apply Laplacian regularization, which constrains the second order gradient for each parameter to be zero.

75 teleseismic P wave records are used in the inversion, from global FDSN broadband seismic stations accessed through the IRIS-DMC. The data were selected from hundreds of available FDSN seismograms to have good azimuthal coverage (Figures A9 and A10) and high signal-to-noise ratios, for epicentral distances from 30° to 90°. The instrument responses are removed from the raw data to recover ground displacement records. A causal band-pass filter with corner frequencies at 0.003-0.9 Hz was applied to the data. The teleseismic Green's functions are generated with a reflectivity method that accounts for interactions in 1-D layered structures on both the source and receiver sides [Kikuchi and Kanamori, 1991]. The

PREM velocity structure is used in the modeling. A 60 s long time window of data with 10 s leader before the initial motion was used.

In finite-fault inversions, we usually start with a large enough fault plane to accommodate the slip zone well within it, with very low seismic moment on outer fringes of the fault model. Thus, it is necessary to trim the final slip distribution for estimating the effective rupture area. Trimming is done here by removing subfaults with a moment smaller than ξ times the moment of the subfault with the largest moment; we call ξ the trimming threshold. The purpose of trimming is twofold. First, it is to remove those subfaults with small amount of slip that can be regarded as noise in the inversion. For this purpose, a trimming threshold of ~10% is commonly used. Second, for purposes of estimating the strain energy, the stress drop to be used is $\Delta\sigma_E = \dfrac{\int_\Sigma \Delta\sigma_1 \Delta u_1 \, dS}{\int_\Sigma \Delta u_1 \, dS}$ which is the spatial average of stress drop weighted by slip. Unfortunately, it is difficult in practice to determine the slip distribution in sufficient detail to estimate its spatial distribution. Numerical models [Noda et al., 2013] have shown that $\Delta\sigma_E$ is always larger than the simple spatial average of the stress drop $\Delta\sigma$. Numerical calculations of $\Delta\sigma_E$ for many heterogeneous stress distributions indicate that a trimming threshold of from 0.15 to 0.3 can be used as a reasonable ratio for the purpose of estimating $\Delta\sigma_E$. We use 0.15 as the trimming parameter for all of our finite-fault models for the mainshock and aftershock. This value is slightly larger than commonly used in assessment of slip models, but it is larger not only to remove the insignificant subfaults but also to account for the effect of slip heterogeneity. Use of somewhat lower or higher trimming thresholds has negligible effects on our conclusions.

Very similar fits to global P waveforms were found for each case, despite large differences in spatial extent (Figure 9.A2). Slightly better fits are found using the horizontal plane, but the preference is subtle. With many-parameter space-time rupture models there is very little resolution of source finiteness for this event, as we also find to be true for the 1994 Bolivia event. Average slip values vary by a factor of 15 and static stress drop estimates by a factor of 50 for these models, so it is necessary to impose independent a priori constraints on *Vr* or fault dimensions to better constrain the source model.

The key equations for our radiation efficiency analysis are for the static stress drop for a buried rectangular fault:

$$\Delta\sigma_s = 16M_0/3\pi S_e W \tag{1}$$

where S_e is the effective rupture area that gives a corresponding estimate $\Delta\sigma_E$ that we equate to the stress drop $\Delta\sigma_s$ and W is the fault width, and the radiation efficiency

$$\eta_R = E_R/\Delta W_0 = 2\mu E_R/(\Delta\sigma_S M_0) \tag{2}$$

From Figure 9.4, for a given rupture velocity, we can infer a radiation efficiency value. With the measured radiated energy and seismic moment, and a rigidity appropriate for the source depth (m = 121 x 10^3 MPa), we then know what value of stress drop will be compatible with the crack theory. For Vr = 4 km/s, η_R = 0.6 for the deep mainshock. This requires $\Delta\sigma_s$ = 15 MPa for the Mode III crack model. Given the fault length required from P wave back-projections, we can then vary the fault width, W, for finite-fault inversions to give an inverted rupture area (for a specified trimming threshold) that yields the required stress drop. This leads to W = 60 km for the Vr = 4 km/s case. The effective rupture area in that case is 9675 km^2, using a trimming parameter of 0.15. For a fixed fault width, the stress drop estimate

varies inversely with the effective source area by (1), or for a fixed stress drop, the width varies inversely with the effective source area. As the stress drop increases the radiated efficiency decreases for a fixed fault width. The degree to which one wants to match the crack theory ideal constrains the precision of the stress drop estimate desired and the corresponding constraint on the rupture model spatial extent.

Final models, constrained by the results of back-projections for apparent fault length and rupture velocity and by the radiation efficiency condition, involve rectangular fault models with asymmetric bilateral grids around the hypocenter. The models with Vr = 4.0 km/s in Figure 9.A9 have 4 grid points along dip and 13 along strike with 15 km spacing. The along-strike spacing for Vr = 4.5 and 5.0 km/s scales proportionally (16.9 km, 18.7 km, respectively), with the number of grid points along dip being kept the same, but along strike the number of grid points reduces to 12 and 11, respectively, to bound the total fault length. Other parameters and the data set are all the same as in the initial, unconstrained models. The data are well fit by these models (Figure 9.A10).

9.5.3 Back-Projection of Teleseismic P waves

Teleseismic P waves from four geographic groupings of broadband seismometers in North America (NA) (Figure 9.A4a,b), Europe (EU) (Figure 9.A4c,d), Alaska (Figure 9.A5), and Australia/Southeast Asia, as well as short-period Hi-net borehole stations in Japan (JA) (Figure 9.A6) were back-projected to the source region [Xu et al., 2009] in order to image the short-period rupture properties of the 24 May 2013 Sea of Okhotsk earthquake and its aftershocks. Seismograms were selected from each region based on uniformity of spatial sampling and similarity of the first 10 s of the unfiltered P wavetrains as defined by the average cross-correlation coefficient (*cc*) determined from a multi-channel cross correlation

algorithm [Vandecar and Crosson, 1990]. This resulted in 74 traces with $cc > 0.7$ (AK), 67 traces with $cc > 0.5$ (AU), 86 traces with $cc > 0.7$ (EU), 409 traces with $cc > 0.75$ (JA), and 164 traces with $cc > 0.65$ (NA). For AU and NA the minimum similarity threshold was decreased slightly to increase the aperture of the array, which in turn increased the slowness resolution. For JA, only traces at distances greater than 15° from the nominal epicenter were selected in order to reduce the influence of waveform complexities created by interaction with the 660-km discontinuity.

For the mainshock back-projections the U. S. Geological Survey National Earthquake Information Center hypocenter of 54.874°N 153.281°E, h=608.9 km, 05:44:49 (UTC) was used as a reference point for aligning the waveforms. The source area was gridded in increments of 0.1° in latitude from 51° to 57° and in longitude from 148° to 159° and depth was held constant at the hypocentral value. Imaging time was sampled in 1 s intervals starting 20 s before the USGS origin time and continuing for 80 s. Power was calculated from a 10-s long, tapered window that slides along beams created with fourth-root stacking. Traces were bandpass filtered between 0.5 and 2 s prior to being stacked (for the results in Figure 9.3), and a 10 s long smoothing filter was applied in post-processing to reduce artifacts. The AK135 reference Earth model was used to calculate travel times. The two arrays show source durations of about 30 s, with beam power extending in a ribbon-like geometry about 40-50 km to NNE and about 120-130 km to the SSE. The dimensions are consistent with an average rupture velocity of 4 to 5 km/s, although three or four short, subevent-like bursts of energy occur during the rupture and we cannot rule out lateral and temporal variations in the rupture velocity. Animations of the time-varying sequences for the NA and EU back-projections are presented in Movie M1.

The spatial resolution of the mainshock radiation for the AK and JA arrays is poorer than that for the EU and NA arrays, however, the AK and JA arrays are aligned more closely to the mainshock rupture direction and have sensitivity to the along-strike source finiteness. We illustrate this with vespagrams of the AK (Figure 9.A5) and JA (Figure 9.A6) data. In each case the aligned traces are filtered between 0.5-2.0 s and beams are created for relative slownesses between -0.4 and 0.4 s/deg (in increments of 0.01 s/deg) using 3rd order phase-weighting stacking [Schimmel and Paulssen, 1997], a technique that amplifies coherent energy yet causes less waveform distortion than Nth root stacking. Power is calculated in a relative, logarithmic sense from envelopes of the stacks. Both arrays show source durations of approximately 30 s, consistent with the back-projection results, but also show a shift in differential slowness as the rupture progresses. Importantly, the AK vespagram shows a drift towards negative relative slowness, indicating steeper rays and thus longer source-receiver distances, while the JA vespagram shows a drift toward positive relative slowness, indicating shallower rays and thus shorter source receiver distances as the rupture progresses. Both vespagrams are thus consistent with southward directivity of the rupture.

We confirmed the mainshock finiteness observed for the NA and EU arrays by back-projecting data from two aftershocks with very simple sources: the M_w 6.7 event that occurred at 14:56:31 (UTC) on 24 May 2013 (52.222°N, 151.515°E, depth 623.0 km), and the m_b 4.4 event that occurred at 08:58:39 (UTC) on 28 May 2013 (54.241°N, 153.395°E, depth of 627.1 km). Results are presented in Figure 9.A7. The NA and EU array configurations used for the three events are very similar, though not exactly the same because of lower quality or missing data for the aftershocks. In fact, not enough high-quality data were available to perform the EU back-projection for the smaller aftershock. Nevertheless, the simplicity of the three aftershock back-projections that were successful confirm that the finiteness observed in

the mainshock back-projections is related to actual source complexity and is not created by any smearing artifact inherent to back-projection or any sort of wave propagation effect.

We further examined the stability of the EU and NA results by performing five additional back-projections in a series of narrow passbands centered at 0.5 s, 1 s, 2 s, 4 s, and 8 s. The gridding was the same as described above however the time averaging was scaled according the dominant period, with beam window lengths of 1.5 s, 3 s, 6 s, 12 s, and 24 s, respectively, and post-processing smoothing filter lengths of 4 s, 6 s, 14 s, 28 s, and 50 s. Results are presented in Figure 9.A8 and show relatively little spatial drift compared to back-projection images for recent megathrust earthquakes, implying that the short-period and long-period energy radiated by the mainshock were not in resolvably different spatial locations for this elongate rupture.

Synthetics were computed for the model in Figure 9.1 for the same stations in Europe and North America used in the back-projections, and processed in the same manner. Resulting images for back-projection of the synthetics in various passbands for rectangular models with Vr = 4.0, 4.5 and 5.0 km/s are very consistent with the observations overall (Figure 9.A11). In detail, the data images appear to sense the rupture front rather than the peak-slip areas, as expected for seismic radiation from a dynamic rupture. The kinematic fault models do not accurately account for high frequency radiation at the crack tip. These results are very stable compared to back-projections for shallow events because there is no interference from surface reflections. We do not include surface reflections in the imaging given uncertainty in the slab structure and strong attenuation of the depth phases.

9.6 Supplementary Figures

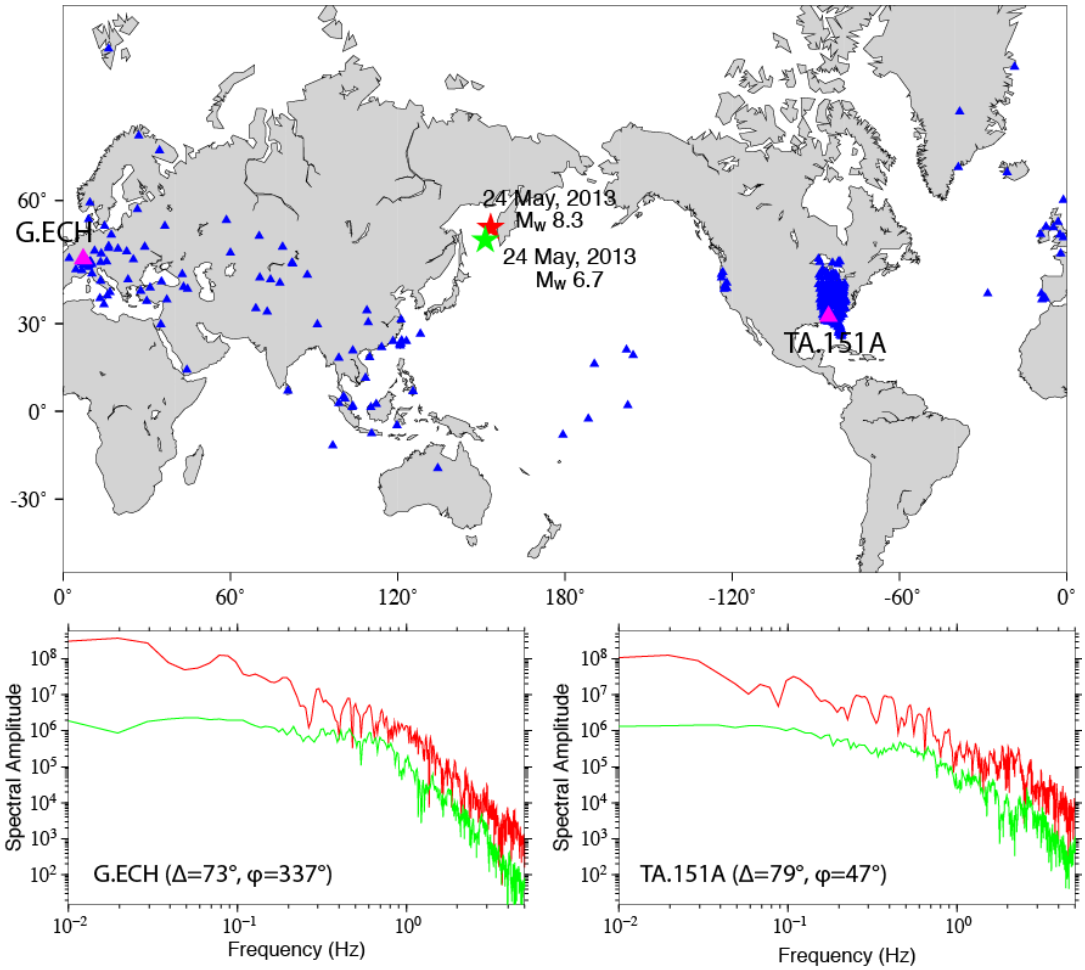

Figure 9.A1. Distribution of seismic stations used for spectral ratio analysis. The map shows the locations of 284 global broadband seismic network stations for which teleseismic P wave spectra were analyzed for the 24 May 2013 mainshock (M_w 8.3) (red star) and aftershock (M_w 6.7) (green star). Only stations with P wave radiation pattern coefficients larger than 0.2 for both events were used in the spectral ratio procedure. Example spectra from the stations with pink triangles on the map are shown below for the mainshock (red) and aftershock (green). Each station's epicentral distance (Δ) and azimuth (ϕ) are indicated. The spectra are corrected for relative radiation pattern and geometric spreading, but not for instrument response, which is common to the two events. The aftershock spectrum begins to drop off with frequency at around 0.5-0.6 Hz, which limits the range for which it serves as an empirical Green's function event. Spectral ratios in the passband 0.03-0.25 Hz are stacked and multiplied by the aftershock moment to obtain the mainshock source spectrum estimate in red in Figure 9. 2.

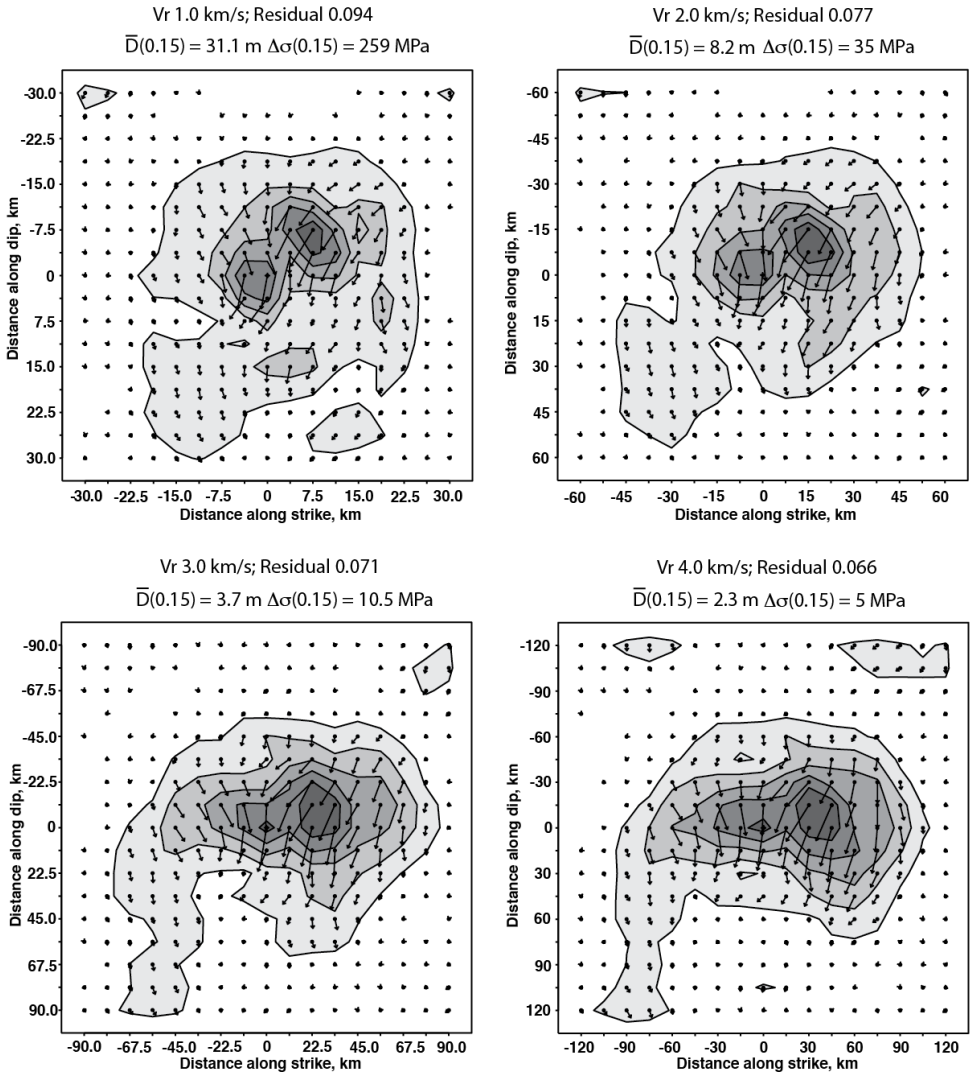

Figure 9.A2 Mainshock finite-fault models for varying rupture velocity for the shallow dipping plane. Slip distributions for four models with different constant rupture velocity with grid spacing scaling proportional to grid velocity. The strike is 184° and dip is 10° for all cases. Large model grids are used, with the hypocenter located at the center of each grid. For small *Vr* the rupture is relatively circular, but as it increases the model tends to elongate in the positive strike direction (toward the south). There is only about 3% greater reduction of the waveform mismatch for the much larger model for *Vr* = 4.0 km/s than for the very concentrated rupture for *Vr* = 1.0 km/s. For each model, the average displacement is computed for only those subfault sources with a seismic moment at least 15% as large as the largest sub-fault seismic moment and these values are given as D(0.15). Using the corresponding area of the remaining subfaults, a static stress drop is calculated using a circular rupture with radius matching the area of significant slip. There is about a factor of 50 range in stress drop estimate.

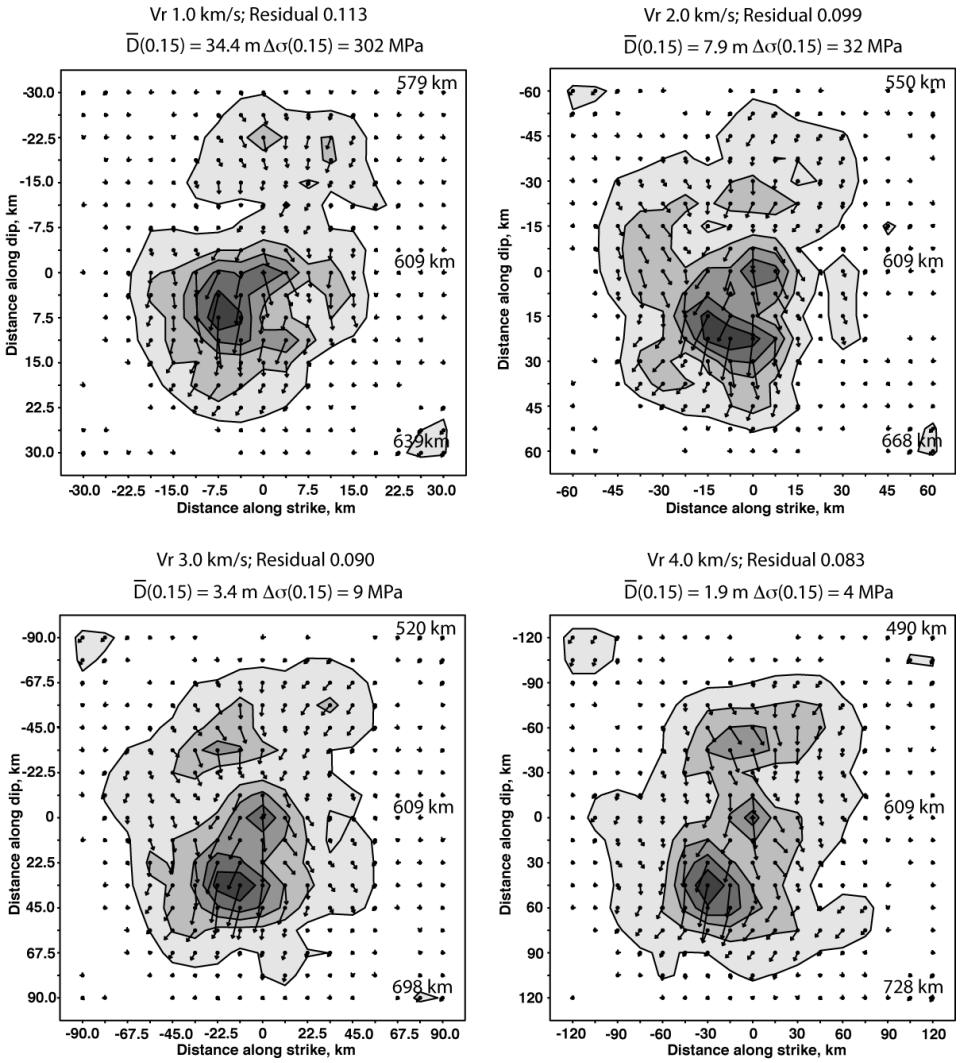

Figure 9.A3 Mainshock finite-fault models for varying rupture velocity for the steeply dipping plane. Slip distributions for four models with different constant rupture velocity with grid spacing scaling proportional to grid velocity. The strike is 12° and dip is 81° for all cases. Large model grids are used, with the hypocenter located at the center of each grid. For small *Vr* the rupture is relatively circular, but as it increases the model tends to elongate in the negative strike direction (toward the south). There is only about 3% greater reduction of the waveform mismatch for the much larger model for *Vr* = 4.0 km/s than for the very concentrated rupture for *Vr* = 1.0 km/s. For each model, the average displacement is computed for only those subfault sources with a seismic moment at least 15% as large as the largest sub-fault seismic moment and these values are given as D(0.15). Using the corresponding area of the remaining subfaults, a static stress drop is calculated using a circular rupture with radius matching the area of significant slip. There is about a factor of 76 range in stress drop estimate.

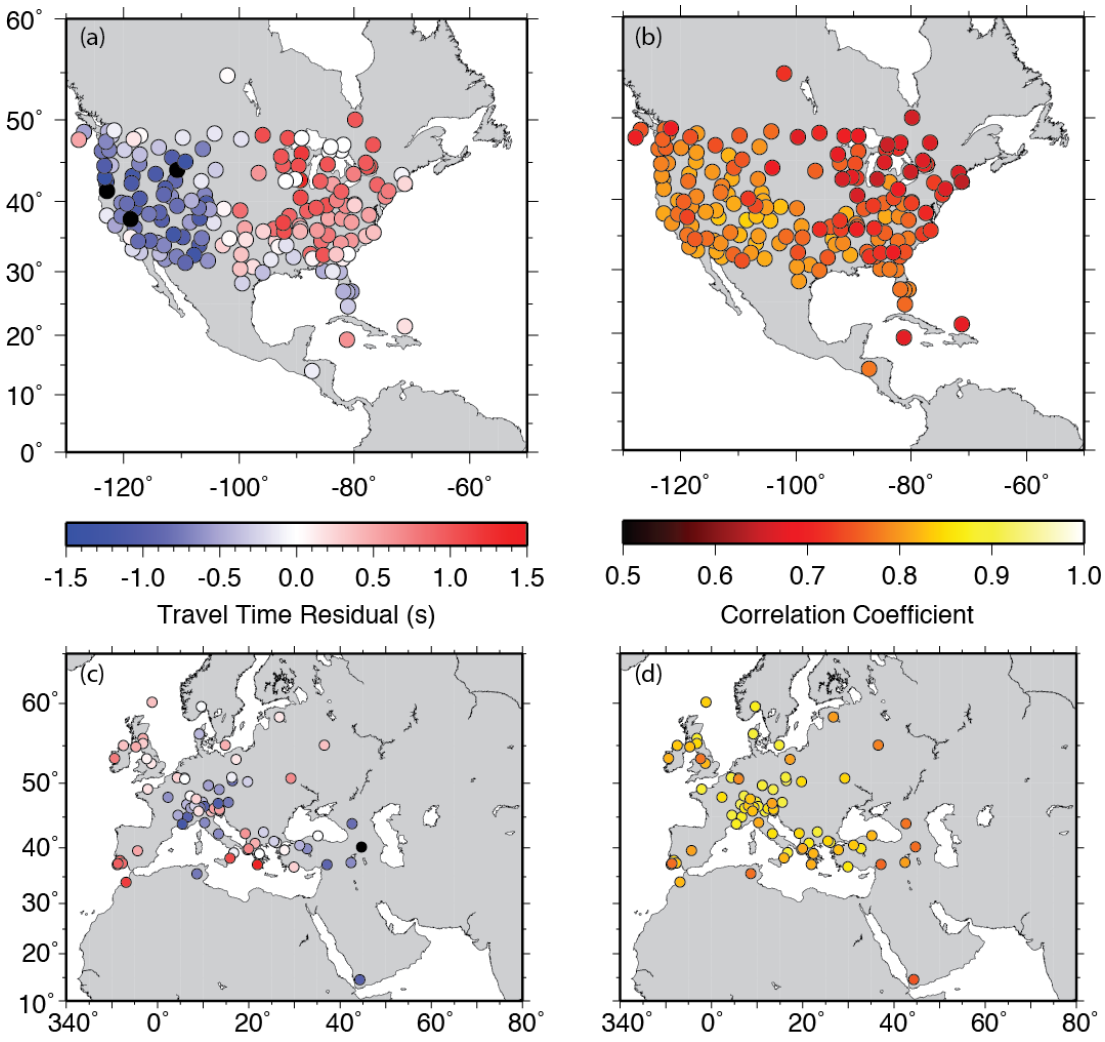

Figure 9.A4 Seismic station networks used for P wave back-projections. Maps of the broadband seismic station distributions in North America (a, b) and Europe (c, d) from which teleseismic P waves are obtained and back-projections to the source region performed. The station travel time residuals used to align the P waves, as determined by cross-correlation analysis are shown in (a) and (c), and the corresponding aligned trace correlation coefficients are shown in (b) and (d). The broadband traces were used for the alignment and then narrow-band filters were applied for back-projections of different passband signals. Figure 9. 3 shows the back-projection results for the 0.5-2.0 Hz passband data for the two networks.

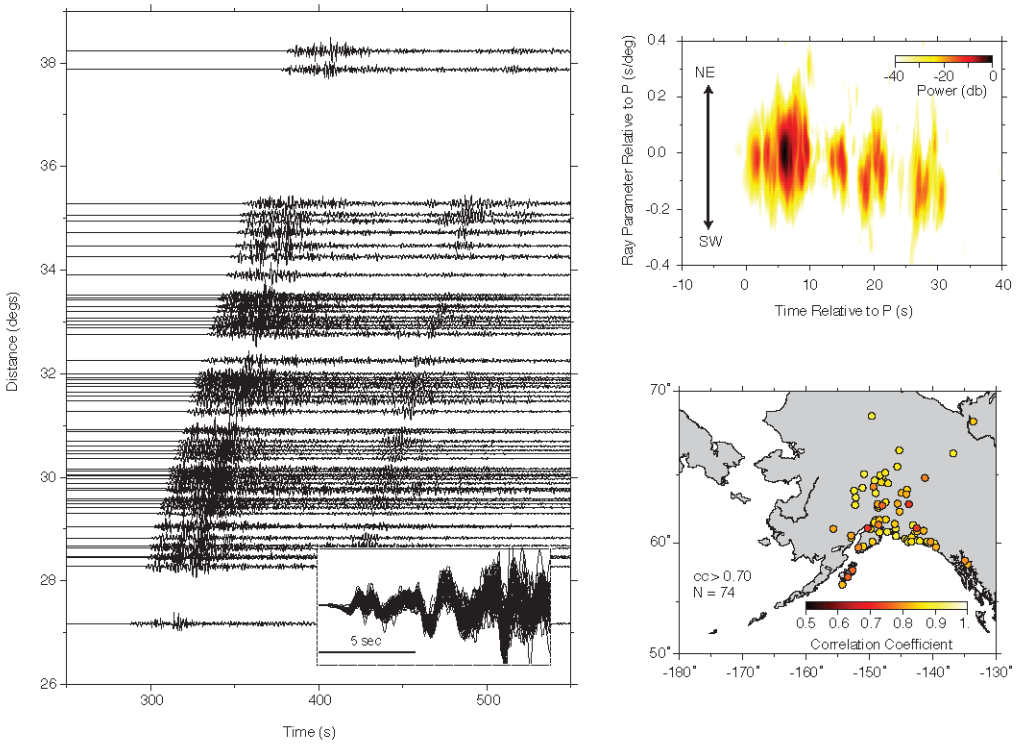

Figure 9.A5 Slowness variations for stations in Alaska. (a) The mainshock was well-recorded at seismic stations in Alaska, with. A profile of data is shown on the left, with the inset showing the well-correlated onset of the waveforms in the first second aligned by multi-channel correlations (the map at lower right shows the correlation coefficients for the aligned stations). The top right is a plot of travel-time ray parameter (slowness) as a function of time (vespagram). The decrease in ray parameter with time indicates that the source in rupturing away from the array (southward).

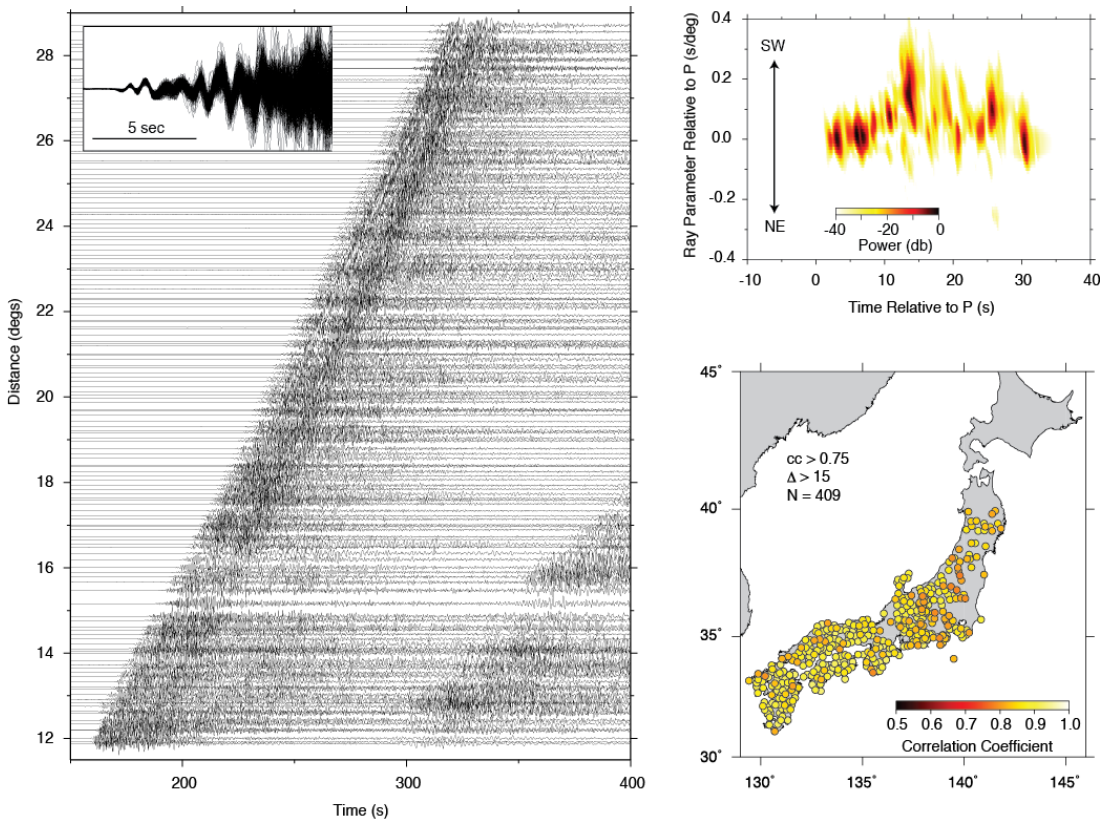

Figure 9.A6 Slowness variations for Hi-net stations in Japan. (a) The mainshock was well-recorded at short-period borehole stations across Japan in the Hi-net array. A profile of data is shown on the left, with the inset showing the highly correlated onset of the waveforms in the first second aligned by multi-channel correlations (the map at lower right shows the correlation coefficients for the aligned stations). The top right plot is a vespagram. The increase in ray parameter with time for the first 15 s of the waveform indicates that the source in rupturing toward the array (southward).

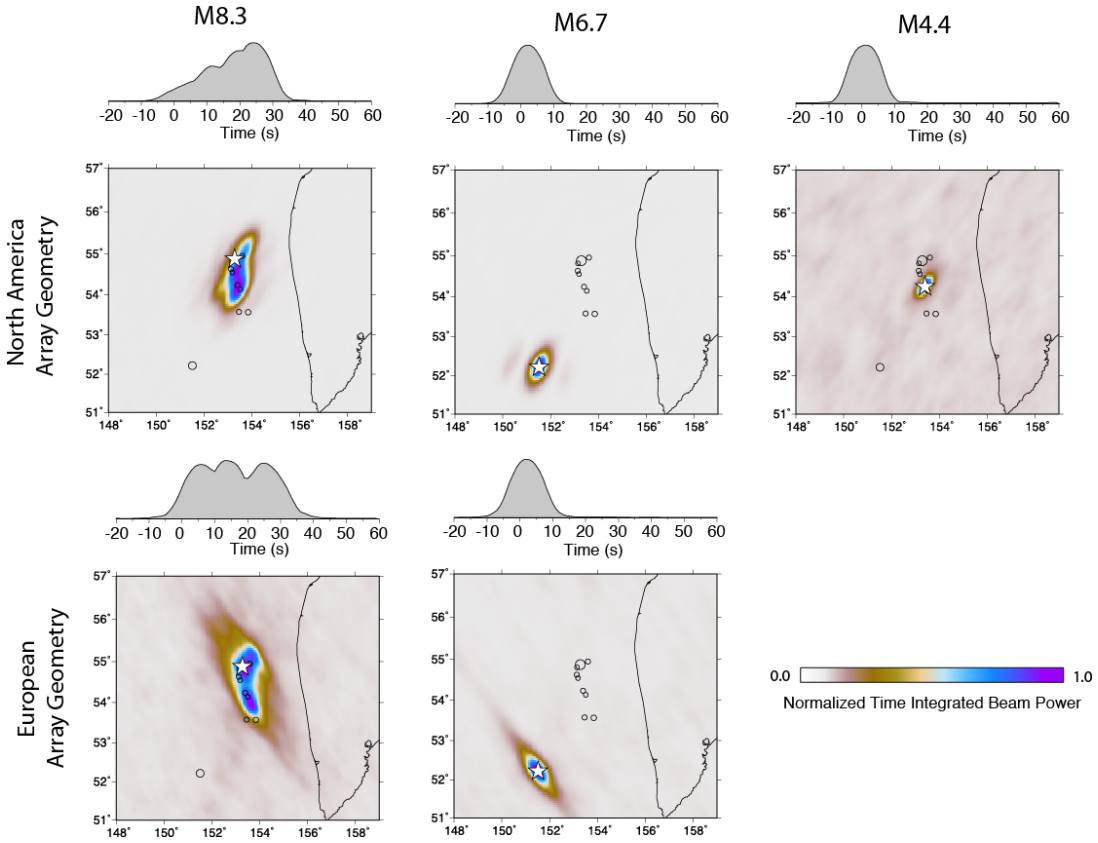

Figure 9.A7 Time-integrated plots of high frequency P wave back-projections for the mainshock and two aftershocks for data from North America and Europe stations. An evaluation of the network response artifacts in the back-projections for the M_w 8.3 mainshock is provided by back-projection of observations from the same stations for the M_w 6.7 aftershock and, for North America only, a m_b 4.4 aftershock. The two aftershocks should essentially be point-sources of energy due to having small spatial and temporal distributions of their energy release, and they are well imaged as spatially concentrated sources for data from both network configurations. The images with southern extension for the mainshock are thus reliable features of the finiteness, with any localized subevent pulses during the mainshock event being smeared out in the images to the same extent as for the aftershocks.

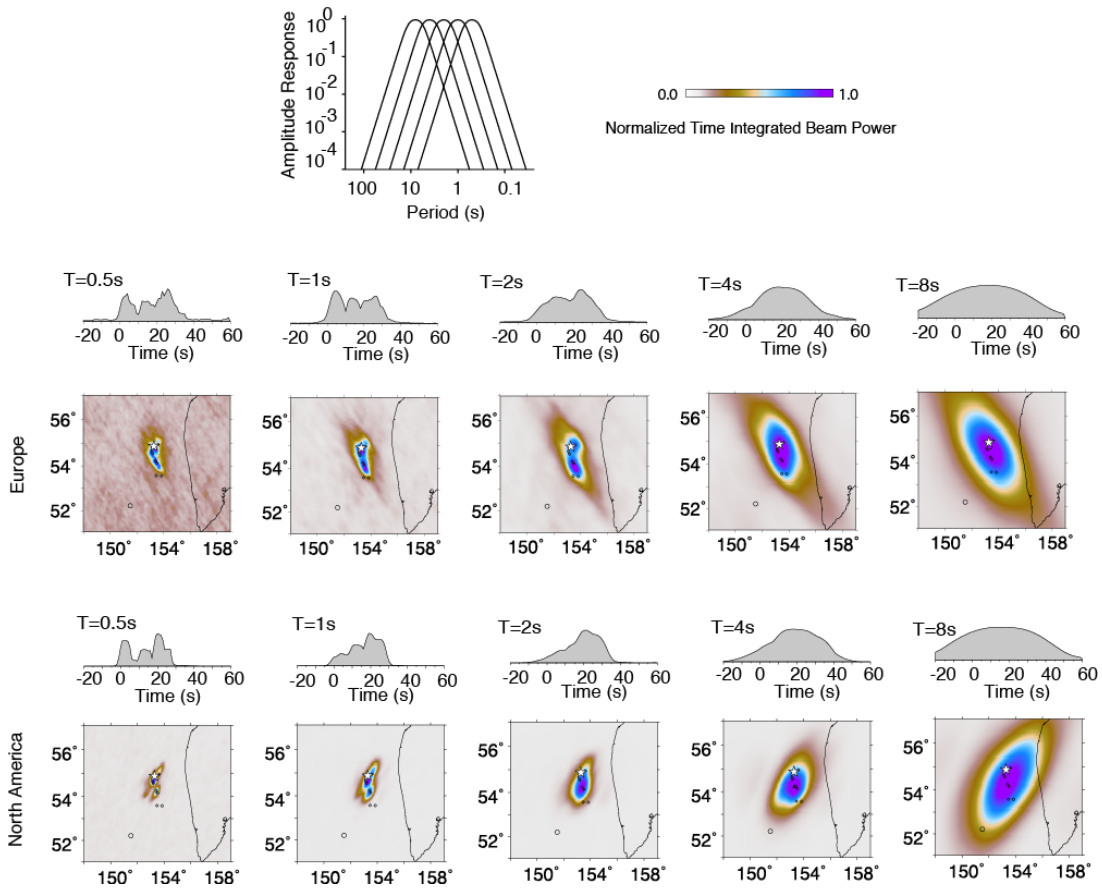

Figure 9.A8 Time-integrations of back-projections for a suite of narrow-band filtered P waves. The results for Europe and North American observations are shown. The narrowband filters are shown at the top left. The time-integrated back-projection for the P waves in each passband, aligned by the broadband signal correlations, are shown in the maps, with time-variation of peak image amplitude shown above each image. The decreasing temporal and spatial resolution with increasing period is a consequence of reduction of the move-out time lags for the finite-rupture relative to the dominant period of the signals.

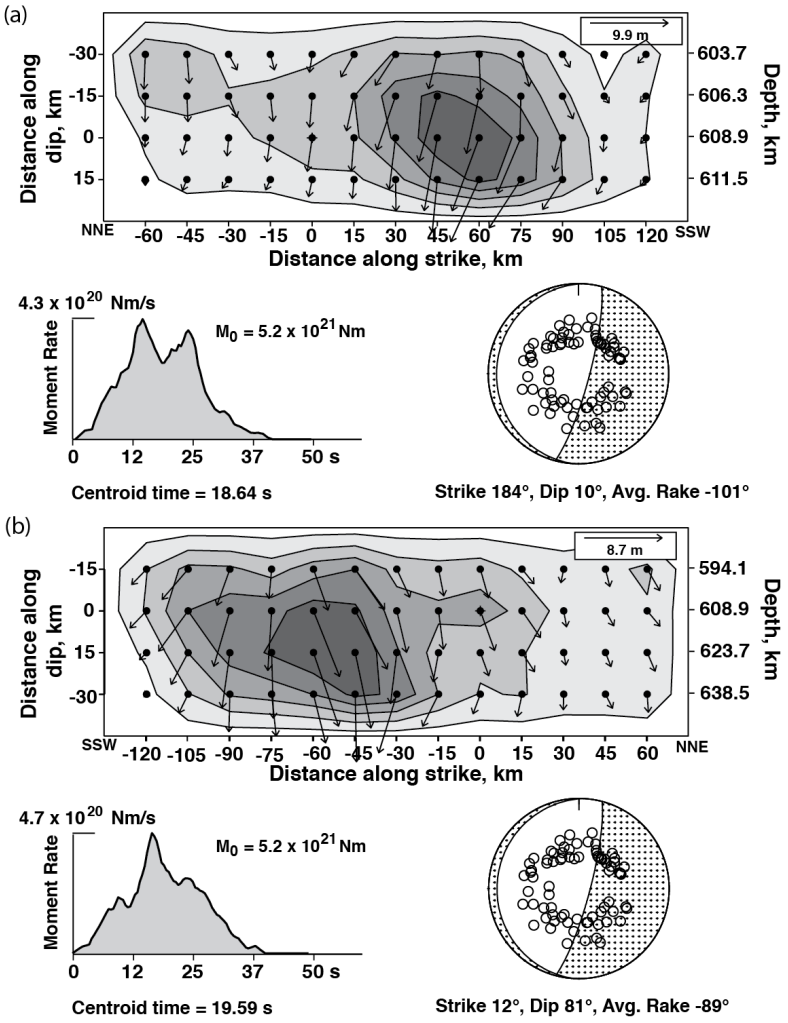

Figure 9.A9 The preferred rupture models. These models are for (a) the shallow dipping fault plane and (b) the steeply dipping fault plane. Both have a rupture velocity of 4.0 km/s, with the along-strike dimension being compatible with the back-projection images in Figure 9.A4, and the along-dip dimension being constrained so that the calculated stress drop for the average slip for subfaults with moment at least 15-20% of the largest subfault moment is 15 MPa, using the formula for a contained dip-slip fault with a width of 60 km. For this stress drop, the radiation efficiency is compatible with a Mode III crack with corresponding rupture velocity (Figure 9. 4). The upper figure in each part shows the slip model with vectors indicating the variable rake on the fault (motion of the upper block relative to the lower block) with slip contoured in m. The source moment rate function is shown at the lower left, and has a centroid time of 18.6 s, compatible with the W-phase inversion centroid time. The focal mechanism shows the faulting geometry and gives the average rake of the fault model (strike and dip are fixed), and the take-off angles of P waves used in each inversion are shown. The corresponding waveform matches for the model in (a) are in Figure 9.A10.

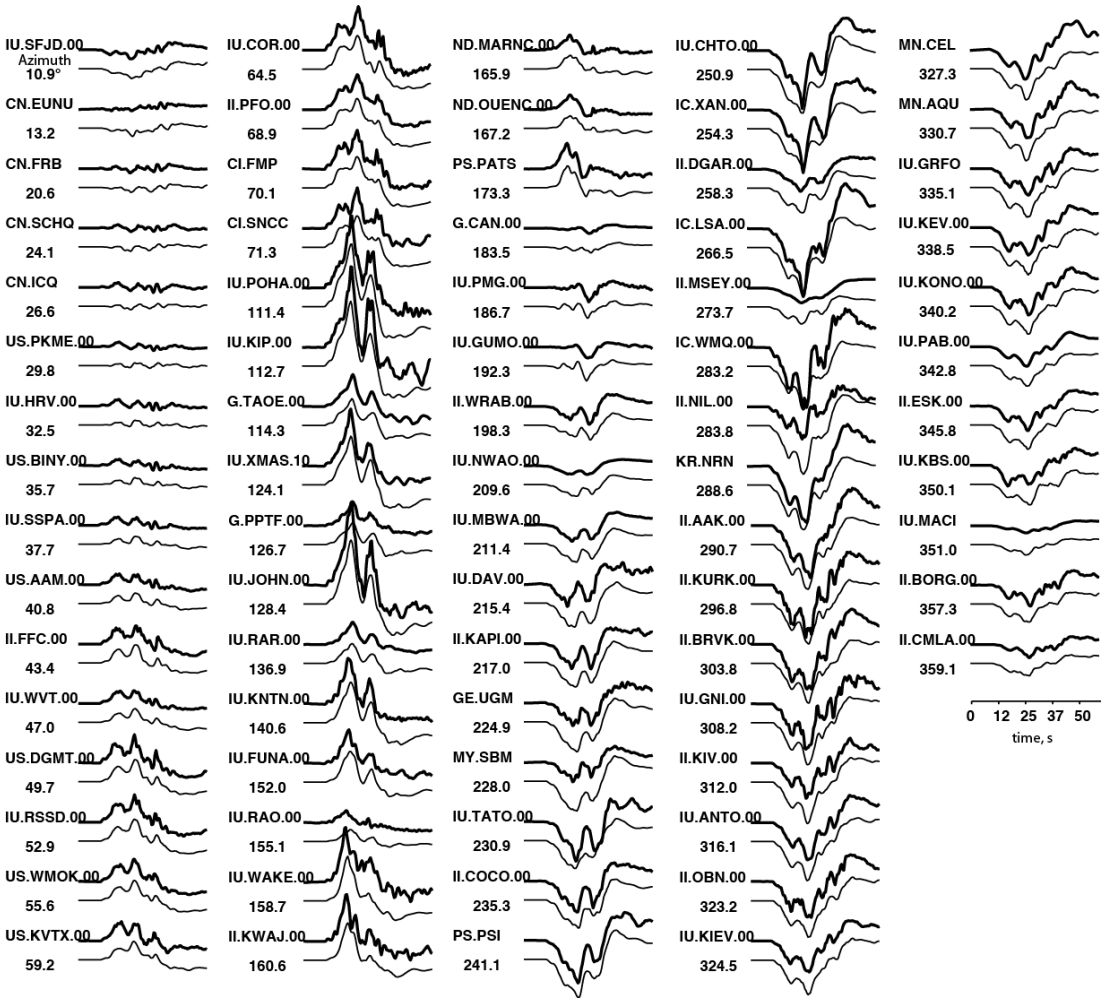

Figure 9.A10 P wave observations and predictions for the preferred shallow dipping model. Comparison of global teleseismic P wave observations (bold lines) and synthetics (light lines) for all data used in the finite-fault inversion in Figure 9.1 and Figure 9.A9a. Each station name and azimuth is given and all amplitudes are on a common scale. A 60 s time window with 10 s leader was used in the inversion.

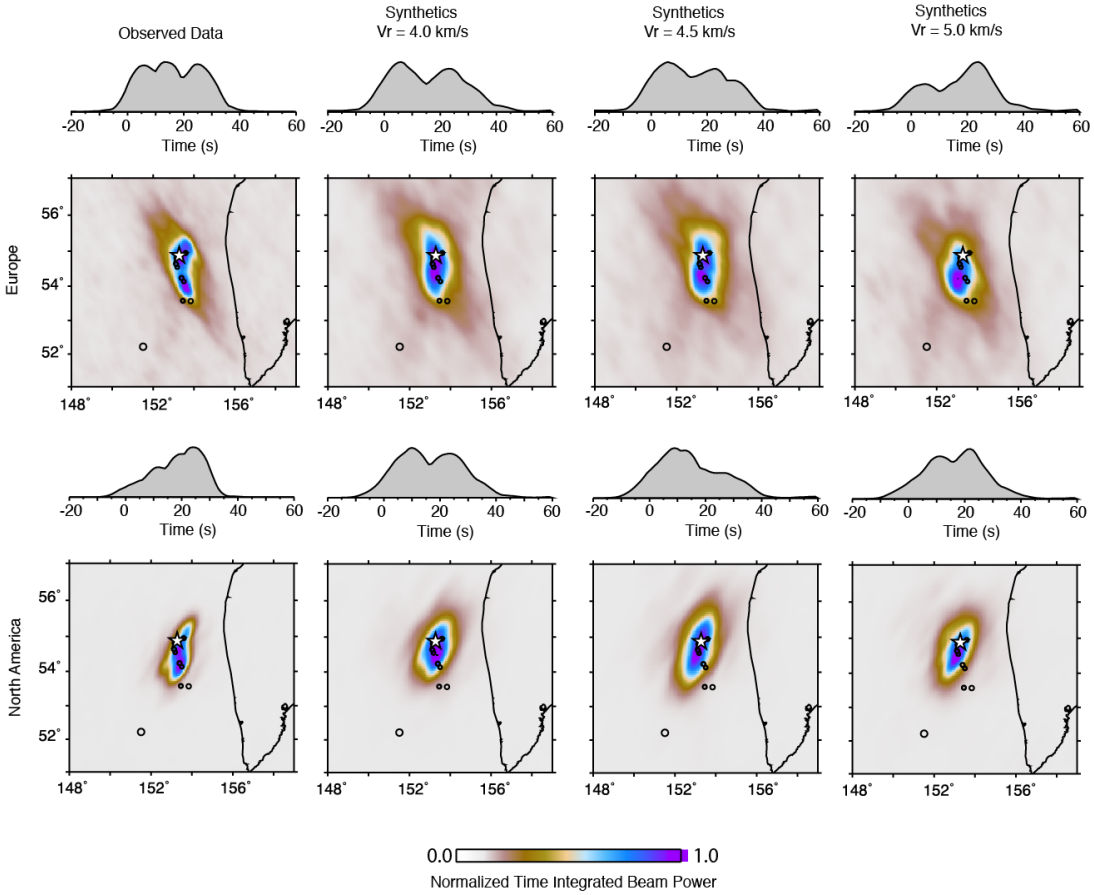

Figure 9.A11 Comparison of observed and synthetic back-projections. The time-integrated maps for back-projections of the data from Europe and North America (left column) are compared with back-projections for rupture models with varying rupture velocity that satisfy the radiation efficiency as shown in Figure 9. 4. The synthetics were made at the same stations and processed the same way as the data. The period range is 0.5-2.0 s. Models for the shallow-dipping fault plane (as in Figure 9.A9a) are shown Very similar comparisons are found for synthetics for models with the steeply dipping fault plane (as in Figure 9.A9b), with somewhat narrower features being imaged.

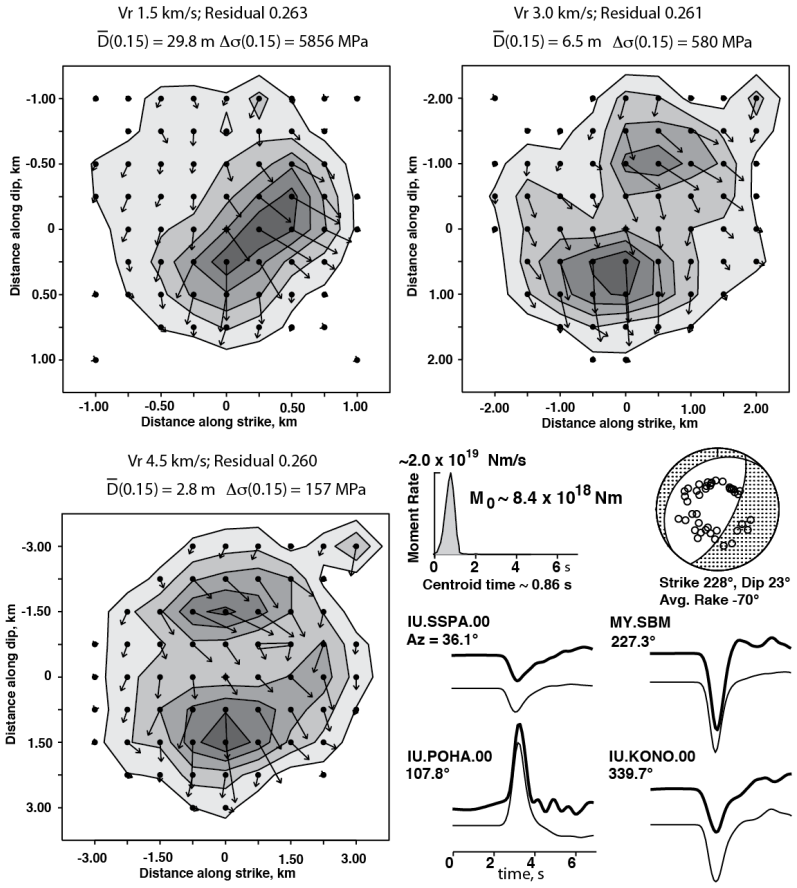

Figure 9.A12 Aftershock finite-fault models for varying rupture velocity. Slip distributions for three models with different constant rupture velocity with grid spacing scaling proportional to grid velocity. The strike is 228° and dip is 23° for all cases. Compact model grids are used, with the hypocenter located at the center of each grid. For small *Vr* the rupture is relatively circular, but as it increases the slip pattern develops two small patches. There is negligible difference in fit to the data for the different rupture models. For each model, the average displacement is computed for only those subfault sources with a seismic moment at least 15% as large as the largest sub-fault seismic moment and these values are given as D(0.15). Using the corresponding area of the remaining subfaults, a static stress drop is calculated using a circular rupture with radius matching the area of significant slip. There is about a factor of 37 range in stress drop estimate, and the stress drop is in the range 157 MPa to 5856 MPa. All of the inversions give similar source time functions, seismic moments and centroid times, with representative values being shown along with the average focal mechanism. Examples of waveform data (bold lines) and synthetics (thin lines) are shown, indicating the very short pulse of the teleseismic P wave signal, with some stations having minor broadening due to attenuation or slab diffraction. The energetic, short-duration impulse nature of the source made it a good empirical Green function event.

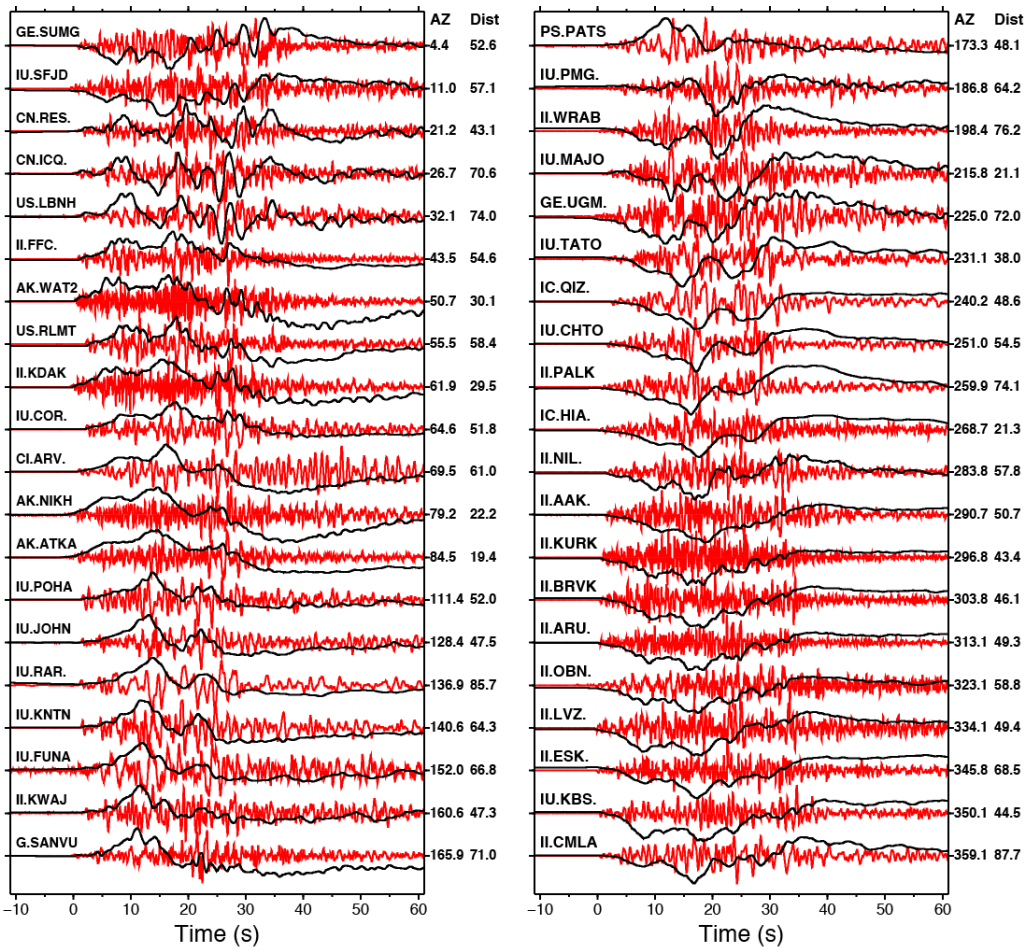

Figure 9.A13 Ground motion accelerations and displacements. Teleseismic P wave recordings from globally distributed broadband seismic stations for the 2013 Sea of Okhotsk event are shown, with the ground displacements given by the black lines and the corresponding ground accelerations given by the red lines. There is good correspondence between the overall temporal distribution of ground accelerations and the displacements (both are free of interference with surface reflections), and this supports use of short-period back-projection as a guide on the rupture kinematics.

Chapter 10

The 2015 isolated deep M_W 7.9 Ogasawara (Bonin) Islands earthquake

This chapter is under submission of:

Ye, L., Z. Zhan, T. Lay, H. Kanamori, and J. Hao (2015),"The isolated deep earthquake 30 May 2015 M_W 7.9 Ogasawara (Bonin) Islands", submitted.

Abstract. Deep-focus earthquakes, located in very high pressure conditions 300 to 700 km below the Earth's surface within sinking slabs of relatively cold oceanic lithosphere, are mysterious phenomena. Seismic waves radiated during rupture provide our primary information about deep earthquake processes, and detailed seismic source characterization is essential for working toward understanding the mechanism of deep events. The largest recorded deep-focus earthquake (M_W 7.9) in the Izu-Bonin slab struck on 30 May 2015 beneath the Ogasawara (Bonin) Islands, isolated from prior seismicity by over 100 km in depth, and followed by only a few small aftershocks. Globally, this is the deepest (680 km centroid depth) event with $M_W \geq 7.8$ in the seismological record. Seismicity indicates along-strike contortion of the Izu-Bonin slab, with horizontal flattening near a depth of 550 km in the Izu region and rapid steepening to near-vertical toward the south above the location of the 2015 event. This event was exceptionally well-recorded by seismic stations around the world, allowing detailed constraints to be placed on the source process. Analyses of a large global data set of P, SH and pP seismic phases using short-period back-projection, subevent directivity, and broadband finite-fault inversion indicate that the mainshock ruptured a shallowly-dipping fault plane with patchy slip that spread over a distance of ~40 km with a

multi-stage expansion rate (~5+ km/s down-dip initially, ~3 km/s up-dip later). During the 17 s total rupture duration the radiated energy was ~3.3 x 10^{16} J and the stress drop was ~38 MPa. The radiation efficiency is moderate (0.34), intermediate to that of the 1994 Bolivia and 2013 Sea of Okhotsk M_W 8.3 deep earthquakes, indicating a continuum of source processes in deep earthquakes from dissipative, more viscous failure to very brittle failure. The isolated occurrence of the event, much deeper than the apparently thermally-bounded distribution of Bonin-slab seismicity above 600 km depth, suggests that localized stress concentration associated with the pronounced deformation of the Izu-Bonin slab and proximity to the 660-km phase transition likely played a dominant role in generating this major earthquake.

Key Words: Deep Earthquakes, Izu-Bonin Slab, Rupture Process, Slab Deformation, Transformational Faulting

10.1 Introduction

Seismic wave radiation from deep-focus earthquakes is essentially indistinguishable from that for shallow stick-slip frictional-sliding earthquakes, but the confining pressure and temperature are so high for deep-focus events that a distinct process is likely needed to account for their abrupt energy release (e.g., Green and Houston, 1995). The two largest recorded deep-focus earthquakes both have seismic wave radiation consistent with shear dislocation on one or more fault planes, but exhibit dramatic differences in rupture characteristics. The 24 May 2013 (M_W 8.3) Sea of Okhotsk earthquake near 609 km depth is the highest seismic moment, longest duration deep event (e.g., Ye et al., 2013; Wei et al., 2013; Chen et al., 2014; Zhan et al., 2014a). The rupture expanded rapidly over a 100+ km long zone, possibly involving several offset faults, at ~4.0 km/s, and the static stress drop of ~15 MPa is comparable to that for shallow intraplate events. This event had large moment-

scaled radiated energy and high radiation efficiency (~0.6). In contrast, the second largest deep event is the 9 June 1994 (M_W 8.3) Bolivia earthquake (e.g., Zhan et al., 2014a; Kikuchi and Kanamori, 1994; Silver et al., 1995; Kanamori et al., 1998), for which the rupture initially had rapid expansion with low energy release and then expanded slowly over about 50 km at ~1.5 km/s, with the static stress drop being ~114 MPa. This event had low moment-scaled radiated energy, and very low radiation efficiency (~0.03), indicative of a very dissipative source process overall. Such profound differences in rupture behavior, comparable to the variability observed for shallow ruptures, challenge efforts to determine the fundamental nature of deep-focus earthquakes.

Currently favored ideas for nucleation and growth of deep-focus earthquakes include transformational faulting triggered by metastable olivine transforming to spinel in the cold, stressed core of the slab (e.g., Green and Burnley, 1989; Wiens et al., 1993; Green and Houston, 1995; Kirby et al., 1996; Green, 2007), thermal instability and run-away shear melting (Kanamori et al., 1998; Ogawa, 1987; Karato et al., 2001), and dehydration embrittlement (possibly involving release of H_2O or CO_2 as hydrous or carbonate phases destabilize with increasing pressure) (e.g., Silver et al., 1995; Omori et al., 2004; Meade and Jeanloz, 1991). All of these proposed mechanisms are influenced by the thermal structure of deep slabs and the deviatoric stress conditions associated with the slabs impinging on the 660-km seismic discontinuity, which resists penetration due to the associated endothermic phase change of spinel to perovskite plus ferropericlase mineralogy (Green and Houston, 1995; Karato et al., 2001).

Distinguishing between the possible mechanisms for deep-focus earthquakes is difficult because resolving their fault dimensions and source processes is very challenging. For many deep-focus events, few aftershocks occur to help constrain the faulting extent and geometry

(Wiens and McGuire, 1995), and the spatial extent of large deep earthquakes tends to be small and difficult to resolve by seismic waves. Various seismological methods have been applied to estimate source dimensions, rupture velocity, and source complexity for large deep events (e.g., Lundgren and Giardini, 1995, Wu and Chen, 2001; Antolik et al., 1996; Goes et al., 1997; Tibi et al., 2003a,b; Kirby et al., 1995, Warren and Silver, 2006; Zhan et al., 2014b). The diversity of rupture characteristics for the two largest deep events is reinforced by observed variable processes of other large deep earthquakes. It is important to increase the observational constraints on large deep-focus earthquakes to add additional information that may help to constrain their basic mechanism.

10.2 The Isolated 2015 Deep Event

The 30 May 2015 Ogasawara (Bonin) earthquake (11:23:02 UTC) has a 664 km deep hypocenter at 27.839°N, 140.493°E [USGS, National Earthquake Information Center (USGS-NEIC), http://earthquake.usgs.gov/earthquakes/eventpage/us20002ki3#scientific_origin:us_us20002ki3]. Figure 10.1 shows the dramatic isolation of this deep event relative to prior seismicity in the Izu-Bonin slab. The rapid Global Centroid Moment Tensor (GCMT) point-source solution for the earthquake shown in Figure 10.1 has a centroid depth of 679.9 km, with a seismic moment of 7.76 x 10^{20} N-m (M_W 7.86). This solution has only 13% non-double couple, suggesting nearly-planar faulting, with the best double couple having nodal planes with strike 162°, dip 74°, rake -111°, and strike 37°, dip 26°, and rake -38°. Only 5 small aftershocks, the largest being an m_b 4.9 event (2 June 2015, 21:04:29 UTC, 681.4 km deep at 27.840°N, 140.616°E) close to the mainshock (depths 673.2 to 686.4 km) were located by the USGS-NEIC within a few days after the earthquake. Eight more smaller events were located

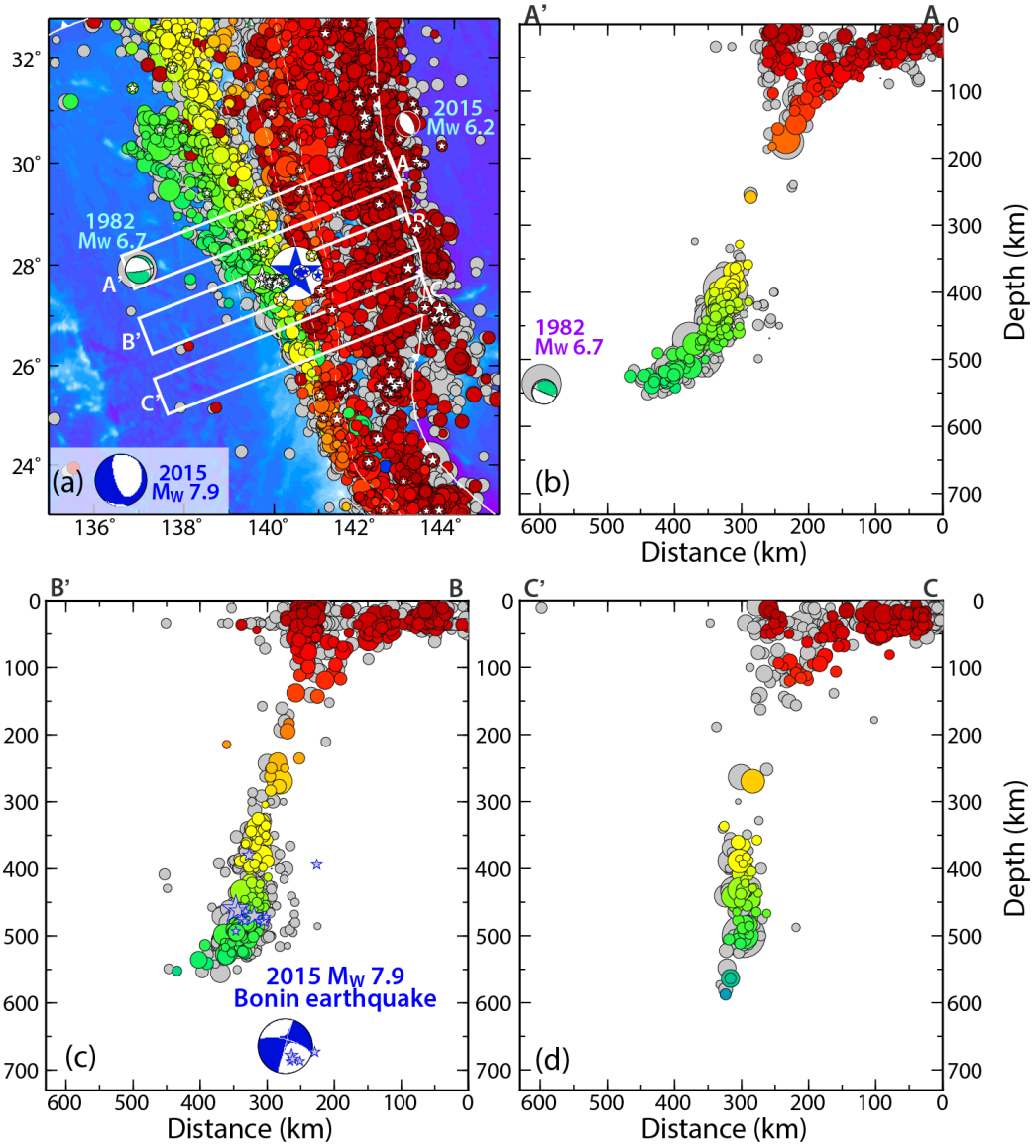

Figure 10.1 The Izu-Bonin subduction zone seismicity distribution. (**a**) Map, and (**b**), (**c**) and (**d**) cross-section of earthquake locations within the westward sinking Pacific plate below the Philippine plate from catalogs of the USGS-NEIC (gray circles) and EHB [Engdahl *et al.*, 1998] (circles color-coded by depth: reddish tones down to 200 km, yellowish from 200-400 km, greenish from 400-600 km, and blue for deeper than 600 km). The map view in (**a**) shows event epicenters including that of the 30 May 2015 event (circle with large blue star) and its gCMT focal mechanism (inset lower hemisphere projection), along with early aftershocks (depth-coded stars), the gCMT mechanism of the isolated 4 July 1982 earthquake (green focal mechanism), and locations of boxes containing the seismicity shown in cross-sections (**b**) for A'-A, (**c**) for B'-B, and (**d**) for C'-C. The focal mechanisms shown in (**b**) and (**c**) are side-view projections onto the far side of the focal sphere perpendicular to the cross-sections. The blue stars in **(c)** are early aftershocks.

nearby by the International Monitoring System as well. The earthquake also activated events throughout the Izu-Bonin slab. A shallow (9.2 km) M_W 6.2 outer rise normal faulting earthquake (Figure 10.1a) occurred about 6 hours after the event (18:49:07), and four m_b 4.1 to 4.4 events occurred above the mainshock at depths of 317-417 km within 15 days of the event. Both the paucity of nearby aftershocks and triggering of distant events in the same slab have previously been observed for some large deep earthquakes (Wiens and McGuire, 1995; Engdahl, et al., 1998; Tibi et al., 2003b). The mainshock was felt widely in Japan to the north, for waves that traveled upward within the slab.

The historical catalog of deep (≥ 300 km) earthquakes along the Izu-Bonin-Mariana (IBM) arc from 1900-2015 from the ISC-GEM (http://www.isc.ac.uk/iscgem; *Storchak et al.*, 2013) and USGS-NEIC catalogs include 14 events with magnitudes ≥ 7.0. The 2015 event is much larger than the two next largest events, which have magnitudes of 7.4 at depths of 300 and 457 km. The 664 km deep hypocenter places the 2015 event much deeper than any earlier M ≥ 7 event along Izu-Bonin (a 559 km deep event with M_W = 7.2 struck in 1955 near 24.3°N) or the Marianas (a 595 km deep event with M_W = 7.1 struck in 1995 near 18.9°N), and more than 100 km deeper than any nearby seismicity. Of the 92 major (M_W ≥ 7.0) deep focus earthquakes globally recorded from 1900 to 2015, only the 19 August 2002 M_W 7.7 Tonga event has a deeper hypocentral depth (675.4 km) (USGS-NEIC).

The seismicity cross-sections in Figure 10.1 indicate that the slab flattens near a depth of 550 km just 100 km north of the 2015 event, with a horizontally isolated M_W 6.7 event in 1982 having a near-vertical nodal plane that may involve tearing of the plate. The cross-section containing the 2015 event (Figure 10.1c) has an almost vertical seismicity distribution, although the deep event is offset eastward from a downward projection of the seismicity trend. The seismicity is even more vertically distributed to the south, and this geometry persists into

the Mariana subduction zone. Thus, the deep Ogasawara event is located in a region of strong along-strike slab distortion, but it is remarkably isolated given that its location suggests tearing, buckling or folding of the slab. Occurrence of isolated large deep earthquakes has been noted for the Izu region to the north and for other subduction zones (Lundgren and Giardini, 1994; Okino et al., 1998, Okal and Kirby, 1998; Okal, 2001), indicating that localized conditions influence otherwise aseismic extensions of the slabs. The tapering-off of the main band of Benioff-zone seismicity within the Bonin slab by a depth of 550-600 km suggests a thermal constraint on the deep earthquake occurrence, but clearly the isolated 1982 and 2015 events indicate that thermal assimilation sufficient to preclude further deep earthquake occurrence after even further slab warming has not occurred. If, for example, disappearance of a central core of metastable olivine within the slab delimits the shallower earthquake activity, one would have to postulate an independent mechanism to account for the isolated deep events.

The variation in seismogenic slab penetration depth along the strike of the IBM arc system has been attributed to lateral variation in trench rollback history and subducted slab age, with significant trench retreat during the interval 30-15 Ma in the north (~1000 km of roll-back, involving subduction of 70-95 Ma lithosphere) than in the south (~400 km of roll-back, involving subduction of 90-115 Ma lithosphere) (Faccenna et al., 2009). This appears to have contributed to horizontal flattening of the deep Izu-Bonin slab at depths near 550 km to the north of 28°N (Lundgren and Giardini, 1994; Okal, 2001), versus the near vertical extension of the Mariana slab to depths of ~800 km to the south of 20°N (Faccenna et al., 2009; Stern et al., 2003; van der Hilst and Seno, 1993). At present, the trench is actually advancing toward the upper Philippine Sea Plate along the entire IBM arc, with clockwise rotation of the upper plate producing back-arc extension along the Marianas. The age of

subducting Pacific plate at the trench currently increases from ~130 Ma to ~150 Ma southward along the IBM, and recent subduction of this very old lithosphere may account for the present advance of the trench (Faccenna et al., 2009). The age of the lithosphere at the depth of the 2015 deep event is ~100 Ma, but lack of constraint on the distorted slab geometry near the event adds large uncertainty to this value and to any associated thermal estimate for the source environment.

10.3 Rupture Analysis

The 2015 Ogasawara deep-focus earthquake is ideally located relative to global seismic stations, with several thousand broadband or high-quality borehole short-period instruments covering most azimuths (Figure 10. 2), and take-off angles ranging from almost directly upward to steeply dipping. We employed the huge data set of ground-motion recordings in a suite of analyses to determine primary features of the energy release. Unusually good resolution of the source process is achieved using the seismological observations, and this is a critical step for gaining direct insight into the basic nature of the event.

10.3.1 W-phase Analysis

The isolated location and depth of the 2015 event in Figure 10.1 is distinctive, and we confirmed the centroid depth by inverting very long-period W-phase signals for a point-source moment tensor. This well-established procedure (Kanamori and Rivera, 2008) was applied to three-component ground displacement recordings filtered in the passband 1-5 mHz from 48 globally well-distributed stations (69-71 traces) at epicentral distances of 8 to 85°. Inversions were performed using starting depths of 650 and 720 km. Stable focal mechanisms were obtained at all depths, with optimal depths of 680.5-690.5 km, and centroid

times of 5.9-9.0 s. The faulting geometry, seismic moment, and small non-double couple component are similar to the GCMT solution and are robust aspects of the rupture. When we allow for an isotropic component, we find it to be less than 1% of the moment, which is below the noise level. An average source depth near 680 km was further validated by waveform inversions of P and pP body waves and analysis of pP arrival times.

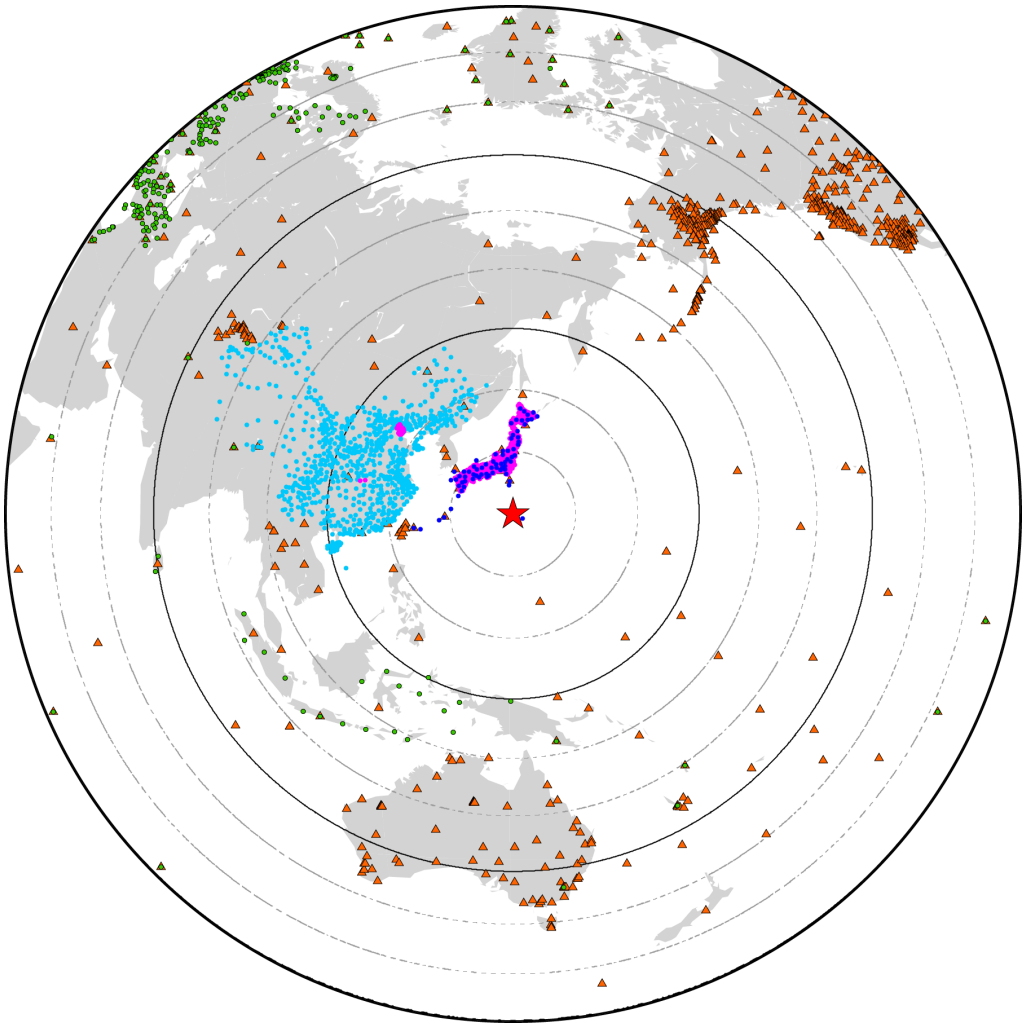

Figure 10.2 Map displaying the locations of all stations from which seismic data were used in this study, color-coded by data source (IRIS data center, brown-triangles; Orpheus data center, green circles; China Earthquake Administration, cyan circles; NIED Hi-net, pink circles; NIED F-net, blue circles).

10.3.2 Back-projection Analysis

The spatial extent and complexity of seismic energy release are the next key source attributes that can be determined by seismology, and toward this end, the superb seismic station distribution provides particular advantage. Back-projection provides a 2D time-varying sequence of images of coherent bursts of P wave energy for a horizontal grid of subevent positions around the hypocenter without assuming a specific faulting process (Xu *et al.*, 2009; Ye *et al.*, 2013). This procedure does not resolve differences in source depth.

We initially performed back-projections for separate large aperture regional networks in different azimuthal and distance bins, using waveform correlations to align the data for each network (Figure 10.A1). The Japan Hi-net borehole short-period network data were used in both 1D slant stacks and in 2D back-projections. The slant stack from northern Hi-net stations spans the largest epicentral range and indicates subevents with concentrated energy release along the NNE direction somewhat north of the hypocenter at 4.5 s and 10.5 s, and to the south at 8 s (Figure 10.A2). For the regional network back-projections a passband of 0.5-2.0 Hz was used in all cases other than for short-period Hi-net stations in Japan, where a 0.5-5.0 Hz passband was used. The regional network back-projections for six different networks consistently indicate three distinct intervals of coherent energy release from approximately 0-4 s, 5-10 s (Figure 10.A3), and 11-16 s (Figure 10.3), with minor azimuthal shifts in timing indicating that the second and third intervals originate 10-20 kilometers south of the hypocenter and 25-35 km to the west/northwest, respectively (Animation S1 shows the corresponding back-projection space-time images). The apparent (horizontal) velocities of the third energy concentration in Figure 10. 3 range from 2.2 to 2.9 km/s. The images from the separate networks are influenced by the array response characteristics, and streaking of features along the great-circle direction to each array contaminates the source images.

However, similar spatial offsets of the discrete features near the same time (Figure 10.3) indicates that basic features of the rupture are sensed, to varying degree, by each network.

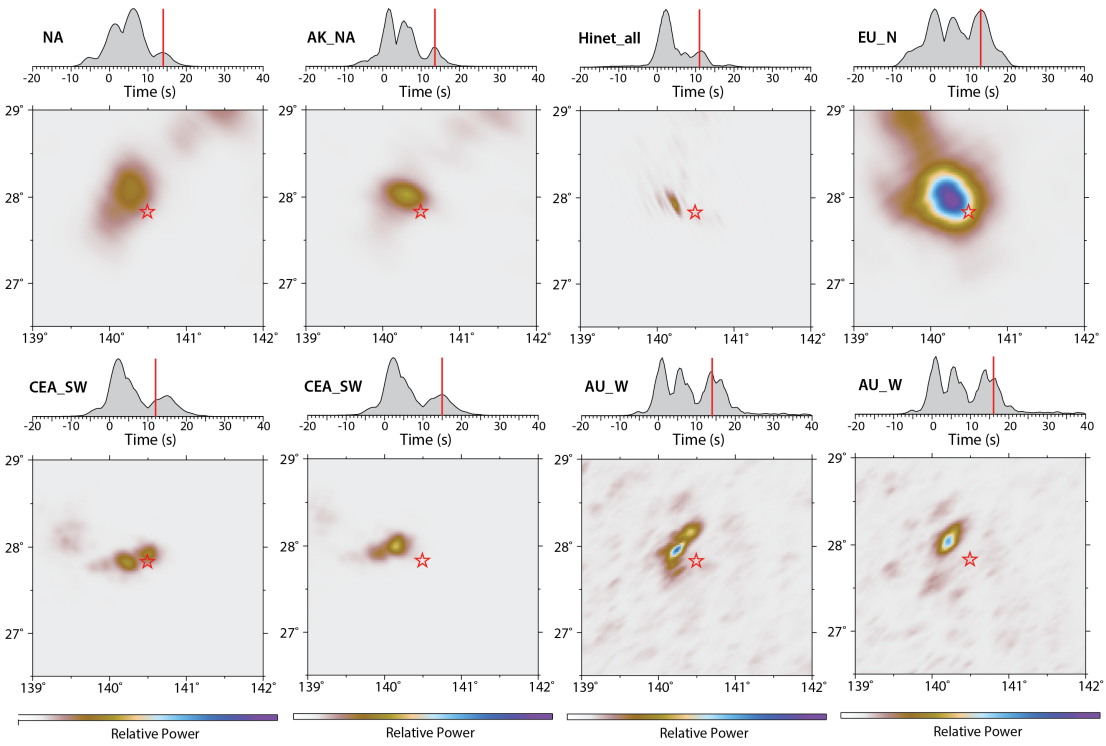

Figure 10.3 The 0.5-2.0 Hz P wave energy near the third peak in the power distributions, 11 to 16 s after the origin time, is imaged by large-aperture networks in the conterminous U.S. and adjacent regions (NA), Alaska and North American (AK_NA), Hi-net in Japan (Hinet_all), Northern Europe (EU_N), China (CEA_SW), and Indonesia-Australia (AU_W). For the CEA_SW and AU_W projections the third peak is split and separate panels are shown for each sub-peak.

The general consistency of the regional network back-projection images, the good signal-to-noise ratios of the data, and the absence of depth-phase interference allowed us to perform joint back-projections of short-period teleseismic P waves at all azimuths (Figures 10.4 and 10.A4) to constrain the overall rupture process. This is an unstable procedure for shallow events, but works well for P waves from deep events as long as polarity reversals are corrected and efforts are made to carefully align the data onsets. The global back-projections use the same data set as used below in finite-fault inversion, with broadband signals aligned by cross-

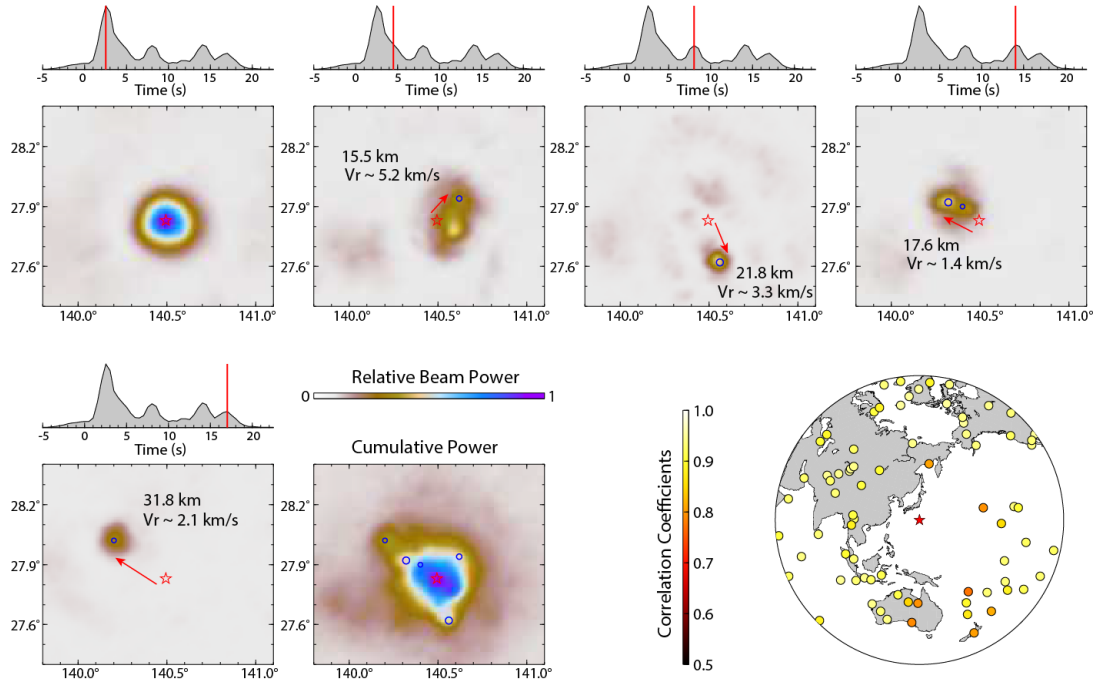

Figure 10.4 The 0.1-2.0 Hz P wave energy back-projected from a global distribution of stations (the same as used later in a finite-fault inversion). The 5 snapshot panels are at 2.5 s, 4.5 s, 8 s, 14 s, and 17 s, with the power in the 4th root stack shown around the source region. The peaks that form at discrete locations (blue circles) are used to estimate the horizontal distance from the hypocenter and an apparent rupture expansion velocity from the origin, assuming a rise-time of 1.5 s. The cumulative power across the grid is shown. The global map shows the station distribution with waveform correlation indicated.

correlation and then filtered in passbands of 0.1-2.0 Hz (Figure 10.4) and 0.5-2.0 Hz (Figure 10.A4). Figure 10.4 and Animation S2 show peak bursts of energy near, east and northeast of the hypocenter in the first 5 s, 22 km to the ESE at 8 s, and from 18 to 32 km to the WNW from 14-17 s. The overall source dimension is ~40 km. The global data set provides good spatial resolution of features that tend to streak along the azimuth to each array in the individual network images. We can estimate effective rupture expansion velocities from the location and timing of these image features (Figure 10.4 shows values of initially 5.2 km/s toward the east and later at 2.1 km/s toward the west assuming horizontal rupture), but accurate rupture velocity estimation requires analysis of vertical distribution of subevents.

10.3.3 Subevent Directivity Analysis

Broadband P and pP waveforms at teleseismic distances are very stable, as displayed in Figure 10.5. These signals are stacks in directivity bins of 0.01 s/km of varying numbers of P or pP waveforms aligned by directivity parameter, $G = -p \cos(f_{sta}-f_{ref})$, where p is the ray parameter, f_{sta} is the station azimuth, and the reference azimuth $f_{ref} = 290°$ corresponds to the average direction of the third peak in the short-period back-projections. Polarity reversals were corrected for in plotting the stacks versus directivity parameter. With the waveform stacks in Figure 10.5 aligned on the first arrival, the relative move-out of two subevents about 12 s and 17 s after the first arrival can be tracked in the P waves over a wide range of azimuths (with the ~2 s of azimuthal variation in arrival times of the arrivals being consistent with both features locating WNW from the hypocenter). Bin-average pP waveforms have generally similar total duration of motion, but the stronger attenuation of these phases (due to their extra paths up and down through the upper mantle near the source) obscures the subevents.

The move-out of secondary pulses in the waveforms was also explored using a 2D multiple sub-event procedure (Zhan et al., 2014a), applied to ground velocity recordings low-pass filtered below 0.3 Hz (Figure 10. 6a). These waveforms show clear move-out for azimuths of 290-300° consistent with that in Figure 10.5, and can be well-modeled using a 5-subevent inversion (Figure 10. 6c) with simple Gaussian subevent source time functions (Figure 10. 6d). The inversion solves for the time, wavelet duration, moment and location of each subevent, assuming a horizontal distribution. The first three subevents locate at the hypocenter, 6 km east of the hypocenter peaking at 3 s, and 6 km south of the hypocenter peaking at 6 s, with two later subevents at an azimuth of about 300° 24 km (11 s) and 42 km (15 s) from the hypocenter. These are generally consistent with the back-projections images

and with the move-out of features in the broadband displacements as seen in Figure 10. 6b.

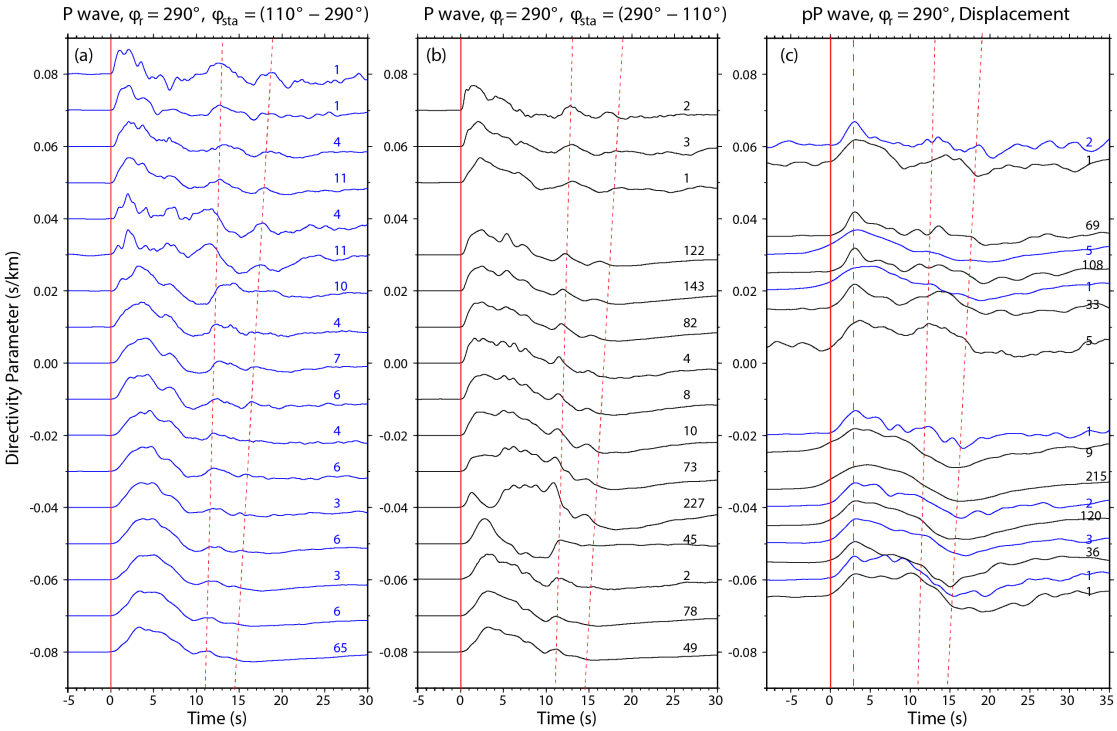

Figure 10.5 Profiles of P and pP ground displacement data plotted with respect to directivity parameter relative to reference azimuth 290°, after binning and stacking the individual data in 0.01±0.05 s/km intervals. The P data are plotted in the two left profiles, separating hemispheres to the NE and SW, with the two hemispheres combined in the pP profile on the right with blue indicating data from the NE hemisphere and black indicating data from the SW hemisphere. The numbers indicate how many traces are stacked in each bin. Negative directivity parameter of -0.08 s/km is in the reference azimuth direction. The data are aligned on onsets. The solid and dotted lines are at the same relative times in all panels. Narrowing of the waveforms toward negative values of directivity parameter indicates a component of rupture toward azimuth 290°. Similarity in duration of the waveforms for P and pP at a given directivity parameter requires small depth extent of the rupture, favoring the shallowly dipping nodal plane.

The back-projection and subevent inversion analyses do not resolve whether the subevents are on a single fault, or involve multiple faults, nor which nodal plane of the focal mechanism is involved. If we assume rupture on the steeply dipping nodal plane, the subevent ~12 s after the source and 25 km to the WNW must locate about 70 km deeper than the hypocenter. If the shallowly-dipping plane is assumed, much less vertical extent of the rupture

is required, ~12 km. Downward rupture on the steeply-dipping plane should broaden the pP depth phases relative to P, but there is no indication of this in the data profiles in Figure 10.5.

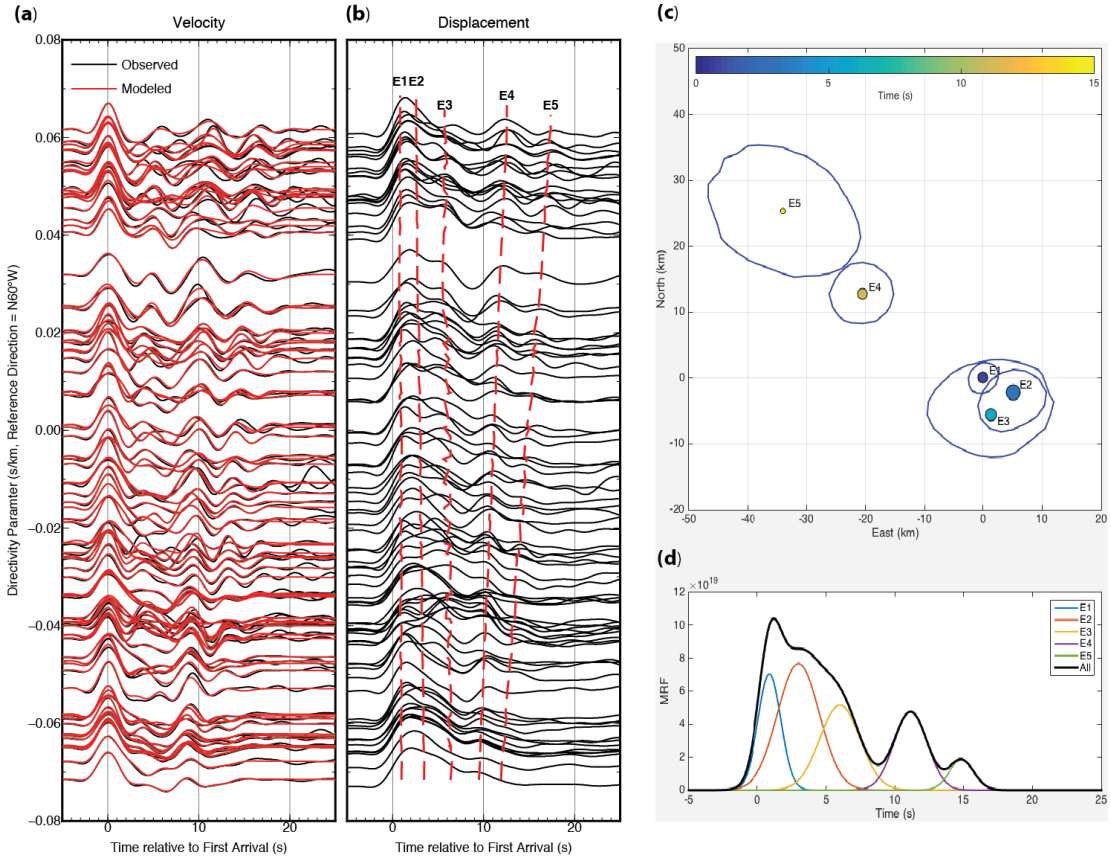

Figure 10.6 (**a**) Observed, and modeled teleseismic P wave ground velocities low-pass filtered at 0.3 Hz, aligned with directivity parameters for a reference azimuth of N60W°. The traces are aligned on the first peak. (**b**) Corresponding broadband ground displacement seismograms. The synthetics in (**a**) are from a spatially distributed 5 subevent-model with relative locations shown in (**c**), with the relative timing of expected arrival peaks indicated by red dashed lines in (**b**). The apparent horizontal spatial dimension of the rupture is less than 45 km, but the actual fault plane is not resolved. (**d**) Plot of individual subevent source time functions (colored curves for E1 to E5) and their cumulative sum approximation of the moment rate function.

Comparison of up-going direct P phases to F-net stations ranging from near-vertical upward take-off angle (to station OSW at an epicentral distance of 1.7°) to horizontal take-off angles (to stations like KGM at about 11° epicentral distance) (Figure 10.7a) show only about

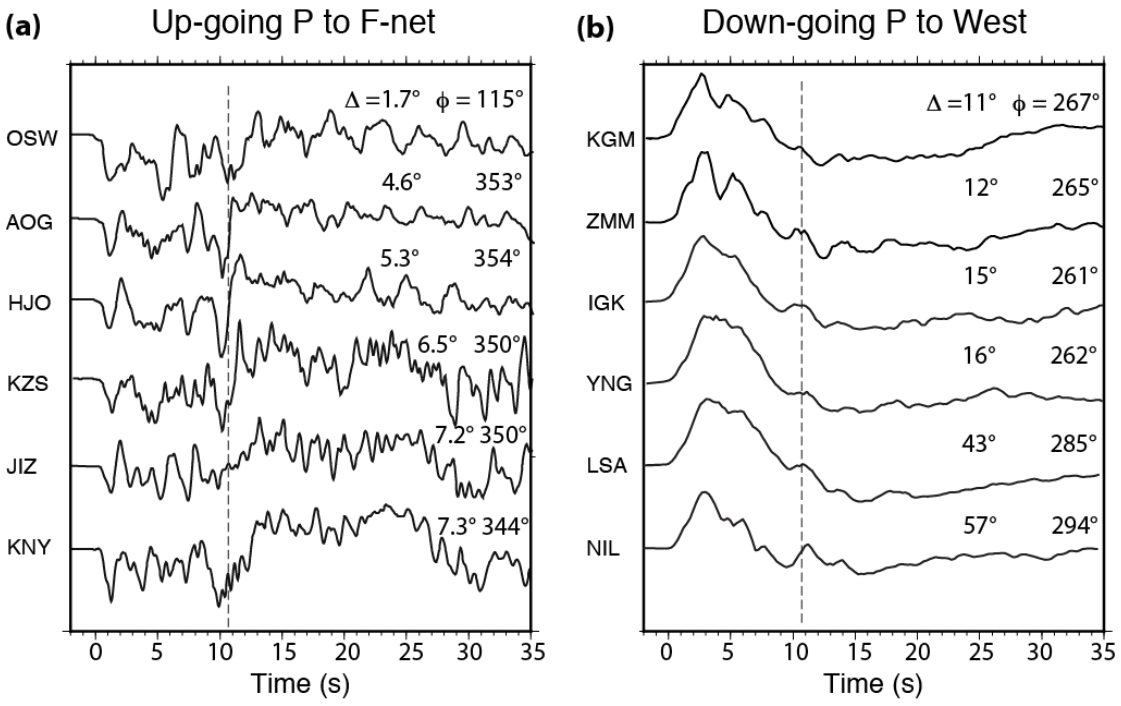

Figure 10.7 Profiles of P waveforms that constrain vertical extent of the rupture. (**a**) Direct P wave ground displacements from F-net stations in Japan spanning a wide range of up-going take-off angles. (**b**) Direct P wave ground displacements at stations to the west of the source spanning take-off angles from near-horizontal at 11° (blue traces) to steeply down-going at teleseismic distances. In both panels the dashed line is a reference line at about the time of a subevent observed in the data in Figures.10.2 and 10.3.

1 s of relative move-out of the feature near 11 s, consistent with the expectations for rupture on the shallowly dipping plane, in contrast to the up to 6 s move-out among F-net stations expected for rupture on the steeply dipping plane (Figure 10.A5). P waves taking off at almost horizontal angles emerge near 11° epicentral distance (station KGM; Figure 10.7b). Compared to steeply diving waves to more distant stations these should have several seconds less move-out for distant stations such as NIL if rupture is on the steeply-dipping plane, but little move-out for the shallowly-dipping plane (Figure 10.A6). The P and pP waveforms in Figure 10.5 and 7 sampling a very large range of take-off angle clearly favor the shallowly dipping nodal plane, or at least a nearly horizontal distribution of subevents. In this case, the

apparent rupture velocities indicated in Figure 10.4 are close to actual rupture velocities, and we can use them to constrain a finite-fault inversion.

10.3.4 Finite-Fault Inversion

A single fault plane least-squares finite-source slip inversion (Harzell and Heaton, 1983; Ye *et al.*, 2013) was performed using a well distributed teleseismic dataset of 85 P waves and 63 SH ground displacement recordings filtered in the passband 0.005-1.9 Hz for the 26° dipping nodal plane of the GCMT solution. Our approach was to impose a priori constraints on the rupture area and expansion rate based on the collective results of back-projection and subevent inversion. The fault model was parameterized with 11 subfaults along the strike direction and 14 subfaults along the dip direction (after exploring larger models), with 5 km by 5 km subfault dimensions. The subfault source time functions were parameterized by six 0.75 s rise-time time triangles offset by 0.75 s time shifts, giving total possible subfault rupture durations of 5.25 s. The rupture expansion velocity was 5.0 km/s in the down-dip (eastward) direction and 3.0 km/s in the up-dip (westward) direction, guided by the back-projection images. The P wave synthetics used a $t_a^* = 0.3$ s, and the SH wave synthetics used a $t_b^* = 1.2$ s, where t^* = travel time/Q, with Q being the quality factor defined by fractional loss of energy per cycle.

The resulting fault-perpendicular moment rate function (Figure 10.8a) has a duration of about 17 s with a total seismic moment of 8.1 x 10^{20} Nm (M_W 7.9); the slip distribution is shown in Figure 10.8b. Peak slip is concentrated near the hypocenter, and rupture initially expands rapidly east to northeastward for 2 s, then southward from 4 to 5 s, followed by slower expansion to the west and northwest from 8 to 15 s. The teleseismic waveforms are well-fit by this inversion (Figure 10.A7), and a rather smooth slip distribution is inferred. The

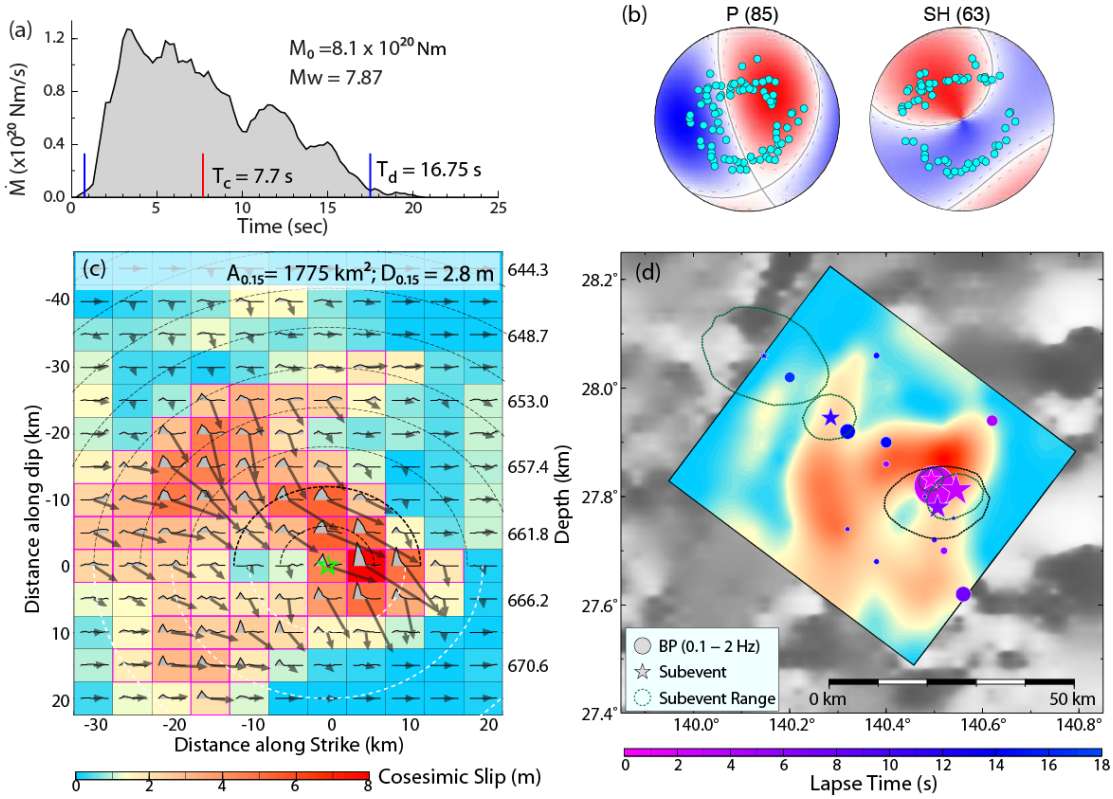

Figure 10.8 Results of linear least-squares inversion for the 2015 Ogasawara earthquake slip model, for a planar fault with strike 37°, dip 26°, and hypocentral depth of 664.0 km. (**a**) The moment rate function, along with the seismic moment, corresponding M_W, centroid time (Tc; red tick) and total duration (Td; time between blue ticks). (**b**) P and SH wave lower hemisphere radiation patterns and sampling positions of the 85 P waves and 63 SH waves used in the inversion. The average rake of the solution is -37.4°. (**c**) Slip model with subfault source time functions and average slip magnitude (color scale and vector length) and direction (vector orientation in the fault-plane coordinate system). The majenta lines outline the subfaults with at least 15% of the peak-subfault moment, indicating the effective rupture area is ~1775 km² and the average slip is ~2.8 m over this area. (**d**) Map view at the surface showing the spatial orientation of the smoothed slip distribution (color coded as in (c)) with early expansion to the east, then southeast and after 10 s toward the west and northwest. The time-coded stars, scaled by relative moment, indicate 5 subevents from the velocity waveform inversion, with dotted uncertainty areas, and the time-coded circles, scaled by relative power, are peaks from the 0.1-2.0 Hz global back-projection in Figure 10.4.

inversion produces subevents from spatial gradients in slip and slip velocity that have good resemblance to the discrete features imaged by back-projection and velocity waveform subevent inversion, allowing for some streaking along isochrones, but there is always a

question of what parameterization is most appropriate for any earthquake rupture process (Ihmlé, 1998). The well-resolved attributes are the ~40 km dimension on a nearly horizontal source region, a 17 s duration with ~8 s centroid time, concentration of slip near the hypocenter compatible with a shear double-couple dislocation, and an M_W = 7.9.

10.3.5 Radiated Energy, Stress Drop and Radiation Efficiency

The radiated energy was calculated by stacking the P wave spectra from teleseismic ground velocities for frequencies from 0.05 – 2 Hz, corrected for t_a^* = 0.3 s. The source spectrum obtained by combining the spectrum of the moment rate function from finite-fault inversion for frequencies <0.05 Hz with the average displacement spectrum from attenuation-corrected P waves for frequencies from 0.05-2.0 Hz was used to apply a correction for the low-frequency radiated energy, giving a final value of 3.26 x 10^{16} J. The moment-scaled radiated energy is found to be 4.2 x 10^{-5}.

The stress drop, $\Delta\sigma$, was estimated by computing the stress at each subfault grid point for the finite-fault slip model (Figure 10.A8) and integrating it weighted by the slip distribution using the slip-weighted stress method (Noda et al., 2013). $\Delta\sigma$ is estimated as 38 MPa. We also trimmed the inverted finite-fault slip model to eliminate subfaults with less than 15% of the peak-subfault moment, and used the total area of significant slip and the average slip in a stress drop calculation for a circular rupture with a uniform slip, finding a value of $\Delta\sigma$ = 25 MPa. We prefer the somewhat larger value from the variable slip calculation. The radiation efficiency, $\eta_R = \frac{E_R}{\Delta W_0} = \frac{2\mu}{\Delta\sigma} \cdot \frac{E_R}{M_0} = 2 \cdot \frac{\sigma_a}{\Delta\sigma}$ = ~0.34, where μ, σ_a, and ΔW_0 are rigidity, apparent stress, and available potential energy, respectively.

10.4 Discussion

The thorough seismological characterization of the 2015 Bonin earthquake slip process described above does not reveal any clear distinctions from shallow earthquakes. The measured radiation efficiency is intermediate compared with estimates for the two largest deep-focus earthquakes as shown in Figure 10.9a. The radiation efficiency for the 2015 Bonin event is fairly consistent with theoretical crack models, and it is clear that deep-focus earthquakes range over a continuum of behavior. For the 1994 Bolivia event the brittle failure component is small relative to a more ductile component, whereas for the 2013 Sea of Okhotsk, the rupture is predominantly brittle. The 2015 Bonin event is intermediate. Like the Bolivia event, it has a two-stage rupture process with initial fast down-dip rupture and relatively brittle behavior followed by slower up-dip rupture with more ductile behavior, but the average rupture expansion velocity is not as slow and the static stress drop is not as high. The overall moderate energy dissipation involved in this event is not that distinct relative to the range of what is found for most shallow earthquakes. However, the lack of large aftershock activity does suggest that conditions in the source zone are distinct from those for shallower events.

The source of the 2015 Bonin event is relatively compact, spanning about 40 km in length and oblique to the trend of the shallower seismogenic slab. However, the aseismic nature of the surrounding slab makes it very difficult to evaluate whether the cold core of the slab, which could potentially host metastable olivine, is aligned with the source or not. The slab has to tear, fold or buckle to extend continuously to the position of this event (Figure 10.9b,c), and such deformation could broaden the horizontal width of the cold region. Alternatively, there could be a chunk of detached slab, but we believe this is unlikely given the progressive steepening of the Benioff-zone seismicity band toward the south of the Bonin slab.

The principal compressional stress axis is not aligned along the down-dip extension of shallower seismicity, and is oriented dipping steeply to the northeast.

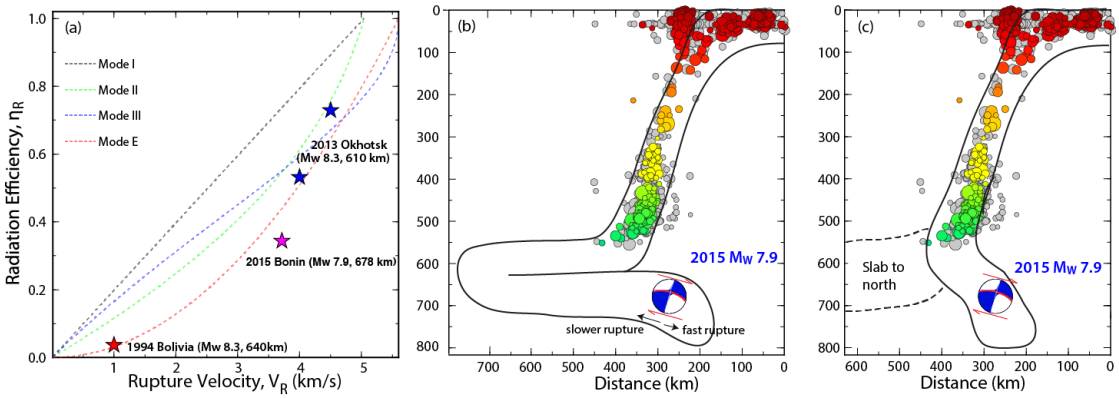

Figure 10.9 (**a**) Comparison of radiation efficiency (from slip-weighted stress distributions) and rupture velocity for the 2015 Bonin deep earthquake and the 1994 Bolivia and 2013 Sea of Okhotsk earthquakes. Results for the 2013 Sea of Okhotsk event for rupture velocities of 4.0 and 4.5 km/s are shown. The 2015 event has intermediate efficiency relative to the 1994 Bolivia and 2013 Sea of Okhotsk events. (**b**) Interpretation of the 2015 event as being in a folded slab continuous along strike; the seismicity from profile B'-B in Figure 10. 1 is shown. The rupture initially expands eastward (toward the right) at high rupture velocity, then toward the west at slower rupture velocity. (**c**) Interpretation of the 2015 event as being in a torn/buckled slab that is recumbent to the north but steeply dipping to the south. The earthquake could also be in a detached piece of slab from earlier subduction.

We infer that the position of the large strain release is due to strong lateral deformation of the Izu-Bonin slab and the proximity to the 660-km phase boundary having concentrated stress in the source zone. This stress concentration appears to have overcome inhibition of faulting due to progressive thermal assimilation that bounds the main Benioff-zone seismicity (Figure 10. 1b,c,d). Even for a buckled slab geometry such as Figure 10.9c, the source region can only be warmer than the region where shallower seismicity terminates, and the lack of large local aftershocks suggests that it is difficult for even small events to occur in the source volume, and very difficult for them to grow into larger ruptures. Similar concentrated slab deformation may account for the isolated event in 1982 that lies well to the west of the

flattened portion of the Izu-Bonin slab (Figure 10.1b). It is not clear why the isolated mainshocks are so large; possibly there are very infrequent mineral transformation or volatile release processes that occur only under particularly high deviatoric stress conditions that allow large dynamic stress relaxations to occur.

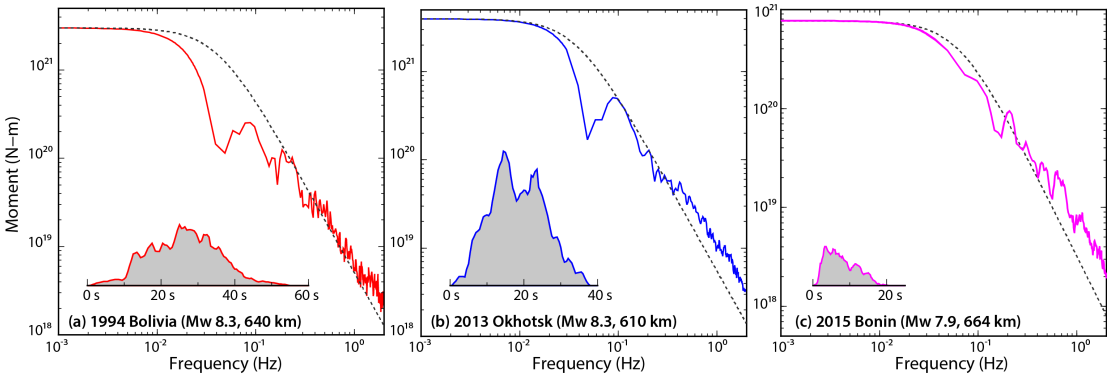

Figure 10.10 Broadband source spectra obtained from finite-fault models for frequencies below 0.05 Hz and averages of teleseismic P wave spectra for higher frequencies are shown for the (**a**) 1994 Bolivia, (**b**) 2013 Sea of Okhotsk, and (**c**) 2015 Bonin events. The dashed lines are reference spectra for w-squared models with the same moment as each event, a 10 MPa stress parameterm and corresponding shear wave velocity around the source.

Comparison of the average source spectra for the three deep events (Figure 10.10) shows that the 1994 Bolivia event is depleted in intermediate period spectral amplitudes, reflecting the smooth, slowly rising source time function for that event, whereas the 2015 Bonin event is relatively enriched in intermediate periods due to the rapid rise time and roughness of the moment rate function. These spectra appear to reflect the relative balance of the brittle and ductile contributions to each rupture, with the 1994 Bolivia event being dominated by the smooth low rupture velocity process and the 2013 Sea of Okhotsk event being dominated by brittle high rupture velocity failure. The early, high rupture velocity stages of the 1994 and 2015 events may be associated with a distinct source process relative to the overall rupture, perhaps associated with nucleation by transformational faulting or dehydration embrittlement,

followed by a more dissipative process of rupture expansion, possibly involving shear band formation or thermal runaway with melting. The occurrence of only very small aftershocks in a previously aseismic region indicates that the source volume was able to nucleate ruptures in the wake of the stress perturbation from the large event, but either limits on available strain energy or failure to achieve a threshold of slip to enable runaway rupture expansion constrained the size of the aftershocks.

10.5 Conclusion

The 30 May 2015 M_W 7.9 Ogasawara (Bonin) deep focus earthquake ruptured near 664 km depth well separated from the main Bonin slab Benioff zone seismicity. The earthquake likely occurred in a buckled region of the slab, with strong contortion of the slab and resistance to penetration of the 660-km discontinuity providing high deviatoric stress concentration that overcame any thermal inhibition of faulting to produce the largest deep earthquake in the region and the deepest $M_W \geq 7.8$ earthquake yet recorded. The absence of any previous recorded seismicity in the source region and the paucity of local aftershocks for the major event indicate that earthquake nucleation in the source region is difficult. The mainshock rupture involved an initial several second long high rupture velocity brittle phase that expanded down-tip, followed by a break-out into a more dissipative process with large strain energy release with lower rupture velocity that expanded in the up-dip direction. The secondary phase was not as low velocity as for the 1994 Bolivia earthquake, and the overall radiation efficiency for the event is intermediate to that for the 1994 Bolivia and 2013 Sea of Okhotsk great deep events. The specific mechanism of the deep failure is not resolved, but it appears likely that high deviatoric stresses played a more important role than temperature in localizing the deformation.

Acknowledgements. The IRIS DMS (http://www.iris.edu/hq/) and Orpheus (http://www.orfeus-eu.org) data centers were used to access the seismic data from Global Seismic Network and Federation of Digital Seismic Network stations, and the Hi-net data center (http://www.hinet.bosai.go.jp/about_data/?LANG=en) of NIED was used to access Hi-net recordings. The Data Management Centre of China National Seismic Network at Institute of Geophysics, China Earthquake Administration, provided waveform data in China. This work made use of GMT and SAC software. K. Koper provided access to and training with his back-projection software. This work was supported by NSF grant EAR1245717 (T.L.).

10.6 Supplementary Figures

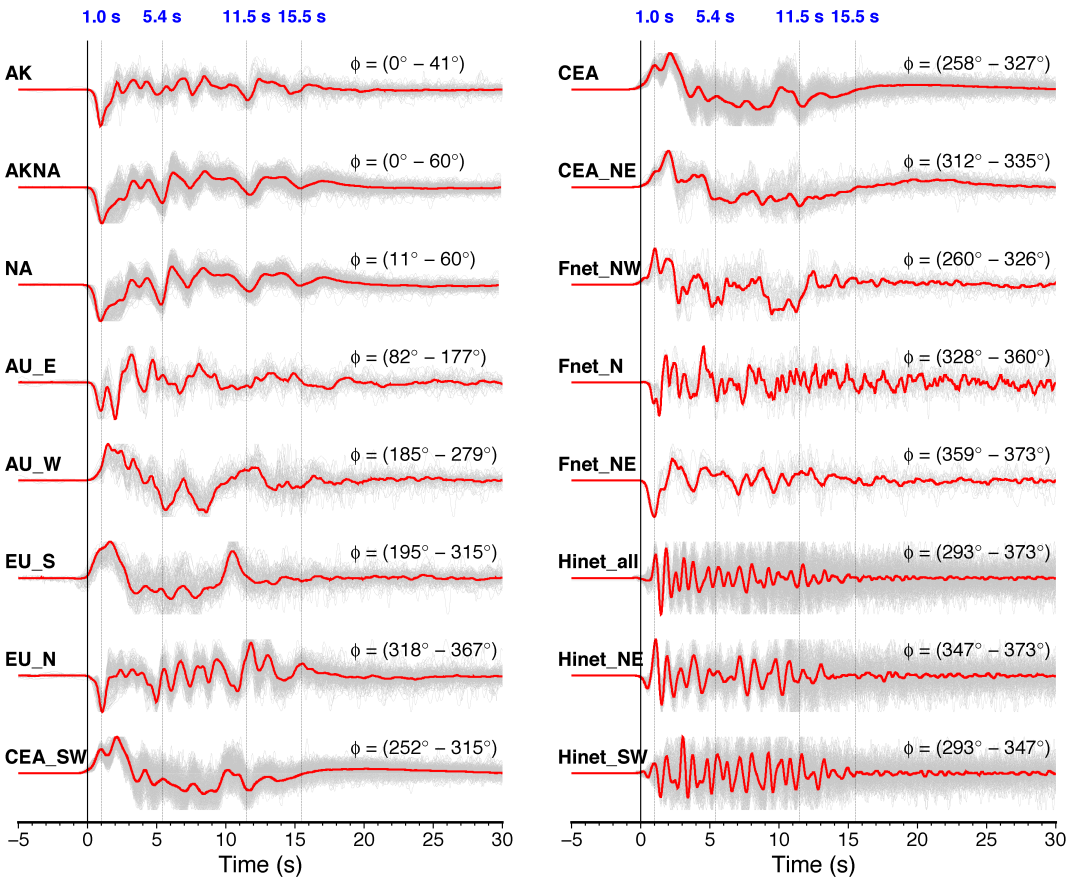

Figure 10.A1 Amplitude-normalized, first-arrival-aligned P waveforms for large-aperture networks at various azimuths from the source (gray traces) and their linear average (red traces). Instrument responses have not been removed. Bandpass filtered versions of these aligned waveforms are used in back-projection imaging for each network separately. A first-motion polarity reversal across the Hi-net stations in Japan was corrected for in joint back-projection of all Hi-net stations.

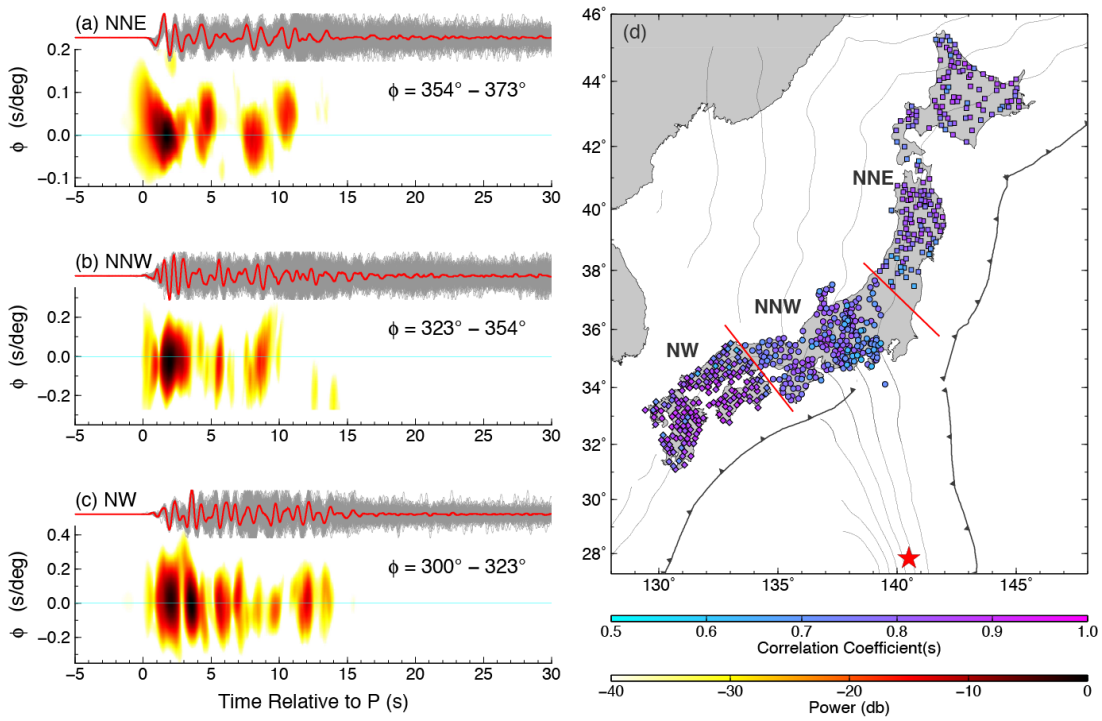

Figure 10.A2 One-dimensional slant-stacks of the short-period Hi-net data in azimuthal bins of (**a**) 354-373°, (**b**) 323-354°, and (**c**) 300-323°. The data are aligned on the P arrivals, and slowness differences are given with respect to the first arrival. The waveforms in each sector are normalized and superimposed (gray traces), along with the linear average (red trace: zero relative slowness stack). The power in the stacks for varying relative slowness is color-contoured. (**d**) shows the groups of stations used in each slant-stack with the correlation coefficient relative to the mean trace color-coded. The red star is the epicentral location of the 2015 event. Positive relative slowness indicates rupture closer to the stations; the lack of strong shifts in slowness throughout the 15 s of significant power indicates a spatially concentrated source.

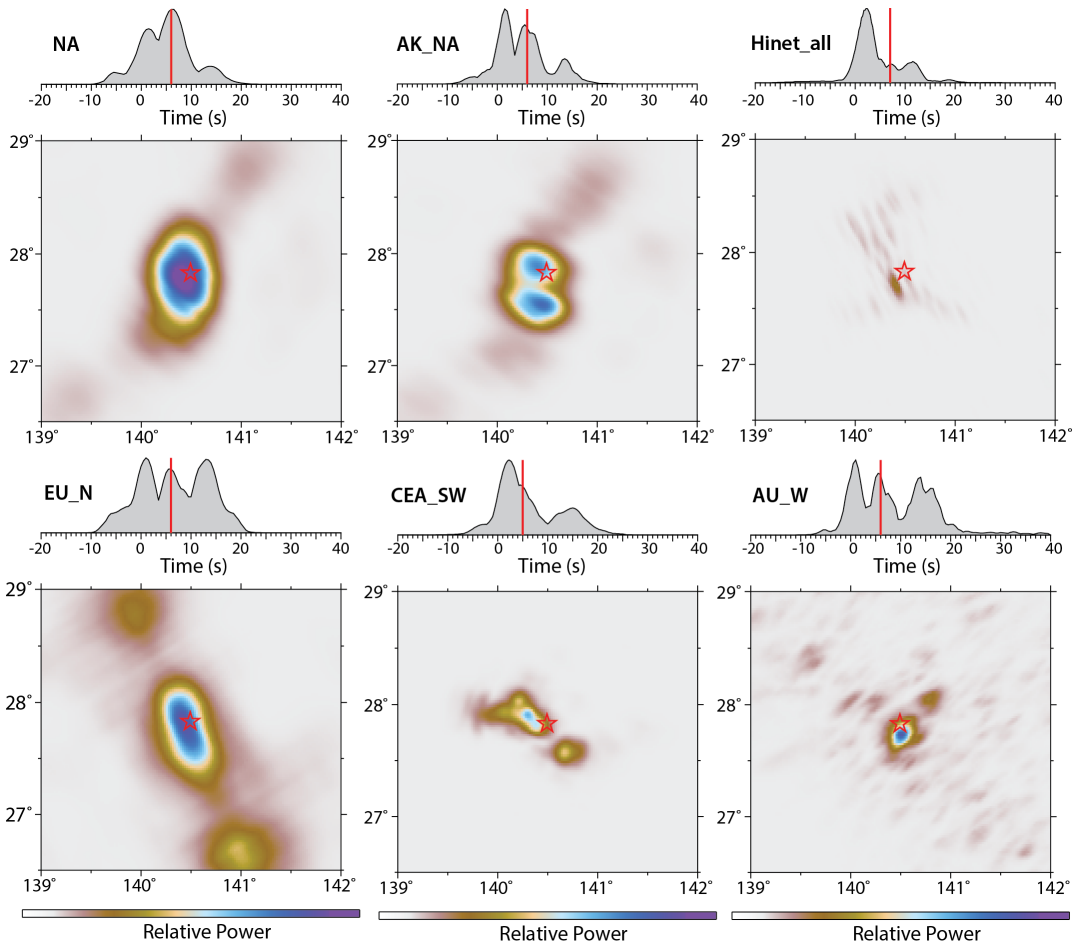

Figure 10.A3 Snapshots from back-projection images (4th root stacks) for signal near the second peak, 5 to 7 s after the origin time from large-aperture networks in the conterminous U.S. and adjacent regions (NA), Alaska and North American (AK_NA), Hi-net in Japan (Hinet_all), Northern Europe (EU_N), China (CEA_SW), and Indonesia-Australia (AU_W).

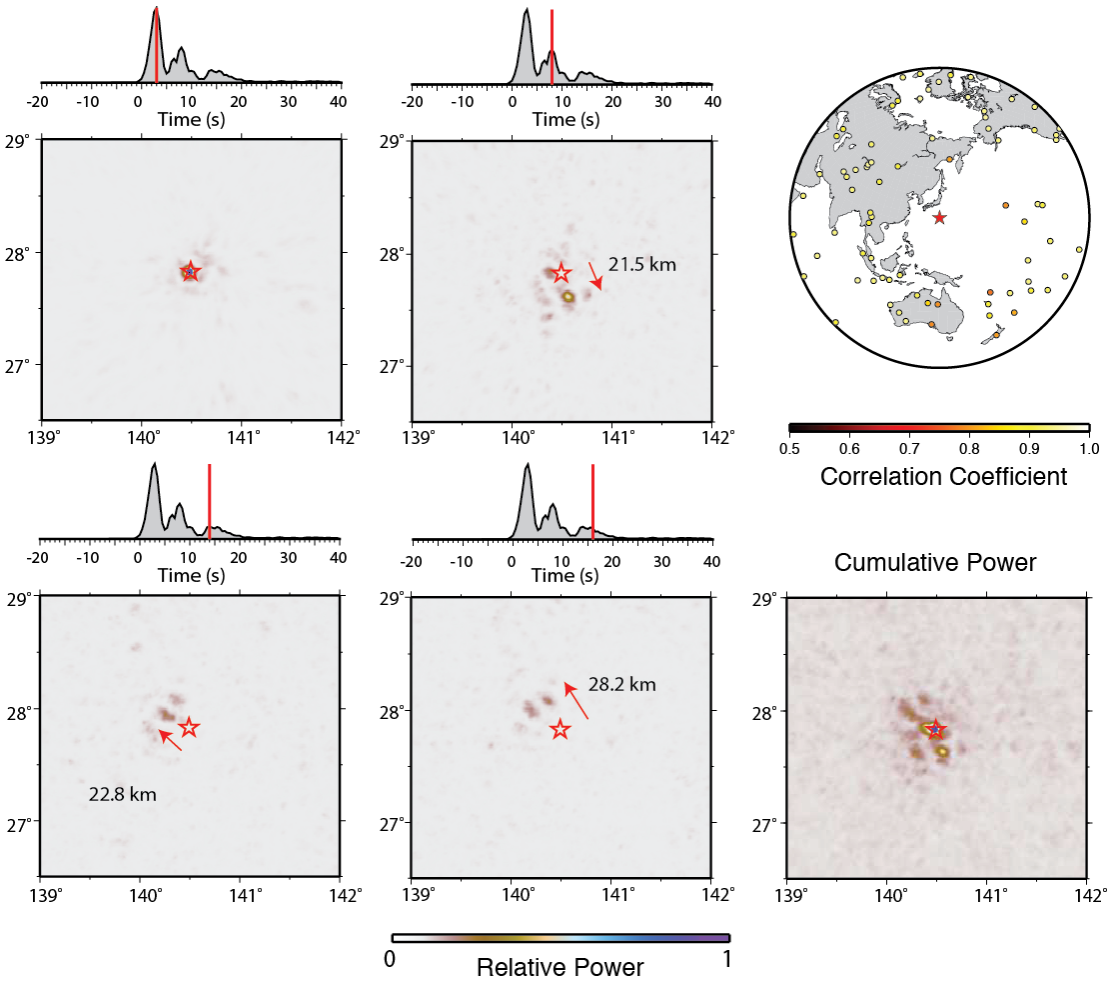

Figure 10.A4 The 0.5-2.0 Hz P wave energy back-projected from a global distribution of stations (the same as used later in a finite-fault inversion). The four panels on the left and center are snapshots at 3 s, 8 s, 14 s, and 16 s, with the power in the 4th root stack shown around the source region. The peaks that form at discrete locations are used to estimate the horizontal distance from the hypocenter and an apparent rupture expansion velocity from the origin. The global map shows the station distribution. The cumulative power of the images integrated over time is shown on the lower right, indicating a total source dimension of about 40 km, slightly elongated to the south and northwest.

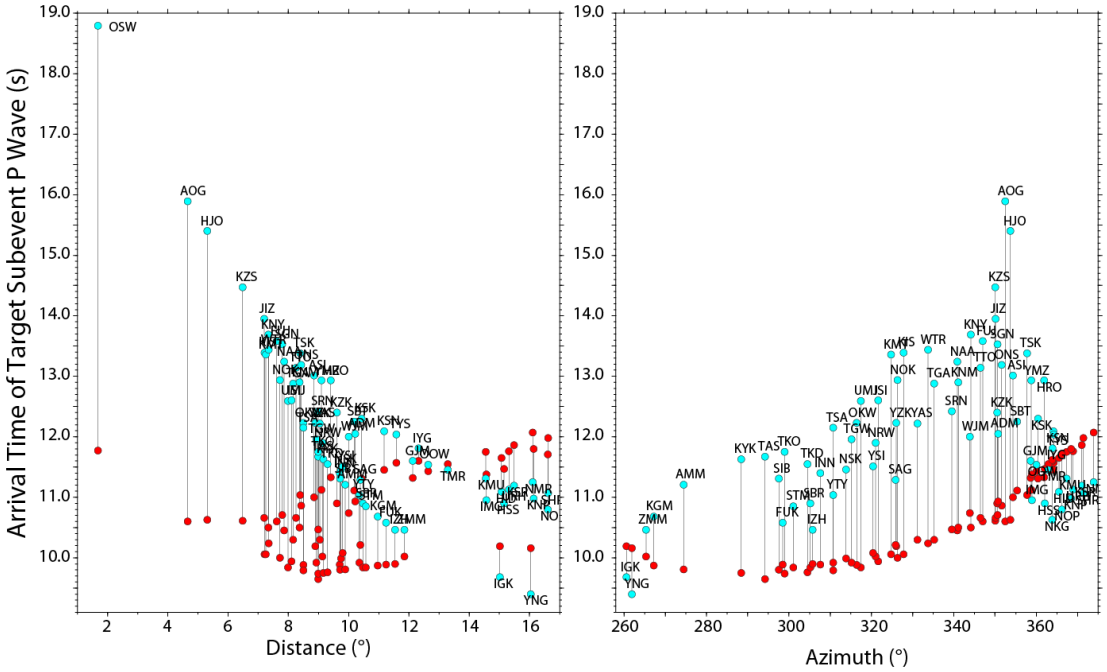

Figure 10.A5 Calculated time differences from the origin to the target third peak 25 km toward the NNW (described in the text) for travel time model IASP91 for up-going p phases (epicentral distances less than 11°) or down-going P phases (epicentral distances greater than 11°) to F-net stations, assuming the target subevent is on either the steeply-dipping (cyan) or the shallowly-dipping (red) dipping fault plane choice at depths of 748 km and 666 km, respectively. Note that much larger time variations due to azimuth and take-off angle variations are expected for the steeply-dipping fault plane.

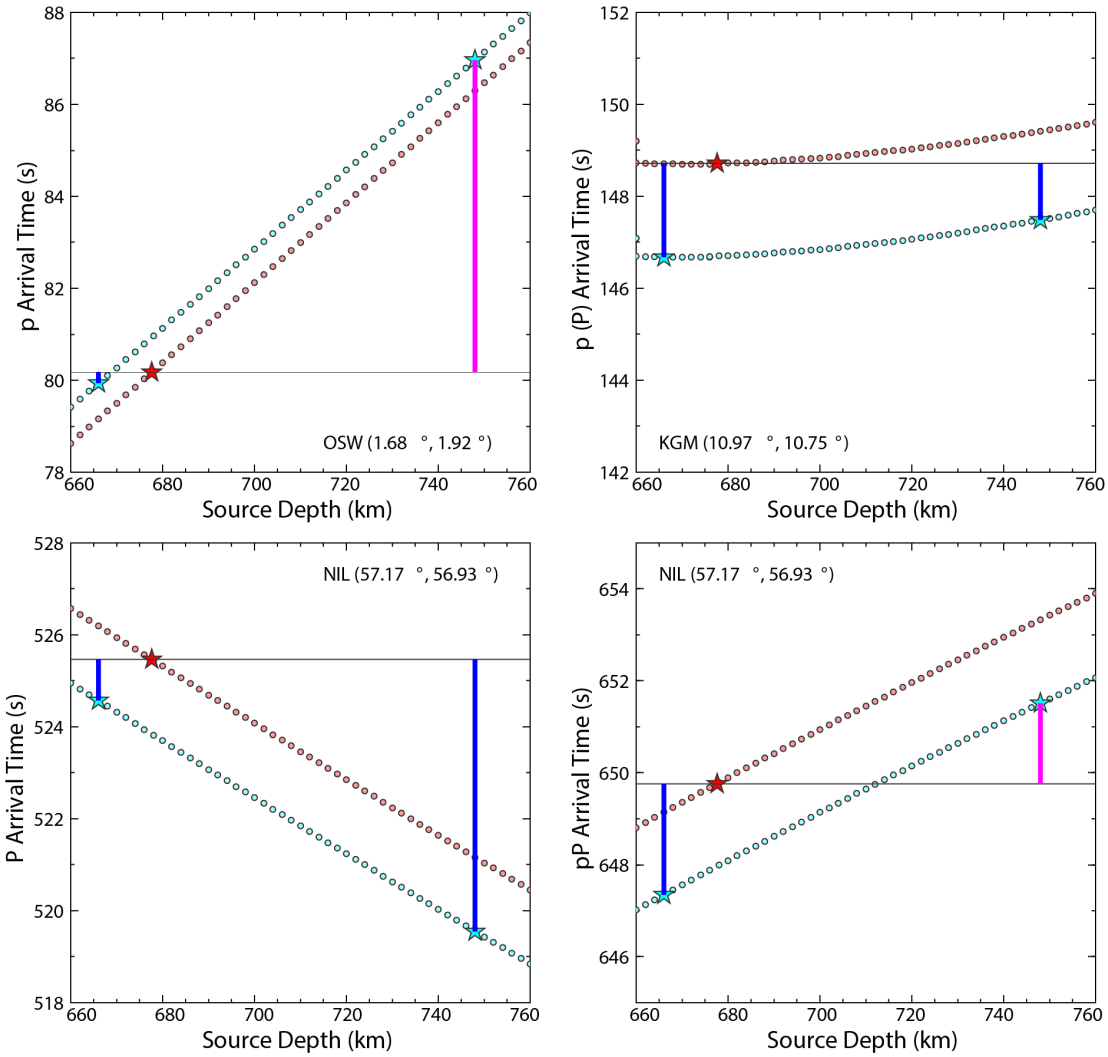

Figure 10.A6 Calculated travel times (IASP91 model) for arrivals of up-going p, and teleseismic P and pP phases at stations OSW, KGM and NIL versus source depth. The hypocenter is indicated by the red star. Target subevent positions 25 km to the NNW projected to the shallowly dipping fault plant (source depth 666 km) and the steeply dipping fault plane (source depth 748 km) and corresponding distance (second distance in name label) to each station are shown by the cyan stars. Blue lines indicates how much time has to be added to the absolute time shift of the subevent (12 s) to calculate the relative arrival time, pink lines indicate how much time has to be subtracted from the absolute time shift of the subevent to calculate the time relative to the first arrival.

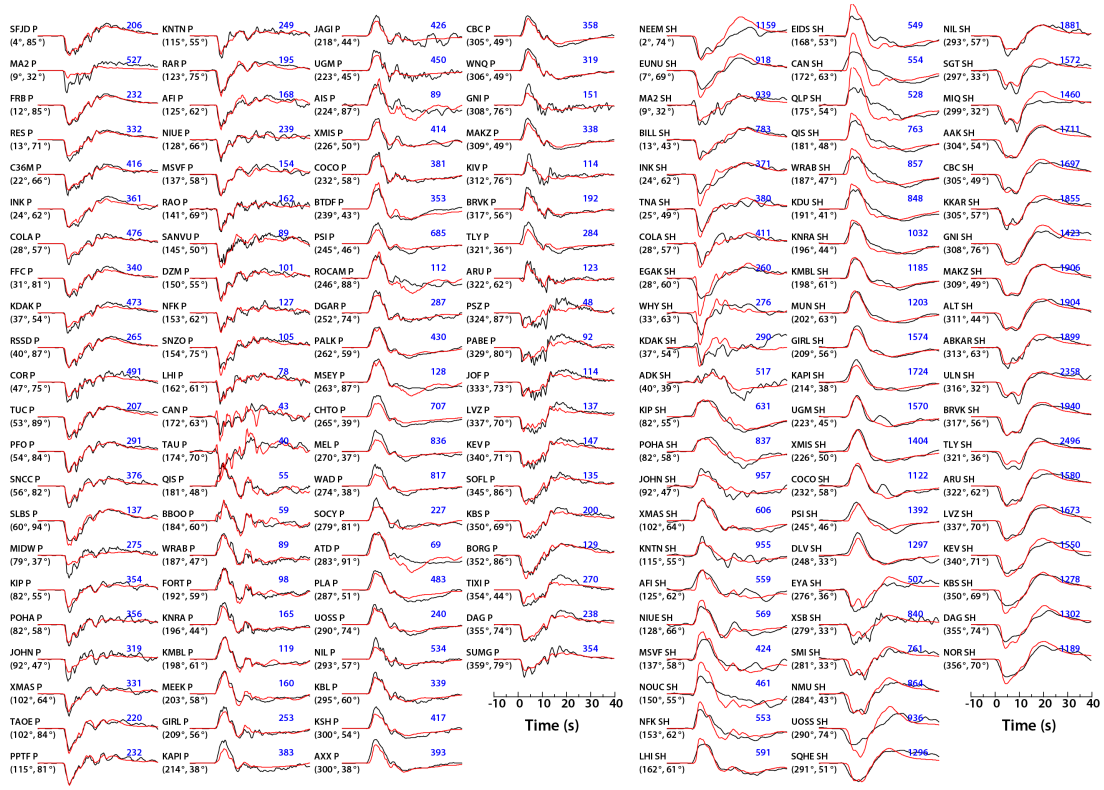

Figure 10.A7 Observed (black lines) and modeled (red lines) P and SH waveforms for the 2015 Bonin earthquake. The synthetic waveforms are for the finite-fault model in Figure 10.8. The peak-to-peak amplitudes in microns are shown by each trace; waveform mismatches for very low amplitude signals indicate that they are near radiation nodes.

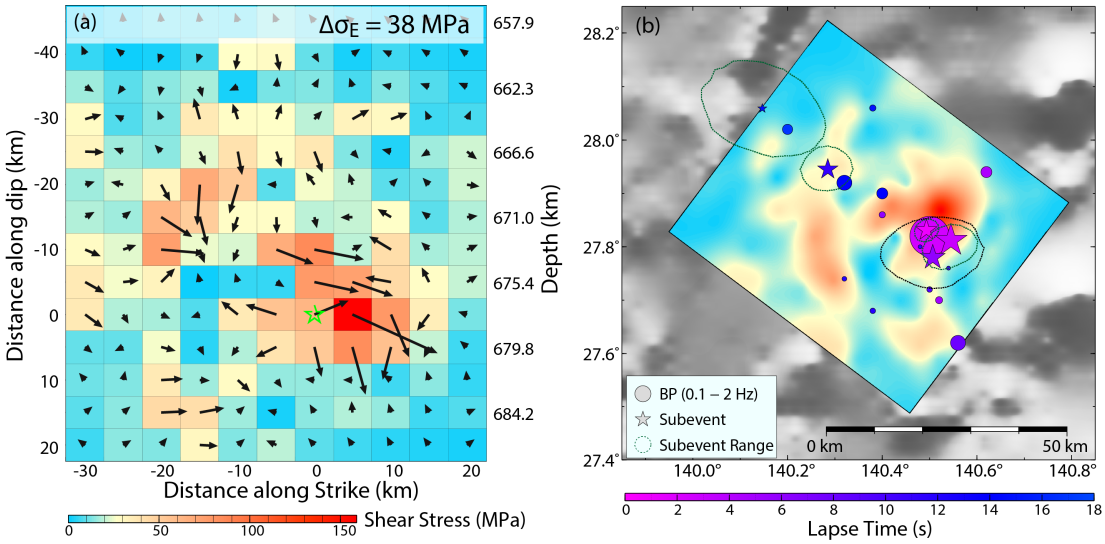

Figure 10.A8 (a) Average shear stress drop $\Delta\sigma_E$ which is the average stress drop weighted by the average slip defined by Noda et al. (2013). The magnitude of $\Delta\sigma_E$ is given by the color code. The arrows give the magnitude and the direction $\Delta\sigma_E$ at the center of each sub-fault for the finite-fault model shown in Figure 10.8. The estimated static stress drop for this rupture model is 38 MPa. (b) Map view at the surface showing the stress variation on the fault model (colors are relative to the shear stress scale in (a)), relative to results of ground velocity subevent inversion and back-projection. The time-coded stars, scaled by relative moment, indicate 5 subevents from the velocity waveform inversion, with dotted uncertainty areas, and the time-coded circles, scaled by relative power, are peaks from the 0.1-2.0 Hz global back-projection in Figure 10.3.

PART III

TRANSFORM FAULT BOUNDARY EARTHQUAKES

Chapter 11

Complementary Slip Distributions of the August 4, 2003 M_W 7.6 and November 17, 2013 M_W 7.8 South Scotia Ridge Earthquakes

This chapter has been published as:

Ye, L., T. Lay, K. D. Koper, R. Smalley, Jr., L. Rivera, M. G. Bevis, A. F. Zakrajsek, and F. N. Teferl (2014), "Complementary slip distributions of the August 4, 2003 M_W 7.6 and November 17, 2013 M_W 7.8 South Scotia Ridge earthquakes", *Earth Planet. Sci. Lett.*, 401, 15–226.

Abstract.The South Scotia Ridge Transform (SSRT) plate boundary between the Scotia and Antarctic plates experienced large strike-slip earthquakes on August 4, 2003 (M_w 7.6) and November 17, 2013 (M_w 7.8). These events have overlapping aftershock zones, which is unusual. A 36°-45° southward dipping fault zone ruptured with left-lateral displacements in each event along the northern margin of the South Orkney micro-continent near 60°S. Slip distributions for the two events are determined using teleseismic body and surface wave recordings along with constraints from GPS ground motion recordings at station BORC on Laurie Island (South Orkney Islands), just south of the SSRT. The aftershock distributions, high-frequency back-projections, and unconstrained body wave finite-fault inversions permit significant overlap of the 2003 and 2013 slip zones; however, the GPS static displacements resolve differences in the large-slip regions of the two ruptures. The 2013 earthquake sequence along the SSRT initiated with M_w 6.1 (November 13) and M_w 6.8 (November 16) foreshocks located ~50 km west of the mainshock hypocenter, and had aftershocks extending ~250 km eastward. The rupture spread primarily eastward at ~2.5 km/s with a total rupture

duration of about 120 s, with two distinct patches of large-slip located northwest and northeast of the South Orkney Islands with a total seismic moment of ~1.1 × 10^{21} N-m. The rupture swept past BORC, with high-rate GPS (HRGPS) ground motion recordings capturing the time-varying slip history of the faulting. Traditional GPS data require that the largest-slip region of the shorter rupture in 2003 (seismic moment ~4.0 × 10^{20} N-m) is located in the gap NNE of BORC between the two patches that ruptured in 2013. There may be some overlap of lower slip regions. The complementary slip distributions comprise a relatively uniform offset along this portion of the SSRT, which is one of the most seismically active regions of the entire Antarctic plate boundary.

11.1 Introduction

Reconstruction of Scotia plate tectonic evolution includes a complicated tectonic history dating back to ~120 Ma, when fragmentation of Gondwanaland initiated differential motion between the South America and Antarctic plates (Dalziel *et al.*, 2013). Subsequent seafloor spreading within what is now the Scotia plate dispersed and stretched continental fragments separated from southern South America and the Antarctic Peninsula during the past ~6-40 Ma. The eastern margin of the Scotia plate is the East Scotia Ridge (ESR). The ESR is an active back-arc spreading ridge associated with subduction of the South American plate beneath the South Sandwich plate along the South Sandwich subduction zone (Figure 11.1). The North and South Scotia Ridge transforms (NSRT and SSRT), now trending roughly EW for ~1000-1500 km, formed at ~20–30 Ma, and are closely associated with spreading of the West Scotia Ridge (WSR), which ended ~6.6 Ma. These boundaries contain a mix of continental and oceanic crust (Civile *et al.*, 2012; Martos *et al.*, 2014), notably the South Georgia and South Orkney Islands along the NSRT and SSRT, respectively.

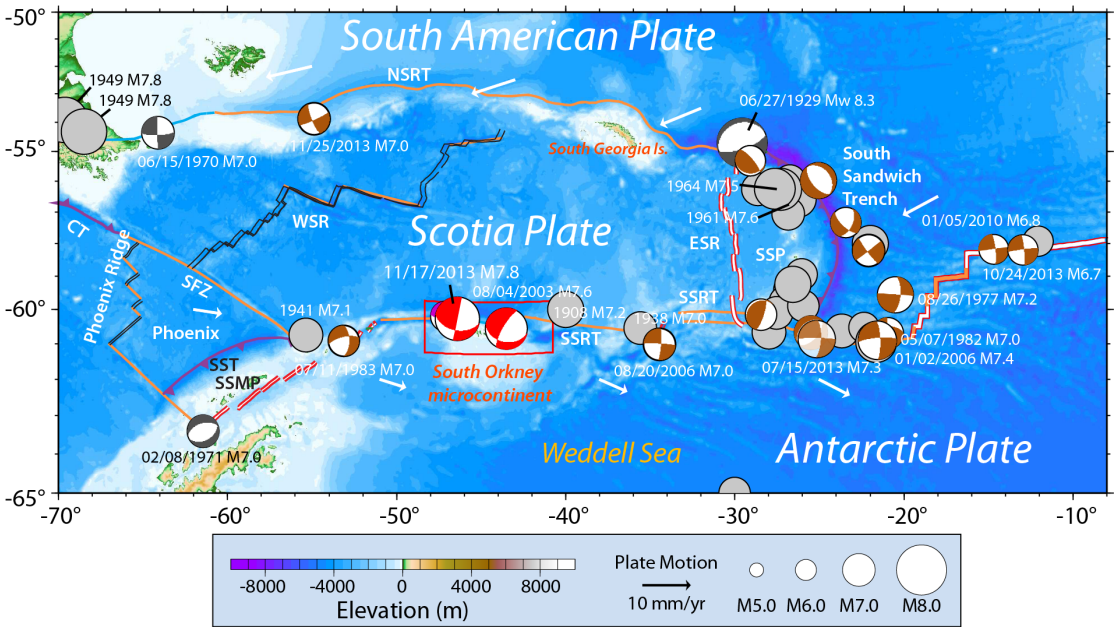

Figure 11.1 Large earthquakes around the Scotia Plate with tectonic structures (after Dalziel *et al.*, 2013). Gray circles indicate epicenters of M ≥ 7.0 events from 1900 to 1975 from PAGER-CAT (Allen *et al.*, 2009). Gray focal mechanisms for 1970 and 1971 events are from Pelayo and Wiens (1989) and that for the 1929 event is from Okal and Hartnady (2009). Brown focal mechanisms are global Centroid Moment Tensor (gCMT) solutions for $M_w \geq 6.5$ events from 1976 to 2014 plotted at the USGS/NEIC epicenters. The red mechanisms are the gCMT solution for the November 17, 2013 M_w 7.8 and August 4, 2003 M_w 7.6 events. Arrows indicate the plate motion directions and rates relative to a fixed Scotia Plate computed using model MORVEL (DeMets *et al.*, 2010). Relative to the Scotia plate, the Antarctic Plate is moving at ~ 6-7 mm/yr eastward with minor tensional obliquity along the South Scotia Ridge transform (SSRT), and the South American Plate at ~ 8-9 mm/yr westward with minor compressional obliquity along the North Scotia Ridge transform (NSRT). The purple curves indicate subduction zones; orange lines show transforms and fracture zones; double red lines indicate the active spreading centers; and black double lines show extinct spreading centers. The West Scotia Ridge (WSR) and the Phoenix Ridge (Livermore *et al.*, 1994; 2000) ceased spreading at approximate 6.5 Ma and 3.3 Ma, respectively. The East Scotia Ridge (ESR) initializes at ~ 9 Ma B.P., and its spreading rate is estimated to be ~ 6-7 cm/yr (Smalley *at el.*, 2007; Thomas et al., 2003). The red box indicates the main study region (Figure 11.8). Other abbreviations: CT, Chile Trench; SFZ, Shackleton Fracture Zone; SST, South Shetlands Trench; SSMP, South Shetlands microplate; SSP, South Sandwich Plate.

Kinematics of the Scotia plate, determined from magnetic lineations, earthquake slip vectors, transform azimuths, gravity anomalies, and GPS crustal velocities indicate that, with its internal structure now stabilized, the Scotia plate essentially serves as a large shear zone between the South America and Antarctic plates. The SSRT and NSRT, with left-lateral motions of ~6-7 mm/yr and ~8-9 mm/yr respectively, partition the total relative movement between the two large plates (DeMets *et al.*, 2010; Forsyth, 1975; Pelayo and Wiens, 1989; Livermore *et al.*, 1994; Smalley *et al.*, 2007; Thomas *et al.*, 2003). The SSRT is the most seismically active portion of the entire Antarctic plate boundary, having experienced about ten M 7+ events since 1908, whereas less seismicity and few large events have been recorded on the NSRT (Figs. 1, S1, S2 and S3). The NSRT and SSRT continue eastward past the ESR forming the northern and southern boundaries of the "D" shaped South Sandwich plate. The NSRT continuation turns southward and changes into the South Sandwich trench (SST) on the north, while the SSRT continuation bifurcates into the SST from the south and a further eastward continuation to form a strike-slip boundary between the Antarctic and South America plates. Additional large events are found on the continuation of the SSRT on the boundaries between the Antarctic and the South Sandwich and South American plates.

On November 17, 2013 (09:04:55 UTC, 60.27°S, 46.40°W; USGS-NEIC), an M_w 7.8 strike-slip earthquake occurred on the SSRT; the largest earthquake yet recorded along this plate boundary. The rupture initiated about 150 km west of the previous largest earthquake, an M_w 7.6 event on August 4, 2003 (04:37:23 UTC, 60.57°S, 43.50°W; USGS-NEIC). The eastern half of the 2013 aftershock zone overlaps that of the 2003 event (Figure 11.A1). Inversions of long-period seismic waves from gCMT (http://www.globalcmt.org/CMTsearch.html) and our own W-phase inversions noted below indicate left-lateral strike-slip displacements on faults striking 97°-102° and dipping 36°-63°

southward for both events (Figure 11.1 and A3). There are two unusual and surprising aspects of the earthquake: the shallow dip of the strike-slip faulting suggests reactivation of a thrust fault which may have formed due to compression from past convergence or continental fragmentation along the SSRT, and the short apparent time for re-rupture of the segment of the plate boundary that failed in 2003 (Vallée and Satriano, 2014). We analyze the rupture characteristics of these two large events to quantify the slip distribution and faulting processes along this complex plate boundary.

11.2 Rupture characteristics of the 2003 and 2013 events

The first-order characteristics of the faulting processes for the two large South Scotia Ridge earthquakes are determined using long-period point-source solutions, back-projection of short-period teleseismic P wave recordings, and surface wave directivity analysis for globally recorded digital seismograms.

11.2.1 Long-period point-source solutions

The long-period point-source moment-tensor best-double-couple solutions from gCMT and our W-phase inversions for both August 4, 2003 and November 17, 2013 events are listed in Table 11.1. The W-phase inversions use three-component long-period signals in the 1.67-5.0 mHz pasband from 29 stations with 50 total channels for the 2003 event, and 28 stations with 53 total channels for the 2013 event. Centroid depths less than 16 km are preferred for both events in the W-phase inversions. The gCMT and W-phase solutions are very consistent for the 2013 event but differ by 27° in dip for the 2003 event. Differences in predicted W-phase waveforms and following fundamental mode surface wave arrivals are small for the range of dips listed in Table 11.1, so we prefer the gCMT dip for the 2003 event

because more data are available for that inversion. Very steep dips, as might be expected for strike-slip events, are not consistent with the long-period data.

Table 11.1 Long-Period Point-Source Solutions

Event	Type	M_0 (N-m)	Centroid Time (s)	Depth (km)	Strike (°)	Dip (°)	Rake (°)
08/04/2003 Scotia event	gCMT	2.73×10^{20}	22.4	15.0	101	36	-23
	Wphase	1.85×10^{20}	15.0	15.5	103	63	-32
11/17/2013 Scotia event	gCMT	5.82×10^{20}	45.5	23.8	102	44	3
	Wphase	6.45×10^{20}	44.4	11.5	97	46	-3

11.2.2 Back-projection analysis

Teleseismic short-period, 0.5-2.0 s, P wave recordings for the November 17, 2013 event from two large networks of stations in Australia (AU) and the Americas (Figure 11.2) are used for back-projections to estimate the rupture speed (V_r) and length following the procedure described by Xu *et al.* (2009). While there are some differences in the back-projections for the two networks, both produce images with two loci of coherent short-period radiation eastward from the hypocenter. The first patch of radiation was released from 10-50 s after the origin time as the rupture extended ~100 km to the east and the secondary patch was released from ~70-100 s after the origin time as the rupture continued eastward another ~150-250 km (Figure 11.2, Supplementary Animations S1, S2). There is a gap between the two regions of coherent short-period emissions. The AU data indicate somewhat longer duration of source radiation, with coherent energy out to ~130 s. The space-time patterns of the short-period radiation indicate a rupture velocity of about 2.0-2.5 km/s (Figure 11.A4). The image from the AU network is spatially less-well resolved overall in the north-south direction than that from the Americas, but provides better east-west separation of the two patches of strong radiation due to more favorable imaging geometry, and both images are blurred by typical

network response distortion of the back-projection. Joint back-projection was not performed because the signal energy distribution differs for the events due to radiation pattern and different depth phase interference effects.

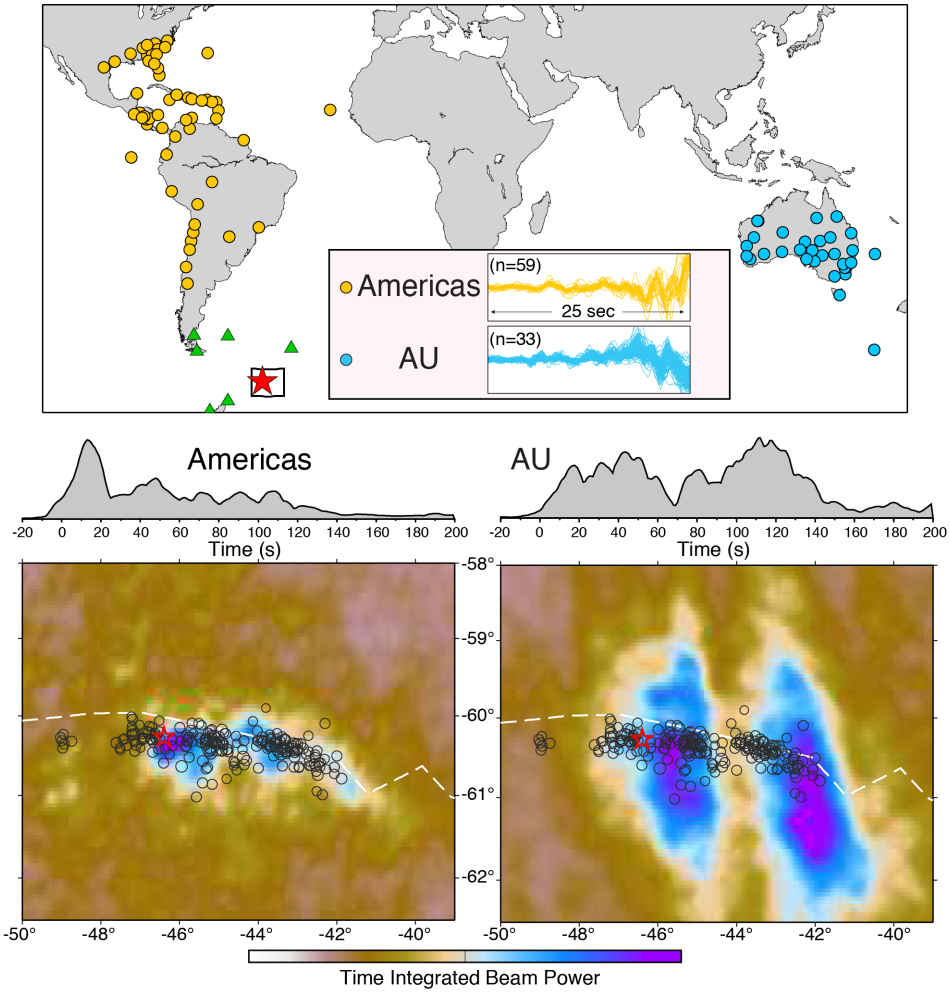

Figure 11.2 Constraints on rupture velocity and rupture length from P wave back-projection. Teleseismic P waves (top panel inset) in the frequency band from 0.5 to 2.0 Hz from large networks (top panel) of stations in the Americas (gold) and Australia (AU) (blue), with the threshold of cross-correlation coefficient for the signals in inset of top panel of 0.6, were used to image the space-time history of coherent high frequency seismic radiation from the November 17, 2013 M_w 7.8 Scotia earthquake. The time-integrated power stacked on a source region grid from each network is shown in the lower panels relative to the mainshock epicenter (red star) and aftershock sequence (black circles). The time sequences of peak beam power are shown in the central panels. The darker blue and light purple colors indicate higher power of coherent energy release with eastward rupture expansion for over 250 km in the images from both networks. A rupture velocity of ~2.0-2.5 km/s is estimated from the space-time history of high-frequency radiation (Figure 11.A4). Supplementary animations, Movies S1 and S2, show the time varying images throughout the rupture process for each network.

The green triangles in the map show the location of the GPS sites used for calibrating the coseismic HRGPS recording at BORC.

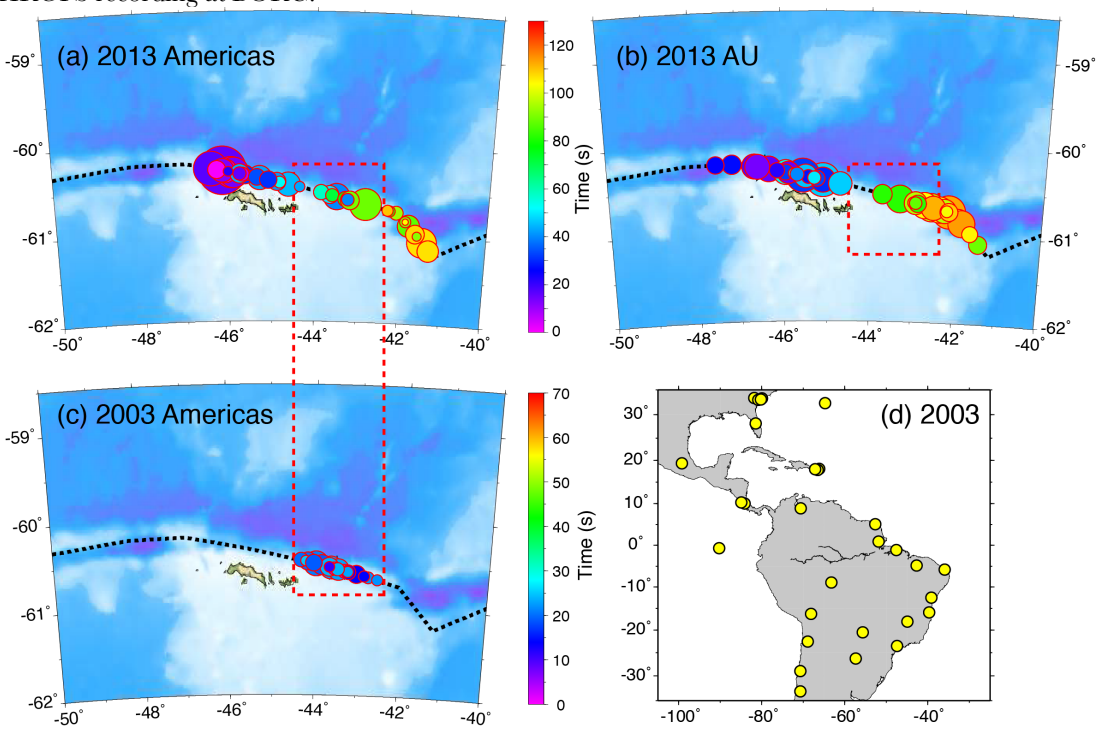

Figure 11.3 The distribution of coherent teleseismic high-frequency (0.5-2.0 Hz) P wave energy obtained by deconvolving the P wave back-projection images from networks in the Americas and Australia (AU) by the corresponding array response functions at 1Hz for the November 17, 2013 M_w 7.8 Scotia earthquake (a and b) and August 4, 2003 M_w 7.6 Scotia earthquake (c) constrained to rupture along the plate boundary (dashed black line). This procedure results in images of discrete bursts of coherent-energy radiation in time and space that are free of the smearing created by the array limitations. The networks used for the 2013 event are shown in Figure 11.2, and the network in the Americas used for the 2003 event is shown in (d). The size of circles in (a), (b) and (c) indicates the relative amplitude after deconvolution, color-coded with the time after origin time. The dashed red box emphasizes the relative location of the coherent energy release of the 2013 and 2003 events. A rupture velocity along the plate boundary of ~2.0-3.0 km/s, is estimated for the 2013 event (see supplementary Figure 11.A5).

To suppress the blurring effects from the network limitations, we perform an iterative deconvolution of the back-projection images by the corresponding array response functions for a 1 s period impulse, constraining the solution to lie along the SSRT boundary. This

deconvolution procedure follows that of Lay *et al.* (2009), and provides a parsimonious characterization of the coherent short-period space-time energy release. The resulting images of the discrete coherent-energy distribution (Figure 11.3) are qualitatively similar to the initial back-projection images, but differences between the two network images are reduced. Estimates of the rupture velocity using the along-boundary length are in the range 2.0-3.0 km/s (Figure 11.A5). The total duration of radiation is about 120 s, with the deconvolved images favoring rupture extending to -41°W, about 300 km eastward from the epicenter, somewhat beyond the 250 km extent of the aftershocks (Figure 11.A1).

We apply the same procedure to the August 4, 2003 earthquake using short-period (0.5-2 s) P recordings from stations in the Americas (Figure 11.3d), giving the deconvolved distribution of coherent high-frequency radiation locations shown in Figure 11.3c. This image suggests bi-lateral rupture expansion with a total rupture length of ~80-100 km. The rupture velocity is not well constrained, but 2.5 km/s is consistent with the data. Comparison of the images for the 2003 and 2013 events from the Americas network indicates strong overlap between the eastern portion of the 2013 event and the 2003 event (Figure 11.3). The westernmost short-period radiation for the 2003 event does lie in the gap between the main high-frequency radiation regions for the 2013 event. The image for the 2013 event extends eastward of the 2003 image, suggesting that the 2013 rupture managed to propagate across the 2003 failure zone. These back-projection images are generally compatible with results in Vallée and Satriano (2014) and those posted on the IRIS website (http://www.iris.edu/spud/backprojection). Given the limited resolution of the back-projections, and the uncertain relation between slip and coherent short-period radiation (Lay *et al.*, 2012), we cannot confidently establish whether the 2013 event re-ruptured the

large-slip area of the 2003 event using back-projection analysis, but the 2013 rupture certainly at least bracketed the 2003 rupture.

11.2.3 Surface wave directivity analysis

To provide further constraint on the rupture directivity, we deconvolve global, teleseismic group-velocity-windowed R1 Rayleigh waves and G1 Love waves for the November 17, 2013 M_w 7.8 earthquake by point-source normal-mode synthetic seismograms computed using the gCMT moment tensor for the PREM Earth model, following the method described by Ammon *et al.* (2006). The resulting propagation-corrected surface wave source time functions (STFs), aligned using the directivity parameter assuming an along-plate boundary rupture azimuth of 98°, show an approximately linear trend for the total durations and two primary intervals of large moment rate (Figure 11.4). This supports the strong unilateral eastward rupture expansion. The STF total durations range from about 60-180s and about 70-180s for R1 and G1, respectively. The estimated rupture length is ~240-250 km, and the rupture velocity is ~2.5 km/s, assuming a unilateral rupture model and reference phase velocities of 4 km/s for R1 and 4.6 km/s for G1. These results are compatible with the back-projection estimates. The STFs show some variations that suggest non-uniform slip, and provide first-order long period source characteristics that we use to constrain the finite-fault modeling below.

11.3 Finite-fault modeling

Finite-fault rupture models for the August 4, 2003 and November 17, 2013 South Scotia Ridge earthquakes are obtained by inverting teleseismic broadband P and SH wave ground displacements in the passband 0.005-0.9 Hz (Figures 11.A6 and 11.A7). We use the least-squares kinematic inversion method with positivity constraint for constant rupture

expansion velocity (V_r), specified fault geometry, and subfault source time functions parameterized by several overlapping triangles developed by Kikuchi and Kanamori (1991).

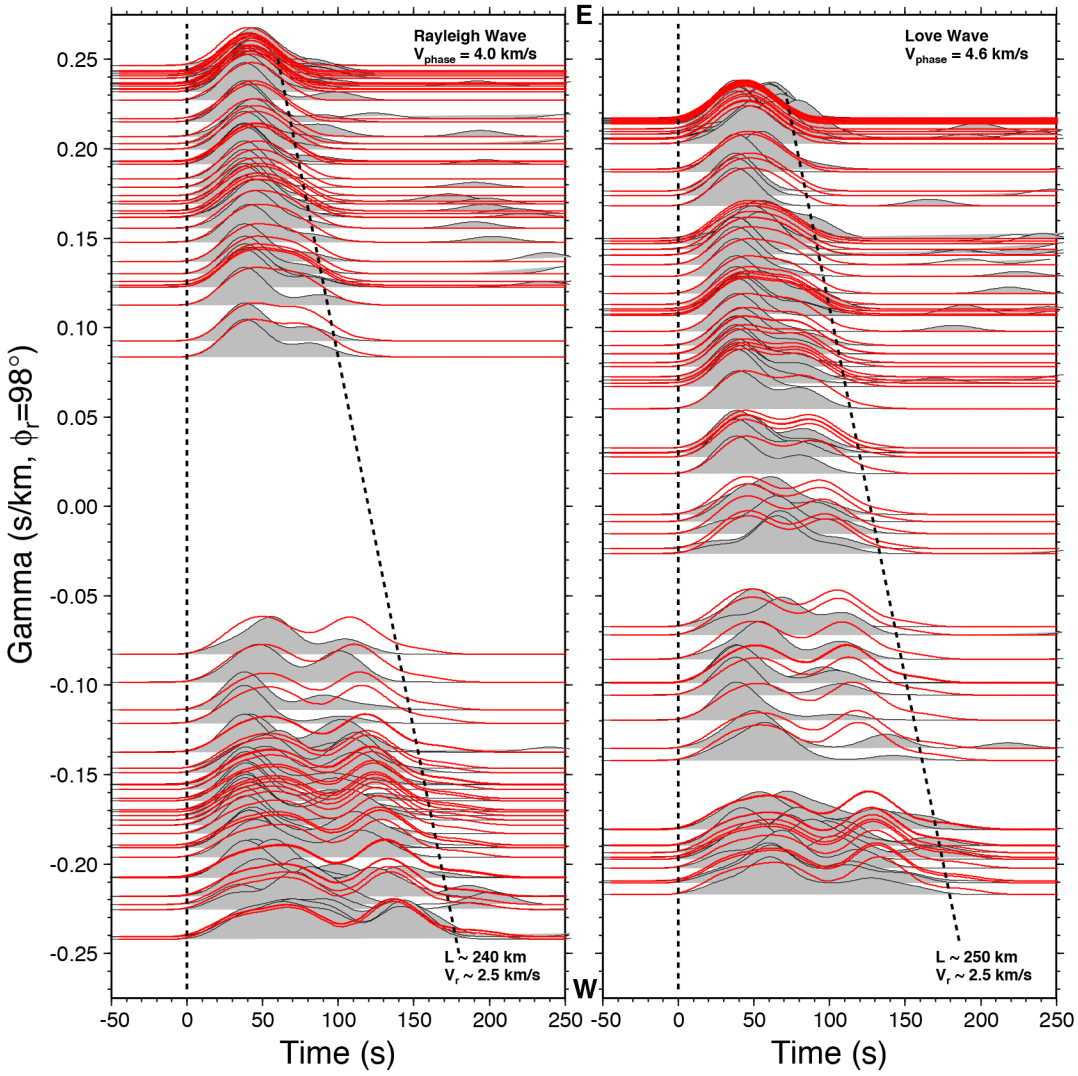

Figure 11.4 Effective source time functions (normalized) for R1 Rayleigh waves and G1 Love waves for the November 17, 2013 M_w 7.8 Scotia earthquake, plotted as a function of directivity parameter, gamma $\cos(\phi-\phi_r)/V_\phi$, for a rupture azimuth ϕ_r of 98° and azimuth of station ϕ , assuming phase velocities V_ϕ of 4.0 km/s (R1) and 4.6 km/s (G1). Each source time function is obtained by deconvolving the group-velocity windowed surface waves by corresponding point-source synthetics from normal model summation using the global Centroid moment tensor source. This removes most propagation effects and allows azimuthal patterns in the source functions to be analyzed for rupture directivity. The red lines are predicted source functions from our preferred finite fault model (Figure 11.5a) at corresponding azimuths. The black dash lines indicate the estimation of the rupture length

and rupture velocity. The source functions narrow toward the east due to the eastward rupture directivity.

We modify the code to allow for several fault segments with different geometries and rupture parameters to explore the complex rupture process of the 2013 event.

In addition to global seismic observations, we model ground motion recordings (Figure 11.5) from GPS station BORC on Laurie Island (South Orkney Islands), just south of the SSRT. We first use the GAMIT/GLOBK daily processing to calculate the co-seismic static offsets for both 2003 and 2013 events. To obtain 2013 high-rate GPS ground motions, we calculate the GPS time series relative to each of 6 regional 1-Hz GPS stations (OHIX, PAL2, FALK, AUTF, UNPA and KEPA, Figure 11.2) which are held fixed, remove the pre- and post-event averages, scale the final coseismic-displacement for each component by the static offsets from GAMIT/GLOBK processing, and average the kinematic estimates to give the HRGPS recordings shown in Figure 11.5a. After scaling, differences between both the

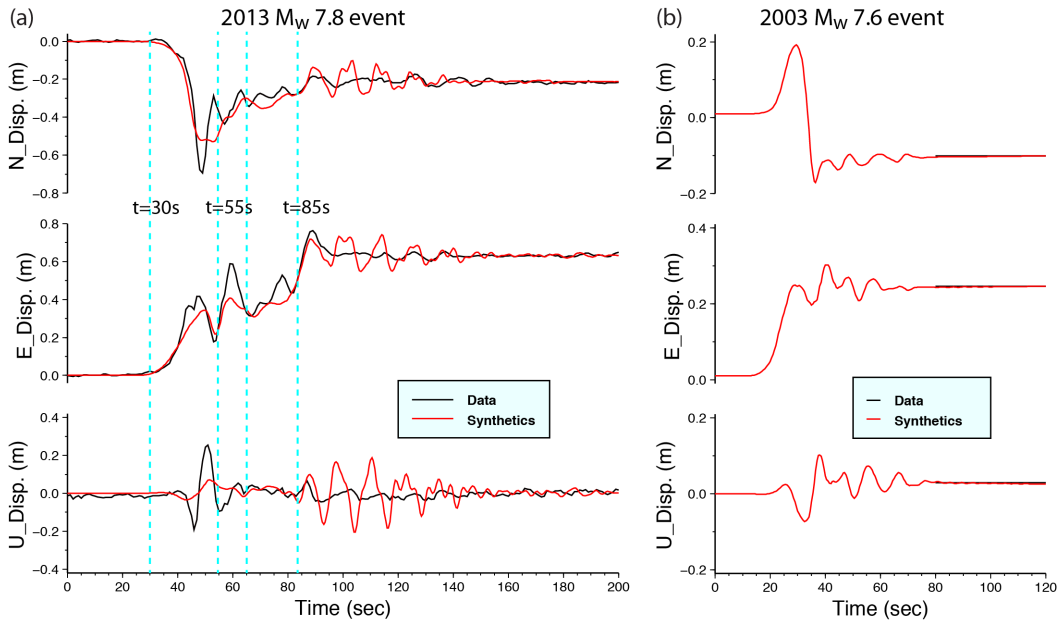

Figure 11.5 Forward modeling predictions of 1-Hz sampled GPS ground motion recordings for the November 17, 2013 M_w 7.8 Scotia earthquake (a) and static displacement offsets for the August 4, 2003

M_w 7.6 Scotia earthquake (b) at station BORC on Laurie Island (South Orkney Islands) (Figures 11.6, 9). The red curves are the predicted displacement from our preferred finite fault models (Figure 11.7).

individual and average, and raw and sidereally filtered seismograms, for both the horizontals and verticals, are negligible at the noise level for HRGPS (~5 mm). The final static offsets are ~0.63 m east, 0.22 m south, and 0.003m vertical (Figure 11.5a). High-rate data are not available from BORC for the 2003 event, but the static offsets are ~0.25 m east, ~0.10 m south, and 0.03 m downward, giving a similar ESE overall displacement direction (Figure 11.5b). The three-component 1-s sampled co-seismic displacements are modeled for the 2013 event; and the static displacement offset is modeled for the 2003 event.

The crustal structure along the SSRT and under the South Orkney microcontinent is not well-known, so we assume a simple two-layer 25-km thick continental crust (Busetti *et al.*, 2000; Vuan *et al.*, 2000) overlain by a thin oceanic layer (1.5km) for computing Green functions for both teleseismic and regional modeling. Complete ground motions including time-varying and static offsets are computed using a frequency-wavenumber (F-K) integration method (Computer Programs in Seismology, Robert Herrmann) for modeling the BORC recordings. Given that the crustal structure is uncertain, we also perform modeling using regional Green functions for other layered structures, finding that the HRGPS waveforms for the 2013 event are primarily dependent on the space-time rupture history, with only secondary dependence on the precise crustal velocity structure used. Changes in source structure mainly give rise to small variations in seismic moment, as rupture velocity trades-off with local wave velocities for aligning arrivals at BORC.

The BORC static offsets provide valuable constraints on the slip distributions for both events due to the proximity of the station to the ruptures. Figure 11.6 indicates initial finite-fault model geometries considered for the 2003 and 2013 events, with the fault planes having

the strike and dip of the corresponding gCMT inversions. The grid depicts the centers of subfaults. For assumed uniform slip at each subfault the vectors at the gridpoints indicate the corresponding contribution to the static offset at BORC. These vectors would be weighted by relative slip on each subfault and summed to match the BORC data. If the slip for 2003 were located within the -44.5° to -42° longitude range indicated by back-projection (Figure 11.3), it would not be possible to match the BORC displacements which are toward the ESE.

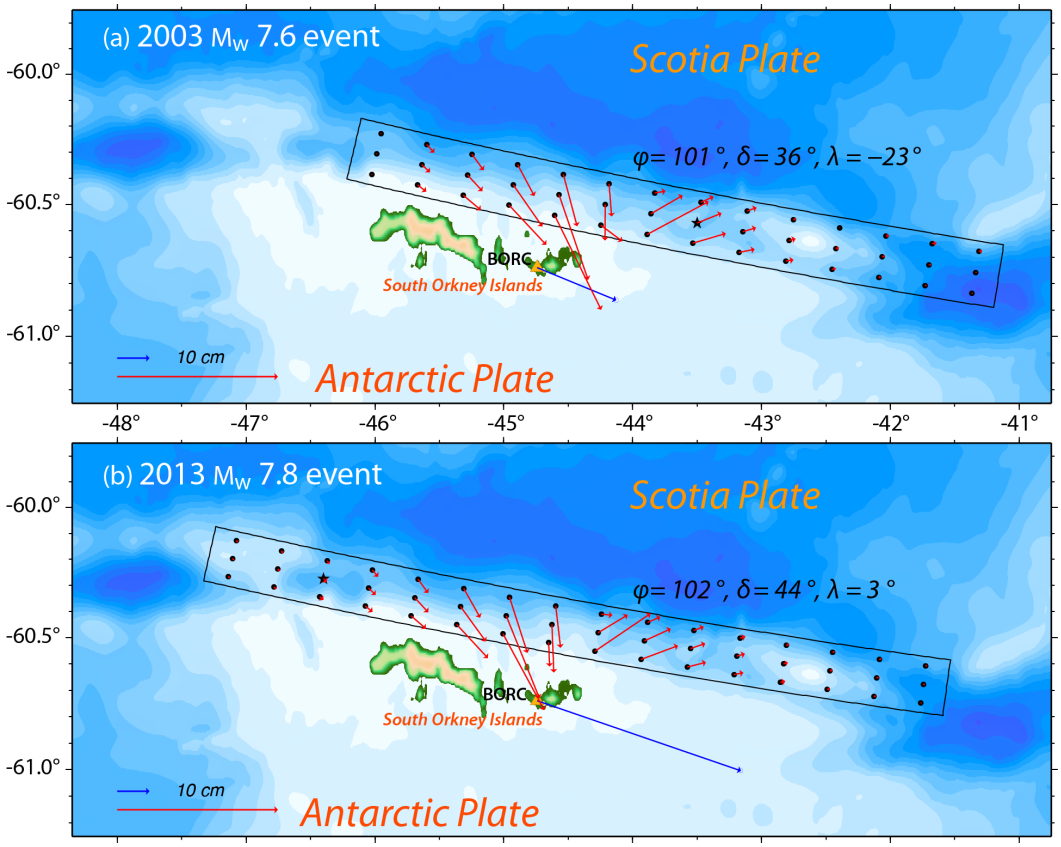

Figure 11.6 Initial finite-fault model framework for the 2003 and 2013 earthquakes, with uniform fault models specified by the gCMT best-double couple solutions. The model grids indicate the center of subfaults in the model representations. The GPS station BORC on Laurie Island is indicated, along with the coseismic static displacement observed for each event, shown with the blue vector. The red vectors indicate the predicted static motion at BORC for a model with uniform slip over each fault model with the indicated strike (ϕ), dip (δ) and rake (λ). For the 2003 event (a), the actual slip on the fault must involve significant slip west of longitude -44°, in order to match the ESE motion at BORC, given

that the rupture begins to the east (star). For the 2013 event (b), the actual slip on the fault must involve significant slip east of -44° to reduce the southerly motion caused by expected large slip west of -44°.

The only way to match those offsets is to have rupture extend further to the west, and to have the southerly offsets from the western slip dominate the northerly offsets from the eastern slip. This holds for different choices of dip or strike of the 2003 segment. Similarly, the 2013 event must involve some balance of western and eastern rupture to match the BORC static motions.

Given only the single HRGPS recording for 2013 and only static offsets for 2003, we adopted a strategy of inverting the teleseismic observations for finite-source models with different parameters (*Vr*, fault strike and dip, subfault source durations), and then forward modeling the BORC observations for the resulting models. We then iteratively constrain the choice of faulting parameters used in the finite-source inversions to those matching the salient features of the BORC observations; relative timing and shape of the time-varying displacements and final static offsets (only the latter for the 2003 event). This iterative inversion/modeling procedure yields good constraints on slip distribution along strike, with much better spatial resolution than the teleseismic inversions on their own. The relatively coarse spatial grid appropriate for the teleseismic inversion produces some roughness in the predicted motions for the portion of the fault where rupture moves away from BORC, but the overall character of the signals is modeled reliably.

The body wave inversion model parameterizations are guided by the gCMT best double couple solutions, aftershock sequences, back-projection images, STF observations, and orientation of the plate boundary. The teleseismic data for the 2013 event can largely be reconciled with a single fault orientation throughout the rupture other than for energy after about 110 s, which indicates a change in fault strike on the eastern end of the rupture. In

modeling the static offset at BORC for 2003, we found the shallower dip of the gCMT solution provided better fit, so we adopt a two-dip, three-segment model for the 2013 rupture with the western segment having the 45° dip of the gCMT solution for 2013, and the eastern segments having the 36° dip of the gCMT solution for 2003. Dip is not tightly resolved, and has uncertainty of 10° or so, but this choice ensures consistency with the long-period mechanisms on average. The V_r, initial timing, source time function, and geometry for each segment are explored over a large range of parameters, under the constraint of matching the HRGPS recordings. This results in a final model with three fault segments (Figure 11.7a) with minor changes in strike and dip from west to east. The HRGPS observations are particularly valuable for constraining the timing and geometry of the first two segments, with little constraint on the remote third segment to the east. In order to match the total seismic moment and geodetic measurements we have to use short source time functions for each subfault, comprised of 3 overlapping triangles with rise times of 3.5 s (western segment), 2.0 s (central segment) and 1.5 s (eastern segment), giving maximum subfault rupture durations of 14-6 s. A rupture velocity of 2.5 km/s is used for the preferred model, as indicated by the surface wave STF directivity and short-period back-projection observations. This value is also preferred from a range of choices considered in modeling the HRGPS recordings.

Given the horizontal grid spacing of 22.5 km and 19.0 km for the first two segments respectively and the specified rupture velocity, the rupture behaves as a slip-pulse sweeping unilaterally toward the east; longer sliding of initially ruptured subfaults is not compatible with the HRGPS data. There is an initial interval of very weak radiation in the P waves, extending for about 10 s prior to onset of strong arrivals. We delay rupture expansion for the first 4.5 s after the origin time based on lack of any offset from the epicenter in the P wave back-projections. The fits to teleseismic data are not affected by this, but the HRGPS

observations are very sensitive to absolute space-time placement of the slip, and a lower rupture velocity would be required if this delay in rupture expansion were not imposed.

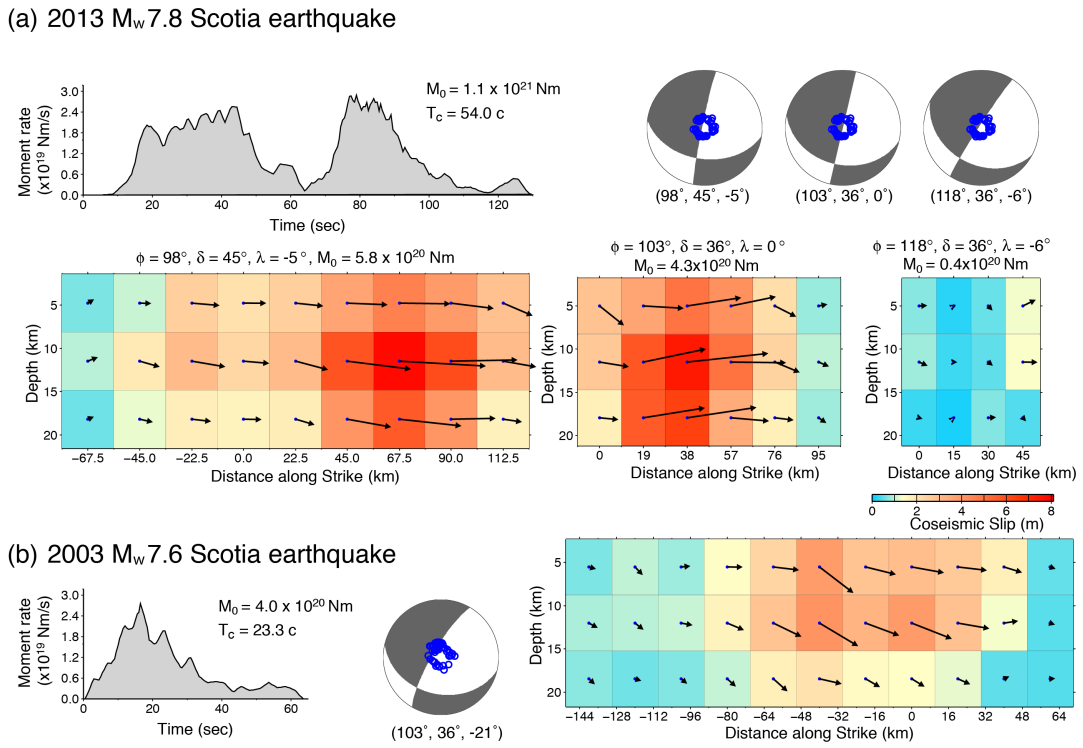

Figure 11.7 Finite-fault slip models from inversion of teleseismic body waves (P and SH) for (a) November, 17, 2013, and (b) August 4, 2003 Scotia earthquakes. The slip distribution on the fault plane is shown with the arrows indicating average rake of each subfault, and slip magnitude being color-coded. Three contiguous fault segments with different geometries are used for the 2013 event with relative locations shown in Figure 11.8a. Rupture expansion velocity of 2.5 km/s is used for both events. The moment-rate functions, seismic moments, centroid time shift (T_c) and the average focal mechanism for each fault segment are shown, with lower hemisphere equal area projections indicating the positions sampled by teleseismic P waves used in the inversions. Observed and synthetic waveform comparisons are shown in the supplementary Figs. 11.A6 and 11.A7.

The E-W HRGPS recording for the 2013 event shows two clear steps in the development of the total static offset (Figure 11.5a). Time-varying motions began about 30 s after the origin time, with initial southward, eastward and downward displacements of 0.7 m, 0.5 m, and 0.2 m, respectively. The rupture begins about 100 km west of the station and sweeps past about

40 km to the north at around 55 s after the origin time. At that time, a second 10-s duration pulse of eastward motion begins with no motion on the N-S and vertical components, followed by about 20 s of minor time-varying motion. At around 85 s, a second eastward step commences, again with minor motions on the N-S and vertical components. The rupture is located well to the east of the station at this time.

The final model for the 2013 event (Figure 11.7a) has several key attributes. (1) The seismic moment of the first segment (5.8×10^{20} Nm) involves up to ~ 8 m of slip with a strike of 98° and southward dip of 45°, with rupture extending ~79 km westward and ~124 km eastward from the epicenter. S and Rayleigh waves from near the hypocenter produce the initial large southeastward motions at BORC with slip near the eastern end producing strong eastward Love waves displacements at BORC. (2) The second segment ruptures from ~70-100 s with a seismic moment (4.3×10^{20} Nm) produced by up to 7.5 m of slip with a strike of 103° and southward dip of 36°. This rupture extends ~100 km eastward of the first segment, and produces ENE displacement at BORC that reduces the total southward static motion. The shallower dip of this segment helped to match the total static offset on the N-S GPS record, which is controlled by interference of the contribution from the slip on the first two segments. (3) Minor seismic moment (0.4×10^{20} Nm) is found on the easternmost segment with strike 118° and southward dip of 36°, from modeling late (110-120 s after origin) P wave signals in the azimuthal range of 100°-200° (observed and final model waveform comparisons are shown in Figure 11.A6). (4) The two large moment rate pulses are compatible with the high-frequency coherent bursts from the back-projections both temporally and spatially. Forward prediction of the surface wave STFs for this model generally matches the directivity and two-pulse character of the data, as seen in Figure 11.4. (5) The average slip on the first segment is ~ 3.4 m and the average stress drop is 3.9 MPa,

with the corresponding values for the second segment being ~ 4.0 m and ~ 5.8 MPa, with these being computed for the subfaults with moment larger than 15% of the peak subfault moment. The total moment of the finite fault inversion with constraint from modeling the GPS recording at BORC is ~ 1.1×10^{21} Nm, which is ~ 65% higher than the moment from long-period point source inversion. This discrepancy may be due to differences in precise fault geometry as well as uncertainty in the absolute location of the fault model relative to the GPS station.

The lack of clear directivity yields fewer constraints on the finite-fault inversion for the 2003 event. The ESE static offset at BORC indicates that the main slip during the 2003 event must be different from the slip in the second segment of the 2013 event, which produced ENE contributions to the total BORC displacement for that event (Figure 11.6). This proves to be a very influential observation for constructing our preferred model; if we adopt the gCMT focal mechanism and allow a bilateral rupture from the 2003 hypocenter, we cannot match the BORC observation although the fit to teleseismic P and SH data is acceptable. By iteratively performing inversions of the seismic data with varying fault orientations, rupture velocity and lateral fault extent and then predicting the BORC static offsets for the resulting models, we established that the main slip during the 2003 event must locate relatively close to BORC, westward of the hypocenter, with a shallow dipping fault (we obtain good fits using the 36° dip of the gCMT solution). The preferred model gives a good fit to teleseismic body waves (Figure 11.A7) and satisfactory match of the GPS offsets (Figure 11.5b), for a fault geometry with strike 103° and southward dip of 36° (Figure 11.7b). This geometry is the same as for the second segment in the 2013 model, thus it is plausibly the same fault surface that ruptured, but the peak slip in 2003 locates further west than in 2013. The seismic moment is 4.0×10^{20} Nm, the total duration is ~60 s, the average slip is 1.7 m, and average stress drop is

1.8 MPa. The slip and stress drop are similar to the values for the two main segments in the 2013 event. The contributions to the static offsets at BORC for the subfaults in the final finite-fault models is shown in Figure 11.A8. The large-slip region in the 2003 model thus locates in the region of low slip between the two patches that ruptured in 2013 (see Figure 11.A9), and this is strongly constrained by the ESE static offset observed at BORC.

11.4 Radiated seismic energy

Slip-pulse rupture processes are indicated for the 2003 and 2013 strike-slip events, with rise-times less than 14 s, much shorter than the total durations of the sources. We calculated the azimuthally-averaged far-field source spectra and seismic moment-scaled radiated energy (E_R/M_0) for both events. The average broadband source spectra (Figure 11.8) were obtained by combining the spectra of the moment-rate functions for the preferred finite-fault models in Figure 11.7 for frequencies less than ~0.05 Hz with averaged P wave spectra for frequencies from 0.05-1.5 Hz. Average radiated energy from individual P wave spectra was estimated following the procedure of Venkataraman and Kanamori (2004), and then the energy distribution across the entire spectrum was scaled up based on the composite spectra in Figure 11.8. Most of the energy is from frequencies >0.05 Hz. For the 2003 event, the radiated energy is 9.1×10^{15} J, and for the 2013 event it is 1.4×10^{16} J. There is at least a factor of two uncertainty in radiated energy estimates, but these values can be compared with those reported in Lay et al. (2012), which were determined by the same procedure. The source spectrum for the 2003 event is similar to the reference w-squared source spectrum with 3 MPa stress parameter, whereas the source spectrum for the 2013 event is somewhat depleted in high-frequency (> 0.5 Hz) radiation. The individual station estimates of P wave radiated

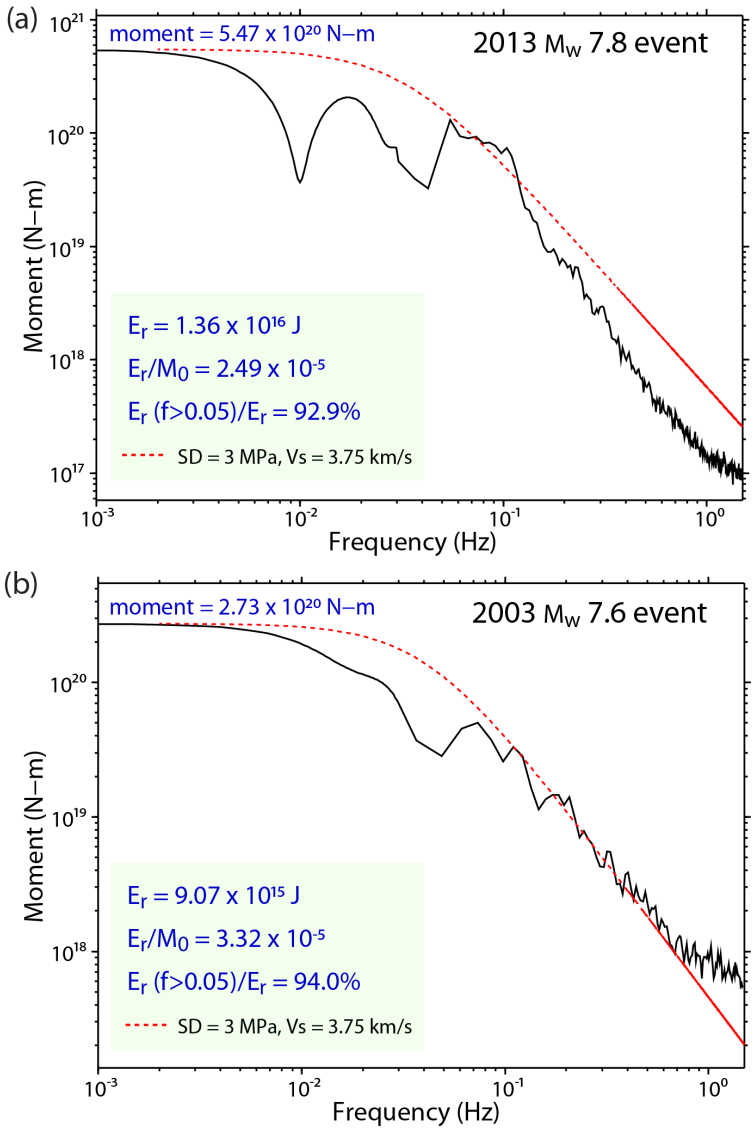

energy for the 2013 event show strong azimuthal variation (Figure 11.A10), as expected given the ~250 km long unilateral rupture. The seismic moment-scaled radiated energy (E_R/M_0) is

Figure 11.8 The average source spectra for (a) November 17, 2013 M_w 7.8 Scotia earthquake, and (b) August 4, 2003 M_w 7.6 Scotia earthquake. The black lines indicate the observed spectra, estimated at frequencies less than ~ 0.05 Hz from the moment-rate functions inverted from teleseismic body wave observations (Figure 11.7) scaled to gCMT seismic moment values, and at frequencies > ~0.05 Hz from stacking of broadband teleseismic P wave spectra. The dashed red lines are reference source spectra for an ω^{-2} model with 3 MPa stress parameter, shear velocity 3.75 km/s, and seismic moments from gCMT solutions. The radiated energy over the full frequency band, E_r, is estimated based on average source spectra and the average radiated energy from 0.05 to 1.5 Hz from teleseismic P waves (see supplementary Figure 11.A10). The high seismic moment scaled radiated energy, ~ 2.5-3.3 x 10^{-5}, is similar to the level for intraplate earthquakes near subduction zones (Lay *et al.*, 2012).

values for intraplate earthquakes (Lay *et al.*, 2012). The relatively high moment-scaled energy values may be associated with the shallow-dipping strike-slip geometry on which there is not large lateral offset.

11.5 Discussion

The finite-fault slip distributions for the 2003 and 2013 events are shown in map view in Figure 11.9, along with their foreshock and aftershock sequences. The GPS static motions and model predictions at station BORC are also shown, illustrating the sensitive location of the station to the two slip distributions. The M_w 7.6 2003 event (Figure 11.9a) appears to have some bilateral character, compatible with the aftershocks and back-projection images, but the primary large slip region is concentrated to the west of the epicenter, NNE of BORC, based on the ESE static motion at that station. The shallow dipping rupture plane is consistent with the gCMT solution, and the sinistral motion parallels the relative motion of the plates closely. The M_w 7.8 2013 earthquake sequence initiated with two left-lateral strike-slip foreshocks with magnitudes M_w 6.1 (November 13) and M_w 6.8 (November 16), located up to ~50 km west of the mainshock. Aftershocks of the mainshock extend ~250 km eastward along the SSRT, extending across the 2003 slip zone and aftershock area. There is minor change in geometry along strike with shallower dip in the eastern segments, but aftershocks tend to cluster around the large slip regions of the 2013 event. The large slip zone for the 2003 event thus lies in between the two main slip patches of the 2013 event, suggesting that while the aftershock zones may overlap, the peak slip patterns are largely complementary and this is not a simple re-rupture of a previously slipped region just ten years later as has been suggested by Vallée and Satriano (2014). The finite-fault models do have overlapping slip in the 2003 rupture area with lower slip, so some re-rupture cannot be excluded, but the peak slip is

largely complementary (Figures 11.9 and 11.A9). Modeling the GPS data at BORC is critical for coming to this conclusion.

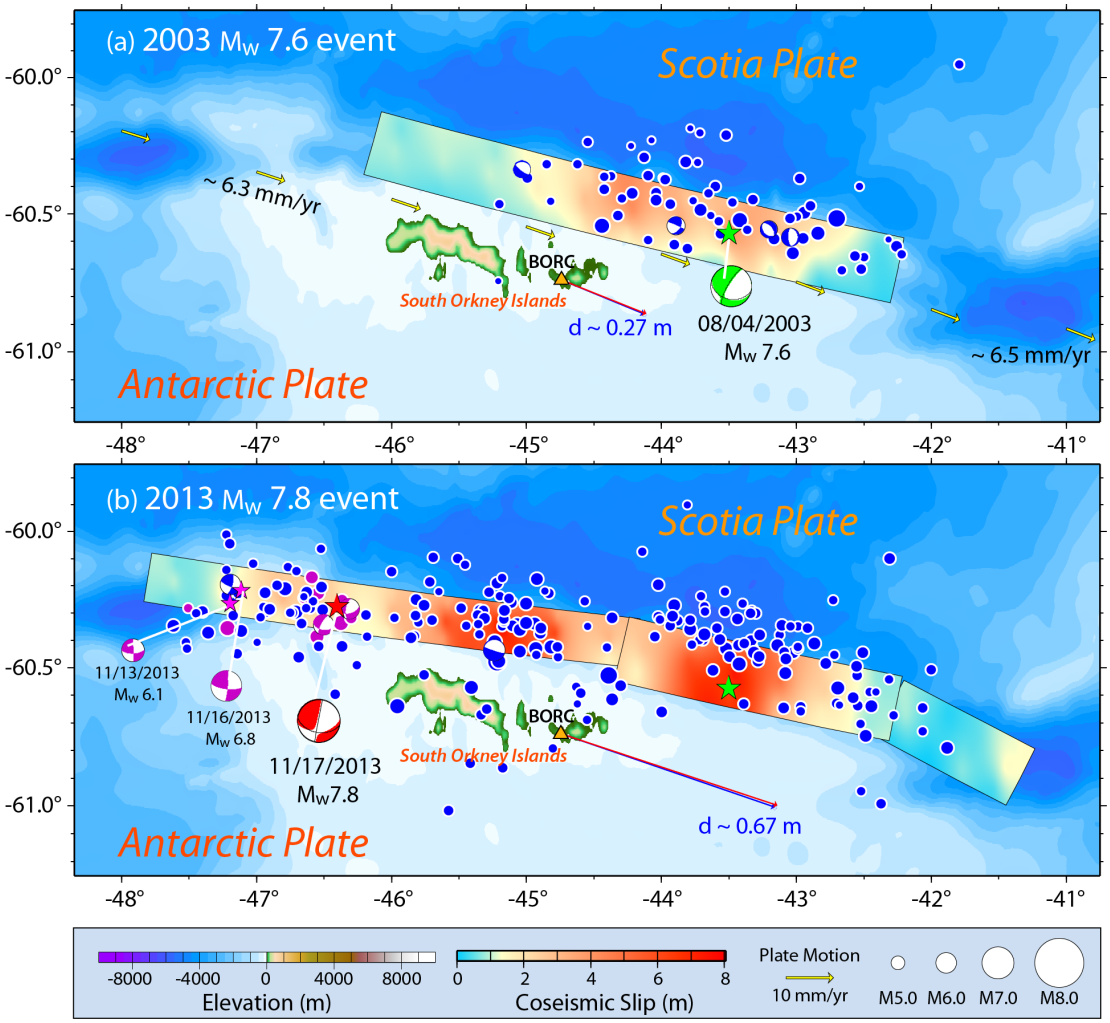

Figure 11.9 Map display of our preferred fault slip models (Figure 11.7), and foreshock (purple circles) and aftershock sequences (blue circles) for August 4, 2003 M_w 7.6 (a) and November 17, 2013 M_w 7.8 (b) events. Focal mechanisms are global Centroid Moment Tensor (gCMT) solutions. Yellow arrows in (a) indicate the plate motion direction and rate along the plate boundary between the Scotia plate and Antarctica plate, relative to the fixed Scotia plate from model MORVEL (DeMets *et al.*, 2010). The observed (blue) and predicted (red) static ground motions at GPS site BORC are shown with arrows.

The 2003 peak slip area may have been delimited between two strongly coupled zones (asperities) that subsequently ruptured in 2013. The latter event may have re-ruptured continuously through the 2003 peak slip zone with low displacement, or the easternmost region may have been dynamically triggered in 2013 by strong shear waves from the western asperity. Our slip models do not have the resolution to establish that there was no slip between the two 2013 asperities. Given the strong eastward directivity of seismic wave radiation evident in the GPS recording at BORC for the western portion of the 2013 rupture, either seismic release of residual or newly accumulated stress in the 2003 zone or jumping of slip across that zone may have occurred.

Dynamic triggering is a possible factor in the occurrence of the November 25, 2013 (06:27:33 UTC, 53.945°S, 55.003°W) M_w 7.0 event on the NSRT (Figure 11.1), which was preceded by magnitude 5.4 and 5.6 earthquakes on November 24, 2013. Examination of broadband recording at station EFI [East Falkland Island (Malvinas)] for the November 17 mainshock could not establish whether any small events were immediately activated in the vicinity of the November 25, 2013 event along the NSRT, though they could have been obscured by observed prolonged T-phase arrivals from the mainshock. The relatively low rate of seismicity along the NSRT suggests that this event was triggered (time advanced). Calculation of the November 17, 2013 Rayleigh wave amplitude at the location of November 25 event indicates that the dynamic strain was about 2×10^{-7}, which is near the threshold for statistically significant levels of dynamic triggering.

These large South Scotia Ridge events are located at the northern margin of the South Orkney micro-continent, spanning longitudes from ~ 48°W to 42°W. This continental fragment has ~25 km thick crust based on gravity modeling. To the north lies an east-west trending depression called the South Orkney trough (Busetti *et al.*, 2000; Civile *et al.*, 2012;

Vuan *et al.*, 2000) along which the main slip patches in the 2003 and 2013 events are located. While the current plate motions are largely left-lateral shear along this ~350 km long east-west segment, a minor convergent component, involving underthrusting of the Scotia plate below the Antarctic Plate is suggested by presence in the west of an accretionary prism. This accretionary prism is manifested in a smooth step morphology, by abrupt change in the seismic characteristics at the outer deformation front, and by continent-ward dipping reflectors in seismic profile (Busetti *et al.*, 2000; Civile et al., 2012; Kavoun and Vinnikovskaia, 1994; Lodolo *et al.*, 2010; Maldonado *et al.*, 1989). This region is distinct from the western SSRT, the Bransfield basin, which appears to be related to back-arc spreading associated with subduction along the South Shetlands Trench (Figure 11.1); and from the eastern SSRT along the boundary of the Brune deep and extending to the Discovery Bank which may be associated with the subduction of the Weddell Sea under the Scotia plate. Earthquake mechanisms along the SSRT include normal fault solutions in small pull-apart basins and some oblique motions, but the purely sinistral motion of the two largest events in the region in 2003 and 2013 indicates that this is the dominant strain release process operating along the central SSRT.

Both the 2003 M_w 7.6 and 2013 M_w 7.8 events have predominantly strike-slip motion on shallow-dipping faults, whereas strike-slip transform faults are typically steeply dipping, as that is energetically more favored. We infer that the fault planes are inherited underthrusting fault geometries from past convergence. The SSRT is predominantly transtensional at present, with restraining and releasing bend structures. The thrust faults along the South Orkney micro-continent are likely to be relic structures from continental break-up that transported to their current configuration. It is not clear how the primarily sinistral relative motion developed, but the current rate of deformation and total offsets on the faults are modest, and

one explanation is that the change in plate motion along the SSRT occurred rapidly enough that slip partitioning did not lead to development of an upper plate vertical strike-slip fault. This has some similarity to the September 24, 2013 M_w 7.6 Pakistan earthquake, which has a purely strike-slip motion on a 45° dipping fault plane that likely originally formed as a thrust fault within the Makran accretionary prism, activated by subsequent left-lateral shear along the Chaman fault system due to India colliding with Eurasia to the east (Avouac *et al.*, 2014). For the slow relative plate rate of ~6-7 mm/yr of sinistral motion along the SSRT (DeMets *et al.*, 2010; Smalley *et al.*, 2007), the recurrence time for the 2003 and 2013 earthquakes with peak slip of ~8 m and average slip of ~4 m, is estimated to be ~600-1300 years.

11.6 Conclusions

The 2003 M_w 7.6 and 2013 M_w 7.8 South Scotia Ridge earthquakes ruptured the plate boundary along the South Orkney microcontinent with the sinistral strike-slip motion on a ~30-45° shallow-dipping fault plate. Using constraints on the faulting geometry and rupture velocity provided by long-period surface wave source time functions and short-period P wave back-projection images, a finite-fault solution for the 2013 event is obtained by iterative inversion of broadband P and SH waves and forward modeling of 1-Hz HRGPS recordings at station BORC, located near the middle of the rupture. The main slip areas for the 2013 event bracket the main slip area for the 2003 event inferred from inverting teleseismic body waves and modeling the static offset at BORC. Thus, the 2013 event appears to have ruptured or triggered across the 2003 zone, yielding largely complementary large slip regions that combine to give relatively uniform slip along the fault strike. The almost purely strike-slip motion of the 2003 and 2013 events may be associated with reactivation of an inherited thrust fault that originally formed from compression across the boundary during continental

fragmentation or possibly seafloor spreading of the Scotia plate as it developed its current configuration.

Acknowledgements. This work made use of GMT and SAC software. The IRIS DMS data center was used to access the seismic data from Global seismic network and Federation of Digital Seismic Network stations. We thank the Argentine National Park Service and Argentine Navy for operation of BORC. We thank R. Abercrombie and an anonymous reviewer for their helpful reviews of the manuscript. This work was supported by NSF grant EAR0635570 (T.L.).

11.7 Supplementary Figures

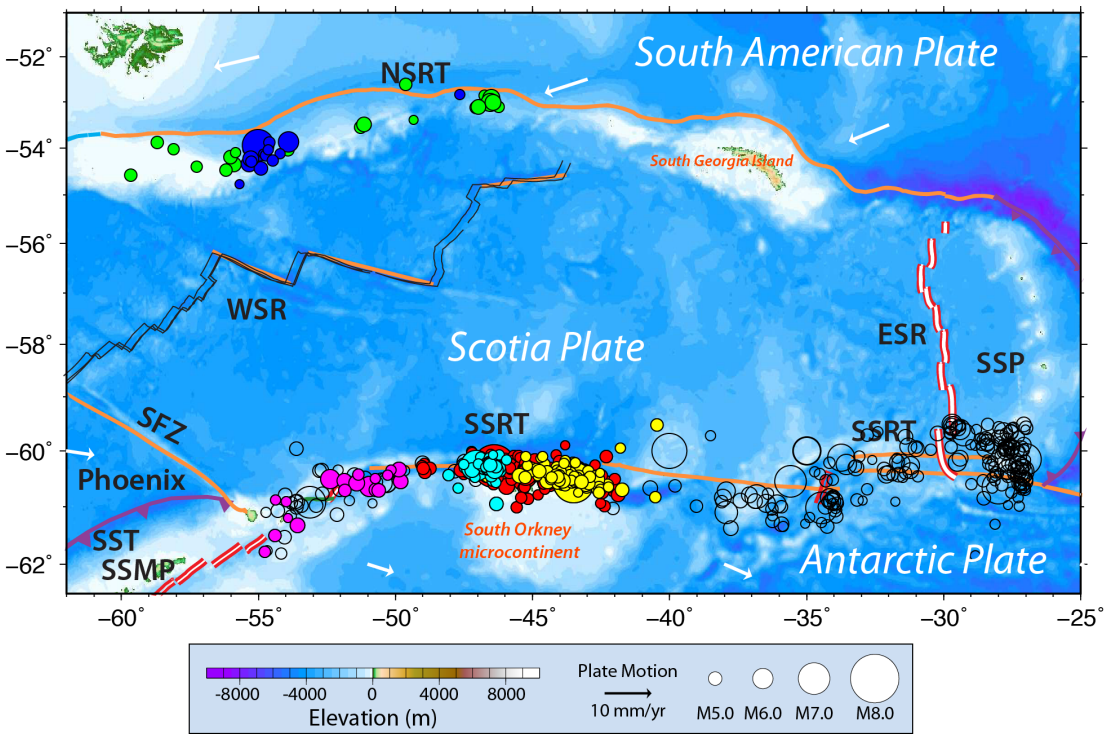

Figure 11.A1 Seismicity around the Scotia Plate. The black circles indicate epicenters of M ≥ 4.0 events from 1900 to 1975 from PAGER-CAT (Allen *et al.*, 2009) and USGS/NEIC catalog from 1976 to 2014 along the South Scotia Ridge plate boundary between the Scotia plate and Antarctica plate. The color-coded circles show the epicenters of M ≥ 4.0 events commencing with the August 4, 2003 M_w 7.6 event following the time line shown in Figure 11.A2. Yellow symbols are local aftershocks of 2003, green symbols are activity along the North Scotia Ridge up until the 2013 mainshock, magenta symbols are events west of the 2013 rupture from 2003-2013, cyan symbols are the 2013 foreshock sequence, red symbols are the 2013 aftershocks, blue symbols are the 2013 activity along the North Scotia Ridge transform including the November 25, 2013 M_w 7.0 event. Arrows indicate the plate motion directions and rates relative to a fixed Scotia plate computed using model MORVEL (DeMets *et al.*, 2010). Other symbols are same as Figure 11.1.

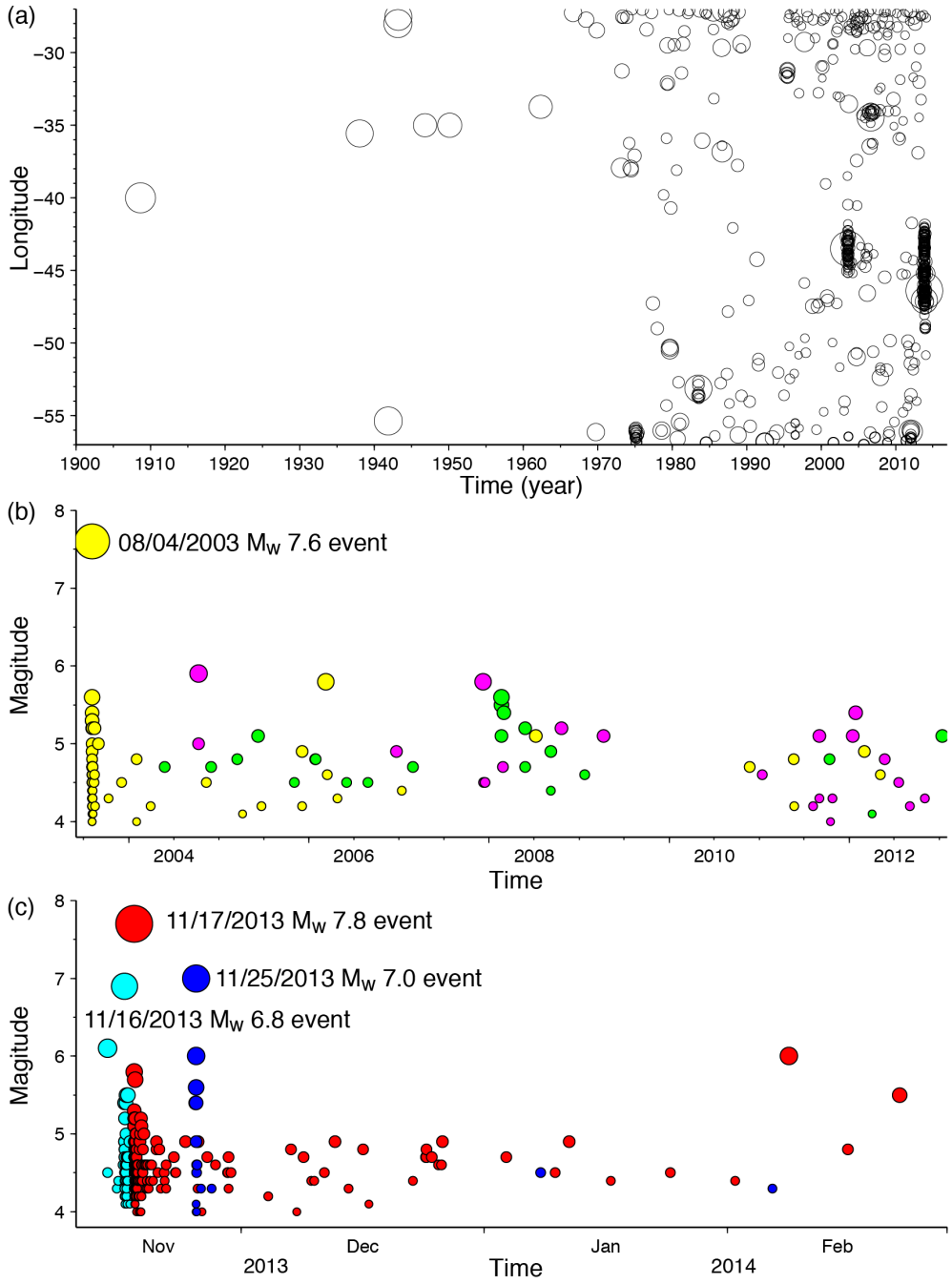

Figure 11.A2 Time series for the seismicity color-coded as Figure 11.A1: (a) M ≥ 4.0 events along the South Scotia Ridge plate boundary between the Scotia plate and Antarctic plate; (b) seismicity from the August 4, 2003 M_w 7.6 event to November 2013; and (c) the foreshock and aftershock sequences for November 17, 2013 M_w 7.8 event.

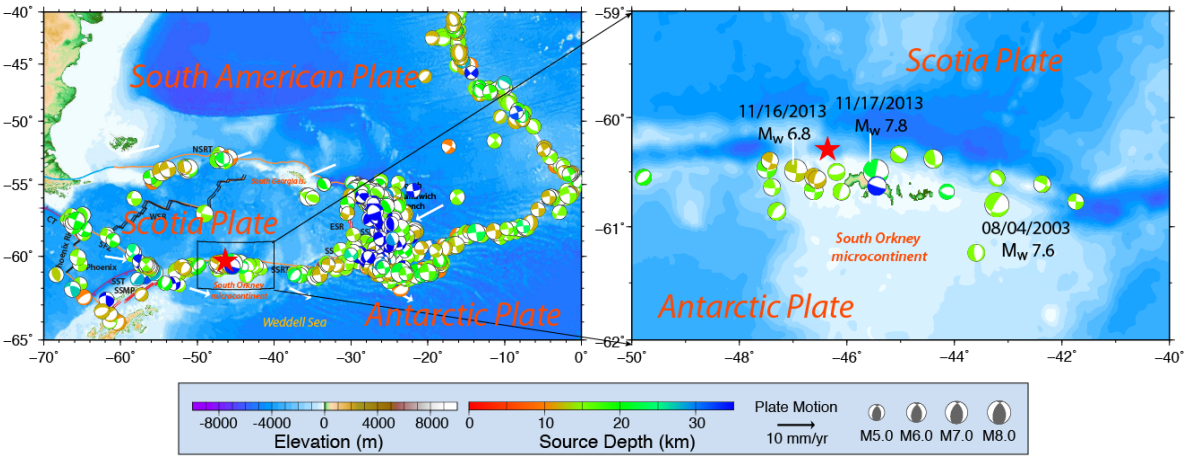

Figure 11.A3 Maps of gCMT focal mechanisms from 1976 to 2014 for earthquakes around the Scotia Sea plate on regional scale (left) and zoomed in on the region around the 2013 event (right). The red star indicates the epicenter for the November 17, 2013 M_w 7.8 event from USGS/NEIC catalog. Other symbols are same as Figure 11.1.

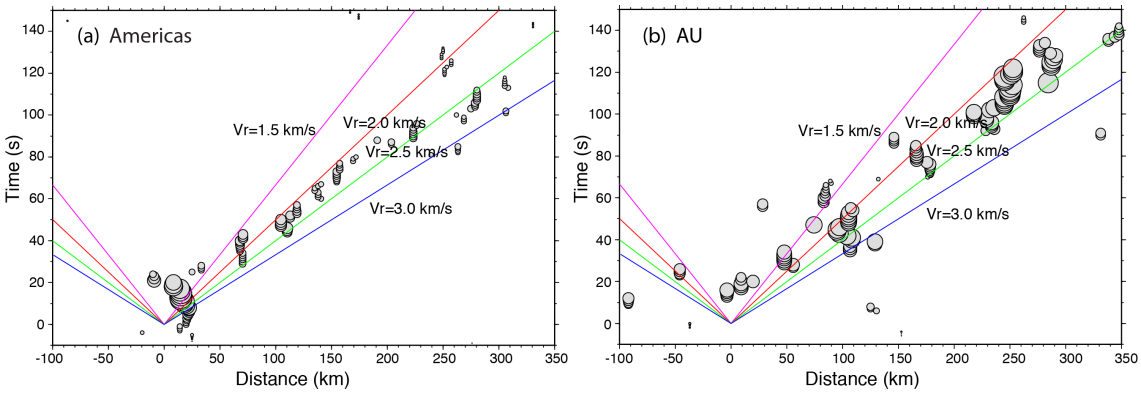

Figure 11.A4 The space-time sequence of coherent high frequency seismic radiation from the November 17, 2013 M_w 7.8 Scotia earthquake from P wave back-projection (Figure 11.2), plotted as distance from the epicenter with positive values eastward. The color-coded lines indicate the slope of different average rupture velocities. A rupture velocity of ~2.0- 2.5 km/s is estimated for back-projections of both Americas and Australia (AU) networks.

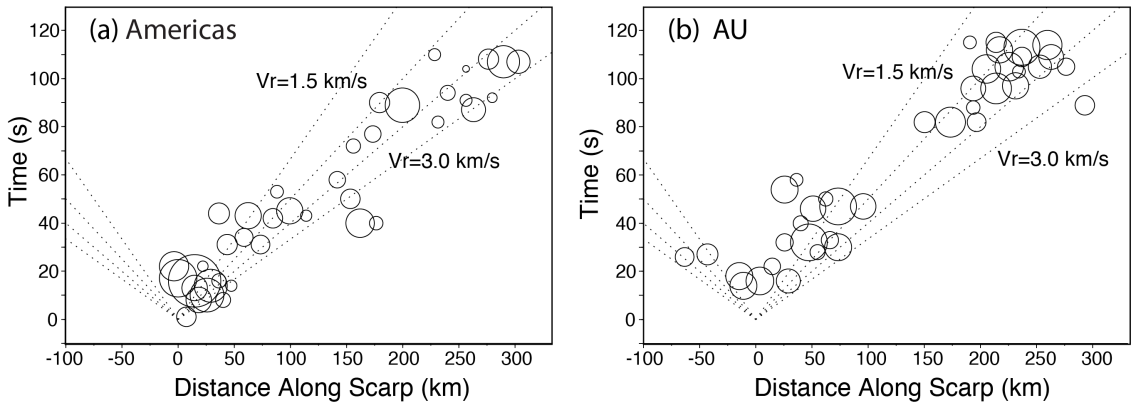

Figure 11.A5 The space-time sequence of coherent high frequency seismic radiation from the November 17, 2013 M_w 7.8 Scotia earthquake obtained by deconvolving array response functions at 1Hz (Figure 11.3), plotted as distance along the plate boundary with positive values eastward. The dashed lines indicate slopes for different rupture velocities. A rupture velocity of ~2.0- 3.0 km/s is estimated for both Americas and Australia (AU) networks.

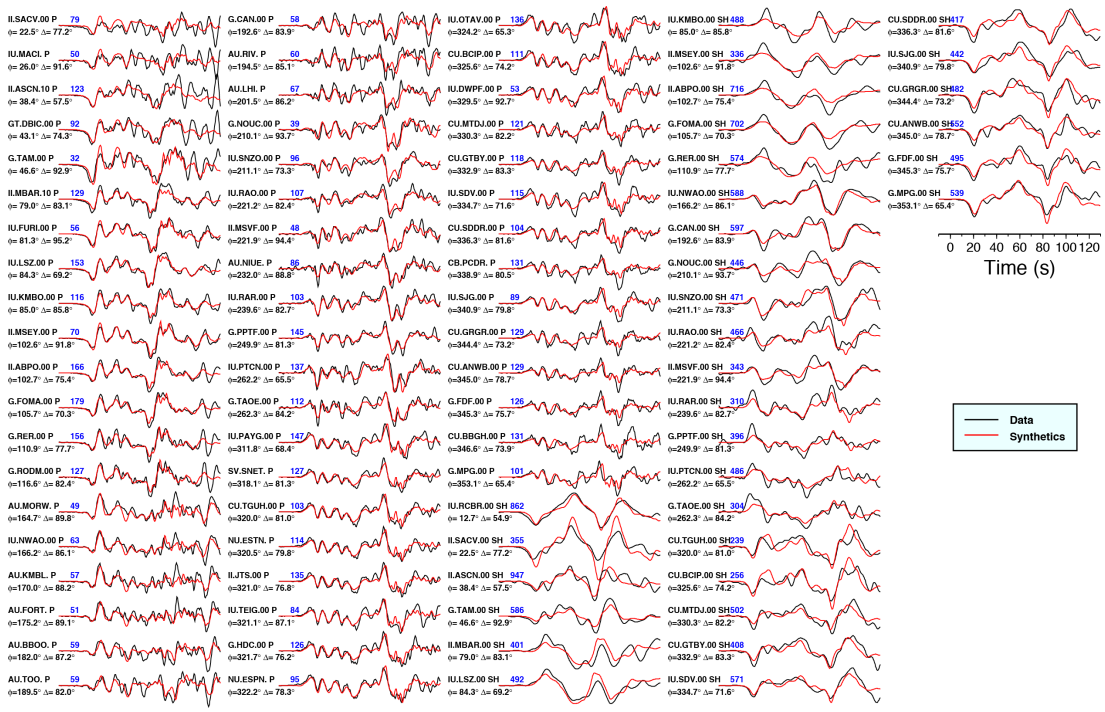

Figure 11.A6 Comparison of observed (black lines) and modeled (red lines) teleseismic body waves for the November 17, 2013 M_w 7.8 Scotia earthquake. The model shown in Figure 11.7a is used for the computations. The signals are broadband ground displacements in the passband 0.005-0.9 Hz. The data and synthetics are normalized by the peak-to-peak amplitude, blue number in unit of 10^{-6} m.

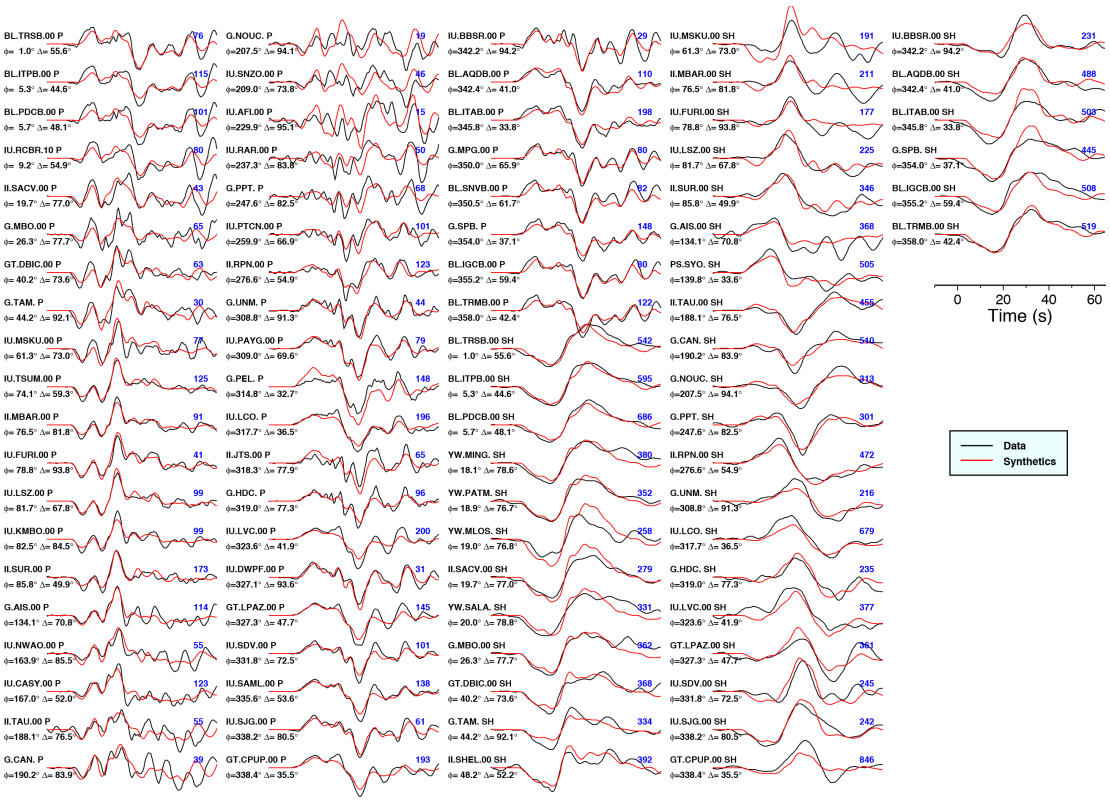

Figure 11.A7 Comparison of observed (black lines) and modeled (red lines) teleseismic body waves for the August 4, 2003 M_w 7.6 Scotia earthquake. The model shown in Figure 11.7b is used for the computations. The signals are broadband ground displacements in the passband 0.005-0.9 Hz. The data and synthetics are normalized by the peak-to-peak amplitude, blue number in unit of 10^{-6} m.

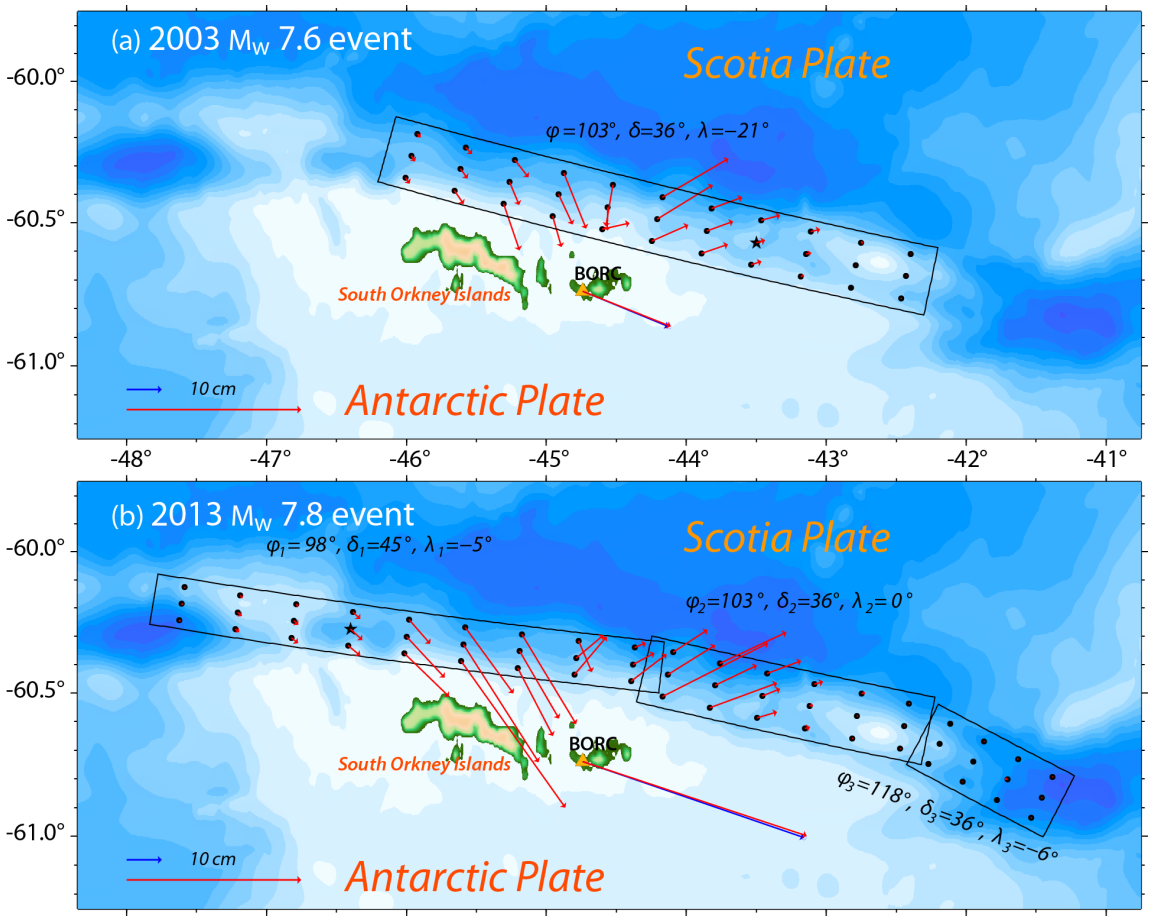

Figure 11.A8 Maps similar to Figure 11.6, but for the final faulting geometries and slip distributions in Figure 11.7, with the contribution to the BORC displacement from each subfault being shown by the red arrows on the subfault grid. The observed (blue) and predicted (red) cumulative displacement at BORC are shown.

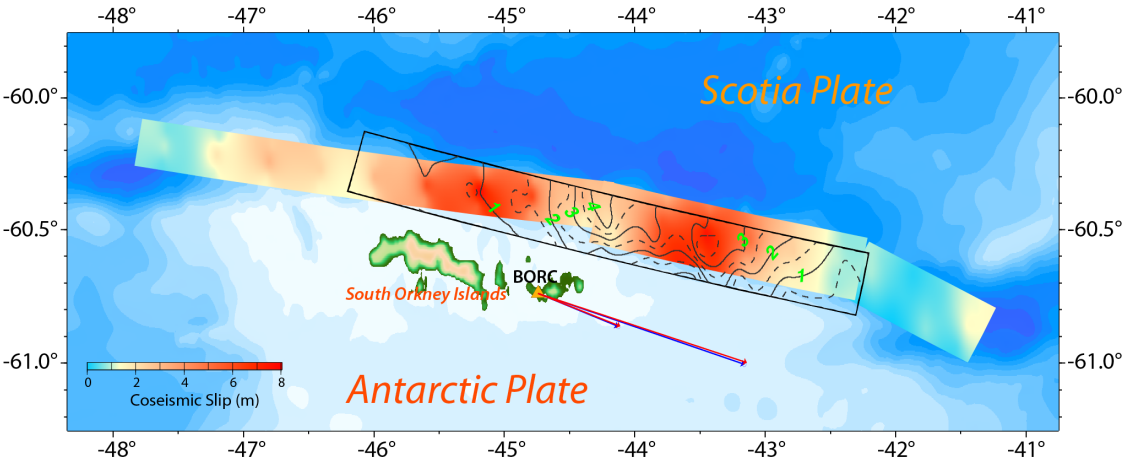

Figure 11.A9 Overlapping comparison of the slip distributions for the 2003 event (contour map with slip magnitudes indicated by the green numbers, and the 2013 event (color slip model). The peak slip of the 2003 event, is located in the low slip area of the 2013 event near a longitude of -44°. There is overlap of slip in the two events further to the East, but the 2013 rupture extends further eastward than the 2003 event.

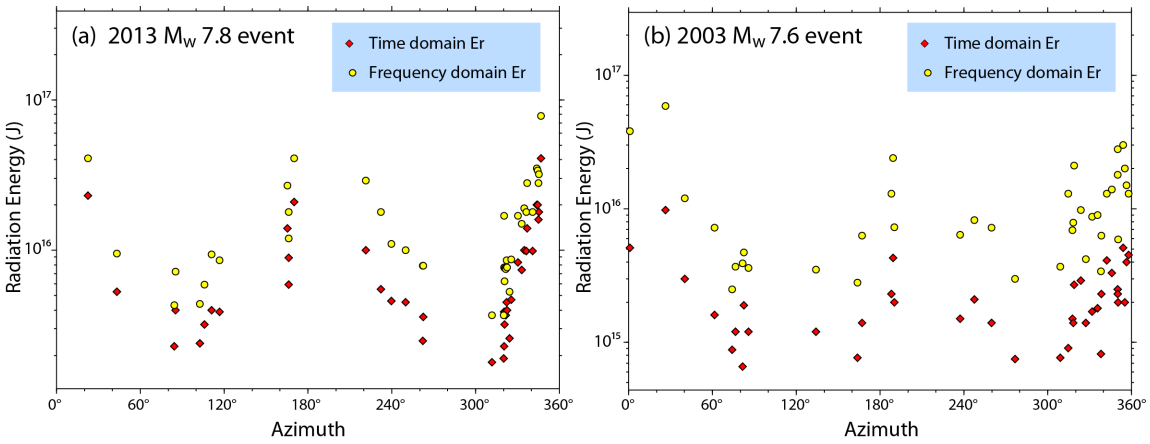

Figure 11.A10 Azimuthal distribution of the radiated energy estimates (Venkataraman and Kanamori, 2004) in the frequency band of ~0.05-1.5 Hz from teleseismic P wave recordings for (a) November 17, 2013 M_w 7.8 Scotia earthquake and (b) August 4, 2003 M_w 7.6 Scotia earthquake. The individual station estimates of P wave radiated energy for the 2013 event show strong azimuthal variation, typical of strike-slip events.

Chapter 12

Conclusion

In this thesis, I have presented a wide range of earthquake rupture studies, including earthquakes located on the shallow megathrust, intra-slab in the outer-rise and mantle transition zone, and on a transform plate boundary. Although the individual studies are relatively independent, they all attempt to extract observational insights to address two fundamental questions, "*how do great earthquake rupture*", and "*what controls large earthquakes*". I approach these two questions by providing an improved seismological understanding of large earthquake rupture processes, exploring the variation of kinematic source parameters, and placing the ruptures into the context of tectonic plate motions that drive the deformation.

However, my analysis of all these 100+ large earthquakes raises puzzles concerning these two questions. There is no "best" or "right" rupture model for a large earthquake overall; just models that account for specific data sets with specific coverage and bandwidth. We remain blind to details of small-scale processes that occurred in the source region during each earthquake failure, limiting our ability to test physical models of the process. The major effort in my Ph.D. program has been to learn assumptions in source modeling, meaning of source parameters, and limitations in the various datasets. For example, whether large earthquake involves multiple point sources, patchy slip, or continuous rupture? What source properties can be extracted from regional or far-field seismic data, static or high-rate GPS recordings, or tsunami data? What limitations arise from our deficient knowledge on earth structure? It is a grand challenge to really understand physical mechanisms of large earthquakes given these practical problems. On the other side, seismology is appealing for seeking more information on both earthquake rupture and earth structure from seismograms.

Reference

1. Abe, K. (1972), Lithospheric normal faulting beneath the Aleutian trench, *Phys. Earth Planet. Inter.*, 5, 190-198.

2. Abe, K., (1977), Tectonic implications of the large Shioya-Oki earthquakes of 1938. *Tectonophysics*, 41, 269-289.

3. Abe, K., (1979), Size of great earthquakes of 1873-1974 inferred from tsunami data, *J. Geophys. Res.*, 84, 1561-1568.

4. Abe, K., (1994), Instrumental magnitudes of historical earthquakes, 1892 to 1898, *Bull. Seism. Soc. Amer.*, 84, 415-425.

5. Abercrombie, R. E. (1995), Earthquake source scaling relationships from-1 to 5 ML using seismograms recorded at 2.5-km depth. *J. geophys. Res,* 100(B2), 24015-24036.

6. Abercrombie, R. E., and J. R. Rice (2005), Can observations of earthquake scaling constrain slip weakening? *Geophys. J. Int.*, 162(2), 406-424.

7. Abercrombie, R. E., M. Antolik, K. Felzer, and G. Ekström (2001), The 1994 Java tsunami earthquake: Slip over a subducting seamount, *J. Geophys. Res*, 106, 6595-6607.

8. Aida, I., (1977), Simulations of large tsunamis occurring in the past off the coast of the Sanriku district. *Bull. Earthq. Res.*, Inst. Univ. Tokyo, 52, 71-101.

9. Aki, K. (1967), Scaling law of seismic spectrum. *J. Geophys. Res*, 72(4), 1217-1231.

10. Aki, K. (1972), Earthquake mechanism, *Tectonophysics*, 13, 423-441.

11. Allen, T. I., K. D. Marano, P. S. Earle, and D. J. Wald (2009), PAGER-CAT: A composite earthquake catalog for calibrating global fatality models, Seism. Res. Lett., 80, 57-62, doi:10.1785/gssrl.80.1.57.

12. Allmann, B. P., and P. M. Shearer (2009), Global variations of stress drop for moderate to large earthquakes, *J. Geophys. Res*, 114, B01310, doi: 10.1029/2008JB005821

13. Alvarado, D., C. DeMets, B. Tikoff, D. Hernández, T. F. Wawrzyniec, C. Pullinger, G. Mattioli, H. L. Turner, M. Rodriguez, and F. Correa-Mora (2011), Forearc motion and deformation between El Salvador and Nicaragua: GPS, seismic, structural, and paleomagnetic observations, Lithosphere, 3(1), 3–21, doi:10.1130/L108.1.

14. Alvarez-Gomez, J. A., P. T. Meijer, J. J. Mart´ınez-D´ıaz, and R. Capote (2008), Constraints from finite element modeling on the active *Tectonics* of northern Central America and the Middle America Trench, *Tectonics*, 27, doi:10.1029/2007TC002162.

15. Ammon, C. J., A. A. Velasco, and T. Lay (2006). Rapid determination of first-order rupture characteristics for large earthquakes using surface waves: The 2004 Sumatra-Andaman earthquake, *Geophys. Res. Lett.*, Vol. 33, L14314, doi:10.1029/2006GL026303.

16. Ammon, C. J., H. Kanamori, and T. Lay (2008). A great earthquake doublet and seismic stress transfer cycle in the central Kuril islands. *Nature,* 451(7178), 561-565.

17. Ammon, C. J., H. Kanamori, T. Lay, and A. A. Velasco (2006), The 17 July 2006 Java tsunami earthquake, *Geophys. Res. Lett.*, 233, L234308, doi:10.10239/2006GL028005.

18. Ammon, C. J., T. Lay, H. Kanamori, and M. Cleveland (2011). A rupture model of the 2011 off the Pacific coast of Tohoku Earthquake, *Earth Planets Space*, 63(693-696).

19. Antolik, M., D. Dreger, and B. Romanowicz (1996), Finite fault source study of the great 1994 deep Bolivia earthquake. *Geophys. Res. Lett.* 23, 1589-1592.

20. Argus, D. F., and R. G. Gordon (1991), No-net-rotation model of current plate velocities incorporating plate motion model NUVEL-1, *Geophys. Res. Lett.*, 18(11), 2039-2042.

21. Asano, Y., T. Saito, Y. Ito, K. Shiomi, H. Hirose, T. Matsumoto, S. Aoi, S. Hori, and S. Sekiguchi (2011), Spatial distribution and focal mechanisms of aftershocks of the 2011 off the Pacific coast of Tohoku Earthquake, *Earth Planets Space* 63 669-673.

22. Assimaki D., W. Li, J. Steidl, and K. Tsuda (2008), Site amplification and attenuation via downhole array inversion: A comparative study of the 2003 Miyagi-Oki aftershock sequence, *Bull. Seism. Soc. Amer.*, 98, No. 1, 301-330.

23. Avouac, J. P., F. Ayoub, S. Wei, J. P. Ampuero, L. Meng, S. Leprince and D. Helmberger (2014). The 2013, Mw 7.7 Balochistan earthquake, energetic strike-slip reactivation of a thrust fault. *Earth Planet. Sci. Lett.*, 391, 128-134.

24. Bai, Y., K. F. Cheung, Y. Yamazaki, T. Lay, and L. Ye (2014). Tsunami surges around the Hawaiian Islands from the 1 April 2014 North Chile Mw 8.1 earthquake. *Geophys. Res. Lett.*, 41(23), 8512-8521.

25. Baltay, A. S., G. C. Beroza, and S. Ide (2014), Radiated energy of great earthquakes from teleseismic empirical Green's function deconvolution, *Pure. Appl. Geophys.,* doi: 10.1007/s00024-014-0804-0.

26. Baltay, A., S. Ide, G. Prieto, and G. C. Beroza (2011), Variability in earthquake stress drop and apparent stress. *Geophys. Res. Lett.*, 38(6).

27. Banerjee, P., F. Pollitz, B. Nagarajan, and R. Bürgmann, (2007), Coseismic slip distributions of the 26 December 2004 Sumatra–Andaman and 28 March 2005 Nias earthquakes from GPS static offsets. *Bull. Seism. Soc. Amer.*, 97(1A), S86-S102.

28. Bassin, C., G. Laske, and G. Masters (2000), The current limits of resolution for surface wave tomography in North America, *EOS* Trans AGU, 81, F897.

29. Bautista, M. L. P., and K. Oike (2000), Estimation of the magnitudes and epicenters of Philippine historical earthquakes, *Tectonophysics*, 317, 137-169.

30. Beck, S. L., and D. H. Christensen (1991), Rupture process of the February 4, 1965, Rat Islands earthquake, *J. Geophys. Res*, 96, 2205-2221.

31. Beck, S. L., P. Silver, T. C. Wallace, and D. James (1995), Directivity analysis of the deep Bolivian earthquake of June 9, 1994. *Geophys. Res. Lett.,* 22(16), 2257-2260.

32. Bilek, S. L., and T. Lay (1998). Variation of interplate fault zone properties with depth in the Japan subduction zone, *Science* 281 1175-1178.

33. Bilek, S. L., and T. Lay (2000). Depth dependent rupture properties in circum-Pacific subduction zones, *GeoComplexity and the Physics of Earthquakes*, Geophysical Monograph 120, American Geophysical Union, 165-186.

34. Bilek, S. L., and T. Lay (2002), Tsunami earthquakes possibly widespread manifestations of frictional conditional stability, *Geophys. Res. Lett.*, 29(14), doi:10.1029/2002GL015215.

35. Bilek, S. L., H. R. DeShon, and E. R. Engdahl (2012), Spatial variations in earthquake source characteristics within the 2011 Mw = 9.0 Tohoku, Japan rupture zone, *Geophys. Res. Lett.*, L09304, doi: 10.1029/2012GL051399.

36. Bilek, S. L., S. Y. Schwartz, and H.R. DeShon (2003), Control of seafloor roughness on earthquake rupture behavior, *Geology*, 31, 455-458.

37. Boatwright, J., and G. L. Choy (1986), Teleseismic estimates of the energy radiated by shallow earthquakes, *J. Geophys. Res*, 91(B2), 2095–2112.

38. Boore, D. M. (1983), Stochastic simulation of high-frequency ground motions based on seismological models of the radiated spectra, *Bull. Seism. Soc. Amer.,* 73 1865-1894.

39. Brune, J. (1970), Tectonic stress and the spectra of seismic shear waves from earthquakes, *J. Geophys. Res*, 75, 4997-5009.

40. Busetti, M., M. Zanolla, and A. Marchetti (2000). Geological structure of the South Orkney microcontinent. *Terra Antartica*, 8(2), 1-8.

41. Carver, G. and G. Plafker (2008), Paleoseismicity and Neo*Tectonics* of the Aleutian Subduction Zone—An Overview, *in Active Tectonics and Seismic Potential of Alaska (eds J. T. Freymueller, P. J. Haeussler, R. L. Wesson and G. Ekström), American Geophysical Union*, Washington, D. C. doi: 10.1029/179GM03

42. Chapple, W. M., and D. W. Forsyth (1979), Earthquakes and bending of plates at trenches, *J. Geophys. Res*, 84, B12, 6729-6749.

43. Chen K. H., R. Burgmann, R. M. Nadeau, T. Chen, and N. Lapusta(2010), Postseismic variations in seismic moment and recurrence interval of small repeating events following the 2004 Parkfield earthquake, *Earth Planet. Sci. Lett.*, 299, 118-125.

44. Chen, W. P. (1995). En echelon ruptures during the great Bolivian earthquake of 1994. *Geophys. Res. Lett.*, 22(16), 2261-2264.

45. Chen, Y., L. Wen, and C. Ji (2014), A cascading failure during the 24 May 2013 great Okhotsk deep earthquake. *J. Geophys. Res.,* 119, 3035-3049.

46. Choy, G. L., A. McGarr, S. H. Kirby, and J. Boatwright (2006), An overview of the global variability in radiated energy and apparent stress, in *Earthquakes: Radiated energy and the physics of faulting, Geophysical Monograph Series*, 170, 43-57.

47. Christensen, D. H., and L. J. Ruff (1988), Seismic coupling and outer rise earthquakes, *J. Geophys. Res*, 93, B11, 13421-13444.

48. Chung, W. Y., and H. Kanamori (1980). Variation of seismic source parameters and stress drops within a descending slab and its implications in plate mechanics. *Phys. Earth Planet. Inter.*, 23(2), 134-159.

49. Civile, D., E. Lodolo, A. Vuan, M. F. Loreto (2012). *Tectonics* of the Scotia–Antarctica plate boundary constrained from seismic and seismological data. *Tectonophysics*, 550, 17-34.

50. Convers, J. A., and A. V. Newman (2011), Global evaluation of large earthquake energy from 1997 through mid-2010, *J. Geophys. Res*, 116, B08304, doi:10.1029/2010JB007928.

51. Correa-Mora, F., C. DeMets, D. Alvarado, H. L. Turner, G. Mattioli, D. Hernandez, C. Pullinger, M. Rodriguez, and C. Tenorio (2009), Evidence for weak coupling of the Cocos plate subduction interface and strong coupling of the volcanic arc faults from modeling of GPS data: El Salvador and Nicaragua, *Geophys. J. Int.*, 179(3), 1279–1291.

52. Craig, T. J., A. Copley, and J. Jackson (2014), A reassessment of outer-rise seismicity and its implications for the mechanics of oceanic lithosphere, *Geophys. J. Int.*, 197, 63-89, doi:10.1093/gji/ggu013.

53. Creager, K. C., and T. M. Boyd (1991), The geometry of Aleutian subduction: Three-dimensional kinematic flow model, *J. Geophys. Res*, 96, 2293-2307.

54. Cross, R. S., and J. T. Freymueller (2008), Evidence for and implications of a Bering plate based on geodetic measurements from the Aleutians and western Alaska. *J. Geophys. Res*, 113(B7).

55. Dalziel, I. W., Lawver, L. A., Norton, I. O., Gahagan, L. M. (2013), The Scotia Arc: genesis, evolution, global significance. *Annu. Rev. Earth Planet. Sci.*, 41, 767-793.

56. Delouis, B., and D. Legrand (2007), Mw 7.8 Tarapaca intermediate depth earthquake of 13 June 2005 (northern Chile): Fault plane identification and slip distribution by waveform inversion, *Geophys. Res. Lett.*, 34, L01304, doi:10.1029/2006GL028193.

57. DeMets, C. (2001), A new estimate for present-day Cocos-Caribbean plate motion: implications for slip along the Central American volcanic arc, *Geophys. Res. Lett.*, 28(21), 4043–4046.

58. DeMets, C., R. G. Gordon, D. F. Argus (2010), Geologically current plate motions. *Geophys. J. Int.*, 181: 1–80.

59. Ding, K., J. T. Freymueller, Q. Wang, and R. Zou (in press), Coseismic and early postseismic deformation of the 5 January 2013 Craig Mw 7.5 earthquake from static and kinematic GPS solutions, Bull. Seismol. Soc. Am, 105(2B), 1153-1164.

60. Dmowska, R., J. R. Rice, L. C. Lovison, and D. Josell (1988), Stress transfer and seismic phenomena in coupled subduction zones during the earthquake cycle, *J. Geophys. Res*, 93, B7, 7869-7884.

61. Duputel, Z., V. C. Tsai, L. Rivera, and H. Kanamori (2013), Using centroid time-delays to characterize source durations and identify earthquakes with unique characteristics, *Earth Planet Sci. Lett.*, 375, 92-100.

62. Dziewonski, A. M. and J. H. Woodhouse (1983), An experiment in systematic study of global seismicity: Centroid-moment tensor solutions for 201 moderate and large earthquakes of 1981. *J. Geophys. Res*, 88(B4), 3247-3271.

63. Dziewonski, A. M., and D. L. Anderson (1981), Preliminary reference Earth model. *Phys. Earth Planet. Inter.*, 25(4), 297-356.

64. Earthquake Research Committee (1998), Seismic Activity in Japan. Headquarters for Earthquake Research Promotion, Prime Minister's Office, Government of Japan, pp. 222.

65. Ekström, G., and E. R. Engdahl (1989), Earthquake source parameters and stress distribution in the Adak Island region of the central Aleutian Islands, Alaska, *J. Geophys. Res*, 94(B11), 15499–15519.

66. El Hariri, M., S. L. Bilek, H. R. DeShon, E. R. Engdahl, and S. Bisrat (2013), Along-strike variability of rupture duration in subduction zone earthquakes, *J. Geophys. Res*, 118, 646–664.

67. Engdahl, E. R., R. van der Hilst, and R. Buland (1998). Global teleseismic earthquake relocation with improved travel times and procedures for depth determination. *Bull. Seismol. Soc. Amer.*, 88(3), 722-743.

68. Faccenna, C., E. D. Giuseep, F. Funiciello, S. Lallemand, and J. van Hunen (2009), Control of seafloor aging on the migration of the Izu-Bonin-Mariana trench. *Earth and Planet. Sci. Lett.*, 288,

386-398.

69. Fernandez, M., E. Molina, J. Havskov, and K. Atakan (2000), Tsunamis and tsunami hazards in Central America, *Natural Hazards*, 22(2), 91-116.

70. Fitch, T. J. (1972), Plate convergence, transcurrent faults, and internal deformation adjacent to Southeast Asia and the western Pacific, *J. Geophys. Res*, 77(23), 4432-4460.

71. Forsyth, D. W. (1975), Fault plane solutions and *Tectonics* of the South Atlantic and Scotia Sea, *J. Geophys. Res*, 80(11), 1429–1443.

72. Fossum, A. F., and L. B. Freund (1975), Nonuniformly moving shear crack model of a shallow focus earthquake mechanism. *J. Geophys. Res.*, 80(23), 3343-3347.

73. Franco, A., C. Lasserre, H. Lyon-Caen, V. Kostoglodov, et al. (2012), Fault kinematics in northern Central America and coupling along the subduction interface of the Cocos Plate, from GPS data in Chiapas (Mexico), Guatemala and El Salvador, *Geophys. J. Int.*, 189, 1223–1236.

74. Freund, L. B. (1972), Energy flux into the tip of an extending crack in an elastic solid. *J. Elasticity*, 2(4), 341-349.

75. Fu, Y., and J. T. Freymueller (2012), Seasonal and Long-term Vertical Deformation in the Nepal Himalaya Constrained by GPS and GRACE Measurements, *J. Geophys. Res*, 117, B03407.

76. Fujii, Y., K. Satake, S. Sakai, M. Shinohara, and T. Kanazawa (2011), Tsunami source of the 2011 off the Pacific coast of Tohoku, Japan earthquake, *Earth Planets Space*, 63(7) 815–820.

77. Furlong, K. P., T. Lay, and C. J. Ammon (2009), A great earthquake rupture across a rapidly evolving three-plate boundary, *Science*, 324, 226-229.

78. Gabsatarove, Y. V., G. M. Steblov, and D. I. Frovlov (2011), The new GPS evidence for the region of Bering Microplate, *Phys. Solid Earth*, 49, 114-118.

79. Gallovič, F., W. Imperatori, and P. M. Mai (2015), Effects of three-dimensional crustal structure and smoothing constraint on earthquake slip inversions: Case study of the Mw6.3 2009 L'Aquila earthquake, *J. Geophys. Res*, 120, 428–449.

80. Gamage, S.S.N., N. Umino, A. Hasegawa, S. H. Kirby (2009), Offshore double planed shallow seismic zone in the NE Japan forearc region revealed by sP depth phases recorded by regional networks. *Geophys. J. Int.* 178, 195-214.

81. Geist, E. L., and T. Parsons (2005), Triggering of tsunamigenic aftershocks from large strike-slip earthquakes: Analysis of the November 2000 New Ireland earthquake sequence, *Geochem., Geophys., Geosyst.*, 6, Q10005.

82. Geist, E. L., J. R.Childs, and D. W. Scholl (1988), The origin of summit basins of the Aleutian Ridge: Implications for block rotation of an arc massif. *Tectonics*, 7(2), 327-341.

83. Goes, S., Ruff, L. & Winslow N. The complex rupture process of the 1996 deep Flores, Indonesia earthquake (MW 7.9) from teleseismic P waves. *Geophys. Res. Lett.* 24, 1295-1298 (1997).

84. Green II, H. W., and H. Houston (1995), The mechanisms of deep earthquakes. *Annu. Rev. Earth Planet. Sci.*, 23, 169-213.

85. Green II, H. W (2007), Shearing instabilities accompanying high-pressure phase transformations and the mechanics of deep earthquakes. *Proc. Natl. Acad. Sci.*, 104, 9133-9138.

86. Green II, H. W., and P. Burnley (1989), A new self-organizing mechanism for deep-focus

earthquakes. *Nature,* 341, 733-737.

87. Guzmán-Speziale, M., and J. M. Gómez-González (2006), Seismic Strain rate along the Middle America Trench reveals significant differences between Cocos–North America and Cocos–Caribbean convergence, *Geophys. J. Int.*, 166(1), 179-185.

88. Harlow, D. H., and R. A. White (1985), Shallow earthquakes along the volcanic chain in Central America: evidence for oblique subduction. *Earthquake Notes*, 55(1), 28.

89. Hartzell, S. H., and T. H. Heaton (1983), Inversion of strong ground motion and teleseismic waveform data for the fault rupture history of the 1979 Imperial Valley, California, earthquake. *Bull. Seismol. Soc. Amer.*, 73(6A), 1553-1583.

90. Hasegawa, A., K. Yoshida, and T. Okada (2011), Nearly complete stress drop in the 2011 M w 9.0 off the Pacific coast of Tohoku Earthquake. *Earth Planets Space*, 63(7), 703-707.

91. Hashimoto, C., A. Noda, T. Sagiya and M. Matsu'ura (2009), Interplate seismogenic zones along the Kuril–Japan trench inferred from GPS data inversion. *Nat Geosci.*, 2, 141-144.

92. Hatori, T. (1974), Tsunami sources on the Pacific side in northeast Japan. *Zisin (J. Seism. Soc. Japan)* Ser. 2, 27, 321-337 (in Japanese).

93. Hayes, G. P. (2011), Rapid source characterization of the 03-11-2011 Mw 9.0 Off the Pacific Coast of Tohoku earthquake, *Earth Planets Space,* 63 529-534.

94. Hayes, G. P., D. J. Wald, and R. L. Johnson (2012), Slab1.0: A three-dimensional model of global subduction zone geometries, *J. Geophys. Res*, 117, B01302.

95. Heki, K., S. I. Miyazaki, and H. Tsuji (1997), Silent fault slip following an interplate thrust earthquake at the Japan Trench. *Nature,* 386, 595-598.

96. Herrmann, R. B. (2013) Computer programs in seismology: An evolving tool for instruction and research, *Seism. Res. Lett.*, 84, 1081-1088.

97. Hino, R., R. Azuma, Y. Ito, et al. (2009). Insight into complex rupturing of the immature bending normal fault in the outer slope of the Japan Trench from aftershocks of the 2005 Sanriku earthquake (Mw = 7.0) located by ocean bottom seismometry, *Geochem. Geophys. Geosys*. 10 Q07018.

98. Hough, S., and L. Seeber (1991), Seismological constraints on source properties of the mb = 4.0 Ardsley, New York earthquake: A characteristic rupture?, *J. Geophys. Res*, 96, 18,183-18,195.

99. Houston, H., and H. Kanamori (1986), Source spectra of great earthquakes: teleseismic constraints on rupture process and strong motion, *Bull. Seism. Soc. Amer.*, 76(1), 19-42.

100. Houston, H., H. M.Benz, and J. E. Vidale (1998), Time functions of deep earthquakes from broadband and short-period stacks. *J. Geophys. Res.*, 103(B12), 29895-29913.

101. Ide, S. (2002), Estimation of radiated energy of finite-source earthquake models. Bull. Seismol. Soc. Am.,, 92(8), 2994-3005.

102. Ide, S., A. Baltay, and G. C. Beroza (2011). Shallow dynamic overshoot and energetic deep rupture in the 2011 Mw 9.0 Tohoku-Oki earthquake, *Science,* 33, 1426-1429.

103. Ide, S., and G. C. Beroza (2001), Does apparent stress vary with earthquake size? *Geophys. Res. Lett.*, 28, 3349-3352.

104. Ide, S., G. C. Beroza, S. G. Prejean, and W. L. Ellsworth (2003), Apparent break in earthquake scaling due to path and site effects on deep borehole recordings. *J. Geophys. Res*, 108(B5).

105. Igarashi, T., T. Matsuzawa, and A. Hasegawa (2003). Repeating earthquakes and interplate aseismic slip in the northeastern Japan subduction zone. *J. Geophys. Res.,* 108, 2249.

106. Ihmlé, P. F (1998), On the interpretation of subevents in teleseismic waveforms: The 1994 Bolivia deep earthquake revisited. *J. Geophys. Res* 103, 17919-17932.

107. Ihmlé, P. F., J. M. Gomez, P. Heinrich, and S. Guibourg (1998), The 1996 Peru tsunamigenic earthquake: Broadband source process. *Geophys. Res. Lett.*, 2691-2694.

108. Iinuma, T., M. Ohzono, Y. Ohta, and S. Miura (2011), Coseismic slip distribution of the 2011 off the Pacific coast of Tohoku Earthquake (M 9.0) estimated based on GPS data – Was the asperity in Miyagi-oki ruptured? *Earth Planets Space,* 63 643-648.

109. Imamura, F., N. Shuto, S. Ide, Y. Yoshida, and K. Abe (1993), Estimate of the tsunami source of the 1992 Nicaraguan earthquake from tsunami data, *Geophys. Res. Lett.*, 20(14), 1515-1518.

110. Irikura, K. (1986), Prediction of strong acceleration motions using empirical Green's function, in *Proc. 7th Japan Earthquake Engineering Symposium*, Tokyo, Japan, 10-12 December 1986, 127-132.

111. Ishii, M. (2011), High-frequency rupture properties of the Mw 9.0 off the Pacific coast of Tohoku earthquake, *Earth Planets Space,* 63 609-614.

112. Ishii, M., P. M. Shearer, H. Houston and J. E. Vidale (2005). Extent, duration and speed of the 2004 Sumatra-Andaman earthquake imaged by the Hi-Net array. *Nature,* 435, 933-936.

113. Ito, T., K. Ozawa, T. Watanabe, T. Sagiya (2011), Slip distribution of the 2011 Tohoku earthquake inferred from geodetic data. *Earth Planets Space*, 63(7), 627-630.

114. Ito, Y., T. Tsuji, Y. Osada, and et al. (2011), Frontal wedge deformation near the source region of the 2011 Tohoku-Oki earthquake, *Geophys. Res. Lett.*, 38 L00G05.

115. Iwata, T., and K.Asano (2011), Characterization of the heterogeneous source model of intraslab earthquakes toward strong ground motion prediction, *Pure Appl. Geophys.*, 168 117-124.

116. Johnson, J. M., Y. Tanioka, L. J. Ruff, K. Satake, H. Kanamori, and L. R. Sykes (1994), The 1957 great Aleutian earthquake, *Pure Appl. Geophys.*, 142, 3-28.

117. Kanamori H., and D. L. Anderson (1975), Theoretical basis of some empirical relations in seismology, *Bull. Seism. Soc. Amer.*, 65, 1073-1095.

118. Kanamori, H. (1971), Seismological evidence for a lithospheric normal faulting – the Sanriku earthquake of 1933, *Phys. Earth Planet. Inter.*, 4, 289, 300.

119. Kanamori, H. (1972), Mechanism of tsunami earthquakes, *Phys. Earth Planet. Inter.*, 6, 246-259.

120. Kanamori, H. (1977). Seismic and aseismic slip along subduction zones and their tectonic implications. *Island Arcs*, Deep Sea Trenches and Back-Arc Basins, 163-174.

121. Kanamori, H. (2014), The diversity of large earthquakes and its implications for hazard mitigation, *Annual Rev. Earth Planet. Sci.*, 42, 7-26.

122. Kanamori, H., and E. E. Brodsky (2004), The physics of earthquakes. *Rep. Prog. Phys.*, 67(8).

123. Kanamori, H., and L. Rivera (2006), Energy partitioning during and earthquake, in *Earthquakes: Radiated Energy and the Physics of Faulting, Geophys. Monograph Series 170*, American Geophysical Union, 3-13, doi: 10.1029/170GM03.

124. Kanamori, H., and L. Rivera (2008), Source inversion of W phase: speeding up seismic tsunami warning, *Geophys. J. Int.*, 175, 222-238.

125. Kanamori, H., and M. Kikuchi (1993), The 1992 Nicaragua earthquake: A slow tsunami earthquake associated with subducted sediments, *Nature,* 361, 714-716.

126. Kanamori, H., and T. H. Heaton (2000), Microscopic and macroscopic physics of earthquakes, in GeoComplexity and the Physics of Earthquakes, Geophysical Monograph, 120, 147-163.

127. Kanamori, H., D. L. Anderson, and T. Heaton (1998), Frictional melting during the rupture of the 1994 Bolivian earthquake. *Science,* 279, 839-842.

128. Kanamori, H., E. Hauksson, L. K. Hutton, and L. M. Jones (1993), Determination of earthquake energy release and ML using TERRAscope, *Bull. Seism. Soc. Amer.*, 83, 330-346.

129. Kanamori, H., M. Miyazawa, and J. Mori (2006), Investigation of the earthquake sequence off Miyagi prefecture with historical seismograms. *Earth Planets Space,* 58, 1533.

130. Kanamori, H., W. H. K. Lee, and K.-F. Ma (2012), The 1909 Taipei earthquake – implications for seismic hazard in Taipei, *Geophys. J. Int.*, 191, 126-146.

131. Karato, S.-i., Riedel, M.R. & Yuen, D. A. Rheological structure and deformation of subducted slabs in the mantle transition zone: implications for mantle circulation and deep earthquakes. *Phys. Earth Planet. Inter.* 127, 83-108 (2001).

132. Kausel, E., and J. Campos (1992), The Mw = 8 tensional earthquake of 9 December 1950 of northern Chile and its relation to the seismic potential of the region, *Phys. Earth Planet. Int.*, 72, 220-235.

133. Kavoun, M., and O. Vinnikovskaya (1994). Seismic stratigraphy and *Tectonics* of the northwestern Weddell Sea (Antarctica) inferred from marine geophysical surveys. *Tectonophysics*, 240(1), 299-341.

134. Kawasaki, I., Y. Asai, and Y. Tamura (2001), Space-time distribution of interplate moment release including slow earthquakes and the seismo-geodetic coupling in the Sanriku-Oki region along the Japan trench. *Tectonophysics* 330, 267-283.

135. Kennett, B. L. N., A. Gorbatov, and E. Kiser (2011). Structural controls on the Mw 9.0 2011 Offshore-Tohoku earthquake, *Earth Planet. Sci. Lett.*, 310(3), 462-467.

136. Kikuchi, M. and H. Kanamori (1991), Inversion of complex body waves—III. *Bull. Seism. Soc. Amer.*, 81(6), 2335-2350.

137. Kikuchi, M. and H. Kanamori (1994), The mechanism of the deep Bolivia earthquake of June 9, 1994. *Geophys. Res. Lett.* 21, 2341-2344.

138. Kikuchi, M., and H. Kanamori (1995), Source characteristics of the 1992 Nicaragua tsunami earthquake inferred from teleseismic body waves, *Pure Appl. Geophys.*, 144(3-4), 441-453.

139. Kirby, S. H., E. A. Okal, and E. R. Engdahl (1995), The 9 June 94 Bolivian deep earthquake: An exceptional event in an extraordinary subduction zone. *Geophys. Res. Lett.* 22, 2233-2236.

140. Kirby, S. H., S. Stein, E. A. Okal, and D. C. Rubie (1996), Metastable mantle phase transformations and deep earthquake in subducting oceanic lithosphere. *Rev. Geophys.*, 34, 261-306.

141. Koketsu, K., Y. Yokota, N. Nishimura, and et al. (2011), A unified source model for the 2011 Tohoku earthquake, *Earth Planet. Sci. Lett.* 310 480-487.

142. Konca, A. O., J. P. Avouac, A. Sladen, A., A. J. Meltzner, et al. (2008), Partial rupture of a locked patch of the Sumatra megathrust during the 2007 earthquake sequence, *Nature,* 456(7222), 631-635.

143. Koper, K. D., A. R. Hutko, and T. Lay (2011a), Along-dip variation of teleseismic short-period radiation from the 11 March 2011 Tohoku Earthquake (Mw 9.0), *Geophys. Res. Lett.* 38 L21309.

144. Koper, K. D., A. R. Hutko, T. Lay, C. J. Ammon, and H. Kanamori (2011b), Frequency-dependent rupture process of the 2011 Mw 9.0 Tohoku Earthquake: Comparison of short-period P wave back-projection images and broadband seismic rupture models, *Earth Planets Space,* 63 599-602.

145. Kostrov, B. V. (1966), Unsteady propagation of longitudinal shear cracks, *J. Appl. Math. Mech. Engl. Transl.*, 30, 1241.

146. Kreemer, C., W. E. Holt, and A. J. Haines (2003), An integrated global model of present-day plate motions and plate boundary deformation, *Geophys. J. Int.*, 154, 8-34.

147. Kuge, K., and H. Kawakatsu (1992), Deep and intermediate-depth non-double couple earthquakes: interpretation of moment tensor inversions using various passbands of very broadband seismic data. *Geophys. J. Int.*, 111(3), 589-606.

148. Kurahashi, S., and K. Irikura (2011). Source model for generating strong ground motions during the 2011 off the Pacific coast of Tohoku Earthquake, *Earth Planets Space* 63 571-576.

149. LaFemina, P., T. H .Dixon, R. Govers, E. Norabuena, and et al. (2009), Fore-arc motion and Cocos Ridge collision in Central America, *Geochem. Geophys. Geosyst.*, 10(5).

150. Lay T., H. Kanamori, C. J. Ammon, K. D. Koper, A. R. Hutko, L. Ye, H. Yue, and T. Rushing (2012), Depth-varying rupture properties of subduction zone megathrust faults, *J. Geophys. Res*, 117, B04311.

151. Lay, T. (2015), The surge of great earthquakes from 2004 to 2014. *Earth Planet. Sci. Lett.*, 409, 133-146.

152. Lay, T., and S. Bilek (2007). Anomalous earthquake ruptures at shallow depths on subduction zone megathrusts. In: *The Seismogenic Zone of Subduction Thrust Faults*, edited by T. H. Dixon, and J. C. Moore, Columbia University Press, New York, pp. 476-511.

153. Lay, T., C. J. Ammon, A. R. Hutko, and H. Kanamori (2010b), Effects of kinematic constraints on teleseismic finite-source rupture inversions: Great Peruvian earthquakes of 23 June 2001 and 15 August 2007, *Bull. Seism. Soc. Amer.*, 100, 969-994.

154. Lay, T., C. J. Ammon, H. Kanamori, K. D. Koper, O. Sufri, and A. R. Hutko (2010a), Teleseismic inversion for rupture process of the 27 February 2010 Chile (Mw 8.8) earthquake, *Geophys. Res. Lett.*, 37, L13301.

155. Lay, T., C. J. Ammon, H. Kanamori, L. Rivera, K. D. Koper, and A. R. Hutko (2010), The 2009 Samoa–Tonga great earthquake triggered doublet, *Nature,* 466, 964-968.

156. Lay, T., C. J. Ammon, H. Kanamori, L. Xue, and M. J. Kim (2011), Possible large near-trench slip during the 2011 Mw 9.0 off the Pacific coast of Tohoku Earthquake, Earth, Planets, and Space, 63(7).

157. Lay, T., C. J. Ammon, H. Kanamori, M. J. Kim, L. Xue (2011a), Outer trench-slope faulting and the great 2011 Tohoku (MW 9.0) earthquake. *Earth Planets Space*, 63(7), 713-718.

158. Lay, T., C. J. Ammon, H. Kanamori, Y. Yamazaki, K. F. Cheung, and A. R. Hutko (2011b), The 25 October 2010 Mentawai tsunami earthquake (Mw 7.8) and the tsunami hazard presented by shallow megathrust ruptures. *Geophys. Res. Lett.*, 38(6).

159. Lay, T., H. Kanamori, C. J. Ammon, A. R. Hutko, K. Furlong, and L. Rivera (2009), The 2006-

2007 Kuril Islands great earthquake sequence, *J. Geophys. Res*, 114, B11308.

160. Lay, T., L. Astiz, H. Kanamori, and D. H. Christensen (1989), Temporal variation of large intraplate earthquakes in coupled subduction zones, *Phys. Earth Planet. Inter.*, 54, 258-312.

161. Lay, T., L. Ye, H. Kanamori, Y. Yamazaki, K. F. Cheung, and C. Ammon (2013a), The February 6, 2013 Mw 8.0 Santa Cruz Islands earthquake and tsunami. *Tectonophysics*, 608, 1109-1121.

162. Lay, T., L. Ye, H. Kanamori, Y. Yamazaki, K. F. Cheung, K. D. Koper, and K. Kwong (2013b), The October 28, 2012 Mw 7.8 Haida Gwaii underthrusting earthquake and tsunami: Slip partitioning along the Queen Charlotte Fault transpressional plate boundary, *Earth Planet. Sci. Lett.*, 375, 57-70.

163. Lee, S.-J., B.-S. Huang, M. Ando, H.-C. Chiu, and J.-H. Wang (2011), Evidence of large scale repeating slip during the 2011 Tohoku-oki earthquake, *Geophys. Res. Lett.*, 38, L19306, doi:10.1029/2011GL049580.

164. Liu, X., and K. C. McNally (1993), Quantitative estimates of interplate coupling inferred from outer rise earthquakes, *Pure Appl. Geophys.*, 140, 211-255.

165. Livermore, R. A., D. McAdoo, and K. Marks (1994), Scotia Sea *Tectonics* from high-resolution satellite gravity. *Earth Planet. Sci. Lett.*, 123 (1), pp. 255–268.

166. Livermore, R., J. C. Balanyá, A. Maldonado, and et al. (2000). Autopsy on a dead spreading center: the Phoenix Ridge, Drake Passage, Antarctica. *Geology*, 28(7), 607-610.

167. Lodolo, E., D. Civile, A. Vuan, A. Tassone, R. Geletti (2010). The Scotia–Antarctica plate boundary from 35 W to 45 W. *Earth Planet. Sci. Lett.*, 293(1), 200-215.

168. Loveless, J.P., Meade, B.J., 2010. Geodetic imaging of plate motions, slip rates, and partitioning of deformation in Japan. *J. Geophys. Res* 115, B02410.

169. Lundgren, P., and D. Giardini (1994), Isolated deep earthquakes and the fate of subduction in the mantle. *J. Geophys. Res* 99, 15,833-15,842.

170. Lundgren, P., and D. Giardini (1995), The June 9 Bolivia and March 9 Fiji deep earthquakes of 1994: I. Source processes. *Geophys. Res. Lett.* 22, 2241-2244.

171. Lyon-Caen, H., E. Barrier, C. Lasserre, A. Franco, and et al. (2006), Kinematics of the North America-Caribbean-Cocos plates in Central America from new GPS measurements across the Polochic-Motagua fault system, *Geophys. Res. Lett.*, 33.

172. Ma, S., and E. T. Hirakawa (2013). Dynamic wedge failure reveals anomalous energy radiation of shallow subduction earthquakes. *Earth Planet. Sci. Lett*, 375, 113-122.

173. Mackey, K. G., K. Fujita, L. V, Gunbina, V. N. Kovalev, V. S. Imaev, B. M. Koz'min, and L. P. Imaeva (1997) Seismicity of the Bering Strait Region: evidence for a Bering Block, Geolog. Soc. Amer. Bull., 25(11), 979-982, doi:10.1130/0091-7613(1997)025.

174. Madariaga, R. (1976), Dynamics of an expanding circular fault, *Bull. Seism. Soc. Amer.*, 66, 639-666.

175. Maeda, T., T. Furumura, S. Sakai, and M. Shinohara (2011), Significant tsunami observed at ocean-bottom pressure gauges during the 2011 off the Pacific coast of Tohoku earthquake, *Earth Planets Space* 63 803-808.

176. Maldonado A., N. Zitellini, G. Leitchenkov, and et al. (1998), Small ocean basin development along the Scotia–Antarctica plate boundary and in the northern Weddell Sea. *Tectonophysics*, 296(3), 371-402.

177. Mansinha, L. and D. E. Smylie (1971), The displacement fields of inclined faults. *Bull. Seism. Soc. Amer.*, 61(5), 1433-1440.

178. Martos, Y. M., J. Galindo-Zaldívar, M. Catalán, F. Bohoyo, A. Maldonado (2014), Asthenospheric Pacific-Atlantic flow barriers and the West Scotia Ridge extinction, *Geophys. Res. Lett.*, 41, 43–49.

179. Matsuzawa, T., T. Igarashi, and A. Hasegawa (2002), Characteristic small-earthquake sequence off Sanriku, northeastern Honshu, Japan. *Geophys. Res. Lett.* 29, 1543.

180. Matsuzawa, T., N. Uchida, T. Igarashi, T. Okada, and A. Hasegawa (2004), Repeating earthquakes and quasi-static slip on the plate boundary east off northern Honshu, Japan. *Earth Planets Space* 56, 803-812.

181. Mazzotti, S., X. Le Pichon, P. Henry, and S. I. Miyazaki (2000), Full interseismic locking of the Nankai and Japan-west Kurile subduction zones: An analysis of uniform elastic strain accumulation in Japan constrained by permanent GPS. *J. Geophys. Res.,* 105, 13159-13113,13177.

182. McCaffrey, R. (1992), Oblique plate convergence, slip vectors, and forearc deformation, *J. Geophys. Res*, 97(B6), 8905-8915.

183. McCloskey, J, D. Lange, F. Tilmann, S. S. Nalbant, A. F. Bell, D. H. Natawidjaja, and A. Rietbrok (2010), The September 2009 Padang earthquake, *Nature* Geoscience, 3, 70-71, doi:10.1038/ngeo753.

184. McGarr, A. (1999), On relating apparent stress to the stress causing earthquake fault slip. *J. Geophys. Res*, 104(B2), 3003-3011.

185. McNally, K. C., and J. B. Minster (1981), Nonuniform seismic slip rates along the Middle America Trench. *J. Geophys. Res*, 86(B6), 4949-4959.

186. Meade, C. and R. Jeanloz (1991), Deep-focus earthquakes and recycling of water into the Earth's mantle. *Science* 252, 68-72.

187. Meng, L., A. Inbal, and J.-P. Ampuero (2011). A window into the complexity of the dynamic rupture of the 2011 Mw 9 Tohoku-oki earthquake, *Geophys. Res. Lett.* 38 L00G07.

188. Minoura, K., F. Imamura, D. Sugawara, Y. Kono, and T. Iwashita (2001), The 869 Jogan tsunami deposit and recurrence interval of large-scale tsunami on the Pacific coast of northeast Japan. *J. Natural Disaster Sci.*, 23, 83.

189. Miyatake, T., Y. Yagi, and T. Yasuda (2004). The dynamic rupture process of the 2001 Geiyo, Japan, earthquake, *Geophys. Res. Lett.* 31 L12612.

190. Molnar, P., B. E. Tucker, and J. N. Brune (1973), Corner frequencies of P and S waves and models of earthquake sources, *Bull. Seism. Soc. Amer.*, 63(6-1), 2091-2104.

191. Moore, G. F., N. L. Bangs, A. Taira, S. Kuramoto, E. Pangborn, and H. J. Tobin (2007), Three-dimensional splay fault geometry and implications for tsunami generation, *Science*, 318, 1128-1131.

192. Morikawa, N., and T. Sasatani (2003). Source spectral characteristics of two large intra-slab earthquakes along the southern Kurile-Hokkaido arc, *Phys. Earth Planet. Inter.* 137, 67-80.

193. Morikawa, N., and T. Sasatani (2004). Source models of two large intraslab earthquakes from broadband strong ground motions, *Bull. Seism. Soc. Amer.* 94 803-817.

194. Mott, N. F. (1948), Fracture of metals: theoretical considerations. *Engineering*, 165(4275), 16-18.

195. Murotani, S., K. Satake, and Y. Fujii (2013), Scaling relations of seismic moment, rupture area, average slip, and asperity size for M~ 9 subduction-zone earthquakes. *Geophys. Res. Lett.*, 40(19), 5070-5074.

196. Nakajima, J., A. Hasegawa, and S. Kita (2011). Seismic evidence for reactivation of a buried hydrated fault in the Pacific slab by the 2011 M9.0 Tohoku earthquake, *Geophys. Res. Lett.* 38 L00G06.

197. Newman, A. V., and E. A. Okal (1998), Teleseismic estimates of radiated seismic energy: The E_R/M_0 discriminant for tsunami earthquakes, *J. Geophys. Res*, 103.

198. Newman, A. V., G. Hayes, Y. Wei, and J. Convers (2011), The 25 October 2010 Mentawai tsunami earthquake, from real-time discriminants, finite-fault rupture, and tsunami excitation, *Geophys. Res. Lett.*, 38, L05302.

199. Nishenko, S. P. (1991), Circum-Pacific seismic potential - 1989-1999, *Pure Appl. Geophys.*, 135, 2, 169-259.

200. Nishimura, T., S. Miura, and et al. (2000), Distribution of seismic coupling on the subducting plate boundary in northeastern Japan inferred from GPS observations. *Tectonophysics* 323, 217-238.

201. Noda, H., and N. Lapusta (2013), Stable creeping fault segments can become destructive as a result of dynamic weakening. *Nature,* 493(7433), 518-521.

202. Noda, H., N. Lapusta, and H. Kanamori (2013), Comparison of average stress drop measures for ruptures with heterogeneous stress change and implications for earthquake physics, *Geophys. J. Int.*, 193, 1691-1712.

203. Ogawa, M. (1987), Shear instability in a viscoelastic material as the cause of deep focus earthquakes. *J. Geophys. Res* 92,13801-13810.

204. Ohnaka, M. (2003), A constitutive scaling law and a unified comprehension for frictional slip failure, shear fracture of intact rock, and earthquake rupture. *J. Geophys. Res*, 108, 2080.

205. Ohta, Y. S. Miura, M. Ohzono, S. Kita, T. Iinuma, T. Demachi, et al. (2011). Large intraslab earthquake (2011 April 7, M 7.1) after the 2011 off the Pacific coast of Tohoku Earthquake (M 9.0): Coseismic fault model based on the dense GPS network data, *Earth Planets Space,* 63, 1207-1211.

206. Okada, T., T. Matsuzawa, and A. Hasegawa (2003), Comparison of source areas of M4. 8±0.1 repeating earthquakes off Kamaishi, NE Japan: are asperities persistent features? *Earth Planet. Sci. Lett.*, 213, 361-374.

207. Okada, Y. (1992), Internal deformation due to shear and tensile faults in a half-space, *Bull. Seism. Soc. Amer.*, 82, 1018-1040.

208. Okal, E. A (2001), "Detached" deep earthquakes: are they really? *Phys. Earth Planet. Inter.* 127, 109-143.

209. Okal, E. A. (2005), A re-evaluation of the great Aleutian and Chilean earthquakes of 1906 August 17. *Geophys. J. Int.*, 161(2), 268-282.

210. Okal, E. A. and S. H. Kirby (1998), Deep earthquakes beneath the Fiji Basin, SW Pacific: Earth's most intense deep seismicity in stagnant slabs. *Phys. Earth Planet. Inter.* 109, 25-63.

211. Okal, E. A., and C. J. Hartnady (2009). The South Sandwich Islands earthquake of 27 June 1929: Seismological study and inference on tsunami risk for the South Atlantic. South African, *J. Geology*, 112(3-4), 359-370.

212. Okino, K., M. Ando, S. Kaneshima, and K. Hirahara (1998), The horizontally lying slab. *Geophys. Res. Lett.* 16, 1059-1062.

213. Omori, S., T. Komabayashi, and S. Maruyama (2004), Dehydration and earthquakes in the subducting slab: empirical link in intermediate and deep seismic zones. *Phys. Earth Planet. Inter.* 146, 297-311.

214. Ozawa, S., T. Nishimura, H. Suito, T. Kobayahi, M. Tobita, and T. Imakiire (2011). Coseismic and postseismic slip of the 2011 magnitude-9 Tohoku-oki earthquake, *Nature* 475 373-376.

215. Pacheco, J. F., L. R. Sykes, and C. H. Scholz (1993), Nature of seismic coupling along simple plate boundaries of the subduction type, *J. Geophys. Res*, 98(B8), 14133-14159.

216. Papadopoulos, G. A., and A. Vassilopoulou (2001), Historical and archeological evidence of earthquakes and tsunamis felt in the Kythira strait, Greece, *Tsunami Research at the End of a Critical Decade*, 119-113, Springer.

217. Peacock, S. M. (2001). Are the lower planes of double seismic zones caused by serpentine dehydration in subducting oceanic mantle?. *Geology*, 29(4), 299-302.

218. Pelayo, A. M., D. A. Wiens (1989), Seismo*Tectonics* and relative plate motions in the Scotia Sea region, *J. Geophys. Res*, 94(B6), 7293–7320.

219. Pérez-Campos, X., S. K. Singh, and G. C. Beroza (2003), Reconciling teleseismic and regional estimates of seismic energy, Bull. Seismol. Soc. Am., 93(5), 2123-2130.

220. Pérez-Campos, X., and G. C. Beroza (2001), An apparent mechanism dependence of radiated seismic energy. *J. Geophys. Res*, 106(B6), 11127-11136.

221. Polet, J., and H. Kanamori (2000), Shallow subduction zone earthquakes and their tsunamigenic potential, *Geophys. J. Int.*, 142, 684-702.

222. Pollitz, F., R. Bürgmann, and P. Banerjee (2011). Geodetic slip model of the 2011 M9.0 Tohoku earthquake, *Geophys. Res. Lett.* 38, L00G08.

223. Prieto, G. A., D. J. Thomson, F. L. Vernon, P. M. Shearer, and R. L. Parker (2007), Confidence intervals for earthquake source parameters. *Geophys. J. Int.*, 168(3), 1227-1234.

224. Prieto, G. A., M. Florez, S. A. Barrett, G. C. Beroza, P. Pedraza, J. F. Blanco, and E. Poveda (2013), Seismic evidence for thermal runaway during intermediate-depth earthquake rupture, *Geophys. Res. Lett.*, 40, 6064-6068.

225. Purvance, M. D., and J. G. Anderson (2003). A comprehensive study of the observed spectral decay in strong-motion accelerations recorded in Guerrero, Mexico, *Bull. Seism. Soc. Amer.*, 93(2), 600-611

226. Raeesi, M., and K. Atakan (2009), On the deformation cycle of a strongly coupled plate interface: The triple earthquakes of 16 March 1963, 15 November 2006, and 13 January 2007 along the Kurile subduction zone, *J. Geophys. Res*, 114, B10301.

227. Rangin, C., X. Le Pichon, S. Mazzottti, M. Pubellier, N. Chamot-Rooke, M. Aurelio, A. Walpersdorf, and R. Quebral (1999), Plate convergence measured by GPS across the Sundaland/Philippine Sea Plate deformed boundary: the Philippines and eastern Indonesia, *Geophys. J. Int.*, 139, 296-316.

228. Redfield, T. F., D. W. Scholl, P. G. Fitzgerald, and M. E. Beck, Jr. (2007), Escape *Tectonics* and the extrusion of Alaska: Past, present and future, *Geology*, 35(11), 1039-1042.

229. Rice, J. R. (2006), Heating and weakening of faults during earthquake slip, *J. Geophys. Res*, 111, B05311.

230. Rivera, L., and H. Kanamori (2005), Representations of the radiated energy in earthquakes, *Geophys. J. Int.*, 162(1), 148-155.

231. Rodriguez, M., C. DeMets, R. Rogers, C. Tenorio, and D. Hernandez, (2009), A GPS and modelling study of deformation in northern Central America, *Geophys. J. Int.*, 178(3), 1733–1754.

232. Ruppert, N. A., N. P. Kozyreva, and R. A. Hansen (2012). Review of crustal seismicity in the Aleutian Arc and implications for arc deformation. *Tectonophysics*, 522, 150-157.

233. Satake, K. (1994), Mechanism of the 1992 Nicaragua tsunami earthquake, *Geophys. Res. Lett.*, 21(23), 2519-2522.

234. Satake, K., Y. Sawai, M. Shishikura, Y. Okamura, Y. Namegaya, and S. Yamaki (2007), Tsunami source of the unusual AD 869 earthquake off Miyagi, Japan, inferred from tsunami deposits and numerical simulations of inundation. *Amer. Geophys. Un., Fall Meeting 2007*, abstract #T31G-03.

235. Savage, J. C. (1972), Relation of corner frequency to fault dimensions, *J. Geophys. Res*, 77(20), 3788-3795.

236. Shao, G., X. Li, C. Ji, and T. Maeda (2011). Focal mechanism and slip history of the 2011 Mw 9.1 off the Pacific coast of Tohoku Earthquake, constrained with teleseismic body and surface waves, *Earth Planets Space.* 63 559-564.

237. Shearer, P. M., G. A. Prieto, and E. Hauksson (2006), Comprehensive analysis of earthquake source spectra in southern California, *J. Geophys. Res*, 111, doi: 10.1029/2005JB003979.

238. Shimamura, K., T. Matsuzawa, T. Okada, N. Uchida, T. Kono, and A. Hasegawa (2011), Similarities and Differences in the Rupture Process of the M 4.8 Repeating-Earthquake Sequence off Kamaishi, Northeast Japan: Comparison between the 2001 and 2008 Events. *Bull. Seismol. Soc. Amer.*, 101, 2355-2368.

239. Si, H., and S. Midorikawa (1999), New attenuation relations for peak ground acceleration and velocity considering effects of fault type and site condition, *J. Struct. Constr. Eng. AIJ*, 523, 63-70.

240. Silver, P. G., S. L. Beck, T. C. Wallace, C. Meade, S. C. Myers, D. E. James, and R. Kuehnel (1995), Rupture characteristics of the deep Bolivian earthquake of 9 June 1994 and the mechanism of deep-focus earthquakes. *Science,* 268, 69-73.

241. Simons, M., S. E. Minson, A. Sladen, et al. (2011), The 2011 Magnitude 9.0 Tohoku-Oki Earthquake: Mosaicking the Megathrust from Seconds to Centuries. *Science,* 332, 1421.

242. Sleep, N. H. (2012), Constraint on the recurrence of great outer-rise earthquakes from seafloor bathymetry, *Earth Planets Space*, 64, 1245-1246.

243. Smalley, R.Jr., I. W. D. Dalziel, M. G. Bevis, E. Kendrick, et al. (2007), Scotia arc kinematics from GPS geodesy, *Geophys. Res. Lett.*, 34, L21308.

244. Song, T. A., and M. Simons (2003), Large Trench-Parallel Gravity Variations Predict Seismogenic Behavior in Subduction Zones, Science, 301, 5633, 630-633.

245. Stern, R. J., M. H. Fouch, and S. L. Klemperer (2003), An overview of the Izu-Bonin-Mariana Subduction factory, in *Inside the Subduction Factory*, Geophysical Monograph 138, AGU, 175-222 (2003).

246. Storchak, D. A., D. Di Giacomo, I. Bondár, E. R. Engdahl, et al. (2013), P. Public Release of the

ISC-GEM Global Instrumental Earthquake Catalogue (1900-2009). *Seism. Res. Lett.*, 84(5), 810-815.

247. Suwa, Y., S. Miura, A. Hasegawa, T. Sato, K. Tachibana (2006), Interplate coupling beneath NE Japan inferred from three-dimensional displacement field. *J. geophys. Res.,* 111, 1997–2002.

248. Suzuki, W., S. Aoi, and H. Sekiguchi (2009), Rupture process of the 2008 Northern Iwate intraslab earthquake derived from strong-motion records, *Bull. Seism. Soc. Amer.* 99 2825-2835.

249. Sykes, L. R. (1971), Aftershock zones of great earthquakes, seismicity gaps, and earthquake prediction for Alaska and the Aleutians. *J. Geophys. Res*, 76(32), 8021-8041.

250. Syracuse, E. M., P. E. van Keken, and G. A. Abers (2010), The global range of subduction zone thermal models. *Phys. Earth Planet. Inter.*, 183(1), 73-90.

251. Tanioka, Y. and K. Sataka (1996), Fault parameters of the 1896 Sanriku tsunami earthquake estimated from tsunami numerical modeling. *Geophys. Res. Lett.* 23, 1549-1552.

252. Taylor, M. A. J., G. Zheng, J. R. Rice, W. D. Stuart, and R. Dmowska (1996), Cyclic stressing and seismicity and strongly coupled subduction zones, *J. Geophys. Res*, 101, B4, 8363-8381.

253. Thomas, C., Livermore, and R., Pollitz, F. (2003), Motion of the Scotia Sea plates. *Geophys. J. Int.*, 155: 789–804.

254. Tibi, R., G. Bock, and D. A. Wiens (2003), Source characteristics of large deep earthquakes: Constraint on the faulting mechanism at great depths. *J. Geohys. Res*., 108, B2 2091.

255. Tibi, R., D. A. Wiens, and H. Inoue (2003), Remote triggering of deep earthquakes in the 2002 Tonga sequences. *Nature,* 424, 921-925 (2003).

256. Toda, S., R. S. Stein, G. C. Beroza, and D. Marsan (2012), Aftershocks halted by static stress shadows, *Nature Geoscience*, 5, 410-413.

257. Todd, E. K., and T. Lay (2013), The 2011 Northern Kermadec earthquake doublet and subduction zone faulting interactions. *J. Geophys. Res.*, 118(1), 249-261.

258. Tsuda, K., J. Steidl, R. Archuleta, and D. Assimaki (2006). Site-response estimation for the 2003 Miyagi-Oki earthquake sequence considering nonlinear site response, *Bull. Seism. Soc. Amer.* 96 1474-1482.

259. Turner, H. L., III, P. LaFemina, A. Saballos, G. S. Mattioli, P. E. Jansma, and T. Dixon (2007), Kinematics of the Nicaraguan forearc from GPS geodesy, *Geophys. Res. Lett.*, 34, L02302.

260. Uchida, N., A. Hasegawa, T. Matsuzawa, and T. Igarashi (2004), Pre-and post-seismic slow slip on the plate boundary off Sanriku, NE Japan associated with three interplate earthquakes as estimated from small repeating earthquake data. *Tectonophysics*, 385, 1-15.

261. Uchida, N., and T. Matsuzawa (2011), Coupling coefficient, hierarchical structure, and earthquake cycle for the source area of the 2011 Tohoku earthquake inferred from small repeating earthquake data *Earth Planets Space*, 63(7), 675-679.

262. Uchida, N., T. Matsuzawa, A. Hasegawa, and T. Igarashi (2003), Interplate quasi-static slip off Sanriku, NE Japan, estimated from repeating earthquakes. *Geophys. Res. Lett.* 30, 1801.

263. Uchida, N., J. Nakajima, A. Hasegawa, and T. Matsuzawa (2009), What controls interplate coupling?: Evidence for abrupt change in coupling across a border between two overlying plates in the NE Japan subduction zone. *Earth Planet. Sci. Lett.*, 283, 111-121.

264. Vallée, M., and C. Satriano (2014), Ten-year recurrence time between two major earthquakes affecting the same fault segment. *Geophys. Res. Lett.*, 41, 2312–2318.

265. van der Hilst, R. T., and T. Seno (1993), Effects of relative plate motion on the deep structure and penetration depth of slabs below the Izu-Bonin and Mariana island arcs. *Earth and Planet. Sci. Lett.*, 120, 395-407.

266. Velasco, A. A., C. J. Ammon, T. Lay, and J. Zhang (1994). Imaging a slow bilateral rupture with broadband seismic waves: The September 2, 1992 Nicaraguan tsunami earthquake, *Geophys. Res. Lett.*, 21, 2629-2632.

267. Venkataraman, A. and H. Kanamori (2004), Observational constraints on the fracture energy of subduction zone earthquakes, *J. Geophys. Res*, 109, B5, B05302.

268. Venkataraman, A., and H. Kanamori (2004), Effect of directivity on estimates of radiated seismic energy. *J. Geophys. Res*,109(B4).

269. Vuan, A., M. Russi, and G. F. Panza (2000), Group velocity tomography in the subantarctic Scotia Sea region. *Pure and Applied Geophysics*, 157(9), 1337-1357.

270. Walter, W. R., K. Mayeda, R. Gok and A. Hofstetter (2006), The scaling of seismic energy with moment: Simple models compared with observations, in *Earthquakes: Radiated Energy and the Physics of Faulting (eds. R. Abercrombie, A. McGarr, G. Di Toro and H. Kanamori)*, AGU, Washington, D. C. doi: 10.1029/170GM05.

271. Wang, D., and J. Mori (2011). Rupture process of the 2011 off the Pacific coast of Tohoku earthquake (Mw 9.0) as imaged with back-projection of teleseismic P waves, *Earth Planets Space,* 63 603-607.

272. Warren, L. M. (2014). Dominant fault plane orientations of intermediate-depth earthquakes beneath South America. *J. Geophys. Res*, 119(7), 5762-5785.

273. Warren, L. M., and P. G. Silver (2006), Measurement of differential rupture durations as constraints on the source finiteness of deep-focus earthquakes, *J. Geophys. Res.,* 111, B06304.

274. Watanabe, H. (2001), Realities of the 869 Jogan earthqauke and tsunami and the inferred tsunami source. *Historical Earthquakes (Rekishi-jishin),* 14, 83-99.

275. Wei, S., D. Helmberger, Z. Zhan, and R. Graves (2013), Rupture complexity of the M_W 8.3 sea of Okhotsk earthquake: Rapid triggering of complementary earthquakes? *Geophys. Res. Lett.,* 40, 5034-5039.

276. Welc, J. L., and T. Lay (1987), The source rupture process of the Great Banda Sea earthquake of November 4, 1963, *Phys. Earth Planet. Inter.*, 45, 242-254.

277. Wessel, P. and W. H. F. Smith (1998). New, improved version of the Generic Mapping Tools released, *Eos Trans. AGU*, 79, 579.

278. White, R. A., and D. H. Harlow (1993), Destructive upper-crustal earthquakes of Central America since 1900, *Bull. Seism. Soc. Amer.*, 83(4), 1115-1142.

279. Wiens, D. A. and J. J. McGuire (1995), The 1994 Bolivia and Tonga events: Fundamentally different types of deep earthquakes? *Geophys. Res. Lett.* 22, 2245-2248.

280. Wiens, D. A., J. J. McGuire, and P. J. Shore (1993), Evidence for transformational faulting from a deep double seismic zone in Tonga. *Nature,* 364, 790793.

281. Winslow, N. W., and L. J. Ruff (1999), A hybrid method for calculating the radiated wave energy

of deep earthquakes. *Phys. Earth Planet. Inter.*, 115(3), 181-190.

282. Wu, F. T., and H. Kanamori (1973), Source mechanism of February 4, 1965, Rat Island earthquake, *J. Geophys. Res.*, 78, 6082-6092.

283. Wu, L.-R., and W.-P. Chen (2001), Rupture of the large (MW 7.8), deep earthquake of 1973 beneath the Japan sea with implications for seismogenesis. *Bull. Seism. Soc. Amer.,* 91, 102-111.

284. Xu, Y., K. D. Koper, O. Sufri, L. Zhu, and A. R. Hutko (2009), Rupture imaging of the Mw 7.9 12 May 2008 Wenchuan earthquake from back projection of teleseismic P waves, *Geochem. Geophys. Geosyst.*, 10, Q04006.

285. Yagi, Y., and Y. Fukahata (2011). Rupture process of the 2011 Tohoku-oki earthquake and absolute elastic strain release, *Geophys. Res. Lett.*, 38, L19307.

286. Yamanaka, Y., and M. Kikuchi (2004), Asperity map along the subduction zone in northeastern Japan inferred from regional seismic data. *J. Geophys. Res.,* 109, B07307.

287. Yamazaki, Y., T. Lay, K. F. Cheung, H. Yue, and H. Kanamori (2011), Modeling near-field tsunami observations to improve finite-fault slip models for the 11 March 2011 Tohoku earthquake, *Geophys. Res. Lett.* 38 L00G15.

288. Yao, H., P. Gerstoft, P. M. Shearer, and C. Mecklenbrauker (2011). Compressive sensing of the Tohuku-oki Mw 9.0 earthquake: Frequency-dependent rupture modes, *Geophys. Res. Lett.,* 38 doi:10.1029/2011GL049223.

289. Ye, L., T. Lay and H. Kanamori (2012), Intraplate and interplate faulting interactions during the August 31, 2012, Philippine Trench earthquake (Mw 7.6) sequence, *Geophys. Res. Lett.*, 39, L24310.

290. Ye, L., T. Lay, and H. Kanamori (2013a), Ground shaking and seismic source spectra for large earthquakes around the megathrust fault offshore of northeastern Honshu, Japan, *Bull. Seismol. Soc. Amer.*, 103(2B).

291. Ye, L., T. Lay, and H. Kanamori (2013b), Large earthquake rupture process variations on the Middle America megathrust, *Earth Planet. Sci. Lett.*, 381,147-155.

292. Ye, L., T. Lay, and H. Kanamori (2014), The 23 June 2014 Mw 7.9 Rat Islands archipelago, Alaska, intermediate depth earthquake, *Geophys. Res. Lett.*, 41, 6389-6395, doi:10.1002/2014GL061153.

293. Ye, L., T. Lay, H. Kanamori, and K. D. Koper (2013c), Energy release of the 2013 Mw 8.3 Sea of Okhotsk earthquake and deep slab stress heterogeneity, *Science*, 341, 1380-1384.

294. Yokota, Y., K. Koketsu, Y. Fujii, K. Satake, S. Sakai, M. Shinohara, and T. Kanazawa (2011), Joint inversion of strong motion, teleseismic, geodetic, and tsunami datasets for the rupture process of the 2011 Tohoku earthquake, *Geophys. Res. Lett.*, 38, L00G21.

295. Yoshida, Y., H. Ueno, D. Muto, and S. Aoki (2011). Source process of the 2011 off the Pacific coast of Tohoku earthquake with the combination of teleseismic and strong motion data, *Earth Planets Space,* 63(7), 565-569.

296. Youngs, R., S. J. Chiou, W. J. Silva, and J. R. Humphrey (1997), Strong ground motion attenuation relationships for subduction zone earthquakes, *Seism. Res. Lett.*, 68(1) 58-73.

297. Yue, H., and T. Lay (2011), Inversion of high-rate (1-sps) GPS data for rupture process of the 11 March 2011 Tohoku earthquake (Mw 9.1), *Geophys. Res. Lett.* 38 L00G09.

298. Yumul Jr., G. P., C. B. Dimalanta, V. B. Maglambayan, and E. J. Marquez (2008), Tectonic

setting of a composite terrane: A review of the Philippine island arc system, *Geosciences J.*, 12, 7-17.

299. Zhan, Z., D. V. Helmberger, H. Kanamori, and P. M. Shearer (2014), Supershear rupture in a M_W 6.7 aftershock of the 2013 Sea of Ohotsk earthquake. *Science,* 345, 204-206.

300. Zhan, Z., H. Kanamori, V. C. Tsai, D. V. Helmberger, and S. Wei (2014), Rupture complexity of the 1994 Bolivia and 2013 Sea of Okhotsk deep earthquakes. *Earth and Planet. Sci. Lett.*, 285, 89-96.

301. Zhang, J., and T. Lay (1989) Duration and depth of faulting of the 22 June 1977 Tonga earthquake, *Bull. Seism. Soc. Amer.,* 79, 41-66.

302. Zhao, D., Z. Huang, N. Umino, A. Hasegawa, and H. Kanamori (2011), Structural heterogeneity in the megathrust zone and mechanism of the 2011 Tohoku-Oki earthquake (Mw 9.0), *Geophys. Res. Lett.*, 38(17).

303. Zumberge, J. F., M. B. Heflin, D. C. Jefferson, M. M. Watkins, and F. H. Webb (1997), Precise point positioning for the efficient and robust analysis of GPS data from large networks, *J. Geophys. Res.*, 102(B3), 5005–5017.